New Views of Carbonates as a Proxy for Ancient Seawater and Paleoenvironments: ^{13}C-^{18}O Clumped Isotopes and Stable Mg Isotopes

By

Nicholas Paul Levitt

A dissertation submitted in partial fulfillment of

the requirements for the degree of

Doctor of Philosophy

(Geoscience)

at the

UNIVERSITY OF WISCONSIN-MADISON

2018

Date of final oral examination: 9/14/2018

The dissertation is approved by the following members of the Final Oral Committee:

Clark M. Johnson, Vilas Distinguished Professor, Geoscience
Pupa Gilbert, Professor, Physics
Eric E. Roden, Albert and Alice Weeks Professor, Geoscience
John W. Valley, Charles R. Van Hise Professor, Geoscience
Huifang Xu, Professor, Geoscience

For my mother and father.
Whose own academic achievements have inspired and filled me with pride.

Acknowledgements

I would like to express my deep appreciation and gratitude to my advisor, Dr. Clark M. Johnson, for the opportunity of a lifetime to study astrobiology and geochemistry at UW-Madison. The steadfast guidance and mentorship he offered has opened my mind to realms of understanding I never expected. Dr. Johnson's intellectual merit and academic prowess is a testament to human ability. I am truly fortunate to have had the opportunity to learn from him.

I also thank my committee members, Drs. Pupa Gilbert, Eric Roden, John Valley, and Huifang Xu for the friendly guidance, thoughtful suggestions, and the general support that each of them offered to me over the years. The science and work ethic they exposed me to will stick with me forever. These paragons of scholarship are excellent examples of why UW-Madison is such a special and outstanding institution.

I extend a special thank you to the ICP-TIMS Isotope Laboratory group. Particular recognition goes to Dr. Brian Beard for shouldering the significant responsibility of managing facilities, equipment, and personnel. He went to great lengths to endow part of his vast knowledge onto me. My educational experience also benefitted greatly from working with Drs. Weiqiang Li, Aaron Satkoski, and Xinyuan Zheng.

My research would not have been possible without funding from NASA Headquarters under the NASA Earth and Space Science Fellowship Program as well as the NASA Astrobiology Institute. My education was also supported through the Dean L. Morgridge Distinguished Graduate Fellowship, the UW-Madison Department of Geoscience Bailey Scholarship, Geological Society of America (GSA) Student Research Grant, and GSA's Mineralogy, Geochemistry, Petrology, and Volcanology Division Student Research Award.

I'd like to recognize Drs. Frank Ettensohn, Alan Fryar, Dave Moecher, and Kent Ratajeski for the contributions that each of them made to my intellectual growth during my years of study at the University of Kentucky and for helping me avoid revocation of my NASA research fellowship. I also thank Dr. Christopher S. Romanek for guiding me into the world of stable isotope geochemistry and isotope ratio mass spectrometry. My gratitude is extended to Dr. John Eiler for sharing his world-class expertise and agreeing to collaborate with me. I also appreciate the Eiler Research Group at Caltech, Nami Kitchen in particular, for technical assistance and general collegiality. I also thank Drs. Greg Henkes, Michael Hren, Max Lloyd, Ben Passey, and Daniel Stolper for working with me to better understand clumped isotopes.

Many others played a significantly positive role during my time as a graduate student. These individuals include technical scientists such as Dr. Suvankar Chakraborty, Dr. John Fournelle, Peter Idstein, and Peter Sobol. I express special appreciation to Drs. Michael Cardiff, Clay Kelly, and Shanan Peters for guidance and mentoring during my teaching assistantships. Cheers to Rubio, Grant, Anastacia, and Mike for company and laughs during long nights and weekends in the clean lab. Additionally, I have shared the past several years with an amazing group of graduate students including M'Bark Baddouh, Ben Barnes, Emilia Cameron, Jake Cammack, Adam Denny, Andria Ellis, Nathan Fortney, Erik Haroldson, Breana Hashman, Shiyun Jin, Mike Johnson, SeungYeol Lee, Ben Linzmeier, Stephanie Napieralski, Liz Percak-Dennett, Ryan Quinn, Thiru Reddy, Gabriel Richarde, Allen Schaen, Debbie Schechtman-Rook, Noah Stern, Rachelle Turnier, Forrest Webb, Olivia Woodruff, and Jody Wycech.

Finally, I offer my sincerest gratitude to my family for their vigilant support. To my parents, Christine, Geri, Raquel, and Steve: thank you for always being there for me. To Tricia, Sara, and Ky: thank you for your patience and understanding. To Richard and Susan: thank you for being the best roommates and amazing grandparents. To Lindsey: you have made innumerable sacrifices including covering far more than your fair share of the parenting and household burdens. You have been everything I've needed and so much more.

Statement of Authorship

Per the University of Wisconsin – Madison Graduate School Office of Academic Services' Academic Policies and Procedures: "A doctoral dissertation must be a dissertator's own work. If it is the result of research enterprises in which others have collaborated, a substantial portion must represent the dissertator's own contribution and the other research participants must be identified. Effective September 1, 2017, dissertations must acknowledge contributions received from other individuals, including co-authors of published work that appears in the document, such as in designing the research, executing the research, analyzing the data, interpreting the data/research, or writing, proofing, or copyediting the manuscript."

This dissertation is, in part, a result of the NASA Astrobiology Institute Cooperative Agreement (Notice, "CAN") 6 endeavor. As a result, several members of the Cooperative Agreement appear as coauthors of publications associated with this work. The following authorship statements describe the contributions from collaborators.

Chapter 1: CS Romanek was involved in the early design of this work and also helped with proofing and copyediting. CM Johnson also helped with proofing and copyediting. CS Romanek's major contribution to this chapter was to insist that all of the experimental data, discussion, and interpretation regarding carbon isotopes be removed.

Chapter 2: This work was designed in part by CS Romanek and CM Johnson who also helped with proofing and copyediting. JM Eiler, BL Beard, and H Xu also helped with proofing and copyediting. JM Eiler, BL Beard, and N Kitchen assisted with technical aspects of data collection and interpretation. H Xu provided laboratory space, equipment, and materials.

Chapter 3: This work was designed in part by CS Romanek, CM Johnson, and W Li who also helped with proofing and copyediting. BL Beard, W Li, John Fournelle, and Aurelien Moy assisted with technical aspects of data collection and interpretation. Calcite used in this study was a subset of experimentally precipitated carbonate provided by CS Romanek ("FU" samples) and S Chakraborty ("Chem/UK" samples). Additionally, CS Romanek and S Chakraborty performed X-Ray diffraction and ICP-AES work.

Appendix A: This work was designed in part by CM Johnson. N Ferralis, JM Eiler, N Kitchen, and S Dutta assisted with technical aspects of data collection and interpretation. A Satkoski, CM Johnson, and N Beukes collected some of the samples used for analysis.

Table of Contents

Dedication i

Acknowledgements ii

Table of Contents iv

Abstract v

Introduction 1

Chapter 1
An "On-Line" Method for Oxygen Isotope Exchange Between Gas-Phase CO_2 and Water 4

Chapter 2
Near Equilibrium ^{13}C-^{18}O Bonding During Inorganic Calcite Precipitation
under Chemo-Stat Conditions 47

Chapter 3
Factors Influencing the Mg Isotope Composition of Magnesian Calcite 157

Bibliography 239

Appendix A
Application of Clumped Isotope Thermometry to Archean Carbonates:
Formation Temperatures, Thermal Histories, and Potential for Biomarker Preservation 266

Appendix B
Laboratory Reports from Outside Sources and Collaborators 297

Appendix C
UW-Madison Thesis Collection Sample Identification Table 390

Abstract

Carbonates chemically precipitated from ocean water are generally considered to be excellent records of seawater chemistry, although these records may be altered through post-depositional processes. Oxygen can potentially constrain critical parameters such as temperature and ocean water O isotope composition. Carbon is a metabolically important element that informs about interaction between the biosphere and ocean sediments. Magnesium has been implicated in processes such as dolomite accumulation variability and sea level fluctuations and contemporary research focuses on determining temporal variation in Mg isotopes in seawater through time.

However, accurate use of geochemical proxies requires interpretations including known physical constants such as equilibrium versus kinetic fractionation factors. Natural carbonates are routinely found with isotope compositions that cannot be fully explained by laboratory results. This study addresses equilibrium processes by limiting kinetic influence through the use of chemo-stat precipitation experiments onto ^{43}Ca-labeled calcite seed crystals.

Results are reported for $^{13}C/^{12}C$, $^{18}O/^{16}O$, $^{26}Mg/^{24}Mg$, and ^{13}C-^{18}O "clumped" isotope analyses of synthetic calcite. Formation rate was controlled to investigate the effect of precipitation rate and temperature on isotope fractionation and ^{13}C-^{18}O bonding, where rates ranged from $10^{-8.4}$ to $10^{-4.9}$ mol m^{-2} s^{-1} at temperatures from 4 to 45°C.

No relation was observed between precipitation rate and ^{13}C-^{18}O bonding proportion. Carbon fractionation factors between calcite and aqueous HCO_3^- as well as the temperature-dependent calcite-water $^{18}O/^{16}O$ fractionation relations are slightly larger than measured in several previous investigations. Significantly, we observe a dependence of the $^{18}O/^{16}O$ isotope fractionation factor on growth rate. Taken together, these findings suggest carbonate growth in our experiments approached equilibrium more closely than previous experiments of this type, yet did not achieve full O isotope equilibrium.

A constant fractionation factor of -2.54±0.12‰ in $^{26}Mg/^{24}Mg$ was measured over all precipitation rates at intermediate temperatures (23-25°C) and a significant temperature dependence has been redefined. We find no relation between Mg concentration in calcite, ionic strength, pCO_2, or solution speciation effects and Mg isotope fractionation. These findings suggest that most biomineralization does not record equilibrium Mg isotope compositions and temperature is the only non-mineralogical or mechanistic factor influencing Mg isotope fractionation during ion-by-ion growth of calcite from solution.

Introduction

The dissertation projects described here fall under the broad theme of using carbonates as a record of seawater chemistry and paleoenvironmental conditions. Today, the ocean covers some 71% of the surface of the Earth, hosts approximately $2x10^4$ Tg of biomass, and is the catchment for $2.8x10^4$ Tg of continentally derived sediment per year (Brown, et al. 2004). Looking to the past, the ocean has been a major component of the Earth system from nearly the very beginning, with evidence of water-lain sediments as old as 3.8 Ga (Nutman et al., 2016). The marine carbonate record is well documented in rocks of 3.5 Ga and younger. Chemically precipitated sediments such as carbonates form directly (or semi-indirectly in the case of most biomineralization) from ocean water, and are generally considered to be one of the best records of seawater chemistry, although these records may be altered through post-depositional processes). Major constituent elements in carbonates (e.g., O), can potentially constrain critical parameters such as temperature and oxygen isotope composition of the ocean. Carbon and Fe are metabolically important elements that inform about the interaction between the biosphere and ocean sediments (Johnson et al., 2013). Magnesium in seawater (and by extension carbonates) has been implicated in mechanisms used to explain processes controlling dolomite accumulation variability, sea level fluctuations, and even RNA biochemistry (Li et al., 2015; Saunders and DeRose, 2016), and a rapidly growing field is stable Mg isotope geochemistry, where the goal is to determine the temporal variation in Mg isotopes in seawater through time. The study of major elements in carbonates, and their isotopic compositions, is complimentary to long-standing approaches using trace elements such as Sr and rare earth elements (REE) that shed light on sources and magnitudes of sediment fluxes to or from the ocean.

The aqueously derived nature of carbonates makes them susceptible to late diagenesis and post lithification alternation that acts to obscure and confound primary signals (Swart, 2015).

A stark illustration of this can be seen by compiling the record of oxygen isotope compositions found for marine carbonates throughout geologic time. Several researchers such as Knauth (2005), Kasting et al. (2006), Jaffres et al. (2007), and Shields (2007) have considered these datasets and attempted to interpret their meaning. The two most notable characteristics of the oxygen isotope record are the 1) wide spread in individual values at a given age, and 2) the seemingly secular trend of decreasing $\delta^{18}O$ with increasing age. A wide range in oxygen isotope compositions of carbonates is commonly interpreted to be related to diagenetic alteration by low $^{18}O/^{16}O$ ratios in meteoric water. However, the extent to which this process has influenced carbonates from any given period in geologic history and whether older strata have experienced a cumulatively larger amount of alteration is up to interpretation. For instance, some researchers ascribe the long term decrease in $^{18}O/^{16}O$ ratios with increasing age observed in carbonates to be a direct result of a changing isotope fractionation factor between calcium carbonate and ocean water due to a progressively hotter ocean (Tartese et al., 2017). However, an alternative explanation could be that the oxygen isotope composition of the ocean changed through time and the fractionation factor (i.e. temperature) was relatively constant.

Turning to other chemical precipitates and proxies, again, a wide range of temperature indications are observed. Alternative records have focused on the oxygen and silicon isotope composition of cherts, but the oxygen isotope composition of serpentine (Pope et al., 2012) and phosphate (Blake et al., 2010) has also been investigated. The interpretation of chert though time generally provides a lower temperature indication compared to carbonate but is consistent with decreasing $^{18}O/^{16}O$ ratios toward the Hadean. Similarly, the observed $^{30}Si/^{28}Si$ ratio of cherts also decreases moving backwards through time. Alternatively, the oxygen isotope composition of Archean phosphate has been interpreted to indicate a much lower ocean temperature of 26-35 °C. Taken together, these proxies illustrate the incomplete nature of our understanding of not

just the Precambrian ocean, but also the extent to which diagenetic alteration can mask records of primary conditions recorded by chemical sediments in the deep rock record.

The dissertation projects described here are intended to advance several components of the use of the isotopic compositions of carbonates as a record of paleoenvironmental conditions and the composition of seawater through time. Three major projects are outlined. The first chapter presents a methods study to fully and efficiently exchange oxygen isotopes between gas phase CO_2 and water and was completed to help perform the experiments described in Chapter 2. The project described in Chapter 2 was completed to assess the reliability of clumped thermometry from a mineral formation rate perspective. Similarly, Chapter 3 was designed to help clarify and quantify the primary variables leading to $^{26}Mg/^{24}Mg$ isotope fractionation between dissolved Mg and calcite. The scientific advancements included in Chapters 2 and 3 will be used to investigate the rock record and place constraints on the temperature of mineral formation water as well as characterization and better understanding of the global Mg isotope composition of the ocean during Earth's history.

All specimens not fully consumed during analysis and referenced in this thesis are in the collections of the Department of Geoscience, University of Wisconsin-Madison, under file number UW2038.

Chapter 1: An "On-Line" Method for Oxygen Isotope Exchange Between Gas Phase CO_2 and Water

Nicholas Paul Levitt[†], Christopher S. Romanek[1]

NASA Astrobiology Institute and
Department of Earth and Environmental Sciences
University of Kentucky
Lexington, Kentucky
40506

[1]NASA Astrobiology Institute and
Department of Earth and Environmental Sciences
Furman University
Greenville SC
29613

[†]Corresponding Author's Current Contact
Address:
NASA Astrobiology Institute and
Department of Geoscience
University of Wisconsin-Madison
1215 W Dayton Street
Madison, Wisconsin
53706

E-mail: nlevitt@wisc.edu
Tel: (608) 262-8960
Fax: (608) 262-0693

Manuscript published in:
AQUATIC GEOCHEMISTRY, 2016, 22:253–269, DOI 10.1007/s10498-016-9291-5

ABSTRACT

An “on-line” mixing system has been developed and evaluated for continuous oxygen isotope exchange between gas phase CO_2 and liquid water. The system is composed of three basic parts: equipment and materials used to introduce water and gas into a mixing reservoir, the mixing and exchange reservoir, and a vessel used to separate gas and water phases exiting the system.

A series of experiments was performed to monitor the isotope exchange process over a range of temperatures (5-40°C) and CO_2 partial pressures (202 to 15200 Pa). Isotopic exchange was evaluated using CO_2 having $\delta^{18}O$ values of 30.4 ‰ and 37.8 ‰, and waters of two distinct oxygen isotope compositions (-6.5 to -5‰ and 6 to 7.5‰). Isotope ratios were determined by isotope ratio mass spectrometry and cavity ring-down spectroscopy.

CO_2 did not reach oxygen isotope equilibrium under the conditions described here. However, oxygen isotope exchange rate constants were determined at different temperatures and regressed to yield the expression $k\ (h^{-1}) = 0.020*T\ (°C) + 0.28$. Using this expression, the residence time required to reach oxygen isotope equilibrium may be estimated for a given set of environmental conditions (e.g., $\delta^{18}O$ value of water, temperature). System parameters can be modified to achieve a specific $\delta^{18}O$ value for CO_2. Consequently, the exchange system described here has the ability to deliver a constant flow of CO_2 at a desired oxygen isotope composition. This ability is attractive for a variety of applications such as experiments that utilize flow-through reactors, environmental chambers, or require static chemical conditions.

Keywords: Carbon Dioxide, Oxygen Isotopes, Isotope Equilibrium, Isotope Kinetics, Dissolved Inorganic Carbon

1 Introduction

The carbonic acid system is one of the most important geochemical systems on the surface of the earth. This system is involved in critical processes that range from intracellular biomineralization to long-term planetary climate regulation. Investigators regularly assess the fractionation of the stable isotopes of H, O, and C in water and solids for a wide range of applications to evaluate and assess chemical and physical processes that involve these ubiquitous elements. Conversely, isotope compositions are also regularly controlled during experimentation in order to extend the utility of established procedures and develop new techniques. For example, isotope labeling is commonly used for tracing metabolic pathways and determining timescales of biological processes. However, despite common and versatile use, the exact details and constants associated with processes such as CO_2-H_2O equilibrium are still an active area of research after decades of investigation (Mills and Urey 1940; O'Neil and Adami 1969; Kim et al. 2014; Zeebe 2014). Today, the burgeoning field of multiply-substituted isotopologues, or "clumped isotopes", has added another dimension of complexity to this key group of elements (Eiler 2011; Huntington and Lechler 2015). This innovative approach to understanding isotope equilibrium carries with it a need for new methods such as those described by Spencer and Kim (2015) that can keep pace with advanced analytical capabilities and computational power that permit the use of clumped isotopes in geosciences (Hill et al. 2014; Tripati et al. 2015).

This communication describes the development and calibration of an "on-line" technique designed to exchange oxygen isotopes between gas phase CO_2 and liquid phase H_2O. According to the work of Affek (2013) and Clog et al. (2015) this method will also allow for the establishment of temperature dependent bonding of multiply-substituted isotopes (i.e., ^{13}C and ^{18}O isotopes) in dissolved inorganic carbon species DIC and gas phase CO_2. The system extensively mixes gas and liquid phases to facilitate the exchange process by forcing the two

phases to repeatedly alternate between flowing through a relatively unrestricted conduit and a narrow restriction. The fluids are simultaneously forced to change direction by 180° between the two flow regimes. This constant turbulence greatly enhances the CO_2 diffusion across the gas-water boundary.

Once dissolved in an aqueous solution, CO_2 becomes involved in the following reactions:

$$CO_2(aq) + H_2O = H_2CO_3 \quad \text{Eq. 1}$$

$$CO_2(aq) + OH^- = HCO_3^- \quad \text{Eq. 2}$$

$$H_2CO_3 = HCO_3^- + H^+ \quad \text{Eq. 3}$$

$$HCO_3^- = CO_3^{2-} + H^+ \quad \text{Eq. 4}$$

Ultimately, the exchange of oxygen isotopes between gas phase CO_2 and water is controlled by equations 1 and 2 as well as diffusion into and out of solution (Zeebe and Wolf-Gladrow 2001). However, oxygen isotope fractionations also occur between individual DIC species. The kinetics and isotope systematics of these reactions have been delineated by such researches as Usdowski et al. (1991, 1993), Beck et al. (2005), Chacko and Deines (2008), Dietzel et al. (2009), and Geisler et al. (2012). At equilibrium, the isotopic composition of species becomes increasingly enriched in ^{18}O according to the sequence: H_2O, CO_3^{2-}, HCO_3^-, H_2CO_3, $CO_2(g)$, and $CO_2(aq)$. Since DIC speciation is pH dependent, it follows that the sum $^{18}O/^{16}O$ ratio of all DIC species is also pH dependent.

The oxygen exchange method presented here utilizes relatively inexpensive, commercially available materials and laboratory equipment and can be used under the range of environmental conditions (e.g., temperature, partial pressure of CO_2, salinity, etc.) that can be found in most natural systems. Finally, the technique can be used to modify CO_2 for two

purposes. First, the response of CO_2 following the interaction with a given set of environmental conditions can be assessed. Second, this method can produce a stream of gas phase CO_2 with a desired oxygen isotope composition. This capability is highly attractive for a variety of applications such as experiments that utilize flow-through reactor cells, environmental chambers, or static chemical conditions. The system described here may also be useful for continuous-flow isotope ratio mass spectrometry since it provides the ability to create a stream of continuously flowing CO_2 at a given oxygen isotope composition. For example, the exchange system effluent could be set to an isotope composition closer to analyte CO_2 and analyzed periodically as a secondary reference gas (Finnigan 2004). This application could also possibly be taken one step further and used to create "equilibrated gases" for the purpose of creating an absolute reference frame (Dennis et al. 2011) during the continuous-flow analysis of multiply-substituted isotopologues of CO_2.

This study describes a series of experiments that monitor oxygen isotope exchange over a range of temperatures (5-40°C) and CO_2 partial pressures (202 to 15200 Pa). Waters with two distinct oxygen isotope composition ranges ($\delta^{18}O \approx$ -6.5 to -5‰ and $\delta^{18}O \approx$ 6 to 7.5‰) were used to explore the exchange process. The first group of experiments used CO_2 with a $\delta^{18}O$ value of 30.4 ‰ while the oxygen isotope composition of the CO_2 used during the second set of the experiments was 37.8 ‰. As described below, this system produces a continuous stream of CO_2 that has exchanged oxygen isotopes with liquid water of a specified stable oxygen isotope content. This feature provides a unique pathway to better understand isotope exchange equilibria in the carbonic acid system.

2 Methods and Materials

The exchange system is composed of three basic parts: 1) equipment and materials used to introduce water and gas into a mixing reservoir, 2) the mixing and exchange reservoir, and 3) a vessel used to separate the gas and water phase exiting the system. The mixing and exchange reservoir is connected to the other components by tubing as specified below. Fig. 1 depicts an annotated photograph of an exchange panel (reservoir) and includes an inset with basic system flow diagrams. The panel was oriented in a horizontal flat-lying position during use. Under steady operating conditions, the lower ~0.25 cm of the panel contained standing water at all times, while the upper ~0.75 cm contained water and gas mixture in a 1:2 volume, respectively (i.e., 0.5 cm gas and 0.25 cm water). Gas parcels move through the system in bubbles of approximately 5 cm x 1 cm x 0.75cm (see Fig. 1 inset). Each gas parcel traverses 120 cells before exiting the exchange panel. During movement through the panel, the gas and water mixture experience extensive mixing at the end of each cell when the gas is transferred turbulently to the next cell.

2.1 System Construction and Components

Four virtually identical exchange panels were constructed and tested for this project. However, all conditions and data reported here were collected during the use of only one panel at a time. Each exchange reservoir was constructed from a single polycarbonate twin-wall panel (United States Plastics Corporation, Lima, OH, USA). One panel is approximately 1.2 m wide by 2.4 m long and consists of 120 cells 1 cm x 1 cm x 2.4 m. Each cell was modified (cut) to connect it to the cell adjacent. The connections were approximately 0.5 cm wide x 2 cm long and alternated at either end of the panel. In this manner, all cells were connected to form one volume with a path length of approximately 288 m (see Fig. 1 inset). The end of each cell was

filled with GE Waterproof Silicon I* caulk (Stock No. GE012A, Fairfield, CT, USA) to create a leak proof seal.

The system was insulated with rigid polyisocyanurate foam sheeting (R-Mate Plus-3, RMAX Inc., Dallas, TX, USA) that matched the dimensions of the exchange panel. Water temperature was monitored at various locations using thermocouples placed between the exchange and insulation panels. Two inlets and one outlet were installed in each panel because gas and water were added to the system separately and removed together. One-quarter inch outer diameter tubing (Bev-A-Line V B-5, Excelon Thermoplastic Processes, Georgetown, DE, USA) was used for water and gas delivery and removal. Gas was delivered by mass flow controllers (model SLA5850, Brooks Instrument, Hatfield, PA, USA). The partial pressure of CO_2 in the gas stream was established by mixing pre-purified CO_2 and N_2 (Scott-Gross Company, Inc., Lexington, KY, USA) to a total flow rate of 100 standard cubic centimeters per minute (sccm). For example, a partial pressure of 15200 Pa (15% of atmospheric pressure) was achieved by combining 15 sccm of CO_2 and 85 sccm of N_2. Flow rates (individual and combined) were verified by a soap film flow meter (model 0101-0113, Hewlett-Packard (HP), Palo Alto, CA, USA).

A refrigerated/heated bath circulator (Isotemp model 4100R20, Fisher Scientific, Fair Lawn, NJ, USA) was filled with deionized water (NANOpure 18.2 MΩ-cm, Thermo Barnstead, Dubuque, IA, USA) that supplied water to the panel at a flow rate of 100 mL/min. The water-gas mixture exiting the system was delivered to a 1000 mL Pyrex filter flask (No. 5340, Corning, NY, USA) located in the circulator reservoir. The flask was modified by creating a hole near the base of the flask to allow water to return to the circulator reservoir. By this method, water mass was conserved and the isotope composition of water remained relatively constant during the

exchange process. In addition to moving fluids though the system, the circulator was used to regulate the temperature of the water entering the panel.

A custom-made water-jacketed distilling/condensing column (Chemglass, Vineland, NJ, USA) was inserted in a filter flask stopper to permit gas phase CO_2/N_2 to exit the system. A column of 18 cm length and smaller internal diameter (7.6 cm) was used to increase the gas flow velocity through the column and minimize the possibility for CO_2-H_2O interaction in the column. Water at approximately 2°C was circulated through the water jacket of the distilling/condensing column to remove water vapor from the gas stream. Water vapor removal prevents condensation of water in the tubing down stream of the filter flask and therefore minimizes the possibility of oxygen isotope exchange after H_2O and CO_2 exit the system.

2.2 System Monitoring and Sample Analysis

Fig. 1 (inset) is a schematic that illustrates the relationship between the exchange system and the analytical sampling setup. System monitoring included temperature, gas phase CO_2 concentration, pH, volume % H_2O of effluent gas, and oxygen isotope composition of CO_2 and H_2O. Temperature was measured at various locations between the exchange and insulation panels using thermocouples (5SC-TT-T-40-36, Omega Engineering Inc., Stamford, CT, USA). The gas phase concentration of CO_2 was measured by a CO_2 analyzer (LI-820 Analyzer, LI-COR, Lincoln, NE, USA) that logged values every 15 seconds. A Picarro (Santa Clara, CA, USA) Cavity Ring-Down Spectroscopy (CRDS) Analyzer Model G1101-i was used to monitor the amount of water vapor exiting the equilibration system. The full range of relative humidity for gas downstream of the exchange system was 1 to 40% (see Online Resource 1 for more details). The pH of the water exiting the panel was regularly monitored by a Cole-Parmer electrode (Item #00289LY, Vernon Hills, IL, USA) connected to an Oakton meter (Bench 2700

Series, Eutech Instruments, Vernon Hills, IL, USA). pH measurements were taken immediately before each gas sample collection event and often more frequently. Measured steady-state pH values agreed with those expected accounting for the percent CO_2 (pCO_2) in the gas entering the panel and relevant equilibrium constants (Zeebe and Wolf-Gladrow 2001). For example, at 25°C measured pH values of approximately 4.3, 4.6, and 5.1 were observed for pCO_2 concentrations of 15, 5, and 0.3%. Modeled pH values for pure water in equilibrium with these CO_2 concentrations are 4.32, 4.56, and 5.17, respectively.

This investigation utilized a Finnigan Delta^{Plus} XP (Thermo Electron Corporation, Bremen, Germany) isotope ratio mass spectrometer (IRMS) to determine oxygen isotope ratios of gas phase CO_2. The instrument was interfaced with a Finnigan Gasbench II (Thermo Electron Corporation, Bremen, Germany) device and GC-PAL (CTC Analytics, Zwigen, Switzerland) autosampler for sample preparation and transfer. Details of the analytical setup and procedure are provided by Levitt (2014). Gas samples were collected in new 5.9-mL flat-bottomed Na-glass containers (exetainers: Labco cat. #718W, Labco Limited, Lampeter, Ceredigion, United Kingdom), designed for use with the Finnigan Gasbench II device. Exetainers were collected no more frequently than once per hour approximately eight times per day. Additional CO_2 sampling details are included in Online Resource 1.

Exchange system water was collected from the bath circulator reservoir once per day with an unused Fisherbrand 9” Disposible Pasteur Pipet (Cat. No. 13-678-20C, Fisher Scientific, Fair Lawn, NJ, USA) and stored in National 12x32 mm sample vial (C4010-1W, Thermo Scientific, Rockwood, TN, USA) until analysis. A Picarro CRDS Analyzer Model G1102-i was used to determine the oxygen isotope composition of liquid water used in the exchange system. This analyzer was connected to a Picarro A0211 High-Precision Vaporizor that converted liquid water to gas phase H_2O for analysis. In-house water standards, Vienna Standard Mean Ocean

Water (VSMOW), Greenland Ice Sheet Precipitation (GISP), and Standard Light Antarctic Precipitation (SLAP) were used to calibrate unknown water sample $\delta^{18}O$ values to the VSMOW scale.

Water having a $\delta^{18}O$ value of ≈ 6 to 7.5‰ was prepared by adding 1 mL of "^{18}O Water" (Part #OLM-240-97-1, Cambridge Isotope Laboratories, Inc., Tewksbury, MA, USA) to the bath circulator reservoir. Fluctuations in water isotope compositions in the exchange system on the multi-day to week timescale are likely due to evaporation and the replenishment of lost water by newly deionized water. While a slightly variable water isotope composition is not ideal, regular and simultaneous monitoring of process water and CO_2 allows for reliable fractionation factor determinations regardless of the absolute values of the individual phases. Therefore, slight temporal drift of water $^{18}O/^{16}O$ ratios (typically ~0.2‰ per week at lower temperatures but up to ~0.2‰ per day at 30-40°C) does not affect the results and conclusions presented here.

2.3 System Operation

A series of experiments was performed to monitor oxygen isotope exchange between $CO_2(g)$ and $H_2O(l)$ over a range of temperatures and CO_2 partial pressures. Temperatures investigated include 5°, 9°, 15°, 25°, 31°, and 40°C while CO_2 partial pressures ranged from 202 to 15200 Pa. These pressures were achieved by mixing 0.2 to 15 percent CO_2 with a N_2 balance. The pH of the system is not artificially controlled. Therefore, higher partial pressures of CO_2 produce more carbonic acid causing a natural decrease in system pH. Waters with two distinct oxygen isotope composition ranges ($\delta^{18}O$ ≈ -6.5 to -5‰ and $\delta^{18}O$ ≈ 6 to 7.5‰) were also used to explore the exchange process. Experimental conditions as well as oxygen isotope compositions of $CO_2(g)$ and $H_2O(l)$ are presented in Table 1. Table 1a includes experiments which utilized

water of $\delta^{18}O \approx$ -6.5 to -5‰. Table 1b includes experiments which utilized water of $\delta^{18}O \approx$ 6 to 7.5‰.

In principle, the exchange system is run continuously. This practice maintains a desired steady operating state under a given set of conditions and therefore limits the need to adjust the amount of fluid in the water bath reservoir and minimizes the time needed to establish a new state of chemical equilibrium with CO_2 gas mixture when changing experimental conditions. The exchange system takes approximately 24 to 72 hours to reach chemical equilibrium depending on factors such as temperature and pCO_2. This is the time needed for CO_2 to dissolve (and speciate) into deionized water that has previously been in contact with air. Most of the experimental conditions reported here were established from pre-existing experiments (i.e. with CO_2 saturated water). In other words, after the establishment of chemical equilibrium under a given set of conditions (temperature, pH, and pCO_2), settings were changed to explore the extent of oxygen isotope exchange under a new set of conditions. For example, Fig. 2 reports $\Delta^{18}O_{CO2\text{-}H2O}$ values, where $\Delta^{18}O_{CO2\text{-}H2O} = \delta^{18}O_{CO2} - \delta^{18}O_{H2O,}$ for various temperatures and pCO_2 conditions over a multi-week time frame. The figure does not chronicle the entire experimental campaign (nor the initial CO_2 addition) but is included to illustrate changing system conditions and responses over time. Similar figures covering other experimental periods are provided in Online Resource 1.

The isotope composition of source CO_2 was determined prior to introduction to the exchange panel to evaluate the magnitude of the change in the oxygen isotope composition of CO_2 due to exchange with H_2O over time. CO_2 samples exiting the exchange system were collected multiple times per day. System water was sampled daily and analyzed for oxygen isotope composition to determine empirical $\Delta^{18}O_{CO2\text{-}H2O}$ values. The oxygen isotope composition

of gas phase CO_2 in equilibrium with system water was calculated under each set of experimental conditions for comparison to the measured values.

Experiments were performed in the absence of enhanced ionic strength. This experimental design best facilitates the objective of the experiments reported here: to facilitate oxygen isotope exchange between CO_2 and H_2O. Addition of salt compounds to the exchange system water would alter (retard in most cases) the exchange of isotopes compared to pure water. This "salt effect" has been well documented experimentally from a reaction rate and $CO_2(g)$-H_2O perspective (Zeebe and Wolf-Gladrow 2001; Horita 2005) while more recent research has investigated this effect on the oxygen isotope partitioning between DIC species (Kim et al. 2014). The data reported here should be considered a baseline reference utilizing pure water and further experimentation would be necessary to understand the magnitude of any salt effects in the exchange system.

2.4 Data Treatment

Exchange system water must become saturated with respect to CO_2 prior to the establishment of a constant oxygen isotope composition for effluent CO_2. This saturation process involves the reaction of CO_2 with H_2O and subsequent speciation into DIC compounds. Once there is no net flux of CO_2 into or out of the solution, oxygen isotope equilibrium can be achieved between CO_2 and H_2O. The time required to reach oxygen isotope equilibrium for a given parcel of CO_2 and H_2O depends on primary factors such as the residence time in the exchange system and system temperature. The extent of oxygen isotope exchange between gas-phase CO_2 and H_2O can be determined by comparing measured $\delta^{18}O$ values for CO_2 and H_2O to calculated values based on system conditions and equilibrium fractionation. The potential for CO_2 to alter the oxygen isotope composition of exchange system water is explored in Online

Resource 1. This assessment documents a negligible affect on water $^{18}O/^{16}O$ ratios. For CO_2, the empirically derived temperature dependent fractionation expression of Brenninkmeijer et al. (1983) was used for this study:

$$\alpha_{CO2\text{-}H2O} = 17.604*T^{-1}\ (K) + 0.98211 \qquad \text{Eq. 5}$$

where

$$\alpha_{CO2\text{-}H2O} = R_{CO2}/R_{H2O} \qquad \text{Eq. 6}$$

and R_{CO2} and R_{H2O} refer to the ratio of $^{18}O/^{16}O$ in CO_2 and H_2O, respectively, divided by the ratio of $^{18}O/^{16}O$ in the reference material VSMOW. The oxygen isotope exchange experiments described here were conducted with a single exchange "unit" with a volume of approximately 28.8 liters. As stated previously, the unit contains approximately equal volumes of water and gas. Given these volumes and flow rates of 100 sccm for gas and water, a residence time for the fluid of 2.4 hours results. The suitability of this residence time for the purpose of reaching oxygen isotope equilibrium is assessed by applying Equation (4) of Clog et al.'s (2015) first order rate expression:

$$\delta^{18}O_{CO2}\ (t) = \delta^{18}O_{CO2,Eq} + (\delta^{18}O_{CO2,In} - \delta^{18}O_{CO2,Eq})*\exp(-k_1*t) \qquad \text{Eq. 7}$$

Here t is the reaction time (or residence time), k_1 is the reaction rate constant, and the values $\delta^{18}O_{CO2}\ (t)$, $\delta^{18}O_{CO2,Eq}$ and $\delta^{18}O_{CO2,In}$ describe the isotope composition of CO_2 at time t, at equilibrium, and initially before exchange.

Equation 7 was used to calculate rate constants as presented for each experiment in Table 1. However, isotope compositions of CO_2 exiting the exchange system can only provide

reliable rate information if the gas has changed isotope composition but not reached equilibrium before exiting the system. Therefore, only CO_2 experiencing ≥ 0.4‰ change and ending distinctly short of equilibrium ("CO_2 offset" < -0.4‰) were considered for this determination. Most experiments utilizing water of isotope composition in the $\delta^{18}O$ range -6.5 to -5‰ produced CO_2 with an isotope composition less than 0.4‰ different than the equilibrium value. This phenomenon can be attributed to the relatively small difference between the starting and equilibrium $^{18}O/^{16}O$ ratio of the CO_2 gas. Conversely, the experiments utilizing water with higher ^{18}O abundance would require much more exchange to move the CO_2 gas isotope within 0.4‰. Therefore, fewer experiments in this group were rejected from rate constant determination due to this criterion. This equilibrium proximity effect can be observed in Online Resource 1 Figure A, which depicts the "reaction progress" as determined by the natural log of CO_2 offset divided by CO_2 isotope composition change. The figure shows that when the isotope composition change is relatively small and the CO2 offset value approaches the analytical precision, the reaction progress determination is inaccurate as evidenced by large variability and a loss of clearly temperature dependent exchange rates. In short, the accuracy of this rate constant determination method is compromised by the lack of sensitivity in isotope composition differences versus measurement precision. Online Resource 1 Figure A is analogous to Figure 2 in Affek (2013) and Figure 3 in Clog et al. (2015). For most conditions, a clear delineation between product CO_2 that was close to oxygen isotope equilibrium and CO_2 that was short of equilibrium is observed starting at -0.4‰.

Another requirement used to group experiments for rate constant determination was invariant temperature and pCO_2 conditions. For representative kinetic rate constant determinations, the following experiments were used: the 5°C average was calculated from data collected at 0.6% or 1% CO_2, the 9°C average was also calculated from data collected at or

below 1% CO_2 (excluding the anomalous value immediately after ^{18}O water was added), and the 31°C average was calculated from data collected at 0.4% CO_2. Only one 25°C experimental result meets the criteria outlined above for reliable rate constant determination; therefore this value was used. Rate constants that meet these requirements are presented in bold font in Table 1.

3 Results and Discussion

Table 1 summarizes the results of exchange experiments performed during this investigation. The table includes experimental conditions (temperature and pCO_2) as well as the isotope composition of source CO_2, system water, and effluent CO_2. Also listed are values that can be used to evaluate extent of oxygen isotope exchange. These values include the magnitude of change in the $\delta^{18}O$ value of CO_2 during a given experiment and the offset from theoretical oxygen isotope equilibrium. Most experimental conditions were reproduced and tested at different and distinct time intervals to verify reproducibility. See Online Resources 1 and 2 for details.

Experimental exchange is depicted in Fig. 2 and Online Resource 2. Measured Δ values are plotted along with equilibrium and kinetic values to illustrate consistency between experimental data and theory. Temperature dependence is clearly shown by the tandem temporal changes in isotope compositions. Increasing the oxygen isotope composition of system water to positive values allowed for a wider range of assessment but did not change the net effect of isotope partitioning. The water enriched in ^{18}O only shifted the oxygen isotope compositions to more positive values and did not affect fractionation factors. The relationship between pCO_2 and isotope partitioning behavior is not entirely clear based on the experiments reported here. This relationship is illustrated in Online Resource 1 Figure B. Changing pCO_2 (and holding other

variables constant) does not lead to a systematic change in offset from equilibrium or calculated equilibrium constants for most temperatures. However, a weak correlation is observed between pCO_2 and rate constants at experiments run between 8.7 and 9.4 °C (0.04 hr^{-1} per 1% pCO_2, R^2 = 0.90, excluding the anomalous value immediately after ^{18}O water was added). This possible relationship may be related to enhanced CO_2 solubility at lower temperatures or the speciation of DIC at lower pH values. Specifically, the pH values measured during the experiments ($\sim 4.2 \leq pH \leq 5.2$) put the DIC speciation regime at the edge of the heavily non-linear transition between HCO_3^- and $CO_2(aq)$ (see Fig. 2 of Beck et al., 2005). For example, at 9°C and a pCO_2 of 0.2%, $CO_2(aq)$ constitutes approximately 96% of DIC compared to 99.4% at a pCO_2 of 15%. Taking reactions 1-4 into account, this speciation difference may explain the possible correlation between pCO_2 and oxygen isotope exchange rates for our experiments similar to DIC effects on carbonate formation (Usdowski and Hoefs 1993; Dietzel et al. 2009). Specifically, at lower pH values, the DIC system is closer to the $CO_2(g) = CO_2(aq)$ realm than at higher pH values.

In some cases, measured values agree more closely with equilibrium than kinetic values. However, it is possible that the similarity between measured and equilibrium values is due to the relatively small difference between the starting CO_2 isotope composition and the equilibrium isotope composition. Another possibility for the larger than predicted $\Delta^{18}O_{CO2\text{-}H2O}$ value for experiments utilizing CO_2 with an oxygen isotope composition of 30.4‰ is kinetic fractionation during preferential dissolution of $C^{16}O_2$ into the exchange water or the forward reaction in Eq. 1 preferentially involving ^{16}O. Equation 1 is the limiting step (Usdowski et al. 1991; Usdowski and Hoefs 1993) and would therefore most heavily involve kinetic effects. This kinetic fractionation would increase the $\delta^{18}O$ value of the residual gas phase CO_2 and make the system appear to be closer to equilibrium than it actually is. $\Delta^{18}O_{CO2\text{-}H2O}$ differences are not as pronounced for experiments utilizing CO_2 with a starting isotope composition of 37.8‰. This is

possibly due to the higher abundance of ^{18}O in the gas phase and a lower apparent impact of kinetic fractionation. This is not to say that any kinetic fractionation process would depend on isotope composition. Rather, that a kinetic effect would be easier to recognize with a starting isotope composition significantly different from the equilibrium isotope composition. It is also worth noting that theoretical kinetic $\Delta^{18}O_{CO2\text{-}H2O}$ values (as opposed to measured values) are lower than equilibrium values during all experiments except those run between 7/13/13 and 7/23/13. Higher kinetically controlled theoretical $\Delta^{18}O_{CO2\text{-}H2O}$ values during this time period are expected due to the fact that CO_2 used during these experiments had an oxygen isotope composition that was enriched in ^{18}O compared to equilibrium CO_2. This was not the case for all other experiments.

The most notable aspect of data collected from experiments covering water with positive $\delta^{18}O$ values is the large difference between measured and equilibrium $\Delta^{18}O_{CO2\text{-}H2O}$ values after the addition of ^{18}O water followed by progressively similar values (compare Table 1b offsets for pCO_2 of 0.2%, 1%, 5%, 10%, and 0.4% in that order). This observation is harder to interpret due to the simultaneous increase of pCO_2 over this period. A temporal depiction of this trend can be observed in Online Resource 1 Figures C-I. The isotope values reported in Table 1 for this time period have been classified as constant. This is not to say that all of the values in the Online Resources have been classified as such, it simply means that a constant operating state was assigned to periods represented in Table 1b. It is possible that the criteria used to identify a constant operating state (and chemical steady state in this case) were not strict enough under these conditions (i.e. low temperature and large initial $\Delta^{18}O_{CO2\text{-}H2O}$) and that oxygen exchange reactions (e.g. $C^{16}O_2(aq) + H_2{}^{18}O = C^{18}O^{16}O(aq) + H_2{}^{16}O$) during this time period were slow. In other words, the drifting $\Delta^{18}O_{CO2\text{-}H2O}$ values during this time may simply be a result of relatively slow equilibration between DIC and water under these conditions compounded by a

stepwise increase in the concentration of gas phase CO_2 between distinct experiments. As the oxygen isotope composition of DIC moved closer to equilibrium, it also allowed the CO_2 to progressively move toward equilibrium. This interpretation is supported by the relatively long residence times predicted in Table 1b and the observation that the exchange system takes approximately 24 to 72 hours to reach a constant operating state when beginning from fresh water at room temperature. This observation also indicates that pCO_2 and water should be balanced to a constant operating state at or above room temperature before moving system temperature to low values. In other words, chemical equilibrium should be attained before changing other experimental parameters such as temperature.

Values presented in Table 1 are considered to have reached a steady oxygen isotope composition. Recognition of steady operating state was based on three variables: pCO_2 stability, temperature, and CO_2 oxygen isotope composition. Online Resource 1 Figure G is a "close-up" view of typical steady operating state conditions. The following criteria were used for consistency when identifying stable operating conditions after changing system conditions. Stable pCO_2 values are defined for time intervals where the standard deviation of CO_2 concentrations is 10% or less of the rolling average value (see Online Resources 1 and 2 for details). Three criteria were used to verify stable temperature. First, a three data point rolling standard deviation was calculated. Temperature measurements that were associated with standard deviations above 0.5°C were excluded. Second, values greater than ± 0.5°C of the cumulative average temperature were also excluded. Finally, only temperatures that contributed to an overall standard deviation of 0.2°C or less were considered stable. Similar criteria were used for oxygen isotope compositions. Individual $\delta^{18}O$ values represented in Table 1 were associated with rolling standard deviations of ≤ 0.4‰ and were also within 0.3‰ of the cumulative average. Finally, only $\delta^{18}O$ values that contributed to an overall standard deviation

of 0.3‰ were considered stable. The composite data representing a given set of experimental conditions is an average of *n* number of samples collected before the system conditions were changed. Many CO_2 isotope analyses were made that are not reflected in Table 1. These measurements document temporal changes in $\delta^{18}O$ values (and other parameters) during the transition between experimental conditions. An example of such measurements is in the central set of data points in Fig. 2 where the evolution of the $\delta^{18}O$ value of CO_2 is recorded during the transition between two temperatures. All individual IRMS analyses and water isotopic compositions, including those not represented in Table 1, have been included in Online Resource 2 with explanations for data collected under non-steady operating conditions.

According to information presented in Table 1, all experimental $\delta^{18}O$ values for CO_2 exiting the exchange system were between the starting CO_2 and equilibrium oxygen isotope composition or within analytical uncertainty of the oxygen equilibrium isotope composition. All experiments conducted with system water of $\delta^{18}O$ values in the 6 to 7.5‰ range failed to reach full equilibrium despite CO_2 changes in $\delta^{18}O$ of up to 13.5‰ over the course of the experiment. The final oxygen isotope composition of CO_2 exiting the exchange system was at least 0.8‰ lower than the calculated equilibrium value in all experiments of this group. Exchange short of equilibrium is likely due to the insufficient reaction time under the experimental operating conditions.

Most experiments conducted with system water in the $\delta^{18}O$ = -6.5 to -5‰ range appear to have reached or at least closely approached equilibrium. However, this is likely related to the coincidental proximity of initial conditions to equilibrium conditions. In this population, only one experiment above 5.7°C had an oxygen isotope composition that did not approach the theoretical equilibrium value within 0.2‰. In any case, CO_2 processed at temperatures near 5°C were found to be short of equilibrium by up to 0.7‰ compared to theoretically calculated values.

The residence time for 5°C experiments was the same as all other experiments reported here: 2.4 hours. According to the reaction rate constant of 0.17 h^{-1} for 5°C reported in Table 2 of Clog et al. (2015), 13.5 hours of exchange is needed to achieve equilibrium. However, if the reaction rate constant determined for this exchange system is used, a time of approximately 5.5 hours is needed (See Table 1 for specific reaction time values). These observations are consistent with the body of work that indicates system temperature is an important factor that determines the time necessary to reach isotope equilibrium between CO_2 and water (Zeebe and Wolf-Gladrow 2001).

Average rate constant values from Table 1 are plotted in Fig. 3 along with values reported by Affek (2013) and Clog et al. (2015). As shown in this figure, the rate constants reported here are higher than those reported by both Clog et al. and Affek. These investigators conducted most of their experiments by promoting gas and liquid phase CO_2 exchange through "shaking". It is probable that the enhanced CO_2/water mixing employed by the exchange system facilitated higher reaction rate constants. Specifically, the system extensively mixes gas and liquid phases to facilitate the exchange process by forcing the two phases to repeatedly alternate between flowing through a relatively unrestricted conduit and a narrow restriction. The fluids are simultaneously forced to change direction by 180° between the two flow regimes. This constant turbulence greatly enhances the CO_2 diffusion across the gas-water boundary. Alternatively, the system may have an effective CO_2 residence time longer than the calculated 2.4 hours. However, a residence time of 4.5 hours is required to derive a 25°C rate constant of 0.39 hr^{-1} which would fall between comparable Affek (2013) and Clog et al. (2015) values of 0.38 and 0.41, respectively. An error-weighted regression of the averaged rate constants in Fig. 3 gives a temperature dependent expression of $k_{\delta 18O}$ (hr^{-1})= 0.020*T (°C) + 0.28. The propagated uncertainty in a give rate constant is close to 20%. Individual rate constant uncertainties are

given in Table 1. This translates to a slope and intercept uncertainty of ± $8.5x10^{-3}$ and 0.10, respectively. The regression slope found for this set of data is similar to that found for Affek's (2013) slope of 0.014 and the Clog et al. (2015) slope of 0.014. The temperature dependent expression found for this study was used to calculate a kinetic rate constant for each experimental condition reported here. These values were then used in Equation 7 to solve for a residence time needed to provide enough exchange to be within analytical error of equilibrium (i.e. 0.0 ± 0.1‰ = $\delta^{18}O_{CO2}$ (t) - $\delta^{18}O_{CO2,Eq}$).

The time required to reach oxygen isotope equilibrium for each experiment is listed in Table 1; values range from 3.5 to 10.0 hours. These residence times can be achieved by 1) reducing the flow rate of fluid though the system to values of 68.6 sccm and 24.0 sccm, respectively, or 2) extending the path length to 422 m and 1198 m. The estimated times are supported by the observation that experiments conducted with positive $\delta^{18}O$ water were off by approximately 0.8 to 5.0‰ compared to equilibrium. It is worth noting that the 3.5 to 10 hours mentioned above does not count the initial dissolution of CO_2 into the system water. As mentioned before, this process takes approximately 24 to 72 hours. However, this initial chemical equilibration is only needed when the entirety of system water is removed and replaced with deionized water that has been in contact with air. Chemical equilibration times due to a shift in system temperature or pCO_2 changes by a few percent are included in the values listed in Table 1.

4 Conclusions

An "online" method has been developed to exchange oxygen isotopes between gas phase CO_2 and liquid water. The system can be constructed with relatively inexpensive and commercially available materials. The system has been tested to assess exchange kinetics under

a variety of conditions including a range of temperatures, CO_2 partial pressures, and isotopic compositions. While CO_2 did not reach oxygen isotope equilibrium under the conditions described here, the experiments allowed the determination of isotope exchange rate constants at temperatures of 5°, 9°, 25°, and 31°C. Empirically determined rate constants predict that exchange system residence times needed to fully exchange oxygen isotopes for the experiments described here range from 3.5 to 10.0 hours. Connecting multiple exchange panels in series or reducing flow rates can accommodate these reaction times. Consequently, the exchange system has the ability to deliver a constant flow of CO_2 at a desired oxygen isotope composition and thermodynamic isotope ordering. This capability is highly attractive for a variety of applications such as experiments that utilize flow-through reactor cells, environmental chambers, or static chemical conditions.

SUPPORTING INFORMATION

Additional figures and data are included in Online Resources 1 and 2 that may be found in the online version of this article.

ACKNOWLEDGEMENTS

Suvankar Chakraborty is recognized for instrument assistance and insightful discussions. The authors wish to thank Clark Johnson and three anonymous reviewers for their helpful comments on earlier versions of this manuscript. Gratitude is also offered to Rolf Arvidson for his editorial handling of this publication. This work was supported by NASA Headquarters under the NASA Earth and Space Fellowship Program – Grant NNX12AN84H as well as the NASA Astrobiology Institute.

Table 1 Experimental Conditions, CO_2 and Oxygen Isotope Compositions for Experiments in the $\delta^{18}O_{water}$ = -6.5 to -5 ‰ range

Number	Source CO_2		System T	Water	IRMS Meas.*	Equilibrium	Change	Offset	Kinetic	Rate Const.	Time
Samples	pCO_2	‰	(° C)*	‰	‰	‰	‰	‰	‰	(h^{-1})	(h)
5	0.2%	37.8	5.5 ± 0.0	-6.5	38.4 ± 0.1	38.5	0.7	-0.1	38.3	0.86 ± 0.17	4.7
3	0.2%	37.8	5.5 ± 0.1	-6.5	38.1 ± 0.1	38.5	0.3	-0.5	38.2	0.19 ± 0.04	4.7
8	0.2%	37.8	5.6 ± 0.1	-6.5	38.4 ± 0.1	38.5	0.6	-0.1	38.2	1.00 ± 0.20	4.6
3	0.3%	30.4	13.6 ± 0.1	-6.5	36.9 ± 0.1	36.8	6.6	0.1	35.1	1.56 ± 0.31	7.3
6	0.3%	30.4	16.7 ± 0.1	-6.3	36.3 ± 0.1	36.3	6.0	0.0	35.0	2.71 ± 0.54	6.6
6	0.3%	30.4	17.2 ± 0.2	-6.3	36.3 ± 0.1	36.2	5.9	0.1	34.9	1.76 ± 0.35	6.4
2	0.3%	37.8	22.6 ± 0.0	-6.3	35.3 ± 0.1	35.1	-2.4	-0.2	35.6	0.96 ± 0.19	4.5
10	0.3%	30.4	24.3 ± 0.2	-6.5	34.8 ± 0.1	34.6	4.5	0.2	33.9	1.21 ± 0.24	5.0
3	0.3%	30.4	24.6 ± 0.1	-6.5	34.4 ± 0.1	34.5	4.1	-0.1	33.8	1.82 ± 0.36	4.9
13	0.3%	30.4	25.2 ± 0.1	-6.4	34.6 ± 0.1	34.4	4.3	0.2	33.8	1.30 ± 0.26	4.8
13	0.3%	30.4	25.3 ± 0.2	-6.6	34.4 ± 0.1	34.2	4.1	0.2	33.6	1.24 ± 0.25	4.7
3	0.3%	37.8	33.4 ± 0.2	-6.1	33.4 ± 0.0	33.2	-4.4	-0.2	33.7	1.32 ± 0.26	4.2
6	0.3%	37.8	40.1 ± 0.1	-4.8	33.4 ± 0.1	33.3	-4.4	-0.1	33.7	1.72 ± 0.34	3.7
2	0.3%	37.8	40.3 ± 0.1	-5.5	32.8 ± 0.0	32.6	-4.9	-0.2	33.1	1.30 ± 0.26	3.8
7	1%	37.8	5.5 ± 0.0	-6.3	38.4 ± 0.0	38.7	0.6	-0.4	38.4	**0.41 ± 0.08**	5.3
3	1%	37.8	5.5 ± 0.0	-6.2	38.4 ± 0.0	38.8	0.6	-0.4	38.4	**0.42 ± 0.08**	5.4
8	1%	37.8	5.4 ± 0.1	-6.5	38.2 ± 0.1	38.6	0.4	-0.4	38.3	**0.34 ± 0.07**	4.8
7	1%	37.8	5.5 ± 0.0	-6.4	38.3 ± 0.0	38.6	0.5	-0.4	38.3	**0.35 ± 0.07**	5.0
6	5%	37.8	5.3 ± 0.0	-6.3	38.1 ± 0.1	38.8	0.3	-0.7	38.4	0.16 ± 0.03	5.4
9	5%	37.8	5.3 ± 0.0	-6.5	38.0 ± 0.1	38.5	0.2	-0.5	38.2	0.12 ± 0.02	4.7
5	10%	37.8	5.3 ± 0.1	-6.4	38.4 ± 0.0	38.6	0.6	-0.2	38.3	0.60 ± 0.12	5.0
6	10%	37.8	5.5 ± 0.0	-6.1	38.6 ± 0.1	38.9	0.9	-0.3	38.5	0.57 ± 0.11	5.7
6	10%	37.8	5.5 ± 0.1	-6.3	38.8 ± 0.1	38.7	1.0	-0.1	38.4	0.78 ± 0.16	5.2
3	10%	37.8	5.7 ± 0.1	-5.9	38.6 ± 0.1	39.1	0.9	-0.4	38.6	0.46 ± 0.09	6.0
7	15%	37.8	5.5 ± 0.1	-6.3	38.9 ± 0.0	38.7	1.1	-0.2	38.4	0.72 ± 0.14	5.2
3	15%	37.8	24.7 ± 0.0	-6.1	35.1 ± 0.1	34.9	-2.7	-0.2	35.3	1.08 ± 0.22	4.4
3	15%	37.8	25.0 ± 0.0	-6.2	34.9 ± 0.2	34.7	-2.9	-0.1	35.2	1.35 ± 0.27	4.4
6	15%	37.8	25.0 ± 0.1	-6.4	35.1 ± 0.0	34.5	-2.7	-0.6	35.0	**0.73 ± 0.15**	4.5
7	15%	37.8	25.5 ± 0.2	-5.9	35.0 ± 0.1	34.9	-2.8	-0.1	35.3	1.33 ± 0.27	4.3

Table 2 Experimental Conditions, CO2 and Oxygen Isotope Compositions for Experiments in the $\delta^{18}O$ = 6 to 7.5 ‰ range

Number	Source CO_2		System	Water	IRMS Meas.*	Equilibrium	Change	Offset	Kinetic	Rate Const.	Time
Samples	pCO_2	‰	Temp. (° C)*	‰	‰	‰	‰	‰	‰	(h^{-1})	(h)
9	0.2%	37.8	8.9 ± 0.1	7.6	51.2 ± 0.1	52.5	13.5	-1.2	47.9	1.04 ± 0.21	10.3
3	0.2%	37.8	9.0 ± 0.1	7.2	47.6 ± 0.1	52.0	9.8	-4.4	47.6	**0.49 ± 0.10**	10.2
8	0.2%	37.8	9.2 ± 0.2	7.6	47.4 ± 0.2	52.4	9.7	-5.0	47.9	**0.45 ± 0.09**	10.2
2	0.4%	37.8	14.1 ± 1.2	6.6	49.1 ± 0.5	50.3	11.3	-1.1	47.1	1.00 ± 0.20	8.4
7	0.4%	37.8	30.8 ± 0.1	6.6	45.4 ± 0.0	46.9	7.6	-1.4	45.7	**0.77 ± 0.15**	5.2
5	0.4%	37.8	30.9 ± 0.1	6.1	45.6 ± 0.0	46.4	7.9	-0.8	45.3	**1.00 ± 0.20**	5.1
8	0.4%	37.8	30.9 ± 0.1	5.9	45.4 ± 0.1	46.1	7.6	-0.8	45.1	**1.00 ± 0.20**	5.1
3	0.4%	37.8	31.0 ± 0.1	6.0	45.0 ± 0.1	46.2	7.3	-1.2	45.2	**0.83 ± 0.17**	5.1
3	1%	37.8	9.1 ± 0.1	7.2	48.8 ± 0.2	52.0	11.1	-3.1	47.6	**0.63 ± 0.13**	10.1
2	1%	37.8	9.4 ± 0.1	7.2	48.4 ± 0.3	51.9	10.6	-3.5	47.6	**0.58 ± 0.12**	10.0
4	5%	37.8	9.1 ± 0.1	7.3	49.2 ± 0.3	52.1	11.5	-2.9	47.7	0.67 ± 0.13	10.2
2	5%	37.8	9.2 ± 0.1	7.3	50.1 ± 0.1	52.1	12.3	-2.0	47.7	0.83 ± 0.17	10.1
2	10%	37.8	8.7 ± 0.1	6.6	49.9 ± 0.1	51.4	12.1	-1.5	47.1	0.91 ± 0.18	10.2
5	10%	37.8	8.9 ± 0.0	6.3	49.7 ± 0.2	51.1	11.9	-1.4	46.9	0.95 ± 0.19	10.1
4	10%	37.8	9.0 ± 0.1	6.2	49.8 ± 0.1	51.0	12.0	-1.2	46.9	0.99 ± 0.20	10.0
4	10%	37.8	9.0 ± 0.1	6.2	49.8 ± 0.1	51.0	12.0	-1.2	46.9	0.99 ± 0.20	10.0
6	10%	37.8	9.0 ± 0.2	6.5	49.6 ± 0.1	51.3	11.8	-1.7	47.1	0.87 ± 0.17	10.1

Delta values reported with respect to VSMOW

* Error values represent 1-SD of n number of samples

Figure Captions

Figure 1 – The background photo is of an exchange panel in a vertical position. The inset shows a schematic diagram of the entire exchange system and monitoring/sampling equipment. Also shown in detail is a side view cartoon of the movement and flow path of bubbles and water inside one cell during system operation.

Figure 2 – Temporal depiction of exchange system conditions, monitoring, and assessment. Annotations include: the isotope composition of the source CO_2 ($\delta^{18}O$ = 30.0‰ before 7/12/13 and 37.8 ‰ afterward) as well as percent CO_2 introduced to the system (experiments before 7/18/13 were conducted with a pCO_2 of 0.3% and 15% afterward).

Figure 3 – Average kinetic rate constants found by this study compared to those determined by Affek (2013) and Clog et al. (2015). The error envelope represents an error-weighted 95% confidence interval. Error bars represent 2-sigma uncertainty.

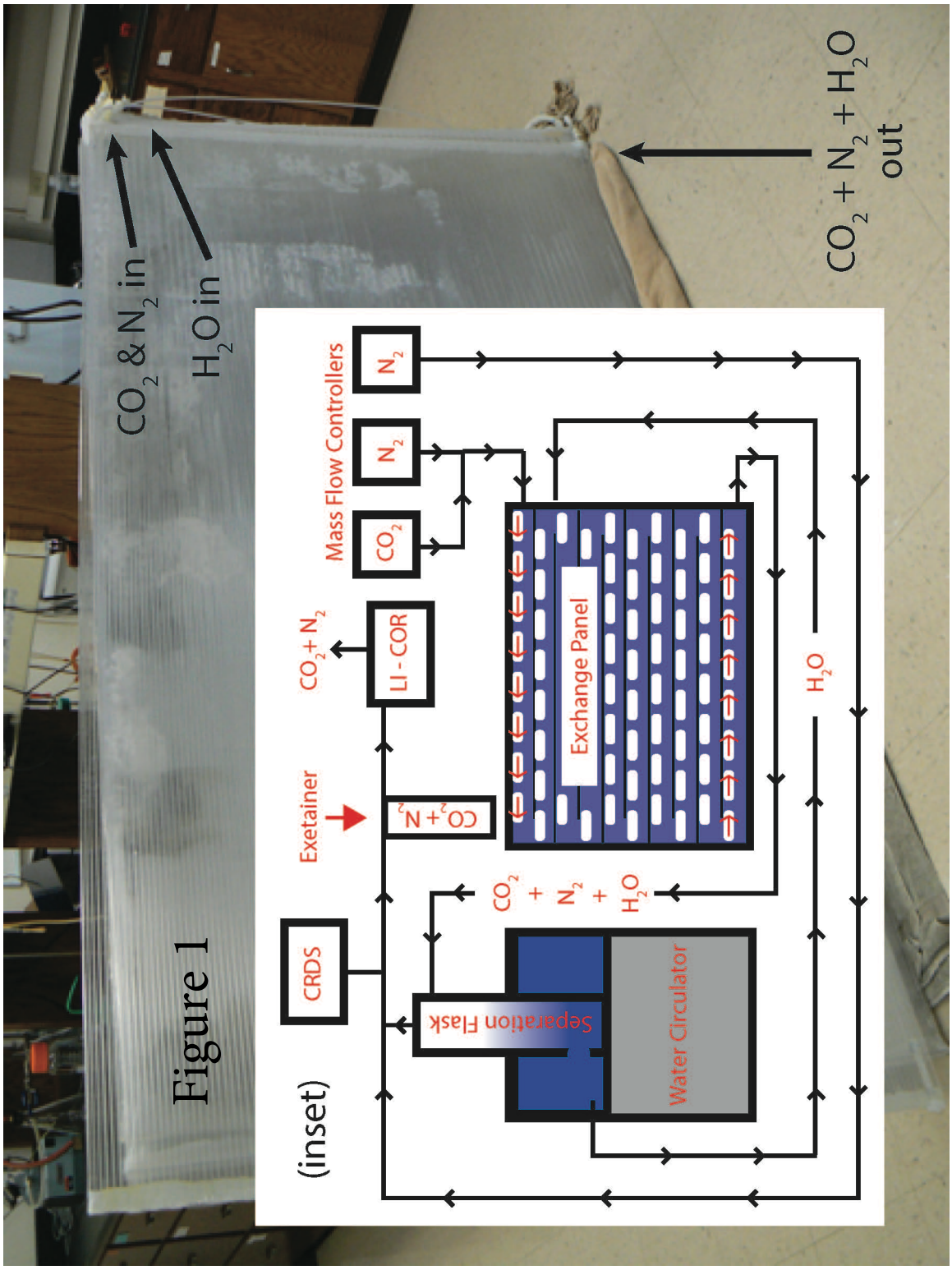

CO_2 & N_2 in
H_2O in
$CO_2 + N_2 + H_2O$ out
(inset)
CRDS
Exetainer
$CO_2 + N_2$
LI - COR
Mass Flow Controllers
CO_2
N_2
N_2
Exchange Panel
H_2O
$CO_2 + N_2 + H_2O$
Separation Flask
Water Circulator

Figure 1

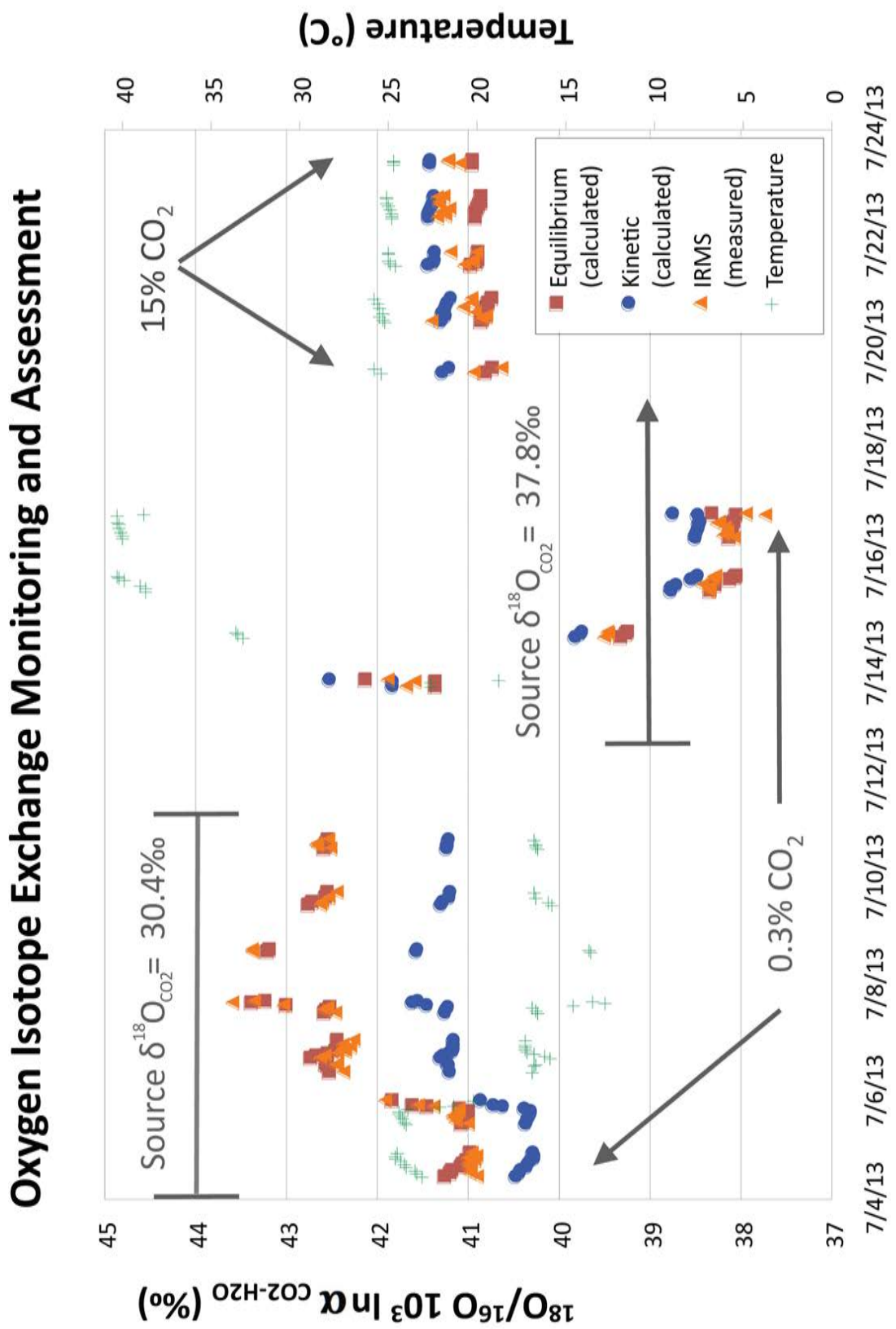
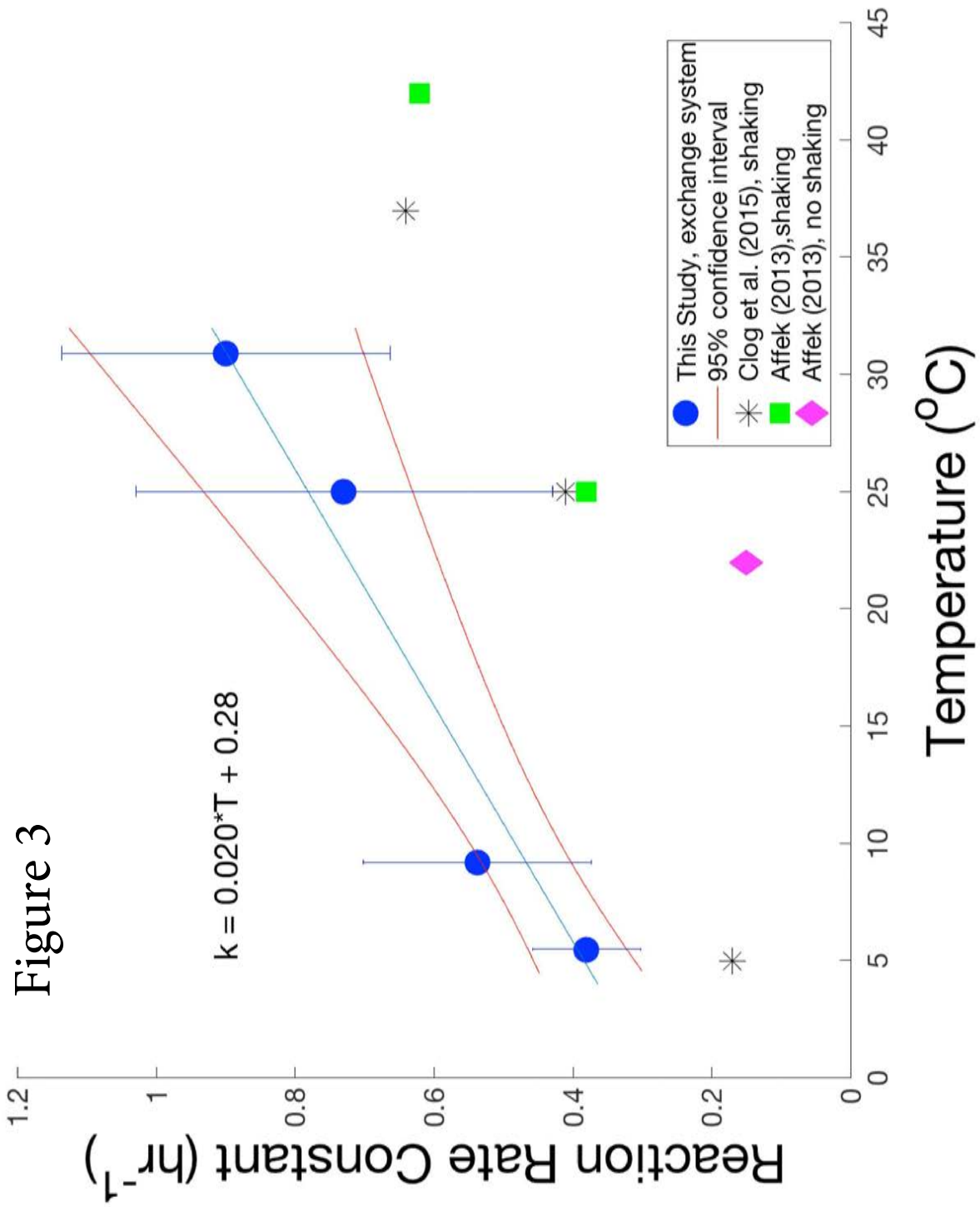

Oxygen Isotope Exchange Monitoring and Assessment
Source $\delta^{18}O_{CO2}$= 30.4‰
15% CO_2
Source $\delta^{18}O_{CO2}$ = 37.8‰
0.3% CO_2
Equilibrium (calculated)
Kinetic (calculated)
IRMS (measured)
Temperature
$^{18}O/^{16}O$ 10^3 ln α $_{CO2-H2O}$ (‰)
Temperature (°C)
7/4/13
7/6/13
7/8/13
7/10/13
7/12/13
7/14/13
7/16/13
7/18/13
7/20/13
7/22/13
7/24/13
Time (Julian Date)

Figure 2

Figure 3


Reaction Rate Constant (hr-1)
Temperature (°C)
k = 0.020*T + 0.28
This Study, exchange system
95% confidence interval
Clog et al. (2015), shaking
Affek (2013),shaking
Affek (2013), no shaking
0
0.2
0.4
0.6
0.8
1
1.2
0
5
10
15
20
25
30
35
40
45

An "On-Line" Method for Oxygen Isotope Exchange Between Gas Phase CO_2 and Water

Online Resource 1

Nicholas Paul Levitt[†], Christopher S. Romanek[1]

NASA Astrobiology Institute and
Department of Earth and Environmental Sciences
University of Kentucky
Lexington, Kentucky
40506

[1]NASA Astrobiology Institute and
Department of Earth and Environmental Sciences
Furman University
Greenville SC
29613

[†]Corresponding Author's Current Contact Address:
NASA Astrobiology Institute and
Department of Geoscience
University of Wisconsin-Madison
1215 W Dayton Street
Madison, Wisconsin
53706

E-mail: nlevitt@wisc.edu
Tel: (608) 262-8960
Fax: (608) 262-0693

Manuscript published in:
AQUATIC GEOCHEMISTRY, 2016, 22:253–269, DOI 10.1007/s10498-016-9291-5

OR 1.1 pCO_2 Measurement and Effluent Stability

All CO_2 evaluated for oxygen isotope composition was collected and analyzed at roughly the same concentration as IRMS monitoring gas. See Levitt (2014) for analysis details. In some cases, gas exiting the exchange system was diluted with pure N_2 at a T-union fitting reduce the concentration of CO_2 to approximately 0.3% prior to pCO_2 and isotopic analysis. Diatomic nitrogen was delivered to the gas stream by a mass flow controller (also model SLA5850). Downstream of the T-union, gas flow passed through a butyl rubber septum-capped exetainer fitted with a 21-gauge syringe. Gas exited the exetainer through a second 21-gauge syringe and was then routed to the LI-COR Analyzer before being vented to the atmosphere. The exetainer flushing procedure allowed the full turnover of air inside the exetainer and effectively filled the vessel with gas that had experienced exchange in the system.

LI-COR measured CO_2 concentrations agreed well with target partial pressures established with the mass flow control devices for lower concentrations. However, less agreement was found when dilution N_2 required the mass flow controllers to be run at a cumulative gas flow rate above the LI-CORE recommended maximum value of 1 L/min. Measurements taken at dilution flow rates greater than 1 L/min are associated with experiments run at pCO_2 concentrations of 5% and higher. Online Resource 2 includes pCO_2 values according to target mass flow controller devices and measured values. Additionally, the table includes values corrected for dilution N_2 flow rates. This correction was made according to the following expression:

$$pCO_{2corr} = pCO_{2meas} * (F_{dil}/F_{un}) \qquad \text{Eq. OR1}$$

Where pCO_{2corr} is the undiluted CO_2 concentration in ppm, pCO_{2meas} is the LI-COR measured CO_2 concentration, F_{dil} is the total diluted flow rate in sccm, and F_{un} is the undiluted flow rate introduced to the exchange system.

While inaccurate pCO_2 measurements at higher CO_2 concentrations are less than ideal, the absolute values are not expected to affect the ability to make qualitative assessments of net mass fluxes into and out of exchange system solution and therefore pCO_2 stability. Furthermore, CO_2 concentration does not appear to influence the rate of exchange under most conditions explored here (as discussed in the main text).

OR 1.2 Stability of Water Oxygen Isotope Composition

The amount of water vapor downstream of the exchange system was monitored as a volume percent of the total gas. Effluent with low pCO_2 (0.2 to 0.3%) contained approximately 0.75% H_2O (or 7 g m^{-3}) translating to ~ 35% relative humidity. The full range of RH for low pCO_2 experiments was 31 to 40%. Higher partial pressures exiting the exchange system were diluted with N_2 for oxygen isotope analysis (see details above), which also diluted the concentration of water vapor in the effluent gas. Gas introduced to the exchange system with 15% CO_2 was treated with the largest amount of dilution N_2. The water vapor content of this diluted gas was approximately 0.03% by volume, which translates to a RH of 1-3%.

Undiluted effluent gas that was saturated with water vapor at the maximum experimental temperature during this study (40°C) would contain approximately 47 g of H_2O per cubic meter. One week's worth of exchange system operation at a total gas flow rate of 100 sccm would use 1008 L or 1.008 m^3 of gas. The 47 g of water lost to evaporation under these conditions (and assuming isotope equilibrium between the two

phases of water) would have an isotope composition 8.4‰ lower than the exchange system water (Horita and Wesolowski 1994).

It is also worthwhile to assess the possibility of CO_2 influencing the oxygen isotope composition of water. The potential for CO_2 to change the isotope composition of system water can be evaluated using the work presented by such researchers as Craig (1957) and Gonfiantini (1981) and summarized by deGroot (2009). According to these authors, the expression that describes the oxygen isotope composition of a given volume of water after equilibration with CO_2 is given by:

$$\delta_w = \delta^i_w + (n_g/n_w)*(\delta^i_g - \delta_g) \qquad \text{Eq. OR2}$$

Where δ^i_w and δ_w are the initial and final isotope compositions of water, δ^i_g and δ_g are the initial and final isotope compositions of gas phase CO_2, and n_w and n_g are the number of moles of water oxygen and CO_2 oxygen atoms, respectively. Using the highest pCO_2 experiments and a volume ratio of gas to liquid in the exchange system of ~1:1 (based on the amount of water added to the system and observed behavior of bubble/liquid flow in the system), a n_g/n_w ratio of 0.000025 (0.2016/800.68) is calculated for the exchange panel. This calculation is based on one liter of 15% pCO_2 gas at 1 kPa and 5°C containing 0.007 moles of CO_2 and a concentration of H_2O molecules in liquid water of 55.6 mol/L. Assuming initial and final CO_2 $\delta^{18}O$ values of 30.4‰ and 38.8‰ (most dissimilar values taken from Table 1a), the δ_w value after exchange to equilibrium would be -6.482‰. If this calculation is performed iteratively holding the δ^i_g constant and using the modified $\delta^{18}O$ value for water at each step, the equilibrium water isotope composition is calculated to be less than 0.01‰ higher after 25 exchange cycles or approximately 60

hours of operation. When this exercise is repeated for δ^{i}_{g}, $\delta_{g,}$ and δ^{i}_{w} values of 37.8‰, 52.5‰, and 5.9‰ (most dissimilar values taken from Table 1b), the δ_{w} values for one and 25 cycles are both less than 0.01‰ lower than the starting isotope composition. Based on these estimates, the reaction between CO_2 and H_2O is not expected to change the isotope composition of water during exchange system operation over the timescale of several hours to a few days.

The assumption of an invariable water isotope composition on shorter timescales is supported by the general temporal consistency of $\delta^{18}O$ values measured for system water on the time scale of days. On longer time scales (several days to weeks) however, there was a pattern of increasing $^{18}O/^{16}O$ ratios over time. For example, the initial isotope composition of system water was $\delta^{18}O$ = -6.7‰. This value increased to $\delta^{18}O$ = -6.1‰ over the period of approximately four weeks of continuous operation and movement through the temperature range of 15-33°C. The observed trend may be attributed to the preferential evaporation of $H_2{}^{16}O$ and to a lesser extent minor isotope exchange with source CO_2. Faster changes in water isotope ratios were observed at higher system temperatures also suggesting that evaporation was the driver for observed variations.

ONLINE RESOURCE 1 FIGURE CAPTIONS AND FIGURES

OR1-Figure A - Graphical representation of "reaction progress" as determined by the natural log of CO_2 $\delta^{18}O$ offset divided by CO_2 isotope composition change (see main text and Table 1 for explanation of these two parameters). This figure is analogous to Figure 2 in Affek (2013) and Figure 3 in Clog et al. (2015). However, the experiments described here only allowed the sampling of reagent CO_2 at one reaction time, while the experiments in Affek (2013) and Clog et al. (2015) were designed with the ability to sample reaction progress at multiple time periods. Open shapes represent all experiments presented in Table 1. Filled shapes correspond to values that are presented in bold font in Table 1. The filled shapes represent single or average values for a given temperature depending on the number of available data points. The equations beside the legend are regressions of the different temperature experiments. The slopes of the lines correspond to reaction rate constants and agree fairly well with the values determined by an alternative method (as described in the main text). While the data points are roughly arranged by temperature (low temperatures closer to the top of the figure) there is a good deal of variability among values of a given temperature and overlap exists between different temperatures. This variability is generally due to analysis of CO_2 that had approached (but likely not reached) equilibrium with the exchange system water. This proximity prevented accurate ratio determinations due to the precision limit of isotope ratio determinations. See the main text for further explanation.

OR1-Figure B - Distance from isotope equilibrium at the end of exchange as a function of percent CO_2 in the gas phase. Different temperature experiments have been plotted as different symbols according to the legend.

Figures OR1-Figure C through OR1-Figure I are analogous to Figure 2 for different time periods of experimentation. Each figure represents a discrete span of time during experimentation and offers details of experimental conditions and findings. Data values are given in terms of the difference between $\delta^{18}O$ of CO_2 and H_2O ($\Delta^{18}O_{CO2\text{-}H2O}$). Calculated equilibrium and kinetic $\delta^{18}O$ values for CO_2 are shown by red boxes and blue circles, respectively. Measured $^{18}O/^{16}O$ ratios are indicated by orange triangles. Finally, exchange system temperature is indicated by green crosses. Axes scales vary to maximize figure space and show detail. Individual values and associated conditions (time, temperature, pCO_2, etc.) are tabulated in Online Resource 2. The following figures include:

OR1-Figure C - June 18, 2013 to August 21, 2013 (full experimental period)

OR1-Figure D - June 18, 2013 to June 21, 2013

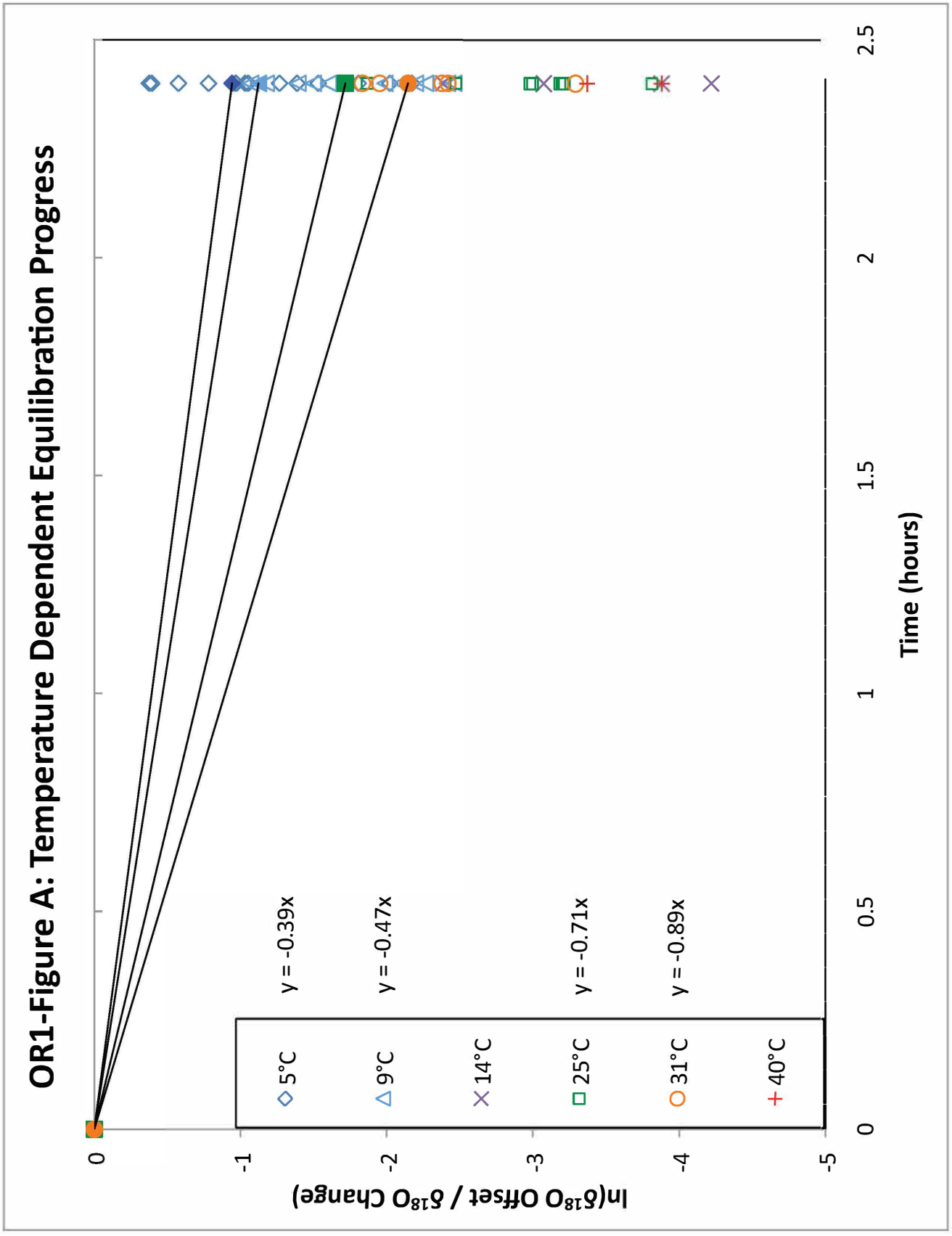
OR1-Figure E - July 1, 2013 to July 11, 2013

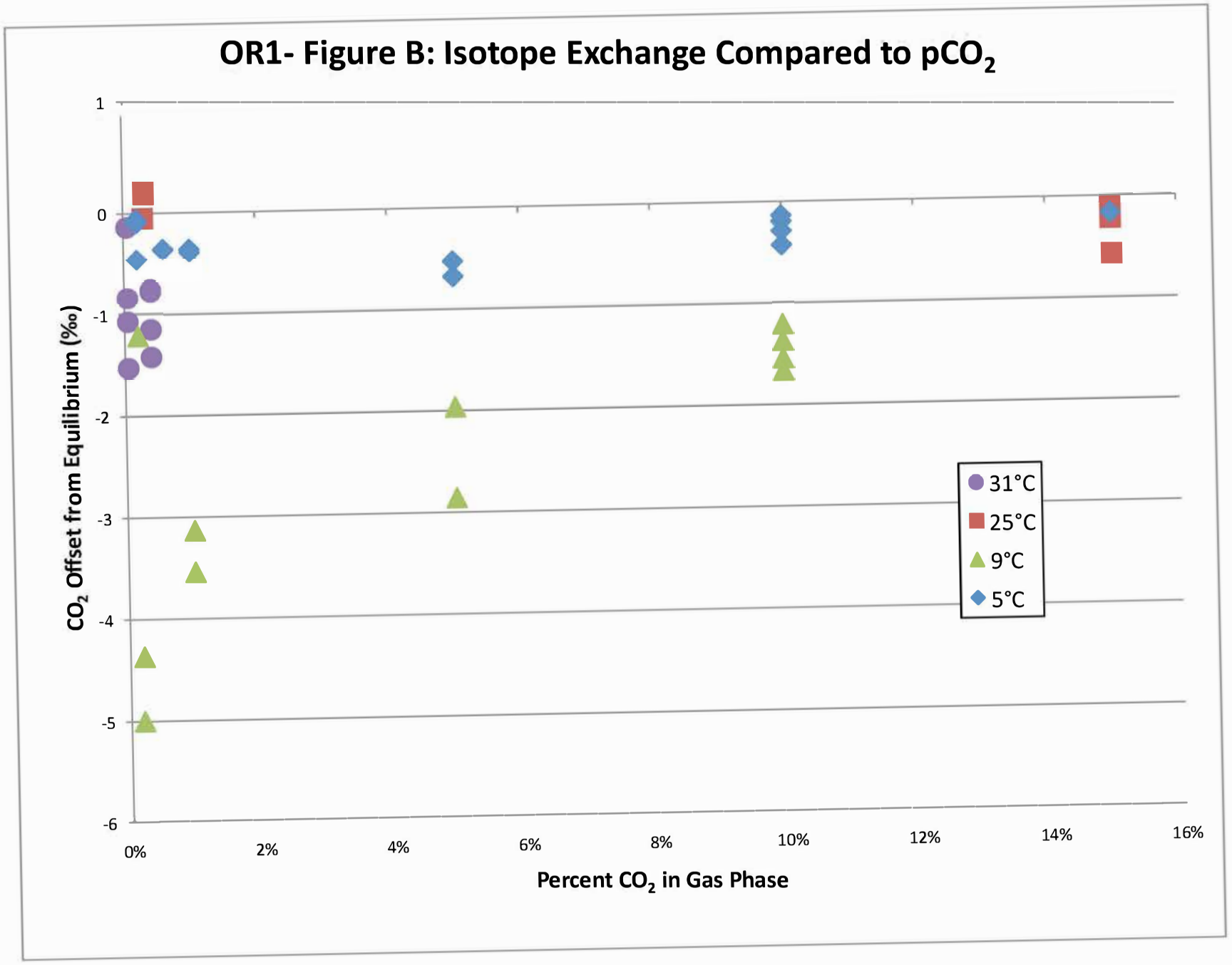
OR1-Figure F - July 14, 2013 to July 24, 2013

OR1-Figure G - July 24, 2013 to August 6, 2013

OR1-Figure H - August 6, 2013 to August 15, 2013

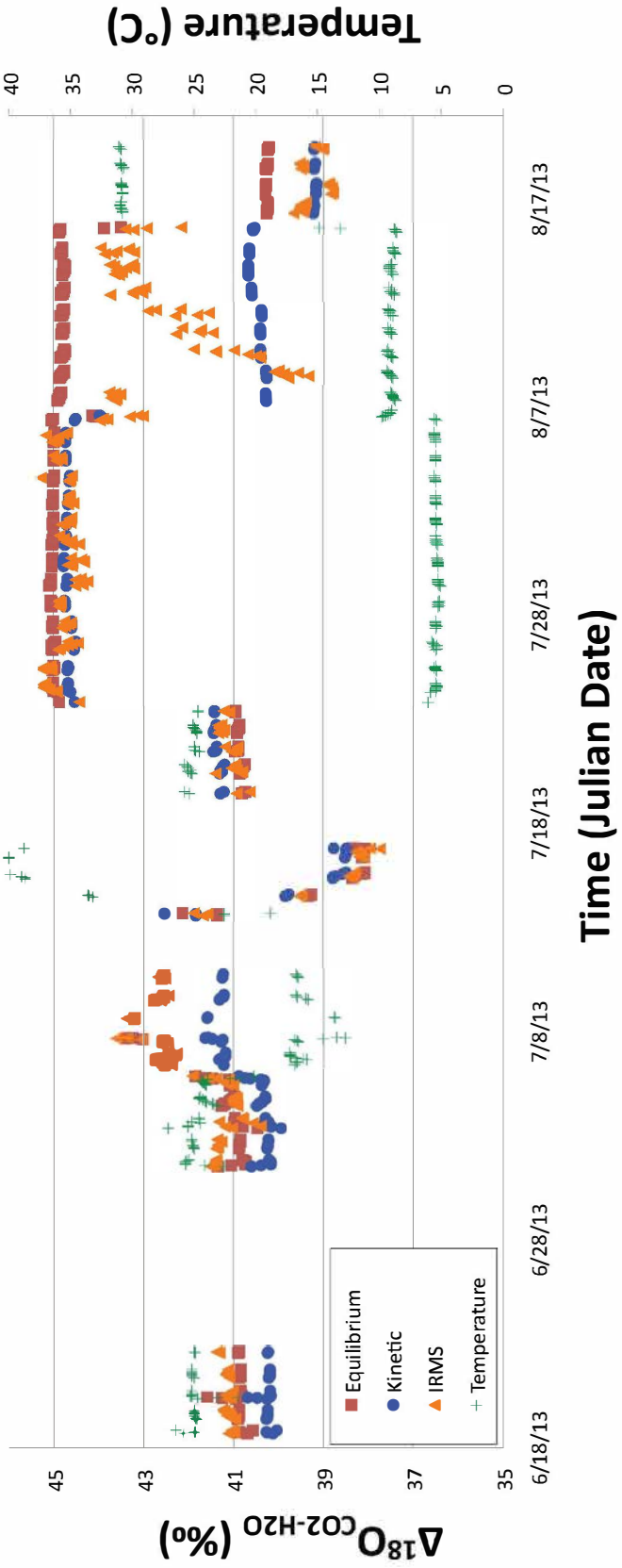
OR1-Figure I - August 14, 2013 to August 21, 2013


OR1-Figure A: Temperature Dependent Equilibration Progress
ln(δ18O Offset / δ18O Change)
Time (hours)
0
-1
-2
-3
-4
-5
0
0.5
1
1.5
2
2.5
5°C
9°C
14°C
25°C
31°C
40°C
y = -0.39x
y = -0.47x
y = -0.71x
y = -0.89x


OR1- Figure B: Isotope Exchange Compared to pCO2
1
0
-1
-2
-3
-4
-5
-6
CO2 Offset from Equilibrium (‰)
0%
2%
4%
6%
8%
10%
12%
14%
16%
Percent CO2 in Gas Phase
31°C
25°C
9°C
5°C

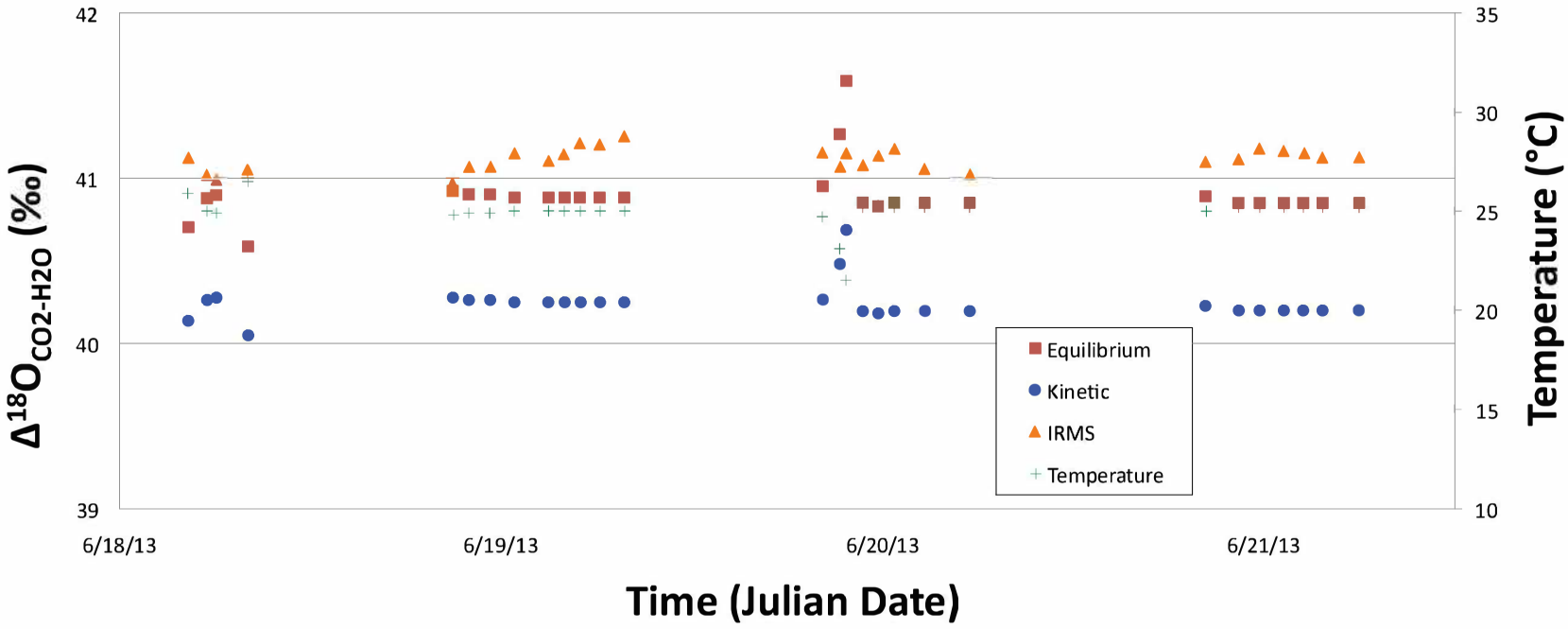
OR1-Figure C

Oxygen Isotope Exchange Monitoring and Assessment



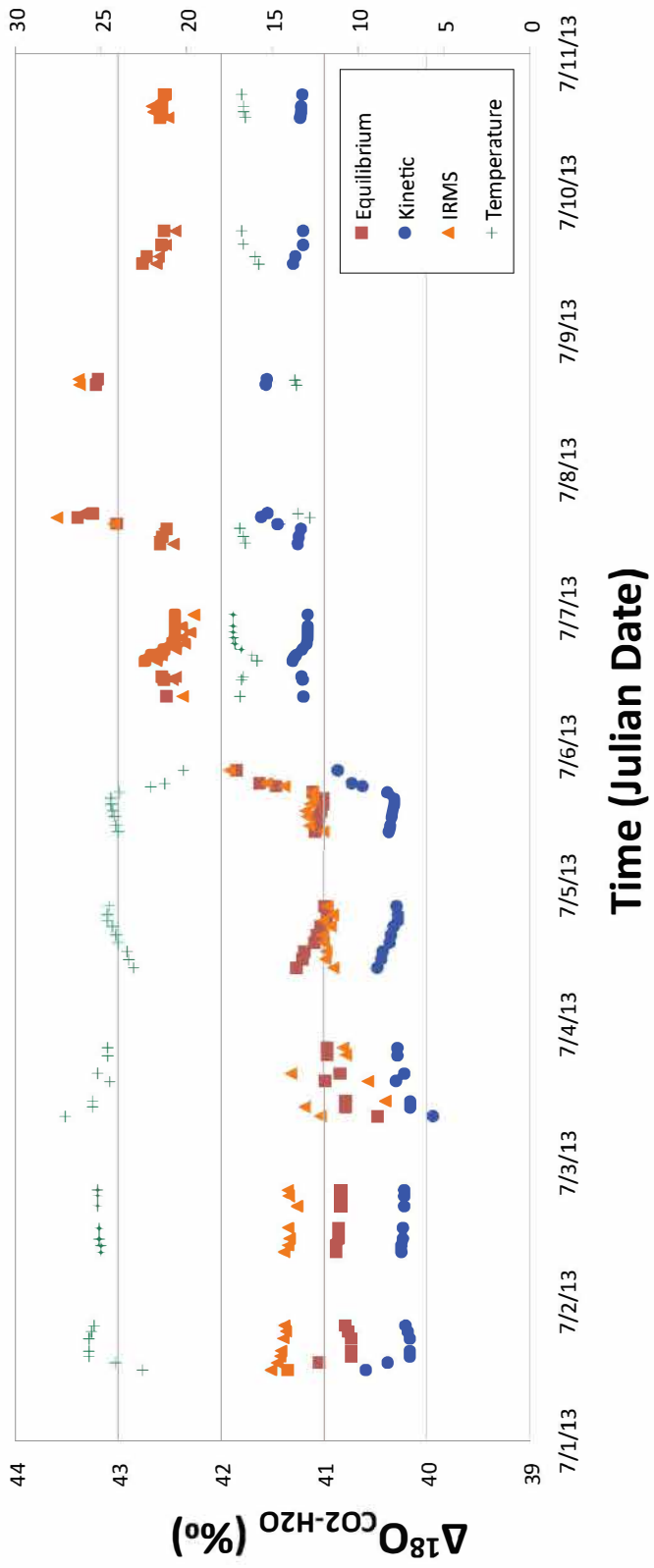
OR1-Figure D

Oxygen Isotope Exchange Monitoring and Assessment



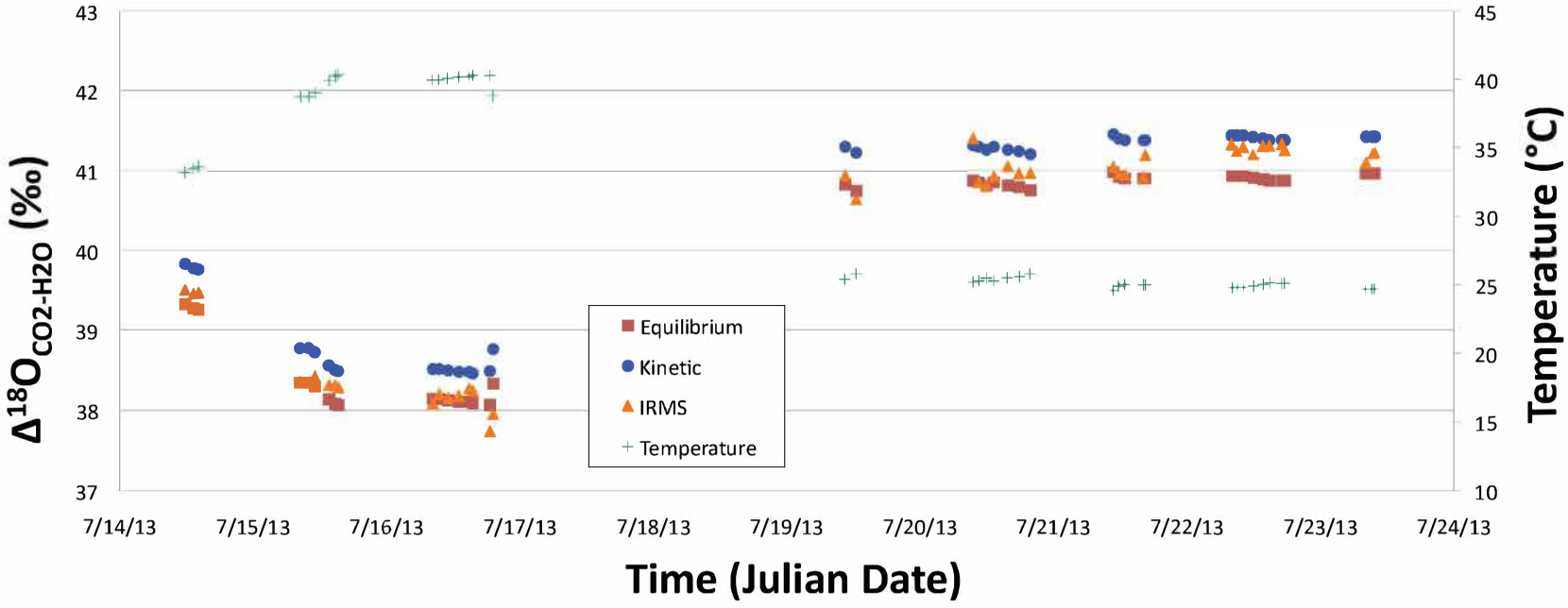
OR1-Figure E

Oxygen Isotope Exchange Monitoring and Assessment



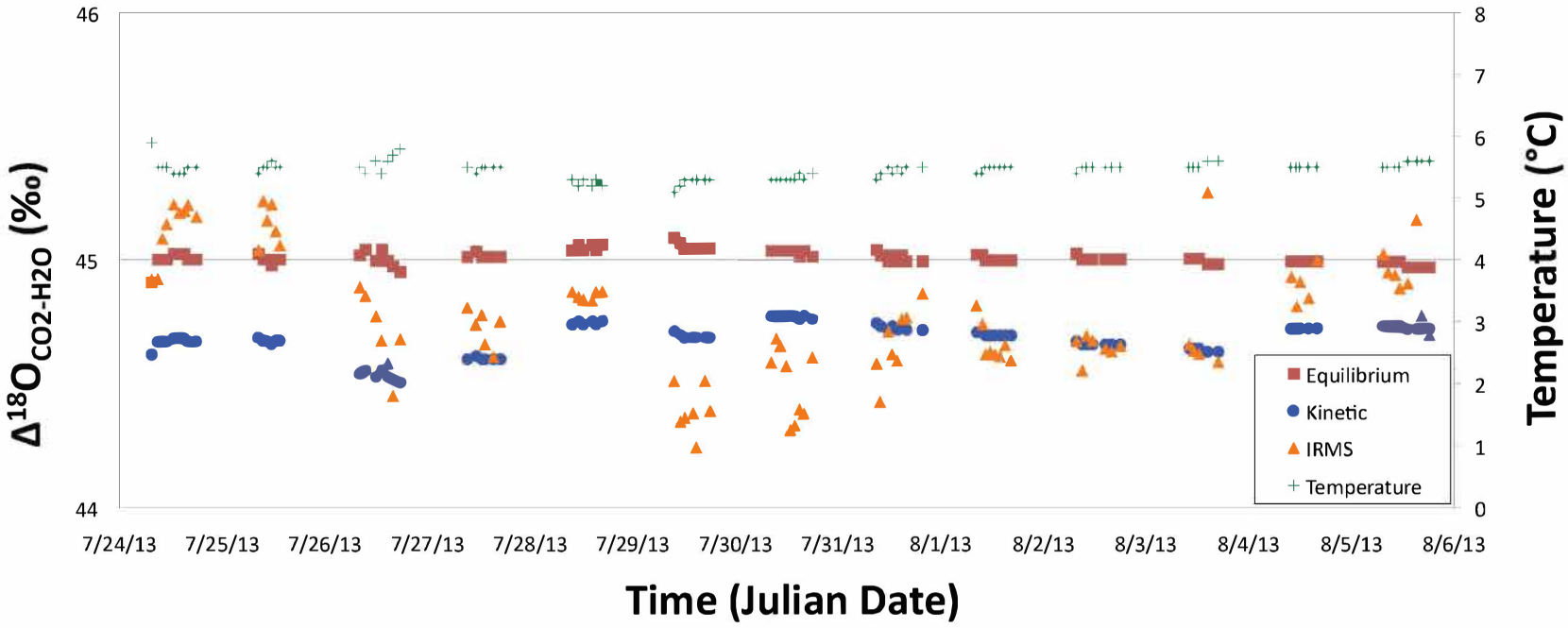
OR1-Figure F

Oxygen Isotope Exchange Monitoring and Assessment



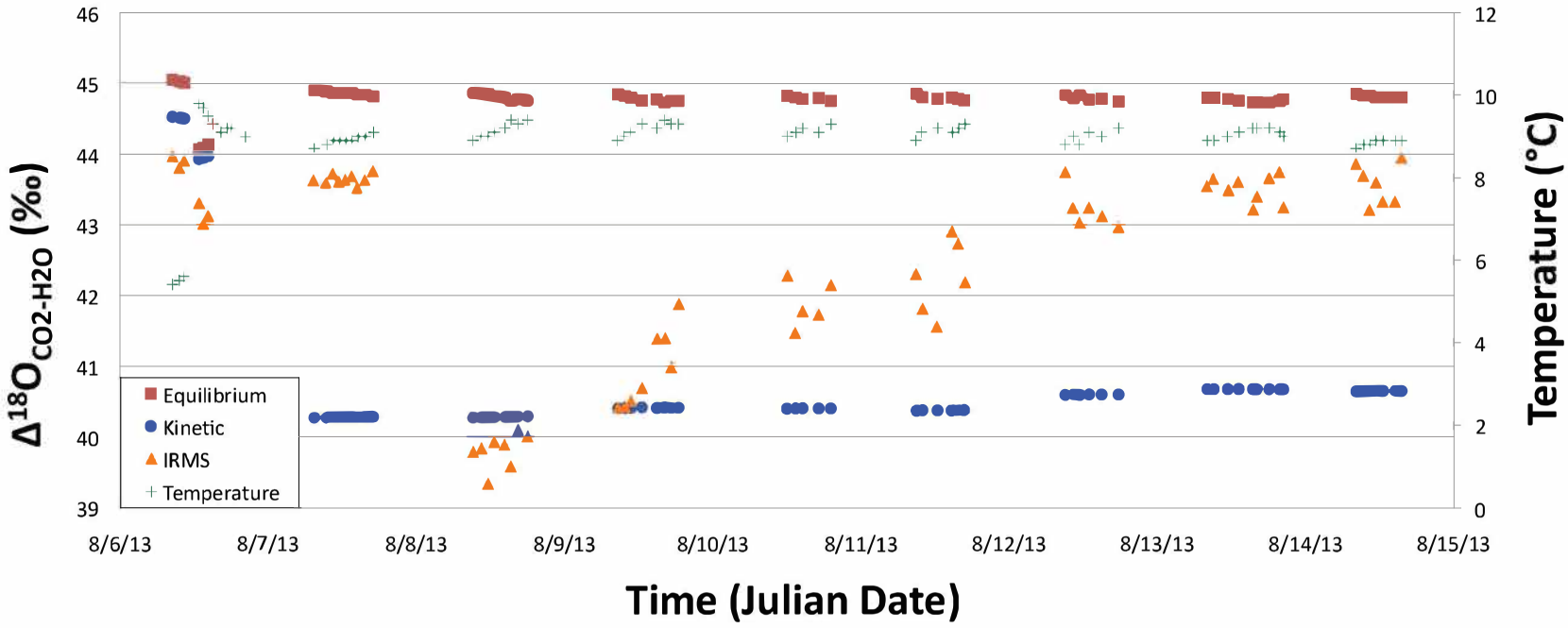
OR1-Figure G

Oxygen Isotope Exchange Monitoring and Assessment



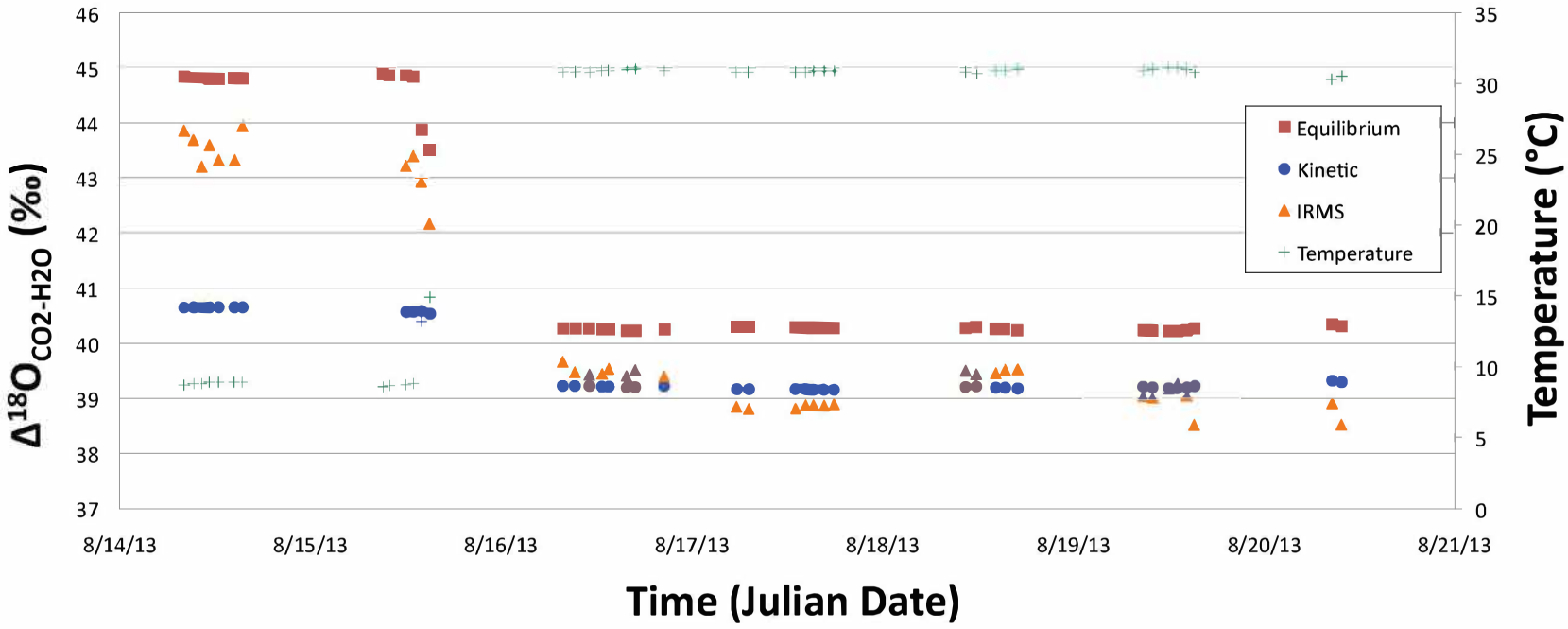
OR1-Figure H

Oxygen Isotope Exchange Monitoring and Assessment



OR1-Figure I

Oxygen Isotope Exchange Monitoring and Assessment



Chapter 2: Near Equilibrium ^{13}C-^{18}O Bonding During Inorganic Calcite Precipitation under Chemo-Stat Conditions

Nicholas P. Levitt[1,†], John M. Eiler[2], Christopher S. Romanek[3], Brian L. Beard[1], Huifang Xu[1], and Clark M. Johnson[1]

[1]NASA Astrobiology Institute and
Department of Geoscience
University of Wisconsin-Madison
1215 W Dayton Street
Madison, Wisconsin, USA
53706

[2]NASA Astrobiology Institute and
Geological and Planetary Sciences
California Institute of Technology
MC 100-23
Pasadena, California, USA
91125

[3]NASA Astrobiology Institute and
Department of Earth and Environmental Sciences
Furman University
Greenville, South Carolina, USA
29613

[†]Corresponding Author's Contact
E-mail: nlevitt@wisc.edu
Tel: (608) 262-8960
Fax: (608) 262-0693

Manuscript published in:
Geochemistry, Geophysics, Geosystems, 2018, 19, 901–920.
https://doi.org/10.1002/2017GC007089

Abstract

We report results of $^{13}C/^{12}C$, $^{18}O/^{16}O$, and ^{13}C-^{18}O "clumped" isotope analyses from a series of calcite precipitation experiments from aqueous solutions under laboratory conditions. Chemo-stat precipitation experiments were performed to synthetically form calcite from aqueous solution onto ^{43}Ca-labeled calcite seed crystals. Formation rate was controlled during the experiments to investigate the effect of precipitation rate and temperature on ^{13}C-^{18}O bonding in calcite, where rates ranged from $10^{-6.88}$ to $10^{-8.20}$ mol m^{-2} s^{-1} at three temperatures (10, 20, and 30°C). No relation was observed between precipitation rate and ^{13}C-^{18}O bonding proportion over the range of precipitation rates used. The relation between Δ_{47} and temperature produced was:

$\Delta_{47} = (0.0461 \pm 0.0094) \times 10^6 T^{-2} + (0.1921 \pm 0.11)$

Comparing solution conditions across multiple experimental data sets indicates an inverse relation between saturation state and ^{13}C-^{18}O bonding, where high super-saturation conditions are likely to be furthest from equilibrium ^{13}C-^{18}O partitioning.

Carbon fractionation factors between calcite and $HCO_3^-{}_{(aq)}$ were found to be a temperature independent value of +1.6‰. Measured $^{18}O/^{16}O$ fractionation factors, yield a temperature relation of:

$10^3 \ln(\alpha_{calcite\text{-}H2O}) = (19.37 \pm 1.0) \times 10^3 T^{-1} + (-35.94 \pm 0.4)$

The temperature-dependent calcite-water $^{18}O/^{16}O$ fractionation relation determined in this study is slightly different (larger $\alpha_{calcite\text{-}H2O}$ value) than those measured in several previous investigations. Significantly, we observe a dependence of the $^{18}O/^{16}O$ isotope fractionation factor on growth rate. Taken together, these findings suggest carbonate growth in our experiments approached equilibrium more closely than previous experiments of this type.

1 Introduction

Oxygen isotope thermometry has a long and important history in geoscience, where, for example, $^{18}O/^{16}O$ fractionation between carbonate and water has been extensively applied as a paleothermometer (Epstein et al., 1953; McCrea, 1950; Urey, 1947;). Application of the O isotope carbonate paleothermometer, however, has been hindered by the large range in temperature-dependent carbonate-water fractionations observed in experimental and empirical studies, such that there is currently no consensus on the correct equilibrium carbonate-water $^{18}O/^{16}O$ fractionation curve (Coplen, 2007; Kim and O'Neil, 1997; Mills and Urey, 1940; O'Neil and Adami, 1969; Watkins and Hunt, 2015; Zeebe, 2014). Recently, a stable isotope thermometer has been proposed involving multiply substituted, or "clumped", isotopologues of carbonate, which has the potential advantage that temperature can be constrained through measurements of carbonate alone, without knowledge of the O isotope composition of the water from which carbonate grew (Dennis and Schrag, 2010; Eiler, 2007; Ghosh et al., 2006; Wang et al., 2004). In addition, clumped isotope analysis allows calculation of the isotopic composition of formation fluid. This technique has been used to investigate the temperatures of deposition and $\delta^{18}O$ of seawater based on measurements of marine carbonates throughout the Phanerozoic, addressing longstanding debates as to whether variations in $\delta^{18}O$ of marine carbonates reflect changes in temperature or seawater O isotope compositions, and in some cases clarifying the role of diagenesis in stable isotope compositions of ancient carbonates (Came et al., 2007; Cummins et al., 2014; Finnegan et al., 2011).

The study of clumped isotopes involves quantification of the preferential bonding between rare stable isotopes (^{13}C to ^{18}O in carbonates) in multiply substituted isotopologues as compared to that predicted from stochastic arrangement. In systems that achieve or closely approach thermodynamic equilibrium, the abundances of multiply substituted isotopologues are

controlled by the effects of isotopic substitution on the reduced masses, and therefore vibration frequencies, of the fundamental modes of molecular vibration (and/or rotation). Singly substituted species generally have lower vibration frequencies than their isotopically "normal" (isotopes of highest abundance) equivalents, and therefore are energetically favored. The doubly substituted species have their vibrational frequencies lowered even more — importantly, usually by slightly more than twice the energy benefit of a single substitution. For that reason, it is energetically favorable to organize the rare heavy isotopes into bonds with each other, where the reduction in system energy is greatest. This energetic effect is counter-acted by configurational entropy, which promotes random distribution of isotopes among all possible isotopologues. In turn, this entropy would produce isotopic ratios that scale with relative atomic abundances and is increasingly important with increasing temperature. It is the balance between the bond-vibration effect and the configurational entropy effect that leads to the temperature dependence of clumped isotope reactions (Eiler, 2007; Urey, 1947; Wang, 2004).

The first empirical clumped isotope thermometry calibration for calcite was determined by Ghosh et al. (2006) using synthetic calcite, and confirmed using natural calcium carbonate precipitated from surface and deep-sea corals that grew at known temperatures. Subsequently, several other calibration studies have been conducted to explore ^{13}C-^{18}O bonding during carbonate precipitation (Bonifacie et al., 2017 [and references therein]; Kelson et al., 2017; Tang et al., 2014; Tripati et al., 2015; Zaarur et al., 2013). With the proliferation of laboratories performing such measurements and calibrations of increasingly diverse materials, it has become clear that there are discrepancies among some calibrations of temperature-dependent carbonate clumped isotope compositions. At least some such discrepancies appear to reflect interlaboratory biases rather than material-specific properties of the carbonates themselves (although there is no consensus as of yet as to exactly why this is so). It is also recognized that some component of

variations in carbonate clumped isotope calibrations can reflect differences in thermodynamically controlled equilibrium constants for different forms of carbonate (HCO_3^- vs. CO_3^{2-}; calcite vs. aragonite; Hill et al., 2014; Schauble et al., 2006; Tripati et al., 2015) or possibly even different acid digestion fractionation factors between calcite and aragonite (Guo et al., 2009).

Some component of these discrepancies, however, likely also reflects different extents of kinetically controlled isotopic fractionation during growth of calibration minerals. It has long been recognized that kinetic effects, and variations in the approach to equilibrium, are likely factors in discrepancies between calibrations of the carbonate-water $^{18}O/^{16}O$ thermometer (Gabitov et al., 2012, Sade and Halevy, 2017; Watkins et al., 2014). By extension, it seems plausible that the same is true of the carbonate clumped isotope thermometer. Such kinetic effects can reflect any of several factors: transport (such as by diffusion); unidirectional hydration, hydroxylation, dehydration or dehydroxilation; solid mineral precipitation rates (Kluge et al., 2014; Tang et al., 2014; Tripati et al., 2015; Watkins and Hunt, 2015); and enzymatic or "vital effects" (Came et al., 2014; Eagle et al., 2013; Petryshyn et al., 2015; Tripati et al., 2010). On short time scales, CO_2 dissolution and degassing have been shown to disrupt clumped isotope equilibrium in the dissolved inorganic C (DIC) pool (Affek et al., 2014; Affek and Zaarur, 2014). However, worth distinguishing is the difference between disequilibrium in the DIC pool related to systems such as speleothems (Daeron et al., 2011; Kluge and Affek, 2012; Kluge et al., 2013) and coral vital effects (Saenger et al., 2012; Spooner et al., 2016) compared to the effect of precipitation rates and mineral surface dynamics that may be partially or fully decoupled from the solution DIC pool (see Discussion below). This body of evidence suggests

that additional experimental work focusing on alternative precipitation regimes may provide further understanding of equilibrium versus kinetic processes during carbonate precipitation. In this study, we systematically assess precipitation rate as a variable in determining equilibrium versus kinetic stable isotope fractionations during synthetic carbonate mineral formation, both in terms of bulk $^{13}C/^{12}C$ and $^{18}O/^{16}O$ fractionations, as well as carbonate clumped (^{13}C-^{18}O) isotope compositions. Most previous experimental work has used CO_2 degassing, diffusion, and/or the manipulation of *p*H to promote carbonate precipitation. For clumped isotope thermometry, such approaches risk producing a DIC pool that is shifted away from clumped and O isotope equilibrium (Affek, 2013) over the course of precipitation. Our approach used constant solution chemical and isotopic compositions ("chemo-stat") to avoid transient changes in clumped isotope composition of the DIC pool. In addition, a unique aspect of this study is our use of seed crystals to remove the potential complicating factor of isotope fractionation attributed to homogenous nucleation mechanisms and/or high initial precipitation rate (Romanek et al., 2011; Gabitov et al., 2012). This approach allowed us to avoid potential CO_2 degassing effects. In addition, we were able to obtain carbonate precipitation using solution compositions that were only slightly supersaturated with respect to calcite (one to four times equilibrium saturation, i.e. Ω = 1 to 4), a much lower level relative to previous studies, which report up to 525 times supersaturation (Dennis and Schrag, 2010; Kelson et al., 2017; Tang et al., 2014). Experiments were conducted over a temperature range of 10°C to 30°C and a range of precipitation rates from 0.006 to 0.132 μmol m^{-2} s^{-1}, significantly slower than those of most previous studies, where documented growth rates were as high as 5.939 umol m^{-2} s^{-1} (Dietzel et al., 2009; Tang et al., 2014). The results of our study show that carbonate growth with these methods, and including the slow rates of precipitation, yields carbonate clumped isotope compositions that are essentially independent of growth rate, and consistent with a sub-set of previous calibrations

(esp., Ghosh et al., 2006, Zaarur et al., 2013, and calibrations of similar slope produced in those two labs).

2 Materials and Methods

This study employed the carbonate precipitation approach commonly referred to as a "chemo-stat" technique (Jimenez-Lopez and Romanek, 2004; Morse, 1974; Mucci and Morse, 1983; Romanek et al., 1992). Conditions were monitored during each experiment to ensure minimal temperature and *p*H variation. Constant chemical conditions (implied by Ca^{2+} and alkalinity concentrations) were maintained by stoichiometric titration of reagent species (Romanek et al., 1992). Additionally, a constant pCO_2 ([gas phase] percent CO_2) was maintained during chemostat carbonate precipitation, which minimizes the potential for kinetically controlled fractionation due to CO_2 degassing or (de)hydration (Affek et al., 2008; Affek and Zaarur, 2014; Daëron et al., 2011; Guo, 2008). Carbonate precipitation was initiated by the introduction of pure calcite seed crystals to a slightly supersaturated solution (Figure 1), which induced heterogeneous growth and avoided the complications that arise from nucleation and growth under high supersaturation and mixed reaction mechanism kinetics. The mass of newly formed carbonate overgrowth was determined in two ways. The first was by mass difference between added seed crystals and final total calcite mass, although this method has the disadvantage of potential mass loss during sample handling. The second, and more precise approach, for determining the mass of carbonate overgrowth used an isotope dilution method (Faure and Mensing, 2009; Gagnon et al., 2012) by incorporating a ^{43}Ca-enriched tracer in the seed crystals (Table S1). This method allowed subtraction of seed crystal mass through measurement of Ca isotope compositions. Table S3 provides a comparison of overgrowth correction by mass balance and isotope dilution, and Table S2 provides analytical details of

standards and equilibrated gases analyzed for Δ_{47}, as well as the calcite seed crystals. Corrections or conversions made based on these materials are described in the Supporting Information. Once the mass of overgrowth was determined, mixing calculations (Affek and Eiler, 2006) were used to calculate the Δ_{47} values of overgrowth carbonate. We note that because the seed crystals were synthesized at 20ºC, and therefore had essentially the same Δ_{47} values as the overgrowth, the correction is very small for 20ºC experiments. The corrections are larger for the 10º and 30ºC experiments. In all cases, uncertainties in the calculated Δ_{47} of newly grown carbonate include propagated errors in both measured Δ_{47} of seeds and overgrowths, and in the mixing ratio of seeds to overgrowths.

2.1 Inorganic Calcite Precipitation

Experiments were conducted at 10, 20, and 30°C for approximately 70 to 240 hours. Calcite was formed from approximately 10 mM solutions of Ca^{2+} and HCO_3^- at *p*H values between 6.3 and 7.0. Chemostat conditions during calcite precipitation were maintained by titrating a master reaction vessel with separate solutions of $NaHCO_3$ and $CaCl_2$ that were independently added. The master solution was prepared by mixing 250 mL of individual $CaCl_2$ and $NaHCO_3$ titrant solutions which had been bubbled with pure CO_2 for approximately 1 hour at room temperature to decrease the *p*H prior to master solution formation so that the mixture would be undersaturated with respect to $CaCO_3$. Soon after mixing, the master solution and new titrant solutions were incorporated into the experimental setup as shown in Figure 1 and introduced to a CO_2/N_2 gas mixture atmosphere as described to allow DIC and pCO_2 to reach a steady state at the desired supersaturation. Master solution *p*H and temperature were monitored during this equilibration period (normally several hours) and after approximately 1 hour of stable *p*H, the experiment was initiated by introduction of seed crystals and commencement of titration.

During experimentation, the solution chemistry was further stabilized by maintaining a constant *p*H via CO_2/N_2 flowing through the master solution reaction vessel. The partial pressure of CO_2 was established by mixing pure CO_2 and N_2 to total mixing ratios as indicated in Table 1. As an example, a pCO_2 of 15% was achieved by combining flow of 15 mL/minute of CO_2 and 85 mL/minute of N_2. Most calculated CO_2 partial pressures were within 1% of values set by mass flow controllers and all values average an offset of -0.1%. The O isotope composition of reagent DIC ($NaHCO_3$) was allowed to exchange with the starting master or titration solution H_2O (see Figure 1) at low *p*H for 4 to 10 days depending on the length of the previous experiment at room temperature and then an additional several hours at the temperature of experimentation (see Supporting Information for further details). This precaution circumvented the need (if any; Kelson et al., 2016) to use carbonic anhydrase for O isotope equilibration (Uchikawa and Zeebe, 2012; Watkins et al., 2013).

Calcite was precipitated in 1 L Pyrex containers that had been custom fitted with glass flow-through style jackets for temperature control (Figure 1). Titrant solutions were likewise jacketed and temperature controlled. Water was circulated by a heating/refrigerating water bath. The reaction vessel was mixed using a magnetic stir bar during carbonate formation. Experiments were designed to produce up to 160 mg of overgrowth carbonate on 80 mg of seed crystals. Master solution titration began immediately upon addition of seed crystals and ended shortly before product collection. Carbonate from the master solution was collected by decanting the reaction fluid into a 0.4 μm filtered vacuum system. The reaction vessel and calcite seeds were rinsed with DI water during filtration to prevent the formation of chloride salts. A small amount of methanol was used to help remove adsorbed water during filtration prior to further drying in an oven at 40°C for approximately 24 hours. Following oven drying,

the experimental product was checked for mineralogy by XRD and then stored in a Dri-Rite filled desiccator until analysis.

2.2 Experimental Conditions

Temperature and precipitation rate were the primary variables explored. Three temperatures were investigated: 10, 20, and 30°C, and these temperatures were controlled to within ±1°C during carbonate formation using a water-jacketed vessel. Temperature was measured with a thermocouple integrated with the Cole-Parmer electrode and the time-weighted standard deviation during mineral growth was ~0.1°C. The CO_2-H_2O exchange system was also maintained at the experimental reaction temperature during CO_2 conditioning. Most reagent solutions were flushed with effluent CO_2/N_2 prior to use to replace the C isotope composition of $NaHCO_3$ reagent (see Supporting Information for details). Carbonate precipitation rates (moles m^{-2} s^{-1}) were varied by changing the rate of titrant solutions to the master solution (Figure 1) for various experimental times. The desired length of a given experiment determined the titration rate needed to add ~ 250 mL of each titrant solution. In all cases, low supersaturation states (2-4 times saturation) were used to remain as close to equilibrium conditions as possible (Watkins and Hunt, 2015; Wolthers, et al., 2012). Actual values in this range were dictated by the accuracy to which pCO_2 could be set by mass-flow controllers (0.2 to 10 ± 0.5% mL min^{-1} for CO_2 and 20 to 1000 ± 0.5% mL min^{-1} for N_2). Master and titrant solutions were prepared such that concentrations of Ca^{2+} and alkalinity would be 10 mM and 10 milli-equivalents (meq) in the master solution during carbonate precipitation. Actual solution concentrations were measured before and after each experiment (Table S1 and see Supporting Information for full details).

Saturation states were modeled with PHREEQC software (Parkhurst and Appelo, 2013) and phreeqc.dat database before and after an experiment.

2.3 Geochemical Analyses and Notation

Stable Ca isotope analysis, XRD, surface area measurements, and determination of solution chemistries were performed at the University of Wisconsin - Madison. Bulk C, bulk O, and clumped isotope compositions for calcite were determined at the California Institute of Technology by isotope ratio mass spectrometry on both of two nearly identical Thermo-Finnigan MAT 253 instruments. Oxygen isotope compositions of solution H_2O, as well as C isotope compositions of DIC, were analyzed at the University of California – Davis. Values of $\delta^{13}C$ reported in this investigation are with respect to international standard Vienna Peedee Belemnite (VPDB), and $\delta^{18}O$ values are with respect to Vienna Standard Mean Ocean Water (VSMOW). Clumped isotope compositions are described in terms of the Absolute Reference Frame (ARF) as described by Dennis et al. (2011). See the Supporting Information for full details, including methodologies as well as precision and accuracy considerations.

Calcium was prepared prior to isotope analysis by ion-exchange chromatography similar to that reported by Li et al. (2012). Approximately 0.25 mg of calcite or 2.5 mL of reaction solution was processed for Ca isolation. Calcite was dissolved in dilute ultra-pure nitric acid and converted to pure $Ca(NO_3)_2$ before purification. Likewise, nitric acid was added to experimental solutions and dried until only solids remained. These solids were repeatedly dissolved with nitric acid and re-dried three times to ensure all cations were transformed into nitrate salts. Calcium was isolated and purified from other cations by ion-exchange chromatography before isotope analysis. Calcium isotope analyses were performed using a Micromass IsoProbe MC-ICP-MS at the University of Wisconsin-Madison. Helium was used as the collision gas for

thermalization and H_2 was used to suppress argide isobars by charge-transfer reactions. Calcium solution concentrations of 10 ppm were introduced to the Ar plasma using a self-aspirating 50 to 100 μL min^{-1} nebulizer coupled to a Cetac Aridus II membrane desolvating system. The cone voltage was set to 200 to 500 V. These settings allowed Ca ion intensities of 44.5, 0.34, 0.07, and 1.22 V at mass numbers 40, 42, 43, and 44, respectively. A 2% HNO_3 solution was used as a rinse solution between individual sample measurements. The sample solutions were also measured using a standard-sample-standard bracketing protocol. Concentration-related matrix effects were corrected according to standard solutions ranging from 5 to 15 ppm Ca, as outlined by Albarède and Beard (2004).

Carbonate C and O isotope analyses as well as clumped isotope analyses were performed on two Thermo-Finnigan MAT 253 (Thermo Scientific, Bremen, Germany) isotope ratio mass spectrometers according to the procedures outlined by Passey et al. (2010). A single analysis consisted of digestion of 8-10 mg calcite in a common phosphoric acid bath at 90°C followed by an automated CO_2 cleaning and purification process. See Passey et al. (2010) for automation and sample preparation details. Carbon and O isotope ratios for sample and standard material were determined by Isodat software with comparison to an Oztech reference gas of known isotope composition. An O isotope acid fractionation factor of 1.00821 (Swart et al., 1991) was used to correct gas phase CO_2 back to calcite $\delta^{18}O$ values. A clumped isotope value of 0.082‰ was used to correct for acid digestion (Deflies et al., 2015). In addition to unknown samples, standard reference material was also analyzed in tandem during each analytical session.

Oxygen isotope ratios for water were determined using a Laser Water Isotope Analyzer V2 (Los Gatos Research, Inc., Mountain View, CA, USA) and standardized using working materials that were calibrated to International Atomic Energy Agency standard reference materials VSMOW, Greenland Ice Sheet Precipitation (GISP), and Standard Light Antarctic

Precipitation (SLAP). DIC C isotope analyses utilized a Delta V Plus (Thermo Scientific, Bremen, Germany) isotope ratio mass spectrometer to determine ratios of evolved trace gas phase CO_2. The IRMS system was interfaced with a Finnigan Gasbench II device for sample preparation and transfer. DIC analysis was similarly standardized according to materials traceable to National Institute of Standards and Technology reference material 8545.

Errors given in Table 2 and throughout the paper represent two standard deviations about the mean for measured values. Propagated errors for derivative values such as precipitation rates and fractionation factors are determined as the square root of the sum of the squares. Isotopic compositions in Table S3 that consider overgrowth mass uncertainty are presented as the difference between the determined overgrowth mass and the 2σ maximum and minimum overgrowth. The expression used to calculate C and O isotope composition of overgrowth carbonate is

$$\boldsymbol{\delta_o = \frac{(\delta_{tot} - \delta_s(1-\chi))}{\chi}} \quad \text{Equation 1}$$

where δ_o is the isotope composition of the overgrowth, δ_{tot} is the measured isotope composition of the overgrowth plus seed crystals, δ_s is the isotope composition of the seed crystals, and χ is the mass fraction of overgrowth to final total carbonate. While this equation is not exact because it assumes linearity in terms of δ notation, tabulated values are accurate to 0.03‰ for the range of $\delta^{13}C$ and $\delta^{18}O$ values reported here, and hence do not significantly affect corrected δ values.

Bulk stable isotope compositions (C, O, Ca) are reported in units of per mil (‰) in standard form:

$$\boldsymbol{\delta^n X = \left(\frac{R_{sa} - R_{std}}{R_{std}}\right) \times 10^3} \quad \text{Equation 2}$$

where *n* is 13 (C), 18 (O), or 43 (Ca), *X* is the element of interest, R_{sa} is the isotope ratio of the sample, and R_{std} is the isotope ratio of a reference standard. Similarly, the convention for describing the magnitude of clumping in a sample is given by the Δ_i value (also in units of per

mil) where *i* is the atomic mass of the isotopologue of interest. Examples include Δ_{47} for $^{13}C^{18}O^{16}O$ and Δ_{63} for $^{13}C^{18}O^{16}O_2^{2-}$. Measured Δ_{47} values do not, however, exactly equal the deviation in $^{13}C^{18}O^{16}O$ species relative to random distribution, as a small fraction of very rare isotopologues also have a mass of 47, although these are unimportant at the current level of precision. Δ_i is defined as

$$\Delta_i = \left(\frac{R_i - R_{i^*}}{R_{i^*}}\right) \times \mathbf{10^3} \quad \text{Equation 3}$$

where Ri is the abundance ratio of the isotopologue of interst, Ri* is an analogous ratio for a population of isotopologues that has the same bulk isotopic composition but a stochastic distribution (Huntington et al., 2009). Both ratios are relative to the most abundant isotopologue.

The partitioning of isotopes between two phases is described here as

$$\mathbf{10^3} ln(\alpha_{a-b}) = \mathbf{10^3} ln\left(\frac{1000 + \delta_a}{1000 + \delta_b}\right) \approx \delta_a - \delta_b \quad \text{Equation 4}$$

where $\alpha_{a\text{-}b}$ is defined as the fractionation factor between the two phases (*a* and *b*) and δ_a and δ_b are the isotope compositions of the two phases ($\delta^{13}C$ and $\delta^{18}O$).

The saturation state convention of Morse and Mackenzie (1990) is used throughout the paper and defined as

$$\Omega_{calcite} = \frac{a_{Ca^{2+}} + a_{CO_3^{2-}}}{K_{calcite}} \quad \text{Equation 5}$$

where *a* denotes the activity of an ionic species and K is the solubility product. Activities and saturation were determined by PHREEQC (Parkhurst and Appelo, 2013) software. The reference state solubility product for calcite in the phreeqc.dat database is $K = 10^{-8.48}$.

3. Results

3.1 Solution Chemistry & Product Carbonate Characterization

Table 1 lists the measured average Ca, alkalinity, pCO_2, and *p*H values, as well as calculated saturation states for all experiments performed during this study. Starting and ending

master solutions were analyzed to verify minimal solution chemistry variation during the experiments. The average of starting and ending aqueous Ca concentrations ranged from 8.1 to 11.2 ± 1.1 mmol L^{-1}. Similarly, alkalinity concentrations were 6.7 to 9.4 ± 0.07 meq. Time-weighted *p*H average values were between 6.3 and 7.0 ± 0.07 *p*H units. These *p*H values were established in part by pCO_2 concentrations in the 5 to 16% range during the experiments. Additionally, a constant partial pressure of CO_2 (pCO_2, reported in terms of volume percent carbon dioxide) helped to minimized drift or fluctuation in solution conditions. These parameters produced saturation states with respect to calcite of 1.1 to 3.8 ± 0.01.

The average mass of overgrowth calcite per experiment was approximately 141 mg (Table S1), which compares to the average mass of seed crystal used of 80.4 mg per experiment. Variation in overgrowth mass between experiments is believed to be due to the small amount of saturation state variability and/or small differences (~ 50 mL) in the actual amount of titrant solution added to the master solution at the end of each experiment. Isotope dilution calculations for the mass of overgrowth have an average uncertainty of ± 2.9% (~4 mg), as determined by the 2-standard deviation value (± 1.07 ‰) about the mean of in-house Ca standard solutions analyzed during ending master solution isotope composition characterization. For Δ_{47} values, this error translates to a propagated maximum average uncertainty due to overgrowth of ± 0.017‰, which is less than the 2-SD external precision (standard deviation about the mean) determined for Δ_{47} analyses of carbonate standards (±0.034‰). The uncertainty in Δ_{47} values reported in Table 2 accounts for overgrowth as well as measurement replication. Errors for each analysis associated with isotopic composition measurement and overgrowth correction are given in Table S3.

The Ca isotope composition was also measured for each master solution after calcite filtration was performed. This analysis was intended to identify any dissolution of seed crystals

during the experiments, which was a possibility given the low saturation state of the experiments. Measured Ca isotope compositions of final solutions were within that of starting master solutions for all but five experiments, where the calculated mass of dissolved seed crystals ranged from 7.0 to 15.8 mg, which is equivalent to dissolution of ~3.8-10.7% of the seed crystals, indicating that these experiments involved some dissolution (possibly due to stir bar grinding and/or Ostwald ripening) despite net growth of new calcite. Although such results provide insights into the dynamic nature of the calcite interface during precipitation, they do not affect the calculated Δ_{47} values for the overgrowths because all five of the experiments that showed minor seed crystal dissolution were performed at 20°C, and hence the Δ_{47} values for the seed crystals were essentially identical to the overgrowths. Therefore, these five experiments remain included in the dataset.

Overgrowth carbonate mineralogy was verified by microscopic inspection as well as XRD. A representative SEM image and XRD patterns are provided in the Supporting Information (Figures S1 and S2). In all cases, only calcite was identified in reaction products. Seed calcite was further characterized by BET surface area analysis (Brunauer et al. 1938) to be 1.2±0.2 $m^2\ g^{-1}$. This value was used to determine precipitation rates, in conjunction with calcite masses (seed and overgrowth), and experiment length. Precipitation rates used during these experiments ranged from 0.006 to 0.034 μmol $m^{-2}\ s^{-1}$ for 10°C experiments, from 0.012 to 0.132 μmol $m^{-2}\ s^{-1}$ for 20°C experiments, and 0.012 to 0.056 μmol $m^{-2}\ s^{-1}$ for 30°C experiments. Error-propagated uncertainties for precipitation rates ranged between 2 and 19%.

3.2 Isotopic Analyses

$\delta^{13}C$ values for overgrowth carbonate ranged from -1.3 to 1.7‰, and $\delta^{18}O$ values for overgrowth carbonate ranged from 19.0 to 24.1‰ (Table 2). The C isotope composition of

starting and ending master solution DIC are reported in Table S1, and $\delta^{13}C$ values for DIC ranged from -6.6 to -1.5‰. Likewise, the O isotope composition of master solution water is given in Table 1 and ranged from $\delta^{18}O$= -9.5 to -8.2‰. Most ending solutions were within 0.3‰ of starting master solution values, confirming maintenance of chemostat conditions in terms of isotopic composition. Individual starting and ending master solution values are presented in Table S1.

Measured O and C isotope compositions allowed for determination of fractionation factors between calcite and water as well as between calcite and calculated values of individual DIC species. Average $^{18}O/^{16}O$ fractionations between calcite and water ($10^3\ln\alpha_{cc\text{-}H2O}$) at 10°C, 20°C, and 30°C were found to be 32.5±0.4‰, 30.0±0.7‰, and 28.1±0.5‰, respectively. Bicarbonate (HCO_3^-) isotope compositions were calculated from measured DIC $\delta^{13}C$ values and used to determine the $^{13}C/^{12}C$ fractionation factors between calcite and bicarbonate($10^3\ln\alpha_{cc\text{-}HCO3}$), which, at 10, 20, and 30°C, were 1.6±0.2‰, 1.6±0.5‰, and 1.6±0.4‰, respectively. Uncertainty in $10^3\ln\alpha$ values represents 2SD external error and seed crystal subtraction. Average fractionation factors only consider experiments that used titrant solutions that had been appropriately pre-flushed with a N_2/ CO_2 gas mixture (see "Next Reagents" section of Figure 1 and the Supporting Information). Specifically, the titrants for experiments UWAI-002, 003, 004, 008, and 009 were not treated with a N_2/ CO_2 gas mixture before use. Additionally, UWAI-016 through 021, as well as UWAI-047 and -048, were treated at a different temperature than the temperature at which they were used during experimentation. For example, if reagents were flushed with CO_2 exiting a 20°C experiment and then those reagents were used for 10°C experiments, their $\alpha_{CaCO3\text{-}HCO3}$ values were found to be systematically different from values obtained where temperature of flushing and experimental temperature was the same. This observation is believed to reflect a fractionation in C isotopes between gas phase and DIC that

was subsequently transferred to the reagent alkalinity used for experiments. These relations are observable in Table 2. Values in bold font average to 1.6‰.

Clumped isotope compositions for overgrowth calcite are presented in Table 2. Additional details regarding standards, heated gasses, and equilibrated gasses analyzed during the same sessions as experimental samples (given in Table S2), whereas information related to raw uncorrected values for C, O, and clumped isotope analyses, which are with respect to an Oztech reference gas (the working gas used in the Caltech lab), are included in Table S3. The latter table also includes corrected clumped isotope values relative to the ARF, seed crystal contribution, and acid digestion fractionation. Clumped isotope compositions for overgrowth carbonate ranged from Δ_{47} = 0.742-0.797‰ for 10°C experiments, from 0.707-0.749‰ for 20°C experiments, and 0.650-0.721‰ for 30°C experiments. Average Δ_{47} values for 10, 20, and 30°C are 0.765 ± 0.036‰, 0.729 ± 0.021‰, and 0.689 ± 0.039‰, respectively. It is also worth noting that that the method used to form seed crystals has been reported to initially form amorphous calcium carbonate which transforms to vaterite and then calcite (Rodriguez-Blanco et al., 2011; see Supporting Information for details). However, despite this pathway, the Δ_{47} value of the seed calcite was found to be 0.735 ± 0.024 ‰ (n=9) which is in good agreement with overgrowth values at this temperature. Uncertainty in Δ_{47} values represents 2SD external error (standard deviation about the mean) which also accounts for seed crystal subtraction.

4. Discussion

Our data set allows assessment of ^{13}C-^{18}O bonding with respect to equilibrium conditions from an O, C, and clumped isotope perspective as well as from a range of solution conditions. In addition to precipitation rate, *p*H and saturation effects have also been considered. We find no direct evidence relating *p*H variability to bulk isotope fractionation (or compositions), as well as

no relation between ^{13}C-^{18}O bonding and *p*H. However, admittedly, our range of *p*H values is limited. ^{13}C-^{18}O bonding, conversely, is shown to increase with decreasing saturation state when multiple data sets are considered. Indirect factors (DIC speciation) related to *p*H are considered through the model of Watkins and Hunt (2015). This model was chosen for consideration due to its treatment of C, O, and clumping isotope partitioning in terms of precipitation rate, parallel to the focus of our study of precipitation rate effects. A detailed description of the Watkins and Hunt model can be found in the Supporting Information. As will be discussed below, we suggest that complete O isotope equilibrium between calcite and water has yet to be obtained for experimental synthesis of calcite, including the current study. Although the information presented here does not exclude the possibility of disequilibrium ^{13}C-^{18}O bonding under some precipitation rates as discussed below, we find no convincing evidence for this phenomenon in our dataset. Our results do, however, add evidence to the argument that faster calcite precipitation and/or higher saturation states can allow kinetic isotope effects to influence the partitioning of C and O during carbonate mineral formation from solution, which is discussed below in more detail.

4.1 Carbon Isotopes

The rate dependence of C isotope fractionations among C species can provide insights into the potential kinetic effects in isotopic partitioning as related to DIC speciation based on equilibrium constants for the system CO_2-H_2O-DIC (Zeebe and Wolf-Gladrow, 2001). Watkins et al. (2014; see also Watkins and Hunt, 2015) explore kinetic isotope fractionation between ions in solution and solid phase carbonate during calcite precipitation, and conclude that deviations from equilibrium can be understood through differences in rates of solid formation versus isotope exchange between DIC species and water. More specifically, at very slow precipitation

rates, isotope fractionation between DIC and calcite is a function of equilibrium partitioning between H_2O, HCO_3^-, CO_3^{2-}, and $CaCO_3$(s). At faster growth rates, however, as the kinetic limit is approached, the isotope composition of precipitating carbonate is determined by the ratio of HCO_3^- to CO_3^{2-} incorporation and kinetic fractionation factors between each species and the mineral phase. Such a model is based on assuming the equilibrium fractionation is recorded by the work of Coplen (2007) and Bottinga (1968) at a log value rate of $\sim \leq$ -9.5 moles m^{-2} s^{-1}, as well as the kinetic fractionations inferred for C isotopes from Romanek et al. (1992).

In Figure 2 we model the kinetic effects on C isotope fractionation at 20°C, following the approach of Watkins and Hunt (2015), illustrating the isotope fractionation between calcite (xtl) and aqueous CO_3^{2-}. Analogous figures for 10 and 30°C are included in the Supporting Information (Figure S3 and S4). When our results are compared with previous work of Romanek et al. (1992), reasonable agreement is observed over a range of precipitation rates in terms of the model of Watkins and Hunt (2015) using a surface speciation ratio of HCO_3^- to CO_3^{2-} of 100:1. The surface speciation ratio is a model parameter determined by the expression $\Theta = 10^{8.6\text{-pH}}$ as reported by Wolthers et al. (2012). A poor fit is observed between the experimental data and modeled fractionation assuming a surface speciation ratio of HCO_3^- to CO_3^{2-} of 0.25:1. The mismatch, however, is likely explained by a C isotope composition of the surface species DIC that is different than that represented by the bulk solution DIC. Romanek et al. (1992) also varied temperature (10, 25, and 40°C) during their study and found an average calcite-bicarbonate fractionation of 1.0 ± 0.2‰ for all temperatures. Regardless of rate considerations, the lack of temperature dependence for this study and Romanek et al. (1992) suggests that O isotopes control isotope partitioning between DIC and calcite, and C isotopes have little to no influence. An alternative explanation would be a scenario where there is little to

no temperature dependence for the C isotope composition of carbonate ions and calcite primarily forms from CO_3^{2-}.

4.2 Oxygen Isotopes

Calcite from Devils Hole cave system of Nevada, USA is often invoked to describe equilibrium isotope fractionation due to its very slow rate of precipitation, and this produces a relatively large $^{18}O/^{16}O$ fractionation factor of $10^3\ln(\alpha_{calcite\text{-}H2O}) = 28.09 \pm 0.13$ at ~34°C (Coplen, 2007; Kluge et al., 2014). The error-weighted slope determined in our study is 19.3 in units of $^{18}O/^{16}O$ $10^3\ln\alpha_{cc\text{-}H2O}$ per 1000 T^{-1} (K). For comparison, the shaded areas of Figure 3 represent a 95% confidence field between temperature and $10^3\ln(\alpha_{calcite\text{-}H2O})$ as reported by Zaarur et al. (2013) and Kim and O'Neil (1997). These temperature-dependent slopes are 17.8 and 18.0 in units of $^{18}O/^{16}O$ $10^3\ln\alpha_{cc\text{-}H2O}$ per 1000 T^{-1} (K) for Zaarur et al. and Kim and O'Neil, respectively. The temperature-dependent equilibrium fractionation derived by Watkins et al. (2013) intersects the proposed fractionation factor for Devils Hole, but is offset to higher $^{18}O/^{16}O$ fractionation than all other experimental studies, including ours (Figure 3). The relations in Figure 3, therefore, most likely reflect a combination of equilibrium and kinetic contributions to the overall O isotope fractionation.

The partitioning of O isotopes during calcite formation from water observed in our experiments are listed in Table 2 and shown in Figure 4 as a function of precipitation rate. The error-weighted slopes for log rate versus $^{18}O/^{16}O$ fractionation at 10, 20, and 30°C are -0.53 ± 0.40, -1.05 ± 0.35, and -0.62 ± 1.21, respectively, in units of $10^3\ln\alpha_{cc\text{-}H2O}$ per log rate (moles m^{-2} s^{-1}). The 20°C relation might be disproportionately weighted toward a steeper slope due to the faster precipitation rates used in those experiments. These slopes are broadly consistent with analogous slopes of -1.288, -1.279, and -0.624 in units of $^{18}O/^{16}O$ $10^3\ln\alpha_{cc\text{-}H2O}$ per log rate (moles

m^{-2} s^{-1}) for the 5, 25, and 40°C syntheses reported by Dietzel et al. (2009). However, a recent study by Devriendt et al. (2017) has asserted that calcite forming from the experiments reported in 2009 was influenced by DIC that was not in equilibrium with solution water. The slightly lower slopes reported here, on the other hand, may be related to the slower precipitation rates, as discussed below, and/or fuller O isotope equilibrium between H_2O and DIC before solid formation.

Oxygen isotope fractionations are a function of precipitation rate (Figure 5), similar to what was found for $^{13}C/^{12}C$ fractionation versus growth rate using the Watkins and Hunt model, but the equivalent trend for $^{18}O/^{16}O$ requires slight modification. The $^{18}O/^{16}O$ fractionation between individual DIC species and calcite inferred by our experiments is lower than those predicted by Watkins and Hunt by up to ~1.5 ‰ (Figures 5, S5, and S6). Possible explanations for this observation include 1) the contribution of HCO_3^- and CO_3^{2-} ions on the surface (Θ, and to the formation) of solid phase carbonate is not proportional to their concentration ratios in the aqueous phase, 2) invalid use of the Devils' Hole calcite fractionation factor as the assumed equilibrium value as extrapolated to other temperatures, 3) invalid fractionation factors between DIC and water, between individual DIC species, and/or DIC species and calcite, 4) O isotope equilibrium between DIC and water was not actually achieved during the experiments of Watkins et al. (2014), or 5) the fractionation-rate dependence used in the model of Watkins and Hunt (2015) is not valid for *p*H values in the 6 to 7 range.

We first explore the assumption that HCO_3^- and CO_3^{2-} contribute to calcite in their aqueous proportions as described by the relation $\Theta = 10^{8.6-pH}$. That both species contribute to the O isotope compositions of calcite is suggested by the fact that the measured data plot between the HCO_3^- and CO_3^{2-} isotope compositions. If, however, CO_3^{2-} contributed a greater proportion of O to calcite, the observed data can be fit using a surface HCO_3^-:CO_3^{2-} ratio of 0.25 (Figure 5).

Such a change in surface HCO_3^-:CO_3^{2-} ratio, relative to the solution proportion of 100, finds support in the recent study of Andersson et al. (2016), who used density functional theory to show that adsorbed carbonate ions are stable on the surface of calcite even when solutions above the surface-bound ions are characterized by low *p*H (2.4 to 6.35), where very little CO_3^{2-} exists in solution. The case of low HCO_3^-:CO_3^{2-} speciation is also consistent with the experimentally derived values of Dietzel et al. (2009), who performed a series of experiments at 5, 25, and 40°C and *p*H between 8.3 and 10.5 (Figure 5, S5, S6). In fact, these data were used to help build a new O isotope fractionation model by Devriendt et al. (2017) that operates on the premise that, at equilibrium, $CaCO_3$ forms exclusively from carbonate ions. We have used this model to predict O isotope fractionation between calcite and H_2O based on average conditions measured during our experiments and find excellent agreement (Figure 3) if a small amount of (deprotonated) HCO_3^- is allowed to be incorporated into precipitated calcite. Details and model parameter values are included in the Supporting Information.

Extrapolation of the Devils Hole results to the conditions of our experiments uses the relation $1000 \ln(\alpha_{xtl\text{-}H2O}) = 17747/T_K - 29.777$. This expression was derived to reconcile assumed equilibrium conditions in the Devils Hole system with the kinetic values in the work of Watkins et al. (2013). This temperature dependence is different than observed in this study (Figure 3), which could explain the poor fit between our results and predicted fractionation at 20 and 30°C, where our regression is most disparate from the Devil's Hole relation (Figure 3). This is supported by the observation that the 10°C experimental data reported here, where our regression is closest to the fractionation expression used by Watkins et al., is more consistent with the predicted model values compared to 20 and 30°C values (see Figures 5, S5, and S6). Although the third and fourth explanations are possible, we consider these unlikely based, in part, on the reproducibility of O isotope fractionation among DIC species described in the work

of Beck et al. (2005), Uchikawa and Zeebe (2013), and Tripati et al. (2015). Additionally, biases in the O isotope fractionation factor between any component pair along the path from $CO_{2(aq)}$ to calcite used in the model would need to be lower than the actual equilibrium partitioning. Because the experiments performed here were close to saturation, and hence suspected to closely reflect calcite-water equilibrium, this possibility seems unlikely. The fourth scenario is based on the possibility that the O isotope composition of DIC from which the carbonates precipitated at 25°C in the work of Watkins et al. (2014) was enriched in $^{18}O/^{16}O$ relative to an equilibrium composition. This situation would artificially increase the $\delta^{18}O$ values of the calcite and, accordingly, the calculated $10^3\ln(\alpha_{xtl\text{-}CO3})$ value (Watkins et al., 2014; Watkins and Hunt, 2015). Watkins et al., however, report that the $CO_2(g)$ used during their experiments was characterized by relatively low $^{18}O/^{16}O$ ratios and would therefore influence the DIC pool toward an anomalously low $\delta^{18}O$ relative to equilibrium with water. This scenario, therefore, seems unlikely.

The final possibility requires that the physical mechanism of calcite growth from solution is different at lower *p*H values, such as, growth at kink sites versus step sites (Morse and Mackenzie, 1990). While this possibility is feasible, actual changes in mechanics during precipitation are impossible to determine from our data. Also, this possibility could be related to differences in accommodating carbonate directly versus indirectly through bicarbonate ions in the calcite lattice upon precipitation. This explanation is supported by an assessment of O isotope fractionation with respect to solution saturation, which suggests that the carbonate formation mechanism may change with increasing supersaturation (see below and Supporting Information for further details); this comparison, however, does not control for possible *p*H

effects. Nonetheless, collectively, these observations may indicate that the HCO_3^-:CO_3^{2-} ratio incorporated in calcite was distinct from that of the fluid.

Broadly, it is possible that one or more explanations are required to explain the discrepancies observed in Figures 3 and 5. At this time, these are difficult to resolve (and more than one might be true), although HCO_3^-:CO_3^{2-} proportions and uncertainties in the temperature extrapolations of previous studies probably play a role based on the modeling of Watkins et al. Importantly, we have shown that O isotope fractionation appears to be influenced by kinetic factors related to precipitation rate, at least to some degree, in all three temperature series explored. An important conclusion, therefore, is that despite conducting our experiments at very low saturation states, and under conditions where nucleation barriers were removed through the use of seed crystals, it may be difficult to attain complete O isotope equilibrium.

4.3 Clumped Isotopes

A significant body of work now exists that has attempted to reconcile discrepant clumped isotope thermometry calibrations (Dennis and Sharag, 2010; Ghosh et al., 2006; Guo et al., 2009), including the standardization efforts of Dennis et al. (2011). Studies of ^{13}C-^{18}O bonding have generally focused on specific carbonates such as deep sea corals (Thiagarajan et al., 2011), mollusk and brachiopod shells (Henkes, et al., 2013), speleothems (Daeron et al., 2011), and a variety of carbonate compositions studied in experiments, including siderite (Fernandez et al., 2014) and dolomite (Bonifacie et al., 2017; Winkelstern et al., 2016). One goal has been to develop generalized calibrations that are independent of carbonate source (Bonifacie et al., 2017;

Deflies et al., 2015; Kelson et al., 2017; Kluge et al., 2015; Murray et al., 2016; Tang et al., 2014; Wacker et al., 2014).

Broadly, the temperature-dependence of ^{13}C-^{18}O bonding can be characterized by "high slopes" or "low slopes" on Δ_{47}–temperature diagrams. Recent work has argued that the "high slope" calibration curves are most likely to be correct, including those of Zaarur et al. (2013) and Tripati et al. (2015). In the former two studies, the authors essentially repeated the experiments of Ghosh et al. (2006) and found temperature dependent ^{13}C-^{18}O bonding very similar to the original clumped isotope thermometry calibration. In the more recent study, $(Ca,Mg)CO_3$ carbonate was investigated and compared to results from $CaCO_3$. Bonifacie et al. (2017) report no difference between Ca-Mg carbonate and Ca carbonate with regard to temperature dependence and ^{13}C-^{18}O bonding. They further integrated calibration data from several other studies to put forth a comprehensive calibration expression to cover $(Ca,Mg,Fe)CO_3$ minerals from -1 to 300°C.

Although the studies described in the previous paragraph provide strong evidence of a single "high slope" Δ_{47} temperature dependence, different calibrations created from data generated in different analytical systems may, in part, still explain observed offsets between calibrations. The temperature dependence of clumped isotope compositions of carbonates grown in our study, in the absolute reference frame, are compared in Figure 6 with the 95% confidence fields for the calibrations of Ghosh et al. (2006), Dennis and Schrag (2010), and Zaarur et al. (2013), as well as the rate-controlled study of Tang et al. (2014). The average values we measure at 10, 20, and 30°C agree well with those predicted by Zaarur et al. (2013), supporting the argument that slow precipitation experiments (as opposed to homogeneous nucleation and subsequent heterogeneous carbonate formation) and/or low saturation states promote lattice equilibrium ^{13}C-^{18}O bond formation at lower temperatures, where calibrations disagree the most.

In general, the temperature-dependence observed for experimental results of this study agree most closely with the "high slope" calibrations over the temperature range explored (Figure 6). For example, the Δ_{47}-temperature dependence found by Zaarur et al. (2013) is described by the equation $\Delta_{47} = (0.0555 \pm 0.0027) \times 10^6\ T^{-2} + (0.0780 \pm 0.0298)$, whereas an error-weighted regression through the data reported here yields $\Delta_{47} = (0.0461 \pm 0.0094) \times 10^6\ T^{-2} + (0.1921 \pm 0.11)$. This regression is also very similar to the combined data calibration reported by Tripati et al. (2015) of $\Delta_{47} = (0.0460 \pm 0.0034) \times 10^6\ T^{-2} + (0.1649 \pm 0.0786)$, as well as the comprehensive calibration of Bonifacie et al. (2017), which is expressed by $\Delta_{47} = (0.0422 \pm 0.0019) \times 10^6\ T^{-2} + (0.1262 \pm 0.0207)$. It should be noted however, that these similarities may be related to, in part, the fact that our data was generated at Caltech and not on the same equipment as the studies of, for example, Dennis and Schrag (2010) or Tang et al. (2014). On the other hand, however, it should be noted that calcite analyzed by Zaarur et al. was digested in McCrea type vessels at 25°C (rather than a common acid bath at 90°C as in this study), which has been suspected as a possible source of disagreement between various calibrations. Additionally, it should be pointed out that while the saturation states used by Zaarur et al. (2013) have not been reported or estimated, it might be assumed that high saturation states existed if homogeneous nucleation occurred near the start of each experiment. Although we do not feel the different results can be explained completely by differences in laboratories, such issues must be kept in mind.

In terms of the experimental approach, the clumped isotope data of this study are most appropriately compared to those of Tang et al. (2014), who controlled calcite precipitation in the range of 0.02 to 4.5 μmol $m^{-2}\ s^{-1}$, which overlaps the range in our study of 0.006 to 0.132 μmol $m^{-2}\ s^{-1}$ (Figure 7, S7-S9), although overall the Tang et al. rates are generally higher. It is important to note, however, that Tang et al. did not use seed crystals, and this is an important

distinction with our study, raising the possibility of nucleation effects in their work. Tang et al. (2014) varied *p*H and ionic strengths, in addition to precipitation rates and temperatures. Their *p*H values ranged from 8.3 to 10.5, whereas $CaCl_2$ solution concentrations started at 35mM and ionic strengths were between 35 mM to 832 mM. Excluding precipitates from high *p*H solutions ($\geq$ 10), average Δ_{47} values determined by Tang et al. for precipitated carbonates ranged from 0.754 ‰ at 5°C to 0.649 ‰ at 40°C. The authors concluded that *p*H may have an influence on Δ_{47} values at higher *p*H values, but that ionic strength and precipitation rate do not influence clumping under their experimental conditions.

Tripati et al. (2015) present a method for identifying isotope compositions of calcite that are influenced by kinetic fractionation. The study included a series of experiments and quantum chemical calculations to determine the Δ_{63} values for individual DIC species. Specifically, the data and conclusions presented in their work indicate that in addition to bulk O isotope composition of DIC, ^{13}C-^{18}O bonding is different among individual DIC species and therefore the clumped isotope composition of total DIC will vary between different *p*H values. Such speciation effects on clumped isotope fractionations are interpreted to be an equilibrium effect in solution but can potentially lead to disequilibrium ^{13}C-^{18}O bonding when DIC is incorporated into solid carbonate. The authors put forth an "interfacial model", which describes the possibility of a precipitation rate/regime where C and O isotope reordering at the solution-mineral interface would allow for mineral lattice equilibrium clumping but kinetically influenced incorporation of bulk isotopes according to DIC compositions. This model predicts three contiguous precipitation rate ranges: one which is slow enough to allow mineral lattice equilibrium for ^{13}C-^{18}O bonding and direct O isotope equilibrium between calcite and water, a second regime where precipitation is slow enough to allow mineral lattice equilibrium for ^{13}C-^{18}O bonding but fast enough to incorporate a kinetic DIC-based fractionation for bulk O isotopes,

and a third rapid precipitation range which requires precipitation of carbonate sufficiently quickly that locks in anomalous DIC bulk and clumped isotope compositions in the mineral lattice. Here it should be noted that, regardless of these proposed precipitation regimes, a DIC pool exists in a bulk solution which is independent of mineral surface boundary layer(s). This DIC pool may or may not be in isotopic equilibrium with water. Questions related to how solution DIC influences precipitated calcite isotopes still remain. However, based on the fastest growth conditions of the "interfacial model", Tripati et al. (2015) were also able to show a kinetically controlled Δ_{47} - $\delta^{18}O$ relation that they suggest can be used to evaluate the possibility of the third type of (kinetically controlled) fractionation in carbonates. This relation has been evaluated for the data reported here, and we find no correlation between Δ_{47} and $10^3\ln(\alpha_{calcite\text{-}H2O})$ (Figure S10).

The treatment of clumped isotopes in the model of Watkins and Hunt (2015) is heavily based on an equilibrium Δ_{63} value of the Devil's Hole calcite and the temperature-dependent ^{13}C-^{18}O bonding determined for calcite, HCO_3^-, and CO_3^{2-} by Hill et al. (2014). However, calculated ^{13}C-^{18}O bonding for DIC species may be underestimated based on a comparison between experimental calcite work and the Δ_{63}-T relation determined by Hill et al (2014). The model predicts an approximately +0.005‰ difference between equilibrium ^{13}C-^{18}O bonding and the (higher frequency) bonding calculated at our precipitation rates (Figures S7-S9). Offsets at this level are not detectable by conventional analytical methods, although, the direction of the offset is worth considering. The positive shift (higher Δ_{63} value) predicted at faster precipitation rates from solutions with *p*H lower than ~ 10 is related to the HCO_3^-:CO_3^{2-} ratio in solution and the higher clumped isotope composition of HCO_3^- compared to CO_3^{2-} (Hill et al., 2014; Tripati et al., 2015). In other words, the model predicts that quickly forming calcite will inherit the species-weighted average of DIC ^{13}C-^{18}O bonding, and therefore disequilibrium calcite can record a

higher Δ_{63} value because aqueous HCO_3^- at equilibrium has a higher Δ_{63} value than equilibrium calcite at the same temperature. This scenario is opposite of the effect expected when saturation state (and by extension, precipitation rate) is increased by raising *p*H. Under these conditions, solution DIC composition shifts to a lower HCO_3^-:CO_3^{2-} ratio causing the composite Δ_{63} to decrease. Above a *p*H of approximately 10, rapid precipitation would cause a negative offset in calcite Δ_{63} according to the model of Watkins and Hunt (2015).

Saturation state is a first-order factor controlling carbonate precipitation rate. The experimental conditions utilized during our study do not include a wide enough range of saturation states to investigate a correlation between degree of saturation and ^{13}C-^{18}O bonding, although the wider range in saturation state of previous studies allow evaluation of this parameter. Calcite precipitation mechanisms and rate laws are thought to change as a function of saturation states, but, within a given saturation state, factors such as *p*H, ionic strength, reagent ion ratios, or substrate morphology are also important (Hong and Teng, 2014; Sand et al., 2016; Teng et al., 2000; van der Weijden and van der Weijden, 2014).

In comparing our results to previous studies, several adjustments must be made to align different studies as closely as possible. Experimentally determined Δ_{47} values from Dennis and Schrag (2010), Tang et al. (2014), and Kelson et al. (2017) have been projected to precipitation temperatures of 10, 20, or 30°C for direct comparison to the results of this study (Figure 8). Additionally, the Devils Hole calcite ($\mathbf{\Omega} = 1.5 \pm 0.09$) may also be considered. Individual experimental values from previous work in the range of 0-14, 15-24, and 25-40°C have been converted to 10, 20, and 30°C, respectively, and these adjustments have been made according to the Δ_{47}-T relations determined in each respective study, retaining data set variability for each set of conditions (see Supporting Information for full details). The following comparison is only qualitative because the experiments conducted by Dennis and Schrag (2010) and Kelson et al.

(2017) were characterized by decreasing saturation state over the course of precipitation, whereas the Tang et al. (2014) experiments likely utilized higher saturation state during carbonate formation initiation by homogenous nucleation.

An apparent correlation of increasing Δ_{47} values with decreasing saturation state can be seen in the collective data sets at lower temperatures (Figure 8). This correlation is most prominent at temperatures between 0 and 14°C, less pronounced between 15 and 24°C, and absent above 24°C. These observations indicate that saturation state is an important factor controlling ^{13}C-^{18}O bonding during calcite formation from solution at lower temperatures where calibrations show maximum divergence. Such relations may be explained in two ways. First, they may indicate that precipitation mechanism may be more sensitive to different saturation states at lower temperatures. Second, the rate of ^{13}C-^{18}O bond reordering at the solution-mineral interface in the interfacial model of Tripati et al. (2015) may be slower at lower temperatures given similar saturation conditions. In other words, at a given medium to high saturation state, ^{13}C-^{18}O bond reordering at the solution-mineral interface may achieve equilibrium at higher temperatures where reordering kinetics are possibly faster but from the same solution at lower temperatures, calcite may not achieve equilibrium ^{13}C-^{18}O bonding where reordering kinetics appear to be slower.

5. Conclusions

Recent developments in the understanding of H_2O-CO_2-carbonate system equilibrium and isotope fractionations associated with carbonate precipitation reactions requires a critical reassessment of ^{13}C-^{18}O bond formation in carbonates and their relations to the DIC system. We have used the chemo-stat synthetic precipitation method to produce slowly growing calcite under slightly supersaturated conditions to explore the relation between formation rate and C and O

isotope fractionation as well as clumped isotope fractionation. The log precipitation rates explored during this study ranged from -6.88 to -8.20 mol m^{-2} s^{-1}, among the slowest precipitation rates obtained in experiments on isotopic fractionation in carbonates. In addition, the use of isotopically labeled seed crystals allowed minimization of kinetic effects that may be produced during mixed precipitation mechanisms during homogeneous nucleation followed by heterogeneous crystal growth. As a result, very low saturation states characterized the experiments, less than four times equilibrium.

We found C isotope fractionation between calcite and bicarbonate ions to exhibit non-temperature-dependent partitioning of approximately 1.6 ± 0.4 ‰ between 10 and 30°C. In contrast, O isotope fractionation between calcite and water was observed to exhibit temperature-dependent isotopic fractionation, but only minor rate-dependent isotopic fractionation over the range of conditions of the experiments. $^{18}O/^{16}O$ fractionation was found to be higher than those measured in many previous experiments, with a temperature relation of $10^3 \ln(\alpha_{calcite\text{-}H2O}) = (19.27 \pm 0.68) \times 10^3 T^{-1} + (-35.60 \pm 2.30)$. Isotopic fractionation for calcite ^{13}C-^{18}O bonding, expressed as Δ_{47}, was also observed to be rate independent over the conditions explored. As expected, formation temperature played a major role in carbonate clumped isotope compositions and we obtained the following relation: $\Delta_{47} = (0.0461 \pm 0.0094) \times 10^6 T^{-2} + (0.1921 \pm 0.11)$. Although our experimental approach was intended to closely approach equilibrium conditions, it is possible, even likely, that kinetic isotope effects remain. We find an average C isotope fractionation that is higher than the study of Romanek et al. (1992) but lower than those of Bottinga (1986) and Coplen (2007). Our C isotope results closely follow the ion-by-ion growth model of Watkins and Hunt (2015). Our results for O isotope fractionation, however, do not fully support the Watkins and Hunt model unless some significant modifications are made, including treatment of surface DIC speciation, among other factors. Although the rate

dependence for O isotope fractionations trend similarly to model predictions, the magnitude of partitioning between calcite and DIC suggests that calcite formed from a surface that disproportionately sequestered carbonate ions instead of bicarbonate ions onto calcite surfaces in our experiments. This mechanism of carbonate formation may be related to saturation state, which has been shown to have a negative correlation with ^{13}C-^{18}O bonding, as well as possibly $^{18}O/^{16}O$ fractionations at lower temperatures. If this conclusion is true, this suggests that equilibrium $^{18}O/^{16}O$ fractionation between calcite and water is higher than commonly believed. This study adds to the growing body of evidence which suggests that O isotope thermometry calibrations including, or at least more similar in magnitude to, the $^{18}O/^{16}O$ fractionation indicated by Devils Hole calcite (Coplen, 2007; Kluge et al., 2014), are preferable to previous experimental studies. Finally, clumped isotope data presented here supports the "higher" slope calibration of Zaarur et al. (2013) over the temperature range explored. This study also supports the "interfacial" calcite formation model presented by Tripati et al. (2015), whereby certain precipitation rate regimes can decouple bulk isotope fractionation and clumped isotope bonding frequency in a mineral lattice.

SUPPORTING INFORMATION

Additional figures, information, and data tables are included in the online Supporting Information.

ACKNOWLEDGEMENTS

Nami Kitchen is recognized for instrument and analytical assistance. The Stable Isotope Facility at UC-Davis is appreciated for supporting analyses. We thank James M. Watkins, Hagit P. Affek, and three anonymous reviewers for helpful comments and suggestions that greatly

improved this document. We also thank Aradhna E. Tripati for her editorial handling. This work was supported by NASA Headquarters under the NASA Earth and Space Science Fellowship Program – Grant NNX13AP40H as well as NASA Astrobiology Institute grant NNA13AA94A. The authors declare no conflicts of interest from their affiliation or funding.

Table 1: Experimental Conditions and Supporting Isotope Compositions

Experiment Identification	Experiment Length (h)	Temperature (° C)*	pCO2 (%)	pH	Ca^{2+} (mmol)	Alkalinity (mmol)	Saturation Ω	log Rate mol m^{-2} s^{-1}	Water $\delta^{18}O$ ‰ (VSMOW)	DIC $\delta^{13}C$ ‰ (VPDB)	HCO_3^- $\delta^{13}C$ ‰ (VPDB)
UWAI-016	94	9.9	10%	6.5	9.7	8.9	1.1	-7.54	-8.9	-2.0	2.0
UWAI-017	93	9.9	10%	6.6	9.7	8.8	1.1	-7.53	-8.8	-1.9	1.5
UWAI-018	138	10.0	10%	6.5	9.8	8.7	1.1	-7.63	-9.0	-2.0	1.9
UWAI-019	136	9.9	10%	6.7	10.1	8.7	1.5	-7.60	-8.9	-1.9	1.0
UWAI-025	206	9.5	6%	6.7	10.3	7.8	1.3	-8.10	-8.8	-3.4	-0.5
UWAI-026	204	10.4	6%	6.8	10.4	7.9	1.7	-8.10	-8.9	-3.2	-0.7
UWAI-027	180	10.0	6%	6.8	10.3	8.0	1.7	-8.19	-8.9	-3.5	-0.9
UWAI-028	178	10.0	6%	6.8	10.4	8.1	1.8	-8.20	-9.0	-3.4	-0.8
UWAI-029	69	10.0	6%	6.8	10.1	8.3	1.8	-7.63	-9.1	-2.7	-0.1
UWAI-030	68	10.9	6%	6.8	10.0	8.5	1.8	-7.70	-9.1	-2.9	-0.6
UWAI-031	232	9.8	6%	6.7	10.3	9.1	1.5	-8.04	-9.1	-4.2	-1.1
UWAI-032	227	9.9	6%	6.7	10.5	9.4	1.6	-8.11	-8.9	-4.0	-1.0
UWAI-033	117	9.9	6%	6.8	10.4	8.5	1.8	-7.47	-8.8	-2.5	0.0
UWAI-034	115	10.5	6%	6.8	10.4	8.6	1.9	-7.48	-8.7	-2.4	0.0
UWAI-002	151	20.0	5%	6.8	10.1	7.9	2.3	-7.45	-8.9	-2.8	-0.9
UWAI-003	143	20.0	5%	6.9	10.4	8.1	3.1	-7.55	-9.1	-2.9	-1.3
UWAI-004	144	20.0	5%	6.9	10.0	8.1	3.0	-7.51	-8.9	-2.8	-1.2
UWAI-005	191	20.0	5%	6.9	10.6	7.9	3.0	-7.65	-8.9	-3.3	-1.7
UWAI-006	93	20.0	5%	6.9	10.0	8.1	3.0	-7.24	-8.7	-2.8	-1.2
UWAI-007	91	19.9	5%	6.8	10.6	6.7	2.1	-7.25	-8.7	-2.6	-0.8
UWAI-008	95	20.0	5%	6.9	9.7	8.1	2.9	-7.23	-8.6	-3.0	-3.1
UWAI-009	94	19.9	5%	6.9	10.0	8.0	2.9	-7.27	-8.8	-2.8	-1.2
UWAI-010	193	20.0	5%	6.9	9.8	7.8	2.8	-7.64	-8.8	-3.0	-1.3
UWAI-011	191	19.9	5%	7.0	9.8	7.8	3.5	-7.59	-8.9	-2.9	-1.5
UWAI-012	109	20.0	5%	7.0	9.9	8.2	3.7	-7.38	-8.8	-2.5	-1.1
UWAI-013	101	19.9	5%	7.0	10.1	8.3	3.8	-7.44	-8.9	-2.5	-1.1
UWAI-014	91	20.0	10%	6.6	10.1	9.1	1.7	-7.50	-8.7	-3.4	-1.7
UWAI-015	89	19.9	10%	6.6	10.5	9.2	1.7	-7.59	-8.8	-3.0	-0.5
UWAI-023	137	20.0	6%	6.8	8.1	8.8	2.2	-7.00	-8.2	-3.2	-1.3
UWAI-024	138	19.9	6%	6.9	8.6	9.0	2.9	-6.88	-8.3	-3.4	-1.7
UWAI-045	200	19.6	13%	6.5	11.0	9.2	1.4	-7.92	-8.7	-4.7	-1.7
UWAI-046	198	19.8	13%	6.5	11.2	9.2	1.4	-7.82	-9.0	-5.0	-1.9
UWAI-020	119	30.0	16%	6.3	9.9	8.0	1.3	-7.40	-8.9	-5.5	-2.0
UWAI-021	121	30.1	16%	6.5	9.8	8.6	1.7	-7.47	-8.6	-6.0	-3.5
UWAI-035	149	30.0	13%	6.6	10.3	8.0	2.0	unknown*	-8.9	-5.1	-2.7
UWAI-036	143	30.2	13%	6.6	10.6	8.5	2.2	-7.51	-8.9	-4.6	-2.5
UWAI-037	235	29.9	13%	6.5	10.2	7.9	1.6	-7.65	-8.5	-4.9	-2.4
UWAI-038	233	29.9	13%	6.5	10.3	7.9	1.6	-7.66	-8.6	-5.0	-2.6
UWAI-039	89	30.0	13%	6.5	10.5	8.0	1.6	-7.25	-8.6	-5.0	-2.5
UWAI-040	87	30.1	13%	6.6	10.9	8.7	2.3	-7.37	-8.7	-4.5	-2.5
UWAI-041	144	30.0	13%	6.5	10.6	8.3	1.7	-7.42	-9.0	-4.9	-2.3
UWAI-042	142	30.0	13%	6.5	10.6	8.3	1.7	-7.47	-9.2	-4.5	-2.0
UWAI-043	240	30.0	13%	6.5	10.6	8.4	1.7	-7.72	-8.7	-5.3	-2.6
UWAI-044	238	30.2	13%	6.6	11.0	9.1	2.4	-7.88	-8.8	-4.4	-2.2
UWAI-047	214	29.5	13%	6.5	11.2	8.3	1.7	-7.92	-9.1	-6.6	-4.1
UWAI-048	211	30.2	13%	6.5	11.2	8.6	2.3	-7.82	-9.5	-6.5	-4.2

* Experiment UWAI-035 homogeneously nucleated, UWAI-036 rate used in figures.

Table 2 Isotope Compositions of Carbonate Overgrowth and Phase Fractionations

	Experiment Identification	System T (° C)	Calcite $\delta^{13}C$ (‰, VPDB)	Calcite $\delta^{18}O$ (‰, VSMOW)	Δ_{47} (‰, ARF)	$\Delta^{13}C_{calcite\text{-}HCO3\text{-}}$ (‰)**	$\Delta^{18}O_{calcite\text{-}H2O}$ (‰)
Experiments Performed at 10°C	UWAI-016	9.9	1.2 ± 0.1	23.7 ± 0.5	0.797 ± 0.017	-0.7 ± 0.1	32.3 ± 0.6
	UWAI-017	9.9	1.4 ± 0.3	23.5 ± 0.4	0.773 ± 0.035	-0.2 ± 0.3	32.2 ± 0.5
	UWAI-018	10.0	1.4 ± 0.2	23.8 ± 0.4	0.777 ± 0.046	0.2 ± 0.2	32.5 ± 0.5
	UWAI-019	9.9	1.3 ± 0.1	23.8 ± 0.3	0.768 ± 0.052	0.6 ± 0.1	32.5 ± 0.5
	UWAI-025	9.5	1.5 ± 0.4	24.0 ± 0.4	0.741 ± 0.021	**1.6 ± 0.4**	32.6 ± 0.7
	UWAI-026	10.4	1.4 ± 0.6	24.0 ± 0.4	0.760 ± 0.035	**1.6 ± 0.6**	32.6 ± 0.8
	UWAI-027	10.0	1.2 ± 0.6	24.1 ± 0.4	0.779 ± 0.040	**1.7 ± 0.6**	32.7 ± 0.4
	UWAI-028	10.0	1.3 ± 1.2	23.8 ± 0.6	0.796 ± 0.070	**1.8 ± 1.2**	32.6 ± 0.6
	UWAI-029	10.0	1.5 ± 0.3	23.9 ± 0.5	0.748 ± 0.066	**1.4 ± 0.3**	32.8 ± 0.5
	UWAI-030	10.9	1.5 ± 0.4	23.9 ± 0.6	0.750 ± 0.080	**1.7 ± 0.4**	32.8 ± 0.6
	UWAI-031	9.8	0.3 ± 0.4	23.8 ± 0.4	0.742 ± 0.039	**1.6 ± 0.4**	32.7 ± 0.4
	UWAI-032	9.9	0.9 ± 0.6	23.9 ± 0.4	0.766 ± 0.060	**1.4 ± 0.6**	32.6 ± 0.4
	UWAI-033	9.9	1.6 ± 0.2	23.7 ± 0.4	0.754 ± 0.082	**1.5 ± 0.2**	32.3 ± 0.5
	UWAI-034	10.5	1.7 ± 0.3	23.7 ± 0.2	0.756 ± 0.051	**1.5 ± 0.3**	32.2 ± 0.3
	Average	**10.1**			**0.765 ± 0.036**	**1.6 ± 0.2**	**32.5 ± 0.4**
Experiments Performed at 20°C	UWAI-002	20.0	-0.5 ± 0.5	21.2 ± 0.4	0.732 ± 0.080	0.0 ± 0.5	30.0 ± 0.5
	UWAI-003	20.0	-0.4 ± 0.3	21.2 ± 0.1	0.726 ± 0.083	-0.1 ± 0.3	30.1 ± 0.4
	UWAI-004	20.0	0.1 ± 0.1	21.6 ± 0.05	0.719 ± 0.010	0.4 ± 0.1	30.3 ± 0.3
	UWAI-005	20.0	0.0 ± 0.1	21.5 ± 0.2	0.726 ± 0.049	**1.7 ± 0.1**	30.2 ± 0.4
	UWAI-006	20.0	0.7 ± 0.1	21.5 ± 0.1	0.729 ± 0.077	**1.9 ± 0.2**	30.0 ± 0.4
	UWAI-007	19.9	0.5 ± 0.5	21.6 ± 0.5	0.726 ± 0.065	**1.2 ± 0.6**	30.1 ± 0.6
	UWAI-008	20.0	0.4 ± 0.03	21.4 ± 0.6	0.721 ± 0.055	0.4 ± 0.1	29.8 ± 0.7
	UWAI-009	19.9	0.4 ± 0.2	21.3 ± 0.4	0.726 ± 0.055	-0.6 ± 0.2	29.9 ± 0.6
	UWAI-010	20.0	0.8 ± 0.5	21.6 ± 0.4	0.749 ± 0.028	**1.9 ± 0.5**	30.1 ± 0.5
	UWAI-011	19.9	-0.1 ± 1.4	21.5 ± 0.2	0.748 ± 0.054	**1.1 ± 1.4**	30.2 ± 0.4
	UWAI-012	20.0	0.4 ± 0.1	21.5 ± 0.4	0.744 ± 0.060	**1.4 ± 0.1**	30.1 ± 0.5
	UWAI-013	19.9	0.6 ± 0.1	21.6 ± 0.5	0.735 ± 0.044	**1.6 ± 0.1**	30.3 ± 0.6
	UWAI-014	20.0	1.1 ± 0.3	21.7 ± 0.3	0.729 ± 0.057	**1.7 ± 0.3**	30.2 ± 0.5
	UWAI-015	19.9	0.5 ± 0.2	21.6 ± 0.5	0.717 ± 0.046	**1.3 ± 0.2**	30.2 ± 0.6
	UWAI-023	20.0	0.2 ± 0.3	21.3 ± 0.1	0.707 ± 0.085	**1.3 ± 0.3**	29.4 ± 0.2
	UWAI-024	19.9	0.3 ± 0.3	21.3 ± 0.04	0.735 ± 0.056	**1.7 ± 0.3**	29.4 ± 0.1
	UWAI-045	19.6	0.5 ± 0.2	21.6 ± 0.3	0.733 ± 0.054	**1.8 ± 0.5**	30.4 ± 1.0
	UWAI-046	19.8	0.5 ± 0.3	21.6 ± 0.4	0.731 ± 0.115	**1.8 ± 0.3**	30.4 ± 0.4
	Average	**19.9**			**0.729 ± 0.021**	**1.6 ± 0.5**	**30.1 ± 0.7**
Experiments Performed at 30°C	UWAI-020	30.0	-1.1 ± 0.3	19.2 ± 0.6	0.703 ± 0.014	0.4 ± 0.3	27.9 ± 0.7
	UWAI-021	30.1	-0.5 ± 0.4	19.5 ± 1.1	0.721 ± 0.067	1.5 ± 0.4	28.0 ± 1.1
	UWAI-035*	30.0	-1.0 ± 0.1	19.2 ± 0.1	0.674 ± 0.077	**2.0 ± 0.2**	28.0 ± 0.1
	UWAI-036	30.2	-0.5 ± 0.3	19.5 ± 0.4	0.672 ± 0.053	**1.6 ± 0.3**	28.2 ± 0.4
	UWAI-037	29.9	-0.9 ± 0.3	19.4 ± 0.5	0.672 ± 0.127	**1.4 ± 0.3**	27.8 ± 0.6
	UWAI-038	29.9	-0.9 ± 0.2	19.3 ± 0.4	0.688 ± 0.077	**1.5 ± 0.2**	27.8 ± 0.4
	UWAI-039	30.0	-0.8 ± 0.4	19.5 ± 0.6	0.679 ± 0.129	**1.5 ± 0.4**	27.9 ± 0.6
	UWAI-040	30.1	-0.1 ± 0.3	19.6 ± 0.4	0.696 ± 0.080	**1.8 ± 0.3**	28.1 ± 0.5
	UWAI-041	30.0	-0.8 ± 0.2	19.4 ± 0.3	0.690 ± 0.108	**1.5 ± 0.2**	28.3 ± 0.3
	UWAI-042	30.0	-0.9 ± 0.1	19.3 ± 0.4	0.688 ± 0.096	**1.3 ± 0.1**	28.4 ± 0.4
	UWAI-043	30.0	-0.7 ± 0.2	19.4 ± 0.4	0.712 ± 0.066	**1.5 ± 0.2**	28.0 ± 0.4
	UWAI-044	30.2	-0.3 ± 0.2	19.5 ± 0.6	0.717 ± 0.129	**1.5 ± 0.2**	28.2 ± 0.6
	UWAI-047	29.5	-0.6 ± 0.4	19.6 ± 0.3	0.687 ± 0.105	2.8 ± 0.5	28.5 ± 0.3
	UWAI-048	30.2	-1.3 ± 0.3	19.0 ± 0.5	0.650 ± 0.115	2.9 ± 0.3	28.3 ± 0.5
	Average	**30.0**			**0.689 ± 0.039**	**1.6 ± 0.4**	**28.1 ± 0.5**

* Experiment UWAI-035 homogeneously nucleated.

** $\Delta^{13}C_{calcite\text{-}HCO3\text{-}}$ values in bold are representative of experimental conditions, see text for details.
Error values represent 2 standard deviations about the mean of multiple (≥ 3) analyses.

Figure Captions

Figure 1 - Schematic of chemo-stat experimental setup illustrating seed crystal and overgrowth details. The source of alkalinity used for these experiments was $NaHCO_3$. The C and O isotopes of the alkalinity produced by this reagent were defined by dissolving $NaHCO_3$ in stock DI water and bubbling with a CO_2/N_2 mixture several (4 to 10) days before being used to precipitate calcite. Before entering the fresh (sodium) bicarbonate solution, the CO_2/N_2 mixture was used to moderate the *p*H of a different actively precipitating master solution. In this way, a fresh solution was thoroughly flushed with "reagent" CO_2 (i.e. CO_2 that had been treated in the CO_2-H_2O exchange system) prior to use.

Figure 2 - Reproduction of the semi-empirical ion-by-ion growth model of Watkins and Hunt (2015) for C isotope fractionation during calcite growth under kinetic and (assumed) equilibrium conditions. The model is based on a "kinetic" regime from the experiments of Romanek et al. (1992, shown by green triangle symbols) and inferred equilibrium from Coplen (2007). The orange dashed line is the modeled fractionation for 20°C, *p*H = 6.6, and a surface HCO_3^-:CO_3^{2-} ratio (Θ) of 100:1. The purple dotted line is modeled fractionation for 20°C, *p*H = 6.6, and a surface HCO_3^-:CO_3^{2-} ratio (Θ) of 0.25:1. Also included are values found during this study at 20°C for partitioning between calcite and aqueous carbonate (red squares).

Figure 3 - Observed temperature dependent calcite-water O isotope fractionation found by this study as compared to other work. The black circle represents Devils Hole calcite (Coplen, 2007). The average propagated 2SD external uncertainty for experimental values is ± 0.47‰. Individual values are given in Table 2.

Figure 4 - Oxygen isotope fractionation between calcite and water as a function of precipitation rate. Error bars represent propagated 2SD external uncertainty. Error envelopes represent 95% confidence intervals. Equations express error weighted regressions of the data.

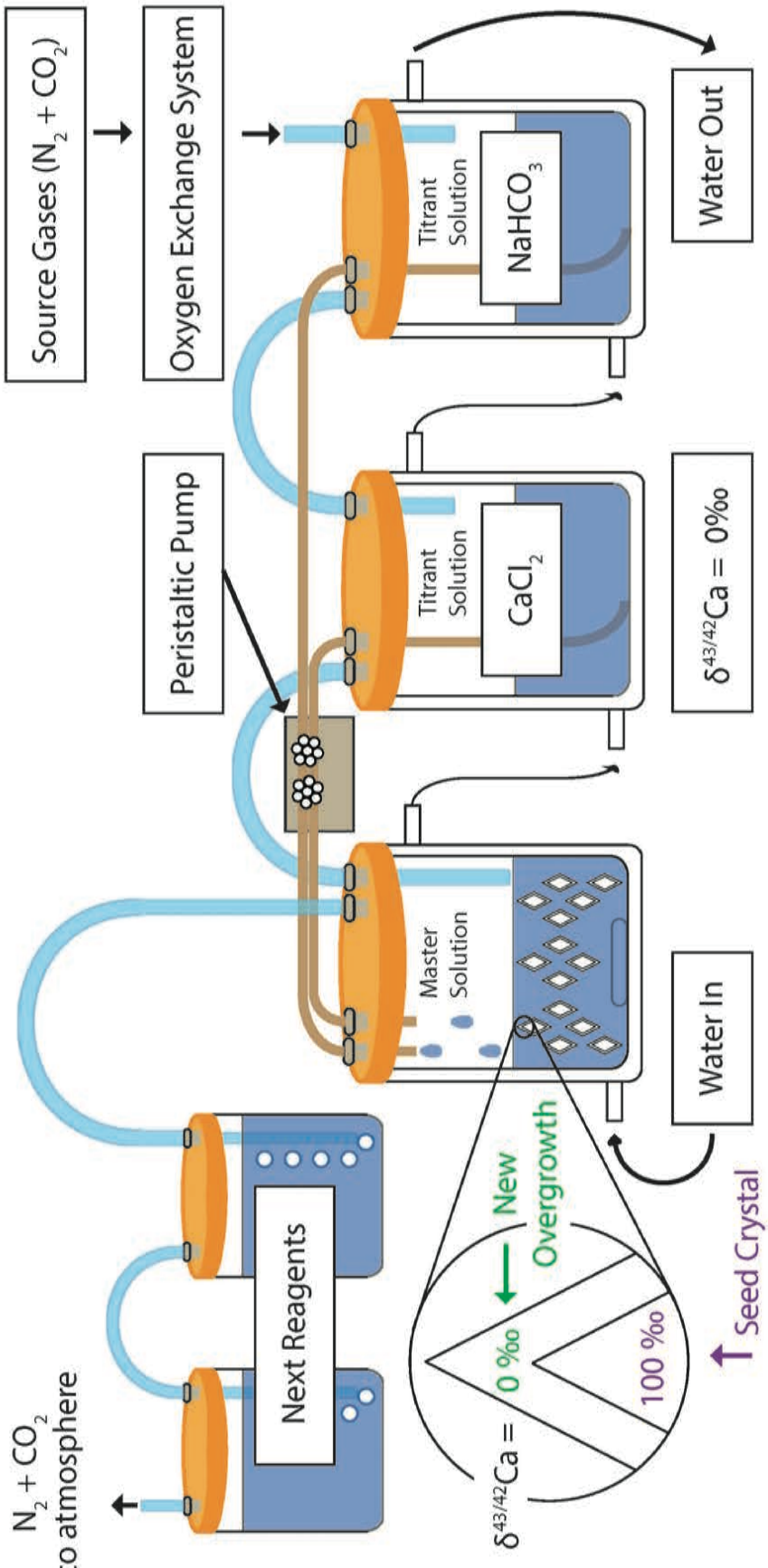
Figure 5 - Reproduction of the semi-empirical ion-by-ion growth model of Watkins and Hunt (2015) for O isotope fractionation during calcite growth under kinetic and (assumed) equilibrium conditions. The model is based on a "kinetic" regime from the experiments of Watkins et al. (2014, shown by green circle symbols) and inferred equilibrium from Bottinga (1968) and Coplen (2007). The orange dashed line is modeled fractionation for 20°C, *p*H = 6.6, and a surface HCO_3^- to CO_3^{2-} ratio (Θ) of 100:1. The purple dotted line is modeled fractionation for 20°C, *p*H = 6.6, and a surface HCO_3^-:CO_3^{2-} ratio (Θ) of 0.25:1. Different equilibrium fractionation is predicted for the two different experimental conditions. Also included are values found during this study at 20°C for partitioning between calcite and aqueous carbonate (red squares). Finally, the adjusted (see Supporting Information text for details) experimental values (T = 20°C, *p*H = 8.3) of Dietzel et al. (2009) are indicated by yellow diamonds.

Figure 6 - Clumped isotope composition (Δ_{47}) of experimentally precipitated calcite as a function of temperature. For comparison, selected clumped isotope thermometry calibrations are included. The work of Ghosh et al. and Zaarur et al. represent "high slope" calibrations, whereas the studies of Dennis and Schrag and Tang et al. represent "low slope" calibrations. Error envelope and shaded regions represent 95% confidence intervals for selected studies.

Figure 7 - Experimentally determined Δ_{47} for calcite as a function of precipitation rate. Error bars represent propagated 2SD external uncertainty. Error envelopes represent 95% confidence intervals. Equations express error weighted regressions of the data.

Figure 8 - Comparison of experimentally determined Δ_{47} for calcite from multiple studies as a function of solution saturation state with respect to calcite. All experimental values represent average conditions for a given experimental run and have been adjusted to represent ^{13}C-^{18}O bonding at 10, 20, and 30°C (See Supporting Information for adjustment description). Error bars for data points from this study represent maximum and minimum saturation based on measured solution conditions. Error bars for the data points of Kelson et al. (2017) and Dennis and Schrag (2010) represent maximum saturation based on reported solution conditions or saturation states. In cases where both starting and ending master solution conditions were not reported, a minimum (end of experiment) saturation state of $\Omega = 1$ was assumed. The saturation states of Tang et al. (2014) were used as reported in Tang et al. (2008). The vertical dotted lines represent saturation (equilibrium, $\Omega = 1$). The temperatures indicated on the second (right side) vertical axes illustrate the equivalent temperatures the range in Δ_{47} values reflect, and are based on the clumped isotope calibration of Zaarur et al. (2013).

Figure 1


Source Gases (N_2 + CO_2)
Oxygen Exchange System
Peristaltic Pump
Water Out
Titrant Solution
$NaHCO_3$
Titrant Solution
$CaCl_2$
$\delta^{43/42}Ca$ = 0‰
Master Solution
Water In
Next Reagents
N_2 + CO_2 to atmosphere
$\delta^{43/42}Ca$ =
0 ‰
New Overgrowth
100 ‰
Seed Crystal

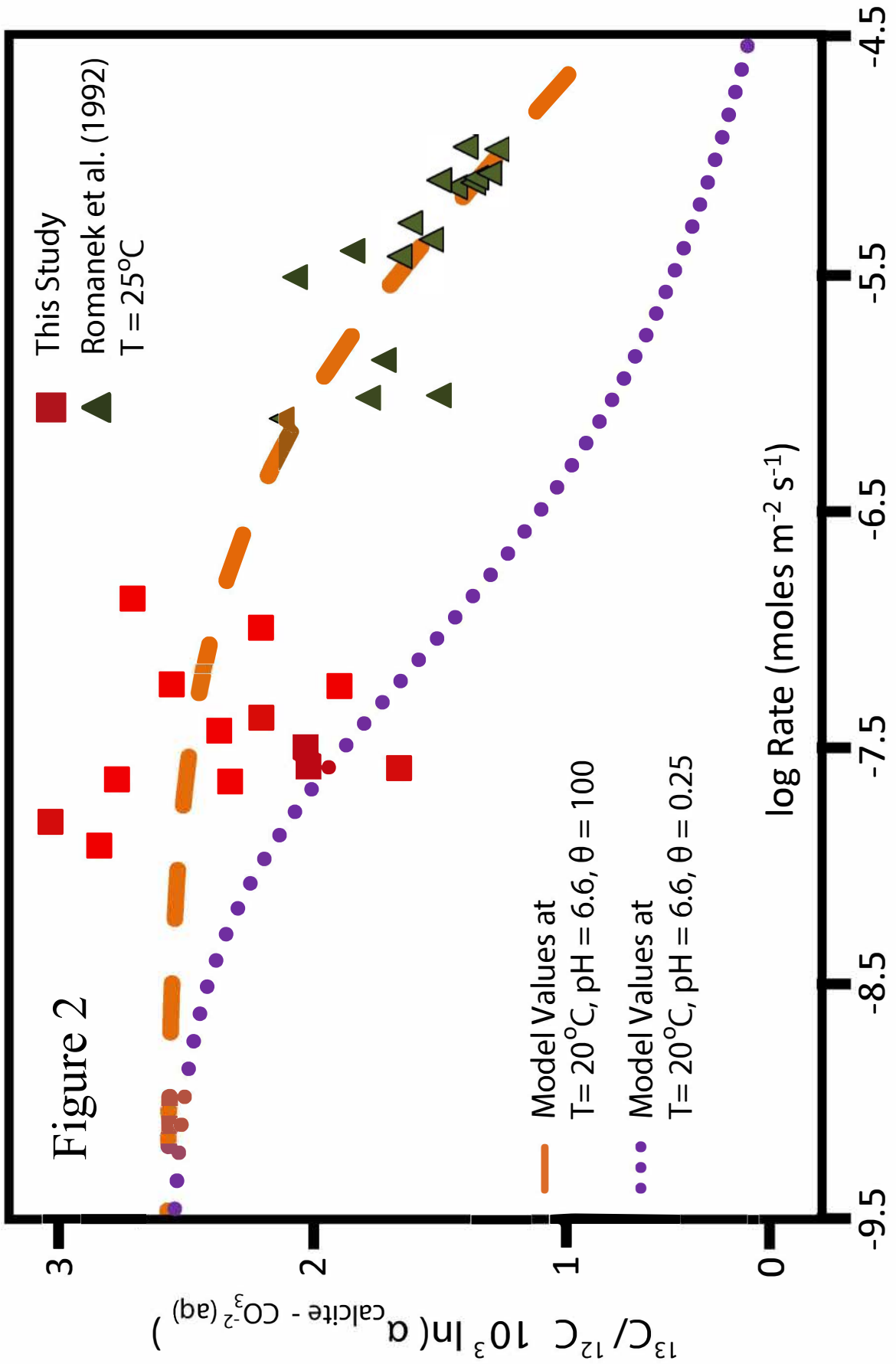
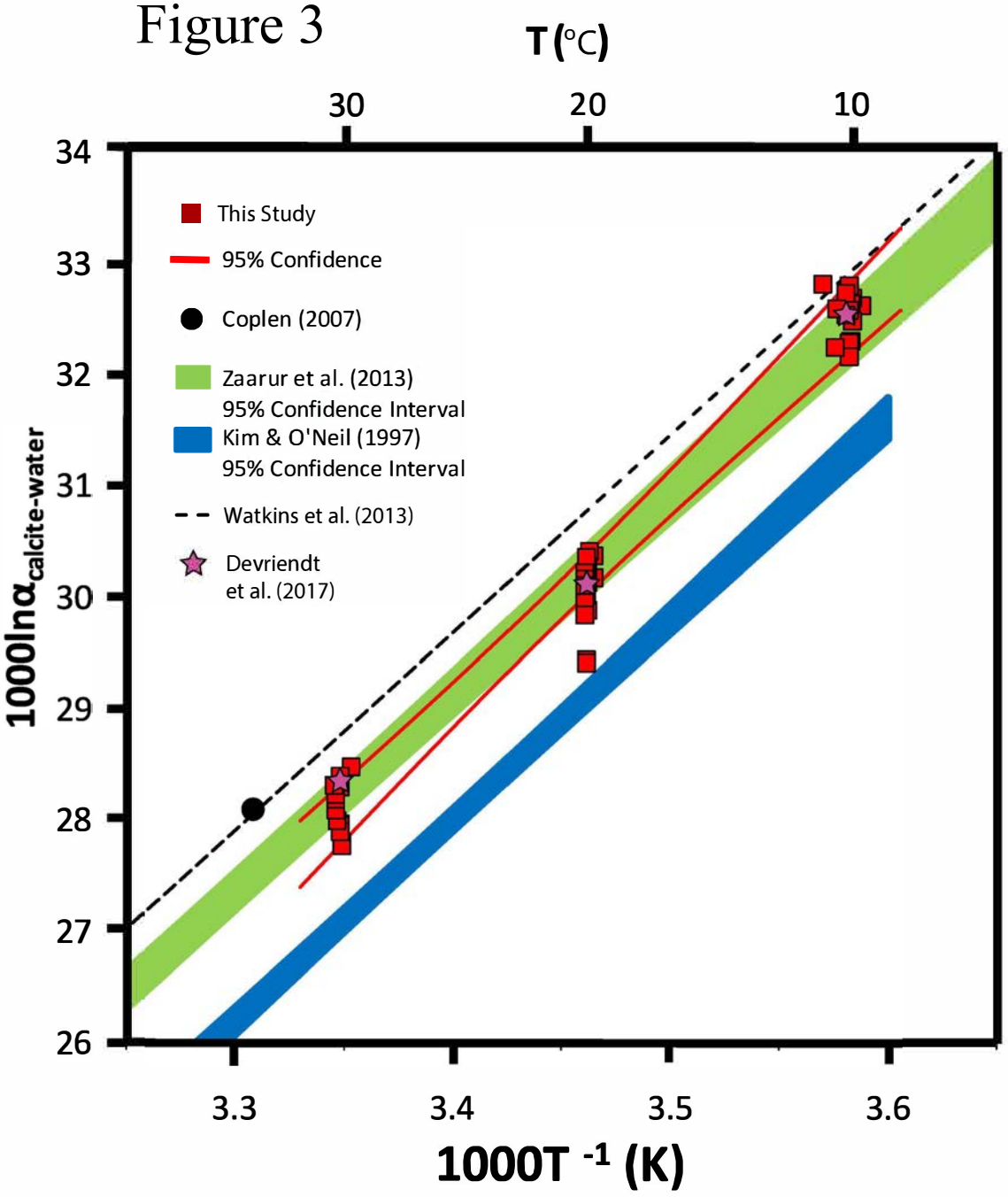
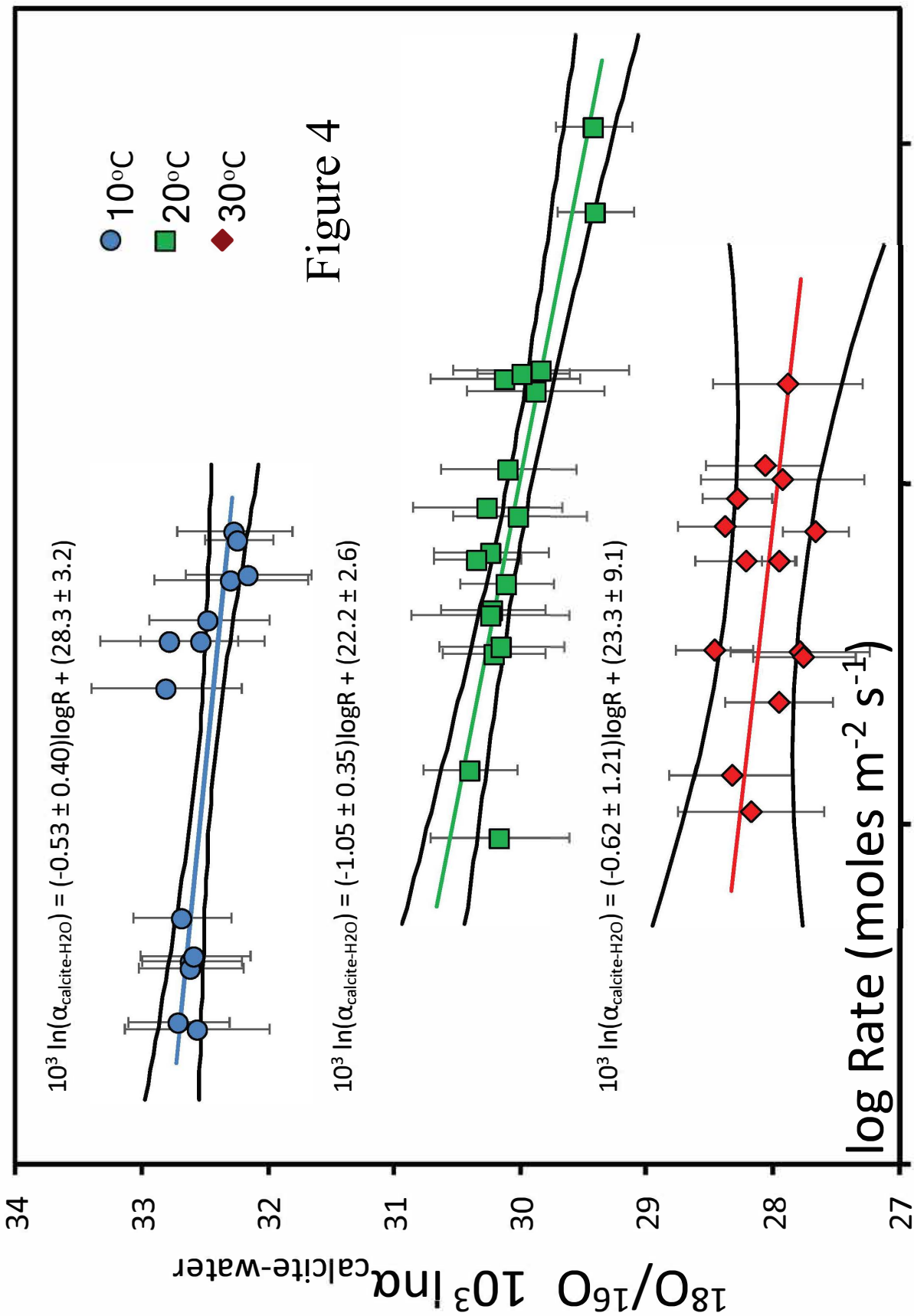

Figure 2
This Study
Romanek et al. (1992)
T = 25°C
Model Values at
T= 20°C, pH = 6.6, θ = 100
Model Values at
T= 20°C, pH = 6.6, θ = 0.25
log Rate (moles m-2 s-1)
-9.5
-8.5
-7.5
-6.5
-5.5
-4.5
0
1
2
3
13C/ 12C 10³ ln(αcalcite - CO3-2 (aq))

Figure 3


T(°C)
30
20
10
34
33
32
31
30
29
28
27
26
1000lnα calcite-water
This Study
95% Confidence
Coplen (2007)
Zaarur et al. (2013)
95% Confidence Interval
Kim & O'Neil (1997)
95% Confidence Interval
Watkins et al. (2013)
Devriendt
et al. (2017)
3.3
3.4
3.5
3.6
1000T -1 (K)


Figure 4
10°C
20°C
30°C
$10^3 \ln(\alpha_{calcite\text{-}H2O}) = (-0.53 \pm 0.40)\log R + (28.3 \pm 3.2)$
$10^3 \ln(\alpha_{calcite\text{-}H2O}) = (-1.05 \pm 0.35)\log R + (22.2 \pm 2.6)$
$10^3 \ln(\alpha_{calcite\text{-}H2O}) = (-0.62 \pm 1.21)\log R + (23.3 \pm 9.1)$
log Rate (moles m^{-2} s^{-1})
-8.4
-7.9
-7.4
-6.9
27
28
29
30
31
32
33
34
$10^3 \ln\alpha_{calcite\text{-}water}$ $^{18}O/^{16}O$

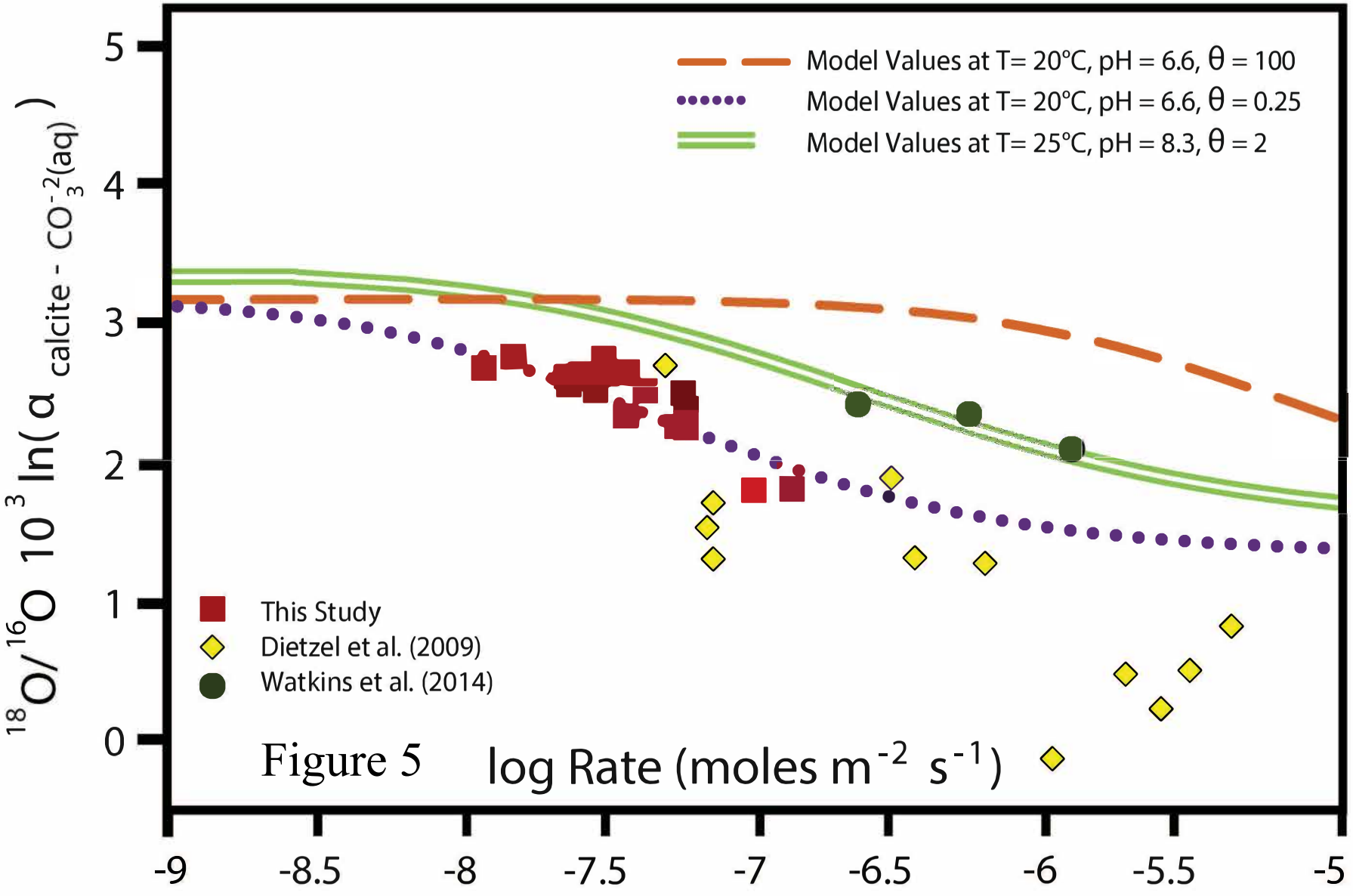
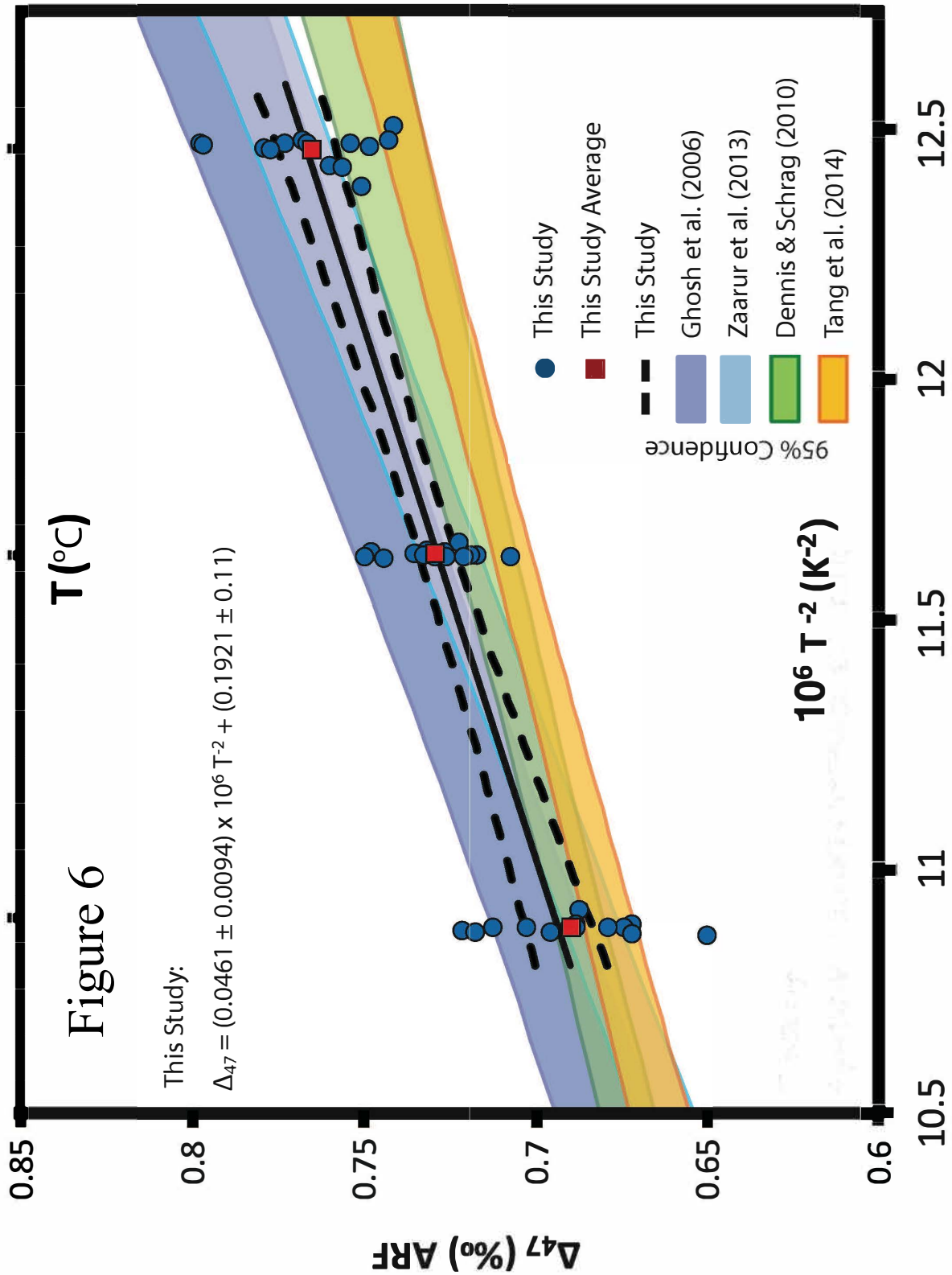

Model Values at T= 20°C, pH = 6.6, θ = 100
Model Values at T= 20°C, pH = 6.6, θ = 0.25
Model Values at T= 25°C, pH = 8.3, θ = 2
This Study
Dietzel et al. (2009)
Watkins et al. (2014)
$^{18}O/^{16}O\ 10^{3}\ \ln(\alpha_{calcite - CO_3^{-2}(aq)})$
log Rate (moles $m^{-2}\ s^{-1}$)
5
4
3
2
1
0
-9
-8.5
-8
-7.5
-7
-6.5
-6
-5.5
-5

Figure 5


Figure 6
T (°C)
30
20
10
This Study:
Δ_{47} = (0.0461 ± 0.0094) x 10^6 T^{-2} + (0.1921 ± 0.11)
Δ_{47} (‰) ARF
0.85
0.8
0.75
0.7
0.65
0.6
10^6 T^{-2} (K^{-2})
10.5
11
11.5
12
12.5
This Study
This Study Average
This Study
Ghosh et al. (2006)
Zaarur et al. (2013)
Dennis & Schrag (2010)
Tang et al. (2014)
95% Confidence

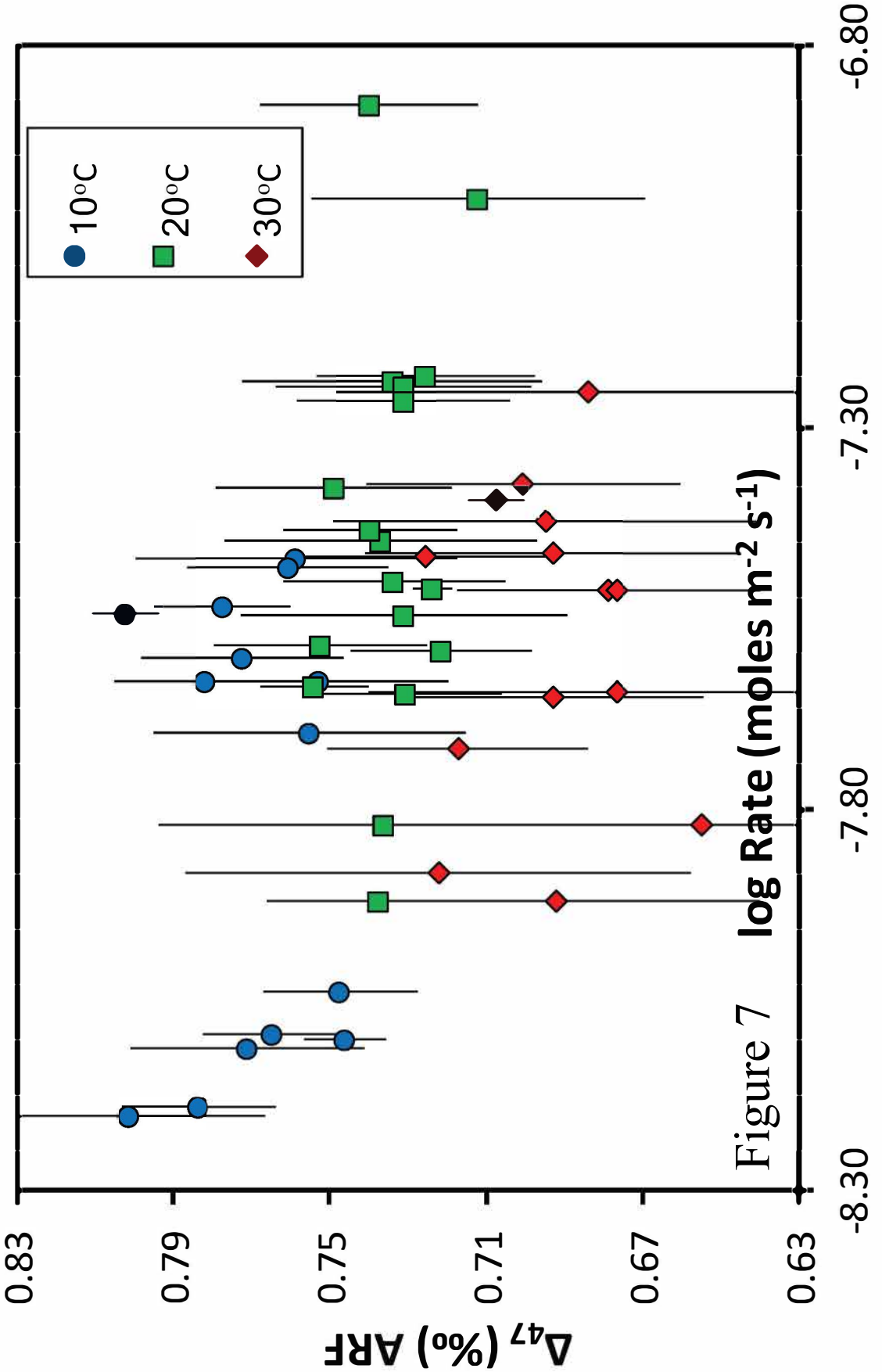
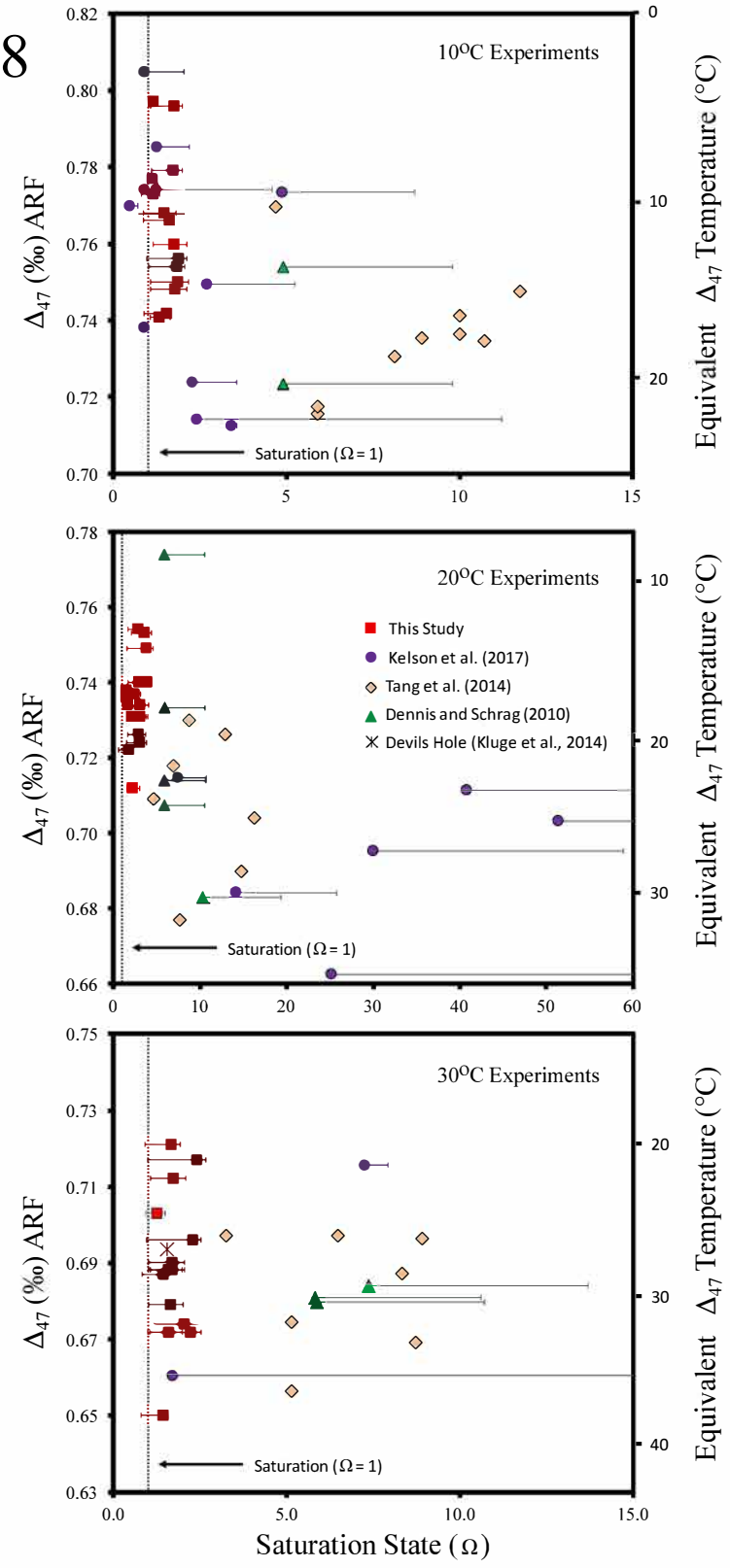

10°C
20°C
30°C
Δ47 (‰) ARF
0.83
0.79
0.75
0.71
0.67
0.63
-8.30
-7.80
-7.30
-6.80
log Rate (moles m-2 s-1)

Figure 7

Figure 8


10°C Experiments
20°C Experiments
30°C Experiments
This Study
Kelson et al. (2017)
Tang et al. (2014)
Dennis and Schrag (2010)
Devils Hole (Kluge et al., 2014)
Saturation (Ω = 1)
Δ47 (‰) ARF
Equivalent Δ47 Temperature (°C)
Saturation State (Ω)

Near Equilibrium ^{13}C-^{18}O Bonding During Inorganic Calcite Precipitation under Chemo-Stat Conditions: Supplementary Material

Nicholas P. Levitt[1,†], John M. Eiler[2], Christopher S. Romanek[3], Brian L. Beard[1], Huifang Xu[1], & Clark M. Johnson[1]

[1]NASA Astrobiology Institute and
Department of Geoscience
University of Wisconsin-Madison
1215 W Dayton Street
Madison, Wisconsin, USA
53706

[2]NASA Astrobiology Institute and
Geological and Planetary Sciences
California Institute of Technology
MC 100-23
Pasadena, California, USA
91125

[3]NASA Astrobiology Institute and
Department of Earth and Environmental Sciences
Furman University
Greenville, South Carolina, USA
29613

[†]Corresponding Author's Contact
E-mail: nlevitt@wisc.edu
Tel: (608) 262-8960
Fax: (608) 262-0693

Manuscript published in:

Geochemistry, Geophysics, Geosystems, 2018, 19, 901–920.
https://doi.org/10.1002/2017GC007089

Supporting Methodology Section

Inorganic Calcite Precipitation

Previous Studies. A common method used to form solid carbonate from aqueous solution is by CO_2 degassing, which initially requires a relatively large amount of dissolved CO_2 that acts to lower pH and saturation state; when CO_2 degassing occurs, the saturation state of the solution increases and causes homogeneous nucleation of solid carbonate. Two sub-types of CO_2 degassing have been used: active (forced CO_2 removal, commonly by N_2) and passive (CO_2 flux due to p CO_2 difference between the solution and atmosphere). In both cases, the loss of gaseous CO_2 increases solution pH and consequently saturation state. A disadvantage of this approach is that CO_2 degassing methods require dynamic changes in solution compositions that lead to variable and sometimes uncontrollable precipitation rates (Kelson et al. 2017), and additionally risks kinetic behavior during homogeneous nucleation.

Tang et al. (2008, 2014, see also Dietzel and Usdowski, 1996 and Dietzel et al., 2009) performed CO_2 diffusion-based experiments and estimated precipitation rate according to an invariant calcite formation pace and modeled time-dependent surface areas. These experiments, however, relied on homogeneous nucleation of calcite from solution, raising the possibility of multiple reaction mechanisms and variable precipitation rates. In these experiments, supersaturation was achieved by titration of NaOH. Watkins et al. (2014) also used NaOH titration to maintain pH and facilitate calcite formation. Similarly, the researchers avoided heterogeneous growth on seed crystals and utilized CO_2(g) diffusion/dissolution to introduce DIC to the experimental solution. Precipitation rate determinations were calculated by reduction in Ca^{2+}

concentrations, experiment length, and a calcite surface area approximation (Tang et al., 2008; 2014).

Current Study. Deionized water (NANOpure 18.2 MΩ, Thermo Barnstead, Bubuque, IA, USA) was used in our study. The source of the water was the Madison, WI, USA municipal water supply. This water was stockpiled in 50 L carboys at the beginning of the project to ensure a water source with a constant O isotope composition throughout the course of experimentation. Reagents used included calcium chloride ($CaCl_2$*$2H_2O$, ACS grade Lot: A0332898, Acros Organics [Geel, Belgium]) and sodium bicarbonate ($NaHCO_3$, 99.5% for analysis grade Lot:A0327974, Acros Organics [Geel, Belgium]). Seed calcite was also produced from these reagents, however a ^{43}Ca spike was mixed into the $CaCl_2$ solution before precipitation to provide a quantitative method to determine overgrowth mass from the Ca isotope composition of the seed and final solid. The Ca spike (80% ^{43}Ca) was obtained from Oakridge National Laboratory (Batch: 219501, Oakridge, TN, USA).

The seed crystals were formed following the procedures of Ogino et al. (1987) and Rodriguez-Blanco et al. (2011). Specifically, 500 mL of a 0.61 M $CaCl_2$ solution was added to 600 mL of a 1.0 M $NaHCO_3$ solution. The reagent solutions had equilibrated at 20°C for 6 days prior to reaction. The reagent solutions were mixed into a water jacketed reaction vessel and maintained at 20°C for 16 days. The reaction solution was mixed with a magnetic stir bar during the 16 days. This time period allowed the conversion of vaterite to calcite. After 12 days an aliquot of the precipitate was collected, dried, and analyzed by X-ray diffraction (XRD) to confirm the presence of pure calcite. The seed crystals were additionally inspected for crystal habit by optical and electron microscopy. Solid was collected by decanting the reaction fluid into a 0.4 μm filtered

(Isopore, HTTP membrane, Reference: HTTP04700, Lot: R4EA68008) vacuum system. The reaction vessel and calcite seeds were rinsed with DI water during filtration to prevent the formation of chloride salts. A small amount of methanol was used to help remove adsorbed water during filtration prior to further drying in an oven at 40°C for approximately 24 hours. Following oven drying, the seed crystals were checked again for mineralogy by XRD and then stored in a Dri-Rite filled desiccator until used. A Nova 4200e surface area and pore size analyzer (Quantachrome Instruments, Boynton Beach, FL, USA) was used to measure the surface area concentration of the seed crystal material according to the BET method (Brunauer et al., 1938). Additionally, the size distribution of seed crystals was assessed by depositing a distributed layer of calcite seeds onto Pelco Tabs (Prod. No. 16084-1, Ted Pella, Inc., Redding, CA, USA) and imaging the seeds with a Hitachi S-3400N scanning electron microscope utilizing backscattered electron (BSE) mode, an accelerating voltage of 15 kV, and a working distance of 10 mm. Image rastering was performed on a 3.8 mm by 1.76 mm area (Figure SM1). A visual inspection of seed crystals indicates a bimodal distribution of (diameter) sizes of approximately 2 and 25 μm.

The experimental setup is shown schematically in Figure 1. Key components of the experimental process include a master solution which hosts precipitation, individual $CaCl_2$ and $NaHCO_3$ titrant solutions, and a separate set of 22 mM $CaCl_2$ and 24 mM $NaHCO_3$ solutions which experience CO_2/N_2 purging prior to use as reagents. After purging, the two reagent solutions were bubbled with pure CO_2 for approximately 1 hour at room temperature to decrease the pH prior to master solution formation so that the mixture would be undersaturated with respect to $CaCO_3$. The master solution was prepared by mixing 250 mL of each reagent solution into a temperature controlled water-

jacketed vessel. Water was circulated through the jackets by a heating/refrigerating water bath (Anova Inc., Model: A&C Series, Stafford, TX, USA). The $CaCl_2$ and $NaHCO_3$ solutions were visually monitored during mixing to verify the absence of homogeneous nucleation as indicated by appearance of a white cloudy area in an otherwise very clear solution. The remaining 750 mL of each reagent solution were transferred to temperature controlled water-jacketed vessels and used as titrant for the following experiment. Soon after mixing, the master solution and new titrant solutions were incorporated into the experimental setup as shown in Figure 1 and introduced to a CO_2/N_2 gas mixture atmosphere as described in detail below to allow DIC and pCO_2 to reach a steady state at the desired supersaturation. Master solution pH and temperature were monitored during this equilibration period (normally several hours) and after approximately 1 hour of stable pH the experiment was initiated by introduction of seed crystals and commencement of titration.

Titration of the master solution was accomplished by moving solutions through Masterflex santoprene tubing (model 6431-26, Gelsenkirchen, Germany) tubing with a Masterflex L/S peristaltic pump (model 7551-10) during experimentation. A Masterflex L/S (model 7534-04) multi-channel pump head was used to accommodate multiple tubes at the same time. The solution pCO_2 was controlled by introducing a CO_2/N_2 gas mixture flowing through the master solution reaction vessel. Gas was delivered by mass flow controllers (model F-201CV, Bronkhorst USA, Bethlehem, PA, USA). The partial pressure of CO_2 was established by mixing pure CO_2 and N_2 to total mixing ratios as indicated in Table 1. As an example, a pCO_2 of 15% was achieved by combining flow of 15 mL/minute of CO_2 and 85 mL/minute of N_2. Flow rates (individual and combined) were verified by a soap film flow meter (model 0101-0113, Hewlett-Packard (HP), Palo

Alto, CA, USA). Measured Ca^{2+}, alkalinity, and pH were used to model solution pCO_2 for each experiment with PHREEQC software (Parkhurst and Appelo, 2013) and phreeqc.dat database to verify static conditions. Most calculated CO_2 partial pressures were within 1% of values set by mass flow controllers and all values average an offset of -0.1%. Individual values are included in Table SM1. Pre-purified tanks of nitrogen gas and a single pre-purified tank of CO_2 gas (both from Scott-Gross Company, Inc. [Madison, WI, USA]) were used for all experiments in this study.

Chemostat precipitation experiments took place in an open-system with respect to O and C, where these elements were constantly moving through the reaction vessel in the form of CO_2 introduced to help maintain pH (further details below). This flux of $CO_2(g)$ may cause changes in the isotope composition of DIC and even H_2O if the CO_2 has not experienced extensive mixing (and reaction) with the solution water before it enters the precipitation system. To avoid this problem, a CO_2-H_2O exchange system was used prior to introducing CO_2/N_2 gas to the master precipitation solution. The design and viability of this equilibration system has been described previously (Levitt and Romanek, 2016). Briefly, the equilibration system is composed of three basic parts: 1) a reservoir to facilitate the mixing and reaction between CO_2 and H_2O, 2) equipment and materials used to introduce water and gas to the mixing reservoir, and 3) a vessel used to separate the reacted gas and water. The reservoir used to facilitate the isotope exchange reactions was approximately 288m long and designed to extensively mix water and gas phases. The same water used for precipitation experiments was also used in the exchange system during the time period of experimentation. This system effectively allows the CO_2 entering the reaction vessel to exchange with the solution water (and by extension DIC) before ever entering the reaction solution.

Another factor to consider during calcite synthesis is the DIC used to form solid carbonate. The source of alkalinity used for these experiments was $NaHCO_3$. The isotope composition of this reagent is unknown. However, the C and O isotope compositions of the DIC produced by this reagent are effectively replaced prior to being used for experimentation. This was achieved through the protocols described in the preceding paragraphs. Again, dissolving $NaHCO_3$ in stock DI water several (4 to 10) days before being used to precipitate calcite allowed this fresh solution to be bubbled with a CO_2/N_2 mixture prior to experimentation. Before entering the fresh (sodium) bicarbonate solution, the CO_2/N_2 mixture was used to help maintain the pH of a different actively precipitating master solution. In this way, a fresh solution was thoroughly flushed with "reagent" CO_2 (i.e. CO_2 that had been treated in the CO_2-H_2O exchange system, see Figure 1) prior to use.

Geochemical Analyses

Solution Ca^{2+} concentrations were determined at the UW-Madison Water Science and Engineering Laboratory with a Dionex (Model ICS-1100 RFIC, Sunnyvale, CA, USA) ion chromatograph. The instrument utilized an ER3b cation assembly cation column (P/N 067803), D56 heated conductivity cell, a 100 µL sample loop, and Dionex CSRS-300 suppressor. The analysis employed 20 mM methanesulfonic acid as an eluent and calibration solution matrices were prepared to mimic those of analyte solutions. Analytical precision is estimated as the 2SD value of concentration standards run as unknowns (± 1.1 mmol L^{-1}, n=3). Alkalinity was measured with a Mettler Toledo (Model DL50 Graphix, Greifensee, Switzerland) auto-titrator using an equivalence point titration (EQP) which was shown to be accurate to within 0.2 milliequivalents L^{-1} (meq)

or 1% of the test solution concentration. Each solution was analyzed for alkalinity three or more times and average 2-standard deviation of individual solution analyses (≥3) was 0.07 meq. pH was monitored before and during reaction with a Cole-Parmer electrode (Item #00289LY, Vernon Hills, IL, USA) and Oakton meter (Bench 2700 Series, Eutech Instruments, Vernon Hills, IL, USA). The electrode was calibrated before each experiment with Fischer Certified buffer solutions (Lots: 133436, 133435, 132388, Waltham, MA, USA). Details regarding solution composition for each experiment are provided in Table 1.

Calcium was purified prior to isotope analysis by ion-exchange chromatography similar to that reported by Li et al. (2012). Approximately 0.25 mg of calcite or 2.5 mL of reaction solution was processed for Ca isolation. Calcite was dissolved in dilute ultra-pure nitric acid and converted to pure $Ca(NO_3)_2$ before purification. Likewise, nitric acid was added to experimental solutions and dried until only solids remained. These solids were repeatedly dissolved with nitric acid and re-dried three times to ensure all cations were transformed into nitrate salts. Calcium was isolated and purified from other cations by ion-exchange chromatography before isotope analysis. Element separation was achieved on Bio-Rad (Hercules, CA, USA) AG 50Wx8 200-400 mesh cation resin. This procedure consisted of following steps: 1) addition of sample to a chromatography column using 0.5 M HNO_3 solution, 2) elution of Na and impurity ions with 7 mL of 0.5 M HNO_3, and 3) removal from resin and collection of Ca with the addition of 3 mL of 8 M HCl.

Calcium isotope analyses were performed using a Micromass IsoProbe MC-ICP-MS at the University of Wisconsin-Madison. Helium was used as the collision gas for thermalization and H_2 was used to suppress argide isobars by charge transfer reactions.

Ca solution concentrations of 10 ppm were introduced to the Ar plasma using a self-aspirating 50 to 100 μL min-1 nebulizer coupled to a Cetac Aridus II membrane desolvating system. The cone voltage was set to 200 to 500 V. These settings allowed Ca ion intensities of 44.5, 0.34, 0.07, and 1.22 V at mass numbers 40, 42, 43, and 44, respectively. A 2% HNO_3 solution was used as a rinse solution between individual sample measurements. The sample solutions were also measured using a standard-sample-standard bracketing protocol. Concentration-related matrix effects were corrected according to standard solutions ranging from 5 to 15 ppm Ca, as outlined by Albarède and Beard (2004). Further data processing included the subtraction of on-peak zero voltages using 60 s on-peak acid blank measurements prior to forty 10 s on-peak integrations of the analyte solution. Typical (2 standard deviation) precision for standards during these analyses was ± 1.07 ‰ for $^{43}Ca/^{42}Ca$. Individual analysis values and uncertainty are presented in Table SM1.

Carbonate C and O isotope analyses as well as clumped isotope analyses were performed on two Thermo-Finnigan MAT 253 (Thermo Scientific, Bremen, Germany) isotope ratio mass spectrometers according to the procedures outlined by Passey et al. (2010). A single analysis consisted of digestion of 8-10 mg calcite in a common phosphoric acid bath at 90°C followed by an automated CO_2 purification process. See Passey et al. (2010) for automation and sample preparation details. Carbon and O isotope ratios for sample and standard material were determined by Isodat software with comparison to an Oztech reference gas of known isotope composition. Data presented in the main document was corrected for ^{17}O according to Santrock et al. (1985). Data was also corrected for ^{17}O using "Brand" parameters (Brand et al. 2010) according to the

recommendations of Daeron et al. (2016). A comparison between the data processed by these two methods is presented below.

An O isotope acid fractionation factor of 1.00821 (Swart et al., 1991) was used to correct the $^{18}O/^{16}O$ ratio of gas phase CO_2 produced by acid digestion back to reactant calcite $\delta^{18}O$ values. All clumped isotope data are reported in the absolute reference frame (ARF) of Dennis et al., 2011 using equilibrated CO_2 gases. Values of Δ_{47} measured for CO_2 produced from acid digestion of calcite at 90 ˚C have been corrected by 0.082‰ to make them equivalent to the frequently used reference frame of carbonates reacted at 25˚C (Deflies et al. 2015). In addition to unknown samples, standard reference material was also analyzed in tandem during each analytical session. Carbonate reference materials included in-house standards "CIT Carrara" and "TV03" as well as National Institute of Standards and Technology Reference Material 8544 NBS19 Limestone (NBS-19). These reference materials averaged -0.31‰, -0.33‰, and +0.012‰ different than their accepted values for $\delta^{13}C$, $\delta^{18}O$, and Δ_{47} during the analytical session of September 2014 (Week 4 in Supporting Information Tables). Therefore, these values were used to correct each individual unknown analysis during this analytical session. After these adjustments, the 2-SD external precision (standard deviation about the mean) of carbonate standards analyzed during all 8 analytical sessions were 0.11‰, 0.27‰, and 0.034‰ for $\delta^{13}C$, $\delta^{18}O$, and Δ_{47} values. Each experimental product was analyzed a minimum of three times (thus standard errors for averages of replicated samples are, on average, 0.06, 0.16 and 0.020 ‰ or better, 2SE, respectively).

Oxygen isotope ratios for water were determined using a Laser Water Isotope Analyzer V2 (Los Gatos Research, Inc., Mountain View, CA, USA) and standardized using working materials that were calibrated to International Atomic Energy Agency

standard reference materials VSMOW, Greenland Ice Sheet Precipitation (GISP), and Standard Light Antarctic Precipitation (SLAP). Water samples analyzed at the UC-Davis Stable Isotope Facility were grouped as follows: Data set #1 includes samples from experiments UWAI-002 through UWAI-019 while data set #2 includes samples from experiments UWAI-020 through UWAI-046. "Internal Checks" for water analyses provided by the UC-Davis Stable Isotope Facility are reported as follows: The data set #1 known value was -4.95‰ and the data set #2 known value was -2.83‰. The measured values for these two internal standards were -4.95 ± 0.34‰ and -2.83 ± 0.10‰, respectively. DIC C isotope analyses utilized a Delta V Plus (Thermo Scientific, Bremen, Germany) isotope ratio mass spectrometer to determine ratios of evolved trace gas phase CO_2. The IRMS system was interfaced with a Finnigan Gasbench II device for sample preparation and transfer. DIC analysis was similarly standardized according to materials traceable to National Institute of Standards and Technology reference material 8545. DIC samples analyzed at the UC-Davis Stable Isotope Facility were grouped as follows: Data set #3 includes samples from experiments UWAI-002 through UWAI-019 while data set #4 includes samples from experiments UWAI-020 through UWAI-046. "Internal Checks" for DIC analyses provided by the UC-Davis Stable Isotope Facility were performed on 0.2 mL of a 10 mM Li_2CO_3 material from Acros2 and are reported as follows: The data set #3 known value was -3.70‰ and the data set #4 known value was -4.00‰. The measured values for these two internal standards were -3.69 ± 0.08‰ (n=8) and -4.04 ± 0.06‰ (n=5), respectively.

Product carbonate was analyzed for mineralogy with a Rigaku (Model: D/max Rapid II-S, Tokyo, Japan) XRD system with a 2-D image plate (Mo Kα radiation) at the S. W. Bailey X-ray Diffraction Laboratory of the University of Wisconsin-Madison.

Overgrowth mineralogy was verified by microscopy inspection as well as XRD. A Hitachi S-3400N scanning electron microscope utilizing backscattered electron (BSE), an accelerating voltage of 15 kV, and a working distance of 10 mm was used for imaging. A representative SEM image and XRD patterns are provided as Figure SM1 and SM2. In all cases, only calcite was identified in reaction products.

Supporting Discussion Section

Data Treatment and Comparisons

The carbonate clumped isotope data reported in this paper have been subject to three corrections that are commonly used in the CO_2 and carbonate clumped isotope literature: 1) we correct measured differences in Δ_{47} between a sample-derived CO_2 gas and an intralaboratory CO_2 standard ('Oztech working gas') to account for non-linearity in 47/44 ratios — that is, a dependence of Δ_{47} on R47. This is done by documenting the correlation of measured Δ_{47} with R47 for gases equilibrated to a uniform temperature (the so-called 'heated gas' method described in Huntington et al., 2009). 2) Linearity-corrected Δ_{47} values are converted to the absolute reference frame of Dennis et al., 2011, by comparison with gases equilibrated at two known temperatures. And 3) Δ_{47} values of CO_2 extracted from calcite at 90˚C are converted to equivalent values for CO_2 extracted from calcite at 25˚C by adding 0.082 ‰.

We also perform a fourth correction to measurements of synthetic calcites grown from seed crystals, to account for the fact that analyzed material is a mixture of seed-crystal calcite and newly grown calcite (see example calculation below). This additional step is applied between corrections 2 and 3, above (though it could be performed at some other stage without significant differences).

As stated in the main document, the expression used to calculate bulk C and O isotope composition of overgrowth carbonate is $\delta_o = ((\delta_{tot} - \delta_s (1-\chi)))/\chi$

where δo is the isotope composition of the overgrowth, δtot is the measured isotope composition of the overgrowth plus seed crystals, δs is the isotope composition of the seed crystals, and χ is the mass fraction of overgrowth to final total carbonate. While this equation is not exact because it assumes linearity in terms of δ notation, tabulated values are accurate to 0.03‰ in the range of $\delta^{13}C$ and $\delta^{18}O$ values reported here, and hence do not significantly affect corrected δ values. An analogous correction for overgrowth Δ_{47} values requires a more complex calculation because mixing of two materials with distinct ^{13}C-^{18}O bonding cannot be treated as linear. We followed the procedure outlined in "Appendix A. Non-linearity of trends in 'Keeling plots' based on Δ_{47}" presented in the work of Affek and Eiler (2006) to isolate the overgrowth Δ_{47} value of reaction products (see example calculation below). This calculation (Equation A7 in Affek and Eiler, 2006) requires knowledge of the C isotope composition, O isotope composition, and Δ_{47} value of the seed crystals as well as the C isotope composition of overgrowth, O isotope composition of overgrowth, ratio of seed crystal mass to overgrowth mass, and Δ_{47} value of the total experimental product (seed crystals plus overgrowth).

There is an additional step in processing raw mass spectrometric data to reported $\delta^{13}C$, $\delta^{18}O$ and Δ_{47} values that has only recently been identified as a possible source of error (Daeron et al. (2016), Olack and Colman (2016), Schauer et al. (2016)). The central issue is that all previously reported clumped isotope measurements of CO_2 (including this study) have been made on sector mass spectrometers that cannot separate $^{13}CO_2$ from $^{12}C^{17}O^{16}O$, or $^{13}C^{18}O^{16}O$ from $^{12}C^{18}O^{17}O$ and $^{13}C^{17}O_2$. For these reasons, it is necessary to estimate the $^{17}O/^{16}O$ ratio of a sample based on the measured $^{18}O/^{16}O$ ratio (which is

constrained by measuring R46). There are two established protocols for making such corrections: Santrock et al. (1985) and Brand et al. (2010). The most important difference between these two is the estimated $^{17}O/^{16}O$ ratio of Vienna Standard Mean Ocean Water (VSMOW). It is now generally recognized that the Brand estimate of this ratio is more nearly accurate. However, most previously reported carbonate clumped isotope data was processed assuming the Santrock parameters. The difference between Δ_{47} values derived from these two sets of parameters scales with the true difference in $\delta^{13}C$ between the sample and reference gases, and can reach ~0.1 ‰ in extreme cases. The community of carbonate clumped isotope researchers is in the process of re-examining and revising previously published works that used the Santrock parameters. Here we present our data using the Santrock parameters in order to maintain consistency with previously published experimental and empirical calibrations of the carbonate clumped isotope thermometer. However, we also processed our data using the Brand parameters to establish what effect this difference makes on our findings.

We used the procedures outlined in Daeron et al. (2016) to reprocess our data according to "Brand" parameters. These values are presented in Table SM4. Similar to the observations of Daeron et al. (2016) and Kelson et al. (2017), the slope of our Δ_{47}-T relation following an error weighted regression is not significantly changed by this conversion (Figure SM14). However, our Δ_{47} values decrease by approximately 0.045‰ at 25°C when cast into the ARF ($\Delta_{47} = (0.0494 \pm 0.012) \times 10^6 T^{-2} + (0.1098 \pm 0.14)$). This observation is consistent with the shifts in Δ_{47} for 23°C CO_2-H_2O equilibrated samples when compared in the "two reference frame" exercise reported by Schauer et al. (2016). Specifically, sample CO_2 will decrease in Δ_{47} when converted from "Santrock" to "Brand" corrected values if reference frame gases have more negative $\delta^{13}C$ values

compared to the analyte C isotope composition. Our calcite (overgrowth + seed) $\delta^{13}C$ values ranged from -1.1 to 4.4‰ while reference frame gas $\delta^{13}C$ values were approximately -10.8‰. Like our data reported with a "Santrock" ^{17}O correction, Δ_{47} values derived with "Brand" parameters do not show a correlation to precipitation rate.

Additional Discussion of Isotope Modeling

Watkins and Hunt (2015) build on the ion-by-ion growth model developed in the work of Wolthers et al. (2012) and Watkins et al. (2014) to account for kinetic fractionation of C, O, and clumped isotopes during calcite precipitation. The model is grounded in the mathematical expressions of ion attachment (Ca and (bi)carbonate) and detachment fluxes at a mineral surface. In this model, calcite grows when the attachment flux outpaces detachment flux and calcite dissolves when detachment flux outpaces attachment flux. The isotope composition of DIC species is accounted for based on a series of equilibrium fractionation factors. Ultimately, isotope fractionation between solution and calcite as a consequence of net ion flux is tied to a "kinetic limit" for a fast precipitation rate and an "equilibrium limit" at a slow precipitation rate. The kinetic limits are based on experimental work of Watkins et al. (2014) for O, Romanek et al. (1992) for C, and the theoretical calculations of Hill et al. (2014) for ^{13}C-^{18}O bonding. The equilibrium limits are based on the publications of Coplen (2007) and Bottinga (1986) for C, Coplen (2007) for O, and Coplen (2007) and Kluge et al. (2014) for clumped isotopes. The calcites in the "kinetic limit" studies exhibit isotope fractionations of lower magnitude compared to the "equilibrium limits". The precipitation rates of reference "limits" are known and isotope fractionation interpolation is tied to the ion-by-ion growth flux."

Watkins and Hunt (2015) provide a compilation (Table 1) of equilibrium fractionation factors used in their model. We follow this convention in our replication of their model calculations. These values have also been used in this work to determine C isotope composition for individual DIC species based on the measured total DIC C isotope composition in our experiments and DIC speciation from PHREEQC calculations. By extension, these alpha values are built into the determination of $^{13}C/^{12}C$ $10^3\ln(\alpha_{calcite\text{-}HCO3})$ values reported in Table 2. The O isotope composition of DIC was not needed to calculate experimental $^{18}O/^{16}O$ 10^3 $\ln(\alpha_{calcite\text{-}H2O})$ values. The treatment of clumped isotopes in the model of Watkins and Hunt (2015) is based on an equilibrium Δ_{63} value of the Devil's Hole calcite and the temperature-dependent ^{13}C -^{18}O bonding determined for calcite, HCO_3^-, and CO_3^{2-} by Hill et al. (2014). However, calculated ^{13}C -^{18}O bonding for calcite DIC species may be underestimated based on a comparison between experimental calcite work and the Δ_{63}-T relation determined by Hill et al (2014). As a first order attempt to account for this, we have modified the clumped isotope component of the Watkins and Hunt (2015) model by applying a constant shift in Δ_{47} values toward more positive values according to the temperature-dependent difference for calcite between values predicted by the Hill et al. (2014) and Zaarur et al. (2013, Equation 7). The Zaarur et al. experimental study matches our data most closely. These adjustments are 0.113, 0.098, and 0.084‰ at pH = 6.6 and 10, 20, and 30ºC, respectively. This adjustment is not meant to be a rigorous correction for an exact comparison to our experimental results (Figures SM7 – SM9), rather, this shift has been included to assist in figure clarity.

It is worth noting that the modeled Δ_{47} values shift in a more positive direction when the surface speciation HCO_3^-:CO_3^{2-} ratio changes from 100 to 0.25 in the

kinetically controlled or influenced regions of precipitation rate. This observation is related to the exclusion of ^{13}C and ^{18}O during kinetic fractionation at more rapid precipitation rates and a disproportionate change in the predicted solid carbonate stochastic ^{13}C -^{18}O bonding compared to pre-existing ^{13}C -^{18}O bonds inherited from DIC. This effect is analogous to the kinetic effects in DIC predicted by Guo (2008) and shown experimentally by Affek and Zaarur (2014) during CO_2 degassing from solutions. The modeled ^{13}C -^{18}O bonding difference imparted by the surface speciation HCO_3^- : CO_3^{2-} ratio is slight. However, the fact that solution phase CO_3^{2-} is believed to have a lower Δ_{63} value than HCO_3^- but may impart a higher calcite Δ_{63} value compared to bicarbonate under certain conditions, all else being equal, implies that considering precipitation rate is critical when using clumped isotopes to investigate kinetic effects and helps support a precipitation mechanism that relies on CO_3^{2-} ions more than solution DIC speciation at circa neutral pH would suggest.

Also supporting our interpretation that CO_3^{2-} contributes more to calcite formation than HCO_3^- is the agreement between our data set and the model presented by Devriendt et al. (2017). This model is based on the kinetic reactions occurring between calcite, DIC, and H_2O to track O isotopes (but not C or clumped isotopes) as they precipitate from solution to form solid. A central tenet of the framework is that carbonate minerals form primarily from CO_3^{2-} ions but can be modified to allow for possible contribution from deprotonated HCO_3^- ions as well. Most parameters used to apply the model to our experiments are determined directly from measured solution chemistry values or other information provided in Table SM1. However, the value of the partial reaction order and reactivity coefficient of HCO_3^- are less straightforward to ascertain. We use a value of 0.22 for the partial reaction order as in the low ionic strength cases explored by Devriendt

et al. (2017). However, the fit between modeled fractionation and our observations decreases if larger partial reaction order values are considered. The final parameter of HCO_3^- reactivity was varied to find a range of values which agree with our dataset. The calculated calcite-water fractionation under our conditions is not sensitive to high values of HCO_3^- availability but requires a minimum contribution of 0.5 mol% HCO_3^- to reproduce the observed $10^3 \ln(\alpha_{calcite\text{-}H2O})$ values we report. Although the Watkins and Hunt (2015) and Devriendt et al. (2017) models are fundamentally unique, they both predict a relatively large contribution of CO_3^- to calcite formation based on our experimental data.

Saturation state is a first-order factor controlling carbonate precipitation rate. The experimental conditions utilized during our study do not include a wide enough range of saturation states to rigorously investigate a correlation between degree of saturation and ^{13}C -^{18}O bonding. To explore this parameter more broadly, however, we have compiled saturation state values from available data for the experimental data sets of Dennis and Schrag (2010), Tang et al. (2014), and Kelson et al. (2017). Starting saturation conditions were directly reported by Dennis and Schrag (2010) and used with the assumption that the starting saturation state was maximum at the initiation of the experiment and that the experiment shifted to exact saturation ($\Omega = 1$) by the end of the experiment. With this assumption, an average saturation for the experiment was calculated. A similar approach was taken for experiments of Kelson et al. (2017) with incomplete experimental condition details. Specifically, a few of the values in the experimental condition tables were missing. In these cases, a minimum saturation state of $\Omega = 1$ was assumed where both starting and ending pH or reagent concentrations were not available for saturation state calculations, but it should be noted this may be far from

the actual conditions. Saturation states for Kelson et al. (2017) experiments were calculated with PHREEQC software (Parkhurst and Appelo, 2013) and phreeqc.dat database. "Critical saturation indices" for Tang et al. (2014) experiments were indirectly reported in the publication of Tang et al. (2008). These values are assumed to be representative of most solid carbonate formation during the experiments reported by Tang et al. (2014) and have been converted to saturation state with no modification.

Temperatures used in the above studies include a wide variety of individual values. In order to make as direct a comparison as possible, the $10^3 \ln(\alpha_{calcite\text{-}H2O})$ and Δ_{47} values reported by Dietzel et al. (2009), Dennis and Schrag (2010), Tang et al. (2014), and Kelson et al. (2017) have been adjusted to correspond to temperatures explored in this study (Figures 5, 8-10, SM5, SM6, SM11-SM13). The work of Dietzel et al. (2009) and Tang et al. (2014) concern the same experiments but the former publication considers O isotopes and the latter publication focuses on clumped isotopes. For all four studies, individual experimental values in the range of 0-14°C, 15-24°C, and 25-40°C have been converted to 10°C, 20°C, and 30°C, respectively. These adjustments have been made according to the Δ_{47}-T or $10^3 \ln(\alpha_{calcite\text{-}H2O})$-T relations determined in each respective study and retain data set variability for each set of conditions. For example, Tang et al. (2014) report a Δ_{47}-T relation in their data of $\Delta_{47}(ARF) = (0.0387 \pm 0.0072) \times 10^6 T^{-2} + (0.2532 \pm 0.0829)$ which implies a Δ_{47} difference of -0.0175‰ between 5 and 10°C. This constant offset has been applied to all 5°C experiments of Tang et al. (2014) while adjustments of +0.0150‰ and +0.0265‰ have been applied to 25 and 40°C experiments, respectively. Similarly, most data points from the studies of Dennis and Schrag (2010) and Kelson et al. (2017) in the range of 0 to 40°C have been shifted to represent temperatures of 10°C, 20°C, and 30°C. Additionally, Devils Hole calcite values as

reported by Kluge et al. (2014) has been considered with the 30°C data. The adjustment from 33.7 to 30°C utilized the Δ_{47}-T and 10^3 ln($\alpha_{calcite\text{-}H2O}$)-T calibrations of Zaarur et al. (2013).

Exceptions to the datasets described in the preceding paragraph include the following: Following the discussion in Tang et al. (2014), we have excluded experiments performed at pH values above 9.0 in our considerations. Also, although Dietzel et al. (2009) report 17 experiments at 40°C, the work of Tang et al. (2014) only considers 7 of those experiments. We have included only the latter 7 experiments in our O isotope fractionation comparison. To limit our cross-study comparison to experimental approaches and conditions which are as similar as possible, we have only considered experiments by Kelson et al. (2017) which utilized "passive degassing" and "mixed solution" experiments. These two methods were also used by Dennis and Schrag (2010). Finally, some experimental details were undetermined or omitted from the publication of Kelson et al. (2017) which prevented the calculation of saturation state and/or 10^3 ln($\alpha_{calcite\text{-}H2O}$) values and such data sets (including all "filtered" experiments) are therefore not discussed here.

CO_2 Mixing Calculation Example (Matlab Format)

```
% The following is an example of overgrowth D47 for calcite grown on
% calcite seed crystals of known isotope composition and clumping.
% This example is based on measured values which apply to UWAI-002. This
% script was developed after the "numerical demonstration of how to calculate
% D47, D48, and D49 from mass spectrometer data" provided by
% Huntington et al. (2009) in the supplemental information.
```

```
% Non-linear D47 mixing calculations following Affek and Eiler (2006).

%%%%%%%%%%%%%%%%%%%%
% Measured Values                %
%%%%%%%%%%%%%%%%%%%%

Cs = 0.0799;       % grams of seed crystal used
Co = 0.1785;       % grams of overgrowth

% total (seed + overgrowth) gas values
d13t = 0.9688;     % d13C_PDB isotope composition
d18t = 30.2633;    % d18O_SMOW isotope composition
D47t = 0.6426;     % D47 value of CO2 gas in preferred reference frame

% seed crystal gas values
d13s = 4.3560;     % d13C_PDB isotope composition
d18s = 31.8090;    % d18O_SMOW isotope composition
D47s = 0.631;      % D47 value of CO2 gas in preferred reference frame

% reference/working gas values
RefGasd13 = -3.56; % dC13_PDB
RefGasd18 = 25.01; % d18O_SMOW

% Constants
```

```
OrigPDBCO2_R13 = 0.0118;     % "Brand Values" from Daeron et al. (2016)
VSMOW_R18 = 0.0020052;       % "Brand Values" from Daeron et al. (2016)
VSMOW_R17 = 0.00038475;      % "Brand Values" from Daeron et al. (2016)
VPDBcalcite_R13 = OrigPDBCO2_R13;
lambda = 0.528;                    % "Brand Values" from Daeron et al. (2016)
VPDBCO2_R13 = VPDBcalcite_R13;
VPDBCO2_R18 = 0.00208839;    % "Brand Values" from Daeron et al. (2016)
VPDBCO2_R17 = 0.00039310;    % "Brand Values" from Daeron et al. (2016)



%%%%%%%%%%%%%%%%%%%%%%%%%%%%
% Scramble reference gas                          %
%%%%%%%%%%%%%%%%%%%%%%%%%%%%
% REF GAS: calculate R13, R17, R18
% minimum value of (R13+2R18-R45)^2+(2R18+2R13R17+(R17)^2-R46)^2

RefGasd13; % defined above
RefGasd18; % defined above
RefGasR13 =((RefGasd13/1000)+1)*VPDBCO2_R13;
RefGasR18 =((RefGasd18/1000)+1)*VSMOW_R18;
RefGasR17 =((RefGasR18/VSMOW_R18)^lambda)*VSMOW_R17;

% REF GAS: calculate abundance of isotopes, assuming stochastic
% distribution of isotopes among isotopologues
```

```
RefGas12C =1/(1+RefGasR13); % [12C]=1/(1+R13)

RefGas13C = 1- RefGas12C; % [13C]=R13/(1+R13)

RefGas16O =1/(1+RefGasR17+RefGasR18); % [16O]=1/(1+R17+R18)

RefGas17O = RefGasR17*RefGas16O; % [17O]=R17/(1+R17+R18)

RefGas18O = RefGasR18*RefGas16O; % [18O]=R18/(1+R17+R18)


% REF GAS: calculate randomly distributed abundance of CO2

% [44]* = [12][16][16]

% [45]* = [13][16][16]+2[12][16][17]

% [46]* = 2[12][16][18]+[12][17][17]+2[13][16][17]

% [47]* = 2[13][16][18]+[13][17][17]+2[12][17][18]


RefGas121616 = RefGas12C*RefGas16O*RefGas16O;

RefGas121617 = RefGas12C*2*RefGas16O*RefGas17O;

RefGas131616 = RefGas13C*RefGas16O*RefGas16O;

RefGas121618 = RefGas12C*2*RefGas16O*RefGas18O;

RefGas121717 = RefGas12C*RefGas17O*RefGas17O;

RefGas131716 = RefGas13C*2*RefGas17O*RefGas16O;

RefGas121718 = RefGas12C*2*RefGas17O*RefGas18O;

RefGas131618 = RefGas13C*2*RefGas16O*RefGas18O;

RefGas131717 = RefGas13C*RefGas17O*RefGas17O;

RefGas121818 = RefGas12C*RefGas18O*RefGas18O;

RefGas131718 = RefGas13C*2*RefGas17O*RefGas18O;
```

```
RefGas131818 = RefGas13C*RefGas18O*RefGas18O;


RefGas44 = RefGas121616;
RefGas45 = RefGas121617 + RefGas131616;
RefGas46 = RefGas121618 + RefGas121717 + RefGas131716;
RefGas47 = RefGas121718 + RefGas131618 + RefGas131717;
RefGas48 = RefGas121818 + RefGas131718;
RefGas49 = RefGas131818;


% REF GAS: calculate ratios by dividing abundance by [44]*


RefGasR45 = RefGas45/RefGas44;
RefGasR46 = RefGas46/RefGas44;
RefGasR47 = RefGas47/RefGas44;
RefGasR48 = RefGas48/RefGas44; % not used in calculations below
RefGasR49 = RefGas49/RefGas44; % not used in calculations below


%%%%%%%%%%%%%%%%%%%%%%%%%%%%
% Scramble seed gas                                  %
%%%%%%%%%%%%%%%%%%%%%%%%%%%%
% seed GAS: calculate R13, R17, R18


sGasd13 = d13s; % defined above
sGasd18 = d18s; % defined above
```

```
sGasR13 = ((sGasd13/1000)+1)*VPDBCO2_R13;
sGasR18 = ((sGasd18/1000)+1)*VSMOW_R18;
sGasR17 = ((sGasR18/VSMOW_R18)^lambda)*VSMOW_R17;

% seed GAS: calculate abundance of isotopes, assuming stochastic
% distribution of isotopes among isotopologues

sGas12C = 1/(1+sGasR13);% [12C]=1/(1+R13)
sGas13C = 1- sGas12C; % [13C]=R13/(1+R13)
sGas16O = 1/(1+sGasR17+sGasR18);  % [16O]=1/(1+R17+R18)
sGas17O = sGasR17*sGas16O; % [17O]=R17/(1+R17+R18)
sGas18O = sGasR18*sGas16O;   % [18O]=R18/(1+R17+R18)

% seed GAS: calculate randomly distributed abundance of CO2
% [44]* = [12][16][16]
% [45]* = [13][16][16]+2[12][16][17]
% [46]* = 2[12][16][18]+[12][17][17]+2[13][16][17]
% [47]* = 2[13][16][18]+[13][17][17]+2[12][17][18]

sGas121616 = sGas12C*sGas16O*sGas16O;
sGas121617 = sGas12C*2*sGas16O*sGas17O;
sGas131616 = sGas13C*sGas16O*sGas16O;
sGas121618 = sGas12C*2*sGas16O*sGas18O;
sGas121717 = sGas12C*sGas17O*sGas17O;
```

```
sGas131716 = sGas13C*2*sGas17O*sGas16O;

sGas121718 = sGas12C*2*sGas17O*sGas18O;

sGas131618 = sGas13C*2*sGas16O*sGas18O;

sGas131717 = sGas13C*sGas17O*sGas17O;

sGas121818 = sGas12C*sGas18O*sGas18O;

sGas131718 = sGas13C*2*sGas17O*sGas18O;

sGas131818 = sGas13C*sGas18O*sGas18O;


sGas44 = sGas121616;

sGas45 = sGas121617 + sGas131616;

sGas46 = sGas121618 + sGas121717 + sGas131716;

sGas47 = sGas121718 + sGas131618 + sGas131717;

sGas48 = sGas121818 + sGas131718;

sGas49 = sGas131818;


% seed GAS: calculate ratios by dividing abundance by [44]*


sGasR45 = sGas45/sGas44; % not used in calculations below

sGasR46 = sGas46/sGas44; % not used in calculations below

sGasR47 = sGas47/sGas44;

sGasR48 = sGas48/sGas44; % not used in calculations below

sGasR49 = sGas49/sGas44; % not used in calculations below
```

```
%%%
```

```
% [47]* = 2[13][16][18]+[13][17][17]+2[12][17][18]

tGas121616 = tGas12C*tGas16O*tGas16O;
tGas121617 = tGas12C*2*tGas16O*tGas17O;
tGas131616 = tGas13C*tGas16O*tGas16O;
tGas121618 = tGas12C*2*tGas16O*tGas18O;
tGas121717 = tGas12C*tGas17O*tGas17O;
tGas131716 = tGas13C*2*tGas17O*tGas16O;
tGas121718 = tGas12C*2*tGas17O*tGas18O;
tGas131618 = tGas13C*2*tGas16O*tGas18O;
tGas131717 = tGas13C*tGas17O*tGas17O;
tGas121818 = tGas12C*tGas18O*tGas18O;
tGas131718 = tGas13C*2*tGas17O*tGas18O;
tGas131818 = tGas13C*tGas18O*tGas18O;

tGas44 = tGas121616;
tGas45 = tGas121617 + tGas131616;
tGas46 = tGas121618 + tGas121717 + tGas131716;
tGas47 = tGas121718 + tGas131618 + tGas131717;
tGas48 = tGas121818 + tGas131718;
tGas49 = tGas131818;

% total GAS: calculate ratios by dividing abundance by [44]*
```

```
tGasR45 = tGas45/tGas44; % not used in calculations below
tGasR46 = tGas46/tGas44; % not used in calculations below
tGasR47 = tGas47/tGas44;
tGasR48 = tGas48/tGas44; % not used in calculations below
tGasR49 = tGas49/tGas44; % not used in calculations below


%%%%%%%%%%%%%%%%%%%%%%%%%%%%%%%%%%%%%%%%%%%%
% Mixing Model Calculations                   %
%%%%%%%%%%%%%%%%%%%%%%%%%%%%%%%%%%%%%%%%%%%%

% R45, R46, R47 expressions are also given by
% Affek and Eiler (2006) Appendix A equations (A2)

Ct = Cs + Co; % total calcite mass
f = Cs/Ct;    % fraction of seed mass to total mass

R13s = ((d13s/1000)+1)*VPDBcalcite_R13;  % mass 13 ratio for seeds
R18s = ((d18s/1000)+1)*VSMOW_R18;        % mass 18 ratio for seeds
R17s = VSMOW_R17*(R18s/VSMOW_R18)^lambda;
R45s = R13s + 2*R17s;                    % Eqn from Santrock et al. (1985)
d45s = (R45s/RefGasR45-1)*1000;
R46s = 2*R18s + 2*R13s*R17s + (R17s)^2;  % Eqn from Santrock et al. (1985)
d46s = (R46s/RefGasR46-1)*1000;
```

```
R47s = ((D47s/1000)+1)*sGasR47;          % mass 47 ratio for seeds
d47s = (R47s/RefGasR47-1)*1000;

R13t = ((d13t/1000)+1)*VPDBcalcite_R13;  % mass 13 ratio for total
R18t = ((d18t/1000)+1)*VSMOW_R18;        % mass 18 ratio for total
R17t = VSMOW_R17*(R18t/VSMOW_R18)^lambda;
R45t = R13t + 2*R17t;                    % Eqn from Santrock et al. (1985)
d45t = (R45t/RefGasR45-1)*1000;
R46t = 2*R18t + 2*R13t*R17t + (R17t)^2;  % Eqn from Santrock et al. (1985)
d46t = (R46t/RefGasR46-1)*1000;
R47t = ((D47t/1000)+1)*tGasR47;          % mass 47 ratio for seeds
d47t = (R47t/RefGasR47-1)*1000;

% The following equations are derived from
% Affek and Eiler (2006) Appendix A equations (A6)

R13o = (R13t-f*R13s)/(1-f); % mass 13 ratio for overgrowth gas
R17o = (R17t-f*R17s)/(1-f); % mass 17 ratio for overgrowth gas
R18o = (R18t-f*R18s)/(1-f); % mass 18 ratio for overgrowth gas
R45o = (R45t-f*R45s)/(1-f); % mass 45 ratio for overgrowth gas
R46o = (R46t-f*R46s)/(1-f); % mass 46 ratio for overgrowth gas
R47o = (R47t-f*R47s)/(1-f); % mass 47 ratio for overgrowth gas
```

```
%%%%%%%%%%%%%%%%%%%%%%
% Overgrowth Values                    %
%%%%%%%%%%%%%%%%%%%%%%

d13o = (d13t-f*d13s)/(1-f); % linear mixing
d18o = (d18t-f*d18s)/(1-f); % linear mixing
d47o = (d47t-f*d47s)/(1-f); % linear mixing

% Non-linear mixing equation (A7) from
% Affek and Eiler (2006) Appendix A
D47o = (R47o/(2*R13o*R18o+2*R17o*R18o+R13o*(R17o^2))...
    -R46o/(2*R18o+2*R13o*R17o+(R17o)^2)...
    -R45o/(R13o+2*R17o)+1)*1000
```

Table SM1: Experimental Conditions and Supporting Isotope Compositions

Experiment Identification	Experiment Date	Experiment Length (h)	System T (° C)*	Flow Rate (mL min^{-1}) N_2	Flow Rate (mL min^{-1}) CO_2	pCO_2 (%)	pCO_2 (%)**	pH	Ca^{2+} Initial (mmol)	Ca^{2+} Final (mmol)	Alkalinity Start (mmol)	Alkalinity End (mmol)	Calcite Saturation State (Ω) Start	Calcite Saturation State (Ω) End
UWAI-016	20140414A	94	9.9	45.0	5.0	10.0	12.1	6.5	9.8	9.5	9.7	8.1	1.0	0.8
UWAI-017	20140414B	93	9.9	45.0	5.0	10.0	9.1	6.6	9.8	9.5	9.7	8.0	1.3	1.1
UWAI-018	20140420A	138	10.0	45.0	5.0	10.0	11.2	6.5	10.7	8.9	9.7	7.7	1.1	0.8
UWAI-019	20140420B	136	9.9	45.0	5.0	10.0	7.0	6.7	10.7	9.6	9.7	7.8	1.8	1.4
UWAI-025	20140607A	206	10.0	47.0	3.0	6.0	6.2	6.7	10.7	9.8	9.6	6.0	1.6	1.0
UWAI-026	20140607B	204	10.0	47.0	3.0	6.0	5.4	6.8	10.7	10.1	9.6	6.2	2.1	1.4
UWAI-027	20140617A	180	10.0	47.0	3.0	6.0	5.5	6.8	10.0	10.6	9.6	6.3	2.0	1.4
UWAI-028	20140617B	178	10.0	47.0	3.0	6.0	5.5	6.8	10.0	10.8	9.6	6.6	2.0	1.5
UWAI-029	20140626A	69	10.0	47.0	3.0	6.0	5.5	6.8	10.8	9.3	9.6	7.1	2.1	1.4
UWAI-030	20140626B	68	10.0	47.0	3.0	6.0	5.4	6.8	10.8	9.1	9.6	7.4	2.2	1.5
UWAI-031	20140630A	232	10.0	47.0	3.0	6.0	8.0	6.7	10.7	9.8	9.6	8.6	1.6	1.4
UWAI-032	20140630B	227	10.0	47.0	3.0	6.0	7.8	6.7	10.7	10.2	9.6	9.1	1.7	1.5
UWAI-033	20140711A	117	10.0	47.0	3.0	6.0	5.5	6.8	10.6	10.2	9.6	7.3	2.1	1.6
UWAI-034	20140711B	115	10.0	47.0	3.0	6.0	5.5	6.8	10.6	10.3	9.6	7.6	2.1	1.7
UWAI-002	20140214	151	20.0	47.5	2.5	5.0	5.9	6.8	11.4	8.8	9.8	6.1	3.1	1.7
UWAI-003	20140221	143	20.0	47.5	2.5	5.0	4.9	6.9	11.7	9.1	9.9	6.4	4.0	2.2
UWAI-004	20140227	144	20.0	47.5	2.5	5.0	4.8	6.9	11.1	9.0	9.9	6.3	3.8	2.2
UWAI-005	20140305	191	20.0	47.5	2.5	5.0	4.7	6.9	11.8	9.5	9.9	5.9	4.0	2.2
UWAI-006	20140314A	93	20.0	47.5	2.5	5.0	4.7	6.9	11.4	8.6	9.8	6.4	4.0	2.2
UWAI-007	20140314B	91	19.9	47.5	2.5	5.0	4.7	6.8	11.4	9.8	9.8	3.7	3.1	1.1
UWAI-008	20140320A	95	20.0	47.5	2.5	5.0	5.1	6.9	11.1	8.3	9.8	6.3	3.7	2.0
UWAI-009	20140320B	94	19.9	47.5	2.5	5.0	5.1	6.9	11.1	8.8	9.8	6.2	3.7	2.1
UWAI-010	20140325A	193	20.0	47.5	2.5	5.0	4.9	6.9	11.1	8.4	9.8	5.9	3.8	2.0
UWAI-011	20140325B	191	19.9	47.5	2.5	5.0	4.2	7.0	11.1	8.5	9.8	5.9	4.3	2.3
UWAI-012	20140403A	109	20.0	47.5	2.5	5.0	4.0	7.0	10.7	9.1	9.7	6.6	4.6	2.9
UWAI-013	20140403B	101	19.9	47.5	2.5	5.0	4.4	7.0	10.7	9.5	9.7	7.0	4.3	3.0
UWAI-014	20140409A	91	20.0	45.0	5.0	10.0	11.8	6.6	11.0	9.2	9.7	8.6	1.8	1.4
UWAI-015	20140409B	89	19.9	45.0	5.0	10.0	10.0	6.6	11.0	10.1	9.7	8.8	2.1	1.8
UWAI-023	20140531A	137	20.0	47.0	3.0	6.0	6.5	6.8	11.5	4.7	9.6	7.9	3.0	1.3
UWAI-024	20140531B	138	20.0	47.0	3.0	6.0	6.1	6.9	11.5	5.6	9.6	8.5	3.8	2.0
UWAI-045	20140823A	200	20.0	43.5	6.5	13.0	13.1	6.5	11.6	10.7	10.0	8.4	1.6	1.3
UWAI-046	20140823B	198	20.0	43.5	6.5	13.0	13.4	6.5	11.6	10.7	10.0	8.4	1.6	1.3
UWAI-020	20140427A	119	30.0	42.0	8.0	16.0	18.8	6.3	10.1	9.8	9.6	6.4	1.5	1.0
UWAI-021	20140427B	121	30.1	42.0	8.0	16.0	14.9	6.5	10.1	9.5	9.6	7.5	1.9	1.5
UWAI-035	20140717A	149	30.0	43.5	6.5	13.0	12.3	6.6	11.2	9.3	9.5	6.5	2.5	1.6
UWAI-036	20140717B	143	30.0	43.5	6.5	13.0	11.2	6.6	11.2	9.9	9.5	7.5	2.5	1.9
UWAI-037	20140724A	235	30.0	43.5	6.5	13.0	13.7	6.5	11.2	9.2	9.5	6.4	2.0	1.2
UWAI-038	20140724B	233	30.0	43.5	6.5	13.0	12.8	6.5	11.2	9.3	9.5	6.4	2.0	1.2
UWAI-039	20140804A	89	30.0	43.5	6.5	13.0	14.5	6.5	11.4	9.6	9.4	6.6	2.0	1.3
UWAI-040	20140804B	87	30.0	43.5	6.5	13.0	11.4	6.6	11.4	10.4	9.4	7.9	2.5	2.0
UWAI-041	20140810A	144	30.0	43.5	6.5	13.0	14.4	6.5	11.4	9.7	9.7	7.0	2.1	1.4
UWAI-042	20140810B	142	30.0	43.5	6.5	13.0	14.1	6.5	11.4	9.8	9.7	7.0	2.1	1.4
UWAI-043	20140817A	240	30.0	43.5	6.5	13.0	15.5	6.5	11.4	9.8	9.9	6.9	2.1	1.4
UWAI-044	20140817B	238	30.0	43.5	6.5	13.0	13.4	6.6	11.4	10.5	9.9	8.3	2.7	2.1
UWAI-047	20140901A	214	30.0	43.5	6.5	13.0	14.2	6.5	12.0	10.1	9.8	6.8	2.1	1.4
UWAI-048	20140901B	211	30.0	43.5	6.5	13.0	13.4	6.5	12.0	10.4	9.8	7.4	2.7	1.9
UWAI-022	Seed Crystals		20.0											
Reagent $CaCl_2$														

Error values represent 2 standard deviations about the mean of multiple analyses

* Experiment UWAI-035 homogeneously nucleated
Precipitation Rate unknown due to homogeneous nucleation, rate estimated based on experiment UWAI-036

** Equilibrium pCO2 calculated by PHREEQC according to solution conditions

Table SM1 (cont.): Experimental Conditions and Supporting Isotope Compositions

Experiment	Experiment	Seed Crystals	Overgrowth Mass Precipitated (g)		Rate	log Rate	Rate	log Rate	δ^{13}C DIC (VPDB, ‰)		δ^{18}O H_2O (VSMOW, ‰)		δ^{43}Ca Calcite (HPS-932016, ‰)			
Identification	Date	(g)	Mass Balance	Isotope Dilution	(μmol m^{-2} h^{-1})	(μmol m^{-2} h^{-1})	(mol m^{-2} s^{-1})	(mol m^{-2} s^{-1})	Start	End	Start	End	Calcite	Num. Analyses	Solution	Num. Analyses
UWAI-016	20140414A	0.080	0.109	0.090	103	2.0	2.9E-08	-7.5	-2.1	-2.0	-8.7	-9.0	44.7 ± 0.4	2	0.3 ± 0.3	3
UWAI-017	20140414B	0.080	0.111	0.091	105	2.0	2.9E-08	-7.5	-2.1	-1.9	-8.7	-9.0	42.4 ± 0.4	2	0.1 ± 0.4	3
UWAI-018	20140420A	0.080	0.128	0.107	84	1.9	2.3E-08	-7.6	-2.8	-2.0	-8.9	-9.0	40.7 ± 0.5	2	0.2 ± 0.6	2
UWAI-019	20140420B	0.081	0.125	0.114	90	2.0	2.5E-08	-7.6	-2.8	-1.9	-8.9	-8.9	39.3 ± 0.5	2	0.8	1
UWAI-025	20140607A	0.081	0.066	0.055	29	1.5	7.9E-09	-8.1	-2.7	-3.4	-8.9	-8.7	59.3 ± 5.1	6	-0.1 ± 1.2	3
UWAI-026	20140607B	0.081	0.062	0.055	29	1.5	8.0E-09	-8.1	-2.7	-3.2	-8.9	-8.8	56.4 ± 2.2	6	-0.2 ± 2.6	3
UWAI-027	20140617A	0.080	0.055	0.039	23	1.4	6.4E-09	-8.2	-2.0	-3.5	-8.9	-8.9	63.9 ± 0.3	2	0.3	1
UWAI-028	20140617B	0.081	0.041	0.038	23	1.4	6.3E-09	-8.2	-2.0	-3.4	-8.9	-9.0	64.5 ± 0.8	2	0.5	1
UWAI-029	20140626A	0.080	0.062	0.053	84	1.9	2.3E-08	-7.6	-2.2	-2.7	-9.2	-9.0	56.9 ± 0.0	2	0.4	1
UWAI-030	20140626B	0.080	0.048	0.045	72	1.9	2.0E-08	-7.7	-2.2	-2.9	-9.2	-9.0	61.4 ± 2.0	2	0.9	1
UWAI-031	20140630A	0.081	0.084	0.072	33	1.5	9.1E-09	-8.0	-3.3	-4.2	-9.3	-9.0	53.4 ± 8.3	2	0.3	1
UWAI-032	20140630B	0.081	0.056	0.059	28	1.4	7.7E-09	-8.1	-3.3	-4.0	-9.3	-8.6	56.1 ± 3.1	2	0.8	1
UWAI-033	20140711A	0.080	0.139	0.132	121	2.1	3.4E-08	-7.5	-1.6	-2.5	-8.7	-8.9	36.3 ± 0.5	2	0.5	1
UWAI-034	20140711B	0.080	0.128	0.126	118	2.1	3.3E-08	-7.5	-1.6	-2.4	-8.7	-8.8	37.1 ± 0.1	2	1.2	1
UWAI-002	20140214	0.080	0.219	0.179	128	2.1	3.6E-08	-7.4	-1.5	-2.8	-8.9	-8.9	29.0 ± 2.4	3	0.9	1
UWAI-003	20140221	0.080	0.194	0.135	102	2.0	2.8E-08	-7.5	-5.5	-2.9	-9.1	-9.0	35.2 ± 0.5	2	0.9	1
UWAI-004	20140227	0.079	0.174	0.146	110	2.0	3.1E-08	-7.5	-2.1	-2.8	-9.0	-8.9	33.5 ± 0.3	2	1.4	1
UWAI-005	20140305	0.080	0.166	0.143	81	1.9	2.2E-08	-7.7	-1.9	-3.3	-9.0	-8.8	34.0 ± 0.6	2	0.7	1
UWAI-006	20140314A	0.081	0.184	0.180	207	2.3	5.8E-08	-7.2	-1.5	-2.8	-8.8	-8.6	28.7 ± 2.2	2	-0.1	1
UWAI-007	20140314B	0.081	0.186	0.174	204	2.3	5.7E-08	-7.2	-1.5	-2.6	-8.8	-8.7	29.5 ± 3.9	2	-0.1	1
UWAI-008	20140320A	0.080	0.189	0.186	210	2.3	5.8E-08	-7.2	-4.8	-3.0	-8.6	-8.6	28.5 ± 1.5	2	0.8	1
UWAI-009	20140320B	0.080	0.189	0.171	195	2.3	5.4E-08	-7.3	-4.8	-2.8	-8.6	-8.9	30.3 ± 2.2	2	-0.2	1
UWAI-010	20140325A	0.081	0.184	0.148	82	1.9	2.3E-08	-7.6	-2.4	-3.0	-8.8	-8.7	33.4 ± 0.7	2	0.8 ± 3.6	2
UWAI-011	20140325B	0.080	0.192	0.166	93	2.0	2.6E-08	-7.6	-2.4	-2.9	-8.8	-9.0	31.0 ± 0.5	2	0.4 ± 0.2	3
UWAI-012	20140403A	0.080	0.149	0.152	150	2.2	4.2E-08	-7.4	-2.4	-2.5	-9.1	-8.4	32.8 ± 0.7	2	-0.7 ± 3.7	2
UWAI-013	20140403B	0.081	0.132	0.125	132	2.1	3.7E-08	-7.4	-2.4	-2.5	-9.1	-8.6	37.3 ± 0.8	2	0.3	1
UWAI-014	20140409A	0.080	0.086	0.095	113	2.1	3.1E-08	-7.5	-4.0	-3.1	-8.7	-8.7	43.3 ± 0.7	2	0.5	1
UWAI-015	20140409B	0.081	0.082	0.076	92	2.0	2.5E-08	-7.6	-4.0	-3.0	-8.7	-8.9	48.5 ± 1.0	2	0.6	1
UWAI-023	20140531A	0.080	0.490	0.454	358	2.6	1.0E-07	-7.0	-2.9	-3.2	-8.4	-8.1	12.7 ± 2.5	4	0.1 ± 1.9	3
UWAI-024	20140531B	0.080	0.470	0.610	477	2.7	1.3E-07	-6.9	-2.9	-3.4	-8.4	-8.1	13.0 ± 4.1	4	1.9 ± 1.3	2
UWAI-045	20140823A	0.080	0.100	0.080	43	1.6	1.2E-08	-7.9	-3.4	-4.7	-8.8	-8.6	47.3 ± 1.0	2	1.0	1
UWAI-046	20140823B	0.080	0.103	0.100	54	1.7	1.5E-08	-7.8	-3.4	-5.0	-8.8	-9.1	41.9 ± 1.4	2	1.2	1
UWAI-020	20140427A	0.080	0.171	0.160	145	2.2	4.0E-08	-7.4	-3.5	-5.5	-9.1	-8.7	31.6 ± 0.6	2	1.8 ± 3.3	3
UWAI-021	20140427B	0.080	0.149	0.136	122	2.1	3.4E-08	-7.5	-3.5	-6.0	-9.1	-8.1	34.9 ± 0.9	2	-1.8 ± 3.9	3
UWAI-035	20140717A	NA	0.187	NA	110*	2.0*	3.1E-08*	-7.5*	-3.9	-5.1	-8.8	-8.9	0.0 ± 0.0	2	1.2	1
UWAI-036	20140717B	0.080	0.149	0.146	110	2.0	3.1E-08	-7.5	-3.9	-4.6	-8.8	-8.9	33.5 ± 1.0	2	0.0	1
UWAI-037	20140724A	0.081	0.187	0.178	81	1.9	2.3E-08	-7.6	-4.0	-4.9	-8.5	-8.6	30.0 ± 0.4	2	0.3	1
UWAI-038	20140724B	0.079	0.191	0.170	80	1.9	2.2E-08	-7.7	-4.0	-5.0	-8.5	-8.7	29.1 ± 3.6	2	0.2	1
UWAI-039	20140804A	0.082	0.173	0.168	200	2.3	5.6E-08	-7.3	-4.0	-5.0	-8.3	-8.9	29.3 ± 5.4	2	0.4	1
UWAI-040	20140804B	0.082	0.118	0.125	152	2.2	4.2E-08	-7.4	-4.0	-4.5	-8.3	-9.1	39.3 ± 4.6	2	0.5	1
UWAI-041	20140810A	0.080	0.179	0.180	136	2.1	3.8E-08	-7.4	-4.0	-4.9	-9.3	-8.7	29.3	1	0.8	1
UWAI-042	20140810B	0.081	0.177	0.164	123	2.1	3.4E-08	-7.5	-4.0	-4.5	-9.3	-9.1	31.9 ± 7.2	3	0.4	1
UWAI-043	20140817A	0.081	0.162	0.154	68	1.8	1.9E-08	-7.7	-4.0	-5.3	-9.2	-8.2	32.5 ± 1.4	2	0.6	1
UWAI-044	20140817B	0.081	0.108	0.105	47	1.7	1.3E-08	-7.9	-4.0	-4.4	-9.2	-8.4	42.8 ± 3.7	2	0.4	1
UWAI-047	20140901A	0.081	0.166	0.164	82	1.9	2.3E-08	-7.6	-5.1	-6.6	-9.2	-8.9	32.7 ± 3.2	2	0.2	1
UWAI-048	20140901B	0.081	0.150	0.106	53	1.7	1.5E-08	-7.8	-5.1	-6.5	-9.2	-9.8	40.1 ± 3.5	2	0.0	1
UWAI-022	Seed Crystals												94.6 ± 2.1			
	Reagent $CaCl_2$												0.4 ± 0.0			

Table SM2: Standards, Heated Gasses, and Equilibrated Gasses Analyzed During Clumped Isotope Analyses

Measurement			$\delta^{13}C$	$\delta^{13}C$	$\delta^{18}O$ gas	$\delta^{18}O$ mineral	$\delta^{18}O$	δ 45 raw	δ 46 raw	δ 47 raw	δ 47 raw	Δ 47 raw	D47	D47	d48	d48	D48	D48	d49	d49	CIT	CIT	ARF	ARF
Week	Type	Name	VPDB (‰)	1σ	VSMOW (‰)	PDB (‰)	1σ	(‰)	(‰)	(‰)	1σ	(v. Oz)	1σ	sterror	(v. Oz)	1σ	(v. Oz)	1σ	(v. Oz)	1σ	slope	intercept	slope	intercept
1	Standard	TV03	3.417	0.005	30.408	-8.578	0.015	6.709	5.276	12.049	0.046	-0.096	0.029	0.010	15.998	0.673	5.361	0.648	-1.425	0.932	0.012	-0.779	1.124	0.012
1	Standard	CIT Carrara	2.115	0.004	37.308	-1.939	0.019	5.728	11.998	17.485	0.036	-0.290	0.021	0.007	35.223	0.769	10.823	0.736	-1.541	0.991	0.012	-0.779	1.124	0.012
1	Standard	TV03	3.348	0.002	30.299	-8.683	0.032	6.641	5.170	11.887	0.049	-0.081	0.029	0.010	16.588	0.873	6.158	0.809	-2.405	0.997	0.012	-0.779	1.124	0.012
1	Standard	CIT Carrara	2.101	0.003	37.329	-1.919	0.036	5.715	12.018	17.536	0.072	-0.246	0.039	0.014	37.149	1.278	12.662	1.179	-3.436	1.113	0.013	-0.691	1.124	0.012
1	Standard	TV03	3.461	0.004	30.545	-8.446	0.054	6.756	5.410	12.288	0.089	-0.037	0.038	0.014	18.875	2.078	7.940	1.952	-3.786	2.035	0.013	-0.691	1.124	0.012
1	Standard	CIT Carrara	2.120	0.003	37.420	-1.831	0.069	5.736	12.107	17.642	0.087	-0.249	0.040	0.014	38.731	1.691	14.028	1.525	-4.747	1.750	0.013	-0.691	1.124	0.012
1	Standard	TV03	3.438	0.004	30.532	-8.458	0.076	6.733	5.397	12.263	0.120	-0.027	0.048	0.017	19.548	1.899	8.630	1.735	-4.902	1.929	0.013	-0.691	1.124	0.012
1	Standard	CIT Carrara	2.127	0.002	37.444	-1.808	0.065	5.743	12.131	17.713	0.086	-0.211	0.044	0.015	39.474	1.794	14.706	1.627	-5.932	1.465	0.013	-0.691	1.124	0.012
1	Standard	CIT Carrara	2.069	0.003	37.102	-2.138	0.007	5.678	11.796	17.255	0.060	-0.268	0.065	0.023	33.013	0.423	9.066	0.415	0.325	0.706	0.013	-0.691	1.124	0.012
1	Standard	TV03	3.373	0.005	30.257	-8.724	0.009	6.661	5.051	11.862	0.051	-0.088	0.049	0.017	13.853	0.470	3.534	0.457	0.659	0.857	0.013	-0.688	1.124	0.012
1	Standard	CIT Carrara	2.071	0.004	37.096	-2.143	0.010	5.680	11.791	17.287	0.030	-0.234	0.029	0.011	32.767	0.436	8.836	0.411	0.419	0.857	0.013	-0.688	1.124	0.012
1	Standard	TV03	3.397	0.005	30.339	-8.645	0.009	6.688	5.208	11.974	0.047	-0.082	0.047	0.017	14.549	0.807	4.063	0.786	0.008	1.338	0.012	-0.688	1.124	0.012
1	Standard	TV03	3.402	0.003	30.317	-8.665	0.006	6.693	5.187	11.951	0.056	-0.088	0.053	0.019	14.231	0.549	3.790	0.539	0.606	0.785	0.012	-0.688	1.124	0.012
1	Heated Gas	BOC	-10.988	0.005	29.382	-9.566	0.023	-6.797	4.244	-3.690	0.034	-0.829	0.027	0.010	11.452	0.530	2.922	0.501	0.461	0.827	0.012	-0.779	1.124	0.012
1	Heated Gas	BOC	-10.906	0.004	30.464	-8.524	0.041	-6.682	5.299	-2.482	0.079	-0.769	0.049	0.017	17.263	1.642	6.567	1.557	-2.686	1.819	0.012	-0.779	1.124	0.012
1	Heated Gas	eBOC	-10.775	0.003	60.274	20.158	0.056	-5.546	34.350	27.455	0.085	-0.397	0.031	0.011	102.693	1.953	30.669	1.722	-4.955	2.078	0.012	-0.779	1.124	0.012
1	Heated Gas	eBOC	-10.726	0.005	54.672	14.767	0.012	-5.690	28.891	21.986	0.078	-0.382	0.075	0.027	82.280	0.740	22.354	0.680	0.100	1.128	0.013	-0.691	1.124	0.012
1	Heated Gas	BOC	-10.164	0.004	31.507	-7.520	0.011	-5.953	6.317	-0.655	0.059	-0.692	0.057	0.020	17.430	0.730	4.696	0.703	0.310	1.268	0.013	-0.691	1.124	0.012
1	Heated Gas	eBOC	-10.661	0.002	58.993	18.926	0.011	-5.483	33.102	26.250	0.041	-0.449	0.048	0.017	95.150	0.561	26.093	0.524	-1.130	0.768	0.013	-0.691	1.124	0.012
1	Heated Gas	eBOC	-10.751	0.003	59.435	19.350	0.015	5.960	6.733	26.647	0.050	-0.400	0.060	0.021	95.917	0.527	25.957	0.472	-0.234	0.808	0.013	-0.691	1.124	0.012
1	Heated Gas	BOC	-10.611	0.026	33.936	-5.184	10.429	-6.406	5.090	-2.187	0.127	-0.556	0.137	0.048	13.958	0.583	3.714	0.577	0.940	1.085	0.013	-0.691	1.124	0.012
1	Heated Gas	BOC	-10.374	0.007	30.505	-8.485	0.014	-6.184	5.340	-1.724	0.128	-0.568	0.141	0.050	15.001	0.624	4.247	0.600	0.514	0.733	0.013	-0.691	1.124	0.012
1	Heated Gas	BOC	-10.739	0.004	31.028	-7.982	0.005	-6.507	5.849	-0.721	0.022	0.275	0.020	0.007	18.590	0.466	6.778	0.460	-2.305	0.389	0.013	-0.691	1.124	0.012
1	Heated Gas	eBOC	-10.565	0.002	59.899	19.797	0.010	-5.363	33.986	27.329	0.062	-0.364	0.065	0.023	96.922	0.574	25.998	0.533	0.423	0.853	0.013	-0.691	1.124	0.012
1	Equilibrated Gas	BOC 25degC	-10.634	0.003	63.367	23.133	0.010	-5.311	37.364	31.417	0.022	0.345	0.024	0.008	105.965	0.355	27.729	0.321	-0.049	0.767	0.012	-0.688	1.124	0.012
1	Equilibrated Gas	BOC 25degC	-10.825	0.003	28.581	-10.336	0.028	-6.923	4.305	-3.544	0.047	-0.049	0.027	0.010	9.986	0.496	3.024	0.497	0.117	0.859	0.013	-0.691	1.124	0.012
1	Equilibrated Gas	BOC 25degC	-10.489	0.003	28.675	-10.246	0.008	-6.354	3.556	-3.118	0.027	-0.041	0.021	0.008	8.956	0.488	1.818	0.471	1.991	0.718	0.012	-0.688	1.124	0.012
2	Standard	TV03	3.397	0.001	30.540	-8.451	0.014	6.763	5.451	12.342	0.036	-0.026	0.042	0.015	17.269	0.137	6.283	0.257	-3.386	0.237	0.019	-0.838	1.006	0.017
2	Standard	CIT Carrera	2.129	0.002	37.382	-1.868	0.003	5.814	12.128	17.740	0.020	-0.233	0.022	0.008	38.327	0.204	13.629	0.245	-2.993	0.177	0.019	-0.838	1.006	0.017
2	Standard	TV03	3.440	0.001	30.525	-8.465	0.006	6.803	5.432	12.351	0.039	-0.043	0.039	0.014	17.318	0.299	6.360	0.111	-2.943	0.397	0.019	-0.838	1.006	0.017
2	Standard	CIT Carrera	2.127	0.001	37.402	-1.849	0.003	5.810	12.128	17.754	0.031	-0.237	0.030	0.010	38.609	0.343	13.865	0.185	-3.008	0.205	0.019	-0.838	1.006	0.017
2	Standard	TV03	3.385	0.002	30.535	-8.456	0.004	6.752	5.440	12.313	0.026	-0.038	0.026	0.009	17.334	0.320	6.356	0.206	-2.549	0.271	0.019	-0.838	1.006	0.017
2	Standard	CIT Carrera	2.139	0.003	37.406	-1.845	0.004	5.820	12.127	17.778	0.020	-0.228	0.016	0.006	38.493	0.258	13.744	0.124	-3.191	0.274	0.019	-0.838	1.006	0.017
2	Standard	TV03	3.422	0.001	30.534	-8.457	0.009	6.786	5.442	12.330	0.015	-0.055	0.015	0.005	17.588	0.197	6.610	0.193	-3.563	0.252	0.019	-0.838	1.006	0.017
2	Standard	TV03	3.414	0.003	30.580	-8.413	0.005	6.782	5.484	12.404	0.024	-0.019	0.025	0.009	17.946	0.245	6.875	0.242	-3.126	0.295	0.019	-0.838	1.006	0.017
2	Standard	CIT Carrera	2.134	0.002	37.417	-1.834	0.004	5.817	12.144	17.792	0.042	-0.220	0.042	0.015	39.037	0.200	14.254	0.387	-2.941	0.390	0.019	-0.838	1.006	0.017
2	Standard	TV03	3.440	0.002	30.531	-8.460	0.004	6.804	5.436	12.360	0.016	-0.040	0.013	0.005	17.567	0.231	6.595	0.250	-3.075	0.299	0.019	-0.838	1.006	0.017
2	Standard	CIT Carrera	2.138	0.002	37.399	-1.851	0.003	5.820	12.086	17.795	0.035	-0.203	0.034	0.012	39.057	14.308	0.252	0.277	-3.993	0.350	0.019	-0.838	1.006	0.017
2	Standard	CIT Carrara	2.135	0.003	37.400	-1.851	0.007	5.817	12.144	17.800	0.039	-0.197	0.038	0.013	38.842	0.228	14.097	0.229	-2.941	0.390	0.019	-0.805	1.006	0.017
2	Standard	CIT Carrara	2.137	0.002	37.396	-1.855	0.002	5.818	12.124	17.782	0.025	-0.212	0.025	0.009	39.177	0.241	14.432	0.239	-2.800	0.322	0.019	-0.805	1.006	0.017
2	Standard	TV03	3.475	0.001	30.505	-8.485	0.003	6.834	5.410	12.384	0.031	-0.024	0.032	0.011	17.606	0.195	6.684	0.190	-3.098	0.250	0.019	-0.805	1.006	0.017
2	Heated Gas	BOC	-11.300	0.001	29.389	-9.559	0.004	-7.021	4.289	-3.948	0.033	-0.899	0.034	0.012	13.458	0.230	4.818	0.168	-2.046	0.199	0.019	-0.805	1.006	0.017
2	Heated Gas	eboc	-10.531	0.001	55.524	15.587	0.010	-5.412	29.758	23.147	0.033	-0.366	0.027	0.010	95.623	0.207	33.207	0.242	-6.115	0.384	0.019	-0.805	1.006	0.017
2	Heated Gas	eBOC	-10.666	0.003	56.880	16.893	0.007	-5.493	31.081	24.329	0.036	-0.390	0.031	0.011	101.015	0.263	35.632	0.206	-4.573	0.299	0.019	-0.805	1.006	0.017
2	Heated Gas	BOC	-10.759	0.002	30.437	-8.550	0.002	-6.480	5.312	-2.364	0.040	-0.873	0.041	0.014	16.871	0.315	6.152	0.293	-2.054	0.248	0.019	-0.805	1.006	0.017
2	Heated Gas	eBOC	-10.779	0.001	55.556	15.618	0.004	-5.645	29.802	22.922	0.027	-0.375	0.025	0.009	96.135	0.1861	33.629	0.243	-2.411	0.272	0.019	-0.805	1.006	0.017
2	Heated Gas	BOC	-10.770	0.002	29.645	-9.312	0.004	-6.517	4.541	-3.137	0.033	-0.855	0.032	0.011	14.362	0.215	5.213	0.215	-1.077	0.217	0.019	-0.805	1.006	0.017
2	Heated Gas	eBOC	-10.485	0.002	55.110	15.189	0.005	-5.384	29.359	22.778	0.022	-0.372	0.020	0.007	95.165	0.192	33.583	0.180	-4.615	0.274	0.019	-0.805	1.006	0.017
2	Equilibrated Gas	25C eBOC	-11.107	0.002	62.055	21.872	0.012	-5.731	36.126	30.061	0.044	0.639	0.034	0.012	117.153	0.376	40.609	0.364	-7.394	0.329	0.019	-0.805	1.006	0.017
2	Equilibrated Gas	25C BOC	-10.466	0.001	28.761	-10.162	0.006	-6.263	3.680	-2.869	0.032	-0.007	0.032	0.011	11.966	0.137	4.559	0.144	-3.428	0.392	0.019	-0.805	1.006	0.017
2	Equilibrated Gas	25C eBOC	-10.836	0.004	60.660	20.529	0.007	-5.525	34.767	28.848	0.016	0.538	0.015	0.005	115.163	0.568	41.486	0.538	-2.994	0.317	0.019	-0.805	1.006	0.017
2	Equilibrated Gas	25C eBOC	-10.704	0.002	60.604	20.476	0.008	-5.403	34.713	28.905	0.043	0.520	0.041	0.015	113.186	0.153	39.748	0.147	-3.617	0.427	0.019	-0.805	1.006	0.017
3	Standard	CIT Carrara	2.105	0.005	37.433	-1.819	0.021	5.715	11.922	17.394	0.044	-0.290	0.035	0.012	33.828	0.483	9.217	0.434	0.026	0.819	0.012	-0.757	1.131	0.012
3	Standard	TV03	3.482	0.012	30.518	-8.473	0.008	6.763	4.792	11.596	0.028	-0.083	0.023	0.008	15.042	0.483	4.201	0.464	-1.269	0.690	0.012	-0.757	1.131	0.012
3	Standard	CIT Carrera*	2.322	0.466	36.506	-2.710	2.418	5.770	12.053	17.578	0.047	-0.312	0.063	0.022	33.711	0.674	9.257	0.637	-0.466	1.021	0.012	-0.757	1.131	0.012
3	Standard	TV03	3.462	0.007	30.501	-8.489	0.012	6.755	5.367	12.169	0.063	-0.111	0.063	0.022	14.503	0.477	3.701	0.457	0.488	0.787	0.012	-0.757	1.131	0.012
3	Standard	CIT Carrera	2.134	0.008	37.330	-1.918	0.022	5.747	12.019	17.502	0.034	-0.313	0.025	0.009	33.122	0.865	8.727	0.807	0.103	1.162	0.012	-0.757	1.131	0.012
3	Standard	CIT Carrera*	1.565	0.010	37.859	-1.409	0.015	5.238	12.538	17.482	0.046	-0.315	0.032	0.011	34.793	0.803	9.325	0.765	-0.291	1.447	0.012	-0.757	1.131	0.012
3	Standard	TV03	3.394	0.006	30.413	-8.574	0.023	6.688	5.281	12.029	0.042	-0.098	0.037	0.013	14.473	0.537	3.843	0.506	-0.456	0.955	0.012	-0.757	1.131	0.012
3	Standard	Carrera	2.104	0.005	37.231	-2.014	0.009	5.715	11.922	17.394	0.055	-0.292	0.046	0.016	32.811	0.552	8.618	0.528	0.026	0.819	0.012	-0.757	1.131	0.012
3	Standard	TV03	3.457	0.006	30.526	-8.465	0.019	6.751	5.391	12.189	0.057	-0.113	0.036	0.013	14.794	0.645	3.940	0.618	0.043	1.027	0.012	-0.757	1.131	0.012
3	Standard	CIT Carrera	2.121	0.008	37.276	-1.970	0.017	5.732	11.967	17.446	0.058	-0.301	0.047	0.017	33.443	0.769	9.146	0.723	-0.873	1.351	0.012	-0.757	1.131	0.012
3	Standard	TV03	2.431	0.017	31.720	-7.316	0.035	5.832	6.552	12.382	0.110	-0.116	0.061	0.022	19.032	2.089	5.808	1.995	-2.303	3.239	0.012	-0.757	1.131	0.012
3	Heated Gas	BOC	-10.923	0.010	29.750	-9.211	0.024	-6.723	4.603	-3.266	0.060	-0.832	0.038	0.013	12.568	1.163	3.309	1.110	-0.521	2.598	0.012	-0.757	1.131	0.012
3	Heated Gas	eBOC	-10.905	0.007	57.005	17.013	0.021	-5.779	31.164	24.002	0.050	-0.489	0.035	0.012	87.530	0.643	22.788	0.590	-0.597	0.852	0.012	-0.757	1.131	0.012
3	Heated Gas	eBOC	-10.948	0.005	56.941	16.951	0.016	-5.821	31.102	23.904	0.029	-0.482	0.019	0.007	87.110	0.573	22.516	0.514	-0.944	0.698	0.012	-0.757	1.131	0.012
3	Heated Gas	BOC	-10.952	0.004	30.011	-8.961	0.016	-6.741	4.857	-3.028	0.040	-0.822	0.039	0.014	13.572	0.606	3.798	0.576	-0.637	1.408	0.012	-0.757	1.131	0.012
3	Heated Gas	eBOC	-10.899	0.005	55.472	15.537	0.013	-5.825	29.670	22.482	0.046	-0.501	0.038	0.013	82.627	0.600	21.134	0.556	-0.514	0.873	0.012	-0.757	1.131	0.012
3	Equilibrated Gas	BOC 25C	-10.523	0.003	28.978	-9.954	0.006	-6.376	3.851	-2.852	0.041	-0.041	0.036	0.013	10.321	0.379	2.583	0.368	0.743	0.542	0.012	-0.757	1.131	0.012
3	Equilibrated Gas	25C eBOC	-10.978	0.006	63.423	23.188	0.018	-5.630	37.419	31.139	0.052	0.355	0.043	0.015	105.718	0.716	27.392	0.646	-0.364	1.158	0.012	-0.757	1.131	0.012
3	Equilibrated Gas	25C eBOC	-10.731	0.003	58.799	18.739	0.023	-5.555	32.913	26.771	0.049	0.313	0.034	0.012	92.946	0.496	24.404	0.446	-0.785	0.766	0.012	-0.757	1.131	0.012
3	Equilibrated Gas	25C BOC	-10.749	0.007	26.220	-12.608	0.010	-6.513	3.735	-3.135	0.045	-0.091	0.033	0.012	2.924	0.592	0.596	0.574	-1.454	0.453	0.012	-0.757	1.131	0.012
3	Equilibrated Gas	25C eBOC	-10.920	0.008	60.312	20.194	0.010	-5.711	34.270	28.135	0.037	0.369	0.031	0.011	102.263	1.070	30.194	0.982	-1.347	0.832	0.012	-0.757	1.131	0.012

Table SM2 (cont): Standards, Heated Gasses, and Equilibrated Gasses Analyzed During Clumped Isotope Analyses

Measurement Week	Type	Name	$\delta^{13}C$ VPDB (‰)	$\delta^{13}C$ 1σ	$\delta^{18}O$ gas VSMOW (‰)	$\delta^{18}O$ mineral PDB (‰)	$\delta^{18}O$ 1σ	δ 45 raw (‰)	δ 46 raw (‰)	δ 47 raw (‰)	δ 47 raw 1σ	Δ 47 raw (v. Oz)	D47 1σ	D47 sterror	d48 (v. Oz)	d48 1σ	D48 (v. Oz)	D48 1σ	d49 (v. Oz)	d49 1σ	CIT slope	CIT intercept	ARF slope	ARF intercept
4	Standard	CIT Carrara	2.020	0.003	37.003	-2.233	0.006	5.628	11.700	17.118	0.024	-0.258	0.022	0.008	34.782	0.270	10.986	0.257	-0.737	0.386	0.013	-0.774	1.078	0.012
4	Standard	TV03	3.309	0.002	30.204	-8.775	0.006	6.602	5.077	11.767	0.025	-0.069	0.026	0.009	15.342	0.378	5.111	0.371	-0.868	0.322	0.013	-0.774	1.078	0.012
4	Standard	NBS-19	1.830	0.002	36.346	-2.865	0.003	5.429	11.060	16.239	0.037	-0.295	0.035	0.013	32.827	0.250	10.355	0.247	-0.747	0.553	0.013	-0.774	1.078	0.012
4	Standard	TV03	3.372	0.002	30.305	-8.678	0.006	6.664	5.175	11.912	0.022	-0.085	0.023	0.008	15.601	0.265	5.170	0.261	-0.740	0.238	0.013	-0.774	1.078	0.012
4	Standard	CIT Carrara	1.355	0.002	37.929	-1.342	0.004	5.038	12.601	17.359	0.032	-0.292	0.032	0.011	37.567	0.397	11.905	0.385	-1.102	0.552	0.013	-0.775	1.078	0.012
4	Standard	TV03	3.282	0.001	30.116	-8.859	0.005	6.573	4.991	11.626	0.022	-0.094	0.025	0.009	14.916	0.237	4.860	0.234	-0.834	0.213	0.013	-0.775	1.078	0.012
4	Standard	CIT Carrara	1.962	0.003	36.841	-2.388	0.003	5.569	11.543	16.854	0.021	-0.304	0.023	0.008	33.843	0.264	10.383	0.258	-0.783	0.329	0.013	-0.777	1.078	0.012
4	Standard	TV03	3.205	0.002	29.945	-9.023	0.004	6.495	4.825	11.378	0.019	-0.097	0.019	0.007	14.356	0.289	4.639	0.285	-0.511	0.430	0.013	-0.777	1.078	0.012
4	Standard	NBS-19	1.758	0.010	36.176	-3.028	0.016	5.355	10.894	15.98	0.027	-0.314	0.028	0.010	31.631	0.456	9.517	0.473	-0.668	0.451	0.013	-0.777	1.078	0.012
4	Standard	TV03	3.149	0.001	30.197	-8.781	0.005	6.451	5.070	11.59	0.030	-0.083	0.028	0.010	14.711	0.275	4.499	0.272	-0.516	0.189	0.013	-0.777	1.078	0.012
4	Standard	CIT Carrara	1.893	0.002	36.669	-2.554	0.005	5.499	11.374	16.602	0.030	-0.315	0.031	0.011	32.439	0.330	9.348	0.326	-0.634	0.193	0.013	-0.777	1.078	0.012
4	Heated Gas	eBOC	-10.554	0.002	55.889	15.939	0.003	-5.489	30.077	23.279	0.044	-0.460	0.043	0.015	90.520	0.281	27.764	0.265	-1.294	0.343	0.013	-0.774	1.078	0.012
4	Heated Gas	eBOC	-10.527	0.003	56.067	16.110	0.005	-5.457	30.251	23.484	0.018	-0.458	0.016	0.005	90.540	0.594	27.437	0.561	-1.289	0.455	0.013	-0.774	1.078	0.012
4	Heated Gas	BOC	-10.983	0.003	30.132	-8.843	0.005	-6.767	4.976	-2.935	0.025	-0.820	0.028	0.010	14.350	0.227	4.331	0.223	-0.247	0.243	0.013	-0.774	1.078	0.012
4	Heated Gas	eBOC	-10.439	0.003	56.162	16.202	0.007	-5.372	30.344	23.654	0.035	-0.469	0.033	0.012	90.662	0.174	27.367	0.158	-1.201	0.337	0.013	-0.774	1.078	0.012
4	Heated Gas	BOC	-10.678	0.002	30.217	-8.762	0.004	-6.479	5.058	-2.562	0.020	-0.825	0.018	0.006	14.829	0.330	4.640	0.323	-0.362	0.156	0.013	-0.775	1.078	0.012
4	Heated Gas	eBOC	-10.375	0.002	53.668	13.802	0.003	-5.396	27.914	21.185	0.040	-0.536	0.037	0.013	80.912	0.287	23.002	0.270	-0.931	0.273	0.013	-0.775	1.078	0.012
4	Heated Gas	BOC	-10.899	0.009	28.741	-10.182	0.023	-6.735	3.620	-4.249	0.050	-0.842	0.028	0.010	10.228	0.227	2.953	0.249	-0.071	0.247	0.013	-0.777	1.078	0.012
4	Equilibrated Gas	BOC 25degC	-10.441	0.002	27.129	-11.733	0.004	-6.362	2.050	-4.635	0.020	-0.079	0.022	0.008	6.244	0.297	2.131	0.299	-0.248	0.453	0.013	-0.777	1.078	0.012
4	Equilibrated Gas	eBOC 25degC	-10.349	0.002	60.439	20.317	0.004	-5.143	34.512	28.846	0.029	0.383	0.027	0.009	106.033	0.368	33.467	0.339	-1.228	0.441	0.013	-0.777	1.078	0.012
4	Equilibrated Gas	eBOC 25degC	-10.927	0.003	60.215	20.101	0.008	-5.691	34.293	28.049	0.040	0.385	0.042	0.015	103.466	0.501	31.506	0.458	-1.363	0.264	0.013	-0.777	1.078	0.012
4	Equilibrated Gas	BOC 25degC	-10.769	0.021	28.770	-10.154	0.045	-6.613	3.648	-3.312	0.066	-0.057	0.036	0.013	10.221	1.833	2.891	1.841	0.428	1.668	0.013	-0.777	1.078	0.012
5	Standard	TV03	3.467	0.004	30.545	-8.446	0.013	6.791	5.459	12.3362	0.033	-0.076	0.023	0.008	15.800	0.227	4.799	0.207	-7.715	0.492	0.012	-0.820	1.028	0.013
5	Standard	CIT Carrara	2.154	0.004	37.413	-1.838	0.015	5.798	12.149	17.6933	0.035	-0.305	0.021	0.007	34.365	0.204	9.683	0.197	-9.049	0.492	0.012	-0.820	1.028	0.013
5	Standard	TV03	3.446	0.010	30.581	-8.412	0.018	6.773	5.494	12.2767	0.035	-0.150	0.028	0.010	15.296	0.186	4.231	0.197	-4.690	0.705	0.012	-0.820	1.028	0.013
5	Standard	CIT Carrara	2.153	0.015	37.381	-1.869	0.020	5.796	12.118	17.6477	0.042	-0.318	0.044	0.016	33.743	0.236	9.137	0.246	-4.390	0.393	0.012	-0.820	1.028	0.013
5	Standard	TV03	3.440	0.014	30.459	-8.529	0.022	6.763	5.375	12.2393	0.048	-0.060	0.023	0.008	15.215	0.216	4.389	0.219	-5.273	0.263	0.012	-0.820	1.028	0.013
5	Standard	CIT Carrara	2.149	0.021	37.380	-1.870	0.034	5.792	12.117	17.6402	0.064	-0.319	0.020	0.007	33.865	0.194	9.259	0.193	-4.242	0.361	0.012	-0.820	1.028	0.013
5	Standard	TV03	3.442	0.017	30.490	-8.499	0.030	6.766	5.405	12.2426	0.058	-0.089	0.038	0.013	15.343	0.228	4.456	0.208	-5.169	0.310	0.013	-0.812	1.028	0.013
5	Standard	CIT Carrara	2.123	0.017	37.319	-1.929	0.027	5.766	12.058	17.5933	0.039	-0.281	0.022	0.008	33.602	0.294	9.120	0.276	-6.091	0.281	0.012	-0.800	1.028	0.013
5	Standard	TV03	3.435	0.015	30.566	-8.426	0.026	6.762	5.479	12.2882	0.044	-0.113	0.041	0.014	15.907	0.244	4.866	0.197	-6.454	0.876	0.012	-0.800	1.028	0.013
5	Standard	TV03	3.457	0.007	30.543	-8.448	0.010	6.782	5.457	12.3132	0.021	-0.086	0.025	0.009	15.794	0.277	4.798	0.256	-6.624	0.508	0.012	-0.800	1.028	0.013
5	Heated Gas	eBOC	-10.719	0.006	58.429	18.383	0.016	-5.527	32.603	25.6749	0.040	-0.491	0.033	0.012	90.826	0.260	23.031	0.250	-11.987	0.900	0.012	-0.800	1.028	0.013
5	Heated Gas	BOC	-10.864	0.002	27.902	-10.989	0.003	-6.702	2.851	-4.9646	0.038	-0.844	0.035	0.012	8.918	0.173	3.189	0.176	-14.909	0.392	0.012	-0.800	1.028	0.013
5	Heated Gas	eBOC	-11.095	0.011	57.889	17.863	0.010	-5.897	32.075	24.7219	0.037	-0.534	0.046	0.016	90.494	0.256	23.766	0.254	-6.741	0.258	0.012	-0.800	1.028	0.013
5	Heated Gas	BOC	-10.670	0.007	31.507	-7.521	0.012	-6.396	6.365	-1.2738	0.020	-0.899	0.019	0.007	17.726	0.303	4.893	0.306	-4.436	0.465	0.012	-0.800	1.028	0.013
5	Heated Gas	eBOC	-10.709	0.018	58.421	18.375	0.032	-5.518	32.595	25.6812	0.058	-0.487	0.019	0.007	91.872	0.162	24.028	0.144	-6.282	0.294	0.012	-0.800	1.028	0.013
5	Heated Gas	BOC	-10.741	0.016	30.231	-8.748	0.027	-6.507	5.121	-2.5339	0.058	-0.831	0.044	0.016	14.417	0.210	4.105	0.246	-6.232	0.510	0.012	-0.800	1.028	0.013
5	Heated Gas	eBOC	-10.749	0.026	58.909	18.845	0.045	-5.539	33.071	26.117	0.063	-0.492	0.028	0.010	93.265	0.197	24.391	0.198	-3.429	0.813	0.012	-0.800	1.028	0.013
5	Heated Gas	BOC	-10.942	0.013	30.157	-8.819	0.025	-6.697	5.049	-2.793	0.047	-0.822	0.024	0.008	14.318	0.188	4.152	0.201	-6.507	0.112	0.012	-0.800	1.028	0.013
5	Heated Gas	eBOC	-10.374	0.016	58.132	18.097	0.029	-5.215	32.314	25.7652	0.040	-0.452	0.016	0.006	91.064	0.306	23.827	0.265	-9.111	0.680	0.012	-0.800	1.028	0.013
5	Heated Gas	BOC	-10.606	0.010	29.988	-8.982	0.017	-6.389	4.885	-2.5912	0.034	-0.779	0.024	0.008	13.670	0.385	3.838	0.359	-9.796	0.568	0.012	-0.800	1.028	0.013
5	Equilibrated Gas	25C BOC	-10.691	0.014	28.139	-10.762	0.044	-5.483	33.621	27.7032	0.045	-0.046	0.021	0.007	9.571	0.466	3.376	0.415	-4.837	0.251	0.012	-0.800	1.028	0.013
5	Equilibrated Gas	25C eBOC	-10.698	0.021	59.529	19.441	0.039	-6.532	3.082	-3.7686	0.059	0.409	0.019	0.007	95.831	0.208	25.596	0.138	-8.654	0.735	0.012	-0.800	1.028	0.013
5	Equilibrated Gas	25C BOC	-10.639	0.007	28.751	-10.172	0.017	-5.471	33.674	27.7055	0.041	-0.043	0.031	0.011	11.516	0.496	4.114	0.473	-6.305	0.265	0.012	-0.800	1.028	0.013
5	Equilibrated Gas	25C eBOC	-10.553	0.024	59.352	19.271	0.052	-5.341	33.503	27.6759	0.086	0.409	0.035	0.012	95.263	0.502	25.405	0.403	-6.655	1.092	0.012	-0.800	1.028	0.013
5	Equilibrated Gas	25C eBOC	-10.615	0.004	58.356	18.313	0.004	-6.561	4.015	-2.905	0.050	0.453	0.050	0.018	100.438	0.567	32.188	0.534	-7.673	0.288	0.012	-0.800	1.028	0.013
5	Equilibrated Gas	25C BOC	-10.725	0.003	28.668	-10.252	0.006	-5.500	33.580	27.677	0.027	-0.033	0.024	0.009	11.168	0.203	3.930	0.194	-4.117	0.286	0.012	-0.800	1.028	0.013
6	Standard	TV03	3.427	0.008	30.511	-8.479	0.020	6.752	5.425	12.288	0.027	-0.050	0.017	0.006	15.632	0.300	4.701	0.302	-6.509	0.721	0.012	-0.800	1.099	0.014
6	Standard	CIT Carrara	2.161	0.006	37.393	-1.857	0.011	5.804	12.130	17.708	0.035	-0.278	0.024	0.008	34.320	0.326	9.676	0.305	-6.571	0.659	0.012	-0.800	1.099	0.014
6	Standard	TV03	3.449	0.009	30.545	-8.446	0.019	6.774	5.459	12.313	0.054	-0.081	0.036	0.013	15.765	0.310	4.765	0.273	-7.007	0.835	0.012	-0.800	1.099	0.014
6	Standard	CIT Carrara	2.154	0.003	37.376	-1.874	0.013	5.797	12.114	17.679	0.040	-0.283	0.029	0.010	34.455	0.156	9.842	0.162	-7.050	0.373	0.012	-0.800	1.099	0.014
6	Standard	TV03	3.479	0.009	30.545	-8.446	0.015	6.803	5.459	12.357	0.027	-0.067	0.016	0.006	15.967	0.502	4.965	0.470	-5.415	0.549	0.012	-0.800	1.099	0.014
6	Standard	CIT Carrara	2.151	0.011	37.449	-1.803	0.016	5.797	12.185	17.752	0.037	-0.280	0.024	0.009	33.845	0.331	9.104	0.301	-6.569	0.649	0.012	-0.800	1.099	0.014
6	Standard	TV03	3.496	0.013	30.571	-8.421	0.029	6.819	5.485	12.392	0.030	-0.073	0.026	0.009	15.895	0.350	4.842	0.308	-6.954	0.409	0.012	-0.800	1.099	0.014
6	Standard	CIT Carrara	2.189	0.022	37.474	-1.780	0.040	5.833	12.209	17.811	0.075	-0.283	0.027	0.010	34.746	0.545	9.936	0.482	-7.482	0.784	0.012	-0.800	1.099	0.014
6	Standard	TV03	3.452	0.005	30.541	-8.450	0.009	6.777	5.455	12.324	0.039	-0.070	0.033	0.012	16.226	0.676	5.229	0.656	-4.391	1.333	0.012	-0.800	1.099	0.014
6	Standard	CIT Carrera	2.160	0.002	37.424	-1.828	0.006	5.805	12.218	17.736	0.033	-0.279	0.034	0.012	35.634	0.254	10.899	0.249	-2.697	0.142	0.012	-0.800	1.099	0.014
6	Standard	CIT Carrera	2.162	0.003	37.435	-1.817	0.005	5.805	12.198	17.802	0.045	-0.227	0.038	0.014	36.432	0.478	11.657	0.459	-2.768	0.251	0.012	-0.800	1.099	0.014
6	Heated Gas	BOC	-10.606	0.010	29.988	-8.982	0.017	-6.389	4.885	-2.591	0.034	-0.779	0.024	0.008	13.670	0.385	3.838	0.359	-9.796	0.568	0.012	-0.800	1.099	0.014
6	Heated Gas	eBOC	-10.974	0.013	58.384	18.340	0.029	-5.767	32.559	25.394	0.049	-0.473	0.040	0.014	93.871	1.686	25.975	1.580	-6.409	0.403	0.012	-0.800	1.099	0.014
6	Heated Gas	BOC	-10.579	0.007	29.439	-9.510	0.015	-6.383	4.350	-3.164	0.044	-0.837	0.042	0.015	12.573	0.166	3.821	0.145	-8.837	0.460	0.012	-0.800	1.099	0.014
6	Heated Gas	eBOC	-11.165	0.040	57.209	17.209	0.080	-5.985	31.413	24.077	0.092	-0.441	0.042	0.015	91.319	0.775	25.857	0.628	-6.237	1.194	0.012	-0.800	1.099	0.014
6	Heated Gas	BOC	-10.827	0.005	29.934	-9.035	0.006	-6.597	4.831	-2.939	0.033	-0.860	0.031	0.011	14.412	0.307	4.681	0.293	-4.116	0.517	0.012	-0.800	1.099	0.014
6	Heated Gas	BOC	-10.579	0.007	29.439	-9.510	0.015	-6.389	4.885	-2.591	0.044	-0.837	0.042	0.015	13.670	0.166	3.821	0.145	-9.796	0.460	0.012	-0.800	1.099	0.014
6	Equilibrated Gas	25C eBOC	-10.709	0.002	59.474	19.388	0.005	-5.483	33.621	27.703	0.045	-0.046	0.021	0.007	109.530	0.466	3.376	0.415	-3.812	0.251	0.012	-0.800	1.099	0.014
6	Equilibrated Gas	25C BOC	-10.691	0.014	28.139	-10.762	0.044	-6.532	3.082	-3.769	0.059	0.409	0.019	0.007	9.571	0.208	25.596	0.138	-8.654	0.735	0.012	-0.800	1.099	0.014
6	Equilibrated Gas	25C eBOC	-10.698	0.021	59.529	19.441	0.039	-5.471	33.674	27.705	0.041	-0.043	0.031	0.011	95.831	0.496	4.114	0.473	-6.305	0.265	0.012	-0.800	1.099	0.014
6	Equilibrated Gas	25C eBOC	-10.553	0.024	59.352	19.271	0.052	-5.341	33.503	27.676	0.050	0.453	0.050	0.018	95.263	0.567	32.188	0.534	-7.673	0.288	0.012	-0.800	1.099	0.014
6	Equilibrated Gas	25C BOC	-10.758	0.003	29.096	-9.840	0.007	-6.561	4.015	-2.905	0.086	0.409	0.035	0.012	13.224	0.502	25.405	0.403	-1.916	1.092	0.012	-0.800	1.099	0.014
6	Equilibrated Gas	25C eBOC	-10.726	0.001	59.432	19.348	0.007	-5.500	33.580	27.677	0.027	-0.033	0.024	0.009	109.908	0.203	3.930	0.194	-4.117	0.286	0.012	-0.800	1.099	0.014

Table SM2 (cont): Standards, Heated Gasses, and Equilibrated Gasses Analyzed During Clumped Isotope Analyses

Measurement Week	Type	Name	$\delta^{13}C$ VPDB (‰)	$\delta^{13}C$ 1σ	$\delta^{18}O$ gas VSMOW (‰)	$\delta^{18}O$ mineral PDB (‰)	$\delta^{18}O$ 1σ	δ 45 raw (‰)	δ 46 raw (‰)	δ 47 raw (‰)	δ 47 raw 1σ	Δ 47 raw (v. Oz)	D47 1σ	D47 sterror	d48 (v. Oz)	d48 1σ	D48 (v. Oz)	D48 1σ	d49 (v. Oz)	d49 1σ	CIT slope	CIT intercept	ARF slope	ARF intercept
7	Standard	CIT Carrera	2.136	0.005	37.574	-1.683	0.013	5.808	12.124	17.625	0.037	-0.470	0.032	0.011	25.225	0.542	0.625	0.528	-0.464	0.204	0.012	-0.834	1.261	0.016
7	Standard	TV03	3.390	0.005	30.627	-8.367	0.011	6.766	5.401	12.14	0.045	-0.234	0.045	0.016	11.637	0.348	0.698	0.327	-0.185	0.454	0.012	-0.834	1.261	0.016
7	Standard	CIT Carrara	2.048	0.004	37.901	-1.369	0.007	5.751	12.016	17.847	0.049	-0.488	0.044	0.016	26.906	0.344	1.636	0.325	-0.558	0.179	0.012	-0.834	1.261	0.016
7	Standard	TV03	3.360	0.007	30.804	-8.197	0.010	6.732	5.403	12.426	0.031	-0.096	0.030	0.010	13.958	0.246	2.668	0.249	-0.281	0.143	0.014	-0.835	1.261	0.016
7	Standard	CIT Carrara	2.179	0.003	37.336	-1.912	0.008	5.801	12.134	17.547	0.045	-0.355	0.037	0.013	30.132	0.260	5.873	0.243	-0.254	0.287	0.014	-0.835	1.261	0.016
7	Standard	TV03	3.423	0.005	30.647	-8.348	0.011	6.778	5.432	12.327	0.039	-0.102	0.040	0.014	13.703	0.224	2.720	0.222	-0.262	0.297	0.014	-0.835	1.261	0.016
7	Standard	CIT Carrara	2.086	0.004	37.730	-1.533	0.009	5.788	12.042	17.89	0.039	-0.316	0.038	0.014	31.135	0.192	6.089	0.174	-0.442	0.320	0.014	-0.835	1.261	0.016
7	Heated Gas	BOC	-11.834	0.004	32.040	-7.008	0.011	-7.423	6.793	-1.92	0.031	-0.897	0.037	0.013	15.316	0.272	1.661	0.265	-1.237	1.649	0.012	-0.834	1.261	0.016
7	Heated Gas	eBOC	-11.189	0.006	33.190	-5.902	0.014	-5.686	31.856	24.812	0.053	-0.877	0.054	0.019	96.716	0.163	4.662	0.156	-0.800	0.222	0.012	-0.834	1.261	0.016
7	Heated Gas	BOC	-11.207	0.002	32.754	-6.320	0.005	-6.813	7.491	-0.531	0.042	-0.822	0.042	0.015	22.664	0.128	7.512	0.130	0.068	0.192	0.012	-0.834	1.261	0.016
7	Heated Gas	BOC	-11.103	0.005	60.649	20.519	0.019	-6.303	7.753	0.329	0.052	-0.453	0.044	0.015	23.345	0.426	21.184	0.376	-0.096	0.163	0.014	-0.835	1.261	0.016
7	Heated Gas	eBOC	-10.992	0.003	32.804	-6.273	0.003	-5.523	31.958	25.172	0.039	-0.823	0.038	0.014	97.939	0.099	4.262	0.096	-1.283	0.180	0.014	-0.835	1.261	0.016
7	Heated Gas	BOC	-11.264	0.004	57.856	17.832	0.008	-7.130	7.480	-0.881	0.024	-0.501	0.027	0.010	22.385	0.392	16.936	0.376	0.044	0.310	0.014	-0.835	1.261	0.016
7	Heated Gas	BOC	-11.061	0.004	60.808	20.672	0.025	-6.578	7.687	-0.075	0.039	-0.472	0.023	0.008	23.020	0.320	20.389	0.265	0.095	0.242	0.014	-0.835	1.261	0.016
7	Heated Gas	eBOC	-10.698	0.004	58.602	18.549	0.009	-5.458	32.681	25.896	0.035	-0.419	0.038	0.014	99.607	0.467	31.111	0.429	-1.266	0.157	0.014	-0.835	1.261	0.016
7	Heated Gas	BOC	-11.269	0.004	33.219	-5.873	0.012	-6.855	7.944	-0.11	0.035	-0.799	0.037	0.013	23.688	0.259	7.615	0.260	-0.274	0.270	0.014	-0.835	1.261	0.016
7	Equilibrated Gas	25degC BOC	-11.034	0.005	28.180	-10.722	0.005	-6.807	3.034	-4.183	0.027	-0.128	0.026	0.009	9.434	0.272	3.336	0.271	0.130	0.365	0.014	-0.835	1.261	0.016
7	Equilibrated Gas	25degC eBOC	-11.133	0.005	56.477	16.505	0.017	-5.937	30.609	24.136	0.040	0.335	0.039	0.014	93.622	0.270	29.626	0.249	-0.555	0.241	0.014	-0.835	1.261	0.016
7	Equilibrated Gas	25degC BOC	-11.152	0.007	29.327	-9.618	0.012	-6.785	2.749	-4.398	0.036	-0.063	0.048	0.017	8.287	0.341	2.412	0.326	-0.023	0.326	0.014	-0.835	1.261	0.016
7	Equilibrated Gas	25degC eBOC	-11.126	0.005	57.926	17.898	0.012	-5.881	32.021	25.651	0.026	0.410	0.029	0.010	87.009	0.254	20.601	0.243	-0.931	0.529	0.014	-0.835	1.261	0.016
8	Standard	TV03	3.429	0.003	30.671	-8.325	0.009	6.801	5.438	12.365	0.035	-0.093	0.035	0.012	13.811	0.223	2.780	0.206	-0.254	0.336	0.014	-0.835	1.174	0.015
8	Standard	CIT Carrara	2.128	0.004	37.469	-1.784	0.005	5.811	12.121	17.675	0.044	-0.311	0.041	0.014	31.105	0.211	6.566	0.207	-0.502	0.233	0.014	-0.835	1.174	0.015
8	Standard	TV03	3.399	0.005	30.677	-8.319	0.009	6.773	5.433	12.34	0.030	-0.094	0.031	0.011	13.899	0.233	2.856	0.224	-0.468	0.172	0.014	-0.835	1.174	0.015
8	Standard	CIT Carrara	2.129	0.003	37.552	-1.704	0.008	5.816	12.152	17.774	0.027	-0.296	0.032	0.011	31.486	0.263	6.776	0.271	-0.334	0.349	0.014	-0.835	1.174	0.015
8	Standard	TV03	3.407	0.003	30.662	-8.334	0.008	6.780	5.436	12.35	0.043	-0.076	0.035	0.012	14.248	0.162	3.231	0.147	-0.191	0.184	0.013	-0.830	1.174	0.015
8	Standard	CIT Carrara	2.133	0.008	37.532	-1.724	0.010	5.816	12.152	17.742	0.047	-0.308	0.048	0.017	31.979	0.290	7.297	0.270	-0.285	0.106	0.013	-0.830	1.174	0.015
8	Standard	TV03	3.442	0.003	30.644	-8.351	0.005	6.809	5.416	12.312	0.043	-0.093	0.046	0.016	14.293	0.242	3.309	0.239	-0.568	0.273	0.013	-0.830	1.174	0.015
8	Standard	CIT Carrara	2.128	0.003	37.526	-1.730	0.006	5.811	12.121	17.719	0.032	-0.272	0.035	0.012	32.124	0.255	7.450	0.246	-0.987	0.199	0.013	-0.837	1.174	0.015
8	Heated Gas	eBOC	-11.264	0.004	57.856	17.832	0.008	-7.130	7.480	-0.881	0.024	-0.501	0.027	0.010	83.064	0.392	16.936	0.376	0.044	0.310	0.014	-0.835	1.174	0.015
8	Heated Gas	BOC	-11.061	0.004	60.808	20.672	0.025	-6.578	7.687	-0.075	0.039	-0.472	0.023	0.008	92.816	0.320	20.389	0.265	0.095	0.242	0.014	-0.835	1.174	0.015
8	Heated Gas	eBOC	-10.698	0.004	58.602	18.549	0.009	-5.458	32.681	25.896	0.035	-0.419	0.038	0.014	99.607	0.467	31.111	0.429	-1.266	0.157	0.014	-0.835	1.174	0.015
8	Heated Gas	BOC	-11.269	0.004	33.219	-5.873	0.012	-6.855	7.944	-0.11	0.035	-0.799	0.037	0.013	23.688	0.259	7.615	0.260	-0.274	0.270	0.014	-0.835	1.174	0.015
8	Heated Gas	eBOC	-11.103	0.005	60.649	20.519	0.019	-5.768	34.675	27.479	0.052	-0.453	0.044	0.016	93.338	0.426	21.284	0.376	-0.358	0.694	0.013	-0.830	1.174	0.015
8	Heated Gas	BOC	-11.040	0.003	33.156	-5.934	0.006	-6.643	7.883	0.038	0.027	-0.812	0.029	0.010	23.644	0.370	7.694	0.364	-0.056	0.261	0.013	-0.830	1.174	0.015
8	Heated Gas	eBOC	-11.092	0.004	59.885	19.784	0.017	-5.784	33.931	26.677	0.053	-0.510	0.055	0.019	92.249	0.248	21.736	0.229	-0.319	0.790	0.013	-0.830	1.174	0.015
8	Heated Gas	BOC	-10.798	0.002	32.181	-6.872	0.007	-6.450	6.933	-0.744	0.034	-0.867	0.036	0.013	18.206	0.160	4.232	0.152	0.253	0.665	0.013	-0.837	1.174	0.015
8	Equilibrated Gas	25degC BOC	-11.034	0.005	28.180	-10.722	0.005	-6.807	3.034	-4.183	0.027	-0.128	0.026	0.009	9.434	0.272	3.336	0.271	0.130	0.365	0.014	-0.835	1.261	0.016
8	Equilibrated Gas	25degC eBOC	-11.133	0.005	56.477	16.505	0.017	-5.937	30.609	24.136	0.040	0.335	0.039	0.014	93.622	0.270	29.626	0.249	-0.555	0.241	0.014	-0.835	1.261	0.016
8	Equilibrated Gas	25degC BOC	-11.152	0.007	29.327	-9.618	0.012	-6.785	2.749	-4.398	0.036	-0.063	0.048	0.017	8.287	0.341	2.412	0.326	-0.023	0.326	0.014	-0.835	1.261	0.016
8	Equilibrated Gas	25degC eBOC	-11.126	0.005	57.926	17.898	0.012	-5.881	32.021	25.651	0.026	0.410	0.029	0.010	87.009	0.254	20.601	0.243	-0.931	0.529	0.014	-0.835	1.261	0.016
9	Standard	TV03	3.423	0.005	30.598	-8.395	0.010	6.773	5.433	12.285	0.030	-0.093	0.034	0.012	14.250	0.287	3.357	0.280	-0.468	0.172	0.014	-0.837	1.198	0.015
9	Standard	CIT Carrara	2.128	0.004	37.542	-1.714	0.009	5.816	12.152	17.742	0.049	-0.316	0.051	0.018	32.642	0.202	7.925	0.195	-0.334	0.349	0.013	-0.837	1.198	0.015
9	Standard	TV03	3.430	0.004	30.606	-8.387	0.007	6.797	5.426	12.317	0.042	-0.077	0.042	0.015	14.562	0.143	3.650	0.144	-0.359	0.257	0.014	-0.847	1.198	0.015
9	Standard	CIT Carrara	2.141	0.004	37.540	-1.716	0.007	5.811	12.121	17.767	0.039	-0.302	0.041	0.015	32.573	0.224	7.860	0.214	-0.502	0.233	0.014	-0.847	1.198	0.015
9	Standard	TV03	3.428	0.004	30.658	-8.337	0.009	6.705	5.377	12.384	0.034	-0.060	0.034	0.012	14.613	0.271	3.598	0.262	-0.285	0.283	0.014	-0.863	1.198	0.015
9	Standard	NBS-19	2.033	0.003	37.157	-2.084	0.008	5.720	11.811	17.28	0.045	-0.302	0.050	0.018	31.779	0.228	7.830	0.230	-0.620	0.379	0.014	-0.863	1.198	0.015
9	Standard	TV03	3.393	0.003	30.746	-8.253	0.004	6.766	5.401	12.422	0.041	-0.076	0.041	0.014	15.116	0.202	3.924	0.196	-0.185	0.454	0.015	-0.867	1.198	0.015
9	Standard	CIT Carrara	2.135	0.003	37.537	-1.719	0.006	5.811	12.121	17.793	0.021	-0.269	0.023	0.008	33.001	0.278	8.285	0.271	-0.502	0.233	0.015	-0.867	1.198	0.015
9	Heated Gas	BOC	-11.269	0.004	33.219	-5.873	0.012	-6.855	7.944	-0.1096	0.035	-0.799	0.037	0.013	23.688	0.259	7.615	0.260	-0.274	0.270	0.014	-0.837	1.198	0.015
9	Heated Gas	eBOC	-11.061	0.004	60.808	20.672	0.025	-5.768	34.675	27.4786	0.039	-0.472	0.023	0.008	93.338	0.320	20.389	0.265	-0.358	0.242	0.013	-0.837	1.198	0.015
9	Heated Gas	BOC	-11.040	0.003	33.156	-5.934	0.006	-6.643	7.883	0.03771	0.027	-0.812	0.029	0.010	23.644	0.370	7.694	0.364	-0.056	0.261	0.014	-0.847	1.198	0.015
9	Heated Gas	eBOC	-11.092	0.004	59.885	19.784	0.017	-5.784	33.931	26.6775	0.053	-0.510	0.055	0.019	92.249	0.248	21.736	0.229	-0.319	0.790	0.014	-0.847	1.198	0.015
9	Heated Gas	BOC	-10.798	0.002	32.181	-6.872	0.007	-6.450	6.933	-0.7442	0.034	-0.867	0.036	0.013	18.206	0.160	4.232	0.152	0.253	0.665	0.014	-0.863	1.198	0.015
9	Heated Gas	eBOC	-10.852	0.003	59.455	19.370	0.005	-5.573	33.511	26.5393	0.055	-0.464	0.057	0.020	91.069	0.169	21.461	0.159	-0.989	0.819	0.014	-0.863	1.198	0.015
9	Heated Gas	BOC	-11.128	0.005	34.164	-4.964	0.012	-6.690	8.865	0.89516	0.036	-0.864	0.033	0.012	23.573	0.329	5.663	0.325	0.916	0.864	0.015	-0.867	1.198	0.015
9	Heated Gas	eBOC	-10.792	0.005	59.294	19.215	0.005	-5.523	33.355	26.4237	0.047	-0.480	0.041	0.014	91.588	0.355	22.255	0.333	-0.259	0.704	0.015	-0.867	1.198	0.015
9	Equilibrated Gas	25degC BOC	-11.034	0.005	28.180	-10.722	0.005	-6.807	3.034	-4.1831	0.027	-0.128	0.026	0.009	9.434	0.272	3.336	0.271	0.130	0.365	0.014	-0.835	1.261	0.016
9	Equilibrated Gas	25degC eBOC	-11.133	0.005	56.477	16.505	0.017	-5.937	30.609	24.136	0.040	0.335	0.039	0.014	93.622	0.270	29.626	0.249	-0.555	0.241	0.014	-0.835	1.261	0.016
9	Equilibrated Gas	25degC BOC	-11.152	0.007	29.327	-9.618	0.012	-6.785	2.749	-4.3985	0.036	-0.063	0.048	0.017	8.287	0.341	2.412	0.326	-0.023	0.326	0.014	-0.835	1.261	0.016
9	Equilibrated Gas	25degC eBOC	-11.126	0.005	57.926	17.898	0.012	-5.881	32.021	25.6509	0.026	0.410	0.029	0.010	87.009	0.254	20.601	0.243	-0.931	0.529	0.014	-0.835	1.261	0.016

Table SM3: Carbon, Oxygen, and Clumped Isotope Analyses

			Analyses*																		
	Measurement		$\delta^{13}C$	$\delta^{13}C$	$\delta^{18}O$ gas	$\delta^{18}O$ mineral	$\delta^{18}O$	δ 45 raw	δ 46 raw	δ 47 raw	δ 47 raw	Δ 47 raw	D47	D47	d48	d48	D48	D48	d49	d49	D47 EGL	D47 ETF
Week	Type	Name	VPDB (‰)	1σ	VSMOW (‰)	VPDB (‰)	1σ	(‰)	(‰)	(‰)	1σ	(v. Oz)	1σ	sterror	(v. Oz)	1σ	(v. Oz)	1σ	(v. Oz)	1σ	Corrected	Corrected
1	Seed Crystals	UWAI-001	4.388	0.003	31.865	-7.177	0.038	7.6679	6.6977	14.5117	0.058	-0.093	0.039	0.014	22.0589	1.296	8.504	1.208	-3.3799	1.297	-0.272	0.637
1	Seed Crystals	UWAI-001	4.398	0.005	31.869	-7.173	0.056	7.6772	6.7016	14.5354	0.080	-0.083	0.034	0.012	22.49894	2.259	8.931	2.122	-3.7376	2.182	-0.262	0.648
1	Experiment Product	UWAI-002	0.978	0.003	30.263	-8.717	0.061	4.4238	5.1297	9.52476	0.075	-0.163	0.027	0.010	18.07963	1.649	7.714	1.519	-3.5852	1.542	-0.280	0.628
1	Experiment Product	UWAI-008	1.594	0.003	30.229	-8.751	0.007	4.9988	5.0971	10.0782	0.051	-0.116	0.050	0.018	13.57014	0.471	3.316	0.462	1.1849	0.783	-0.240	0.673
1	Experiment Product	UWAI-009	1.679	0.003	30.168	-8.809	0.007	5.0759	5.0382	10.1139	0.041	-0.102	0.044	0.016	13.80813	0.629	3.669	0.616	0.6918	0.811	-0.226	0.688
1	Experiment Product	UWAI-010	2.053	0.004	30.483	-8.506	0.004	5.4364	5.3463	10.792	0.043	-0.102	0.041	0.015	14.6544	0.501	3.892	0.490	0.6436	0.752	-0.235	0.678
1	Experiment Product	UWAI-011	0.824	0.004	30.477	-8.512	0.005	4.2872	5.3372	9.58756	0.035	-0.106	0.034	0.012	14.60137	0.451	3.857	0.438	1.0681	0.667	-0.224	0.690
1	Experiment Product	UWAI-012	1.750	0.003	30.435	-8.553	0.006	5.152	5.2982	10.455	0.029	-0.097	0.031	0.011	15.22758	0.303	4.555	0.296	-0.858	0.464	-0.225	0.689
1	Experiment Product	UWAI-013	2.055	0.003	30.474	-8.515	0.004	5.4377	5.3372	10.7851	0.035	-0.101	0.031	0.011	14.925	0.659	4.177	0.648	-0.0548	1.135	-0.234	0.679
1	Experiment Product	UWAI-014	2.639	0.004	30.802	-8.199	0.011	5.9951	5.6579	11.6952	0.066	-0.087	0.053	0.019	15.56054	0.688	4.166	0.663	0.3743	1.371	-0.231	0.683
1	Experiment Product	UWAI-015	2.447	0.005	30.759	-8.241	0.010	5.8145	5.6155	11.4586	0.039	-0.094	0.030	0.011	15.23709	0.621	3.930	0.603	0.6243	0.888	-0.235	0.678
1	Experiment Product	UWAI-016	2.713	0.002	31.823	-7.216	0.006	6.0994	6.654	12.8172	0.036	-0.059	0.033	0.012	18.38288	0.427	4.964	0.413	0.5713	0.643	-0.217	0.699
1	Experiment Product	UWAI-016	2.753	0.004	31.859	-7.182	0.008	6.1381	6.6888	12.8906	0.029	-0.060	0.032	0.011	18.86399	0.638	5.370	0.618	-0.3083	1.034	-0.219	0.696
1	Experiment Product	UWAI-017	2.701	0.003	31.788	-7.250	0.005	6.087	6.6193	12.7705	0.013	-0.069	0.012	0.004	18.17516	0.589	4.829	0.571	0.7835	0.906	-0.226	0.689
1	Experiment Product	UWAI-017	2.723	0.003	31.779	-7.259	0.010	6.1074	6.6102	12.7741	0.015	-0.091	0.017	0.006	18.13223	0.364	4.804	0.346	0.5726	0.762	-0.248	0.664
1	Experiment Product	UWAI-018	2.606	0.003	31.891	-7.152	0.009	6.0022	6.7191	12.7943	0.030	-0.046	0.026	0.009	18.95528	0.608	5.399	0.586	-0.2811	0.851	-0.203	0.714
1	Experiment Product	UWAI-019	2.561	0.004	31.905	-7.138	0.010	5.9605	6.7328	12.7626	0.037	-0.048	0.032	0.011	18.61975	0.445	5.041	0.423	0.362	0.773	-0.205	0.712
1	Experiment Product	UWAI-020	0.753	0.004	28.817	-10.109	0.009	4.1637	3.7197	7.79477	0.039	-0.173	0.029	0.010	10.04146	0.597	2.569	0.578	0.4816	1.228	-0.269	0.641
1	Experiment Product	UWAI-020	0.775	0.002	28.911	-10.019	0.007	4.1879	3.8112	7.9059	0.042	-0.177	0.040	0.014	10.35275	0.249	2.695	0.243	0.4836	0.255	-0.274	0.634
1	Experiment Product	UWAI-021	1.217	0.003	29.074	-9.862	0.008	4.6063	3.9709	8.53588	0.017	-0.138	0.018	0.006	10.63055	0.503	2.652	0.495	0.8491	0.721	-0.243	0.669
1	Experiment Product	UWAI-021	1.260	0.003	29.183	-9.756	0.009	4.6501	4.0778	8.67984	0.031	-0.145	0.033	0.012	11.25616	0.351	3.059	0.337	-0.1249	0.487	-0.252	0.659
1	Seed Crystals	UWAI-022	4.342	0.006	31.815	-7.224	0.071	7.6226	6.6496	14.4345	0.111	-0.076	0.040	0.014	22.75994	2.030	9.292	1.869	-4.4652	2.154	-0.254	0.657
1	Seed Crystals	UWAI-022	4.356	0.003	31.636	-7.397	0.012	7.6297	6.4747	14.2216	0.022	-0.065	0.022	0.008	17.99584	0.619	4.940	0.594	0.2003	0.936	-0.240	0.672
2	Seed Crystals	UWAI-001	4.381	0.003	31.867	-7.174	0.016	7.728	6.740	14.687	0.023	0.034	0.022	0.008	21.577	0.202	7.944	0.189	-3.466	0.275	-0.210	0.670
2	Experiment Product	UWAI-004	1.601	0.004	30.630	-8.365	0.005	5.086	5.527	10.648	0.029	-0.063	0.030	0.010	17.843	0.243	6.684	0.247	-3.841	0.376	-0.239	0.640
2	Experiment Product	UWAI-005	1.568	0.003	30.585	-8.408	0.002	5.054	5.484	10.552	0.034	-0.082	0.031	0.011	17.824	0.405	6.751	0.401	-4.274	0.411	-0.257	0.622
2	Experiment Product	UWAI-005	1.518	0.004	30.688	-8.309	0.007	5.011	5.584	10.627	0.047	-0.061	0.041	0.014	17.826	0.218	6.554	0.221	-2.916	0.263	-0.237	0.642
2	Experiment Product	UWAI-005	1.569	0.002	30.553	-8.438	0.007	5.054	5.453	10.581	0.021	-0.023	0.021	0.008	17.576	0.239	6.569	0.246	-2.972	0.227	-0.199	0.681
2	Experiment Product	UWAI-006	1.743	0.002	30.509	-8.481	0.004	5.215	5.411	10.635	0.037	-0.093	0.035	0.013	17.583	0.338	6.660	0.335	-4.867	0.346	-0.269	0.610
2	Experiment Product	UWAI-006	1.785	0.003	30.524	-8.467	0.004	5.255	5.425	10.751	0.014	-0.033	0.018	0.006	17.442	0.245	6.492	0.242	-2.938	0.338	-0.212	0.668
2	Experiment Product	UWAI-007	1.811	0.002	30.552	-8.440	0.003	5.280	5.452	10.778	0.031	-0.059	0.029	0.010	17.382	0.297	6.379	0.291	-4.108	0.335	-0.238	0.642
2	Experiment Product	UWAI-008	1.598	0.004	30.626	-8.369	0.005	5.083	5.523	10.643	0.037	-0.060	0.038	0.013	17.904	0.402	6.752	0.396	-3.232	0.450	-0.237	0.643
2	Experiment Product	UWAI-009	1.739	0.003	30.426	-8.560	0.005	5.208	5.330	10.580	0.043	-0.061	0.044	0.016	17.231	0.217	6.474	0.215	-3.052	0.423	-0.237	0.643
2	Experiment Product	UWAI-010	1.903	0.002	30.650	-8.345	0.005	5.369	5.548	10.977	0.045	-0.047	0.041	0.014	17.935	0.295	6.733	0.290	-3.274	0.214	-0.229	0.651
2	Experiment Product	UWAI-011	1.592	0.002	30.458	-8.530	0.004	5.072	5.360	10.461	0.024	-0.070	0.022	0.008	17.638	0.224	6.815	0.223	-3.248	0.189	-0.243	0.636
2	Experiment Product	UWAI-012	1.779	0.002	30.706	-8.292	0.006	5.255	5.602	10.890	0.056	-0.070	0.051	0.018	18.233	0.238	6.920	0.236	-2.876	0.331	-0.250	0.629
2	Experiment Product	UWAI-013	2.111	0.001	30.814	-8.188	0.005	5.569	5.708	11.346	0.029	-0.045	0.030	0.011	18.424	0.249	6.897	0.250	-2.969	0.189	-0.233	0.646
2	Experiment Product	UWAI-014	2.608	0.003	30.970	-8.038	0.006	6.040	5.861	11.988	0.029	-0.042	0.030	0.011	18.869	0.224	7.031	0.222	-4.409	0.317	-0.241	0.639
2	Experiment Product	UWAI-015	2.491	0.003	31.062	-7.949	0.004	5.933	5.950	11.967	0.032	-0.041	0.028	0.010	19.061	0.168	7.041	0.164	-4.015	0.379	-0.239	0.640
2	Experiment Product	UWAI-016	2.685	0.003	31.951	-7.094	0.008	6.145	6.818	13.112	0.047	0.024	0.039	0.014	21.817	0.202	8.026	0.192	-4.803	0.434	-0.193	0.686
2	Experiment Product	UWAI-018	2.673	0.003	32.119	-6.931	0.004	6.139	6.982	13.258	0.015	0.015	0.012	0.004	22.226	0.320	8.100	0.311	-3.515	0.324	-0.205	0.675
2	Experiment Product	UWAI-019	2.596	0.004	32.111	-6.939	0.004	6.075	6.979	13.165	0.034	0.005	0.033	0.012	22.105	0.393	7.997	0.389	-2.665	0.272	-0.214	0.666
2	Experiment Product	UWAI-019	2.604	0.002	32.116	-6.935	0.003	6.067	6.974	13.176	0.028	0.003	0.027	0.010	22.407	0.205	8.285	0.206	-2.831	0.270	-0.215	0.664
2	Experiment Product	UWAI-020	0.933	0.002	29.294	-9.650	0.005	4.415	4.225	8.607	0.021	-0.120	0.023	0.008	13.493	0.279	4.983	0.274	-3.222	0.223	-0.263	0.616
2	Experiment Product	UWAI-021	1.432	0.002	29.744	-9.217	0.007	4.897	4.664	9.548	0.030	-0.114	0.028	0.010	15.003	0.347	5.600	0.347	-2.738	0.179	-0.272	0.607
2	Seed Crystals	UWAI-022	4.383	0.003	31.920	-7.123	0.018	7.732	6.791	14.732	0.037	0.024	0.040	0.014	22.159	0.372	8.417	0.357	-3.171	0.312	-0.220	0.659
3	Seed Crystals	UWAI-001	4.378	0.009	31.703	-7.333	0.017	7.653	6.540	14.301	0.034	-0.075	0.024	0.009	18.397	0.707	5.206	0.679	-0.736	1.212	-0.243	0.651
3	Experiment Product	UWAI-002	0.917	0.003	30.183	-8.795	0.008	4.364	5.051	9.338	0.038	-0.153	0.029	0.010	13.603	0.527	3.441	0.508	0.410	0.759	-0.263	0.629
3	Experiment Product	UWAI-003	1.309	0.005	30.367	-8.617	0.014	4.737	5.232	9.908	0.043	-0.147	0.040	0.014	14.391	0.600	3.860	0.586	0.079	1.002	-0.264	0.628
3	Experiment Product	UWAI-004	1.614	0.005	30.607	-8.387	0.011	5.030	5.466	10.461	0.053	-0.130	0.041	0.015	14.922	0.520	3.917	0.496	0.535	0.965	-0.254	0.640
3	Experiment Product	UWAI-004	1.645	0.011	30.636	-8.359	0.020	5.060	5.495	10.529	0.076	-0.122	0.049	0.017	15.985	1.117	4.911	1.073	-1.533	1.892	-0.246	0.649
3	Experiment Product	UWAI-005	1.571	0.005	30.514	-8.476	0.013	4.993	5.389	10.351	0.064	-0.126	0.049	0.017	14.839	0.435	3.990	0.411	-0.041	0.537	-0.248	0.646
3	Experiment Product	UWAI-006	1.812	0.007	30.473	-8.515	0.014	5.211	5.336	10.496	0.048	-0.154	0.032	0.011	14.197	0.845	3.459	0.811	0.432	1.308	-0.278	0.613
3	Experiment Product	UWAI-007	1.439	0.006	30.783	-8.217	0.007	4.872	5.637	10.449	0.028	-0.148	0.025	0.009	15.074	0.382	3.726	0.370	0.498	0.698	-0.271	0.620
3	Experiment Product	UWAI-007	1.829	0.006	30.530	-8.461	0.018	5.229	5.392	10.591	0.032	-0.133	0.020	0.007	14.364	0.702	3.514	0.669	0.479	1.378	-0.258	0.635
3	Experiment Product	UWAI-008	1.577	0.004	30.297	-8.685	0.009	4.985	5.163	10.091	0.038	-0.154	0.028	0.010	13.628	0.423	3.241	0.403	0.603	0.703	-0.273	0.617
3	Experiment Product	UWAI-009	1.699	0.006	30.297	-8.685	0.010	5.099	5.164	10.220	0.038	-0.144	0.031	0.011	14.008	0.325	3.616	0.310	0.243	0.806	-0.265	0.627
3	Experiment Product	UWAI-009	1.603	0.008	30.500	-8.490	0.013	5.016	5.361	10.337	0.062	-0.136	0.047	0.017	15.203	0.764	4.405	0.733	-0.958	1.188	-0.258	0.634
3	Experiment Product	UWAI-010	2.199	0.006	30.713	-8.284	0.012	5.581	5.571	11.165	0.043	-0.102	0.037	0.013	15.258	0.678	4.040	0.651	0.086	1.089	-0.234	0.662
3	Experiment Product	UWAI-012	1.808	0.006	30.538	-8.453	0.012	5.209	5.399	10.601	0.044	-0.109	0.031	0.011	14.613	0.573	3.745	0.548	0.098	1.102	-0.234	0.661
3	Experiment Product	UWAI-013	2.140	0.006	30.750	-8.249	0.014	5.444	5.610	11.040	0.252	-0.126	0.053	0.019	15.491	0.718	4.193	0.693	-0.114	1.209	-0.256	0.637
3	Experiment Product	UWAI-014	2.500	0.009	30.891	-8.113	0.018	5.868	5.745	11.611	0.041	-0.125	0.024	0.008	15.934	0.627	4.361	0.590	-0.143	1.105	-0.262	0.630
3	Experiment Product	UWAI-015	2.556	0.009	30.960	-8.047	0.013	5.924	5.812	11.733	0.027	-0.127	0.023	0.008	16.571	0.623	4.856	0.597	-0.875	0.988	-0.265	0.627
3	Experiment Product	UWAI-015	2.541	0.008	30.983	-8.025	0.014	5.910	5.835	11.748	0.056	-0.120	0.042	0.015	16.310	0.772	4.553	0.740	-0.819	1.600	-0.259	0.634
3	Experiment Product	UWAI-016	2.685	0.007	32.124	-6.927	0.006	6.083	6.947	13.086	0.058	-0.064	0.053	0.019	19.194	0.375	5.181	0.363	-0.391	0.759	-0.218	0.680
3	Experiment Product	UWAI-017	2.747	0.004	32.008	-7.038	0.018	6.138	6.834	13.057	0.035	-0.087	0.025	0.009	18.785	0.361	5.001	0.347	0.299	1.009	-0.241	0.654
3	Experiment Product	UWAI-018	2.706	0.007	32.048	-7.000	0.015	6.101	6.873	13.019	0.042	-0.075	0.035	0.012	18.628	0.468	4.770	0.447	0.153	0.763	-0.229	0.668
3	Experiment Product	UWAI-018	2.729	0.007	32.094	-6.956	0.019	6.124	6.918	13.086	0.063	-0.078	0.043	0.015	19.138	0.573	5.182	0.549	-0.439	1.038	-0.232	0.664
3	Experiment Product	UWAI-019	2.627	0.007	32.041	-7.007	0.011	6.026	6.866	12.922	0.039	-0.088	0.035	0.012	18.575	0.570	4.731	0.551	0.260	1.027	-0.241	0.654
3	Experiment Product	UWAI-020	0.777	0.010	28.919	-10.011	0.007	4.190	3.819	7.934	0.045	-0.159	0.038	0.013	10.214	0.537	2.542	0.529	0.084	0.665	-0.252	0.641
3	Experiment Product	UWAI-020	0.560	0.007	29.241	-9.701	0.012	3.998	4.132	8.033	0.034	-0.171	0.026	0.009	11.321	0.660	3.014	0.637	0.001	0.953	-0.266	0.626
3	Seed Crystals	UWAI-022	4.342	0.006	31.815	-7.224	0.071	7.623	6.650	14.434	0.111	-0.076	0.040	0.014	22.760	2.030	9.292	1.869	-4.428	2.543	-0.254	0.657
3	Seed Crystals	UWAI-022	4.396	0.005	31.788	-7.250	0.023	7.672	6.623	14.396	0.029	-0.082	0.014	0.005	17.871	0.608	4.521	0.574	0.605	0.888	-0.252	0.641

Table SM3 (cont): Carbon, Oxygen, and Clumped Isotope Analyses

			Analyses*																		
Week	Measurement Type	Name	δ ^{13}C VPDB (‰)	δ ^{13}C 1σ	δ ^{18}O gas VSMOW (‰)	δ ^{18}O mineral VPDB (‰)	δ ^{18}O 1σ	δ 45 raw (‰)	δ 46 raw (‰)	δ 47 raw (‰)	δ 47 raw 1σ	Δ 47 raw (v. Oz)	D47 1σ	D47 sterror	d48 (v. Oz)	d48 1σ	D48 (v. Oz)	D48 1σ	d49 (v. Oz)	d49 1σ	D47 EGL Corrected	D47 ETF Corrected
4	Experiment Product	UWAI-003	1.178	0.003	29.968	-9.002	0.006	4.600	4.842	9.387	0.018	-0.142	0.021	0.008	14.080	0.239	4.330	0.234	-0.330	0.198	-0.258	0.658
4	Experiment Product	UWAI-006	1.538	0.002	30.091	-8.883	0.005	4.941	4.963	9.905	0.025	-0.098	0.024	0.009	14.397	0.216	4.401	0.212	-0.390	0.239	-0.220	0.699
4	Experiment Product	UWAI-006	1.554	0.001	30.084	-8.890	0.004	4.956	4.956	9.879	0.031	-0.131	0.030	0.011	14.371	0.287	4.391	0.282	-0.336	0.317	-0.254	0.663
4	Experiment Product	UWAI-017	2.552	0.002	31.523	-7.505	0.006	5.939	6.361	12.349	0.031	-0.070	0.028	0.010	18.420	0.208	5.585	0.196	-0.489	0.247	-0.223	0.696
4	Experiment Product	UWAI-017	2.611	0.002	31.637	-7.395	0.004	5.998	6.472	12.508	0.031	-0.083	0.028	0.010	18.617	0.225	5.558	0.221	-0.284	0.209	-0.238	0.680
4	Experiment Product	UWAI-025	3.356	0.001	31.932	-7.099	0.004	6.408	6.437	12.895	0.036	-0.087	0.039	0.014	18.416	0.418	5.430	0.413	-0.542	0.476	-0.247	0.670
4	Experiment Product	UWAI-026	3.317	0.002	31.958	-7.074	0.007	6.372	6.462	12.912	0.024	-0.081	0.021	0.007	18.651	0.228	5.611	0.215	-0.503	0.235	-0.240	0.677
4	Experiment Product	UWAI-027	3.490	0.002	31.926	-7.105	0.004	6.533	6.432	13.031	0.041	-0.075	0.041	0.014	18.463	0.312	5.487	0.313	-0.359	0.278	-0.237	0.681
4	Experiment Product	UWAI-028	3.631	0.002	31.849	-7.179	0.002	6.663	6.357	13.102	0.031	-0.065	0.030	0.011	18.245	0.290	5.421	0.286	-0.337	0.321	-0.227	0.691
4	Experiment Product	UWAI-029	3.302	0.001	31.850	-7.178	0.005	6.354	6.357	12.762	0.030	-0.085	0.034	0.012	18.348	0.168	5.522	0.162	-0.326	0.259	-0.243	0.674
4	Experiment Product	UWAI-030	3.433	0.001	31.822	-7.205	0.003	6.476	6.330	12.881	0.029	-0.086	0.027	0.010	18.183	0.107	5.414	0.104	-0.516	0.150	-0.245	0.672
4	Experiment Product	UWAI-031	2.594	0.002	31.851	-7.177	0.003	5.692	6.356	12.107	0.030	-0.101	0.032	0.011	18.384	0.283	5.560	0.281	-0.261	0.239	-0.250	0.666
4	Experiment Product	UWAI-032	3.057	0.002	31.886	-7.144	0.004	6.127	6.391	12.575	0.036	-0.069	0.034	0.012	18.556	0.324	5.661	0.324	-0.323	0.185	-0.225	0.693
4	Experiment Product	UWAI-033	2.731	0.002	31.822	-7.205	0.004	5.820	6.329	12.176	0.038	-0.088	0.040	0.014	18.288	0.244	5.520	0.243	-0.660	0.265	-0.239	0.678
4	Experiment Product	UWAI-034	2.844	0.002	31.907	-7.123	0.003	5.928	6.412	12.393	0.030	-0.086	0.027	0.010	18.915	0.243	5.974	0.239	-0.613	0.354	-0.239	0.679
4	Experiment Product	UWAI-035	-0.956	0.003	27.536	-11.328	0.005	2.225	2.144	4.180	0.026	-0.227	0.025	0.009	6.277	0.401	1.976	0.394	-0.220	0.211	-0.279	0.635
4	Experiment Product	UWAI-036	1.394	0.002	29.073	-9.850	0.004	4.475	3.647	8.043	0.033	-0.175	0.031	0.011	11.034	0.285	3.700	0.281	-0.439	0.213	-0.274	0.641
4	Experiment Product	UWAI-037	0.844	0.003	28.827	-10.086	0.005	3.953	3.406	7.279	0.029	-0.161	0.032	0.011	10.183	0.337	3.337	0.327	-0.639	0.369	-0.251	0.666
4	Experiment Product	UWAI-038	0.853	0.002	28.792	-10.120	0.005	3.959	3.371	7.255	0.040	-0.157	0.040	0.014	10.074	0.377	3.298	0.374	-0.527	0.411	-0.247	0.670
4	Experiment Product	UWAI-039	1.026	0.003	28.922	-9.995	0.006	4.126	3.499	7.545	0.029	-0.165	0.030	0.011	10.686	0.431	3.650	0.418	-0.732	0.398	-0.259	0.657
4	Experiment Product	UWAI-040	1.767	0.003	29.251	-9.679	0.005	4.830	3.820	8.604	0.040	-0.152	0.040	0.014	11.496	0.312	3.811	0.308	-0.535	0.299	-0.259	0.657
4	Experiment Product	UWAI-041	0.916	0.003	28.881	-10.035	0.007	4.021	3.458	7.405	0.024	-0.157	0.021	0.008	10.413	0.318	3.461	0.304	-0.361	0.391	-0.249	0.668
4	Experiment Product	UWAI-042	0.886	0.003	28.866	-10.049	0.005	3.994	3.444	7.335	0.032	-0.135	0.031	0.011	10.409	0.312	3.486	0.306	-0.547	0.489	-0.227	0.692
4	Experiment Product	UWAI-043	1.088	0.002	28.943	-9.975	0.005	4.185	3.519	7.610	0.030	-0.181	0.035	0.012	10.790	0.498	3.713	0.486	-0.957	0.381	-0.276	0.639
4	Experiment Product	UWAI-044	1.801	0.003	29.392	-9.543	0.002	4.866	3.958	8.793	0.034	-0.138	0.032	0.011	12.070	0.263	4.105	0.259	-0.868	0.258	-0.247	0.670
4	Experiment Product	UWAI-045	2.545	0.002	30.713	-8.272	0.005	5.607	5.248	10.877	0.036	-0.097	0.032	0.011	15.726	0.269	5.149	0.261	-0.742	0.302	-0.232	0.686
4	Experiment Product	UWAI-046	2.362	0.002	30.668	-8.316	0.003	5.435	5.203	10.640	0.016	-0.110	0.013	0.005	15.441	0.191	4.956	0.187	-0.629	0.278	-0.242	0.676
4	Experiment Product	UWAI-047	1.263	0.002	29.090	-9.834	0.002	4.354	3.662	7.955	0.010	-0.153	0.010	0.005	11.381	0.121	4.014	0.119	-1.858	3.258	-0.251	0.666
4	Experiment Product	UWAI-048	1.260	0.002	29.088	-9.835	0.004	4.351	3.661	7.956	0.025	-0.148	0.023	0.008	11.260	0.159	3.896	0.154	-0.822	0.420	-0.246	0.671
5	Experiment Product	UWAI-003	1.368	0.003	30.431	-8.556	0.005	4.886	5.939	10.778	0.042	-0.109	0.039	0.014	16.827	0.396	6.047	0.390	-6.426	0.749	-0.239	0.605
5	Experiment Product	UWAI-023	0.967	0.002	30.094	-8.880	0.007	4.438	5.014	9.379	0.026	-0.153	0.020	0.007	14.604	0.223	4.506	0.221	-6.524	0.406	-0.273	0.615
5	Experiment Product	UWAI-023	0.787	0.013	30.009	-8.962	0.028	4.266	4.931	9.135	0.042	-0.137	0.025	0.009	14.309	0.392	4.380	0.342	-6.202	0.673	-0.254	0.597
5	Experiment Product	UWAI-024	0.934	0.009	29.974	-8.996	0.018	4.403	4.897	9.268	0.041	-0.112	0.023	0.008	13.880	0.236	4.023	0.214	-4.819	0.354	-0.230	0.622
5	Experiment Product	UWAI-024	0.912	0.002	29.986	-8.984	0.005	6.592	6.940	9.285	0.031	-0.086	0.031	0.011	14.779	0.313	4.890	0.304	-5.956	0.367	-0.205	0.640
5	Experiment Product	UWAI-025	3.140	0.014	32.008	-7.039	0.022	6.535	6.884	13.529	0.024	-0.064	0.022	0.008	19.273	0.173	5.384	0.160	-4.449	0.315	-0.237	0.650
5	Experiment Product	UWAI-025	3.230	0.033	32.114	-6.937	0.059	6.623	6.987	13.729	0.095	-0.013	0.029	0.010	20.967	0.783	6.848	0.686	-4.660	1.661	-0.189	0.666
5	Experiment Product	UWAI-025	3.199	0.006	32.065	-6.984	0.009	6.535	6.884	13.528	0.037	-0.064	0.030	0.011	19.782	0.369	5.774	0.367	-4.449	0.315	-0.238	0.650
5	Experiment Product	UWAI-026	3.107	0.013	31.990	-7.056	0.024	6.504	6.866	13.457	0.045	-0.050	0.029	0.010	19.332	0.221	5.478	0.179	-4.409	0.360	-0.222	0.645
5	Experiment Product	UWAI-027	3.299	0.027	32.016	-7.031	0.043	6.684	6.892	13.680	0.060	-0.040	0.036	0.013	19.646	0.384	5.736	0.305	-6.227	0.307	-0.215	0.657
5	Experiment Product	UWAI-027	3.318	0.004	32.051	-6.997	0.008	6.703	6.926	13.750	0.022	-0.025	0.022	0.008	20.078	0.590	6.093	0.571	-3.588	1.102	-0.201	0.654
5	Experiment Product	UWAI-028	3.402	0.013	31.878	-7.164	0.020	6.776	6.757	13.640	0.022	-0.042	0.027	0.010	19.153	0.265	5.518	0.236	-5.585	0.319	-0.217	0.655
5	Experiment Product	UWAI-028	3.451	0.005	32.010	-7.037	0.005	6.826	6.887	13.835	0.029	-0.028	0.024	0.008	20.220	0.557	6.312	0.540	-3.775	0.814	-0.205	0.639
5	Experiment Product	UWAI-029	3.184	0.015	31.946	-7.098	0.025	6.575	6.823	13.497	0.038	-0.042	0.022	0.008	19.361	0.191	5.591	0.177	-4.750	0.168	-0.215	0.659
5	Experiment Product	UWAI-029	3.205	0.005	32.065	-6.983	0.005	6.592	6.940	13.658	0.041	-0.021	0.037	0.013	21.801	0.403	7.765	0.389	-5.956	0.367	-0.209	0.608
5	Experiment Product	UWAI-032	2.939	0.027	32.080	-6.969	0.054	6.350	6.954	13.394	0.082	-0.040	0.032	0.011	20.077	0.413	6.036	0.316	-6.712	0.316	-0.212	0.641
5	Experiment Product	UWAI-033	2.631	0.008	31.967	-7.078	0.014	6.058	6.843	12.953	0.030	-0.068	0.021	0.007	20.010	0.384	6.193	0.363	-7.416	0.362	-0.234	0.621
5	Experiment Product	UWAI-033	2.637	0.003	32.113	-6.938	0.004	6.068	6.985	13.146	0.019	-0.028	0.016	0.006	20.627	0.222	6.517	0.216	-4.239	0.498	-0.196	0.648
5	Experiment Product	UWAI-034	2.680	0.007	32.006	-7.040	0.013	6.105	6.881	13.063	0.039	-0.046	0.029	0.010	19.976	0.512	6.082	0.484	-7.273	0.660	-0.213	0.642
5	Experiment Product	UWAI-034	2.692	0.003	31.995	-7.052	0.007	6.129	6.895	13.082	0.034	-0.027	0.028	0.010	20.718	0.450	6.838	0.432	-7.455	0.645	-0.194	0.650
5	Experiment Product	UWAI-037	0.692	0.025	28.911	-10.019	0.043	4.140	3.860	7.931	0.047	-0.152	0.028	0.010	10.975	0.196	3.216	0.168	-4.602	0.255	-0.253	0.613
5	Experiment Product	UWAI-038	0.698	0.012	28.971	-9.960	0.016	4.148	3.919	7.997	0.030	-0.152	0.034	0.012	11.252	0.218	3.372	0.204	-4.094	0.298	-0.255	0.612
5	Experiment Product	UWAI-038	0.772	0.015	29.099	-9.838	0.024	4.221	4.043	8.176	0.052	-0.171	0.040	0.014	12.120	0.368	3.986	0.332	-6.690	0.337	-0.276	0.577
5	Experiment Product	UWAI-041	0.812	0.019	29.095	-9.841	0.038	4.258	4.040	8.225	0.076	-0.158	0.031	0.011	11.890	0.308	3.763	0.255	-4.677	0.188	-0.272	0.550
5	Experiment Product	UWAI-042	0.849	0.009	29.110	-9.827	0.010	4.293	4.054	8.270	0.026	-0.164	0.011	0.004	11.582	0.253	3.429	0.249	-4.213	0.140	-0.269	0.614
5	Experiment Product	UWAI-042	0.853	0.003	29.068	-9.868	0.007	4.321	4.098	8.338	0.025	-0.137	0.026	0.009	12.720	0.381	4.641	0.370	-6.827	0.502	-0.243	0.600
5	Experiment Product	UWAI-044	1.678	0.022	29.582	-9.373	0.036	5.085	4.516	9.587	0.064	-0.122	0.034	0.012	12.922	0.098	3.835	0.162	-4.511	0.279	-0.245	0.622
5	Experiment Product	UWAI-045	2.397	0.017	30.877	-8.127	0.028	5.802	5.780	11.606	0.054	-0.097	0.019	0.007	16.510	0.175	4.860	0.173	-5.460	0.290	-0.246	0.621
6	Experiment Product	UWAI-030	3.281	0.004	32.072	-6.977	0.005	6.673	6.893	13.651	0.028	0.003	0.025	0.009	20.460	0.400	6.428	0.388	-4.710	0.726	-0.155	0.688
6	Experiment Product	UWAI-035	-1.030	0.003	27.602	-11.278	0.009	2.484	2.581	4.904	0.036	-0.204	0.033	0.012	7.688	0.181	2.507	0.170	-6.361	0.460	-0.271	0.543
6	Experiment Product	UWAI-036	1.273	0.005	29.229	-9.713	0.008	4.694	4.171	8.840	0.024	-0.124	0.024	0.009	12.194	0.198	3.803	0.190	-5.930	0.738	-0.246	0.571
6	Experiment Product	UWAI-037	0.872	0.045	29.250	-9.692	0.089	4.320	4.191	8.404	0.143	-0.192	0.027	0.009	13.123	0.541	4.685	0.386	-7.902	0.724	-0.307	0.521
6	Experiment Product	UWAI-039	0.875	0.007	29.038	-9.896	0.013	4.315	3.984	8.194	0.029	-0.193	0.027	0.010	11.875	0.321	3.859	0.300	-6.660	0.733	-0.309	0.522
6	Experiment Product	UWAI-040	1.683	0.006	29.470	-9.481	0.011	5.086	4.407	9.483	0.046	-0.120	0.033	0.012	13.344	0.319	4.471	0.296	-7.726	0.415	-0.251	0.573
6	Experiment Product	UWAI-041	0.786	0.017	29.024	-9.910	0.032	4.232	3.970	8.141	0.041	-0.146	0.033	0.012	11.278	0.217	3.295	0.205	-4.677	0.188	-0.250	0.616
6	Experiment Product	UWAI-042	0.877	0.012	29.155	-9.784	0.022	4.321	4.098	8.313	0.052	-0.143	0.034	0.012	12.229	0.261	3.983	0.244	-6.827	0.502	-0.258	0.583
6	Experiment Product	UWAI-043	1.052	0.009	29.217	-9.724	0.020	4.487	4.159	8.562	0.052	-0.126	0.034	0.012	12.417	0.288	4.047	0.275	-5.913	0.765	-0.245	0.593
6	Experiment Product	UWAI-044	1.709	0.009	29.608	-9.348	0.016	5.085	4.516	9.533	0.062	-0.114	0.041	0.014	13.677	0.777	4.531	0.745	-4.511	0.279	-0.247	0.566
6	Experiment Product	UWAI-046	2.238	0.004	30.814	-8.187	0.006	5.651	5.719	11.382	0.030	-0.104	0.028	0.010	16.800	0.405	5.270	0.397	-6.990	1.245	-0.261	0.575
6	Experiment Product	UWAI-047	0.962	0.022	29.190	-9.750	0.036	4.402	4.133	8.456	0.056	-0.137	0.024	0.008	11.826	0.128	3.515	0.106	-5.060	0.251	-0.254	0.581
6	Experiment Product	UWAI-048	1.074	0.004	29.264	-9.679	0.009	4.509	4.205	8.667	0.040	-0.139	0.036	0.013	12.299	0.279	3.839	0.261	-6.459	0.249	-0.258	0.565
6	Experiment Product	UWAI-048	1.137	0.009	29.369	-9.578	0.015	4.572	4.308	8.817	0.040	-0.155	0.021	0.008	12.532	0.208	3.865	0.201	-6.426	0.749	-0.277	0.542

Table SM3 (cont): Carbon, Oxygen, and Clumped Isotope Analyses

			Analyses*																			
	Measurement		$\delta^{13}C$	$\delta^{13}C$	$\delta^{18}O$ gas	$\delta^{18}O$ mineral	$\delta^{18}O$	δ 45 raw	δ 46 raw	δ 47 raw	δ 47 raw	Δ 47 raw	D47	D47	d48	d48	D48	D48	d49	d49	D47 EGL	D47 ETF
Week	Type	Name	VPDB (‰)	1σ	VSMOW (‰)	VPDB (‰)	1σ	(‰)	(‰)	(‰)	1σ	(v. Oz)	1σ	sterror	(v. Oz)	1σ	(v. Oz)	1σ	(v. Oz)	1σ	Corrected	Corrected
7	Experiment Product	UWAI-026	3.082	0.001	32.129	-6.922	0.003	6.529	6.914	13.564	0.025	-0.036	0.027	0.009	20.797	0.324	6.827	0.317	-0.3573	0.2565	-0.250	0.673
7	Experiment Product	UWAI-031	2.446	0.004	32.058	-6.991	0.010	5.931	6.843	12.858	0.035	-0.061	0.028	0.010	20.714	0.273	6.887	0.268	-0.3774	0.1819	-0.263	0.657
7	Experiment Product	UWAI-031	2.353	0.004	32.037	-7.010	0.003	5.845	6.823	12.745	0.037	-0.083	0.039	0.014	20.840	0.233	7.052	0.227	-0.2496	0.2345	-0.284	0.631
7	Experiment Product	UWAI-031	2.397	0.003	32.035	-7.012	0.006	5.885	6.821	12.793	0.050	-0.066	0.049	0.017	20.330	0.244	6.563	0.235	-0.1655	0.3271	-0.267	0.651
7	Experiment Product	UWAI-032	2.803	0.003	32.046	-7.002	0.010	6.265	6.832	13.210	0.014	-0.068	0.023	0.008	20.552	0.260	6.750	0.258	-0.3999	0.3307	-0.276	0.641
7	Experiment Product	UWAI-032	2.824	0.003	32.072	-6.977	0.004	6.286	6.858	13.246	0.028	-0.026	0.028	0.010	20.970	0.251	7.122	0.248	-0.3932	0.1754	-0.235	0.692
7	Experiment Product	UWAI-035	-1.128	0.003	27.617	-11.264	0.009	2.437	2.507	4.743	0.058	-0.242	0.058	0.021	7.631	0.297	2.599	0.298	0.0546	0.1948	-0.317	0.589
7	Experiment Product	UWAI-035	-1.083	0.002	27.657	-11.225	0.006	2.480	2.546	4.841	0.048	-0.227	0.049	0.017	7.892	0.318	2.786	0.319	-0.1377	0.2777	-0.303	0.606
7	Experiment Product	UWAI-036	1.162	0.002	29.412	-9.536	0.007	4.640	4.262	8.851	0.033	-0.145	0.031	0.011	12.914	0.260	4.336	0.260	-0.2251	0.3047	-0.285	0.629
7	Experiment Product	UWAI-036	1.219	0.002	29.333	-9.612	0.008	4.692	4.185	8.817	0.044	-0.156	0.044	0.016	12.577	0.303	4.167	0.292	-0.1271	0.1782	-0.295	0.616
7	Experiment Product	UWAI-039	0.733	0.003	29.397	-9.551	0.008	4.239	4.246	8.401	0.035	-0.129	0.035	0.012	12.709	0.326	4.164	0.313	-0.3607	0.2774	-0.262	0.658
7	Experiment Product	UWAI-039	0.847	0.003	29.159	-9.780	0.009	4.338	4.014	8.283	0.057	-0.155	0.060	0.021	12.110	0.219	4.043	0.221	-0.1531	0.1186	-0.286	0.628
7	Experiment Product	UWAI-040	1.563	0.004	29.535	-9.418	0.007	5.019	4.382	9.377	0.021	-0.132	0.021	0.007	13.184	0.142	4.362	0.138	-0.3347	0.3036	-0.280	0.635
7	Experiment Product	UWAI-040	1.621	0.006	29.568	-9.387	0.008	5.075	4.414	9.486	0.030	-0.112	0.031	0.011	13.306	0.291	4.431	0.296	-0.2248	0.1817	-0.262	0.658
7	Experiment Product	UWAI-043	0.962	0.003	29.158	-9.781	0.006	4.445	4.013	8.422	0.027	-0.126	0.030	0.010	12.061	0.277	3.987	0.265	-0.1767	0.3499	-0.259	0.662
7	Experiment Product	UWAI-043	0.987	0.002	29.274	-9.669	0.008	4.472	4.127	8.566	0.036	-0.122	0.042	0.015	12.597	0.260	4.301	0.260	-0.1494	0.2795	-0.257	0.664
7	Experiment Product	UWAI-045	2.378	0.004	31.006	-8.003	0.011	5.833	5.817	11.705	0.048	-0.067	0.040	0.014	17.531	0.208	5.795	0.200	-0.3156	0.257	-0.252	0.671
8	Experiment Product	UWAI-002	1.218	0.003	30.458	-8.530	0.004	4.729	5.281	9.999	0.051	-0.098	0.053	0.019	15.799	0.270	5.162	0.265	-0.397	0.292	-0.250	0.698
8	Experiment Product	UWAI-003	1.474	0.003	30.598	-8.395	0.010	4.973	5.418	10.396	0.027	-0.089	0.023	0.008	16.207	0.314	5.294	0.310	-0.305	0.246	-0.247	0.701
8	Experiment Product	UWAI-011	1.648	0.003	30.607	-8.386	0.006	5.136	5.427	10.541	0.026	-0.121	0.030	0.011	16.380	0.396	5.446	0.389	-0.280	0.172	-0.281	0.661
8	Experiment Product	UWAI-023	0.723	0.003	30.018	-8.953	0.009	4.251	4.851	9.047	0.031	-0.129	0.030	0.011	14.370	0.276	4.606	0.269	-0.366	0.259	-0.267	0.678
8	Experiment Product	UWAI-024	0.690	0.002	29.956	-9.013	0.004	4.218	4.791	8.947	0.037	-0.134	0.034	0.012	14.335	0.263	4.694	0.255	-0.298	0.164	-0.270	0.674
8	Experiment Product	UWAI-027	3.296	0.002	32.089	-6.961	0.008	6.728	6.875	13.703	0.029	-0.044	0.023	0.008	20.791	0.219	6.913	0.210	-0.280	0.148	-0.252	0.695
8	Experiment Product	UWAI-029	3.180	0.004	32.078	-6.971	0.008	6.619	6.865	13.582	0.035	-0.043	0.033	0.012	20.682	0.266	6.825	0.015	-0.350	0.266	-0.249	0.699
8	Experiment Product	UWAI-029	3.178	0.004	32.123	-6.928	0.009	6.618	6.908	13.590	0.033	-0.076	0.030	0.011	20.822	0.252	6.876	0.260	-0.322	0.184	-0.283	0.660
8	Experiment Product	UWAI-033	2.625	0.003	32.131	-6.921	0.005	6.102	6.914	13.102	0.035	-0.035	0.038	0.013	20.590	0.190	6.633	0.187	-0.281	0.233	-0.234	0.716
8	Experiment Product	UWAI-034	2.659	0.002	32.103	-6.947	0.006	6.133	6.888	13.090	0.046	-0.052	0.045	0.016	20.774	0.291	6.868	0.296	-0.351	0.405	-0.251	0.697
8	Experiment Product	UWAI-037	0.699	0.003	29.124	-9.814	0.005	4.198	3.979	8.084	0.028	-0.175	0.032	0.011	11.908	0.336	3.911	0.330	-0.088	0.350	-0.298	0.642
8	Experiment Product	UWAI-038	0.710	0.004	29.078	-9.858	0.007	4.207	3.935	8.035	0.025	-0.190	0.028	0.010	11.963	0.258	4.055	0.256	-0.086	0.208	-0.312	0.625
8	Experiment Product	UWAI-041	0.737	0.002	29.062	-9.874	0.005	4.231	3.919	8.074	0.026	-0.160	0.027	0.009	11.780	0.326	3.906	0.317	0.066	0.121	-0.283	0.659
8	Experiment Product	UWAI-044	1.664	0.003	29.801	-9.162	0.004	5.123	4.642	9.718	0.044	-0.085	0.048	0.017	13.868	0.325	4.532	0.317	-0.351	0.343	-0.234	0.717
8	Experiment Product	UWAI-045	2.366	0.002	31.020	-7.989	0.007	5.821	5.831	11.661	0.026	-0.112	0.027	0.009	17.620	0.365	5.868	0.358	-0.232	0.401	-0.289	0.652
8	Experiment Product	UWAI-046	2.146	0.003	30.818	-8.183	0.005	5.609	5.634	11.290	0.032	-0.068	0.032	0.011	17.011	0.329	5.659	0.321	-0.218	0.191	-0.240	0.710
8	Experiment Product	UWAI-046	2.229	0.002	30.926	-8.079	0.006	5.690	5.740	11.428	0.037	-0.119	0.038	0.013	17.481	0.417	5.912	0.406	-0.269	0.467	-0.293	0.648
8	Experiment Product	UWAI-047	0.939	0.002	29.336	-9.610	0.008	4.430	4.186	8.560	0.050	-0.144	0.047	0.017	12.573	0.130	4.158	0.132	-0.261	0.331	-0.274	0.670
8	Experiment Product	UWAI-048	1.095	0.002	29.407	-9.541	0.007	4.578	4.257	8.742	0.038	-0.185	0.037	0.013	12.649	0.257	4.093	0.255	-0.243	0.278	-0.318	0.618
9	Experiment Product	UWAI-028	3.159	0.003	32.038	-7.010	0.006	6.598	6.825	13.523	0.009	-0.040	0.011	0.004	20.592	0.139	6.816	0.135	-0.196	0.265	-0.249	0.716
9	Experiment Product	UWAI-030	3.277	0.002	32.074	-6.975	0.000	6.709	6.861	13.678	0.038	-0.036	0.038	0.013	20.637	0.248	6.789	0.244	-0.363	0.270	-0.242	0.613
9	Experiment Product	UWAI-030	3.304	0.004	32.039	-7.009	0.004	6.733	6.826	13.670	0.041	-0.035	0.041	0.015	20.470	0.162	6.694	0.156	-0.438	0.306	-0.241	0.615

Table SM3 (cont): Carbon, Oxygen, and Clumped Isotope Analyses

			Overgrowth by Isotope Dilution**										Overgrowth by Mass Balance									
	Measurement		$\delta^{13}C$	$\delta^{13}C$ Mixing	$\delta^{13}C$ Mixing	$\delta^{18}O$ mineral	$\delta^{18}O$ mineral	$\delta^{18}O$ Mixing	D_{47} Mixing	Mixing	Mixing	Acid	$\delta^{13}C$	$\delta^{13}C$ Mixing	$\delta^{13}C$ Mixing	$\delta^{18}O$ mineral	$\delta^{18}O$ mineral	$\delta^{18}O$ Mixing	D_{47} Mixing	Mixing	Mixing	Acid
Week	Type	Name	VPDB (‰)	+ 2σ	- 2σ	VSMOW (‰)	+ 2σ	- 2σ	Correction	+ 2σ	- 2σ	Corrected	VPDB (‰)	+ 2σ	- 2σ	VSMOW (‰)	+ 2σ	- 2σ	Correction	+ 2σ	- 2σ	Corrected
1	Seed Crystals	UWAI-001	4.388	NA	NA	23.462	NA	NA	NA	NA	NA	0.718	4.388	NA	NA	23.462	NA	NA	NA	NA	NA	0.718
1	Seed Crystals	UWAI-001	4.398	NA	NA	23.466	NA	NA	NA	NA	NA	0.729	4.398	NA	NA	23.466	NA	NA	NA	NA	NA	0.729
1	Experiment Product	UWAI-002	-0.545	-0.013	0.013	21.189	-0.006	0.006	0.613	-2.3E-04	2.2E-04	0.694	-0.262	-0.002	0.002	21.316	-0.001	0.001	0.607	3.8E-05	-3.8E-05	0.688
1	Experiment Product	UWAI-008	0.393	-0.010	0.010	21.165	-0.006	0.006	0.678	2.5E-05	-4.9E-05	0.759	0.412	-0.002	0.003	21.176	-0.001	0.001	0.668	9.9E-06	-1.0E-05	0.749
1	Experiment Product	UWAI-009	0.408	-0.011	0.012	21.015	-0.007	0.007	0.701	5.7E-05	-1.7E-05	0.782	0.533	-0.002	0.002	21.090	-0.001	0.001	0.690	-3.5E-06	3.5E-06	0.771
1	Experiment Product	UWAI-010	0.789	-0.012	0.013	21.380	-0.007	0.007	0.688	-6.4E-05	3.0E-05	0.769	1.034	-0.002	0.002	21.518	-0.001	0.001	0.676	5.1E-06	-5.1E-06	0.757
1	Experiment Product	UWAI-011	-0.893	-0.016	0.016	21.449	-0.006	0.006	0.704	-7.1E-06	-2.6E-05	0.785	-0.664	-0.003	0.003	21.534	-0.001	0.001	0.693	-5.2E-06	5.3E-06	0.774
1	Experiment Product	UWAI-012	0.360	-0.013	0.014	21.325	-0.007	0.007	0.705	2.7E-05	-2.8E-05	0.786	0.332	-0.004	0.004	21.311	-0.002	0.002	0.692	-7.8E-06	7.8E-06	0.773
1	Experiment Product	UWAI-013	0.546	-0.017	0.017	21.226	-0.009	0.010	0.692	8.7E-06	3.3E-05	0.773	0.628	-0.004	0.004	21.273	-0.002	0.002	0.676	8.2E-06	-8.2E-06	0.757
1	Experiment Product	UWAI-014	1.172	-0.019	0.019	21.570	-0.011	0.011	0.705	-5.8E-12	0.0E+00	0.786	1.006	-0.008	0.008	21.475	-0.004	0.004	0.683	-1.1E-13	3.3E-13	0.764
1	Experiment Product	UWAI-015	0.408	-0.029	0.030	21.271	-0.016	0.016	0.699	-8.8E-05	7.7E-05	0.780	0.552	-0.009	0.009	21.348	-0.005	0.005	0.673	2.4E-05	-2.4E-05	0.754
1	Experiment Product	UWAI-016	1.228	-0.019	0.020	23.437	0.000	0.000	0.739	1.5E-04	-1.9E-04	0.820	1.479	-0.005	0.005	23.434	0.000	0.000	0.711	-4.3E-05	4.3E-05	0.792
1	Experiment Product	UWAI-016	1.304	-0.019	0.020	23.503	0.001	-0.001	0.733	1.2E-04	-1.5E-04	0.814	1.549	-0.004	0.004	23.495	0.000	0.000	0.705	-3.4E-05	3.5E-05	0.786
1	Experiment Product	UWAI-017	1.215	-0.019	0.020	23.370	0.000	0.000	0.720	7.0E-05	-6.8E-05	0.801	1.482	-0.004	0.004	23.373	0.000	0.000	0.693	-1.5E-05	1.5E-05	0.774
1	Experiment Product	UWAI-017	1.257	-0.019	0.020	23.353	0.000	0.000	0.672	-2.1E-04	2.3E-04	0.753	1.520	-0.004	0.004	23.358	0.000	0.000	0.650	5.0E-05	-5.0E-05	0.731
1	Experiment Product	UWAI-018	1.276	-0.016	0.016	23.551	0.001	-0.001	0.759	3.1E-04	-2.8E-04	0.840	1.489	-0.003	0.004	23.541	0.000	0.000	0.733	-6.1E-05	6.1E-05	0.814
1	Experiment Product	UWAI-019	1.277	-0.015	0.015	23.571	0.001	-0.001	0.753	2.9E-04	-2.4E-04	0.834	1.391	-0.004	0.004	23.565	0.000	0.000	0.731	-5.9E-05	6.0E-05	0.812
1	Experiment Product	UWAI-020	-1.060	-0.017	0.017	18.959	-0.014	0.014	0.627	-2.8E-04	2.3E-04	0.708	-0.938	-0.004	0.004	19.058	-0.003	0.003	0.619	5.4E-05	-5.4E-05	0.700
1	Experiment Product	UWAI-020	-1.026	-0.017	0.017	19.098	-0.013	0.014	0.616	-2.3E-04	2.7E-04	0.697	-0.905	-0.004	0.004	19.194	-0.003	0.003	0.609	6.1E-05	-6.1E-05	0.690
1	Experiment Product	UWAI-021	-0.634	-0.019	0.019	19.109	-0.016	0.017	0.670	-1.1E-04	1.2E-04	0.751	-0.474	-0.005	0.005	19.246	-0.004	0.004	0.660	2.7E-05	-2.7E-05	0.741
1	Experiment Product	UWAI-021	-0.566	-0.019	0.019	19.282	-0.016	0.016	0.654	-1.8E-04	1.7E-04	0.735	-0.408	-0.004	0.004	19.413	-0.004	0.004	0.644	4.1E-05	-4.1E-05	0.725
1	Seed Crystals	UWAI-022	4.342	NA	NA	23.413	NA	NA	NA	NA	NA	0.738	4.342	NA	NA	23.413	NA	NA	NA	NA	NA	0.738
1	Seed Crystals	UWAI-022	4.356	NA	NA	23.235	NA	NA	NA	NA	NA	0.753	4.356	NA	NA	23.235	NA	NA	NA	NA	NA	0.753
2	Seed Crystals	UWAI-001	4.381	NA	NA	23.464	NA	NA	NA	NA	NA	0.751	4.381	NA	NA	23.464	NA	NA	NA	NA	NA	0.751
2	Experiment Product	UWAI-004	0.112	-0.015	0.015	21.569	-0.006	0.006	0.630	-2.4E-04	2.4E-04	0.711	0.354	-0.003	0.003	21.673	-0.001	0.001	0.620	4.5E-05	-4.5E-05	0.701
2	Experiment Product	UWAI-005	-0.005	-0.016	0.016	21.404	-0.007	0.007	0.601	-2.6E-04	2.1E-04	0.682	0.213	-0.003	0.003	21.504	-0.001	0.001	0.628	4.4E-05	-4.4E-05	0.709
2	Experiment Product	UWAI-005	-0.010	-0.016	0.016	21.514	-0.007	0.007	0.632	-3.8E-04	3.4E-04	0.713	0.209	-0.003	0.003	21.608	-0.001	0.001	0.592	7.1E-05	-7.2E-05	0.673
2	Experiment Product	UWAI-005	-0.088	-0.016	0.016	21.673	-0.006	0.006	0.693	-2.5E-04	2.3E-04	0.774	0.135	-0.003	0.003	21.759	-0.001	0.001	0.622	4.8E-05	-4.8E-05	0.703
2	Experiment Product	UWAI-006	0.664	-0.010	0.010	21.492	-0.005	0.005	0.588	-3.0E-04	2.7E-04	0.669	0.686	-0.002	0.002	21.503	-0.001	0.001	0.582	6.7E-05	-6.8E-05	0.663
2	Experiment Product	UWAI-006	0.563	-0.010	0.010	21.543	-0.005	0.005	0.672	-2.4E-04	2.8E-04	0.753	0.586	-0.003	0.003	21.554	-0.001	0.001	0.578	7.0E-05	-7.0E-05	0.659
2	Experiment Product	UWAI-007	0.624	-0.011	0.011	21.585	-0.005	0.005	0.634	-2.6E-04	2.7E-04	0.715	0.698	-0.002	0.002	21.621	-0.001	0.001	0.593	5.9E-05	-5.9E-05	0.674
2	Experiment Product	UWAI-008	0.397	-0.010	0.010	21.729	-0.004	0.004	0.636	-2.2E-04	2.5E-04	0.717	0.417	-0.002	0.003	21.737	-0.001	0.001	0.626	3.6E-05	-3.6E-05	0.707
2	Experiment Product	UWAI-009	0.437	-0.011	0.012	21.203	-0.006	0.006	0.635	-1.9E-04	2.5E-04	0.716	0.561	-0.002	0.002	21.273	-0.001	0.001	0.603	5.1E-05	-5.1E-05	0.684
2	Experiment Product	UWAI-010	1.015	-0.012	0.012	21.732	-0.006	0.006	0.647	-1.3E-04	1.2E-04	0.728	1.245	-0.002	0.002	21.846	-0.001	0.001	0.653	2.0E-05	-2.0E-05	0.734
2	Experiment Product	UWAI-011	0.206	-0.012	0.013	21.480	-0.006	0.006	0.625	-1.8E-04	2.1E-04	0.706	0.388	-0.002	0.002	21.563	-0.001	0.001	0.616	4.2E-05	-4.2E-05	0.697
2	Experiment Product	UWAI-012	0.400	-0.013	0.014	21.622	-0.006	0.006	0.613	-1.1E-04	1.2E-04	0.694	0.372	-0.004	0.004	21.610	-0.002	0.002	0.649	3.2E-05	-3.3E-05	0.730
2	Experiment Product	UWAI-013	0.618	-0.016	0.017	21.634	-0.008	0.008	0.638	-3.8E-04	3.4E-04	0.719	0.699	-0.004	0.004	21.672	-0.002	0.002	0.609	8.6E-05	-8.6E-05	0.690
2	Experiment Product	UWAI-014	1.116	-0.019	0.020	21.877	-0.009	0.009	0.624	-6.0E-04	5.7E-04	0.705	0.946	-0.008	0.008	21.798	-0.004	0.004	0.598	1.9E-04	-1.9E-04	0.679
2	Experiment Product	UWAI-015	0.632	-0.027	0.028	21.681	-0.013	0.013	0.622	-8.7E-04	8.6E-04	0.703	0.768	-0.009	0.009	21.744	-0.004	0.004	0.572	2.7E-04	-2.7E-04	0.653
2	Experiment Product	UWAI-016	1.177	-0.020	0.020	23.676	0.002	-0.002	0.715	-3.4E-06	3.9E-05	0.796	1.431	-0.005	0.005	23.654	0.000	0.000	0.688	-7.6E-06	7.7E-06	0.769
2	Experiment Product	UWAI-018	1.392	-0.015	0.016	23.948	0.003	-0.003	0.691	-7.2E-05	7.5E-05	0.772	1.597	-0.003	0.003	23.911	0.001	-0.001	0.670	1.6E-05	-1.6E-05	0.751
2	Experiment Product	UWAI-019	1.389	-0.014	0.015	23.802	0.002	-0.002	0.675	-1.4E-04	1.4E-04	0.756	1.498	-0.004	0.004	23.787	0.000	0.000	0.655	3.5E-05	-3.5E-05	0.736
2	Experiment Product	UWAI-019	1.337	-0.015	0.015	23.920	0.002	-0.003	0.671	-1.6E-04	1.5E-04	0.752	1.448	-0.004	0.004	23.902	0.001	-0.001	0.652	3.9E-05	-3.9E-05	0.733
2	Experiment Product	UWAI-020	-0.790	-0.016	0.016	19.669	-0.012	0.012	0.590	-3.5E-04	3.4E-04	0.671	-0.675	-0.004	0.004	19.752	-0.003	0.003	0.583	7.8E-05	-7.9E-05	0.664
2	Experiment Product	UWAI-021	-0.293	-0.018	0.018	20.164	-0.012	0.013	0.574	-4.2E-04	4.8E-04	0.655	-0.144	-0.004	0.004	20.267	-0.003	0.003	0.565	1.1E-04	-1.1E-04	0.646
2	Seed Crystals	UWAI-022	4.383	NA	NA	23.517	NA	NA	NA	NA	NA	0.740	4.383	NA	NA	23.517	NA	NA	NA	NA	NA	0.740
3	Seed Crystals	UWAI-001	4.378	NA	NA	23.301	NA	NA	NA	NA	NA	0.732	4.378	NA	NA	23.301	NA	NA	NA	NA	NA	0.732
3	Experiment Product	UWAI-002	-0.546	-0.013	0.013	20.874	-0.007	0.007	0.614	-2.0E-04	2.1E-04	0.695	-0.264	-0.002	0.002	21.020	-0.001	0.001	0.609	3.7E-05	-3.7E-05	0.690
3	Experiment Product	UWAI-003	-0.487	0.000	0.038	21.134	-0.009	0.009	0.608	-3.0E-04	3.5E-04	0.689	0.039	-0.003	0.003	21.387	-0.001	0.001	0.605	4.8E-05	-4.8E-05	0.686
3	Experiment Product	UWAI-004	0.159	-0.015	0.015	21.614	-0.006	0.006	0.630	-2.1E-04	1.9E-04	0.711	0.399	-0.003	0.003	21.715	-0.001	0.001	0.620	4.5E-05	-4.5E-05	0.701
3	Experiment Product	UWAI-004	0.092	-0.015	0.015	21.604	-0.006	0.006	0.644	-2.2E-04	2.4E-04	0.725	0.335	-0.003	0.003	21.706	-0.001	0.001	0.633	3.6E-05	-3.6E-05	0.714
3	Experiment Product	UWAI-005	-0.009	-0.016	0.016	21.465	-0.007	0.007	0.638	-4.4E-05	1.4E-05	0.719	0.210	-0.003	0.003	21.561	-0.001	0.001	0.680	2.9E-06	-2.9E-06	0.761
3	Experiment Product	UWAI-006	0.625	-0.010	0.010	21.564	-0.005	0.005	0.592	-6.0E-05	5.8E-05	0.673	0.648	-0.002	0.002	21.575	-0.001	0.001	0.661	1.5E-05	-1.5E-05	0.742
3	Experiment Product	UWAI-007	0.650	-0.010	0.011	21.554	-0.005	0.005	0.602	-2.4E-04	2.1E-04	0.683	0.724	-0.002	0.002	21.590	-0.001	0.001	0.614	4.5E-05	-4.5E-05	0.695
3	Experiment Product	UWAI-007	0.624	-0.011	0.011	21.585	-0.005	0.005	0.624	-2.0E-04	1.8E-04	0.705	0.698	-0.002	0.002	21.621	-0.001	0.001	0.624	3.9E-05	-3.9E-05	0.705
3	Experiment Product	UWAI-008	0.368	-0.010	0.010	21.262	-0.005	0.006	0.598	-1.7E-04	1.5E-04	0.679	0.388	-0.003	0.003	21.272	-0.001	0.001	0.589	6.0E-05	-6.0E-05	0.670
3	Experiment Product	UWAI-009	0.296	-0.012	0.012	21.499	-0.005	0.006	0.611	-1.8E-04	2.2E-04	0.692	0.425	-0.002	0.002	21.559	-0.001	0.001	0.626	3.6E-05	-3.7E-05	0.707
3	Experiment Product	UWAI-009	0.496	-0.011	0.011	21.392	-0.006	0.006	0.622	-1.6E-04	1.8E-04	0.703	0.619	-0.002	0.002	21.455	-0.001	0.001	0.613	4.4E-05	-4.5E-05	0.694
3	Experiment Product	UWAI-010	0.557	-0.013	0.013	21.635	-0.006	0.006	0.664	-1.7E-04	1.8E-04	0.745	0.819	-0.002	0.002	21.756	-0.001	0.001	0.637	3.1E-05	-3.1E-05	0.718
3	Experiment Product	UWAI-012	0.404	-0.013	0.014	21.736	-0.006	0.006	0.662	-2.3E-04	2.9E-04	0.743	0.376	-0.004	0.004	21.725	-0.002	0.002	0.600	7.8E-05	-7.9E-05	0.681
3	Experiment Product	UWAI-013	0.639	-0.016	0.017	21.782	-0.007	0.007	0.623	-3.1E-04	2.7E-04	0.704	0.719	-0.004	0.004	21.817	-0.002	0.002	0.623	6.9E-05	-6.9E-05	0.704
3	Experiment Product	UWAI-014	0.805	-0.021	0.021	20.989	-0.014	0.014	0.607	-4.2E-04	4.7E-04	0.688	0.620	-0.008	0.009	20.864	-0.006	0.006	0.580	2.3E-04	-2.3E-04	0.661
3	Experiment Product	UWAI-015	0.601	-0.028	0.029	21.728	-0.012	0.013	0.595	-6.9E-04	7.5E-04	0.676	0.738	-0.009	0.009	21.789	-0.004	0.004	0.586	2.3E-04	-2.3E-04	0.667
3	Experiment Product	UWAI-015	0.499	-0.028	0.029	21.888	-0.011	0.011	0.609	-6.2E-04	6.6E-04	0.690	0.640	-0.009	0.009	21.943	-0.003	0.004	0.598	2.0E-04	-2.1E-04	0.679
3	Experiment Product	UWAI-016	1.175	-0.020	0.020	24.000	0.004	-0.004	0.704	4.3E-05	-3.3E-05	0.785	1.430	-0.005	0.005	23.952	0.001	-0.001	0.678	8.7E-06	-8.7E-06	0.759
3	Experiment Product	UWAI-017	1.251	-0.019	0.020	22.806	-0.004	0.004	0.654	-3.0E-04	3.5E-04	0.735	1.514	-0.004	0.004	22.856	-0.001	0.001	0.633	7.6E-05	-7.7E-05	0.714
3	Experiment Product	UWAI-018	1.450	-0.015	0.015	23.824	0.002	-0.002	0.679	-1.5E-04	1.4E-04	0.760	1.651	-0.003	0.003	23.795	0.000	0.000	0.658	3.0E-05	-3.0E-05	0.739
3	Experiment Product	UWAI-018	1.491	-0.015	0.015	23.905	0.003	-0.003	0.672	-1.8E-04	1.8E-04	0.753	1.689	-0.003	0.003	23.870	0.001	-0.001	0.652	3.8E-05	-3.8E-05	0.733
3	Experiment Product	UWAI-019	1.350	-0.014	0.015	23.929	0.003	-0.003	0.654	-2.3E-04	2.3E-04	0.735	1.460	-0.004	0.004	23.910	0.001	-0.001	0.635	5.9E-05	-6.0E-05	0.716
3	Experiment Product	UWAI-020	-1.023	-0.017	0.017	19.110	-0.013	0.014	0.627	-2.0E-04	2.3E-04	0.708	-0.903	-0.004	0.004	19.206	-0.003	0.003	0.619	5.3E-05	-5.3E-05	0.700
3	Experiment Product	UWAI-020	-1.348	-0.018	0.018	19.589	-0.012	0.012	0.605	-3.3E-04	3.0E-04	0.686	-1.221	-0.004	0.004	19.674	-0.003	0.003	0.597	6.9E-05	-6.9E-05	0.678
3	Seed Crystals	UWAI-022	4.342	NA	NA	23.413	NA	NA	NA	NA	NA	0.738	4.342	NA	NA	23.413	NA	NA	NA	NA	NA	0.738
3	Seed Crystals	UWAI-022	4.396	NA	NA	23.386	NA	NA	NA	NA	NA	0.722	4.396	NA	NA	23.386	NA	NA	NA	NA	NA	0.722

Table SM3 (cont): Carbon, Oxygen, and Clumped Isotope Analyses

			Overgrowth by Isotope Dilution**										Overgrowth by Mass Balance									
	Measurement		$\delta^{13}C$	$\delta^{13}C$ Mixing	$\delta^{13}C$ Mixing	$\delta^{18}O$ mineral	$\delta^{18}O$ mineral	$\delta^{18}O$ Mixing	D_{47} Mixing	Mixing	Mixing	Acid	$\delta^{13}C$	$\delta^{13}C$ Mixing	$\delta^{13}C$ Mixing	$\delta^{18}O$ mineral	$\delta^{18}O$ mineral	$\delta^{18}O$ Mixing	D_{47} Mixing	Mixing	Mixing	Acid
Week	Type	Name	VPDB (‰)	+ 2σ	- 2σ	VSMOW (‰)	+ 2σ	- 2σ	Correction	+ 2σ	- 2σ	Corrected	VPDB (‰)	+ 2σ	- 2σ	VSMOW (‰)	+ 2σ	- 2σ	Correction	+ 2σ	- 2σ	Corrected
4	Experiment Product	UWAI-003	-0.230	-0.018	0.018	21.048	-0.009	0.009	0.655	-2.1E-04	1.7E-04	0.736	0.285	-0.002	0.002	21.311	-0.001	0.001	0.647	2.3E-05	-2.3E-05	0.728
4	Experiment Product	UWAI-006	0.708	-0.010	0.010	21.438	-0.005	0.005	0.716	1.5E-05	-5.4E-05	0.797	0.730	-0.002	0.002	21.450	-0.001	0.001	0.705	-1.4E-05	1.4E-05	0.786
4	Experiment Product	UWAI-006	0.733	-0.010	0.010	21.427	-0.005	0.005	0.664	-7.3E-05	8.1E-05	0.745	0.755	-0.002	0.002	21.439	-0.001	0.001	0.653	2.1E-05	-2.1E-05	0.734
4	Experiment Product	UWAI-017	1.510	-0.018	0.018	23.521	0.001	-0.001	0.731	1.7E-04	-1.5E-04	0.812	1.751	-0.004	0.004	23.511	0.000	0.000	0.705	-3.3E-05	3.3E-05	0.786
4	Experiment Product	UWAI-017	1.621	-0.017	0.017	23.734	0.002	-0.002	0.702	-4.2E-05	3.6E-05	0.783	1.854	-0.004	0.004	23.706	0.000	0.000	0.678	7.9E-06	-7.9E-06	0.759
4	Experiment Product	UWAI-025	1.850	-0.025	0.026	23.746	0.003	-0.003	0.723	-3.9E-04	3.5E-04	0.804	2.099	-0.008	0.008	23.712	0.001	-0.001	0.653	1.0E-04	-1.1E-04	0.734
4	Experiment Product	UWAI-026	1.760	-0.026	0.027	23.808	0.004	-0.004	0.739	-3.3E-04	3.0E-04	0.820	1.936	-0.009	0.009	23.781	0.001	-0.001	0.658	9.9E-05	-1.0E-04	0.739
4	Experiment Product	UWAI-027	1.652	-0.034	0.036	23.811	0.005	-0.005	0.770	-1.2E-03	1.4E-03	0.851	2.187	-0.009	0.010	23.731	0.001	-0.001	0.609	3.4E-04	-3.4E-04	0.690
4	Experiment Product	UWAI-028	2.025	-0.030	0.032	23.581	0.002	-0.002	0.804	-1.9E-03	2.2E-03	0.885	2.156	-0.014	0.015	23.571	0.001	-0.001	0.548	9.1E-04	-9.3E-04	0.629
4	Experiment Product	UWAI-029	1.694	-0.027	0.028	23.546	0.001	-0.001	0.732	-1.9E-03	2.0E-03	0.813	1.908	-0.009	0.009	23.535	0.000	0.000	0.510	6.4E-04	-6.5E-04	0.591
4	Experiment Product	UWAI-030	1.753	-0.030	0.031	23.486	0.001	-0.001	0.721	-2.2E-03	2.3E-03	0.802	1.855	-0.013	0.013	23.482	0.000	0.000	0.494	1.0E-03	-1.0E-03	0.575
4	Experiment Product	UWAI-031	0.574	-0.030	0.031	23.527	0.001	-0.001	0.705	-8.4E-04	8.2E-04	0.786	0.869	-0.008	0.008	23.517	0.000	0.000	0.581	2.3E-04	-2.4E-04	0.662
4	Experiment Product	UWAI-032	1.242	-0.029	0.030	23.623	0.002	-0.002	0.772	1.8E-04	-1.9E-04	0.853	1.146	-0.014	0.014	23.629	0.001	-0.001	0.704	-8.2E-05	8.3E-05	0.785
4	Experiment Product	UWAI-033	1.730	-0.011	0.011	23.451	0.000	0.000	0.712	1.6E-04	-2.1E-04	0.793	1.780	-0.003	0.003	23.450	0.000	0.000	0.735	-5.4E-05	5.5E-05	0.816
4	Experiment Product	UWAI-034	1.867	-0.011	0.011	23.589	0.001	-0.001	0.713	1.2E-04	-9.9E-05	0.794	1.882	-0.003	0.003	23.588	0.000	0.000	0.706	-2.7E-05	2.7E-05	0.787
4	Experiment Product	UWAI-035	-0.956	NA	NA	19.182	NA	NA	0.649	-7.9E-12	0.0E+00	0.730	-0.956	NA	NA	19.182	NA	NA	0.676	2.1E-04	-2.1E-04	0.757
4	Experiment Product	UWAI-036	-0.244	-0.016	0.017	19.228	-0.015	0.015	0.646	-4.0E-04	4.5E-04	0.727	-0.208	-0.004	0.004	19.260	-0.004	0.004	0.567	1.1E-04	-1.1E-04	0.648
4	Experiment Product	UWAI-037	-0.756	-0.014	0.014	19.132	-0.012	0.012	0.681	-1.9E-04	1.8E-04	0.762	-0.683	-0.003	0.003	19.193	-0.003	0.003	0.622	4.3E-05	-4.4E-05	0.703
4	Experiment Product	UWAI-038	-0.787	-0.015	0.015	19.045	-0.012	0.013	0.687	-2.4E-04	2.8E-04	0.768	-0.615	-0.003	0.003	19.190	-0.003	0.003	0.599	5.6E-05	-5.6E-05	0.680
4	Experiment Product	UWAI-039	-0.598	-0.054	0.015	19.179	-0.046	0.013	0.670	-2.5E-04	1.0E-03	0.751	-0.558	-0.004	0.004	19.212	-0.003	0.003	0.600	6.6E-05	-6.7E-05	0.681
4	Experiment Product	UWAI-040	0.060	0.096	0.019	19.237	0.092	0.019	0.672	-2.1E-04	-1.0E-03	0.753	-0.056	-0.006	0.006	19.125	-0.006	0.006	0.639	6.6E-05	-6.7E-05	0.720
4	Experiment Product	UWAI-041	-0.614	0.001	0.013	19.241	0.001	0.011	0.685	-8.0E-05	-7.5E-06	0.766	-0.628	-0.003	0.003	19.229	-0.003	0.003	0.646	3.0E-05	-3.0E-05	0.727
4	Experiment Product	UWAI-042	-0.834	-0.141	0.016	19.072	-0.117	0.013	0.717	-4.0E-04	3.6E-03	0.798	-0.707	-0.004	0.004	19.177	-0.003	0.003	0.560	9.2E-05	-9.2E-05	0.641
4	Experiment Product	UWAI-043	-0.643	-0.107	0.017	19.092	-0.092	0.015	0.644	-1.0E-04	7.8E-04	0.725	-0.552	-0.004	0.004	19.171	-0.003	0.003	0.653	2.9E-05	-2.9E-05	0.734
4	Experiment Product	UWAI-044	-0.187	-0.081	0.025	19.189	-0.075	0.023	0.694	3.0E-04	-1.0E-03	0.775	-0.129	-0.007	0.007	19.242	-0.007	0.007	0.741	-8.8E-05	8.9E-05	0.822
4	Experiment Product	UWAI-045	0.707	-0.393	0.026	21.263	-0.229	0.015	0.728	-3.5E-04	6.7E-03	0.809	1.079	-0.006	0.006	21.480	-0.003	0.003	0.627	9.8E-05	-9.9E-05	0.708
4	Experiment Product	UWAI-046	0.742	-0.069	0.021	21.393	-0.038	0.011	0.709	-3.6E-04	1.2E-03	0.790	0.791	-0.006	0.006	21.420	-0.003	0.003	0.621	1.0E-04	-1.1E-04	0.702
4	Experiment Product	UWAI-047	-0.275	-0.033	0.014	19.400	-0.028	0.012	0.682	-8.7E-05	1.9E-04	0.763	-0.256	-0.004	0.004	19.416	-0.003	0.003	0.662	2.1E-05	-2.1E-05	0.743
4	Experiment Product	UWAI-048	-1.127	-0.723	0.030	18.670	-0.621	0.025	0.691	-4.6E-04	1.6E-02	0.772	-0.425	-0.004	0.004	19.273	-0.004	0.004	0.581	1.0E-04	-1.0E-04	0.662
5	Experiment Product	UWAI-003	-0.412	-0.018	0.019	21.235	-0.008	0.009	0.572	-5.2E-04	4.9E-04	0.653	0.123	-0.003	0.003	21.477	-0.001	0.001	0.572	6.7E-05	-6.8E-05	0.653
5	Experiment Product	UWAI-023	0.368	-0.003	0.003	21.408	-0.001	0.001	0.589	-5.2E-06	5.4E-05	0.670	0.412	0.000	0.000	21.430	0.000	0.000	0.604	9.2E-06	-9.3E-06	0.685
5	Experiment Product	UWAI-023	0.156	-0.003	0.003	21.309	-0.001	0.001	0.576	-3.5E-05	6.8E-05	0.657	0.202	0.000	0.000	21.332	0.000	0.000	0.583	1.2E-05	-1.2E-05	0.664
5	Experiment Product	UWAI-024	0.483	-0.001	0.001	21.349	-0.001	0.001	0.607	-1.1E-05	2.7E-05	0.688	0.348	0.000	0.000	21.278	0.000	0.000	0.611	9.1E-06	-9.1E-06	0.692
5	Experiment Product	UWAI-024	0.457	-0.001	0.001	21.362	-0.001	0.001	0.637	-4.6E-05	1.9E-05	0.718	0.322	-0.001	0.001	21.292	0.000	0.000	0.632	6.5E-06	-6.5E-06	0.713
5	Experiment Product	UWAI-025	1.316	-0.030	0.031	23.899	0.005	-0.005	0.612	-9.1E-04	8.6E-04	0.693	1.617	-0.009	0.009	23.851	0.001	-0.002	0.608	2.6E-04	-2.6E-04	0.689
5	Experiment Product	UWAI-025	1.540	-0.028	0.029	24.158	0.007	-0.008	0.659	-4.8E-04	4.8E-04	0.740	1.819	-0.009	0.009	24.084	0.002	-0.002	0.643	1.4E-04	-1.5E-04	0.724
5	Experiment Product	UWAI-025	1.462	-0.029	0.030	24.039	0.006	-0.006	0.609	-9.5E-04	8.7E-04	0.690	1.749	-0.009	0.009	23.977	0.002	-0.002	0.608	2.6E-04	-2.6E-04	0.689
5	Experiment Product	UWAI-026	1.243	-0.031	0.032	23.854	0.004	-0.005	0.649	-1.1E-04	1.8E-04	0.730	1.453	-0.011	0.011	23.824	0.002	-0.002	0.677	3.8E-05	-3.9E-05	0.758
5	Experiment Product	UWAI-027	1.064	-0.042	0.043	24.043	0.008	-0.008	0.671	2.7E-04	-3.3E-04	0.752	1.716	-0.011	0.012	23.918	0.002	-0.002	0.710	-9.2E-05	9.3E-05	0.791
5	Experiment Product	UWAI-027	1.124	-0.041	0.043	24.150	0.009	-0.010	0.621	2.1E-04	-2.5E-04	0.702	1.764	-0.011	0.011	24.003	0.003	-0.003	0.704	-1.1E-04	1.1E-04	0.785
5	Experiment Product	UWAI-028	1.304	-0.040	0.041	23.628	0.003	-0.003	0.665	1.2E-03	-1.4E-03	0.746	1.476	-0.019	0.019	23.616	0.001	-0.001	0.777	-5.6E-04	5.7E-04	0.858
5	Experiment Product	UWAI-028	1.459	-0.038	0.039	24.041	0.008	-0.009	0.607	-2.7E-04	2.5E-04	0.688	1.622	-0.018	0.018	24.005	0.004	-0.004	0.662	8.2E-05	-8.3E-05	0.743
5	Experiment Product	UWAI-029	1.403	-0.030	0.031	23.750	0.003	-0.004	0.668	3.2E-04	-3.4E-04	0.749	1.640	-0.010	0.010	23.723	0.001	-0.001	0.718	-1.1E-04	1.1E-04	0.799
5	Experiment Product	UWAI-029	1.454	-0.029	0.030	24.045	0.006	-0.007	0.641	-6.2E-04	6.5E-04	0.722	1.687	-0.010	0.010	23.994	0.002	-0.002	0.628	2.1E-04	-2.1E-04	0.709
5	Experiment Product	UWAI-032	0.962	-0.032	0.033	24.049	0.006	-0.006	0.604	-4.1E-06	3.1E-05	0.685	0.858	-0.015	0.015	24.069	0.003	-0.003	0.675	7.8E-06	-7.9E-06	0.756
5	Experiment Product	UWAI-033	1.570	-0.011	0.011	23.661	0.001	-0.001	0.582	-7.4E-05	2.7E-05	0.663	1.623	-0.003	0.003	23.656	0.000	0.000	0.677	7.5E-06	-7.5E-06	0.758
5	Experiment Product	UWAI-033	1.578	-0.011	0.011	23.893	0.002	-0.002	0.646	-2.8E-04	2.9E-04	0.727	1.631	-0.003	0.003	23.884	0.001	-0.001	0.616	8.0E-05	-8.0E-05	0.697
5	Experiment Product	UWAI-034	1.599	-0.012	0.012	23.729	0.001	-0.001	0.616	7.0E-12	0.0E+00	0.697	1.616	-0.003	0.003	23.727	0.000	0.000	0.714	5.5E-03	-8.8E-03	0.795
5	Experiment Product	UWAI-034	1.618	-0.012	0.012	23.710	0.001	-0.001	0.648	-4.8E-13	0.0E+00	0.729	1.635	-0.003	0.003	23.708	0.000	0.000	0.640	1.5E-03	-2.9E-03	0.721
5	Experiment Product	UWAI-037	-0.978	-0.015	0.015	19.233	-0.011	0.012	0.599	-7.4E-05	9.8E-05	0.680	-0.901	-0.003	0.003	19.292	-0.003	0.003	0.662	1.9E-05	-1.9E-05	0.743
5	Experiment Product	UWAI-038	-1.013	-0.015	0.015	19.286	-0.012	0.012	0.598	-1.3E-04	5.4E-04	0.679	-0.833	-0.003	0.003	19.424	-0.002	0.002	0.642	3.6E-05	-3.6E-05	0.723
5	Experiment Product	UWAI-038	-0.905	-0.015	0.015	19.471	-0.011	0.011	0.524	-7.8E-04	2.8E-03	0.605	-0.729	-0.003	0.003	19.602	-0.002	0.002	0.444	1.8E-04	-1.8E-04	0.525
5	Experiment Product	UWAI-041	-0.801	0.001	0.014	19.427	0.001	0.011	0.539	-4.2E-05	-1.3E-05	0.620	-0.816	-0.004	0.004	19.415	-0.003	0.003	0.693	-5.2E-07	5.2E-07	0.774
5	Experiment Product	UWAI-042	-0.890	-0.143	0.016	19.414	-0.108	0.012	0.574	-2.5E-04	1.7E-03	0.655	-0.762	-0.004	0.004	19.511	-0.003	0.003	0.614	6.4E-05	-6.4E-05	0.695
5	Experiment Product	UWAI-042	-0.848	-0.141	0.016	19.481	-0.106	0.012	0.570	-5.1E-04	3.1E-03	0.651	-0.721	-0.004	0.004	19.576	-0.003	0.003	0.546	1.2E-04	-1.2E-04	0.627
5	Experiment Product	UWAI-044	-0.349	-0.084	0.026	19.545	-0.069	0.021	0.602	6.7E-05	-5.6E-04	0.683	-0.289	-0.007	0.007	19.594	-0.006	0.006	0.688	-8.2E-06	8.3E-06	0.769
5	Experiment Product	UWAI-045	0.411	-0.425	0.028	21.562	-0.197	0.013	0.462	-8.3E-04	1.7E-02	0.543	0.813	-0.006	0.006	21.749	-0.003	0.003	0.541	2.5E-04	-2.5E-04	0.622
6	Experiment Product	UWAI-030	1.332	-0.035	0.036	24.137	0.008	-0.009	0.685	-2.2E-03	2.3E-03	0.766	1.450	-0.015	0.015	24.109	0.004	-0.004	0.499	9.7E-04	-9.9E-04	0.580
6	Experiment Product	UWAI-035	-1.030	NA	NA	19.234	NA	NA	0.576	-2.5E-04	2.8E-04	0.657	-1.030	NA	NA	19.234	NA	NA	0.616	7.0E-05	-7.0E-05	0.697
6	Experiment Product	UWAI-036	-0.432	-0.017	0.017	19.446	-0.014	0.014	0.574	-3.7E-04	4.1E-04	0.655	-0.394	-0.004	0.004	19.477	-0.004	0.004	0.578	1.0E-04	-1.0E-04	0.659
6	Experiment Product	UWAI-037	-0.715	-0.014	0.014	19.722	-0.010	0.010	0.488	-2.7E-04	3.4E-04	0.569	-0.643	-0.003	0.003	19.774	-0.002	0.002	0.580	6.8E-05	-6.8E-05	0.661
6	Experiment Product	UWAI-039	-0.823	-0.057	0.016	19.330	-0.044	0.012	0.529	-2.5E-04	-1.2E-03	0.610	-0.781	-0.004	0.004	19.363	-0.003	0.003	0.636	7.4E-05	-7.5E-05	0.717
6	Experiment Product	UWAI-040	-0.078	0.099	0.020	19.575	0.085	0.017	0.557	-4.3E-05	-5.8E-06	0.638	-0.197	-0.006	0.006	19.472	-0.005	0.006	0.658	2.3E-05	-2.3E-05	0.739
6	Experiment Product	UWAI-041	-0.763	0.001	0.014	19.529	0.001	0.010	0.604	-3.4E-04	3.1E-03	0.685	-0.778	-0.004	0.004	19.518	-0.003	0.003	0.580	7.7E-05	-7.7E-05	0.661
6	Experiment Product	UWAI-042	-0.884	-0.142	0.016	19.352	-0.110	0.013	0.559	-1.7E-04	8.7E-04	0.640	-0.756	-0.004	0.004	19.450	-0.003	0.003	0.650	3.2E-05	-3.2E-05	0.731
6	Experiment Product	UWAI-043	-0.698	-0.108	0.017	19.487	-0.083	0.013	0.622	-1.8E-04	5.7E-04	0.703	-0.605	-0.004	0.004	19.558	-0.003	0.003	0.658	4.9E-05	-5.0E-05	0.739
6	Experiment Product	UWAI-044	-0.349	-0.084	0.026	19.545	-0.069	0.021	0.562	-6.4E-04	1.3E-02	0.643	-0.289	-0.007	0.007	19.594	-0.006	0.006	0.572	2.0E-04	-2.0E-04	0.653
6	Experiment Product	UWAI-046	0.519	-0.073	0.022	21.632	-0.034	0.010	0.596	-1.2E-04	2.6E-04	0.677	0.572	-0.006	0.006	21.656	-0.003	0.003	0.655	2.8E-05	-2.8E-05	0.736
6	Experiment Product	UWAI-047	-0.725	-0.036	0.016	19.529	-0.027	0.012	0.608	-1.7E-04	4.6E-03	0.689	-0.704	-0.004	0.004	19.545	-0.003	0.003	0.662	2.7E-05	-2.7E-05	0.743
6	Experiment Product	UWAI-048	-1.457	-0.766	0.031	18.954	-0.584	0.024	0.479	-4.3E-12	0.0E+00	0.560	-0.712	-0.005	0.005	19.522	-0.004	0.004	0.647	4.9E-03	-4.6E-03	0.728
6	Experiment Product	UWAI-048	-1.344	-0.751	0.031	19.138	-0.559	0.023	0.450	-2.3E-05	0.0E+00	0.531	-0.615	-0.005	0.005	19.682	-0.003	0.003	0.656	5.2E-04	-1.0E-03	0.737

Table SM3 (cont): Carbon, Oxygen, and Clumped Isotope Analyses

			Overgrowth by Isotope Dilution**										Overgrowth by Mass Balance									
Measurement			$\delta^{13}C$	$\delta^{13}C$ Mixing	$\delta^{13}C$ Mixing	$\delta^{18}O$ mineral	$\delta^{18}O$ mineral	$\delta^{18}O$ Mixing	D_{47} Mixing	Mixing	Mixing	Acid	$\delta^{13}C$	$\delta^{13}C$ Mixing	$\delta^{13}C$ Mixing	$\delta^{18}O$ mineral	$\delta^{18}O$ mineral	$\delta^{18}O$ Mixing	D_{47} Mixing	Mixing	Mixing	Acid
Week	Type	Name	VPDB (‰)	+ 2σ	- 2σ	VSMOW (‰)	+ 2σ	- 2σ	Correction	+ 2σ	- 2σ	Corrected	VPDB (‰)	+ 2σ	- 2σ	VSMOW (‰)	+ 2σ	- 2σ	Correction	+ 2σ	- 2σ	Corrected
7	Experiment Product	UWAI-026	1.181	-0.031	0.032	24.194	0.008	-0.008	0.817	-1.1E-03	1.3E-03	0.898	1.395	-0.011	0.011	24.141	0.003	-0.003	0.616	3.0E-04	-3.1E-04	0.697
7	Experiment Product	UWAI-031	0.259	-0.032	0.033	23.936	0.004	-0.004	0.764	1.7E-04	-2.3E-04	0.845	0.579	-0.009	0.009	23.895	0.001	-0.001	0.707	-9.8E-05	1.0E-04	0.788
7	Experiment Product	UWAI-031	0.063	-0.034	0.035	23.893	0.004	-0.004	0.717	-9.3E-04	1.0E-03	0.798	0.398	-0.009	0.009	23.855	0.001	-0.001	0.579	4.4E-04	-4.5E-04	0.660
7	Experiment Product	UWAI-031	0.156	-0.033	0.034	23.890	0.004	-0.004	0.717	-9.0E-04	1.0E-03	0.789	0.483	-0.009	0.009	23.852	0.001	-0.001	0.580	4.3E-04	-4.4E-04	0.661
7	Experiment Product	UWAI-032	0.640	-0.035	0.036	23.968	0.005	-0.005	0.745	-3.5E-04	4.0E-04	0.826	0.526	-0.016	0.016	23.986	0.002	-0.002	0.585	1.0E-04	-1.0E-04	0.666
7	Experiment Product	UWAI-032	0.690	-0.034	0.035	24.030	0.006	-0.006	0.848	-2.1E-04	2.3E-04	0.929	0.578	-0.016	0.016	24.049	0.003	-0.003	0.628	5.8E-05	-5.8E-05	0.709
7	Experiment Product	UWAI-035	-1.128	NA	NA	19.248	NA	NA	0.644	-6.0E-04	6.7E-04	0.725	-1.128	NA	NA	19.248	NA	NA	0.509	1.7E-04	-1.7E-04	0.590
7	Experiment Product	UWAI-035	-1.083	NA	NA	19.289	NA	NA	0.659	-2.9E-04	3.3E-04	0.740	-1.083	NA	NA	19.289	NA	NA	0.598	8.4E-05	-8.4E-05	0.679
7	Experiment Product	UWAI-036	-0.603	-0.017	0.018	19.728	-0.013	0.013	0.688	-9.4E-05	1.0E-04	0.769	-0.565	-0.005	0.005	19.756	-0.003	0.003	0.656	2.4E-05	-2.4E-05	0.737
7	Experiment Product	UWAI-036	-0.515	-0.017	0.018	19.607	-0.013	0.014	0.671	-6.8E-04	6.5E-04	0.752	-0.477	-0.005	0.005	19.637	-0.004	0.004	0.449	1.5E-04	-1.6E-04	0.530
7	Experiment Product	UWAI-039	-1.032	-0.059	0.016	19.858	-0.039	0.011	0.723	-9.1E-04	-4.2E-03	0.804	-0.989	-0.004	0.004	19.886	-0.003	0.003	0.495	2.7E-04	-2.7E-04	0.576
7	Experiment Product	UWAI-039	-0.864	-0.057	0.016	19.508	-0.042	0.012	0.685	-4.3E-04	-1.9E-03	0.766	-0.822	-0.004	0.004	19.539	-0.003	0.003	0.600	1.2E-04	-1.2E-04	0.681
7	Experiment Product	UWAI-040	-0.278	0.103	0.021	19.682	0.082	0.017	0.700	-2.2E-04	-1.8E-05	0.781	-0.402	-0.007	0.007	19.582	-0.005	0.005	0.584	7.3E-05	-7.3E-05	0.665
7	Experiment Product	UWAI-040	-0.181	0.101	0.020	19.734	0.081	0.016	0.734	-5.6E-04	-3.5E-05	0.815	-0.303	-0.007	0.007	19.636	-0.005	0.005	0.489	1.4E-04	-1.4E-04	0.570
7	Experiment Product	UWAI-043	-0.835	-0.111	0.018	19.397	-0.085	0.014	0.728	-5.6E-04	2.0E-03	0.809	-0.741	-0.004	0.004	19.469	-0.003	0.003	0.575	1.8E-04	-1.8E-04	0.656
7	Experiment Product	UWAI-043	-0.797	-0.110	0.018	19.573	-0.082	0.013	0.732	-1.1E-03	3.8E-03	0.813	-0.703	-0.004	0.004	19.643	-0.003	0.003	0.477	3.3E-04	-3.3E-04	0.558
7	Experiment Product	UWAI-045	0.374	-0.429	0.029	21.816	-0.170	0.011	0.765	-1.1E-04	2.7E-04	0.846	0.780	-0.006	0.006	21.977	-0.003	0.003	0.670	2.3E-05	-2.3E-05	0.751
8	Experiment Product	UWAI-002	-0.198	-0.012	0.012	21.469	-0.005	0.005	0.735	3.3E-05	-5.4E-05	0.816	0.065	-0.002	0.002	21.580	-0.001	0.001	0.703	-9.5E-06	9.5E-06	0.784
8	Experiment Product	UWAI-003	-0.244	-0.018	0.018	21.499	-0.007	0.008	0.748	1.5E-04	-1.1E-04	0.829	0.272	-0.002	0.002	21.711	-0.001	0.001	0.708	-1.5E-05	1.5E-05	0.789
8	Experiment Product	UWAI-011	0.328	-0.012	0.012	21.642	-0.005	0.005	0.687	-7.1E-05	9.9E-05	0.768	0.504	-0.002	0.002	21.718	-0.001	0.001	0.652	1.9E-05	-2.0E-05	0.733
8	Experiment Product	UWAI-023	0.080	-0.003	0.003	21.319	-0.001	0.001	0.700	2.6E-05	5.4E-06	0.781	0.127	0.000	0.000	21.342	0.000	0.000	0.677	9.2E-07	-9.2E-07	0.758
8	Experiment Product	UWAI-024	0.228	-0.002	0.002	21.317	-0.001	0.001	0.695	-1.4E-05	4.7E-06	0.776	0.085	-0.001	0.001	21.245	0.000	0.000	0.679	7.4E-07	-7.4E-07	0.760
8	Experiment Product	UWAI-027	1.056	-0.042	0.043	24.264	0.011	-0.011	0.822	-1.3E-03	1.5E-03	0.903	1.709	-0.011	0.012	24.095	0.003	-0.003	0.596	6.0E-04	-6.1E-04	0.677
8	Experiment Product	UWAI-029	1.392	-0.030	0.031	24.077	0.007	-0.007	0.798	-3.9E-04	3.9E-04	0.879	1.630	-0.010	0.010	24.023	0.002	-0.002	0.652	1.7E-04	-1.7E-04	0.733
8	Experiment Product	UWAI-029	1.387	-0.030	0.031	24.187	0.008	-0.008	0.709	2.6E-05	-4.0E-05	0.790	1.625	-0.010	0.010	24.125	0.003	-0.003	0.693	-2.0E-05	2.0E-05	0.774
8	Experiment Product	UWAI-033	1.559	-0.011	0.011	23.921	0.002	-0.002	0.774	-2.1E-04	2.4E-04	0.855	1.613	-0.003	0.003	23.911	0.001	-0.001	0.629	6.4E-05	-6.5E-05	0.710
8	Experiment Product	UWAI-034	1.564	-0.012	0.012	23.886	0.002	-0.002	0.746	-7.4E-12	0.0E+00	0.827	1.581	-0.003	0.003	23.883	0.001	-0.001	0.544	2.1E-03	-4.5E-03	0.625
8	Experiment Product	UWAI-037	-0.967	-0.015	0.015	19.540	-0.010	0.011	0.658	-4.6E-04	5.0E-04	0.739	-0.891	-0.003	0.003	19.595	-0.002	0.002	0.531	9.8E-05	-9.8E-05	0.612
8	Experiment Product	UWAI-038	-0.996	-0.015	0.015	19.441	-0.011	0.011	0.636	-1.3E-04	5.0E-04	0.717	-0.816	-0.003	0.003	19.573	-0.002	0.002	0.644	3.3E-05	-3.3E-05	0.725
8	Experiment Product	UWAI-041	-0.872	0.001	0.014	19.480	0.001	0.010	0.681	-4.6E-04	4.3E-03	0.762	-0.886	-0.004	0.004	19.469	-0.003	0.003	0.535	1.1E-04	-1.1E-04	0.616
8	Experiment Product	UWAI-044	-0.429	-0.086	0.026	19.884	-0.063	0.019	0.779	-1.0E-04	2.6E-03	0.860	-0.368	-0.008	0.008	19.929	-0.005	0.006	0.661	3.8E-05	-3.8E-05	0.742
8	Experiment Product	UWAI-045	0.349	-0.431	0.029	21.845	-0.167	0.011	0.679	-1.0E-03	3.7E-03	0.760	0.758	-0.006	0.006	22.003	-0.002	0.002	0.491	3.2E-04	-3.3E-04	0.572
8	Experiment Product	UWAI-046	0.353	-0.076	0.023	21.640	-0.033	0.010	0.773	-5.2E-04	1.2E-03	0.854	0.408	-0.007	0.007	21.664	-0.003	0.003	0.529	1.3E-04	-1.3E-04	0.610
8	Experiment Product	UWAI-046	0.503	-0.073	0.022	21.833	-0.030	0.009	0.672	-5.4E-04	1.2E-03	0.753	0.555	-0.006	0.006	21.854	-0.003	0.003	0.517	1.4E-04	-1.4E-04	0.598
8	Experiment Product	UWAI-047	-0.759	-0.036	0.016	19.745	-0.026	0.011	0.696	-9.7E-04	3.4E-02	0.777	-0.739	-0.004	0.004	19.760	-0.003	0.003	0.464	2.1E-04	-2.1E-04	0.545
8	Experiment Product	UWAI-048	-1.419	-0.761	0.031	19.205	-0.551	0.023	0.625	-3.0E-05	0.0E+00	0.706	-0.679	-0.005	0.005	19.740	-0.003	0.003	0.661	-6.4E-03	-1.1E-03	0.742
9	Experiment Product	UWAI-028	2.025	-0.030	0.032	23.581	0.002	-0.002	0.849	-6.9E-04	6.7E-04	0.930	2.156	-0.014	0.015	23.571	0.001	-0.001	0.626	2.2E-04	-2.2E-04	0.707
9	Experiment Product	UWAI-030	1.321	-0.035	0.036	24.142	0.008	-0.009	0.686	-2.5E-04	2.6E-04	0.796	1.439	-0.015	0.015	24.113	0.004	-0.004	0.650	7.5E-05	-7.5E-05	0.731
9	Experiment Product	UWAI-030	1.395	-0.034	0.035	24.045	0.007	-0.008	0.686	-4.4E-04	4.0E-04	0.021	1.511	-0.015	0.015	24.020	0.003	-0.003	0.632	1.2E-04	-1.2E-04	0.713

* Error values for individual values represent internal instrument error.
** Overgrowth error values represent propagated uncertainty including overgrowth amount and seed crystal standard deviation about the mean

Table SM4: Carbon, Oxygen, and Clumped Isotope Data Reprocessed with "Brand" Parameters

			Bulk Values								Overgrowth Correction by Isotope Dilution			
	Measurement		$\delta^{13}C$	$\delta^{18}O$ gas	$\delta^{18}O$ gas	$\delta^{18}O$ mineral	Δ_{47} raw	Δ_{48} raw	Δ_{49} raw	Δ_{47} ARF	$\delta^{13}C$	$\delta^{18}O$ mineral	Δ_{47} mixing	Δ_{47} acid
Week	Type	Name	VPDB (‰)	VPDB (‰)	VSMOW (‰)	VSMOW (‰)	(v. Oz)	(v. Oz)	(v. Oz)	Corrected	VPDB (‰)	VSMOW (‰)	Corrected	Corrected
1	Seed Crystals	UWAI-001	4.371	0.975	31.865	23.462	-0.036	8.504	-24.343	0.640	NA	NA	NA	0.722
1	Seed Crystals	UWAI-001	4.381	0.978	31.869	23.466	-0.026	8.931	-24.710	0.651	NA	NA	NA	0.733
1	Experiment Product	UWAI-002	0.969	-0.579	30.263	21.874	-0.105	7.715	-18.183	0.643	-0.547	29.571	0.645	0.727
1	Experiment Product	UWAI-008	1.583	-0.613	30.229	21.839	-0.115	3.316	-14.022	0.622	0.388	29.547	0.615	0.697
1	Experiment Product	UWAI-009	1.668	-0.671	30.168	21.779	-0.101	3.669	-14.474	0.637	0.404	29.396	0.637	0.719
1	Experiment Product	UWAI-010	2.041	-0.366	30.483	22.092	-0.102	3.892	-15.491	0.626	0.785	29.764	0.620	0.702
1	Experiment Product	UWAI-011	0.815	-0.372	30.476	22.085	-0.105	3.857	-13.855	0.641	-0.894	29.833	0.643	0.725
1	Experiment Product	UWAI-012	1.739	-0.413	30.434	22.043	-0.096	4.555	-16.580	0.637	0.357	29.708	0.638	0.720
1	Experiment Product	UWAI-013	2.042	-0.375	30.474	22.083	-0.101	4.177	-16.163	0.627	0.813	29.764	0.622	0.704
1	Experiment Product	UWAI-014	2.625	-0.057	30.802	22.408	-0.086	4.166	-16.938	0.629	1.510	30.152	0.625	0.707
1	Experiment Product	UWAI-015	2.434	-0.098	30.759	22.365	-0.094	3.930	-16.423	0.624	0.409	29.652	0.613	0.695
1	Experiment Product	UWAI-016	2.700	0.935	31.823	23.421	-0.058	4.964	-18.764	0.643	1.227	31.836	0.653	0.735
1	Experiment Product	UWAI-016	2.740	0.969	31.859	23.456	-0.059	5.370	-19.733	0.640	1.299	31.904	0.648	0.730
1	Experiment Product	UWAI-017	2.688	0.900	31.788	23.386	-0.067	4.829	-18.476	0.644	1.214	31.769	0.655	0.737
1	Experiment Product	UWAI-017	2.710	0.891	31.779	23.377	-0.090	4.804	-18.687	0.634	1.255	31.752	0.638	0.720
1	Experiment Product	UWAI-018	2.594	1.000	31.890	23.488	-0.045	5.399	-19.623	0.658	1.273	31.952	0.679	0.761
1	Experiment Product	UWAI-019	2.549	1.013	31.905	23.502	-0.047	5.041	-18.975	0.656	1.274	31.972	0.675	0.757
1	Experiment Product	UWAI-020	0.743	-1.982	28.817	20.439	-0.173	2.569	-11.180	0.593	-1.061	27.323	0.567	0.649
1	Experiment Product	UWAI-020	0.766	-1.891	28.911	20.532	-0.177	2.695	-11.380	0.587	-1.027	27.464	0.557	0.639
1	Experiment Product	UWAI-021	1.206	-1.733	29.074	20.694	-0.138	2.652	-11.767	0.621	-0.659	27.454	0.607	0.689
1	Experiment Product	UWAI-021	1.249	-1.626	29.183	20.803	-0.145	3.059	-12.981	0.611	-0.568	27.648	0.591	0.673
1	Seed Crystals	UWAI-022	4.324	0.927	31.815	23.413	-0.019	9.293	-25.267	0.661	NA	NA	NA	0.743
1	Seed Crystals	UWAI-022	4.339	0.753	31.636	23.235	-0.065	4.940	-20.372	0.612	NA	NA	NA	0.694
2	Seed Crystals	UWAI-001	4.363	0.977	31.868	23.465	0.034	7.944	-24.570	0.632	NA	NA	NA	0.714
2	Experiment Product	UWAI-004	1.590	-0.223	30.630	22.237	-0.062	6.684	-19.887	0.613	0.089	29.990	0.601	0.683
2	Experiment Product	UWAI-005	1.557	-0.267	30.585	22.193	-0.081	6.751	-20.196	0.595	-0.013	29.899	0.571	0.653
2	Experiment Product	UWAI-005	1.508	-0.167	30.688	22.295	-0.060	6.554	-19.007	0.616	-0.090	30.059	0.604	0.686
2	Experiment Product	UWAI-005	1.558	-0.297	30.554	22.162	-0.022	6.569	-18.856	0.657	-0.011	29.849	0.669	0.751
2	Experiment Product	UWAI-006	1.731	-0.340	30.510	22.118	-0.092	6.660	-20.806	0.581	0.558	29.929	0.556	0.638
2	Experiment Product	UWAI-006	1.774	-0.326	30.524	22.132	-0.033	6.492	-18.977	0.642	0.620	29.949	0.645	0.727
2	Experiment Product	UWAI-007	1.799	-0.299	30.552	22.160	-0.058	6.379	-20.206	0.615	0.618	29.971	0.605	0.687
2	Experiment Product	UWAI-008	1.587	-0.227	30.626	22.233	-0.059	6.752	-19.276	0.616	0.393	30.116	0.608	0.690
2	Experiment Product	UWAI-009	1.728	-0.421	30.426	22.036	-0.060	6.474	-18.858	0.616	0.492	29.776	0.607	0.689
2	Experiment Product	UWAI-010	1.891	-0.204	30.650	22.257	-0.046	6.733	-19.662	0.623	0.554	30.021	0.617	0.699
2	Experiment Product	UWAI-011	1.581	-0.390	30.458	22.067	-0.069	6.815	-18.969	0.609	0.241	29.806	0.596	0.678
2	Experiment Product	UWAI-012	1.768	-0.150	30.706	22.313	-0.069	6.920	-19.256	0.601	0.400	30.123	0.583	0.665
2	Experiment Product	UWAI-013	2.099	-0.045	30.814	22.420	-0.044	6.898	-19.876	0.618	0.899	30.285	0.609	0.691
2	Experiment Product	UWAI-014	2.595	0.106	30.970	22.574	-0.041	7.031	-22.072	0.608	1.460	30.429	0.591	0.673
2	Experiment Product	UWAI-015	2.478	0.196	31.062	22.666	-0.040	7.041	-21.746	0.609	0.499	30.274	0.584	0.666
2	Experiment Product	UWAI-016	2.672	1.058	31.951	23.548	0.026	8.026	-24.393	0.656	1.171	32.078	0.678	0.760
2	Experiment Product	UWAI-018	2.660	1.222	32.120	23.715	0.016	8.100	-23.438	0.643	1.389	32.352	0.652	0.734
2	Experiment Product	UWAI-019	2.591	1.219	32.117	23.712	0.005	8.285	-22.532	0.632	1.346	32.334	0.633	0.715
2	Experiment Product	UWAI-019	2.583	1.214	32.111	23.707	0.006	7.997	-22.677	0.634	1.333	32.325	0.637	0.719
2	Experiment Product	UWAI-020	0.923	-1.519	29.295	20.913	-0.120	4.983	-16.076	0.593	-0.791	28.039	0.568	0.650
2	Experiment Product	UWAI-021	1.421	-1.082	29.745	21.359	-0.113	5.600	-16.948	0.581	-0.296	28.537	0.546	0.628
2	Seed Crystals	UWAI-022	4.365	1.028	31.920	23.517	0.024	8.417	-24.382	0.621	NA	NA	NA	0.703
3	Seed Crystals	UWAI-001	4.361	0.817	31.703	23.301	-0.075	5.206	-21.438	0.605	NA	NA	NA	0.687
3	Experiment Product	UWAI-002	0.908	-0.657	30.183	21.794	-0.152	3.441	-14.033	0.597	-0.635	29.455	0.578	0.660
3	Experiment Product	UWAI-003	1.299	-0.478	30.367	21.977	-0.146	3.860	-15.096	0.594	-0.507	29.515	0.567	0.649
3	Experiment Product	UWAI-004	1.603	-0.245	30.607	22.215	-0.129	3.917	-15.405	0.604	0.109	29.955	0.587	0.669
3	Experiment Product	UWAI-004	1.634	-0.217	30.636	22.244	-0.121	4.912	-17.526	0.613	0.156	30.000	0.601	0.683
3	Experiment Product	UWAI-005	1.566	-0.322	30.528	22.136	-0.125	3.990	-15.785	0.611	0.001	29.809	0.597	0.679
3	Experiment Product	UWAI-006	1.801	-0.375	30.473	22.082	-0.153	3.459	-15.445	0.576	0.659	29.876	0.550	0.632
3	Experiment Product	UWAI-007	1.428	-0.075	30.783	22.389	-0.147	3.726	-15.606	0.584	0.076	30.309	0.560	0.642
3	Experiment Product	UWAI-007	1.818	-0.320	30.530	22.138	-0.132	3.514	-15.524	0.599	0.646	29.939	0.582	0.664
3	Experiment Product	UWAI-008	1.566	-0.547	30.297	21.907	-0.154	3.241	-14.708	0.582	0.364	29.645	0.559	0.641
3	Experiment Product	UWAI-009	1.687	-0.546	30.297	21.907	-0.143	3.616	-15.183	0.592	0.433	29.586	0.571	0.653
3	Experiment Product	UWAI-009	1.592	-0.350	30.500	22.108	-0.136	4.405	-16.659	0.599	0.293	29.884	0.582	0.664
3	Experiment Product	UWAI-010	2.187	-0.142	30.713	22.320	-0.101	4.040	-16.623	0.625	1.010	30.119	0.620	0.702
3	Experiment Product	UWAI-012	1.797	-0.313	30.538	22.146	-0.109	3.745	-15.892	0.626	0.444	29.866	0.621	0.703
3	Experiment Product	UWAI-013	2.039	-0.103	30.754	22.360	-0.122	4.193	-16.752	0.603	0.808	30.193	0.586	0.668
3	Experiment Product	UWAI-014	2.487	0.030	30.891	22.496	-0.124	4.361	-17.481	0.591	1.282	30.299	0.564	0.646
3	Experiment Product	UWAI-015	2.543	0.097	30.960	22.565	-0.126	4.856	-18.387	0.588	0.633	30.066	0.538	0.620
3	Experiment Product	UWAI-015	2.528	0.119	30.983	22.588	-0.120	4.553	-18.361	0.594	0.602	30.113	0.553	0.635
3	Experiment Product	UWAI-016	2.672	1.226	32.124	23.719	-0.062	5.181	-20.250	0.639	1.170	32.404	0.647	0.729
3	Experiment Product	UWAI-017	2.734	1.114	32.008	23.605	-0.037	5.001	-19.416	0.670	1.301	32.185	0.704	0.786
3	Experiment Product	UWAI-018	2.693	1.153	32.048	23.644	-0.074	4.770	-19.594	0.627	1.447	32.227	0.624	0.706
3	Experiment Product	UWAI-018	2.716	1.197	32.094	23.690	-0.076	5.182	-20.285	0.623	1.488	32.308	0.617	0.699
3	Experiment Product	UWAI-019	2.614	1.146	32.041	23.637	-0.087	4.731	-19.398	0.613	1.385	32.204	0.601	0.683
3	Experiment Product	UWAI-020	0.768	-1.883	28.919	20.540	-0.158	2.542	-11.793	0.612	-1.024	27.475	0.595	0.677
3	Experiment Product	UWAI-020	0.552	-1.571	29.241	20.859	-0.171	3.014	-12.279	0.596	-1.348	27.958	0.572	0.654
3	Seed Crystals	UWAI-022	4.324	0.927	31.815	23.413	-0.019	9.293	-25.230	0.667	NA	NA	NA	0.749
3	Seed Crystals	UWAI-022	4.379	0.900	31.788	23.386	-0.082	4.521	-20.304	0.595	NA	NA	NA	0.677

Table SM4 (cont): Carbon, Oxygen, and Clumped Isotope Data Reprocessed with "Brand" Parameters

			Bulk Values								Overgrowth Correction by Isotope Dilution			
	Measurement		$\delta^{13}C$	$\delta^{18}O$ gas	$\delta^{18}O$ gas	$\delta^{18}O$ mineral	Δ_{47} raw	Δ_{48} raw	Δ_{49} raw	Δ_{47} ARF	$\delta^{13}C$	$\delta^{18}O$ mineral	Δ_{47} mixing	Δ_{47} acid
Week	Type	Name	VPDB (‰)	VPDB (‰)	VSMOW (‰)	VSMOW (‰)	(v. Oz)	(v. Oz)	(v. Oz)	Corrected	VPDB (‰)	VSMOW (‰)	Corrected	Corrected
4	Experiment Product	UWAI-003	1.168	-0.866	29.968	21.581	-0.141	4.330	-14.606	0.603	-0.223	29.421	0.564	0.646
4	Experiment Product	UWAI-006	1.527	-0.746	30.091	21.703	-0.097	4.401	-15.256	0.645	0.711	29.816	0.632	0.714
4	Experiment Product	UWAI-006	1.543	-0.753	30.084	21.695	-0.131	4.391	-15.203	0.607	0.735	29.805	0.577	0.659
4	Experiment Product	UWAI-017	2.539	0.644	31.524	23.124	-0.069	5.585	-19.077	0.637	1.517	31.912	0.621	0.703
4	Experiment Product	UWAI-017	2.598	0.754	31.637	23.237	-0.082	5.558	-19.149	0.621	1.628	32.126	0.589	0.671
4	Experiment Product	UWAI-025	3.037	0.718	31.600	23.200	-0.086	5.430	-19.761	0.609	1.864	32.134	0.548	0.630
4	Experiment Product	UWAI-026	2.998	0.743	31.626	23.226	-0.057	5.611	-19.734	0.642	1.775	32.197	0.630	0.712
4	Experiment Product	UWAI-027	3.171	0.713	31.595	23.194	-0.075	5.487	-19.702	0.620	1.676	32.194	0.561	0.643
4	Experiment Product	UWAI-028	3.311	0.638	31.518	23.118	-0.064	5.421	-19.671	0.631	2.051	31.962	0.593	0.675
4	Experiment Product	UWAI-029	2.982	0.639	31.518	23.119	-0.084	5.522	-19.341	0.613	1.698	31.933	0.557	0.639
4	Experiment Product	UWAI-030	3.113	0.612	31.490	23.091	-0.065	5.414	-19.601	0.634	1.772	31.869	0.605	0.687
4	Experiment Product	UWAI-031	2.276	0.639	31.519	23.119	-0.050	5.560	-18.586	0.664	0.586	31.915	0.675	0.757
4	Experiment Product	UWAI-032	2.738	0.673	31.554	23.154	-0.069	5.661	-19.166	0.635	1.258	32.010	0.611	0.693
4	Experiment Product	UWAI-033	2.413	0.612	31.491	23.091	-0.087	5.520	-19.059	0.620	1.733	31.844	0.593	0.675
4	Experiment Product	UWAI-034	2.526	0.694	31.575	23.175	-0.065	5.974	-19.284	0.642	1.870	31.983	0.629	0.711
4	Experiment Product	UWAI-035	-1.266	-3.546	27.204	18.840	-0.227	1.976	-6.774	0.590	-0.956	27.545	0.578	0.660
4	Experiment Product	UWAI-036	1.078	-2.055	28.742	20.365	-0.175	3.700	-12.276	0.587	-0.203	27.619	0.538	0.620
4	Experiment Product	UWAI-037	0.530	-2.294	28.496	20.120	-0.161	3.337	-11.459	0.615	-0.678	27.552	0.585	0.667
4	Experiment Product	UWAI-038	0.538	-2.328	28.460	20.085	-0.157	3.298	-11.288	0.620	-0.610	27.549	0.592	0.674
4	Experiment Product	UWAI-039	0.711	-2.202	28.591	20.215	-0.165	3.650	-11.912	0.606	-0.553	27.572	0.569	0.651
4	Experiment Product	UWAI-040	1.450	-1.883	28.919	20.540	-0.152	3.811	-13.077	0.603	-0.049	27.482	0.556	0.638
4	Experiment Product	UWAI-041	0.601	-2.242	28.549	20.173	-0.157	3.461	-11.357	0.617	-0.623	27.589	0.588	0.670
4	Experiment Product	UWAI-042	0.572	-2.256	28.534	20.159	-0.184	3.486	-11.483	0.587	-0.702	27.536	0.543	0.625
4	Experiment Product	UWAI-043	0.773	-2.181	28.611	20.235	-0.181	3.713	-12.237	0.586	-0.546	27.529	0.539	0.621
4	Experiment Product	UWAI-044	1.484	-1.746	29.060	20.680	-0.138	4.105	-13.711	0.617	-0.122	27.599	0.577	0.659
4	Experiment Product	UWAI-045	2.227	-0.464	30.382	21.991	-0.097	5.149	-16.844	0.630	1.086	29.855	0.604	0.686
4	Experiment Product	UWAI-046	2.044	-0.508	30.336	21.946	-0.109	4.956	-16.466	0.619	0.798	29.795	0.586	0.668
4	Experiment Product	UWAI-047	0.948	-2.039	28.758	20.380	-0.153	4.014	-13.580	0.614	-0.252	27.777	0.581	0.663
4	Experiment Product	UWAI-048	0.945	-2.041	28.756	20.379	-0.148	3.896	-12.551	0.619	-0.419	27.632	0.588	0.670
5	Experiment Product	UWAI-003	1.361	0.187	31.053	22.657	-0.130	9.816	-21.732	0.578	-0.409	30.606	0.544	0.626
5	Experiment Product	UWAI-023	0.918	-0.733	30.104	21.716	-0.150	4.506	-20.872	0.574	0.314	29.805	0.563	0.645
5	Experiment Product	UWAI-023	0.738	-0.816	30.019	21.632	-0.135	4.380	-20.217	0.596	0.102	29.705	0.588	0.670
5	Experiment Product	UWAI-024	0.885	-0.850	29.984	21.597	-0.110	4.023	-18.930	0.624	0.430	29.745	0.622	0.704
5	Experiment Product	UWAI-024	3.144	1.179	32.075	23.671	-4.327	0.840	-26.217	0.609	0.233	29.611	0.605	0.687
5	Experiment Product	UWAI-025	3.085	1.123	32.018	23.614	-0.027	5.384	-24.575	0.656	1.218	32.325	0.694	0.776
5	Experiment Product	UWAI-025	3.176	1.226	32.124	23.719	-0.021	6.848	-25.070	0.659	1.442	32.587	0.702	0.784
5	Experiment Product	UWAI-025	3.085	1.123	32.018	23.614	-0.027	5.885	-24.575	0.654	1.218	32.325	0.654	0.736
5	Experiment Product	UWAI-026	3.052	1.106	32.000	23.596	-0.048	5.477	-24.470	0.632	1.147	32.279	0.634	0.716
5	Experiment Product	UWAI-027	3.244	1.131	32.026	23.622	-0.038	5.736	-26.486	0.640	0.952	32.473	0.659	0.741
5	Experiment Product	UWAI-027	3.263	1.166	32.062	23.657	-0.023	6.092	-23.986	0.656	1.010	32.582	0.710	0.792
5	Experiment Product	UWAI-028	3.347	0.997	31.888	23.485	-0.040	5.518	-25.696	0.638	1.189	32.057	0.653	0.735
5	Experiment Product	UWAI-028	3.396	1.126	32.020	23.617	-0.026	6.312	-24.221	0.651	1.343	32.472	0.696	0.778
5	Experiment Product	UWAI-029	3.130	1.063	31.956	23.553	-0.040	5.591	-24.796	0.640	1.305	32.175	0.654	0.736
5	Experiment Product	UWAI-029	3.144	1.179	32.075	23.671	-0.012	7.766	-26.217	0.670	1.342	32.471	0.730	0.812
5	Experiment Product	UWAI-032	2.885	1.194	32.090	23.686	-0.038	6.036	-26.734	0.645	0.871	32.476	0.664	0.746
5	Experiment Product	UWAI-033	2.578	1.084	31.977	23.574	-0.066	6.193	-26.913	0.618	1.500	32.079	0.611	0.693
5	Experiment Product	UWAI-033	2.584	1.225	32.123	23.718	-0.025	6.517	-24.079	0.663	1.509	32.314	0.683	0.765
5	Experiment Product	UWAI-034	2.627	1.122	32.017	23.613	-0.044	6.082	-26.894	0.643	1.529	32.148	0.650	0.732
5	Experiment Product	UWAI-034	2.651	1.135	32.030	23.626	-0.062	6.788	-27.121	0.621	1.568	32.171	0.615	0.697
5	Experiment Product	UWAI-037	0.642	-1.881	28.921	20.542	-0.150	3.216	-16.448	0.596	-0.961	27.674	0.575	0.657
5	Experiment Product	UWAI-038	0.648	-1.822	28.982	20.602	-0.151	3.372	-16.069	0.595	-0.893	27.806	0.574	0.656
5	Experiment Product	UWAI-038	0.722	-1.699	29.109	20.729	-0.170	3.985	-18.949	0.570	-0.788	27.986	0.539	0.621
5	Experiment Product	UWAI-041	0.762	-1.702	29.105	20.725	-0.157	3.763	-16.993	0.584	-0.838	27.901	0.557	0.639
5	Experiment Product	UWAI-042	0.799	-1.688	29.120	20.740	-0.162	3.429	-16.600	0.577	-0.823	27.894	0.547	0.629
5	Experiment Product	UWAI-042	0.827	-1.644	29.165	20.785	-0.166	4.470	-19.295	0.573	-0.782	27.960	0.540	0.622
5	Experiment Product	UWAI-044	1.626	-1.230	29.592	21.208	-0.121	3.835	-18.605	0.606	-0.416	27.933	0.579	0.661
5	Experiment Product	UWAI-045	2.344	0.027	30.887	22.493	-0.095	4.860	-22.704	0.604	0.739	30.152	0.580	0.662
6	Experiment Product	UWAI-030	3.232	1.132	32.027	23.623	-0.056	6.536	-24.990	0.646	1.241	32.413	0.674	0.756
6	Experiment Product	UWAI-035	-1.076	-3.151	27.612	19.244	-0.202	2.507	-13.991	0.615	-1.076	27.612	0.615	0.697
6	Experiment Product	UWAI-036	1.222	-1.573	29.239	20.858	-0.123	3.803	-18.936	0.647	-0.459	27.861	0.649	0.731
6	Experiment Product	UWAI-037	0.823	-1.552	29.260	20.878	-0.190	4.685	-20.532	0.566	-0.702	28.159	0.532	0.614
6	Experiment Product	UWAI-039	0.825	-1.757	29.048	20.669	-0.192	3.859	-18.905	0.567	-0.842	27.745	0.531	0.613
6	Experiment Product	UWAI-040	1.632	-1.338	29.480	21.097	-0.119	4.471	-21.568	0.640	-0.267	27.857	0.639	0.721
6	Experiment Product	UWAI-041	0.737	-1.771	29.034	20.654	-0.144	3.295	-16.832	0.632	-0.876	27.798	0.626	0.708
6	Experiment Product	UWAI-042	0.827	-1.644	29.165	20.785	-0.191	3.983	-19.295	0.566	-0.782	27.960	0.530	0.612
6	Experiment Product	UWAI-043	1.002	-1.584	29.227	20.846	-0.174	4.047	-18.683	0.583	-0.668	27.942	0.553	0.635
6	Experiment Product	UWAI-044	1.626	-1.230	29.592	21.208	-0.174	4.583	-18.605	0.616	-0.416	27.933	0.597	0.679
6	Experiment Product	UWAI-046	2.186	-0.034	30.825	22.430	-0.102	5.270	-23.934	0.627	0.498	30.059	0.621	0.703
6	Experiment Product	UWAI-047	0.912	-1.610	29.200	20.819	-0.166	3.515	-17.700	0.597	-0.766	27.929	0.574	0.656
6	Experiment Product	UWAI-048	1.023	-1.539	29.274	20.892	-0.137	3.839	-19.331	0.631	-0.776	27.905	0.625	0.707
6	Experiment Product	UWAI-048	1.087	-1.436	29.379	20.997	-0.154	3.865	-19.560	0.607	-0.678	28.067	0.587	0.669

Table SM4 (cont): Carbon, Oxygen, and Clumped Isotope Data Reprocessed with "Brand" Parameters

			Bulk Values								Overgrowth Correction by Isotope Dilution			
Week	Measurement Type	Name	$\delta^{13}C$ VPDB (‰)	$\delta^{18}O$ gas VPDB (‰)	$\delta^{18}O$ gas VSMOW (‰)	$\delta^{18}O$ mineral VSMOW (‰)	Δ_{47} raw (v. Oz)	Δ_{48} raw (v. Oz)	Δ_{49} raw (v. Oz)	Δ_{47} ARF Corrected	$\delta^{13}C$ VPDB (‰)	$\delta^{18}O$ mineral VSMOW (‰)	Δ_{47} mixing Corrected	Δ_{47} acid Corrected
7	Experiment Product	UWAI-026	3.078	1.153	32.048	23.644	-0.015	6.827	-20.617	0.642	1.185	32.598	0.659	0.741
7	Experiment Product	UWAI-031	2.443	1.084	31.977	23.573	-0.030	6.887	-19.881	0.640	0.260	32.339	0.650	0.732
7	Experiment Product	UWAI-031	2.351	1.064	31.956	23.553	-0.032	7.052	-19.626	0.639	0.064	32.296	0.650	0.732
7	Experiment Product	UWAI-031	2.395	1.062	31.955	23.551	-0.025	6.552	-19.583	0.646	0.157	32.292	0.664	0.746
7	Experiment Product	UWAI-032	2.799	1.072	31.965	23.562	-0.014	6.750	-20.228	0.650	0.645	32.370	0.678	0.760
7	Experiment Product	UWAI-032	2.820	1.098	31.991	23.588	-0.025	7.110	-20.292	0.637	0.695	32.433	0.646	0.728
7	Experiment Product	UWAI-035	-1.123	-3.224	27.536	19.169	-0.242	2.599	-7.432	0.559	-1.133	27.617	0.559	0.641
7	Experiment Product	UWAI-035	-1.079	-3.186	27.576	19.208	-0.226	2.780	-7.744	0.575	-1.089	27.656	0.575	0.657
7	Experiment Product	UWAI-036	1.161	-1.483	29.332	20.950	-0.145	4.336	-13.425	0.587	-0.567	28.127	0.558	0.640
7	Experiment Product	UWAI-036	1.219	-1.559	29.252	20.871	-0.156	4.156	-13.233	0.575	-0.479	28.005	0.539	0.621
7	Experiment Product	UWAI-039	0.734	-1.497	29.316	20.934	-0.164	4.164	-13.108	0.574	-0.991	28.258	0.541	0.623
7	Experiment Product	UWAI-039	0.848	-1.728	29.078	20.698	-0.155	4.033	-12.559	0.587	-0.824	27.908	0.560	0.642
7	Experiment Product	UWAI-040	1.561	-1.363	29.455	21.072	-0.132	4.362	-14.163	0.592	-0.404	27.951	0.557	0.639
7	Experiment Product	UWAI-040	1.619	-1.332	29.487	21.104	-0.112	4.419	-14.174	0.613	-0.305	28.006	0.593	0.675
7	Experiment Product	UWAI-043	0.962	-1.730	29.077	20.697	-0.126	3.987	-12.692	0.618	-0.743	27.838	0.605	0.687
7	Experiment Product	UWAI-043	0.987	-1.616	29.194	20.813	-0.123	4.291	-12.913	0.618	-0.706	28.013	0.606	0.688
7	Experiment Product	UWAI-045	2.376	0.063	30.925	22.530	-0.066	5.795	-17.753	0.620	0.778	30.365	0.610	0.692
8	Experiment Product	UWAI-002	1.208	-0.389	30.459	22.068	-0.097	5.154	-15.653	0.636	-0.201	29.854	0.635	0.717
8	Experiment Product	UWAI-003	1.463	-0.254	30.598	22.206	-0.088	5.284	-16.079	0.639	-0.246	29.883	0.641	0.723
8	Experiment Product	UWAI-011	1.637	-0.245	30.607	22.215	-0.121	5.437	-16.243	0.601	0.324	30.027	0.584	0.666
8	Experiment Product	UWAI-023	0.714	-0.816	30.018	21.631	-0.128	4.599	-14.294	0.618	0.075	29.704	0.614	0.696
8	Experiment Product	UWAI-024	0.681	-0.877	29.956	21.569	-0.134	4.686	-14.075	0.613	0.200	29.713	0.610	0.692
8	Experiment Product	UWAI-027	3.281	1.192	32.089	23.685	-0.043	6.899	-20.673	0.632	1.065	32.666	0.635	0.717
8	Experiment Product	UWAI-029	3.165	1.182	32.079	23.674	-0.041	6.812	-20.609	0.636	1.394	32.480	0.644	0.726
8	Experiment Product	UWAI-029	3.163	1.226	32.123	23.719	-0.076	6.863	-20.664	0.599	1.389	32.591	0.552	0.634
8	Experiment Product	UWAI-033	2.612	1.233	32.131	23.726	-0.034	6.622	-20.099	0.652	1.555	32.326	0.666	0.748
8	Experiment Product	UWAI-034	2.646	1.207	32.104	23.699	-0.051	6.856	-20.150	0.633	1.559	32.291	0.635	0.717
8	Experiment Product	UWAI-037	0.690	-1.684	29.124	20.744	-0.175	3.902	-12.281	0.583	-0.893	27.965	0.556	0.638
8	Experiment Product	UWAI-038	0.701	-1.728	29.078	20.698	-0.189	4.045	-12.203	0.568	-0.818	27.943	0.536	0.618
8	Experiment Product	UWAI-041	0.727	-1.744	29.062	20.682	-0.160	3.896	-12.046	0.600	-0.889	27.838	0.579	0.661
8	Experiment Product	UWAI-044	1.653	-1.027	29.801	21.416	-0.154	4.521	-14.787	0.577	-0.369	28.300	0.529	0.611
8	Experiment Product	UWAI-045	2.353	0.155	31.020	22.624	-0.111	5.856	-17.684	0.593	0.755	30.391	0.560	0.642
8	Experiment Product	UWAI-046	2.134	-0.040	30.819	22.425	-0.068	5.647	-17.073	0.646	0.406	30.049	0.654	0.736
8	Experiment Product	UWAI-046	2.217	0.065	30.927	22.532	-0.118	5.901	-17.410	0.589	0.553	30.241	0.554	0.636
8	Experiment Product	UWAI-047	0.929	-1.479	29.336	20.954	-0.144	4.148	-13.095	0.609	-0.740	28.130	0.592	0.674
8	Experiment Product	UWAI-048	1.085	-1.409	29.407	21.025	-0.184	4.083	-13.368	0.562	-0.681	28.111	0.518	0.600
9	Experiment Product	UWAI-028	3.145	1.143	32.038	23.634	-0.039	6.803	-20.360	0.618	0.555	32.527	0.590	0.672
9	Experiment Product	UWAI-030	3.262	1.178	32.075	23.670	-0.036	6.775	-20.708	0.619	1.325	32.545	0.598	0.680
9	Experiment Product	UWAI-030	3.289	1.144	32.039	23.635	-0.034	6.680	-20.740	0.620	1.400	32.446	0.603	0.685

Supporting Figures Section

Figures SM3-SM4 and SM5-SM6 are equivalent to Figures 2 and 5 in the main text, respectively, but at different temperatures.

Figure SM1 - Scanning electron microscopy imagery of calcite seed crystals. Main Figure: A 3.8 mm by 1.76 mm mosaic image of calcite seed crystals deposited on an adhesive surface. The scale bar at the bottom of the image is 100 μm. Inset: Typical grain size and crystal habit.

Figure SM2 - X-ray diffraction patterns for experimental products and calcite seed crystals. These analyses confirm calcite was the sole mineral product.

Figure SM3 - Reproduction of the semi-empirical ion-by-ion growth model of Watkins and Hunt (2015) for calcite growth under kinetic and (assumed) C equilibrium conditions. The model is based on a "kinetic" regime from the experiments of Romanek et al. (1992, shown by green triangle symbols for 10°C) and inferred equilibrium from Coplen (2007). The orange dashed line is modeled fractionation for 10°C, pH = 6.6, and a surface HCO_3^-:CO_3^{2-} ratio (Θ) of 100. The purple dotted line is modeled fractionation for 10°C, pH = 6.6, and a surface HCO_3^-:CO_3^{2-} ratio (Θ) of 0.25. Also included are values found during this study at 10°C for partitioning between calcite and aqueous carbonate (red squares).

Figure SM4 - As in Figure S3 but for 30°C modeled values and 25°C values for Romanek et al. (1992).

Figure SM5 - Reproduction of the semi-empirical ion-by-ion growth model of Watkins and Hunt (2015) for calcite growth under kinetic and (assumed) O equilibrium conditions. The model is based on a "kinetic" regime from the experiments of Watkins et al. (2014) and inferred equilibrium from Bottinga (1968) and Coplen (2007). The orange dashed line is modeled fractionation for 10°C, pH = 6.6, and a surface HCO_3^-:CO_3^{2-} ratio (Θ) of 100. The purple dotted line is modeled fractionation for 10°C, pH = 6.6, and a surface HCO_3^-:CO_3^{2-} ratio (Θ) of 0.25. Also included are red squares values found during this study at 10°C for partitioning between calcite and aqueous carbonate (red squares). Finally, the adjusted experimental values (T = 10°C, pH = 8.3 to 9.0) of Dietzel et al. (2009) are indicated by yellow diamonds.

Figure SM6 - As in Figure S5 but for 30°C modeled values. Green circle symbols indicate experimental values of Watkins et al. (2014). The green double line represents modeled values at 25°C, pH = 8.3, and a surface HCO_3^-:CO_3^{2-} ratio (Θ) of 2.

Figure SM7 - Reproduction of the semi-empirical ion-by-ion growth model of Watkins and Hunt (2015) for calcite growth under kinetic and (assumed) clumped equilibrium conditions. The model is based on a "kinetic" regime from the work of Hill et al. (2014), inferred equilibrium from Kluge et al. (2014), and adjusted to account for the difference in calcite Δ_{47} between Hill et al. (2014) and Zaarur et al. (2013). The orange dashed line is modeled clumping for 10°C, pH = 6.6, and a surface HCO_3^-:CO_3^{2-} ratio (Θ) of 100. The purple dotted line is modeled clumping for 10°C, pH = 6.6, and a surface HCO_3^-:CO_3^{2-} ratio (Θ) of 0.25. Also included are values found during this study at 10°C (red squares). Finally, the work of Tang et al. (2014) is represented by peach-colored

diamonds. These values are associated with experimental temperatures of 5°C (pH = 8.3 to 9.0), but have been adjusted to 10°C in the figure according to the Δ_{47}-T relation reported by Tang et al. (2014).

Figure SM8 - As in Figure S7 but for 20°C.

Figure SM9 - As in Figure S7 but for 30°C.

Figure SM10 - Experimental Δ_{47} plotted against O isotope fractionation between overgrowth calcite and water. Per Tripati et al. (2015), a correlation between these two values (at a given temperature) can indicate disequilibrium due to kinetic effects.

Figure SM11 - Comparison of four studies and experimental O isotope fractionation between calcite and water as a function of solution saturation state with respect to calcite. All experimental values represent average experiment conditions and have been adjusted to represent $10^3 \ln(\alpha_{calcite\text{-}H2O})$ at 10°C (See Supporting Information for adjustment description). Error bars for data points from this study represent maximum and minimum saturation based on measured solution conditions. Error bars for the data points of Kelson et al. (2017) and Dennis and Schrag (2010) represent maximum saturation based on reported solution conditions or saturation states. In cases where both starting and ending solution conditions were not reported, an assumed minimum (end of experiment) saturation state of $\Omega = 1$ was assumed. The saturation states of Dietzel et al. (2009) were used as reported in Tang et al. (2008). The vertical dotted line represents saturation

(equilibrium, $\Omega = 1$). The temperatures indicated on the second vertical axis are based on the work of Zaarur et al. (2013).

Figure SM12 - As in Figure S11 but for 20°C.

Figure SM13 - As in Figure S11 but for 30°C.

Figure SM14 - Clumped isotope composition of experimental calcite as a function of temperature. Blue circles indicate values determined by "Santrock" ^{17}O correction parameters and red squares indicate values re-processed with "Brand" ^{17}O correction values according to Daeron et al. (2016). Error envelopes represent error weighted 95% confidence intervals.

Figure SM1

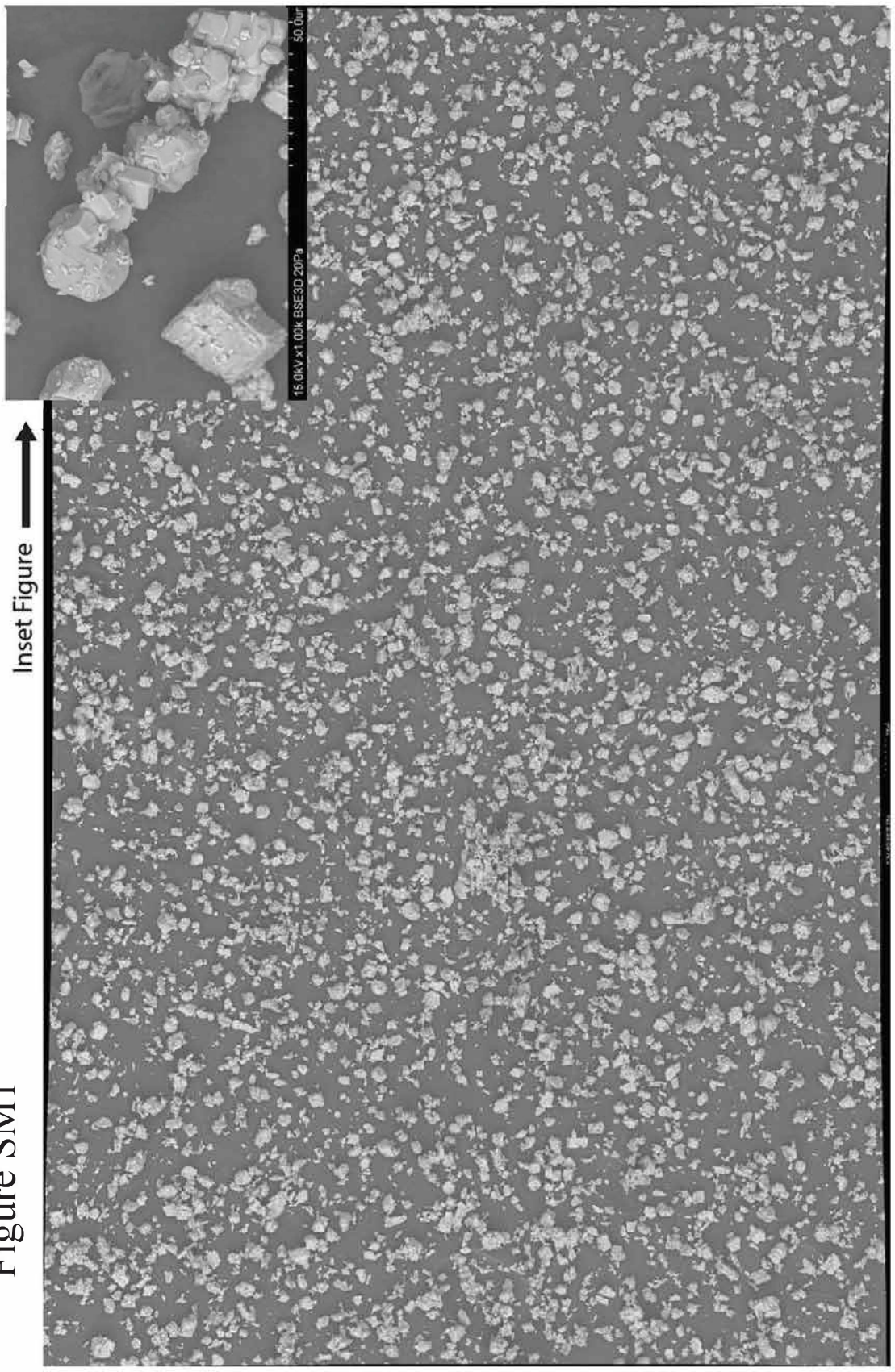
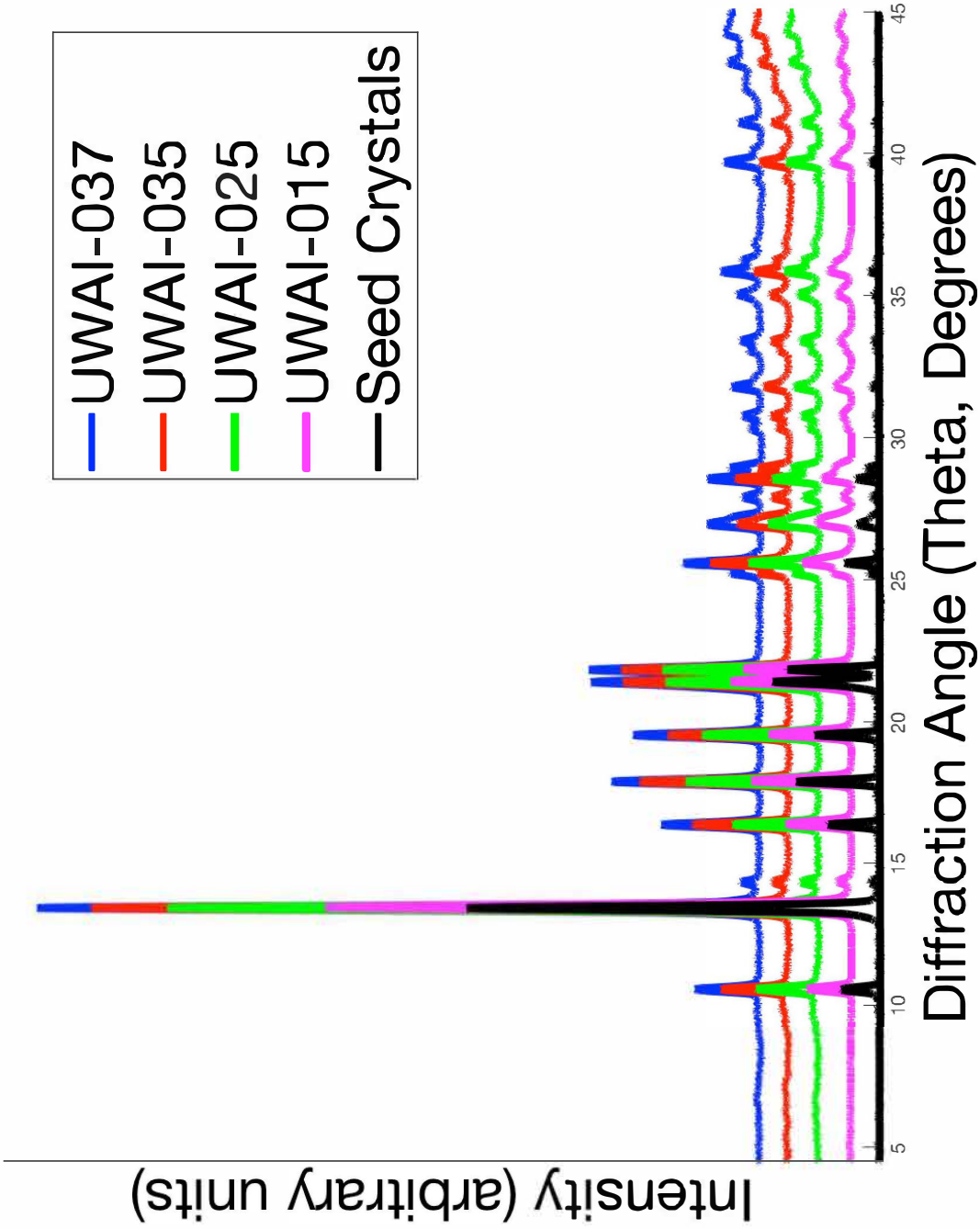
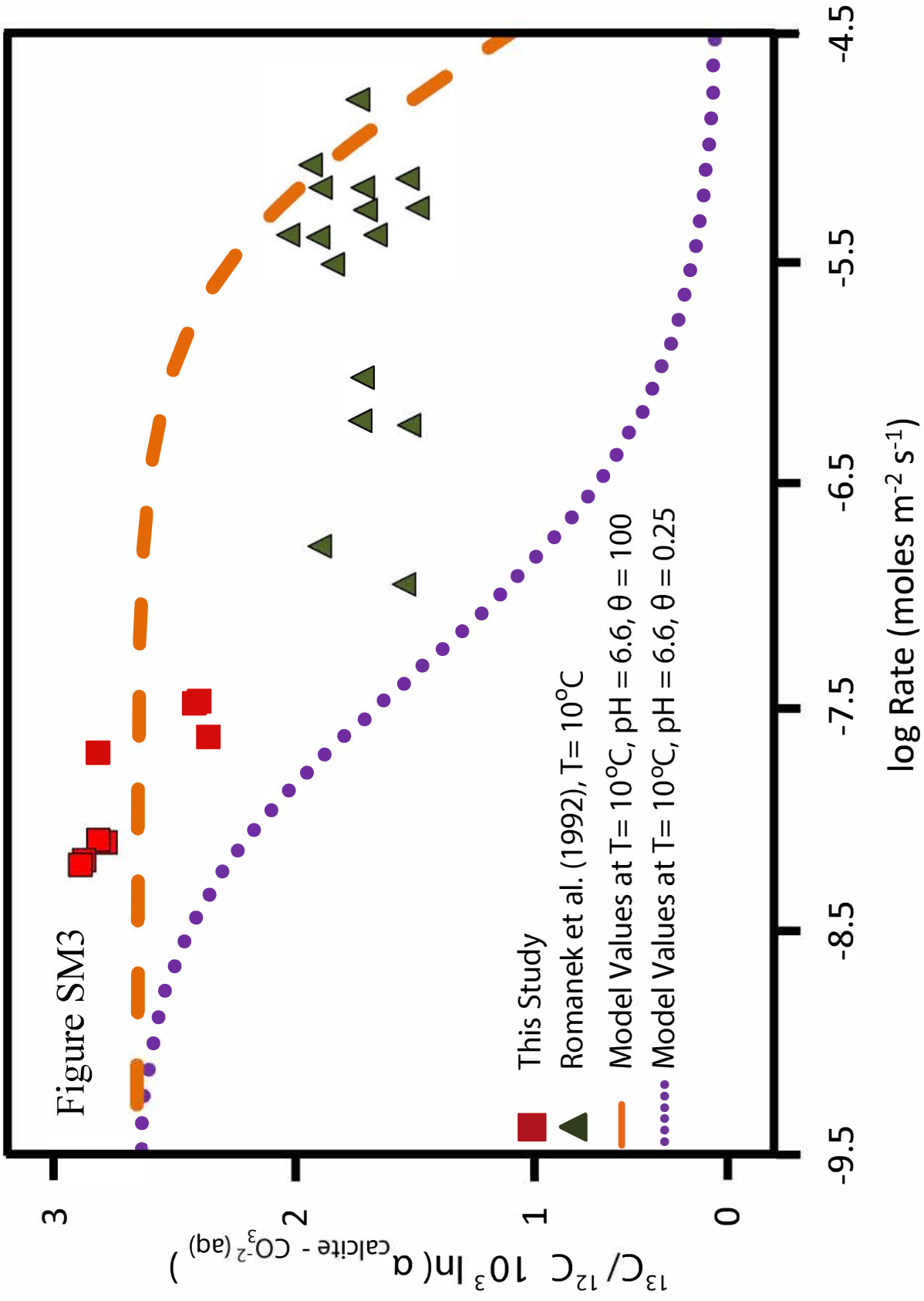
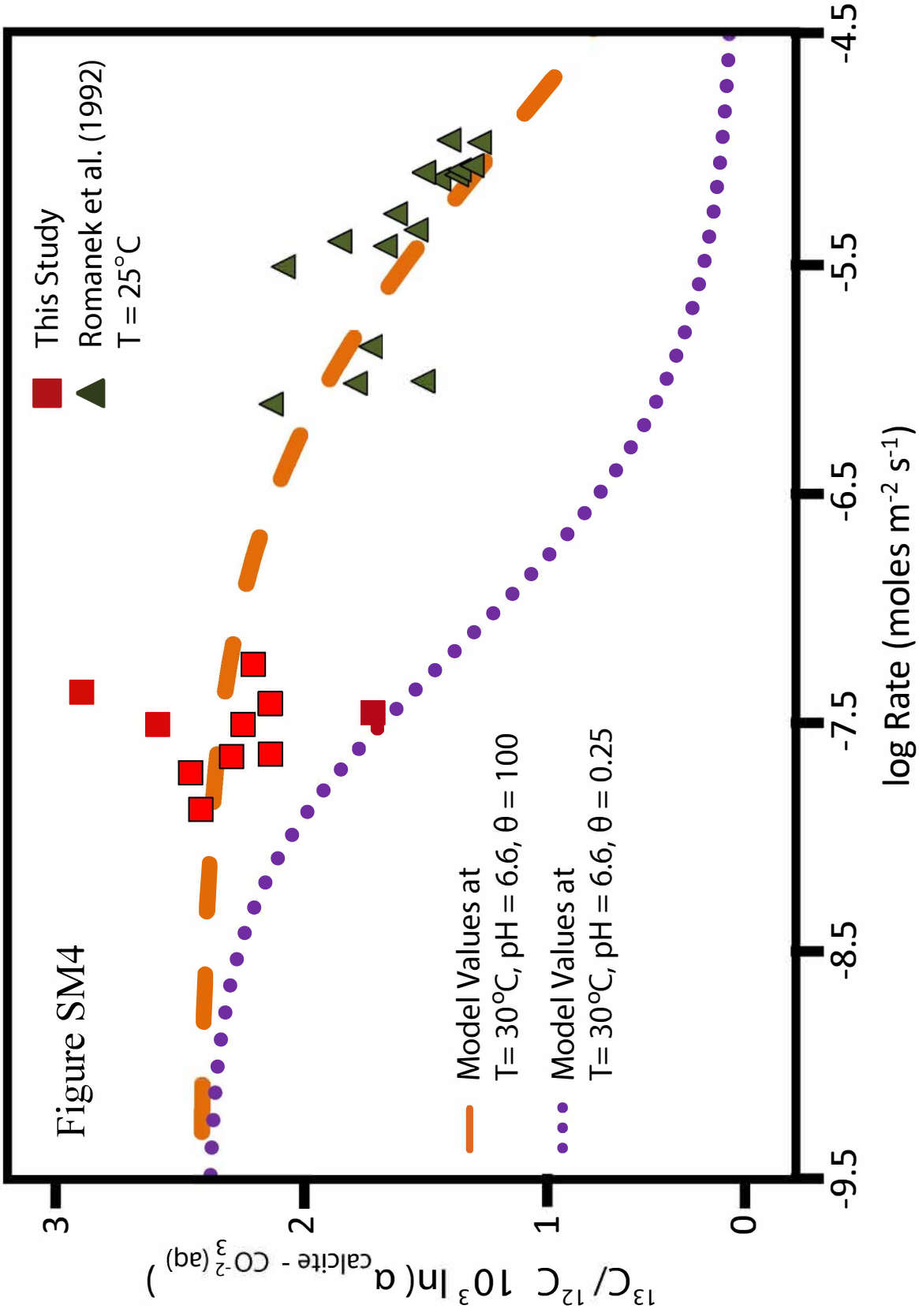
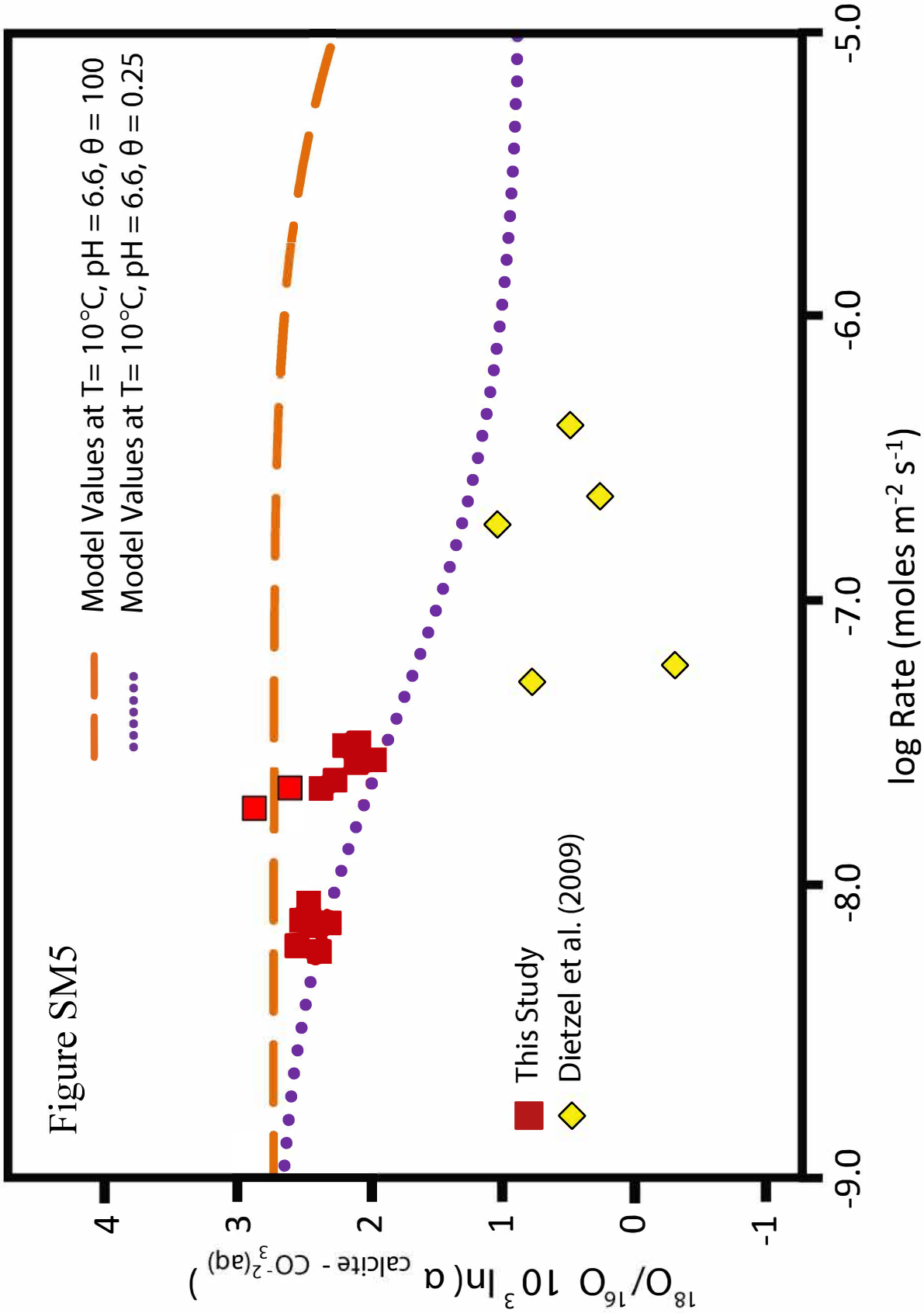


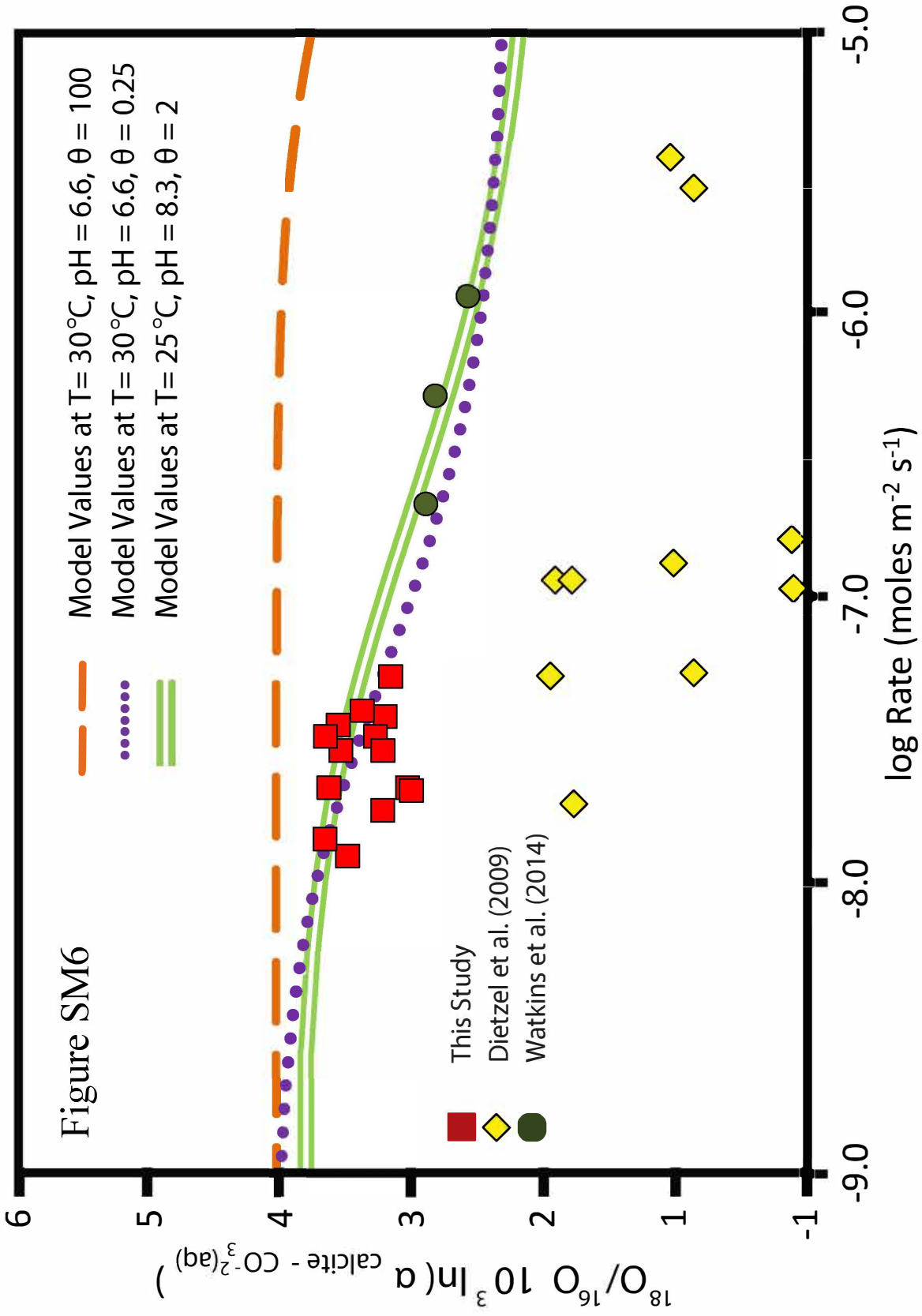
Figure SM2 Seed & Product Diffraction Patterns




Figure SM3
This Study
Romanek et al. (1992), T= 10°C
Model Values at T= 10°C, pH = 6.6, θ = 100
Model Values at T= 10°C, pH = 6.6, θ = 0.25
log Rate (moles m-2 s-1)
-9.5
-8.5
-7.5
-6.5
-5.5
-4.5
0
1
2
3
13C/ 12C 10³ ln(α calcite - CO3-2 (aq))


Figure SM4
This Study
Romanek et al. (1992)
T = 25°C
Model Values at
T= 30°C, pH = 6.6, θ = 100
Model Values at
T= 30°C, pH = 6.6, θ = 0.25
3
2
1
0
-9.5
-8.5
-7.5
-6.5
-5.5
-4.5
log Rate (moles m-2 s-1)
13C/ 12C 10³ ln(α calcite - CO-2 3 (aq))


Figure SM5
Model Values at T= 10°C, pH = 6.6, θ = 100
Model Values at T= 10°C, pH = 6.6, θ = 0.25
This Study
Dietzel et al. (2009)
log Rate (moles m-2 s-1)
-9.0
-8.0
-7.0
-6.0
-5.0
-1
0
1
2
3
4
18O/16O 10 3 ln(α calcite - CO-2 3(aq))


Figure SM6
Model Values at T= 30 °C, pH = 6.6, θ = 100
Model Values at T= 30 °C, pH = 6.6, θ = 0.25
Model Values at T= 25 °C, pH = 8.3, θ = 2
This Study
Dietzel et al. (2009)
Watkins et al. (2014)
log Rate (moles m-2 s-1)
-9.0
-8.0
-7.0
-6.0
-5.0
-1
1
2
3
4
5
6
18O/16O 10 3 ln(α calcite - CO-2 3(aq))

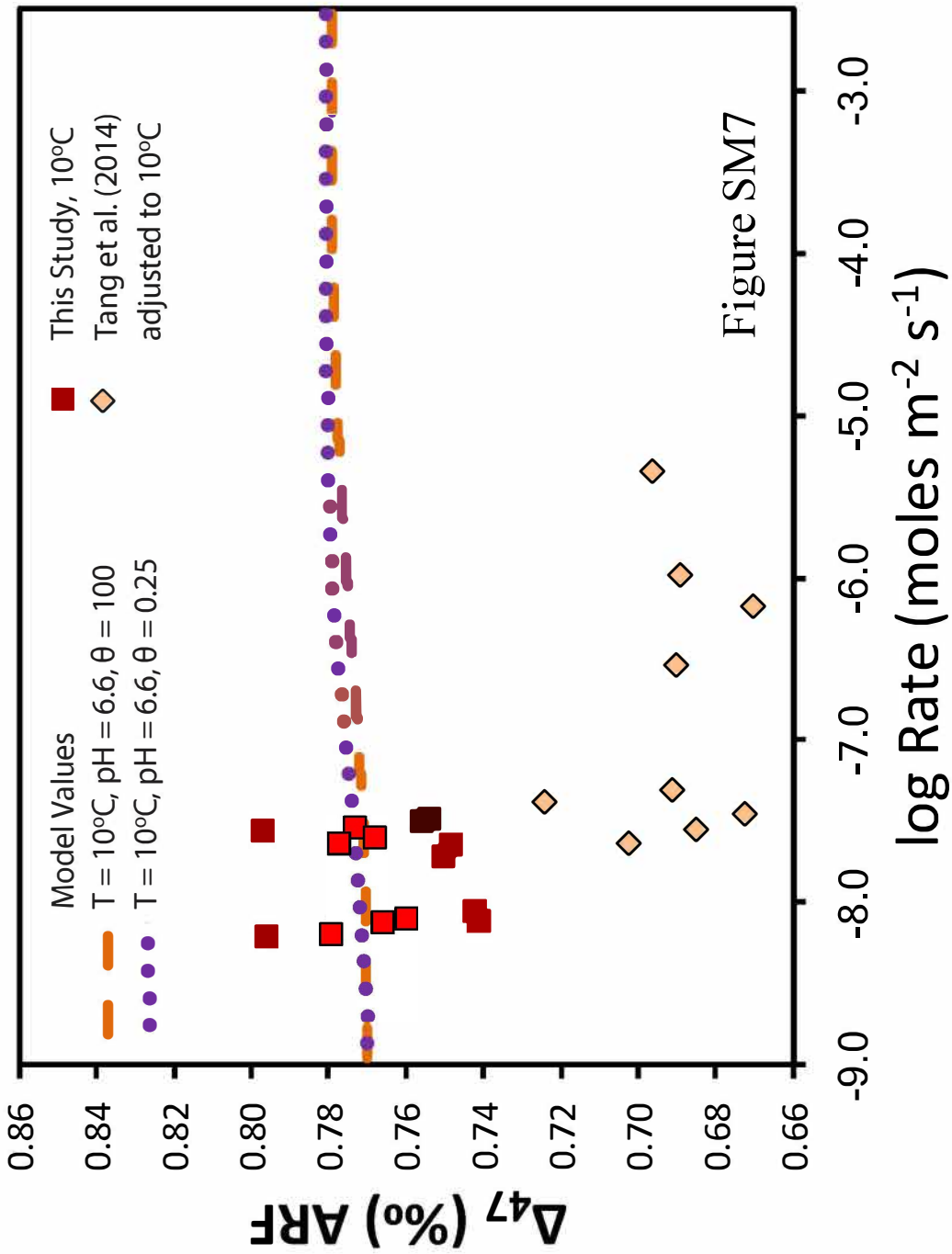
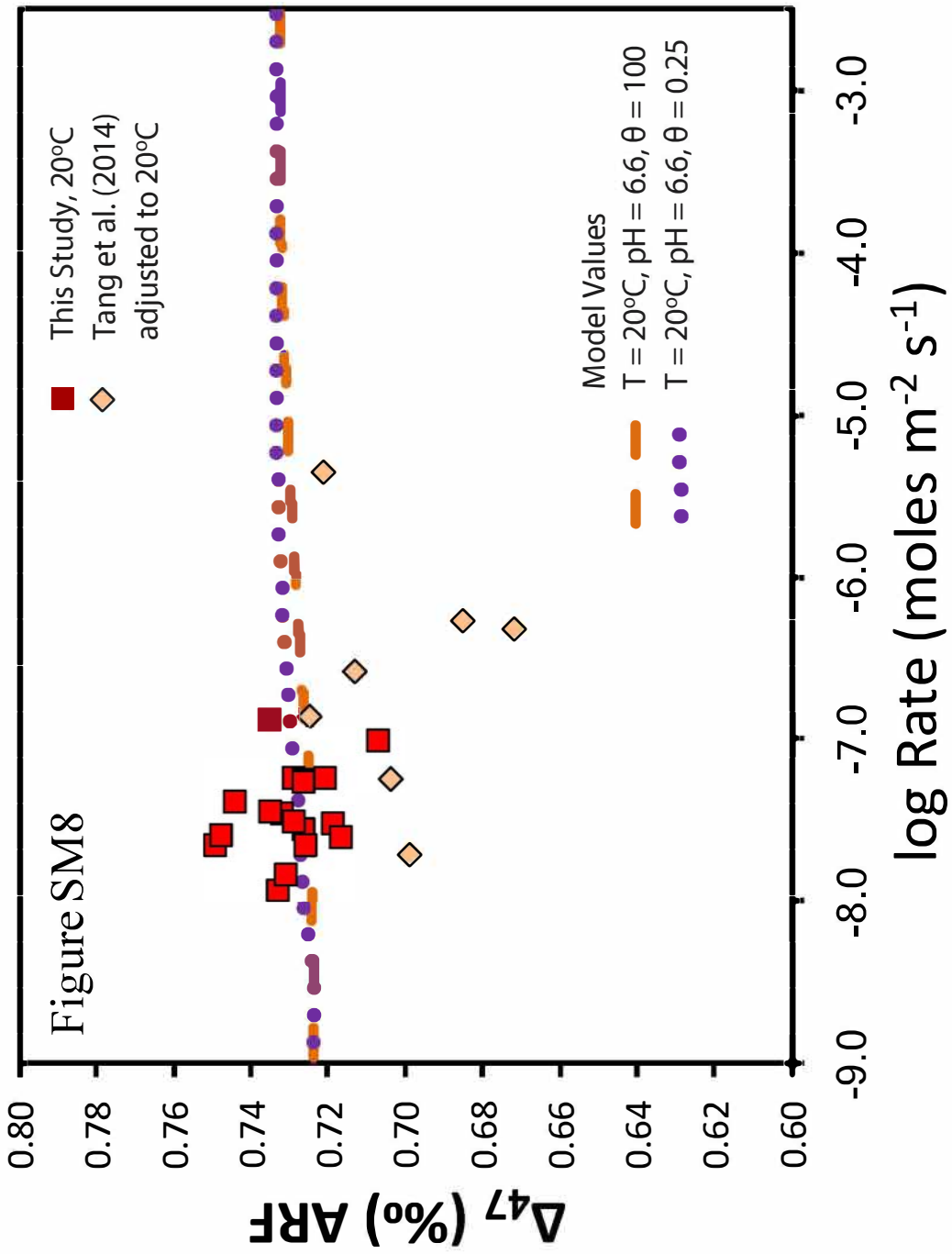
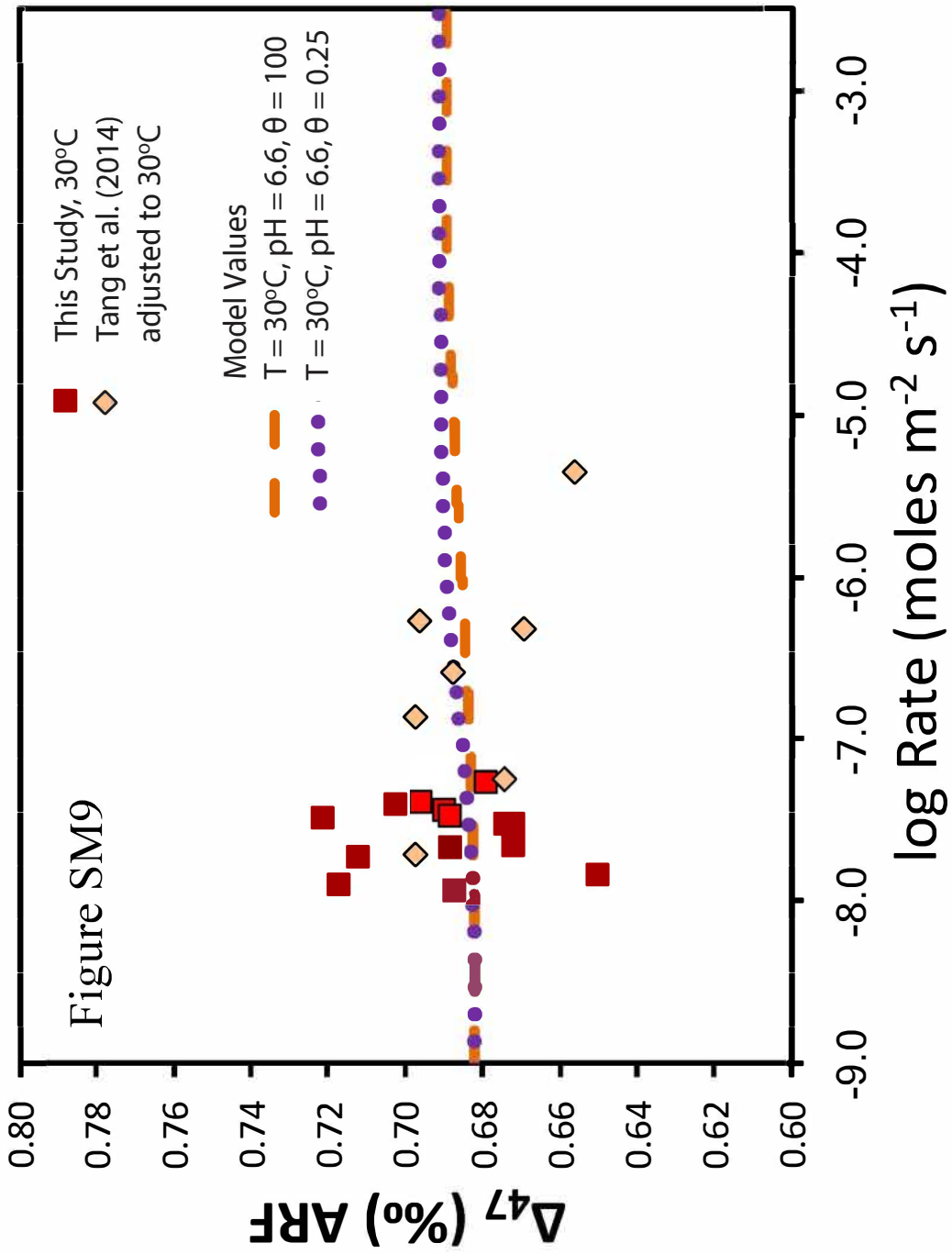

Model Values
T = 10°C, pH = 6.6, θ = 100
T = 10°C, pH = 6.6, θ = 0.25
This Study, 10°C
Tang et al. (2014) adjusted to 10°C
Δ47 (‰) ARF
log Rate (moles m-2 s-1)
0.86
0.84
0.82
0.80
0.78
0.76
0.74
0.72
0.70
0.68
0.66
-9.0
-8.0
-7.0
-6.0
-5.0
-4.0
-3.0

Figure SM7


Figure SM8
This Study, 20°C
Tang et al. (2014) adjusted to 20°C
Model Values
T = 20°C, pH = 6.6, θ = 100
T = 20°C, pH = 6.6, θ = 0.25
Δ47 (‰) ARF
log Rate (moles m-2 s-1)
0.80
0.78
0.76
0.74
0.72
0.70
0.68
0.66
0.64
0.62
0.60
-9.0
-8.0
-7.0
-6.0
-5.0
-4.0
-3.0


Figure SM9
This Study, 30°C
Tang et al. (2014) adjusted to 30°C
Model Values
T = 30°C, pH = 6.6, θ = 100
T = 30°C, pH = 6.6, θ = 0.25
Δ47 (‰) ARF
log Rate (moles m-2 s-1)
0.80
0.78
0.76
0.74
0.72
0.70
0.68
0.66
0.64
0.62
0.60
-9.0
-8.0
-7.0
-6.0
-5.0
-4.0
-3.0

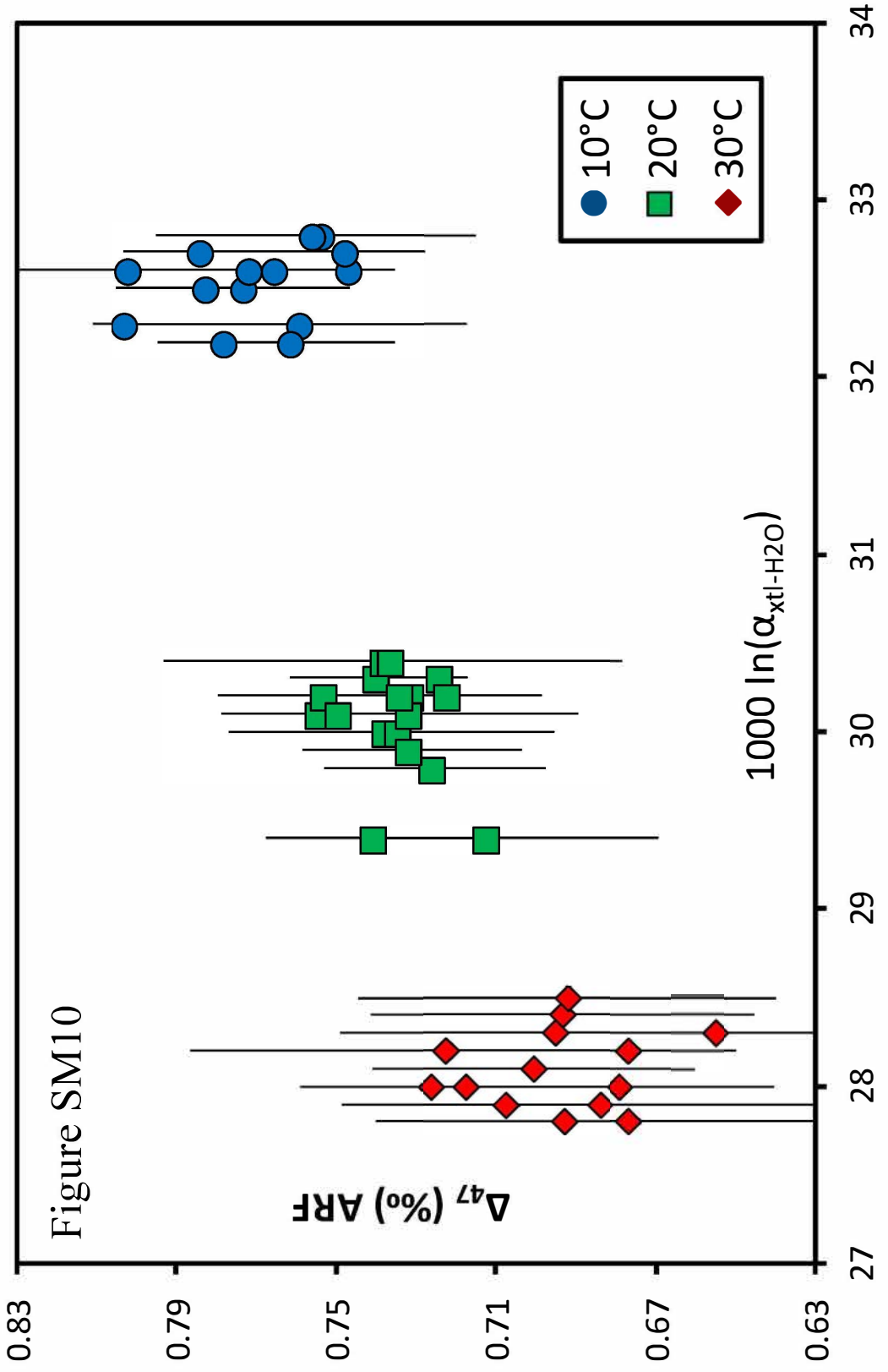
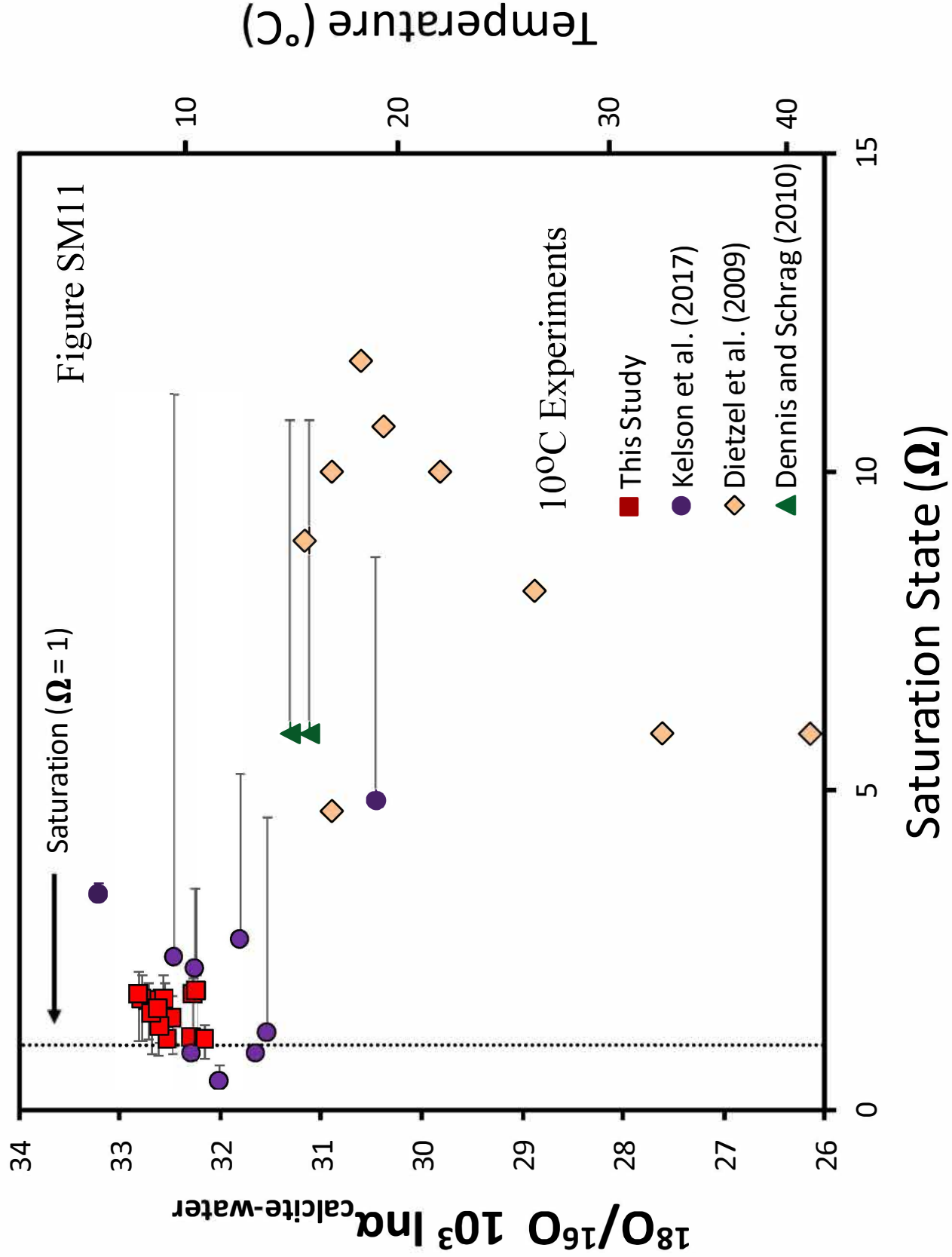
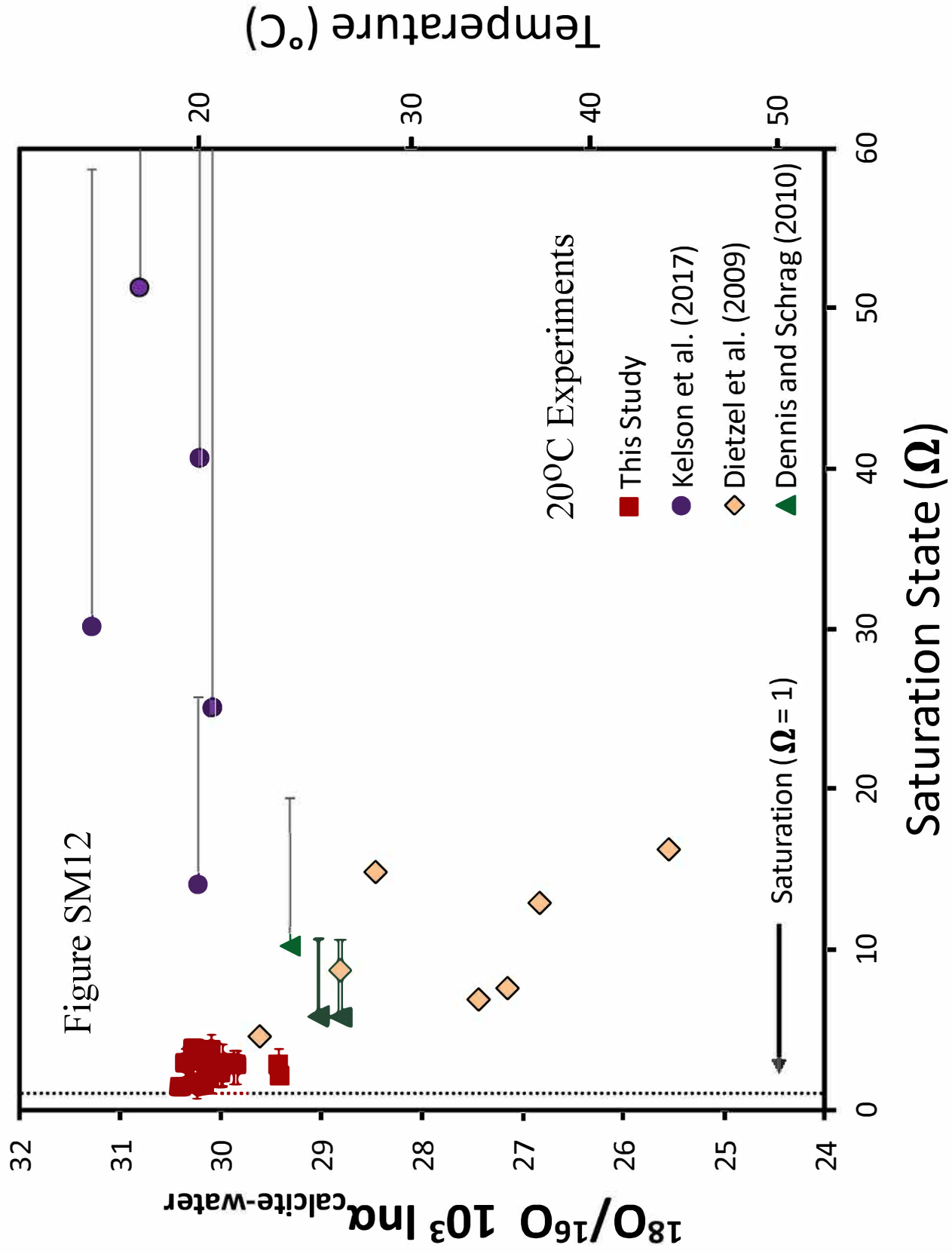
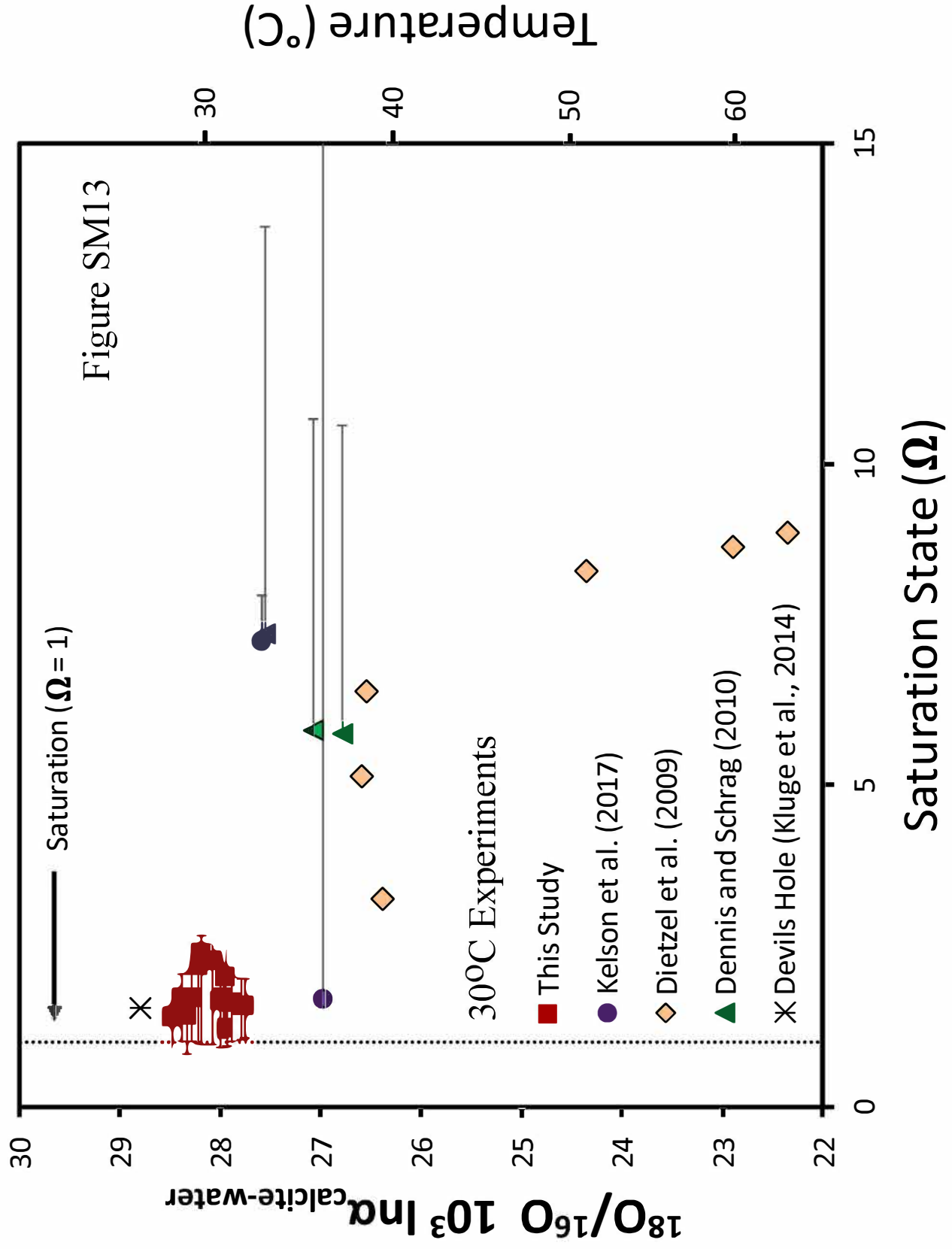

10°C
20°C
30°C
1000 ln(αxtl-H2O)
Δ47 (‰) ARF
0.83
0.79
0.75
0.71
0.67
0.63
27
28
29
30
31
32
33
34

Figure SM10


Figure SM11
Saturation (Ω = 1)
10°C Experiments
This Study
Kelson et al. (2017)
Dietzel et al. (2009)
Dennis and Schrag (2010)
Saturation State (Ω)
Temperature (°C)
$\delta^{18}O/^{16}O$ 10^3 $\ln\alpha_{calcite\text{-}water}$
34
33
32
31
30
29
28
27
26
0
5
10
15
10
20
30
40


Figure SM12
20°C Experiments
This Study
Kelson et al. (2017)
Dietzel et al. (2009)
Dennis and Schrag (2010)
Saturation (Ω = 1)
Saturation State (Ω)
Temperature (°C)
$^{18}O/^{16}O$ 10^3 $\ln\alpha_{calcite\text{-}water}$
32
31
30
29
28
27
26
25
24
0
10
20
30
40
50
60
20
30
40
50


Figure SM13
Saturation (Ω = 1)
30°C Experiments
This Study
Kelson et al. (2017)
Dietzel et al. (2009)
Dennis and Schrag (2010)
Devils Hole (Kluge et al., 2014)
Saturation State (Ω)
Temperature (°C)
$10^3 \ln\alpha_{calcite\text{-}water}$
$^{18}O/^{16}O$

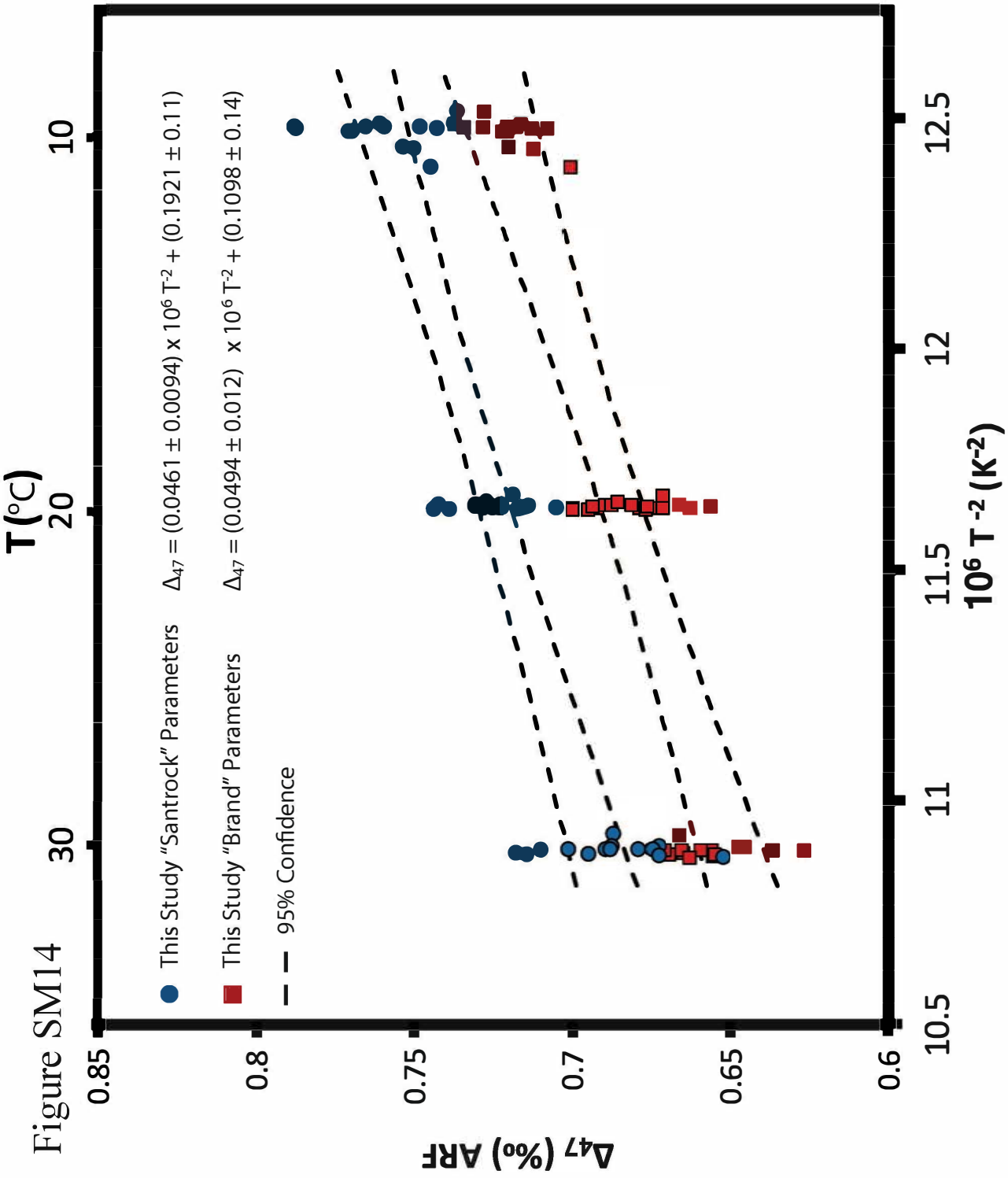

T (°C)
10
20
30
0.85
0.8
0.75
0.7
0.65
0.6
Δ47 (‰) ARF
10.5
11
11.5
12
12.5
10⁶ T⁻² (K⁻²)
This Study "Santrock" Parameters Δ47 = (0.0461 ± 0.0094) x 10⁶ T⁻² + (0.1921 ± 0.11)
This Study "Brand" Parameters Δ47 = (0.0494 ± 0.012) x 10⁶ T⁻² + (0.1098 ± 0.14)
95% Confidence

Figure SM14

Chapter 3: Factors Influencing the Mg Isotope Composition of Magnesian Calcite

Nicholas P. Levitt[1,†], Christopher S. Romanek[2], Brian L. Beard[1], Weiqiang Li[1,3], Suvankar Chakraborty[4], and Clark M. Johnson[1]

[1]NASA Astrobiology Institute and
Department of Geoscience
University of Wisconsin-Madison
1215 W Dayton Street
Madison, Wisconsin, USA
53706

[2]NASA Astrobiology Institute and
Department of Earth and Environmental Sciences
Furman University
Greenville, South Carolina, USA
29613

[3]State Key Laboratory for Mineral Deposits Research, School of Earth Sciences and Engineering, Nanjing University, Nanjing, Jiangsu 210093, PR China

[4]Department of Biology and Department of Geology and Geophysics
University of Utah
257 S 1400 E
Salt Lake City, Utah, USA
84112

[†]Corresponding Author's Contact
E-mail: nlevitt@wisc.edu
Tel: (608) 262-8960
Fax: (608) 262-0693

Manuscript to be submitted to Geochimica et Cosmochimica Acta
Submission Date: TBD

ABSTRACT

A very wide range in Mg isotope fractionation between magnesian calcite and aqueous Mg has been determined to date, and this limits the application of this system to studies of critical Earth system processes such as elemental fluxes and mineral composition, as well as seafloor spreading rates and sea level change. This study reports the results of a series of chemo-stat experiments that explore $^{26}Mg/^{24}Mg$ fractionation between Mg-calcite and Mg-bearing solutions, as well as the determination of Mg partition coefficients. The growth of calcite was obtained using calcite seed crystals as nuclei, and solution chemistry was controlled to investigate the effect of precipitation rate, temperature, ionic strength, pCO_2 and aqueous Mg/Ca ratio on Mg isotope fractionation between calcite and aqueous Mg.

A constant Mg isotope fractionation factor ($1000\ln \boldsymbol{\alpha}_{cc\text{-}sol}$) of -2.54±0.12‰ (2 $\boldsymbol{\sigma}$ stdev; n = 25) was measured at an intermediate temperature of 23° to 25°C over a range of precipitation rates ($10^{-8.4}$ to $10^{-4.9}$ mol m^{-2} s^{-1}), ionic strengths (0.04 to 0.93 mol kg^{-1}), pCO_2 (0.003 to 1.0), and molar aqueous Mg/Ca (0.41 to 3.39) ratios. The observed Mg isotope fractionation relation as a function of temperature (4°-45°C) was:

$$10^3 \ln(\alpha_{cc\text{-}sol}) = (-0.172\pm0.030) \times 10^6\ T^{-2} + (-0.60\pm0.34)$$

Which is significant, although modest relative to O isotopes. The experiments produced Mg concentrations in the precipitated calcite that ranged from 0.9 to 10.2 mol% Mg. No relation was observed between the mol% Mg of the overgrowth and Mg isotope composition, which contrasts with previous experimental and theoretical work. Likewise, no solution speciation effects on Mg isotope fractionation were observed. Such observations greatly simplify application of Mg isotopes to natural systems.

The Mg partition coefficient (D_{Mg}) between calcite and solution ranged from 0.00063 to 0.0536 (23°-25°C) and may be described by the following expression:

$D_{Mg} = 0.0308*(R_{Mg/Ca})^{-0.374}$

where D_{Mg} is the molar $(Mg/Ca_{solid})/(Mg/Ca_{soln})$ ratio and $R_{Mg/Ca}$ is the molar (Mg/Ca_{soln}) ratio. Unlike previous studies, the results of this study showed no dependence of D_{Mg} on precipitation rate or Mg isotope fractionation.

1 Introduction

Chemically precipitated marine carbonates form directly from ocean water and are generally considered to be one of the best records of seawater chemistry, although these records may be altered through post-depositional processes. Magnesium concentrations in seawater (and by extension, carbonates) have been used to explain processes controlling variations in the mineralogy of marine carbonates, as well as atmospheric pCO_2, sea level fluctuations, hydrothermal activity, and even early Earth biochemistry (Dalai et al., 2018; Li et al., 2015; Ries, 2004; Saunders and DeRose, 2016; Stanley and Hardie, 1998). Stable Mg isotope geochemistry is a rapidly growing field, where a major aim is to understand the Mg cycle over Earth history. Specific goals include identifying primary factors that control the Mg content and isotope composition of various carbonate minerals, and the processes and conditions that affect equilibrium or kinetic isotope fractionation. The study of major elements in carbonates, and their isotopic compositions (e.g., C, O, Mg, Ca, and Fe), is complimentary to long-standing approaches using trace elements such as Sr and rare earth elements, all of which can shed light on sources and magnitudes of sediment fluxes to or from the ocean, paleocondition proxies, and indicators of diagenetic alteration processes.

Magnesium has a long ocean residence time of ~13 million years and therefore the isotope composition of seawater can be considered homogeneous at any one time (Saenger and Wang, 2014; Teng, 2017). This element is continuously delivered to the ocean though

continental weathering, and leaves seawater through quantitative removal at hydrothermal seafloor spreading centers, as well as carbonate precipitation. Recent reviews of Mg isotope geochemistry highlight the wide range of ~ 6‰ in $^{26}Mg/^{24}Mg$ ratios in sediments and fluids, although many questions remain as to the reasons behind this relatively large variation due to incomplete understanding of Mg isotope fractionation factors (Saenger and Wang, 2014). Abiotic variables that have been proposed or shown to influence $^{26}Mg/^{24}Mg$ fractionation include temperature, precipitation rate, solution ion speciation, and mineral phase (e.g., Mavromatis et al., 2017a). A potentially important factor for kinetic effects is the high activation energy needed to dehydrate the $Mg(H_2O)_6^{2+}$ ion, and this reaction barrier is widely considered to be at the crux of many "dolomite problem" related issues, including the wide absence of low-temperature dolomite forming in nature today or laboratory experiments (e.g., Gregg et al., 2015; Hong et al., 2016; Land, 1998; Zhang et al., 2015). A limited number of both organic and inorganic catalyst studies have been shown to facilitate Mg dehydration and incorporation into carbonate mineral lattices (Romanek et al. 2009; Zhang et al., 2013; Shen et al., 2015; Zhang et al., 2015). Possible catalytic influence and lack of a consensus Mg isotope fractionation factor suggest that one or more unidentified or poorly understood kinetic processes and/or growth mechanisms may influence carbonate mineral formation.

Two well-cited Mg isotope studies of Mg-bearing calcite are at apparent odds. Li et al. (2012) observed a slight temperature dependence to Mg isotope partitioning between Mg calcite and experimental solution and report an equilibrium $^{26}Mg/^{24}Mg$ fractionation factor between calcite and fluid of -2.6‰ at 22°C. In contrast, Mavromatis et al. (2013) suggest a strong precipitation rate influence on Mg isotope fractionation and infer an equilibrium fractionation factor for $^{26}Mg/^{24}Mg$ of -3.5‰ at 25°C. In an attempt to resolve these discrepancies, $^{26}Mg/^{24}Mg$ isotope fractionation between calcite and dissolved Mg has been investigated through the chemo-

stat laboratory experiments. Major factors that control Mg isotope incorporation into the calcite mineral lattice were explored, including, precipitation rate, ionic strength, pCO_2, aqueous Mg/Ca ratio, mole % Mg incorporation in calcite overgrowth, aqueous Mg speciation effects, and growth substrate cation composition.

2 Methods and Materials

This study employed the carbonate precipitation approach commonly referred to as a "chemo-stat" technique (e.g., Mucci and Morse, 1983,) to form Mg-bearing calcite from supersaturated solutions. Constant chemical conditions were maintained by the titration of reagent species (i.e., Ca, Mg, carbonate alkalinity) into a reacting solution at the same rate they are removed by the precipitation of a solid phase. Additionally, a constant pCO_2 was maintained by bubbling the solution with a CO_2 gas mixture, which maximizes the potential for gas-solution equilibria during the precipitation reaction. This precaution is particularly important to prevent the buildup or depletion of aqueous CO_2 due to the kinetics of CO_2 exchange across the gas-liquid interface (Daëron et al., 2011; Affek and Zaarur, 2014; Sade and Halevy, 2017). Carbonate precipitation was initiated by the introduction of calcite seed crystals, which induced heterogeneous growth and minimized potential for the nucleation and growth of other solid phases (e.g., vaterite, aragonite). The Mg content and isotope composition of calcite and fluids were determined to assess elemental and isotopic partitioning among the various components of this system.

2.1 Inorganic Calcite Precipitation

Chemo-stat conditions during calcite precipitation were maintained by titrating a master reaction vessel with separate solutions of $NaHCO_3$ and a mixture of $CaCl_2$ and $MgCl_2$ that were

independently added (Fig. 1). The solution chemistry was further stabilized by maintaining a constant *p*H via CO_2/N_2 flowing through the master solution reaction vessel. The partial pressure of CO_2 in the gas stream was established by mixing CO_2 and N_2 gas streams at various flow rates using proportional flow controllers prior to the introduction of gas into the system. Calcite was precipitated in a 1 L Pyrex container that contained a magnetic stir bar suspended from the bottom of the vessel. Experiments were designed to produce up to 200 mg of overgrowth carbonate on approximately 70 mg of seed crystals. Master solution titration began immediately upon addition of seed crystals and ended shortly before product collection. Experiments were allowed to proceed from 24 minutes to 646 hours. Carbonate from the master solution was collected by vacuum filtration through a 0.4 μm polycarbonate filter, after which the solid was rinsed with methanol and dried overnight in an oven at 40ºC. The mass of newly formed carbonate overgrowth was determined by mass difference between added seed crystals and final total calcite mass. Table 1 provides values for seed crystal and overgrowth masses. The accuracy of mass recovery is estimated to be 4 mg (see below). In all cases, uncertainty in the mass of overgrowth is factored into the estimation of error for precipitation rates and Mg isotope compositions (Table 2).

This work integrates three distinct experimental programs. The major difference among the groups (Set A, B, and M) is the type of calcite seed crystals used. The seed crystals used in experimental Set A were the same as those used in the study of Li et al. (2012), which are calcite rhombs of 1-5 μm edge length that contain no detectable Mg. The seed crystals used in experimental Set B were reagent grade calcite powder (~1-5 μm) purchased from J.T. Baker (J.T. Baker, Baker Analyzed™ reagent $CaCO_3$, Lot H22339), which also had no detectable Mg. In contrast, the seed crystals used in experimental Set M were reagent-grade calcite powder (~1-5 μm) purchased from ACROS (ACROS Organics $CaCO_3$, 99+%, Lot: A0350502), which

contained an average of 1.61 ± 0.9 mol% Mg. The Set M seed crystals provided an opportunity to study the potential pathway dependence of Mg calcite formation on a Mg-bearing solid susceptible to dissolution/re-precipitation.

2.2 Experimental Conditions

Carbonate precipitation rates (moles m^{-2} s^{-1}) were varied by changing the length of experimentation and solution conditions. Temperatures ranged from 4 to 45°C and were maintained to within ± 1°C using water-jacketed vessels which were connected to a circulating heating and cooling bath. In most cases, supersaturation states in the range of 1 to 5 times saturation with respect to pure calcite were chosen to remain relatively close to equilibrium conditions. In five experiments, however, a saturation state of ≥8 times saturation was used (Table 1). Master and titrant solutions were prepared such that concentrations of Ca^{2+}, Mg^{2+}, and alkalinity would be in the ranges of 3-50 mmol L^{-1} (mM), 5-50 mM, and 7-37 meq L^{-1}, respectively, in the master solution during carbonate precipitation. Average experiment conditions are reported in Table 1 while initial and final solution concentrations are reported in Table S1. Reagent grade NaCl (Fisher Certified ACS NaCl, Lot 167532) was added to the master solution of some experiments at concentrations of 200, 400, 600, or 800 mM to explore the effects of ionic strength on Mg isotope fractionation. Cation titrant solutions were adjusted with NaCl to maintain these concentrations during experimentation. Saturation states, as well as speciated ion pair concentrations, were modeled with PHREEQC software (Parkhurst and Appelo, 2013) and the llnl.dat database for each experiment. Following Schott et al. (2016) and Mavromatis et al. (2017a), our llnl.dat database was modified to include updated carbonic-acid dissociation constants (Millero et al., 2007; Stefansson et al., 2013), the first Mg^{2+} hydrolysis equilibrium constant (Palmer and Wesolowski, 1997), and Mg bicarbonate and carbonate pairs

(Stefansson et al., 2014). Table S3 provides information on ion-pair concentrations as determined by PHREEQC.

2.3 Geochemical Analyses and Notation

Magnesium was purified prior to isotope analysis by ion-exchange chromatography according to procedures reported by Li et al. (2012, 2014, 2015). Approximately 30 mg of calcite or 300 μL of reaction solution (target of 100 μg of Mg) was processed for Mg separation and isotope analysis. Calcite was dissolved in 2.2M ultra-pure HCl acid, and cations were converted to pure chloride salts before purification. Likewise, HCl was added to experimental solutions and repeatedly dried three times until only solids remained. Magnesium was purified from other cations by ion-exchange chromatography before isotope analysis. Cation resin from Bio-Rad (Hercules, CA, USA) was used including AG MP-50 (100-200 mesh) for the first two stages and AG 50Wx8 (200-400 mesh) for the third stage. A fourth separation was performed to ensure any remaining Ca was removed using Eichrom (Lisle, IL, USA) Normal DGA resin (50-100 μm). Specific acid concentrations and volumes used as well as additional information are included in the Supplemental Material. It should be noted that this extensive ion-exchange column work was needed because the carbonates analyzed in this study consisted of both the calcite seed crystals and only small amounts of the Mg-bearing carbonate overgrowth.

Stable Mg isotope analyses were performed using a Nu Plasma II MC-ICPMS under low mass resolution (0.3mm source slit) at the University of Wisconsin - Madison. Samples bracketed by similar concentration (1 ppm) in-house standard solutions were input to the ICP via a Glass Expansion self-aspirating nebulizer with an uptake rate of ~ 40 μL/min and a peltier cooled Glass Expansion twisty spray chamber cooled to 7°C. Ion signal backgrounds were determined using an on-peak acid blank measured for 60 s prior to each standard and unknown

analysis. Isotope ratio determinations were made from sixty 5-s integrations which yielded a typical internal precision better than ±0.04‰ (2SD) for $^{26}Mg/^{24}Mg$ ratios. External precision is discussed in the Supplementary Material. See Li et al. (2014) for further details on mass spectrometry procedures.

The Mg content of the calcite overgrowth was determined in two ways. First, solids were digested in a small volume of trace metal grade HCl, diluted to volume with 1% HNO_3 concentration and analyzed by ICP-AES (Liberty Series II using Liberty Expert Ver.3.0 software) to determine the mass of Mg for a given experimental product. This mass was converted to mol% Mg of overgrowth calcite based on measured seed crystal and overgrowth masses. Overgrowth mol% Mg values for experimental Set M include a correction for the average amount of Mg determined for seed crystals. Second, seed crystals and experimental products were analyzed *in situ* by a CAMECA SXFive field-emission electron microprobe (EPMA) with an estimated analytical spatial resolution of ~500 nm. Calcite was mounted in epoxy plugs, polished, and carbon coated before EPMA analysis. The instrument was operated at 7kV and 10nA with a fully focused beam for mapping and spot/point analyses on overgrowth rims and with a 10 µm beam diameter for spot/point analyses on seed crystals and bulk grains of experimental Set M. Signal counting duration was low (10 ms) to minimize specimen damage. Background correction was achieved by the Mean Atomic Number method and validated for trace levels of Mg with seeds that contained no Mg (as determined by ICP-AES). The Mg detection limit was determined to be 0.07 wt.% or ~0.3 mol% Mg based on calibration of in-house Mg-bearing carbonate standards. Magnesium concentration detection accuracy was also verified during analytical sessions by analysis of an in-house dolomite standard. EPMA was used for spot/point assessments as well as X-ray mapping. Wavelength dispersive spectroscopy

(WDS) was achieved by analyzing Mg K$\boldsymbol{\alpha}$ emission with a LTAP crystal and Ca K$\boldsymbol{\alpha}$ with a LPET crystal.

Magnesium and Ca concentrations in the solid and solution phase can be considered together to determine the Mg partition coefficient (D_{Mg}) for the system. The homogeneous distribution coefficient definition of Henderson and Kracek (1927) was used:

$$D_{Mg} = \frac{M_{Mg_{cc}^{2+}}/M_{Ca_{cc}^{2+}}}{M_{Mg_{sol}^{2+}}/M_{Ca_{sol}^{2+}}} \qquad \text{Equation 1}$$

for consistency with previous chemo-stat precipitation studies (Burton and Walter, 1991; Hartley and Mucci, 1996; Mucci, 1986, 1987; Mucci and Morse, 1983, 1984; Zhong and Mucci, 1989), where M_{Mg2+} and M_{Ca2+} are molar concentrations in calcite (cc) and solution (sol). Application of D_{Mg} to chemo-stat experiments contrasts with heterogeneous distribution coefficients, which are determined using solution ion concentrations which vary over time due to chemical reaction between solid and solution phases (Doerner and Hoskins, 1925; Katz, 1973; Oomori et al., 1987).

Errors given in Table 2 and throughout the paper represent two standard deviations about the mean for measured compositions. Propagated errors for derivative values such as precipitation rates and fractionation factors were calculated as the square root of the sum of the squares. For Set M experiments, which used seed crystals that contained Mg, the expression used to calculate the Mg isotope composition of overgrowth carbonate is

$$\delta_o = \frac{(\delta_{tot} - \delta_s(1-\chi))}{\chi} \qquad \text{Equation 2}$$

where δ_o is the isotope composition of the overgrowth, δ_{tot} is the measured isotope composition of the overgrowth plus seed crystals, δ_s is the isotope composition of the seed crystals, and χ is the mass fraction of overgrowth to final total carbonate. Although Equation 2 is not exact

because it assumes linearity in terms of δ notation, this approximation introduces an error that is far below analytical uncertainties in δ^{26}Mg values.

Bulk stable isotope compositions are reported in units of per mil (‰) in standard form:

$$\delta^{n}Mg = \left(\frac{R_{sa}-R_{std}}{R_{std}}\right) \times 10^{3} \quad \text{Equation 3}$$

where *n* is 26 or 25 for ^{26}Mg/^{24}Mg or ^{25}Mg/^{24}Mg, respectively, R_{sa} is the isotope ratio of the sample, and R_{std} is the isotope ratio of a reference standard. Values of δ^{26}Mg reported in this investigation are relative to international standard DSM3 (Galy et al., 2003).

The partitioning of isotopes between two phases is described here as

$$10^{3} ln(\alpha_{a-b}) = 10^{3} ln\left(\frac{1000+\delta_a}{1000+\delta_b}\right) \approx \delta_a - \delta_b = \Delta^{n}\mathrm{Mg}_{a-b} \quad \text{Equation 4}$$

where $\alpha_{a\text{-}b}$ is defined as the fractionation factor between the two phases (*a* and *b*), δ_a and δ_b are the isotope compositions of the two phases (e.g., δ^{26}Mg), and n is the same variable used in Equation 3.

The saturation state convention of the PHREEQC llnl.dat database with respect to pure calcite is used throughout the paper and defined as

$$\Omega_{calcite} = \frac{a_{Ca^{2+}} * a_{HCO_3^-}}{K_{calcite}} = \frac{IAP}{Ksp} \quad \text{Equation 5}$$

where *a* denotes the activity of an ionic species, IAP is the ion activity product, and *K,* as well as *Ksp,* are the solubility product constant. Activities and saturation were determined by PHREEQC software. The reference state solubility for the reaction $CaCO_3 + H^+ = Ca^{2+} + HCO_3^-$ in the llnl.dat database is $K_{calcite} = 10^{1.8487}$ at 25°C.

3. Results

3.1 Solution Chemistry & Product Carbonate Characterization

Experimental results are summarized in Table 1. Average aqueous Ca and Mg concentrations ranged from 2.6 to 54.8 and 5.1 to 50.1 mmol L^{-1}, respectively. Similarly, average alkalinity concentrations varied from 6.3 to 40.0 meq L^{-1}. Average *p*H values were between 6.0 and 8.2 *p*H units. These *p*H values were established in part by pCO_2 concentrations, which ranged from 0.3 to 100%. These parameters produced saturation states with respect to calcite of 1.1 to 18.5, which in turn produced a range of precipitation rates of $10^{-8.4}$ to $10^{-4.9}$ mol m^{-2} s^{-1} (or $10^{-6.8}$ to $10^{-3.3}$ μm s^{-1}). Error-propagated uncertainties for precipitation rates ranged between 2 and 19%.

Seed crystal and overgrowth carbonate mineralogy were verified by microscopic inspection as well as XRD and EPMA analysis. Specifically, XRD patterns were inspected for peaks that could not be attributed to calcite, and carbonate grain morphology was monitored by secondary election imaging during EPMA work. In most cases, only calcite was identified in reaction products. Aragonite (111 and 021) peaks, however, were identified in the product of experiments A1, A4, A5, A6, A8, and A12, which were performed at higher temperatures (35-45°C). The amount of aragonite in these experiments is approximately 53, 48, 35, 16, 26, and 57 volume %, respectively, based on quantitative XRD analysis, and were accounted for when determining overgrowth mol% Mg and partition coefficients. The presence of aragonite in the precipitated carbonate material is not estimated to change the Mg isotope fractionation between calcite and solution more than ±0.05‰ due to the small amount of Mg accommodated by the aragonite lattice and a fractionation factor that is not largely different from calcite (Morse and Mackenzie, 1990; Wang et al., 2013).

The uncertainties in overgrowth Mg contents, as well as Mg isotope compositions for Set M experiments, were evaluated in several ways. The average mass of calcite overgrowth per experiment was approximately 40, 390, and 95 mg for experiment Sets A, B, and M, respectively (Table 1). The average seed crystal masses were approximately 75, 65, and 55 mg for experimental Sets A, B, and M, respectively. These relative masses between overgrowth and seed crystals are consistent with average seed crystal diameters of approximately 7, 1.1, and 2.5 μm, respectively, assuming a 1 μm overgrowth.

Some seed material and final solids were analyzed by EPMA to better understand the distribution and content of Mg in the overgrowths. The seed crystals used for Experimental Set A and B contained Mg in concentrations below detection limit (≤ 0.3 mol% compared to < 0.02 mol% reported by Li et al., 2012), whereas the Mg content of seed crystals used for experimental set M ranged from ≤ 0.3 to 3.5 mol%, with an average value of 1.6 ± 0.9 mol% (n = 25) based on random spot/point analyses. Measured bulk (seeds + overgrowth) concentrations range from 0.7 to 4.6 mol% Mg, and this range translates to 0.9 to 10.2% mol% Mg for magnesian calcite overgrowth. Mass-balance calculations for the amount of overgrowth have an average uncertainty of 2.2% (±4 mg), as determined by seed crystal recovery experiments at $\boldsymbol{\Omega}$=1, which is in good agreement with a rigorous comparison between gravimetry and isotope dilution for similar experiments reported by Levitt et al. (2018). This error factors into an average overgrowth mol% Mg uncertainty of ±0.9% (reported as 2SD relative to mol% Mg; Table S1). For δ^{26}Mg values of Experimental Set M, which involves a correction for the Mg-bearing seed crystals, overgrowth uncertainty translates to a propagated maximum uncertainty of ±0.11‰ in $^{26}Mg/^{24}Mg$ ratios, which is approximately the same as the 2-SD external precision (Table S2). Errors for each analysis for Set M experiments associated with overgrowth correction are given in Table S1; Sets A and B do not have such uncertainties.

X-ray mapping by EPMA revealed that overgrowth rims of Experimental Sets A and B averaged approximately 1 micron in width (Fig. 2). This distance is only twice as wide as the minimum spatial resolution of the technique and therefore EPMA analyses of the rim provide only semi-quantitative information compared to bulk dissolution. Regardless, the Mg content of Experimental Sets A and B determined by EPMA agreed with bulk ICP-AES measurements. Significantly, Mg was observed to be homogeneously distributed in overgrowths at the level of EPMA mapping precision. Concentration variability based on spot/point analyses among overgrowths of a given experimental grain population was ≤ ±0.5 mol% Mg. The distribution of Mg in the experimental products of Set M varied widely, however, and overgrowth rims were always not distinguishable from seed crystals via EPMA analysis (Fig. 2). See the Supplemental Material for further details.

Partition coefficients (D_{Mg}) varied greatly across the experimental conditions studied. For Set A experiments, D_{Mg} varied from 0.0063 to 0.0233 for Set A experiments conducted at 25°C and averaged 0.0130 ± 0.0152 (2**σ** SD; n =6; Table 1; Fig. 3). Set B experiments performed at 23°C produced D_{Mg} values that ranged from 0.0320 to 0.0536 and averaged 0.0427 ± 0.0138 (2**σ**; n =19; Fig. 3). The absolute concentration of aqueous Ca and Mg did not influence D_{Mg} except in Set A where two 25°C experiments had aqueous Ca and Mg values of ~15 and 50 mM, respectively, and larger D_{Mg} values (0.0227 ±0.0019) than four other 25°C experiments having aqueous Ca and Mg values of ~3 and 10 mM, respectively, and lower D_{Mg} values (0.0081 ± 0.0026). D_{Mg} values for Set M ranged from 0.0147 to 0.0413, with an average value of 0.0292 ± 0.0173. The range in D_{Mg} values is relatively large for experimental set M (0.0266) compared to set A (0.0171) or B (0.0216).

3.2 Mg Isotope Compositions

The initial δ^{26}Mg value of reagent Mg was -2.35±0.07‰ (2**σ** SD, n = 7) for experimental group A, -0.96±0.09‰ (2**σ** SD, n = 16) for group B, and -0.96±0.05‰ (2**σ** SD, n=7) for experimental group M. The reagent $MgCl_2 \bullet 6H_2O$ used for experimental group A was the same reagent used by Li et al. (2012) so it is not surprising that the measured values for group A solutions (Table 2) agree with the value reported previously ($\delta^{26}Mg_{DSM}$ = -2.39±0.08‰, n=38) by Li et al. (2012). An aliquot of Mg from several master solutions was analyzed after experimentation in each experimental group and solid product filtration to confirm a constant isotope composition during calcite precipitation. The δ^{26}Mg value of ending master solutions for experimental sets A, B, and M were -2.35±0.10‰ (n=8), -0.97±0.09‰ (n=19), and -0.94±0.05‰ (n=8), respectively, which are within error of the starting compositions for each experimental group, confirming that a constant Mg-isotope composition was maintained for each experiment.

The observed error-weighted Mg isotope composition of seed crystals for experimental Set M was -3.02±0.04‰ (n = 6, with each value representing three separate measurements). At the scale of the Mg isotope analysis of the solid (~ 27 mg), this indicates no sample heterogeneity, although it is possible there could be Mg isotope variation at the scale of single crystals, given the range in Mg content for the Mg-bearing seed crystals observed by EPMA (Fig. 2). For comparison, the average δ^{26}Mg value of the overgrowths on the M seed crystals was -3.43±0.47‰ (n = 13), which is 0.41‰ lower than the δ^{26}Mg value of the initial seed crystals, indicating that the bulk seed crystal correction is relatively small.

The $^{26}Mg/^{24}Mg$ fractionation between magnesian calcite and solution (1000ln $\boldsymbol{\alpha}_{cc\text{-}soln}$) is reported for experimental sets A and B, along with the results of Li et al. (2012) in Fig. 4 as a function of temperature. The values are not subdivided by mol% Mg in the overgrowth, for which experimental sets A and B varied from 0.9 to 10.2 mol% Mg, and for Li et al. (2012),

which varied from 1.2 to 12.6 mol% Mg. In addition, the results in Fig. 4 cover a wide range in the calcite precipitation rate ($10^{-8.4}$ to $10^{-4.9}$ mol m^{-2} s^{-1}) and ionic strength (0.04 to 0.93 mol kg^{-1}). All the data are highly consistent, despite the fact that they represent three independent sets of experiments, showing a modest temperature gradient in isotope fractionation of ~ 0.014‰/°C over the range of 4-45°C. Importantly, the precision and accuracy of experimental sets A and B in the current study are significantly better than the results of Li et al. (2012) due to differences in mass spectrometers (i.e., Micromass Isoprobe vs. Nu Plasma II). The results from experimental Set M, which are more complicated due to the presence of Mg in the seed crystals, therefore do not provide a direct measurement of equilibrium Mg isotope fractionation, will be discussed below in Section 4.2.

4. Discussion

A large body of work on Mg incorporation into carbonate minerals sets the foundation for understanding Mg isotope partitioning between calcite and solution. Early studies related to the calcite endmember focused on quantifying differences between material produced inorganically versus biogenically in terms of growth mechanisms, Mg partitioning between carbonate and solution, and precise determination of solubility constants for magnesian calcites (Morse and Mackenzie, 1990). The findings of this study are compared to pioneering and more recent studies, and are evaluated within the context of D_{Mg} values and solution ion speciation, mol% Mg in the overgrowth, precipitation rate, and temperature. The discussion concludes with an overview of the implications of the results with regard to biomineralization and environmental reconstructions from the Mg isotope composition of fossils.

4.1 Mg Incorporation into Calcite

The convention "magnesian calcite" will be used to describe calcite containing detectible Mg up to 25 mol% Mg without differentiating between low Mg calcite (LMC) or high Mg calcite (HMC) unless required when discussing a referenced work. The Mg isotope compositions are interpreted within the context of Mg-free seed material used in experimental Sets A and B, after which they are compared to results obtained using the Mg-bearing seed material in experimental Set M. From a high temperature formation perspective, the amount of Mg in magnesian calcite is a function of exchange with other Mg sources and solvi. For example, a large miscibility gap exists between calcite and dolomite when Mg-bearing carbonate is allowed to cool slowly from metamorphic conditions (Bucher and Grapes, 2011). However, magnesian calcite inclusions with relatively high mol% Mg contents have been observed to stabilize in equilibrium with forsterite and not exsolve dolomite (Ferry, 2001). At the low temperature end of the spectrum, an extensive literature exists for Mg partitioning between calcite and aqueous solution, as compiled and reviewed by various authors (e.g., Morse and Mackenzie, 1990; Bischoff et al., 1993, Morse et al., 2007; Radha and Navrotsky, 2013). We highlight representative studies in the main text, but present a brief review in the Supplemental Material.

Recent focus has moved away from bulk system characteristics and centered on formation pathways, the influence of organic compounds, growth inhibition by surface adsorption, and a host of diagenetic factors such as fluid vs sediment buffering of sediment reagents (e.g., Zhu et al., 2010; Chanda and Fantle, 2016; Purgstaller et al., 2016; Hong et al., 2016; Mavromatis et al., 2017b; Gorski and Fantle, 2017; Higgins et al., 2018). Experimental studies demonstrate that at first order, D_{Mg} is a function of Mg/Ca ratios of aqueous solutions (e.g., Fig. 3), and this has been discussed in terms of: 1) thermodynamics where the mixture of cations in the substituted calcite increases the entropy of the system (Morse and Mackenzie,

1990), 2) theoretical considerations of Mg partitioning (Busenburg and Plummer, 1989; Konigsberger and Gamsjager, 1992; Konigsberger et al., 1999), and 3) experimental studies that provide empirical evidence for Mg partitioning (Navrotsky and Capobianco, 1987; Bischoff, 1998). Importantly, and seemingly counterintuitively, it is observed that under equivalent conditions, calcite that contains modest amounts of Mg (~1-10 mol%) is less soluble than pure calcite and also magnesian calcite of higher Mg compositions (≥15 mol%) in Mg-bearing aqueous solutions (Bischoff et al., 1987; Mucci and Morse, 1984; Walter and Morse, 1984). A related and also poorly understood process has recently been termed "pseduomorphic replacement" by Putnis (2014), is described as a feedback mechanism initiated by "the dissolution of even a few monolayers of a mineral surface (which) can supersaturate an interfacial layer with respect to another solid phase." This dissolution-reprecipitation process creates a formation pathway that "allows the parent solid phase to be replaced by a product phase with different composition while maintaining its original dimensions."

Pseudomorphic replacement may explain the relatively low D_{Mg} values for experimental Set M where the concentration of Mg in the seed crystals varied widely. The spatial heterogeneity and wide range of Mg concentrations identified by spot/point EPMA analyses (up to 3.5 mol% Mg) observed in the Mg-bearing seed crystals of experimental set M suggest that small-scale domains of the seed crystals are differentially soluble with respect to the solution and potentially susceptible to dissolution-reprecipitation reactions. Any unaccounted-for dissolution of seed material with less than average Mg content (1.61 mol%) would have made the apparent overgrowth Mg partitioning lower. Specifically, underestimated Mg/Ca ratios in newly formed magnesian calcite could have resulted from mass balance calculations assuming low Mg concentrations in seed crystals and/or overestimating total seed crystal mass. In addition to replacement of surface calcite, the low D_{Mg} values observed for experimental Set M may have

also been influenced by a similar interior crystal dissolution-reprecipitation process facilitated by the heterogeneous nature of seed calcite. Similar examples of carbonate ion replacement are reported by Tribble and Mackenzie (1998) for magnesian calcite rinds that evolved over time to grow in size and stabilize to Mg contents of a few mol%, and by Jonas et al. (2015) who reacted pure calcite with 1 M $MgCl_2$ solution and documented a time-dependent reaction front of Mg into carbonate coupled to a loss of Ca to solution. Therefore, it is likely that the mol% Mg values calculated for overgrowth calcite on Mg-bearing seeds include an unquantifiable degree of inaccuracy as a result of alteration of the Mg-bearing seed crystals during experimentation.

Magnesium-free calcite seeds would not have experienced differential solubility, precluding pathways for Mg penetration below the solid-liquid interface, and are therefore interpreted to have been uniformly coated until disconnected from the solution phase (Fig. 2c). In the absence of any dissolution-precipitation processes, the Mg composition of overgrowth calcite was dominantly directed by solution Mg/Ca ratio. The results for D_{Mg} from experimental sets A and B are broadly similar to the relations described for D_{Mg} and solution Mg/Ca outlined by Mucci and Morse (1983) for magnesian calcite grown from seawater-type solutions on a pre-existing Mg-free calcite surface at 22 to 25°C (Fig. 3). The combined data demonstrate that D_{Mg} values are relatively high when aqueous Mg/Ca ratio is low and they decrease to an asymptotic value of ~0.01 as aqueous Mg/Ca increases. Mucci and Morse (1983) suggest that at a relatively low aqueous Mg/Ca ratio, the calcite surface is preferentially enriched in Mg compared to the bulk solution, and this leads to an enhancement of Mg in the solid phase. Our experimental results, along with the work of Katz (1973), expand the mathematical description of D_{Mg} as a function of solution Mg/Ca ratio to lower Mg/Ca ratios (Fig. 3). For comparison, the D_{Mg} values reported by Mavromatis et al. (2013) are generally lower that the values from Mucci and Morse (1983; see Fig. 3) and appear to display a strong positive correlation with precipitation rate in

agreement with the prediction by Wang and Xu (2001). On the other hand, Gabitov et al. (2014) observed a range of D_{Mg} values (0.009-0.0363) at relatively low aqueous Mg/Ca ratio (0.098-0.153) that displayed a negative correlation with precipitation rate. They hypothesized that the highest D_{Mg} value (0.0363) at the slowest rate ($10^{-7.42}$ mol m^{-2} s^{-1}) represented chemical equilibria, with all lower D_{Mg} values (0.009-0.0301) reflecting a kinetic effect. D_{Mg} values determined in the current study show no dependence on precipitation rate, nor do the studies of Burton and Walter (1991), Howson et al. (1987), Lopez et al. (2009), Li et al. (2012), Mucci and Morse (1983), Mucci et al. (1985, 1989), and Zhong and Mucci (1989). See the Supplemental Material for further discussion.

The wide range in D_{Mg} values observed at relatively low aqueous Mg/Ca ratio (Fig 3.) may be related to the formation of magnesian calcite via an amorphous calcium carbonate (ACC) (Giuffre et al., 2015; Blue et al., 2017) and/or hydrated precursor (Fukushi et al., 2017; Jimenez-Lopez et al., 2004, 2006; Oelkers et al., 2018). For example, Purgstaller et al. (2016) report experiments that involved initial rapid formation of Mg-bearing ACC followed by a significant increase in Mg content during transformation of the initial precipitate to calcite. The authors explain the observed cation concentration and mineralogy transition through a dissolution-reprecipitation process. The process is further described by Mavromatis et al. (2017a) as an ion exchange and/or dissolution-reprecipitation process that occurs in a nanoporous solid which contains a system of interconnected "percolating channels". The final and time-point averaged Mg partition coefficients of their study are lower than those observed by Mucci and Morse (1983). Collectively, these experiments indicate that transformation of ACC or hydrated carbonate to magnesian calcite can produce anomalously low D_{Mg} values.

We infer based on the discussion above, that the relatively low D_{Mg} values reported by Gabitov et al. (2014) and Mavromatis et al. (2013, 2017b) reflect a Mg incorporation mechanism

that is not exclusively dependent on exterior surface calcite growth by ions from bulk solution. Gabitov et al. (2014) used a supersaturated solution to initiate solid growth and observed increasing D_{Mg} values as carbonate accumulation slowed, reflecting an increase in solution Mg/Ca ratio with time. They interpret to record a kinetic effect and invoke a growth entrapment model where precipitating carbonate is not representative of the bulk solution under conditions where the advancing mineral lattice front is faster than diffusion in solution. However, if the initial precipitate was ACC or another phase, recrystallization to calcite and subsequent growth could have limited Mg incorporation in the same way as reported by Purgstaller et al. (2016). Mavromatis et al. (2013, 2017b) prepared initial solutions by dissolving and equilibrating calcite in Mg-bearing solutions under a pure CO_2 atmosphere. The authors filtered calcite from the initial solutions before reseeding with new calcite (V. Mavromatis personal communication; 25 September 2018) and commencing reagent titration. It is possible, however, that filtration of the initial solution removed dissolved CO_2 and supersaturated the solution before addition of new seed calcite or titrants. This experimental procedure has been reported to produce vaterite in addition to calcite (Kim and O'Neil, 1997; Tarutani et al., 1969) and has been shown to be influenced by recrystallization of carbonate (O'Neil et al., 1969).

If only calcite existed throughout the experiments of Mavomatis et al. (2013, 2017b), a solid-solution interfacial mechanism is required to interpret the anomalously low D_{Mg} values. The authors relied on solution characteristics to determine the concentration of Mg in calcite, based on the amount of Mg and Ca added and removed from the solution at steady-state during titration (Equation 1 of Mavromatis et al., 2013). In addition, they determined the mass of Mg in the solid using atomic absorption spectrometry. It is not possible, however, to know changes in calcite Mg contents prior to steady-state conditions. For example, experiments were performed for 12-15 days, however, solution Ca concentrations varied for ~2.8 days before plateauing and

Mg concentrations did not level off until 5.6 to 6.9 days after seed crystal introduction. Mavomatis et al. (2013) report that addition of titrant solutions shifted the solution phase to higher saturation states and "precipitation rate increase(d) with time until attainment of steady-state". Therefore, the carbonate phase was likely out of steady-state conditions, forming from a solution of decreasing Mg/Ca ratio for a large portion of the experiment. We speculate that falling Mg and increasing Ca solution concentrations may have induced a forward and back reaction couple that produced an interfacial dynamic similar to pseudomorphic replacement. An assessment of the Mg concentration difference between the initial solution and steady-state conditions reveals a correlation with D_{Mg} as well as saturation state (Fig. 5). This relation may indicate that at higher saturation states (and higher precipitation rates), growth dynamics suppressed surface dissolution-reprecipitation and Mg incorporation was more similar to the experiments reported here and by Mucci and Morse (1983, Fig. 3).

4.2 Mg Isotope Fractionation Between Calcite and Solution

$\Delta^{26}Mg_{cc\text{-}sol}$ fractionations ranged from -2.73±0.14‰ (at 4°C) to -2.03±0.12‰ (at 45°C) for experimental sets A and B over all conditions explored. Li et al. (2012) conducted free-drift experiments and observed $\Delta^{26}Mg_{cc\text{-}sol}$ fractionations ranging from -2.73 ± 0.16‰ (at 10°C) to -2.22 ± 0.24‰ (at 45°C) over a similar temperature range. The study of Mavromatis et al. (2013) reported measured $\Delta^{26}Mg_{cc\text{-}sol}$ fractionations ranging from -3.16 to -1.88‰ for experiments conducted at 25ºC, where they estimate an equilibrium fractionation of $\Delta^{26}Mg_{cc\text{-}sol}$ = -3.5‰, which was revised to -3.1‰ (Mavromatis et al., 2017a) based on the Mg solution speciation work of Schott et al. (2016). Although Mavromatis et al. (2013, 2017a) utilized calcite as a growth substrate, instead of adding the seed crystals to a supersaturated solution of constant composition, as was done in the current study, they report adding calcite to a saturated solution

and adding titrant solutions to slowly move toward a supersaturated steady-state condition. Given these changes in saturation state, Mg overgrowths in the study of Mavromatis et al. were not produced in the same manner as the current study where chemo-stat conditions were maintained at all times.

No correlation was observed between $\Delta^{26}Mg_{cc\text{-}sol}$ fractionation and mol% Mg for the overgrowths of experimental Sets A or B (Fig. 6), which contrasts with the experiments of Mavromatis et al. (2013) and the predictions of Rustad et al. (2010), Pinilla et al. (2015), and Wang et al. (2017). Combining the reduced partition function ratios of Rustad et al. (2010) and Pinilla et al. (2015) suggest that for the two Mg calcite compositions that were modeled, at 25°C, calcite that has 3.12 and 6.25 mol% Mg should have $\Delta^{26}Mg_{cc\text{-}sol}$ fractionations that are 0.9 and 1.8‰ higher than those of "infinitely dilute" magnesian calcite (see polynomial regression line in Fig. 6). Our experimental results, however, provide no evidence for the predicted Mg concentration effect on isotope fractionation, and we therefore conclude that a compositional effect is not an important determining factor for inorganic magnesian calcite formation under conditions related to our experiment Sets A and B.

Five experiments from set M (M3, M10, M12, M13, and M14) have $\Delta^{26}Mg_{cc\text{-}sol}$ fractionations that are greater (more positive) than those from experimental Sets A and B, and these approach the most positive fractionations of two experiments (CaMg113a and CaMg114s) reported by Mavromatis et al. (2013) (Fig. 6). Two experiments from Set M (M2 and M5) have $\Delta^{26}Mg_{cc\text{-}sol}$ fractionations that are more negative than those from experimental Sets A and B. EPMA X-ray analyses of Mg in the seed crystals, as well as consideration of Mg-calcite solubility data, raise the possibility that the measured Mg-isotope fractionation for Set M may be related to incongruent dissolution, which has been explored in other studies. Pearce et al. (2012) observed Mg isotope fractionation during the dissolution of magnesite, and attributed it to the

"stoichiometric release of all Mg isotopes during dissolution and coincident incorporation of lighter Mg isotopes back into the solid", which has the effect of producing more negative $\Delta^{26}Mg_{cc\text{-}sol}$ fractionations. In contrast, Perez-Fernandez et al. (2017) performed similar experiments on natural dolomite at experimental temperatures above 100°C and they observed a preferential release of light Mg isotopes into solution followed by a period of less negative $\Delta^{26}Mg_{dol\text{-}sol}$ fractionations until the Mg isotope composition of the solution was approximately equal to the starting dolomite.

Oelkers et al. (2018) monitored the Mg isotope composition of hydromagnesite and host solutions over periods of several months and concluded that "the transfer of material from the solid to the fluid phase may not be conservative during stoichiometric dissolution and that the isotopic compositions of carbonate minerals can evolve even when the mineral is in bulk chemical equilibrium with its coexisting fluid." Although this work does not prove congruent or incongruent dissolution of carbonate minerals (or Mg isotope fractionation related to these processes), it does indicate that $^{26}Mg/^{24}Mg$ fractionations could be variable under different calcite formation conditions. We speculate that incongruent dissolution of some seed material occurred during experiments of Set M, as suggested by bulk carbonate Mg compositions observed by EPMA (Fig. 2), which could explain the anomalously high and low $\Delta^{26}Mg_{cc\text{-}sol}$ fractionations for these experiments compared to those of experimental Sets A and B (Table 2).

4.3 Potential speciation effects

The control of solution Mg/Ca concentrations on Mg incorporation into the calcite crystal lattice, and attendant changes in solution speciation, bears on recent calculations of reduced partition function ratios for $^{26}Mg/^{24}Mg$ fractionation as a function of solution speciation (Schott et al., 2016). Ions relevant to this study include $Mg(H_2O)_6^{2+}$, $MgCl_2(H_2O)_4$, $MgCl(H_2O)_5^{+}$,

$MgOH(H_2O)_5^+$, $MgHCO_3(H_2O)_4^+$, and $MgCO_3(H_2O)_4$. By far the most abundant form of Mg in dilute solutions is $Mg(H_2O)_6^{2+}$, therefore we compare the predictions of Schott et al. (2016) for various Mg species relative to $Mg(H_2O)_6^{2+}$ in Fig. 7. The relative difference in $\delta^{26}Mg$ values between $Mg(H_2O)_6^{2+}$ and $MgCl_2(H_2O)_4$, $MgCl(H_2O)_5^+$, $MgOH(H_2O)_5^+$, $MgHCO_3(H_2O)_4^+$, and $MgCO_3(H_2O)_4$ are 0.79, 0.07, -2.07, -3.99, and -5.16‰ at 25°C, respectively, based on the calculated reduced partition function ratios (see Supplemental Material for more details), and these can be scaled to predict changes in the total $\Delta^{26}Mg_{cc\text{-}sol}$ fractionation as a function of speciation. For example, very large changes in $\Delta^{26}Mg_{cc\text{-}sol}$ fractionation would occur for a solution of $Mg(H_2O)_6^{2+}$ and $MgCO_3(H_2O)_4$ at only a few percent $MgCO_3(H_2O)_4$, but little change for a solution of $Mg(H_2O)_6^{2+}$ and $MgCl(H_2O)_5^+$ at even high percentages of $MgCl(H_2O)_5^+$. As shown in Table S3, $Mg(H_2O)_6^{2+}$ comprised >80% of aqueous Mg in our experiments, and the most important minor species were $MgHCO_3(H_2O)_4^+$ and $MgCl(H_2O)_5^+$, the former of which should impart a strong isotopic effect. We find no indication that varying the concentration of complexed Mg has an effect on Mg isotope fractionation over the range of conditions studied (Fig. 7). The data set from Mavromatis et al. (2013) is also plotted in Fig. 7 based on the speciation calculations in Table A3, which are very similar to the current study, where a significant isotopic effect is predicted for $MgHCO_3(H_2O)_4^+$, producing an increasingly negative $\Delta^{26}Mg_{cc\text{-}sol}$ fractionation with decreasing $Mg(H_2O)_6^{2+}$, which is not observed (Fig. 7). We conclude that the predicted speciation effects of Schott et al. (2016) are not observed in the experiments from the current study nor those of Mavromatis et al. (2013). Although there is an apparent linear relation between speciation and $\Delta^{26}Mg_{cc\text{-}sol}$ fractionation in the experiments of Mavromatis et al. (2013) (Fig. 7), such a relation lies at high angles to that predicted by the major speciation control, $Mg(H_2O)_6^{2+}$ and $MgHCO_3(H_2O)_4^+$, suggesting another origin for this apparent relation.

4.4 Equilibrium versus kinetic isotope fractionation

A common approach for investigating equilibrium versus kinetic isotope effects during precipitation is to explore isotope fractionation as a function of precipitation rates. Li et al. (2012) did not observe a relation between $\Delta^{26}Mg_{cc\text{-}sol}$ fractionation and precipitation rate in the range of $10^{-9.5}$ to $10^{-6.5}$ mol m^{-2} s^{-1}. In contrast, Mavromatis et al. (2013) reported a range of Mg isotope fractionation from $\Delta^{26}Mg_{cc\text{-}sol}$ = -3.16 to -1.88‰, which were interpreted to reflect a kinetic fractionation for precipitation rates from $10^{-8.3}$ to $10^{-6.6.}$ mol m^{-2} s^{-1} (Fig. 8), and they inferred an equilibrium $\Delta^{26}Mg_{cc\text{-}sol}$ fractionation at very slow precipitation rates to be ~ -3.5‰. The chemo-stat experiments of this study extend to a wider range in precipitation rates beyond that explored by Mavromatis et al. (2013), from $10^{-8.4}$ to $10^{-4.9}$ mol m^{-2} s^{-1}, and no evidence was found that precipitation rate influenced Mg isotope fractionation (Fig. 8). Therefore, the average $\Delta^{26}Mg_{cc\text{-}sol}$ value of Sets A and B probably reflect an equilibrium $^{26}Mg/^{24}Mg$ fractionation for magnesian calcite.

The most apparent differences between the experiments reported here and those of Mavromatis et al. (2013) are 1) the filtration method used to create a saturated starting solution, 2) a changing solution Mg/Ca ratio during initial carbonate growth, and 3) the amount of time needed for experimental solutions to reach steady-state conditions. Aside from the two experiments with the fastest precipitation rates (CaMg113s and CaMg114s, which precipitated from solutions reported to have non-mass dependent relations between $^{26}Mg/^{24}Mg$ and $^{25}Mg/^{24}Mg$ by Mavromatis et al. [2013, Table 2]), the reported amount of Mg in calcite appears to correlate with $\Delta^{26}Mg_{cc\text{-}sol}$ fractionation in the study of Mavromatis et al. (Fig. 6). We suggest that this may be related to a mineral lattice effect that did not influence our experiments, reflecting different formation mechanisms between the studies. As discussed in Section 4.2, this observation may reflect variable amounts of carbonate recrystallization to calcite or surface

alteration before steady-state conditions were attained with regard to saturation state and precipitation rate. Considering D_{Mg} and $\Delta^{26}Mg_{cc\text{-}sol}$ fractionation (Fig 8), as well as ACC-to-calcite transformation experiments (Purgstaller et al., 2016; Mavromatis et al., 2017a), some broad relations emerge. In all three studies, the solution Mg/Ca ratio decreases until a steady-state condition is reached, lower solution saturation is associated with lower mol% Mg concentrations, and Mg isotope fractionation is tied to calcite formation rate. In the words of Purgstaller et al. (2016), "calcite precipitated inorganically from high supersaturated solutions is not in equilibrium with the Mg/Ca ratio of its parent fluid. Specifically, the reaction pathway of calcite nucleation and precipitation via precursor phases and Rayleigh type distillation processes may impose nonequilibrium processes that may as well affect the isotope distribution of Mg in the solid phase (cf. Mavromatis et al., 2013)." These issues seem likely to underlie the discrepancies between our study and that of Mavromatis et al. (2013).

We speculate that the higher and lower than equilibrium $\Delta^{26}Mg_{cc\text{-}sol}$ fractionation values reported by Mavromatis et al. (2013) may be explained by the initial presence of non-calcite carbonate and/or surface alteration leading up to steady-state solution conditions. In the case of non-calcite carbonate recrystallization, a range of Mg isotope compositions is expected according to the amount of time allowed for recrystallization, as explained by Mavromatis et al. (2017a). Slower precipitation rates allow more time for preferential loss of heavy Mg to solution through dissolution-recrystallization in percolating channels, whereas faster precipitation rates lock in relatively positive isotope compositions inherited from hydrated Mg. The $\Delta^{26}Mg_{cc\text{-}sol}$ fractionation values reported by Mavromatis et al. (2013) are intermediate compared to Mg-bearing ACC and fully recrystallized magnesian calcite (Fig. 8). Support for this explanation comes from the identification of H_2O by FTIR in the calcite lattice for all product carbonate, reflecting incorporation of hydrated Mg, as reported by Mavromatis et al. (2013). Alternatively,

a calcite formation mechanism that includes surface alteration during non-steady-state conditions likely followed a pseudomorphic replacement process at low saturation states and slow precipitation rates. Under solution conditions of progressively lower aqueous Mg/Ca ratios leading up to steady-state conditions, incongruent loss of heavy Mg to solution can explain anomalously negative $\Delta^{26}Mg_{cc\text{-}sol}$ fractionations. Higher saturation states and fast precipitation rates likely retarded the surface replacement process and blocked equilibrium Mg isotope fractionation during hexaquo-Mg dehydration, burying unequilibrated horizons below the solution-solid interface, which, in essence, locks in Mg isotope disequilibrium. Such processes at fast precipitation rates are generally compatible with the description of kinetic Mg isotope fractionation given by Mavromatis et al. (2013) for more positive than equilibrium $\Delta^{26}Mg_{cc\text{-}sol}$ fractionations.

4.5 Temperature

We report four experiments in the range of 4 to 15°C and nine experiments in the range of 35 to 45°C. The former group of experiments is characterized by $\Delta^{26}Mg_{cc\text{-}sol}$ fractionations ranging from -2.70 ± 0.12‰ to -2.52 ± 0.07‰, whereas the latter group of experiments is characterized by $\Delta^{26}Mg_{cc\text{-}sol}$ fractionations ranging from -2.49 ± 0.12‰ to -2.03 ± 0.12‰. Considering Sets A and B together produces a significant temperature relation (Fig. 4) of $\Delta^{26}Mg_{cc\text{-}sol} = (-0.208 \pm 0.057) \times 10^6\ T^{-2} + (-0.20 \pm 0.64)$, which is within analytical error of the expression determined by Li et al. (2012), who studied a narrower range of experimental conditions. We therefore agree with the conclusion of Li et al. (2012) that Mg isotope fractionation between calcite and aqueous Mg has a significant temperature dependency. Combining both studies produces an error weighted temperature relation of $\Delta^{26}Mg_{cc\text{-}sol} = (-0.191 \pm 0.035) \times 10^6\ T^{-2} + (-0.38 \pm 0.39)$ where the fractionation factor varies by 0.014‰/°C in

$^{26}Mg/^{24}Mg$ over the temperature range 4°–45°C. These synthetic calibrations are consistent with the conclusions of Galy et al. (2002), who also observed Mg isotope fractionation as a function of mean annual temperature (4°-18°C) in four caves covering different climates, and report an error weighted relation of 0.017‰/°C (Fig 4), which lies within error of the temperature relation from the current study.

4.6 Implications for Mg Isotopes in Biogenic Materials

A major focus of Mg isotope studies on carbonates has been distinguishing kinetic "vital" effects from equilibrium fractionation, and the equilibrium $^{26}Mg/^{24}Mg$ fractionations we determined in the current study allow us to consider previous Mg isotope studies of biogenic systems (Fig. 9). The findings of our experiments that show there is a moderate temperature relation in calcite-solution $^{26}Mg/^{24}Mg$ fractionation, but no dependence on Mg contents in calcite, or aqueous speciation, greatly simplify application of Mg isotopes to natural carbonate systems.

Several recent studies have analyzed the Mg isotope composition of marine calcifiers and find $\Delta^{26}Mg_{cc\text{-}sol}$ fractionations ranging from -4.74 to -0.21‰ (Saenger and Wang, 2014; Teng, 2017). Some of the variability in fractionation factors is likely due to temperature differences (Hippler et al., 2009), although, based on the temperature relation determined here, this can only explain a range of < 0.5‰ over a reasonable temperature range. It seems most likely, therefore, that the effect of biological species-specific influences and mineralogy are the dominant explanations for the wide range in isotopic compositions (Chang et al., 2004; Wombacher et al., 2006; Pogge von Strandmann, 2008; Hippler et al., 2009; Ra et al., 2010; Ma et al., 2018; Muller et al., 2011; Wombacher et al., 2011). Vital effects have been proposed for Mg isotope fractionations in previous studies (Immenhauser et al., 2010; Rollion-Bard et al., 2016; Cusack et

al., 2008; Hippler et al., 2009; Mavromatis et al., 2017b; Politi et al., 2010; Purgstaller et al., 2016; Mavromatis et al., 2017a), and we summarize several examples in Figure 9. Several mechanisms have been proposed to explain observed fractionations, including kinetic isotope effects related to precipitation rate (Immenhauser et al., 2010; Rollion-Bard et al., 2016), isotope fractionation during transport of Mg across membranes (Cusack et al., 2008; Hippler et al., 2009), binding to organic molecules (Mavromatis et al., 2017b), involvement of ACC as an initial stabilizing phase (Politi et al., 2010; Purgstaller et al., 2016; Mavromatis et al., 2017a), and effects due to variable aqueous Mg concentrations and/or pH (Saenger and Wang, 2014).

As an example, we highlight one recent study of biogenic calcite formation, by Rollion-Bard et al. (2016), who performed a detailed study of the C, O, and Mg isotope composition of Mg-bearing calcite of three brachiopod shells. These authors analyzed a bulk composite sample of a modern *Frieleia halli*, a modern *Terebratalia transversa*, and a fossilized Plio-quaternary *Terebratula scillae*, and concluded that only *T. transversa* grew in partial isotope equilibrium with the formation water. Focusing on the *T. transversa* samples, which were divided into the primary calcite outermost surface (TP), the innermost surface (TI), and 12 sections of secondary calcite that divided the dorsal valve into roughly equal volumes, Rollion-Bard et al. measured an average $\Delta^{26}Mg_{cc\text{-}sol}$ fractionation of -1.83 ± 0.84‰. For sub-sampling of TP and TI, they determined a Mg isotope fractionation between calcite and seawater of -1.85 ± 0.11‰ and -3.18 ± 0.07‰, respectively.

Rollion-Bard et al. (2016) considered a relatively large range in $\Delta^{26}Mg_{cc\text{-}sol}$ fractionation that bracketed the studies of Saulnier et al. (2012) and Mavromatis et al. (2013). A (upper) threshold $\delta^{26}Mg$ value of -2.95‰ was used to discriminate between "equilibrium" or "disequilibrium" shell values based on a minimum Mg isotope fractionation between calcite and seawater. Two portions of the *T. transversa* (layer TI and section 12) were found to have $\delta^{26}Mg$

values at or more negative than -2.95‰ (Fig. 10). The samples with the highest Mg concentrations (samples 1-4 of the secondary layer, closest to the outer primary layer) have the most positive $\delta^{26}Mg$ values, whereas the areas with the lowest Mg concentrations have the lowest $\delta^{26}Mg$ values (samples 9-12 of the secondary layer, closest to the inner layer which is characterized by the most negative $\delta^{26}Mg$ value). Accordingly, the middle secondary layer (samples 5-8) is intermediate in Mg concentration as well as isotope composition (Fig. 10 Inset). The average Mg isotope composition of the middle section is within 0.1‰ of the primary calcite layer and also the average of the inner and outer secondary calcite.

Rollion-Bard et al. (2016) propose three possibilities to explain the large variability and relatively high $^{26}Mg/^{24}Mg$ ratios obtained for the brachiopod calcite: 1) temperature-dependent $\Delta^{26}Mg_{cc\text{-}sol}$ for a given organism at different mineralization time periods, 2) pH dependent $\Delta^{26}Mg_{cc\text{-}sol}$, and 3) kinetic Mg isotope fractionation due to variable formation rates. Additionally, they consider a fourth possibility: post precipitation biogeochemistry. As discussed by Rollion-Bard et al. (2016), different precipitation rates may indicate variable mechanisms of calcite formation, and they build on work by Griesshaber et al. (2009) and Cusack et al. (2010) who have reported ACC as a precursor to calcite in brachiopod biomineralization (see also Radha et al., 2012; Long et al., 2014; Immenhauser et al., 2016), although they do not conclude that ACC is an explanation for their observed fractionations. Finally, if we accept that the Mg isotope fractionations in the study of Rollion-Bard et al. (2016) do not reflect equilibrium conditions, the relations in Figure 10 might also indicate that C and O isotope equilibrium was not attained. Exploring such possibilities through additional combined Mg-C-O isotope studies, see for example Ma et al. (2018), will be important for fully understanding which elements are most likely to record equilibrium isotopic effects in biogenic carbonates.

Research specific to Mg-calcite and biomineralization in brachiopods has suggested that the isotopic composition may be controlled by biological mechanisms (Cusack et al., 2007) at the structural layer (England et al., 2007; Perez-Huerta et al., 2008), as well as crystallographic orientation levels (Cusack et al., 2008; Perez-Huerta et al., 2011), and changes with ontogenetic age (Immenhauser et al., 2016). Any of these issues may explain the variability in the Mg isotope composition reported by Rollion-Bard et al. (2016). Specifically, magnesian calcite may be subject to continued Mg exchange after initial calcite formation in terms of Mg diffusion and/or migration during recrystallization. The driving force for this phenomenon may be due to greater thermodynamic stability of the mineral lattice (Morse and Mackenzie, 1990; Bischoff et al., 1993, Morse et al., 2007; Elstnerova et al., 2010; Radha and Navrotsky, 2013) and/or promotion of enhanced mechanical strength due to higher Mg content (Wang et al., 1997; Griesshaber et al., 2007; Kunitake et al., 2012, 2013; Long et al., 2012, 2014).

The microstructure of brachiopod shells is conducive to mm to cm scale transport of ions due to specialized secretory cells which operate in the mantle and migrate from the peristracum to the outer epithelium membrane, forming a layer of primary and then secondary calcite in a continuous process (Griesshaber et al., 2007; Immenhauser et al., 2016). Additionally, brachiopod calcite includes mineral vesicles which store ionic building blocks and help facilitate removal and expulsion of harmful metals (Immenhauser et al., 2016). Brachiopod biomineralization includes a complex array of characteristics and processes which allow for continual shell maintenance and repair (Cusack et al., 2008; Griesshaber et al., 2009; Ye et al., 2017) that may also facilitate the redistribution of Mg depending on where enhanced shell strength is needed most. In the case of *T. transversa*, the highest Mg concentrations in the outermost secondary layer corresponds to the area most vulnerable to predation and the high δ^{26}Mg values associated with these sections are consistent with a redistribution mechanism that

takes advantage of stronger Mg-O bonds, which should concentrate heavier Mg isotopes when hydrated (Riechelmann et al., 2016). Although direct evidence of Mg mobilization by brachiopods after initial carbonate formation is currently lacking, many recent advances in our understanding of biomineralization (Cusack et al., 2007, 2008; England et al., 2007; Griesshaber et al., 2007, 2009; Perez-Huerta et al., 2008, 2011; Immenhauser et al., 2016; Ye et al., 2017) and carbonate mechanical strength related to Mg composition (Wang et al., 1997; Griesshaber et al., 2007; Kunitake et al., 2012, 2013; Long et al., 2012, 2014) indicate that caution should be exercised when using Mg isotopes in biominerals to reconstruct paleo-conditions. Such conclusions become apparent given the restricted range of Mg isotope fractionation under equilibrium conditions as determined in this study.

5. Conclusions

To address the fundamental controls on Mg isotope fractionation during precipitation of calcite, the chemo-stat precipitation method was used to produce magnesian calcite under a wide range of solution conditions to explore the relations between precipitation rate and Mg isotope fractionation, where rates ranged from $10^{-8.4}$ to $10^{-4.9}$ mol m^{-2} s^{-1} at temperatures from 4 to 45°C. Solution Mg/Ca concentrations ranged from 0.41 and 3.39 during calcite formation, and ionic strength was increased in some experiments by adding NaCl in concentrations up to 800 mM. These conditions produced Mg concentrations in the precipitated calcite ranging from 0.9 to 10.2 mol% Mg, producing a Mg partitioning relation of $D_{Mg} = 0.0308*(R_{Mg/Ca})^{-0.374}$ between calcite and aqueous solution under the conditions studied, where D_{Mg} is the molar $(Mg/Ca_{solid})/(Mg/Ca_{soln})$ ratio and $R_{Mg/Ca}$ is the molar (Mg/Ca_{soln}) ratio. In addition, we used both Mg-free and Mg-bearing calcite seeds to gain insight into possible mechanistic growth processes which can cause variability in Mg isotope compositions. We hypothesize that the presence of

Mg in the near-surface calcite lattice influences Mg transport and dehydration effects during dissolution-reprecipitation when the mineral is not in chemical equilibrium or at least steady-state with an aqueous solution, producing spurious (non-equilibrium) Mg isotope fractionations and D_{Mg} values.

The results obtained here agree with the study of Li et al. (2012), producing a constant $\Delta^{26}Mg_{cc\text{-}sol}$ fractionation of -2.54 ± 0.12‰ over all precipitation rates investigated at intermediate temperatures (23-25°C), independent of Mg speciation in solution or mol % Mg in calcite. We take this constant fractionation, at a given temperature, to be representative of equilibrium conditions, as it seems unlikely that a kinetic effect would be constant over the wide range of conditions encompassed by the experiments. Demonstration of an equilibrium Mg isotope fractionation factor that is independent of solution chemistry or the extent of Mg substitution in calcite greatly simplifies application of Mg isotopes to ancient carbonates where such parameters are unknown. This conclusion is contrary to the interpretations of Mavromatis et al. (2013), who report a strong rate-control of Mg isotope fractionation and infer a much lower negative isotope fractionation factor under equilibrium conditions. We interpret the contrasts in these studies to indicate that carbonate growth mechanisms are sensitive to the chemical state between calcite and solution in terms of mobilization of pre-existing Mg at the calcite surface, and that deviations from isotope equilibrium occur when mineral accumulation dynamics diverge from an ion-by-ion growth model at the solid-solution interface under conditions where diffusion to the interface is not limited.

The observed Mg isotope fractionation found over a range of temperatures in this and the study of Li et al. (2012) is expressed by $^{26}Mg/^{24}Mg\ 10^3 \ln(\alpha_{cc\text{-}sol}) = (-0.172 \pm 0.030) \times 10^6\ T^{-2} + (-0.60 \pm 0.34)$ where temperature is Kelvin. If we take this temperature dependence to reflect equilibrium conditions, this provides a reference frame with which to interpret non-equilibrium

"vital effects" during biomineralization. For example, our re-interpretation of the work by Rollion-Bard et al. (2016) indicates that the brachiopods studied did not form magnesian calcite in Mg isotope equilibrium with seawater, and that these species likely serve as poor archives for reconstructing the Mg isotope composition of ancient seawater. Taken together, our findings suggest that temperature is the only non-mineralogical or mechanistic factor influencing Mg isotope fractionation during ion-by-ion growth of calcite from solution, and, although significant, the temperature dependence is modest relative to O isotopes.

Acknowledgements

John Fournelle and Aurelien Moy are appreciated for EPMA assistance and informative discussions. John Valley is thanked for constructive comments on an earlier version of this manuscript. This work was supported by NASA Astrobiology Institute grant NNA13AA94A. The authors declare no conflicts of interest from their affiliation(s) or funding.

Table 1: Average Experimental Conditions

	Experiment Identification	Experiment Length (h)	Temp (° C)	pCO_2 (%)	pH	Ca^{2+} (mM)	Mg^{2+} (mM)	Soln Mg/Ca	Alkalinity (meq)	NaCl (mM)	Ionic Strength (mol kg^{-1})	Saturation Ω	DMg ($x10^2$)	Seed Calcite (mg)	Overgrowth Calcite (mg)	Overgrowth Mol% Mg	log Rate mol m^{-2} s^{-1}
*	C-22	151	22	3.0%	6.8	14.8	50.1	3.4	10.0	0	0.20	4.7	2.33	78.7	56.0	7.3%	-7.6
Experimental Set "A"	A1	48	35	3.0%	7.2	13.7	49.6	3.6	9.6	0	0.19	6.6	5.10	81.9	127.4	7.4%	-6.7
	A2	72	25	3.0%	7.1	14.8	49.9	3.4	10.2	0	0.20	4.7	2.33	74.8	35.0	7.3%	-7.4
	A3	72	25	2.1%	7.2	14.8	50.0	3.4	10.1	0	0.20	6.2	2.20	75.3	60.9	6.9%	-7.2
	A4	72	35	2.1%	7.2	14.7	50.0	3.4	6.3	0	0.19	4.2	5.45	74.0	90.4	8.2%	-7.0
	A5	36	40	2.1%	7.5	2.8	10.0	3.6	9.7	0	0.05	5.6	4.88	75.1	67.9	9.6%	-6.9
	A6	8	45	2.1%	7.5	2.8	10.0	3.6	10.0	0	0.05	6.7	4.08	72.5	50.7	10.2%	-6.3
	A7	72	25	2.1%	7.4	2.9	10.0	3.4	10.1	0	0.05	3.2	0.63	71.3	14.1	2.1%	-7.8
	A8	7	40	1.7%	7.6	2.7	10.0	3.7	9.8	0	0.05	6.9	3.47	72.0	60.8	8.1%	-6.2
	A9	96	25	1.7%	7.5	2.8	10.1	3.6	10.1	0	0.05	3.8	0.91	72.9	18.2	3.1%	-7.8
	A10	120	15	2.1%	7.2	14.9	50.0	3.4	10.1	0	0.20	4.6	1.19	77.0	15.3	3.8%	-8.0
	A11	120	25	1.7%	7.5	3.1	10.3	3.3	10.7	0	0.05	4.6	0.91	71.7	16.1	2.9%	-8.0
	A12	72	35	1.7%	7.6	2.7	10.3	3.8	10.1	0	0.05	5.9	6.85	80.3	75.7	9.3%	-7.1
	A13	36	35	1.7%	7.6	2.9	9.6	3.3	10.0	0	0.05	7.5	2.99	75.4	15.0	8.9%	-7.5
	A14	0.4	45	1.7%	7.6	2.9	10.0	3.4	10.0	0	0.05	10.2	1.85	78.0	5.0	5.9%	-6.2
	A15	0.5	25	0.3%	8.2	2.7	10.2	3.7	10.3	0	0.05	18.5	0.82	74.0	16.4	3.0%	-5.6
	A16	18	10	0.3%	8.1	3.2	10.5	3.3	10.0	0	0.05	11.4	0.88	75.8	19.7	2.8%	-7.1
	A17	18	15	0.3%	8.2	2.6	10.3	3.9	10.5	0	0.05	12.1	1.04	78.1	38.6	3.9%	-6.8
	A18	60	4	0.3%	8.1	2.9	10.2	3.5	10.8	0	0.05	8.0	0.61	75.4	27.1	2.1%	-7.5
	A19**	72	45	3.0%	7.3	4.9	50.1	10.2	9.5	0	0.17	3.7	0.25	77.5	31.7	2.5%	-7.6
	A20	--	--	--	--	--	--	--	--	--	--	--	--	--	--	--	--
Experimental Set "B"	B1	71	23	70%	6.2	23.3	21.8	0.9	32.5	0	0.16	2.0	3.20	58.6	78.6	2.9%	-7.0
	B2	71	23	70%	6.3	23.2	21.0	0.9	33.8	200	0.35	2.0	4.15	79.7	4.4	3.6%	-8.4
	B3	71	23	40%	6.5	22.1	21.9	1.0	30.4	0	0.15	3.4	3.84	70.5	252.7	3.7%	-6.6
	B4	71	23	40%	6.5	21.9	21.1	1.0	31.5	200	0.35	2.7	4.28	64.8	219.7	4.0%	-6.6
	B5	71	23	40%	6.5	23.4	21.6	0.9	33.5	400	0.55	3.3	3.40	64.8	14.9	3.0%	-7.7
	B6	65	23	75%	6.2	32.3	16.0	0.5	26.2	0	0.16	2.7	4.84	54.2	378.4	2.3%	-6.2
	B7	65	23	75%	6.2	40.7	21.0	0.5	32.9	200	0.40	3.1	4.81	58.3	568.8	2.4%	-6.1
	B8	65	23	75%	6.2	48.6	25.5	0.5	35.8	400	0.64	3.3	4.66	63.6	1061.5	2.4%	-5.8
	B9	43	23	100%	6.1	33.7	16.7	0.5	27.3	0	0.17	1.7	5.12	64.0	555.7	2.5%	-5.9
	B10	43	23	100%	6.2	42.5	21.2	0.5	35.3	200	0.42	2.4	4.13	71.0	579.8	2.0%	-6.0
	B11	43	23	100%	6.1	54.8	27.3	0.5	39.4	400	0.66	3.4	5.36	71.5	1239.4	2.6%	-5.6
	B12	5	23	100%	6.0	34.3	16.3	0.5	29.6	0	0.17	1.3	3.45	57.0	179.3	1.6%	-5.5
	B13	5	23	100%	6.2	43.0	20.7	0.5	37.6	200	0.41	2.5	3.20	75.2	165.0	1.5%	-5.6
	B14	5	23	100%	6.1	45.8	25.3	0.6	39.4	400	0.63	1.2	3.50	66.8	903.7	1.9%	-4.9
	B15	70	23	50%	6.3	22.5	10.9	0.5	19.5	0	0.11	1.7	5.12	65.2	165.1	2.4%	-6.7
	B16	72	23	50%	6.1	23.0	10.8	0.5	21.1	0	0.12	1.1	4.30	72.8	79.2	2.0%	-7.1
	B17	47	23	30%	6.7	22.2	20.8	0.9	31.2	400	0.54	4.9	4.47	62.0	203.6	4.0%	-6.4
	B18	47	23	30%	6.6	21.7	20.5	0.9	30.7	600	0.74	3.8	4.22	70.0	260.2	3.8%	-6.4
	B19	47	23	30%	6.6	20.6	20.2	1.0	29.1	800	0.93	2.5	5.02	67.1	427.2	4.7%	-6.1
Experimental Set "M"	M1	144	23	7%	6.7	11.5	5.4	0.5	8.7	0	0.06	1.9	3.96	61.0	143.6	1.8%	-7.0
	M2	144	23	7%	7.0	6.6	5.1	0.8	9.0	0	0.04	2.9	3.77	50.2	80.6	2.8%	-7.2
	M3	646	23	11%	6.7	13.2	5.5	0.4	9.7	0	0.06	2.5	4.13	51.1	29.0	1.7%	-8.3
	M4	98	23	50%	6.3	21.3	9.8	0.5	11.7	0	0.10	1.7	3.18	63.9	74.7	1.4%	-7.2
	M5	98	23	50%	6.4	12.4	9.9	0.8	15.4	0	0.08	1.7	3.61	57.7	125.7	2.8%	-6.9
	M6	70	23	63%	6.4	12.6	17.2	1.4	12.4	0	0.10	1.5	3.40	74.4	23.9	4.4%	-7.6
	M7	89	23	97%	6.1	32.7	14.9	0.5	8.1	0	0.15	1.1	3.66	65.4	211.1	1.6%	-6.7
	M8	89	23	97%	6.2	22.2	19.4	0.9	11.7	0	0.13	1.4	2.57	54.8	83.1	2.2%	-7.0
	M9	89	23	97%	6.2	24.5	29.0	1.2	13.9	0	0.17	1.7	2.33	52.6	400.5	2.7%	-6.3
	M10	42	23	75%	6.3	36.6	15.2	0.4	30.0	0	0.17	6.2	2.16	48.8	15.9	0.9%	-7.4
	M11	42	23	75%	6.4	26.8	29.1	1.1	40.0	0	0.19	6.9	1.47	45.5	39.0	1.6%	-6.9
	M12	47	23	75%	6.4	23.5	19.6	0.8	26.9	0	0.15	4.6	2.00	55.7	50.0	1.6%	-7.0
	M13	73	23	33%	6.5	14.6	12.3	0.8	21.5	0	0.10	3.3	1.84	66.5	40.3	1.5%	-7.3
	M14	43	23	75%	6.4	23.7	19.8	0.8	30.5	0	0.15	4.8	2.83	45.5	17.8	2.3%	-7.3

* Chemo-stat experiment reported by Li et al. (2012)

** Only experiment at solution Mg/Ca > 3.9 so data point excluded from D_{Mg} figures.

Table 2: Mg isotope composition of solutions and carbonates and corresponding isotope fractionations.

Experiment Identification	Measured Values Initial Solution δ^{26}Mg ‰ (DSM)	2SD	n	Measured Values Final Solution δ^{26}Mg ‰ (DSM)	2SD	n	Calcite Overgrowth δ^{26}Mg ‰ (DSM)	2SD	n	cc-soln Δ^{26}Mg ‰	2SD
C-22*	-2.39	0.08	38	-2.34	0.22	7	-4.89	0.15	10	-2.54	0.27
A1	--	--	--	--	--	--	-4.81	0.07	6	-2.46	0.08
A2	--	--	--	--	--	--	-4.82	0.06	6	-2.47	0.05
A3	--	--	--	-2.38	0.10	3	-4.83	0.08	5	-2.48	0.07
A4	-2.38	0.13	2	--	--	--	-4.76	0.10	5	-2.41	0.11
A5	--	--	--	--	--	--	-4.82	0.07	5	-2.47	0.08
A6	--	--	--	-2.40	0.27	2	-4.80	0.06	5	-2.45	0.07
A7	-2.36	0.02	2	--	--	--	-4.92	0.09	5	-2.57	0.15
A8	--	--	--	-2.40	0.04	2	-4.84	0.11	6	-2.49	0.12
A9	--	--	--	-2.27	0.10	3	-4.98	0.17	5	-2.63	0.20
A10	-2.36	0.11	3	--	--	--	-4.87	0.06	3	-2.52	0.07
A11	-2.40	0.19	3	--	--	--	-4.97	0.11	5	-2.62	0.11
A12	--	--	--	-2.36	0.13	3	-4.76	0.06	6	-2.41	0.07
A13	-2.30	0.11	3	--	--	--	-4.82	0.13	4	-2.47	0.13
A14	--	--	--	-2.35	0.12	3	-4.73	0.08	4	-2.38	0.09
A15	-2.33	0.11		--	--	--	-4.94	0.09	6	-2.59	0.09
A16	--	--	--	-2.35	0.22	5	-5.12	0.10	6	-2.77	0.12
A17	-2.32	0.10	2	--	--	--	-5.06	0.06	6	-2.71	0.14
A18	--	--	--	-2.29	0.09	2	-5.08	0.11	6	-2.73	0.14
A19	-2.34	0.16	3	--	--	--	-4.38	0.10	6	-2.03	0.12
A20	--	--	--	--	--	--	--	--	--	--	--
B1	-0.96	0.08	3	-0.97	0.13	3	-3.52	0.07	6	-2.59	0.07
B2	--	--	--	-0.96	0.09	3	-3.44	0.06	3	-2.48	0.06
B3	-0.96	0.02	3	-0.98	0.01	3	-3.48	0.04	3	-2.52	0.05
B4	-1.03	0.05	3	-0.99	0.03	3	-3.49	0.06	3	-2.53	0.06
B5	-0.98	0.05	4	-0.96	0.02	3	-3.37	0.06	6	-2.39	0.06
B6	-0.98	0.03	3	-0.98	0.02	3	-3.48	0.13	6	-2.47	0.13
B7	-0.95	0.16	3	-0.97	0.07	3	-3.56	0.05	3	-2.60	0.05
B8	-0.98	0.01	2	-0.95	0.02	3	-3.59	0.03	3	-2.63	0.03
B9	-0.98	0.12	3	-0.94	0.09	3	-3.53	0.03	3	-2.57	0.03
B10	-1.02	0.16	2	-0.99	0.08	3	-3.55	0.07	6	-2.58	0.07
B11	-0.91	0.03	3	-0.96	0.01	3	-3.51	0.07	3	-2.55	0.07
B12	-0.95	0.03	3	-1.09	0.11	3	-3.49	0.12	3	-2.53	0.12
B13	-0.87	0.05	3	-0.95	0.23	5	-3.51	0.05	3	-2.55	0.05
B14	--	--	--	-0.85	0.16	6	-3.54	0.07	6	-2.55	0.07
B15	-0.97	0.03	3	-0.97	0.09	3	-3.53	0.06	4	-2.57	0.06
B16	-0.97	0.09	3	-0.95	0.01	3	-3.48	0.09	4	-2.50	0.06
B17	-0.89	0.08	3	-1.02	0.08	3	-3.45	0.17	3	-2.49	0.17
B18	--	--	--	-1.01	0.11	3	-3.42	0.11	3	-2.48	0.11
B19	-0.93	0.06	3	-0.96	0.06	3	-3.56	0.01	4	-2.60	0.02
M1	--	--	--	--	--	--	-3.55	0.11	3	-2.59	0.12
M2	--	--	--	-0.93	0.08	15	-3.72	0.08	3	-2.76	0.09
M3	-0.97	0.06	18	-0.93	0.09	12	-3.24	0.08	3	-2.28	0.10
M4	--	--	--	--	--	--	-3.58	0.12	3	-2.62	0.13
M5	-0.96	0.08	6	-0.94	0.10	6	-3.69	0.09	3	-2.73	0.10
M6	--	--	--	--	--	--	-3.56	0.07	3	-2.60	0.08
M7	-0.98	0.05	6	-0.96	0.03	4	-3.48	0.04	3	-2.52	0.05
M8	-0.95	0.04	4	-0.96	0.13	4	-3.58	0.06	3	-2.62	0.08
M9	-0.93	0.11	4	-0.91	0.05	4	-3.54	0.10	3	-2.58	0.11
M10	--	--	--	-0.92	0.15	8	-3.00	0.07	3	-2.32	0.08
M11	-0.93	0.06	3	-0.98	0.09	3	-3.39	0.07	3	-2.43	0.09
M12	--	--	--	--	--	--	-2.98	0.06	3	-2.12	0.07
M13	-0.99	0.04	4	--	--	--	-3.32	0.09	3	-2.36	0.10
M14	-0.95	0.10	3	-0.95	0.06	6	-2.94	0.02	3	-2.01	0.09
M-seeds	--	--	--	--	--	--	-3.02	0.04	18	--	--

* Chemo-stat experiment from Li et al. (2012).

Figure Captions

Figure 1 – Schematic of chemo-stat experimental setup. Temperature-controlled water flows through jacketed glass vessels for experiments that deviated from room temperature. The master solution hosts magnesian calcite growth on calcite seed crystals. Titrant solutions of $CaCl_2$ and $MgCl_2$, and $NaHCO_3$ are transferred to the master solution by a peristaltic pump to replace ions removed from solution due to calcite precipitation. Experiments are conducted under a constant partial pressure of CO_2 to facilitate gas-solution exchange of aqueous and gaseous CO_2.

Figure 2 – Representative X-ray maps (left) showing Mg concentrations and secondary electron images (right) produced by CAMECA SXFive field emission electron microprobe analysis of experimental products resulting from Mg-free seed crystals (top and middle) and Mg-bearing seed crystals (bottom). For comparison, the overgrowth of A19 is 2.3 mol% Mg by bulk dissolution and ICP-AES analysis.

Figure 3 – Relation between aqueous Mg/Ca ratio and Mg partition coefficient for synthetic magnesian calcite from experiments of this study and previous studies at near room temperature (22-25°C). The purple regression was calculated as a power function by Microsoft® Excel for Mac (Version 16.12) from average D_{Mg} values reported here at average solution Mg/Ca ratios of ~0.50, 0.95, and 3.4, as well as average D_{Mg} values reported by Katz (1973) at average solution Mg/Ca ratios of 0.09, 0.18, and 0.35, and values reported in Table 3 of Mucci and Morse (1983). The closed blue and open diamonds are the equilibrium (exp DC-1) and kinetically influenced (exps DC-1, DC-3, and DSC-4) D_{Mg} values, respectively, as reported by Gabitov et al. (2014). This figure is modified after Mucci and Morse (1983). Importantly, D_{Mg} values appear anomalously low for the Mg isotope study of Mavromatis et al. (2013), as well as Set M from

this study, which used Mg-bearing seed crystals. Additional distribution coefficients from the literature are discussed in the Supplemental Material.

Figure 4 – Observed calcite-solution Mg isotope fractionation (1000ln $\boldsymbol{\alpha}_{cc\text{-}soln}$) determined in this study (experimental set A and B) and Li et al. (2012). The solid purple line represents the composite error weighted regression for the two studies. The dashed green line represents an error-weighted relation observed in speleothem calcite as reported by Galy et al. (2002). Individual propagated 2SD external uncertainty for experimental values are represented by error bars for this study. Individual values are given in Table 2. Note that analytical uncertainties in the current study are substantially smaller than those of Li et al. (2012).

Figure 5 – Mg isotope fractionation between calcite and solution (1000ln $\boldsymbol{\alpha}_{cc\text{-}soln}$) and Mg partition coefficient from experiments of Mavromatis et al. (2013) are compared to the difference in Mg concentration between the initial solution and that at steady-state. The left y-axis corresponds to both saturation state ($\boldsymbol{\Omega}$x10^2) and distribution coefficient. The right y-axis corresponds to Mg isotope fractionation between calcite and steady-state solution. Individual 2SD uncertainty for isotope fractionation is represented by error bars. Note Mavromatis et al. (2013) report conditions for thirty experiments and fourteen $\Delta^{26}Mg_{cc\text{-}sol}$ fractionation values. The correlation between solution difference, fractionation, saturation state, and D_{Mg} suggests non-equilibrium conditions.

Figure 6 – Mg isotope fractionation between calcite and solution (1000ln $\boldsymbol{\alpha}_{cc\text{-}soln}$) compared to mol% Mg in overgrowth calcite (experimental set A, B, and M) for this study. Predicted Mg isotope fractionation as a function of mol% Mg is plotted as a solid black line from Pinilla et al.

(2015), described by the expression: ß = -0.0306*(mol% Mg)^2 -0.097*(mol% Mg) + 18.9. Individual propagated 2SD external uncertainty for experimental values are represented by error bars. Individual values determined by this study are given in Table 2. Data from Mavromatis et al. (2013) are reported for comparison. The data from this study show no correlation between Mg-isotope fractionation and mol % Mg, in contrast to experimental data from Mavromatis et al. (2013) or theoretical predictions of Pinilla et al. (2015).

Figure 7 – Measured Mg isotope fractionation between calcite and solution (1000ln $\boldsymbol{\alpha}_{cc\text{-}soln}$) as a function of fluid speciation (as the fraction of total Mg represented by hexaquo-Mg as calculated by PHREEQC; see text for details) at near room temperature (22-25°C). Deviations from 100% hexaquo Mg for different ionic complexes are shown as straight lines calculated according to the work of Schott et al. (2016), assuming a two-component mixture of hexaquo Mg and the indicated species. Individual propagated 2SD external uncertainty for experimental values are represented by error bars. Individual values determined by this study are given in Table 2. Mg speciation in solution for individual experimental conditions is given in Table S3. There is no correlation between fractionation and Mg solution speciation, indicating that over the range of compositions studied, speciation effects are insignificant.

Figure 8 – Mg isotope fractionation between calcite (or ACC precursor) and solution compared to precipitation rate. MgCaX samples are reported by Purgstaller et al. (2016) and Mavromatis et al. (2017a). The bottom x-axis applies to this study and Mavromatis et al. (2013) and the top x-axis applies to samples MgCaX from Purgstaller et al. (2016). Therefore, the Mg fractionation values as a function of apparent growth rate are not directly comparable to values as a function of precipitation rate. Individual propagated 2SD external uncertainty for experimental values is

represented by error bars. Error bars for samples MgCaX are smaller than the symbols. Individual values measured by this study are given in Table 2. For our study, we observe no correlation between fractionation and precipitation rate, suggesting that our results (sets A and B) reflect equilibrium isotope fractionation.

Figure 9 – Mg isotope fractionation between calcite and solutions for a variety of inorganic experiments and biogenic materials. Experimental studies are shown as colored data fields, with sources noted. Biogenic low Mg calcite (LMC) and high Mg calcite (HMC) have been reported by Saenger and Wang (2014) with additional data points reported by Pogge von Strandmann et al. (2014). The data points for *T. transversa*, *F. hali*, and *T. scillae* have been reported by Rollion-Bard et al. (2016). The red lines represented a 95% confidence interval of the regression reported in Figure 4.

Figure 10 – Re-interpretation of the Mg isotope compositions (primary vertical axis) of a modern brachiopod specimen (*T. transversa*) reported by Rollion-Bard et al. (2016). We use the Mg isotope fractionation and uncertainty measured in this study to establish an equilibrium Mg isotope composition, assuming a seawater δ^{26}Mg value of -0.82‰ (secondary vertical axis). Similarly, the Mg isotope composition of ACC formed from seawater calculated based on the work of Mavromatis et al. (2017a). A general trend of decreasing Mg isotope fractionation with increasing Mg concentration is reported by Rollion-Bard et al. (2016). The fields of equilibrium fractionation for C and O isotopes are based on seawater compositions of between 0.5 and 2.0‰ (VPDB) and -0.2‰ (VSMOW) as measured by Santos et al. (2011) and listed in The Global Seawater Oxygen-18 Database (Epstein and Mayeda, 1953), respectively, and isotope fractionation factors determined by Levitt et al. (2018). Rollion-Bard et al. (2016) interpret

variable $\delta^{18}O$ values to reflect variable degrees of kinetic fractionation. The inset image is a cartoon replication of the *T. transversa* shell depicted in Figure 2a of Rollion-Bard et al. (2016).

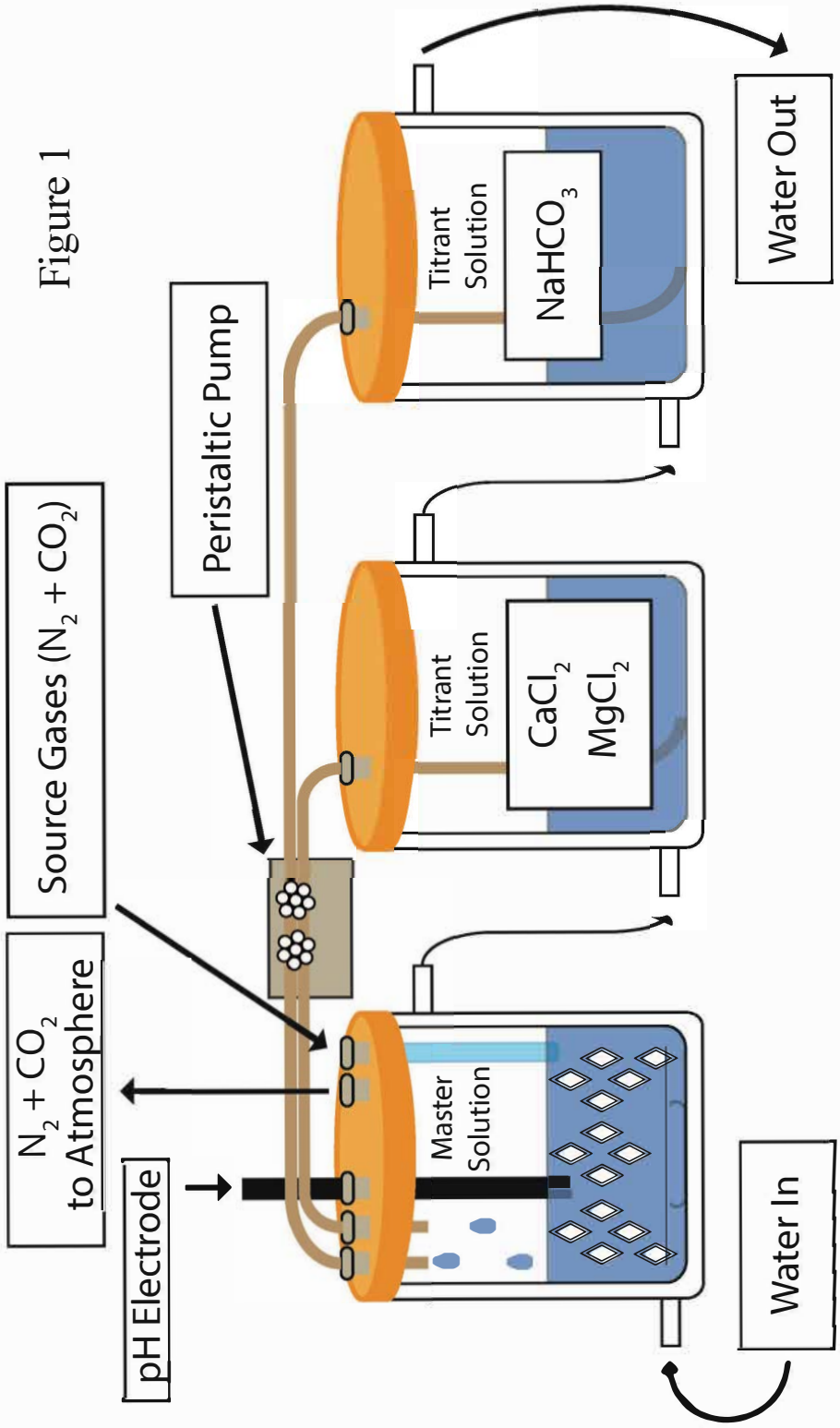
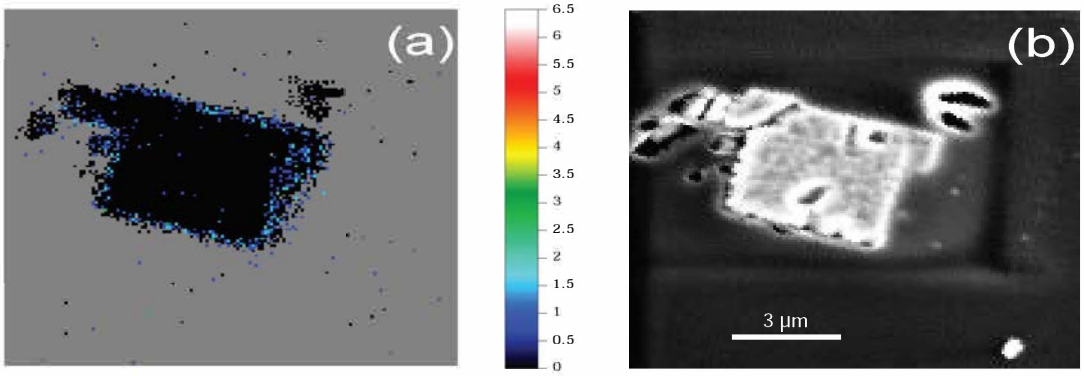

Water Out
Titrant Solution
NaHCO3
Titrant Solution
CaCl2
MgCl2
Peristaltic Pump
Source Gases (N2 + CO2)
N2 + CO2 to Atmosphere
pH Electrode
Master Solution
Water In

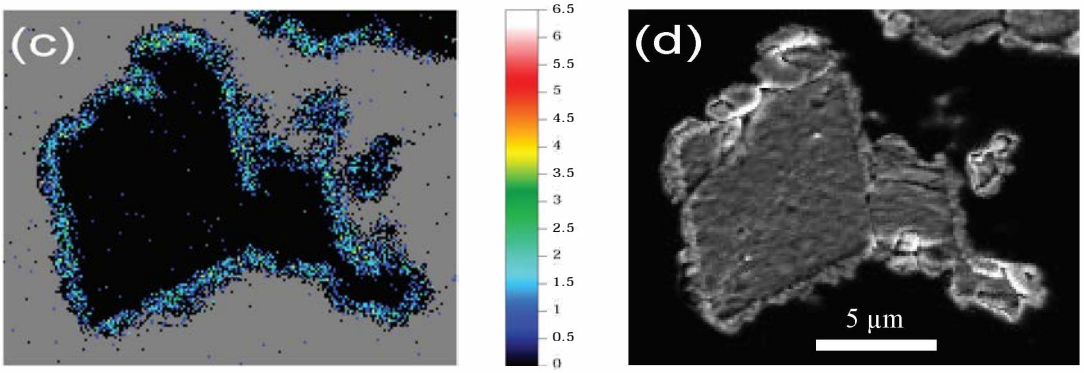
Figure 1

Figure 2



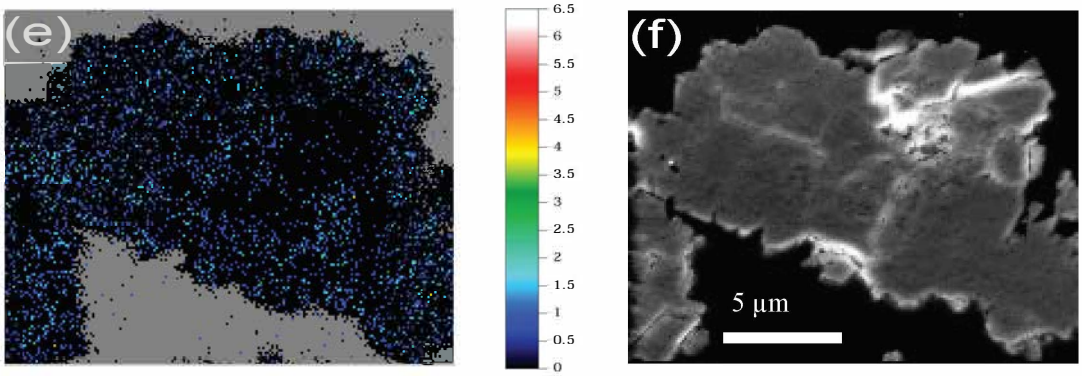
Experiment A19 Product

Mg Wt%

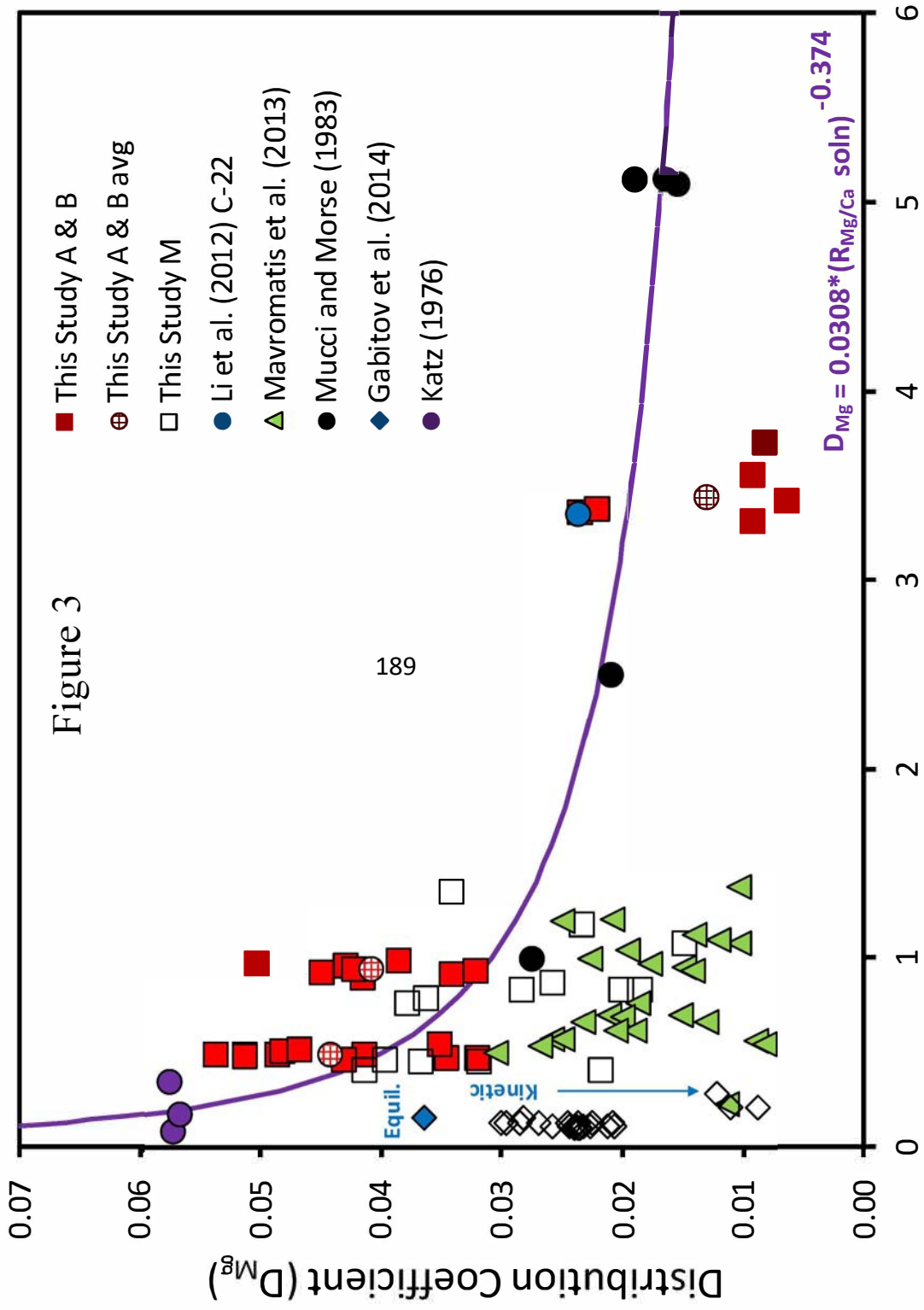


Experiment A20 Product

Mg Wt%



Experiment M6 Product


Figure 3
189
This Study A & B
This Study A & B avg
This Study M
Li et al. (2012) C-22
Mavromatis et al. (2013)
Mucci and Morse (1983)
Gabitov et al. (2014)
Katz (1976)
$D_{Mg} = 0.0308*(R_{Mg/Ca\ soln})^{-0.374}$
Equil.
Kinetic
Distribution Coefficient (D_{Mg})
Mg:Ca Ratio in Solution (mol/mol)
0.00
0.01
0.02
0.03
0.04
0.05
0.06
0.07
0
1
2
3
4
5
6

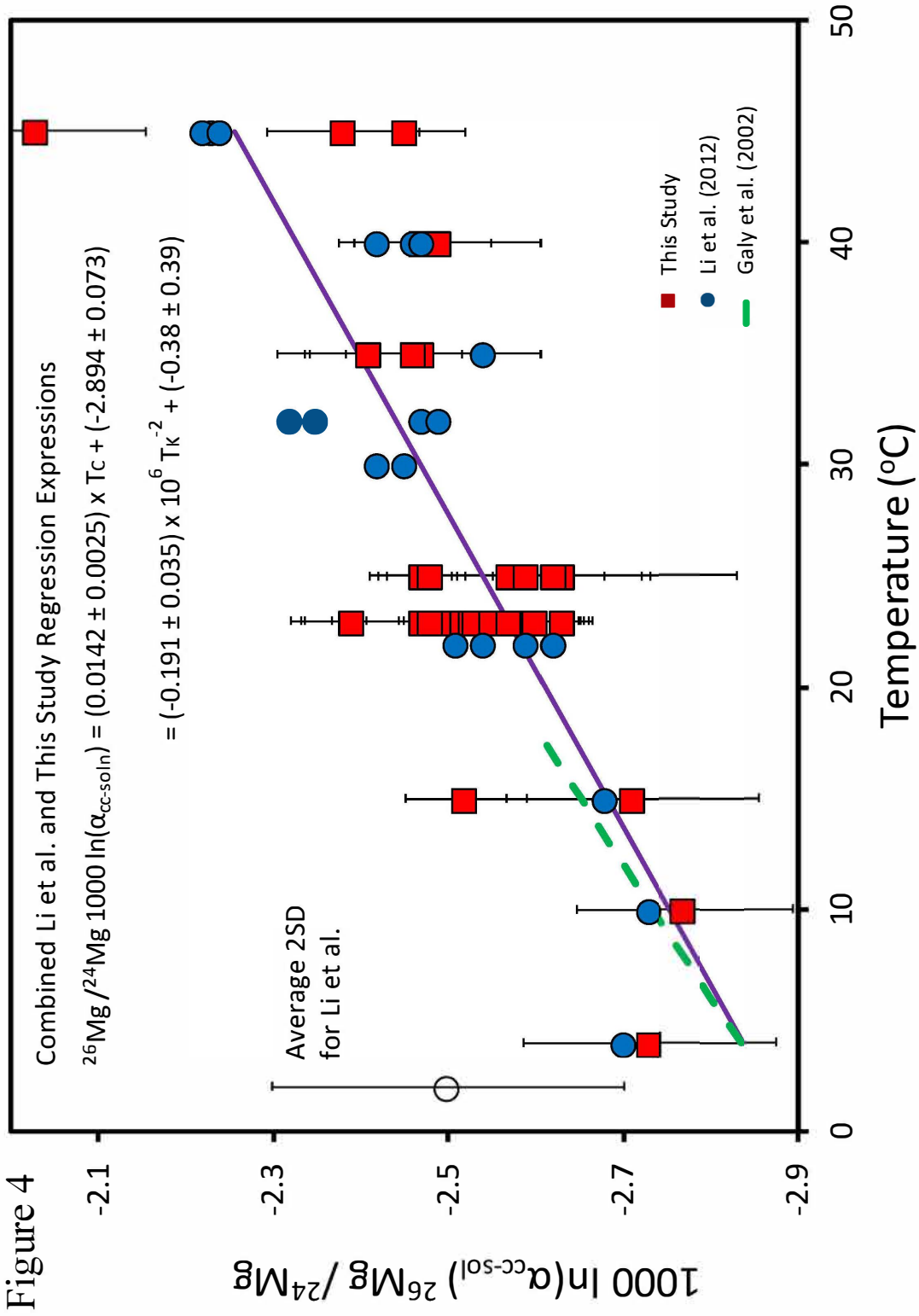
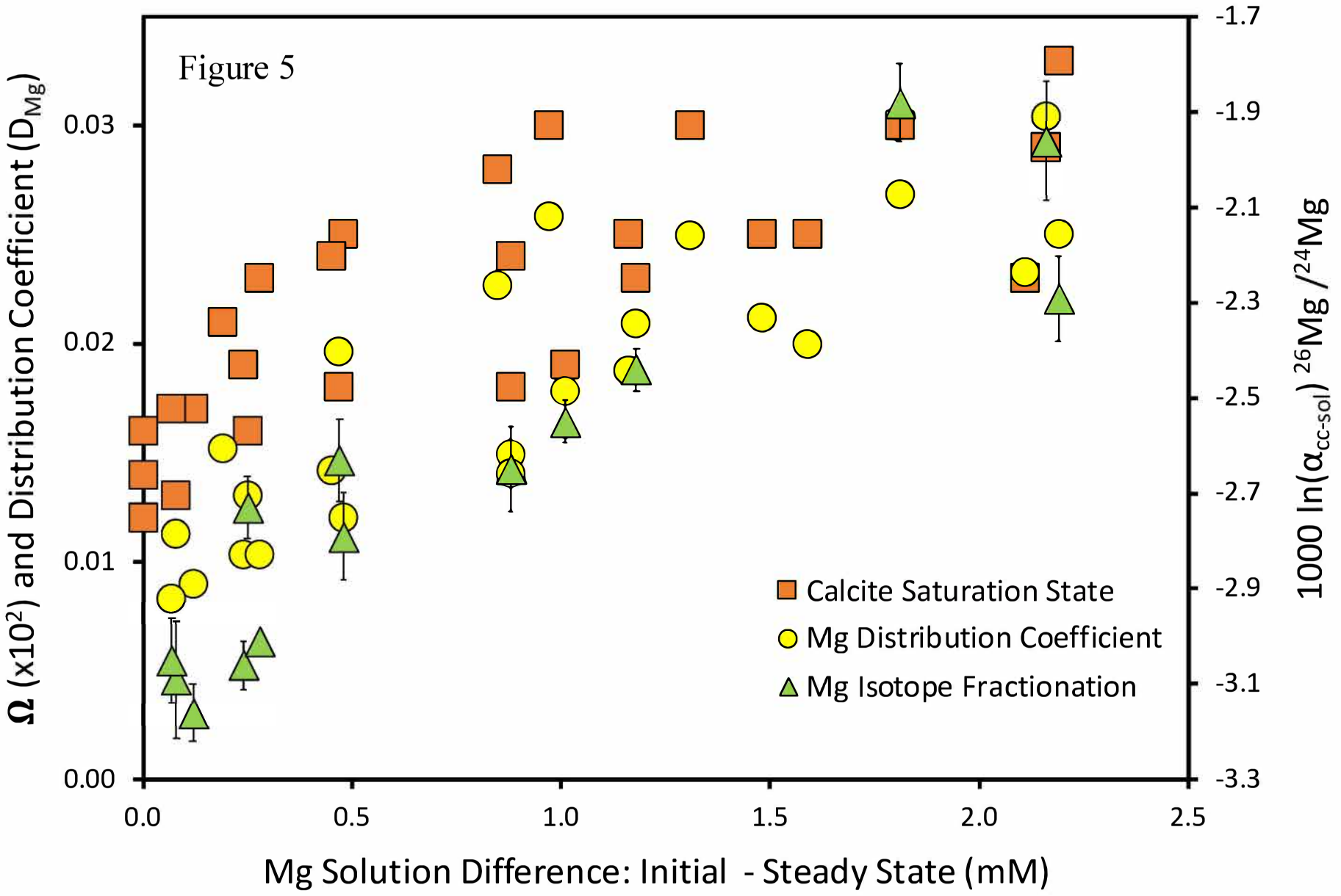
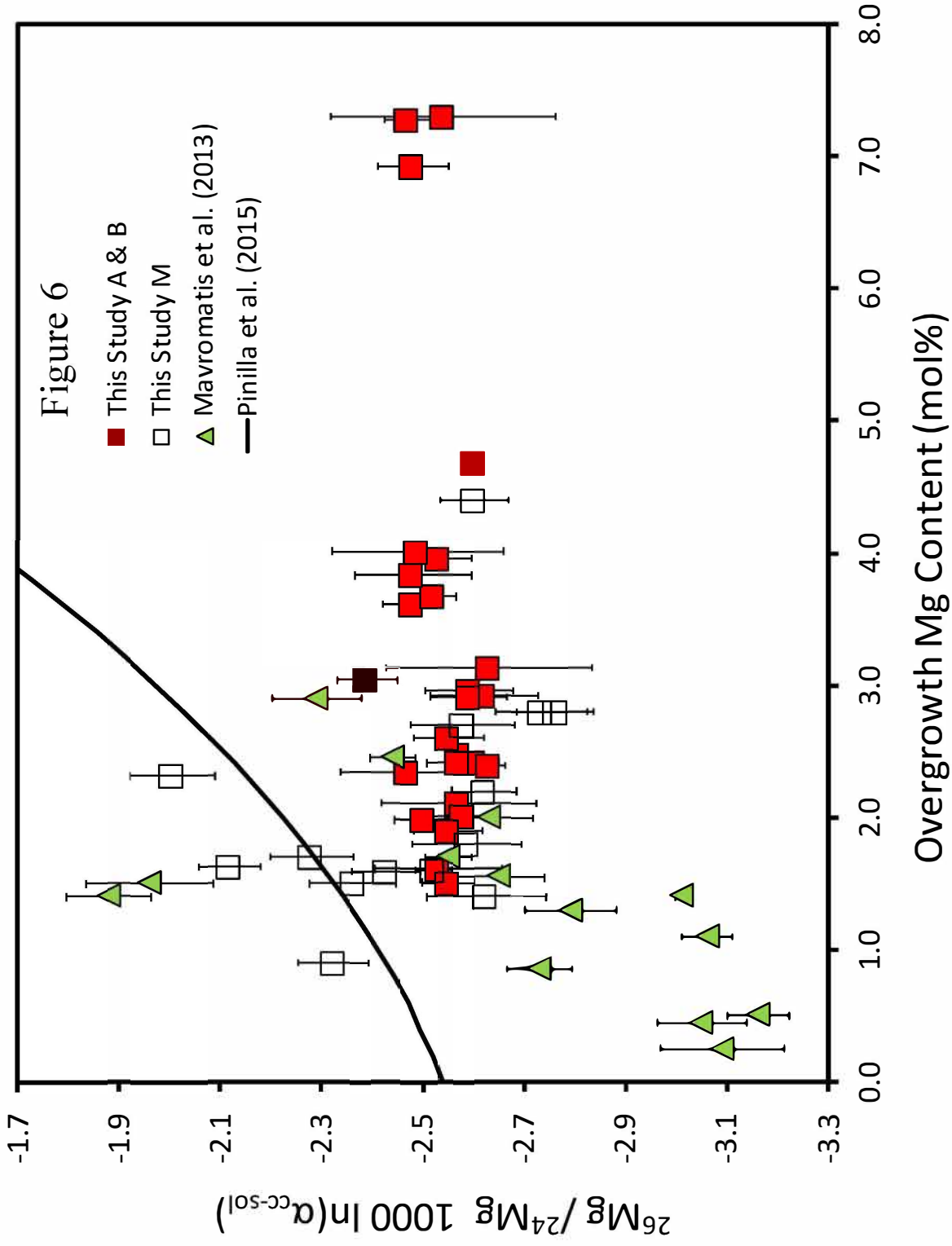
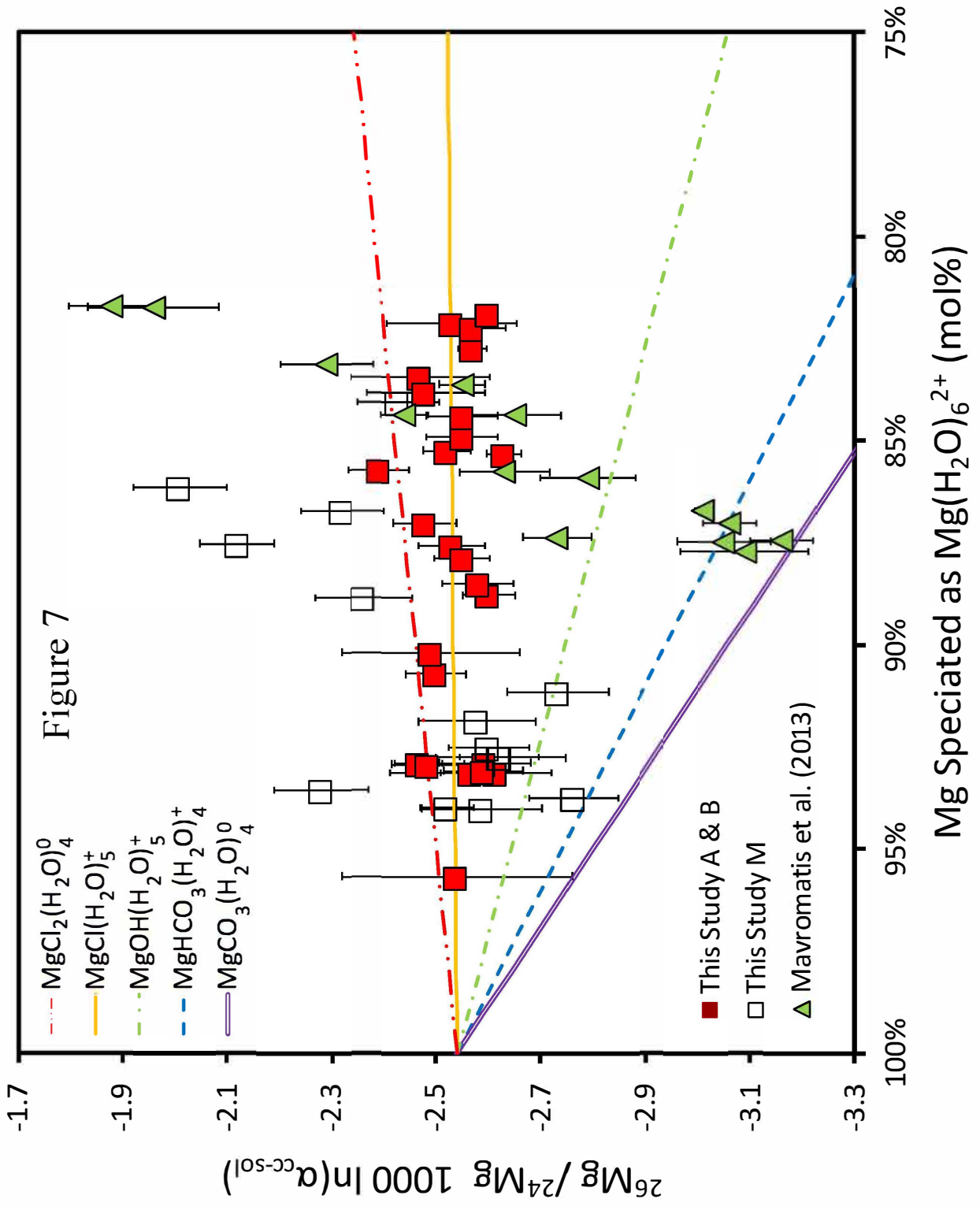

Combined Li et al. and This Study Regression Expressions
$^{26}Mg/^{24}Mg\ 1000\ ln(\alpha_{cc\text{-}soln}) = (0.0142 \pm 0.0025) \times T_C + (-2.894 \pm 0.073)$
$= (-0.191 \pm 0.035) \times 10^6\ T_K^{-2} + (-0.38 \pm 0.39)$
Average 2SD for Li et al.
This Study
Li et al. (2012)
Galy et al. (2002)
1000 ln($\alpha_{cc\text{-}sol}$) $^{26}Mg/^{24}Mg$
Temperature (°C)
-2.1
-2.3
-2.5
-2.7
-2.9
0
10
20
30
40
50

Figure 4


Figure 5
Ω (x10²) and Distribution Coefficient (D_Mg)
1000 ln(α_cc-sol) ²⁶Mg /²⁴Mg
Mg Solution Difference: Initial - Steady State (mM)
Calcite Saturation State
Mg Distribution Coefficient
Mg Isotope Fractionation
0.00
0.01
0.02
0.03
0.0
0.5
1.0
1.5
2.0
2.5
-1.7
-1.9
-2.1
-2.3
-2.5
-2.7
-2.9
-3.1
-3.3


Figure 6
This Study A & B
This Study M
Mavromatis et al. (2013)
Pinilla et al. (2015)
$^{26}Mg/^{24}Mg$ 1000 ln($\alpha_{cc\text{-}sol}$)
-1.7
-1.9
-2.1
-2.3
-2.5
-2.7
-2.9
-3.1
-3.3
0.0
1.0
2.0
3.0
4.0
5.0
6.0
7.0
8.0
Overgrowth Mg Content (mol%)


Figure 7
$MgCl_2(H_2O)^0_4$
$MgCl(H_2O)^+_5$
$MgOH(H_2O)^+_5$
$MgHCO_3(H_2O)^+_4$
$MgCO_3(H_2O)^0_4$
This Study A & B
This Study M
Mavromatis et al. (2013)
$^{26}Mg/^{24}Mg$ 1000 ln(α_{cc-sol})
-1.7
-1.9
-2.1
-2.3
-2.5
-2.7
-2.9
-3.1
-3.3
100%
95%
90%
85%
80%
75%
Mg Speciated as $Mg(H_2O)_6^{2+}$ (mol%)

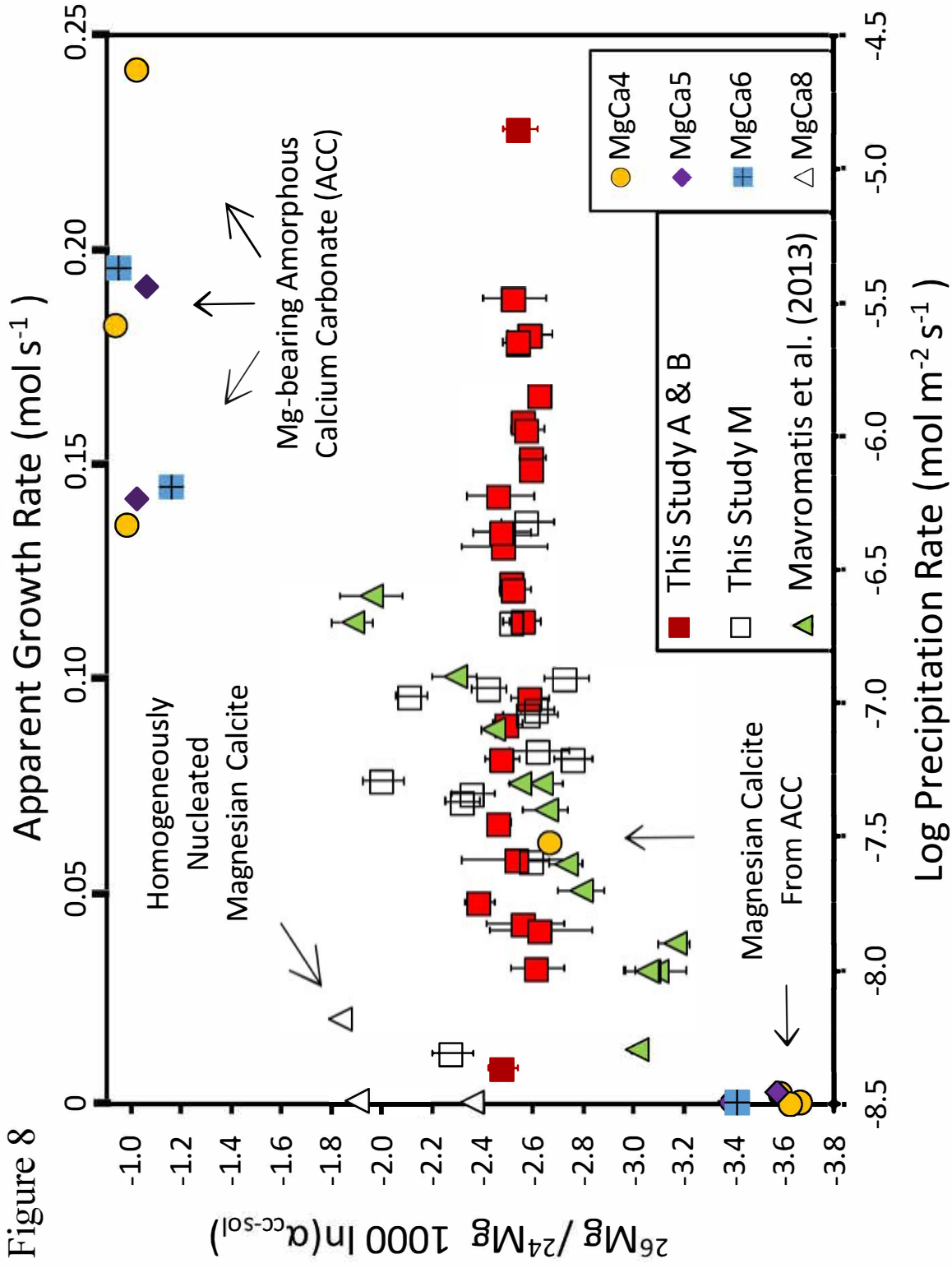
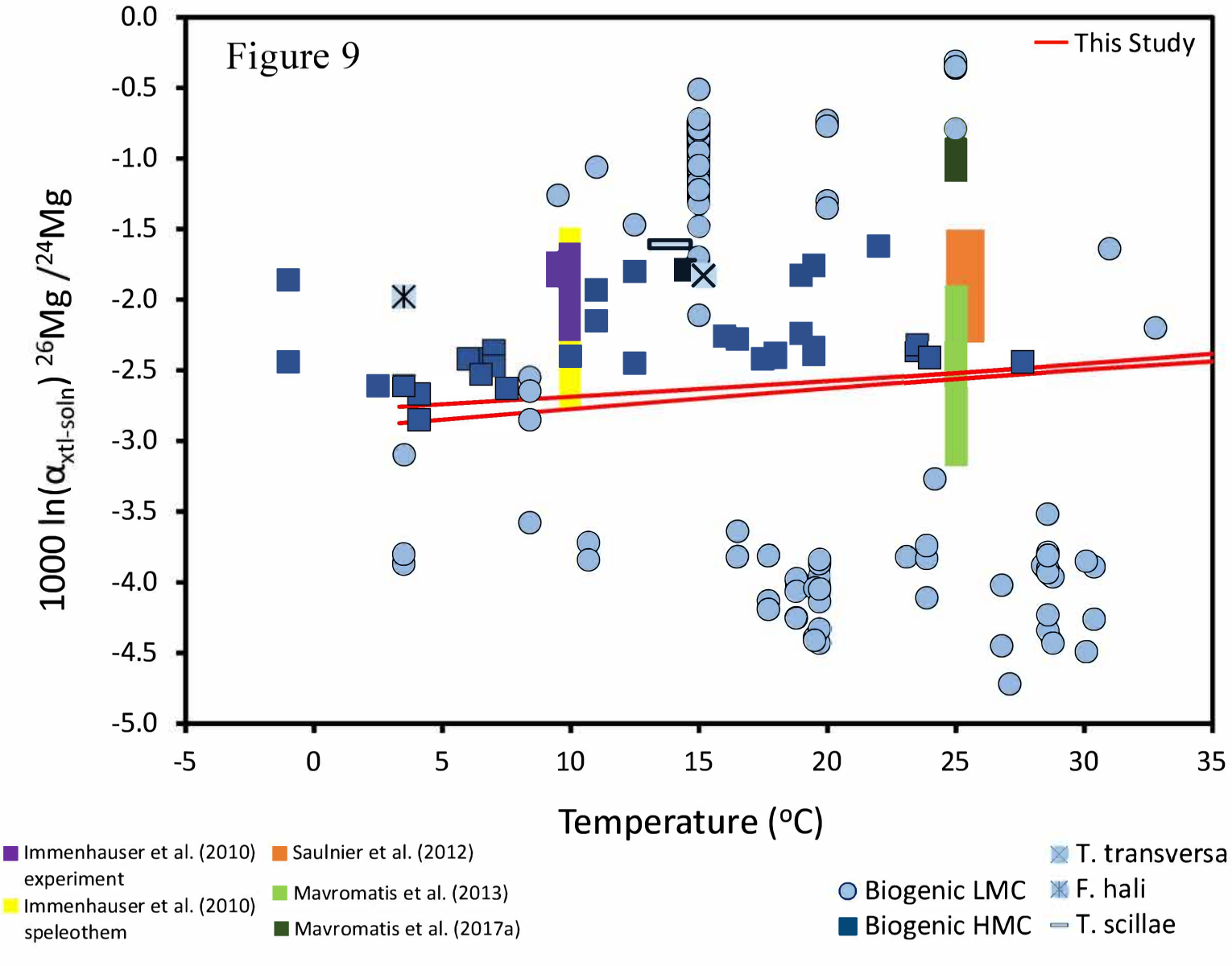
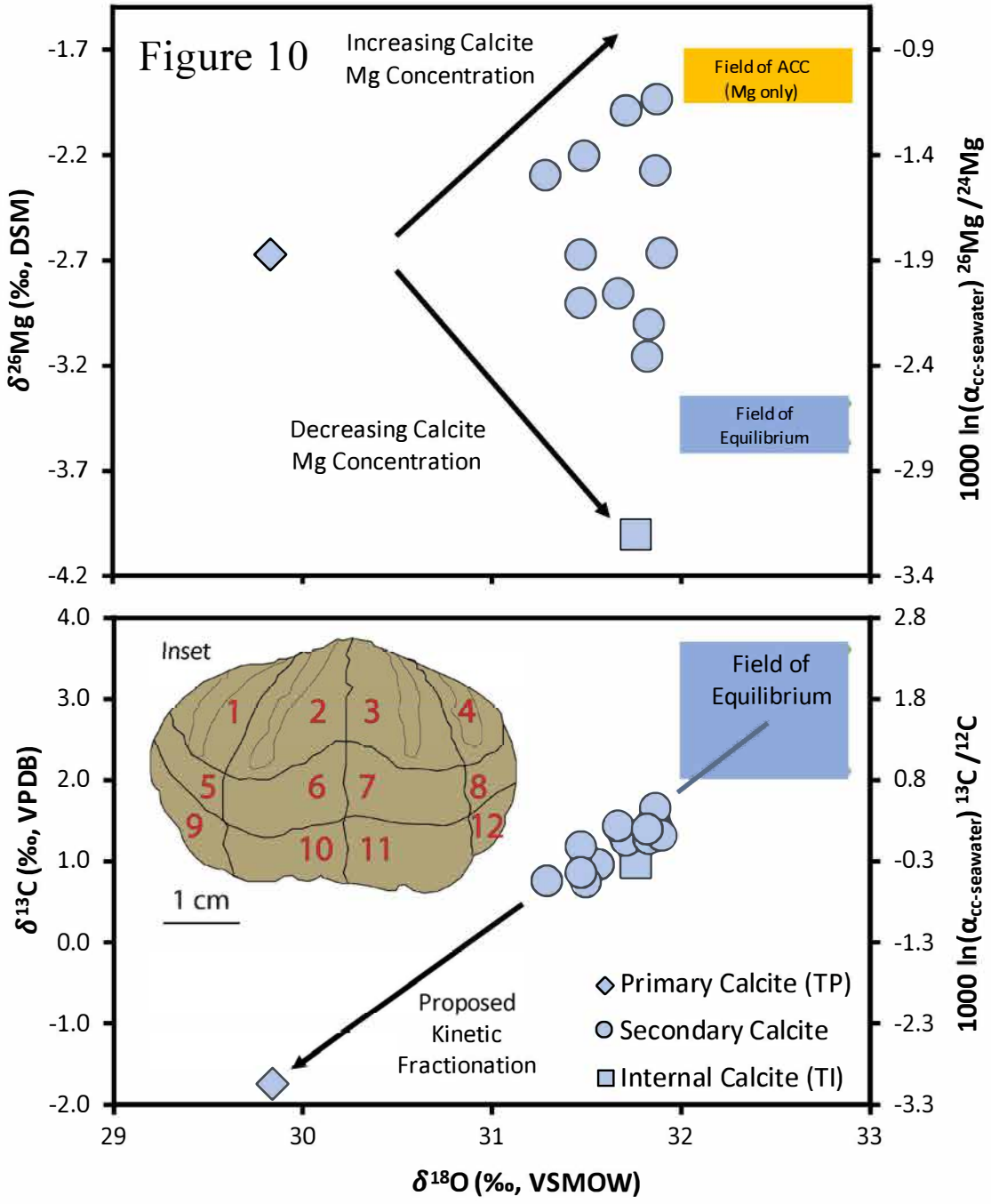

Apparent Growth Rate (mol s-1)
Log Precipitation Rate (mol m-2 s-1)
26Mg /24Mg 1000 ln(αcc-sol)
Homogeneously Nucleated Magnesian Calcite
Mg-bearing Amorphous Calcium Carbonate (ACC)
Magnesian Calcite From ACC
MgCa4
MgCa5
MgCa6
MgCa8
This Study A & B
This Study M
Mavromatis et al. (2013)

Figure 8


Figure 9
This Study
0.0
-0.5
-1.0
-1.5
-2.0
-2.5
-3.0
-3.5
-4.0
-4.5
-5.0
1000 ln(α xtl-soln) 26Mg /24Mg
-5
0
5
10
15
20
25
30
35
Temperature (°C)
Immenhauser et al. (2010) experiment
Immenhauser et al. (2010) speleothem
Saulnier et al. (2012)
Mavromatis et al. (2013)
Mavromatis et al. (2017a)
Biogenic LMC
Biogenic HMC
T. transversa
F. hali
T. scillae


Figure 10
Increasing Calcite
Mg Concentration
Field of ACC
(Mg only)
Field of
Equilibrium
Decreasing Calcite
Mg Concentration
-1.7
-2.2
-2.7
-3.2
-3.7
-4.2
-0.9
-1.4
-1.9
-2.4
-2.9
-3.4
δ26Mg (‰, DSM)
1000 ln(αcc-seawater) 26Mg /24Mg
Inset
1
2
3
4
5
6
7
8
9
10
11
12
1 cm
Field of
Equilibrium
Proposed
Kinetic
Fractionation
Primary Calcite (TP)
Secondary Calcite
Internal Calcite (TI)
4.0
3.0
2.0
1.0
0.0
-1.0
-2.0
2.8
1.8
0.8
-0.3
-1.3
-2.3
-3.3
δ13C (‰, VPDB)
1000 ln(αcc-seawater) 13C /12C
29
30
31
32
33
δ18O (‰, VSMOW)

Factors Influencing the Magnesium Isotope Composition of Magnesian Calcite: Supplemental Material

Nicholas P. Levitt[1,†], Christopher S. Romanek[2], Brian L. Beard[1], Weiqiang Li[1,3], Suvankar Chakraborty[4], and Clark M. Johnson[1]

[1]NASA Astrobiology Institute and
Department of Geoscience
University of Wisconsin-Madison
1215 W Dayton Street
Madison, Wisconsin, USA
53706

[2]NASA Astrobiology Institute and
Department of Earth and Environmental Sciences
Furman University
Greenville, South Carolina, USA
29613

[3]State Key Laboratory for Mineral Deposits Research, School of Earth Sciences and Engineering, Nanjing University, Nanjing, Jiangsu 210093, PR China

[4]Department of Biology and Department of Geology and Geophysics
University of Utah
257 S 1400 E
Salt Lake City, Utah, USA
84112

[†]Corresponding Author's Contact
E-mail: nlevitt@wisc.edu
Tel: (608) 262-8960
Fax: (608) 262-0693

Manuscript to be submitted to Geochimica et Cosmochimica Acta
Submission Date: TBD

1 Supplemental Methodology Section

1.1 Accuracy of Mg Isotope Measurements

Accuracy of sample analysis was appraised by analyzing test solutions prepared using an in-house Mg standard (HPS Mg solution, Lot# 909104, High Purity Standards, Charleston, South Carolina, USA) and a calcite matrix designed to mimic the experimental products. Specifically, the high Ca/Mg ratios (average of 94, Table SM1) of precipitation products requires a rigorous demonstration of effective Mg isolation without alteration of its isotope composition. Table SM2 contains representative reproducibility for unknowns, which are typically ±0.10‰ or better for $^{26}Mg/^{24}Mg$. The external reproducibility and accuracy of Mg isotope compositions was assessed using several approaches. During the course of this study four standards were analyzed for their Mg isotope composition. The $\delta^{26}Mg$ for DSM3 was 0.03 ±0.09‰ (n= 111; 2-SD), Cambridge 1 was -2.58 ±0.13‰ (n= 98; 2-SD), HPS-932001 was -2.88 ±0.12‰ (n= 58; 2-SD), and SRM-980 was -4.10 ±0.15‰ (n= 71; 2-SD). The accepted values of these standards are 0.01‰, -2.57‰, -2.91‰, and -4.14‰, respectively (Galy et al., 2003). All unknowns were measured at least twice and all but eight experimental products were measured three or more times. Several products were measured multiple times during different analytical sessions and/or processed and analyzed as completely separate samples, including ion-exchange chromatography. Several formulations of test solutions were analyzed concurrently with the unknown samples, including formulations that included Fe, Mn, and Al (Table SM2a). Ca/Mg ratios of test solutions ranged up to 330 without significant deviation in $^{26}Mg/^{24}Mg$ ratios ($\leq \pm$ 0.2‰) compared to the known isotope composition (Table SM2). Figure SM1 is a plot of deviation in $\delta^{26}Mg$ relative to yield.

Magnesium was isolated and purified from other cations by ion-exchange chromatography before isotope analysis. Cation resin from Bio-Rad (Hercules, CA, USA) was used including AG MP-50 (100-200 mesh) for the first two stages and AG 50Wx8 (200-400 mesh) for the third stage. A fourth separation stage was performed to ensure any remaining Ca was removed using Eichrom (Lisle, IL, USA) Normal DGA resin (50-100 μm). Specific acid concentrations and volumes used, as well as additional information, are included in Section 2.2 below. All acids used in the procedure were prepared by sub-boiling distillation, water was from a water polisher that produces 18.2 megaohm-cm water, and acetone was Optima grade from Fisher Scientific. Recovery of Mg was 93± 27% (*n*=134, 2SD), as determined by MC-ICP-MS analysis of test solutions that were treated as samples. Total procedural blanks for the ion-exchange procedure were < 150 ng, which are negligible. Magnesium loss during processing, which may occur due to dry down and/or sorption to collection beakers and pipet tips, did not result in isotope fractionation, as shown by the Mg isotope analysis of test solutions prepared with Mg of known isotope compositions (Table SM2, Fig. SM1).

1.2 Mg purification

Magnesium was purified prior to isotope analysis by ion-exchange chromatography according to procedures reported by Li et al. (2012, 2014, 2015). Approximately 30 mg of calcite or 300 μL of reaction solution (target of 100 μg of Mg) was processed for Mg separation and isotope analysis. Calcite was dissolved in 2.2M ultra-pure HCl acid, and cations were converted to pure chloride salts before purification. Likewise, HCl was added to experimental solutions and repeatedly dried three times until

only solids remained. Magnesium was purified from other cations by ion-exchange chromatography before isotope analysis according to the following procedure:

Stage 1: Bio-Rad (Hercules, CA, USA) AG MP-50 (100-200 mesh) with column of 6.25mm ID and 93mm resin height

1) Condition resin with 10 mL of 2.2M HCl
2) Load sample in 0.25 mL of 2.2M HCl
3) Pass 0.2 mL of 2.2M HCl five times (5X)
4) Pass 0.5 mL of 2.2M HCl
5) Pass 1.0 mL of 2.2M HCl
6) Collect Mg by passing 8.75 mL of 2.2M HCl
7) Clean resin (of Ca) with 30 mL of 8M HCl twice (2X)
8) Rinse resin with 30 mL of de-ionized water twice (2X)
9) Perform this stage [Stage 1: Bio-Rad (Hercules, CA, USA) AG MP-50 (100-200 mesh) with column of 6.25mm ID and 93mm resin height] 2-3 times until the majority of Ca is removed as indicated by visual inspection (i.e. dried residual salt size and yellow color are consistent with standards processed as unknowns).

Stage 2: Bio-Rad (Hercules, CA, USA) AG MP-50 (100-200 mesh) with column of 4.9mm ID and 18.5mm resin height

1) Clean resin with 1 mL of 8M HCl
2) Rinse resin with 1 mL of de-ionized water twice (2X)
3) Condition resin with 1 mL total volume of a 7% 0.5M HCl and 93% acetone mixture by volume. The solution made fresh each day.

4) Load sample in 0.5 mL total volume of a 7% 0.5M HCl and 93% acetone mixture by volume.
5) Pass 0.5mL of HCl/acetone solution four times (4X) to elute Mn
6) Collect Mg by passing 1 mL of 8M HCl three times (3X)
7) Clean resin with 1 mL of 8M HCl three times (3X)
8) Rinse resin with 1 mL of de-ionized water three times (3X)

Stage 3: Bio-Rad (Hercules, CA, USA) AG 50Wx8 (200-400 mesh) with column of 4.9mm ID and 18.5mm resin height

1) Clean resin with 1 mL of 4.5M HNO_3 three times (3X)
2) Condition resin with 1 mL of 0.5M HNO_3
3) Load sample in 0.2 mL of 0.5M HNO_3
4) Pass 1 mL of 0.5M HNO_3 five times (5X) to elute Na
5) Collect Mg by passing 1 mL of 1.0M HNO_3 five times (5X)
6) Collect Mg by passing 0.5 mL of 1.5M HNO_3 five times (5X)
7) Clean resin (of Al and Fe) with 1 mL of 4.5M HNO_3 three times (3X)
8) Rinse resin with 1 mL of de-ionized water three times (3X)
9) Alternatively, discard resin after Mg collection

Stage 4: Eichrom (Lisle, IL, USA) Normal DGA resin (50-100 µm) with column of 4.9mm ID and 18.5mm resin height

1) Clean resin with 1 mL of 0.1M HCl
2) Wash resin with 1 mL of de-ionized water two times (2X)
3) Condition resin with 1 mL of 2.0M HNO_3
4) Load sample in 0.2 mL of 2.0M HNO_3

5) Collect Mg by passing 1 mL of 2.0M HNO_3 three times (3X)
6) Clean resin (of Ca) with 1 mL of 0.1M HCl twice (2X)
7) Rinse resin with 1 mL of de-ionized water three times (3X)
8) DGA resin will react with HNO_3 over time. Replace often.

2. Calcite Seed Crystals and Overgrowths

Electron microprobe micro analysis (EPMA) inspection of seed crystals and experimental products confirm the analyses performed by ICP-AES. The seed crystals used for Experimental Set B contained Mg in concentrations below the EPMA detection limit (≤ 0.3 mol%, Fig. SM2(a)). The Mg content of seed crystals used for Experimental Set M ranged from ≤ 0.3 to 3.5 mol%, with an average value of 1.6 ± 0.9 mol% (n = 25). EPMA used for spot/point assessments and X-ray mapping revealed that overgrowth rims of experimental products A19 and A20 averaged approximately 1 micron in width (Fig. 2(a and c)). This distance is only twice as wide as the spatial resolution of the technique and therefore provides only semi-quantitative information compared to bulk dissolution. The Mg content of Experimental Sets A and B was observed to generally agree with bulk ICP-AES measurements and vary between different grains of a given experimental product by up to 0.5 mol% Mg. The concentration distribution of Mg in the experimental products of Set M vary widely. Some calcite grains of this group show a relatively homogeneous Mg distribution across seed crystals and overgrowths (Fig. 2(e)). Magnesium was also observed to be concentrated at the interior or exterior of individual grains for the majority of experiments and material produced (Fig. SM2(e)). Specifically, these products have overgrowth Mg concentrations lower than the seed crystals, Mg concentrated in the overgrowth of a grain, or zones of high Mg between the center of a

grain and the rim. No apparent solution chemistry relation can be used to explain the observed behavior, and Mg concentration patterns are often mixed within a set of experimental product grains for set M. It is clear, therefore, that the distribution of Mg in product calcite of Experimental Set M is quite heterogeneous and complex. For this reason, the data resulting from Experimental Set M is not factored into our assessment of the equilibrium Mg isotope fractionation between Mg calcite and solution, although Set M may provide insight into the effects of pre-existing Mg during Mg isotope fractionation.

3. Other Studies of Mg Partitioning as a Function of Solution Chemistry

In this section, we review several records of magnesian calcite (and precursors) formation and outline some possible explanations for deviations from the (apparent equilibrium) relation between solution Mg/Ca ratio and D_{Mg} (Fig 3). To enhance figure symbol visibility/clarity and accommodate the large range of reported solution Mg/Ca and D_{Mg} values in the literature, we have prepared two figures for lower values (Fig. SM3) and higher values (Fig. SM4). Previous investigators have published extensively on magnesian calcite precipitated under a variety of experimental conditions utilizing the chemo-stat method, and many have used solutions similar to seawater with Mg/Ca ratios of approximately 5. The D_{Mg} values resulting from the experiments of Mucci and Morse (1984), as well as the Gulf Stream seawater experiments of Burton and Walter (1987; 1991), all at 25°C, agree with the relation between Mg/Ca ratio in solution and Mg composition of calcite described by Mucci and Morse (1983, Figs. S3-S4). Slight positive deviations from the expected D_{Mg} value of ~0.018 for chemo-stat experiments

were attributed to the presence of sulfate in seawater for Zhong and Mucci (1989) and Mucci et al. (1989).

Studies of magnesian calcite formation using Mg/Ca solution ratios below those of seawater (Figs. S3-S4) include Howson et al. (1987), Huang and Fairchild (2001), Oomori et al. (1987), Mavromatis et al. (2017), and Saulnier et al. (2012). The D_{Mg} values determined from these studies are generally lower than those predicted by the relation described by Mucci and Morse (1983), which may be due to differences in precipitation mechanism (e.g., Huang and Fairchild, 2001) or an underestimation of calcite Mg/Ca ratio (e.g., Howson et al., 1987). Importantly, most of these studies were done before the influence of amorphous or hydrated calcium carbonate was formally investigated, and it is possible ACC may have played a role in Mg partitioning. For example, Saulnier et al. (2012) report D_{Mg} values that are both significantly higher and lower than that predicted for calcite under their experimental conditions (Fig. SM4). The authors report occurrences of aragonite, magnesite, and vaterite along with calcite that was homogeneously nucleated, but they do not mention the possibility of an amorphous or hydrated phase prior to calcite growth. Based on recent work, both higher-than-predicted and lower-than-predicted D_{Mg} values could result from ACC precursors, depending on experimental conditions. Specifically, Purgstaller et al. (2016) report a significant decrease in D_{Mg} over time as ACC recrystallizes to calcite. Additional evidence for the confounding effects of ACC and hydrated calcium carbonate are provided by the large range of D_{Mg} values (Fig. SM4) for pure ACC reported by Blue and Dove (2015), and calcite formed from these precursors according to Loste et al. (2003) and Jimenez-Lopez et al. (2004).

4. Detailed Relations between D-Mg and Experimental Conditions

Over the range of experimental conditions in the present study, there are no correlations between D_{Mg} and parameters other than temperature and solution Mg/Ca ratio. We have investigated Mg concentrations that range an order of magnitude from 5.1 to 50.1 mM (Fig. SM5) and Mg/Ca ratios between 0.41 to 3.93. We have also added NaCl to experimental solutions in the concentration range of 200 mM to 800 mM (Fig. SM6) and employed pCO_2 conditions which explore a wide range of values from 0.3% to 100% (Fig. SM7). Additionally, we find no correlation between D_{Mg} and precipitation rate (Fig. SM8) or saturation state (Fig. SM9). Our observed lack of relation between D_{Mg} and most parameters is in agreement with several previous chemo-stat studies, including those that studied the effects of pCO_2 (Hartley and Mucci, 1996), salinity (Zhong and Mucci, 1989), sulfate (Mucci et al., 1989), phosphate (Mucci, 1986), and precipitation rate (Mucci et al., 1989; Zhong and Mucci, 1989).

5. Additional Factors Potentially Related to Mg Isotope Fractionation

In Figures SM10-SM13, we plot the relation between Mg isotope fractionation and solution Mg concentration, D_{Mg}, ionic strength, and PCO_2. Specifically, we have investigated Mg concentrations that range an order of magnitude from 5.1 to 50.1 mM (Fig. SM10) and Mg/Ca ratios between 0.41 to 3.93. These concentrations produce partition coefficients that similarly do not correlate with isotope fractionation (Fig. SM11). We have also added NaCl to experimental solutions in the concentration range of 200 mM to 800 mM in order to assess a possible salt effect related to the work of Mavromatis et al. (2013, Fig. SM12). Additionally, we have employed pCO_2 conditions which explore a wide range of values from 0.3% to 100% (Fig. SM13). This parameter is

also indirectly considered in speciation calculations (Table SM3) because dissolved CO_2 contributes to DIC that can couple with Mg to form ion pairs. Recent work also suggests that DIC plays a role in the kinetics and mechanisms of carbonate mineral growth as related to isotope fractionation (Kluge et al., 2014; Bajnai et al., 2018; Levitt et al., 2018). Despite this, we find no first-order effect on Mg isotope partitioning related to the partial pressure of CO_2 used during our experiments (Fig. SM13). In summary, solution Mg concentration, D-Mg, ionic strength, and pCO_2 have no effect on Mg isotope fractionation over the range of experimental conditions studied.

Table S1: Starting and Ending Experimental Conditions and Uncertainty due to Overgrowth

	Experiment Identification	Experiment Length (h)	Temp (° C)*	pCO2 (%)	Start pH	End pH	Start Ca^{2+} (mM)	End Ca^{2+} (mM)	Start Mg^{2+} (mM)	End Mg^{2+} (mM)	Start Alkalinity (meq)	End Alkalinity (meq)	Start Ionic Strength (mol kg^{-1})	End Ionic Strength (mol kg^{-1})	Start Saturation Ω	End Saturation Ω	Seed Calcite (mg)	Over-growth Mass (mg)	Total Bulk Calcite Ca:Mg	Total Carbonate Mol% Mg	Over-growth** Mol% Mg	Overgrowth Uncertainty Minimum Mol% Mg	Overgrowth Uncertainty Maximum Mol% Mg
*	C-22	151	22	3.0%	7.1	6.5	15.0	14.7	50.2	50.1	10.0	10.0	0.20	0.20	4.7	4.6	79	56	33	3.0%	7.3%	7.1%	7.6%
Experimental Set "A"	A1	48	35	3.0%	7.2	7.2	14.9	12.4	49.8	49.4	10.0	9.1	0.20	0.19	6.0	7.1	82	127	127	4.5%	7.4%	7.2%	7.7%
	A2	72	25	3.0%	7.1	7.1	15.0	14.7	49.9	49.8	10.5	9.9	0.20	0.20	4.8	4.6	75	35	43	2.3%	7.3%	6.5%	8.2%
	A3	72	25	2.1%	7.2	7.2	15.0	14.5	50.0	49.9	10.4	9.8	0.20	0.20	6.5	5.9	75	61	32	3.1%	6.9%	6.5%	7.4%
	A4	72	35	2.1%	7.2	7.2	15.0	14.4	50.0	49.9	7.1	5.6	0.20	0.19	3.7	4.6	74	90	90	4.5%	8.2%	7.8%	8.6%
	A5	36	40	2.1%	7.5	7.5	3.0	2.5	10.0	10.0	10.3	9.1	0.05	0.05	5.1	6.1	75	68	68	4.6%	9.6%	9.0%	10.2%
	A6	8	45	2.1%	7.5	7.5	3.0	2.6	10.0	10.0	10.6	9.3	0.05	0.04	5.9	7.5	73	51	24	4.2%	10.2%	9.5%	11.1%
	A7	72	25	2.1%	7.4	7.4	3.0	2.9	10.0	10.0	10.2	10.0	0.05	0.05	3.2	3.1	71	14	287	0.3%	2.1%	1.6%	2.9%
	A8	7	40	1.7%	7.6	7.6	3.0	2.4	10.0	10.0	10.2	9.4	0.05	0.04	6.2	7.5	72	61	27	3.7%	8.1%	7.6%	8.7%
	A9	96	25	1.7%	7.5	7.5	3.0	2.7	10.1	10.1	10.1	10.0	0.05	0.05	4.1	3.5	73	18	160	0.6%	3.1%	2.6%	4.0%
	A10	120	15	2.1%	7.2	7.2	15.0	14.8	50.0	49.9	10.2	10.1	0.20	0.20	4.6	4.6	77	15	157	0.6%	3.8%	3.0%	5.2%
	A11	120	25	1.7%	7.5	7.5	3.1	3.0	10.3	10.3	10.9	10.5	0.05	0.05	4.6	4.6	72	16	186	0.5%	2.9%	2.3%	3.9%
	A12	72	35	1.7%	7.6	7.6	3.0	2.4	10.3	10.2	10.9	9.3	0.05	0.05	5.1	6.6	80	76	22	4.5%	9.3%	8.8%	9.8%
	A13	36	35	1.7%	7.6	7.6	3.0	2.9	9.6	9.6	10.0	10.0	0.05	0.05	7.4	7.6	75	15	68	1.5%	8.9%	7.0%	12.1%
	A14	0.4	45	1.7%	7.6	7.6	3.0	2.9	10.0	9.9	10.0	10.0	0.05	0.05	10.0	10.5	78	5	281	0.4%	5.9%	3.3%	29.5%
	A15	0.5	25	0.3%	8.2	8.2	2.9	2.6	10.2	10.2	10.6	10.1	0.05	0.05	20.0	17.0	74	16	187	0.5%	3.0%	2.4%	3.9%
	A16	18	10	0.3%	8.1	8.1	3.3	3.1	10.6	10.5	10.0	10.0	0.05	0.05	11.2	11.6	76	20	173	0.6%	2.8%	2.3%	3.5%
	A17	18	15	0.3%	8.2	8.2	2.7	2.6	10.3	10.3	10.9	10.1	0.05	0.05	11.5	12.6	78	39	77	1.3%	3.9%	3.6%	4.4%
	A18	60	4	0.3%	8.1	8.1	3.0	2.8	10.2	10.2	10.9	10.8	0.05	0.05	7.6	8.5	75	27	182	0.5%	2.1%	1.8%	2.4%
	A19	72	45	3.0%	7.3	7.2	5.0	4.9	50.5	50.5	9.9	9.1	0.17	0.17	4.1	3.3	78	32	40	0.7%	2.5%	2.2%	2.8%
	A20	--	--	--	--	--	--	--	--	--	--	--	--	--	--	--	--	--	--	--	--	--	--
Experimental Set "B"	B1	71	23	70%	6.3	6.1	23.3	23.3	21.4	22.2	32.9	32.1	0.15	0.16	2.9	1.2	59	79	67	1.0%	2.9%	2.8%	3.1%
	B2	71	23	70%	6.3	6.3	22.9	23.5	20.8	21.2	33.0	34.6	0.35	0.35	2.2	1.8	80	4	637	0.2%	3.6%	1.9%	39.7%
	B3	71	23	40%	6.5	6.5	23.1	21.2	21.8	22.1	32.3	28.4	0.15	0.15	5.0	1.8	71	253	37	1.6%	3.7%	3.6%	3.7%
	B4	71	23	40%	6.6	6.5	22.6	21.3	20.9	21.3	32.6	30.3	0.35	0.34	4.1	1.4	65	220	35	1.7%	4.0%	3.9%	4.0%
	B5	71	23	40%	6.5	6.5	23.6	23.2	22.3	20.9	32.4	34.5	0.55	0.55	3.3	3.2	65	15	213	0.4%	3.0%	2.4%	4.2%
	B6	65	23	75%	6.4	6.0	33.7	30.9	15.6	16.4	29.8	22.6	0.17	0.15	4.5	0.9	54	378	35	1.1%	2.3%	2.3%	2.4%
	B7	65	23	75%	6.3	6.1	43.5	38.0	20.8	21.1	39.0	26.7	0.31	0.39	4.7	1.4	58	569	35	1.1%	2.4%	2.3%	2.4%
	B8	65	23	75%	6.3	6.0	54.1	43.0	25.4	25.6	48.5	23.0	0.66	0.61	5.6	0.9	64	1062	26	1.2%	2.4%	2.4%	2.4%
	B9	43	23	100%	6.2	6.0	32.7	34.7	15.2	18.1	30.7	23.8	0.16	0.17	2.3	1.1	64	556	51	1.2%	2.5%	2.4%	2.5%
	B10	43	23	100%	6.2	6.1	44.0	41.0	20.8	21.6	38.8	31.8	0.41	0.40	3.3	1.5	71	580	47	0.9%	2.0%	2.0%	2.0%
	B11	43	23	100%	6.3	6.0	63.2	46.5	28.7	25.9	48.1	30.7	0.70	0.63	5.6	1.1	72	1239	45	1.3%	2.6%	2.6%	2.6%
	B12	5	23	100%	6.0	6.0	34.9	33.7	16.0	16.6	30.8	28.3	0.17	0.17	1.5	1.0	57	179	46	0.7%	1.6%	1.6%	1.6%
	B13	5	23	100%	6.2	6.2	43.7	42.2	20.7	20.7	38.2	36.9	0.41	0.41	2.6	2.3	75	165	57	0.6%	1.5%	1.5%	1.6%
	B14	5	23	100%	6.1	6.0	-	45.8	-	25.3	48.1	30.6	-	0.63	-	1.2	67	904	41	0.9%	1.9%	1.9%	1.9%
	B15	70	23	50%	6.3	6.3	23.1	21.8	10.7	11.0	21.2	17.7	0.11	0.11	1.9	1.4	65	165	88	1.0%	2.4%	2.4%	2.5%
	B16	72	23	50%	6.3	5.9	23.0	23.1	10.5	11.0	20.7	21.5	0.31	0.11	1.3	0.9	73	79	103	0.6%	2.0%	1.9%	2.1%
	B17	47	23	30%	6.7	6.7	22.7	21.8	20.6	20.9	31.7	30.6	0.55	0.54	5.5	4.3	62	204	58	1.7%	4.0%	3.9%	4.1%
	B18	47	23	30%	6.7	6.5	22.5	20.8	20.3	20.6	31.9	29.4	0.74	0.74	5.0	2.5	70	260	62	1.6%	3.8%	3.8%	3.9%
	B19	47	23	30%	6.6	6.5	22.0	19.2	20.0	20.4	31.9	26.2	0.94	0.93	3.4	1.5	67	427	108	2.1%	4.7%	4.6%	4.7%
Experimental Set "M"	M1	144	23	7%	6.8	6.7	-	11.5	-	5.4	-	8.7	-	0.06	-	1.9	61	144	55	1.8%	1.8%	1.8%	1.8%
	M2	144	23	7%	7.0	7.0	-	6.6	-	5.1	-	9.0	-	0.04	-	2.9	50	81	35	2.4%	2.8%	2.8%	2.9%
	M3	646	23	11%	6.6	6.7	11.6	14.7	4.9	6.0	11.1	8.3	0.06	0.07	2.2	2.8	51	29	59	1.6%	1.7%	1.7%	1.7%
	M4	98	23	50%	6.3	6.3	21.9	20.7	9.7	9.9	9.5	13.9	0.10	0.10	1.6	1.9	64	75	69	1.5%	1.4%	1.4%	1.5%
	M5	98	23	50%	6.4	6.3	13.3	11.6	9.9	9.8	14.0	16.7	0.08	0.08	1.7	1.7	58	126	36	2.4%	2.8%	2.8%	2.8%
	M6	70	23	63%	6.4	6.4	10.2	15.1	19.2	15.2	11.1	13.6	0.10	0.10	1.0	2.0	74	24	23	2.3%	4.4%	4.0%	5.0%
	M7	89	23	97%	6.2	6.1	32.9	32.4	14.7	15.0	8.9	7.2	0.15	0.15	1.3	0.9	65	211	61	1.6%	1.6%	1.6%	1.6%
	M8	89	23	97%	6.2	NA	23.0	21.4	19.8	19.1	12.7	10.6	0.14	0.13	1.5	1.2	55	83	45	2.0%	2.2%	2.2%	2.2%
	M9	89	23	97%	6.3	6.2	25.6	23.5	28.5	29.6	13.9	13.8	0.17	0.17	2.0	1.3	53	401	37	2.6%	2.7%	2.7%	2.7%
	M10	42	23	75%	6.4	6.3	35.2	38.0	14.7	15.7	29.9	30.0	0.17	0.18	6.5	6.0	49	16	112	1.4%	0.9%	0.6%	1.0%
	M11	42	23	75%	6.4	6.4	25.7	27.9	28.0	30.2	42.8	37.1	0.19	0.20	6.9	6.9	46	39	64	1.6%	1.6%	1.6%	1.6%
	M12	47	23	75%	6.4	6.4	22.7	24.2	19.0	20.3	32.0	21.7	0.15	0.15	5.2	3.9	56	50	61	1.6%	1.6%	1.6%	1.6%
	M13	73	23	33%	6.5	6.4	11.4	17.8	9.6	15.1	16.7	26.3	0.08	0.12	2.4	4.2	67	40	65	1.6%	1.5%	1.5%	1.5%
	M14	43	23	75%	6.4	6.3	22.6	24.8	19.1	20.7	30.0	31.0	0.15	0.16	5.3	4.3	46	18	42	1.8%	2.3%	2.2%	2.5%

* Chemo-stat experiment reported by Li et al. (2012)

**Experimental Set "M" calculated based on a seed calcite content of 1.61 mol% Mg.

Table S2: Mg Isotope analyses of unknowns and Test Solutions illustrating typical precision and accuracy.

			Singe Day Average							Multi-Day Replication Average							Complete Replication Average						
Sample ID	Lab ID	Analysis Date	$\delta^{26/24}Mg_{DSM3}$	2-SD	$\delta^{25/24}Mg_{DSM3}$	2-SD	$\delta^{26/25}Mg_{DSM3}$	2-SD	number of analyses	$\delta^{26/24}Mg_{DSM3}$	2-SD	$\delta^{25/24}Mg_{DSM3}$	2-SD	$\delta^{26/25}Mg_{DSM3}$	2-SD	number of analyses	$\delta^{26/24}Mg_{DSM3}$	2-SD	$\delta^{25/24}Mg_{DSM3}$	2-SD	$\delta^{26/25}Mg_{DSM3}$	2-SD	number of analyses
M3	6M-028	1-Jul-16	-1.01	0.11	-0.54	0.09	-0.48	0.03	4														
Starting		20-Jun-16	-0.96	0.08	-0.50	0.04	-0.47	0.04	2	-0.99	0.10	-0.53	0.08	-0.48	0.03	6							
Solution	6M-029	1-Jul-16	-0.96	0.07	-0.50	0.04	-0.47	0.06	4														
		20-Jun-16	-0.95	0.02	-0.50	0.02	-0.46	0.02	2	-0.96	0.06	-0.50	0.03	-0.46	0.05	6							
	6M-030	1-Jul-16	-0.97	0.10	-0.51	0.05	-0.47	0.06	4														
		20-Jun-16	-0.96	0.04	-0.50	0.02	-0.49	0.04	2	-0.96	0.08	-0.50	0.04	-0.47	0.05	6	-0.97	0.08	-0.51	0.06	-0.47	0.04	18
M5	6M-40	6-Jul-17	-0.97	0.07	-0.51	0.06	-0.46	0.03	3														
Starting Soln.	6M-41	6-Jul-17	-0.95	0.09	-0.49	0.04	-0.46	0.07	3	–	--	–	–	–	–	–	-0.96	0.08	-0.50	0.05	-0.46	0.05	6
M7	6M-82	6-Jul-17	-0.98	0.05	-0.50	0.03	-0.49	0.03	3														
Starting Soln.	6M-83	6-Jul-17	-0.98	0.06	-0.53	0.01	-0.45	0.08	3	–	--	–	–	–	–	–	-0.98	0.05	-0.51	0.04	-0.47	0.06	6
B13	7M-31	16-Jul-17	-0.81	0.10	-0.44	0.04	-0.39	0.11	3														
Ending Soln.	7M-32	15-Jul-17	-0.90	0.18	-0.48	0.10	-0.40	0.03	3	–	--	–	–	–	–	–	-0.85	0.16	-0.46	0.08	-0.39	0.08	6
M2	6M-013	1-Jul-16	-0.89	--	-0.47	--	-0.44	--	1														
Ending		20-Jun-16	-0.88	0.03	-0.48	0.02	-0.42	0.03	2	-0.89	0.03	-0.48	0.02	-0.42	0.03	3							
Solution	6M-026	1-Jul-16	-0.94	0.03	-0.50	0.02	-0.45	0.02	4														
		20-Jun-16	-0.92	0.11	-0.47	0.03	-0.46	0.08	2	-0.93	0.07	-0.49	0.04	-0.45	0.05	6							
	6M-027	1-Jul-16	-0.93	0.10	-0.50	0.05	-0.44	0.04	4														
		20-Jun-16	-0.94	0.04	-0.51	0.03	-0.45	0.04	2	-0.94	0.08	-0.50	0.04	-0.44	0.04	6	-0.93	0.08	-0.49	0.04	-0.44	0.04	15
M3	6M-031	1-Jul-16	-0.96	0.03	-0.50	0.04	-0.48	0.03	4														
Ending		20-Jun-16	-0.92	0.09	-0.49	0.02	-0.44	0.08	2	-0.95	0.06	-0.49	0.04	-0.47	0.06	6							
Solution	6M-032	1-Jul-16	-0.89	0.07	-0.48	0.02	-0.43	0.05	4														
		20-Jun-16	-0.92	0.00	-0.48	0.04	-0.45	0.01	2	-0.90	0.06	-0.48	0.02	-0.44	0.05	6							
	6M-033	1-Jul-16	-0.96	0.12	-0.50	0.07	-0.47	0.05	3	–	--	–	–	–	–	–	-0.93	0.09	-0.49	0.04	-0.46	0.06	15
M5	6M-40	6-Jul-17	-0.92	0.04	-0.50	0.03	-0.44	0.01	3														
Ending Soln.	6M-41	6-Jul-17	-0.97	0.12	-0.51	0.06	-0.47	0.06	3	–	--	–	–	–	–	–	-0.94	0.10	-0.50	0.04	-0.45	0.05	6
M7	6M-85	6-Jul-17	-0.96	0.03	-0.51	0.04	-0.45	0.01	2														
Ending Soln.	6M-86	6-Jul-17	-0.95	0.01	-0.50	0.00	-0.44	0.02	2	–	--	–	–	–	–	–	-0.96	0.03	-0.51	0.03	-0.46	0.05	4
M10	6M-125	24-May-17	-0.88	0.16	-0.46	0.09	-0.43	0.07	4														
Ending Soln.		17-Jul-17	-0.96	0.09	-0.51	0.03	-0.45	0.06	4	-0.92	0.15	-0.49	0.08	-0.44	0.06	8	–	–	--	–	–	–	–
M14	3M-46	24-May-17	-0.92	0.01	-0.47	0.04	-0.46	0.05	3														
Ending Soln.		17-Jul-17	-0.97	0.05	-0.51	0.01	-0.48	0.06	3	-0.95	0.06	-0.49	0.05	-0.47	0.05	6	–	–	--	–	–	–	–
A1	3M-46	19-Dec-13	-4.78	0.01	-2.47	0.06	-2.33	0.05	3														
Calcite		11-Sep-17	-4.84	0.02	-2.48	0.04	-2.36	0.02	3	-4.81	0.07	-2.47	0.04	-2.34	0.05	6	–	–	--	–	–	–	–
A2	3M-47	19-Dec-13	-4.80	0.07	-2.49	0.04	-2.33	0.02	3														
Calcite		11-Sep-17	-4.83	0.03	-2.49	0.02	-2.35	0.03	3	-4.82	0.06	-2.49	0.03	-2.34	0.04	6	–	–	--	–	–	–	–
A3	3M-49	19-Dec-13	-4.85	0.09	-2.50	0.02	-2.37	0.07	3														
Calcite		12-Sep-17	-4.81	0.06	-2.48	0.08	-2.34	0.05	2	-4.83	0.08	-2.68	0.05	-2.56	0.07	5	–	–	--	–	–	–	–
A4	3M-50	19-Dec-13	-4.76	0.05	-2.48	0.02	-2.31	0.08	3														
Calcite		12-Sep-17	-4.76	0.19	-2.44	0.02	-2.33	0.15	2	-4.76	0.10	-2.65	0.04	-2.52	0.10	5	–	–	--	–	–	–	–
A5	3M-51	19-Dec-13	-4.83	0.03	-2.49	0.02	-2.35	0.05	3														
Calcite		12-Sep-17	-4.82	0.13	-2.46	0.10	-2.37	0.02	2	-4.82	0.07	-2.67	0.06	-2.56	0.04	5	–	–	--	–	–	–	–
A6	3M-52	19-Dec-13	-4.80	0.07	-2.47	0.03	-2.35	0.03	3														
Calcite		12-Sep-17	-4.78	0.03	-2.47	0.03	-2.31	0.03	2	-4.80	0.06	-2.66	0.03	-2.54	0.04	5	–	–	--	–	–	–	–
A7	3M-53	19-Dec-13	-4.93	0.06	-2.55	0.03	-2.40	0.04	3														
Calcite		12-Sep-17	-4.89	0.15	-2.55	0.10	-2.37	0.02	2	-4.92	0.09	-2.74	0.06	-2.59	0.05	5	–	–	--	–	–	–	–
A8	3M-55	19-Dec-13	-4.83	0.05	-2.50	0.01	-2.36	0.04	3														
Calcite		14-Sep-17	-4.86	0.16	-2.49	0.06	-2.37	0.10	3	-4.84	0.11	-2.50	0.04	-2.37	0.07	6	–	–	--	–	–	–	–
A9	3M-56	19-Dec-13	-4.94	0.05	-2.56	0.01	-2.38	0.01	2														
Calcite		14-Sep-17	-5.01	0.20	-2.59	0.11	-2.44	0.09	3	-4.98	0.17	-2.57	0.08	-2.41	0.09	5	–	–	--	–	–	–	–
A11	3M-58	19-Dec-13	-4.92	0.03	-2.55	0.01	-2.39	0.00	2														
Calcite		14-Sep-17	-4.99	0.10	-2.57	0.07	-2.44	0.05	3	-4.97	0.11	-2.57	0.05	-2.42	0.06	5	–	–	--	–	–	–	–
A12	3M-59	19-Dec-13	-4.77	0.10	-2.46	0.02	-2.31	0.06	2														
Calcite		15-Sep-17	-4.76	0.04	-2.46	0.01	-2.31	0.04	4	-4.76	0.06	-2.46	0.01	-2.31	0.04	6	–	–	--	–	–	–	–
A13	3M-60	20-Dec-13	-4.81	0.02	-2.49	0.04	-2.33	0.03	3														
Calcite		15-Sep-17	-4.83	0.18	-2.49	0.09	-2.35	0.11	4	-4.82	0.13	-2.49	0.07	-2.34	0.08	7	–	–	--	–	–	–	–
A14	3M-61	19-Dec-13	-4.76	0.05	-2.47	0.06	-2.31	0.02	3														
Calcite		14-Sep-17	-4.71	0.08	-2.44	0.10	-2.29	0.05	4	-4.73	0.08	-2.45	0.09	-2.30	0.04	7	–	–	--	–	–	–	–
A15	3M-62	19-Dec-13	-4.97	0.10	-2.55	0.03	-2.44	0.05	2														
Calcite		14-Sep-17	-4.93	0.08	-2.53	0.07	-2.41	0.02	4	-4.94	0.09	-2.54	0.06	-2.42	0.04	6	–	–	--	–	–	–	–
A17	3M-65	20-Dec-13	-5.09	0.14	-2.63	0.05	-2.47	0.10	3														
Calcite		12-Sep-17	-5.03	0.01	-2.59	0.03	-2.45	0.01	3	-5.09	0.11	-2.64	0.05	-2.47	0.06	6	–	–	--	–	–	–	–
A18	6M-191	11-Nov-16	-5.08	0.08	-2.63	0.05	-2.47	0.06	3														
Calcite		12-Sep-17	-5.10	0.14	-2.65	0.06	-2.47	0.07	3	-5.09	0.11	-2.64	0.05	-2.47	0.06	6	–	–	--	–	–	–	–

Table S2 (cont.): Mg Isotope analyses of unknowns and Test Solutions illustrating typical precision and accuracy.

			Singe Day Average							Multi-Day Replication Average							Complete Replication Average						
Sample ID	Lab ID	Analysis Date	$\delta^{26/24}Mg_{DSM3}$	2-SD	$\delta^{25/24}Mg_{DSM3}$	2-SD	$\delta^{26/25}Mg_{DSM3}$	2-SD	number of analyses	$\delta^{26/24}Mg_{DSM3}$	2-SD	$\delta^{25/24}Mg_{DSM3}$	2-SD	$\delta^{26/25}Mg_{DSM3}$	2-SD	number of analyses	$\delta^{26/24}Mg_{DSM3}$	2-SD	$\delta^{25/24}Mg_{DSM3}$	2-SD	$\delta^{26/25}Mg_{DSM3}$	2-SD	number of analyses
B1	7M-43	12-Jul-17	-3.55	0.02	-1.82	0.03	-1.75	0.01	3														
Calcite		11-Sep-17	-3.50	0.07	-1.81	0.06	-1.71	0.00	3	-3.52	0.07	-1.81	0.04	-1.73	0.05	6	–	–	--	–	–	–	–
B4	7M-46	12-Jul-17	-3.35	0.04	-1.74	0.04	-1.63	0.04	3														
Calcite		11-Sep-17	-3.39	0.04	-1.76	0.04	-1.65	0.06	3	-3.37	0.06	-1.75	0.04	-1.64	0.05	6	–	–	--	–	–	–	–
B5	7M-50	13-Jul-17	-3.44	0.05	-1.83	0.05	-1.64	0.01	3														
Calcite		11-Sep-17	-3.54	0.12	-1.88	0.08	-1.67	0.06	3	-3.48	0.13	-1.85	0.08	-1.64	0.06	6	–	–	--	–	–	–	–
B9	7M-54	13-Jul-17	-3.53	0.01	-1.84	0.03	-1.70	0.03	3														
Calcite		11-Sep-17	-3.56	0.10	-1.84	0.07	-1.74	0.07	3	-3.55	0.07	-1.84	0.05	-1.72	0.06	6	–	–	--	–	–	–	–
B13	7M-58	13-Jul-17	-3.51	0.02	-1.83	0.01	-1.69	0.00	3														
Calcite		11-Sep-17	-3.57	0.03	-1.84	0.07	-1.76	0.05	3	-3.54	0.07	-1.83	0.04	-1.73	0.08	6	–	–	--	–	–	–	–
A18	3M-66	20-Dec-13	-5.06	0.21	-2.62	0.12	-2.46	0.12	3	–	--	–	–	–	–	–							
Calcite	6M-191	11-Nov-16	-5.08	0.08	-2.63	0.05	-2.47	0.06	3														
	6M-191	12-Sep-17	-5.10	0.14	-2.65	0.06	-2.47	0.07	3	-5.09	0.11	-2.64	0.05	-2.47	0.06	6	-5.08	0.14	-2.63	0.08	-2.46	0.08	9
Test Solution 1	6M-189	17-Oct-16	-0.66	0.07	-0.33	0.07	-0.31	0.07	4	–	--	–	–	–	–	–							
	6M-219	12-Nov-16	-0.62	0.04	-0.32	0.03	-0.30	0.03	2	–	--	–	–	–	–	–							
	6M-257	11-Jul-17	-0.67	0.03	-0.35	0.02	-0.34	0.02	3	–	--	–	–	–	–	–							
	6M-258	12-Jul-17	-0.65	0.00	-0.34	0.04	-0.32	0.03	3	–	--	–	–	–	–	–	-0.65	0.02	-0.34	0.01	-0.32	0.02	12
Test Solution 2	6M-158	19-Jul-16	-0.72	0.00	-0.40	0.04	-0.34	0.06	2	–	--	–	–	–	–	–							
	6M-159	19-Jul-16	-0.64	0.08	-0.35	0.07	-0.30	0.03	2	–	--	–	–	–	–	–							
	6M-265	11-Jul-17	-0.65	0.07	-0.34	0.05	-0.31	0.02	3	–	--	–	–	–	–	–							
	6M-266	11-Jul-17	-0.70	0.03	-0.37	0.03	-0.35	0.05	3	–	--	–	–	–	–	–	-0.68	0.04	-0.36	0.02	-0.33	0.02	10
Test Solution 3	6M-161	19-Jul-16	-0.64	0.00	-0.32	0.02	-0.32	0.01	2	–	--	–	–	–	–	–							
	6M-163	19-Jul-16	-0.61	0.04	-0.33	0.01	-0.29	0.08	2	–	--	–	–	–	–	–	-0.62	0.02	-0.33	0.01	-0.30	0.02	4
Test Solution 4	6M-136	16-Jul-16	-0.63	0.08	-0.34	0.03	-0.30	0.03	4	–	--	–	–	–	–	–							
	6M-137	16-Jul-16	-0.70	0.15	-0.37	0.12	-0.34	0.05	4	–	--	–	–	–	–	–							
	6M-138	16-Jul-16	-0.66	0.02	-0.37	0.00	-0.30	0.02	2														
		18-Jul-16	-0.69	0.04	-0.34	0.03	-0.34	0.03	2	-0.67	0.02	-0.35	0.02	-0.32	0.03	4	-0.67	0.11	-0.35	0.07	-0.32	0.05	12
Test Solution 5	6M-140	16-Jul-16	-0.72	0.01	-0.39	0.01	-0.34	0.08	2														
		18-Jul-16	-0.69	0.07	-0.38	0.03	-0.33	0.05	2	-0.70	0.02	-0.38	0.01	-0.34	0.03	5							
	6M-141	16-Jul-16	-0.68	–	-0.34	–	-0.34	–	1														
		18-Jul-16	-0.68	0.02	-0.35	0.06	-0.35	0.06	2	-0.68	0.01	-0.35	0.02	-0.34	0.02	3							
	6M-142	16-Jul-16	-0.67	–	-0.36	–	-0.32	–	1														
		18-Jul-16	-0.66	0.00	-0.35	0.00	-0.32	0.00	2	-0.66	0.01	-0.35	0.01	-0.32	0.00	3	-0.69	0.05	-0.36	0.04	-0.33	0.04	11
Test Solution 6	6M-144	16-Jul-16	-0.67	0.06	-0.35	0.05	-0.33	0.04	7	–	--	–	–	–	–	–							
	6M-145	16-Jul-16	-0.68	–	-0.35	–	-0.33	–	1	–	--	–	–	–	–	–							
	6M-146	18-Jul-16	-0.66	0.10	-0.35	0.08	-0.33	0.07	2	–	--	–	–	–	–	–	-0.67	0.06	-0.35	0.05	-0.33	0.04	10
Test Solution 7	6M-167	24-Aug-16	-0.59	0.03	-0.31	0.06	-0.28	0.03	3	–	--	–	–	–	–	–	–	–	--	–	–	–	–
Test Solution 8	6M-168	24-Aug-16	-0.50	0.15	-0.30	0.06	-0.23	0.08	3	–	--	–	–	–	–	–	–	–	--	–	–	–	–
Test Solution 9	6M-169	24-Aug-16	-0.61	0.05	-0.34	0.06	-0.28	0.02	3	–	--	–	–	–	–	–	–	–	--	–	–	–	–
Test Solution 10	6M-170	24-Aug-16	-0.59	0.06	-0.32	0.03	-0.28	0.03	3	–	--	–	–	–	–	–	–	–	--	–	–	–	–
Test Solution 11	6M-171	24-Aug-16	-0.62	0.03	-0.35	0.00	-0.28	0.02	3	–	--	–	–	–	–	–	–	–	--	–	–	–	–
Test Solution 12	6M-172	24-Aug-16	-0.62	0.03	-0.32	0.03	-0.31	0.00	3	–	--	–	–	–	–	–							
	6M-178	24-Aug-16	-0.67	0.05	-0.35	0.00	-0.33	0.06	3	–	--	–	–	–	–	–	-0.65	0.09	-0.33	0.05	-0.32	0.07	6

Test Solutions are made from in-house standard HPS-909104 with a $\delta^{26}Mg$ value of -0.66‰.

Table S2a: Chemical composition of Test Solutions used to assess analytical accuracy.

Test Solution #	Ion Concentration (ppm, µg/ml)					
Number	Mg	Ca	Fe	Mn	Al	Molar Ratio Mg:Ca:Fe:Mn:Al
1	52	82	28	3	0	1:3:1:0:0
2	52	83	347	3	0	1:3:15:0:0
3	25	4	235	3	0	1:0:21:0:0
4	100	200	0	0	0	1:3:0:0:0
5	100	6000	0	0	0	1:99:0:0:0
6	100	0	1000	0	0	1:0:23:0:0
7	50	3000	0	0	75	1:99:0:0:2
8	50	5000	0	0	75	1:165:0:0:2
9	50	10000	0	0	75	1:330:0:0:2
10	50	3000	0	0	0	1:99:0:0:0
11	50	5000	0	0	0	1:165:0:0:0
12	50	10000	0	0	0	1:330:0:0:0

Table S3: Solution Speciation of Mg according Schott et al. (2016).

	Major solution phase species (moles/L) calculated by PHREEQC.							Fraction of each species in solution.						
Sample ID	Mg^{+2}_{aq}	$MgHCO_3^+$	$MgCl^+$	$MgCO_3$	$Mg(OH)^+$	$Mg_4(OH)_4^{+4}$	Mg TOTAL	Mg^{+2}_{aq}	$MgHCO_3^+$	$MgCl^+$	$MgCO_3$	$Mg(OH)^+$	$Mg_4(OH)_4^{+4}$	Mg TOTAL
Li et al. 2012														
C-22	4.82E-02	1.09E-03	1.08E-03	1.31E-05	1.92E-07	1.03E-18	5.04E-02	0.96	0.02	0.02	0.00	0.00	0.00	1.00
22a	4.84E-02	1.03E-03	9.74E-04	1.51E-05	2.47E-07	2.76E-18	5.04E-02	0.96	0.02	0.02	0.00	0.00	0.00	1.00
22c	4.68E-02	1.13E-03	1.04E-03	1.28E-05	1.74E-07	6.97E-19	4.89E-02	0.96	0.02	0.02	0.00	0.00	0.00	1.00
22d	4.71E-02	1.78E-03	1.07E-03	1.32E-05	1.88E-07	1.10E-18	4.99E-02	0.94	0.04	0.02	0.00	0.00	0.00	1.00
22e	3.77E-02	1.20E-03	8.81E-04	1.24E-05	1.71E-07	6.68E-19	3.98E-02	0.95	0.03	0.02	0.00	0.00	0.00	1.00
This Study														
A1	4.65E-02	1.69E-03	1.71E-03	7.19E-05	1.49E-06	3.78E-17	5.00E-02	0.93	0.03	0.03	0.00	0.00	0.00	1.00
A2	4.67E-02	1.76E-03	1.76E-03	4.88E-05	7.60E-07	2.82E-17	5.02E-02	0.93	0.03	0.04	0.00	0.00	0.00	1.00
A3	4.68E-02	1.74E-03	1.77E-03	5.59E-05	8.81E-07	5.08E-17	5.03E-02	0.93	0.03	0.04	0.00	0.00	0.00	1.00
A4	4.74E-02	1.13E-03	1.78E-03	4.66E-05	1.46E-06	3.59E-17	5.03E-02	0.94	0.02	0.04	0.00	0.00	0.00	1.00
A5	9.31E-03	5.77E-04	9.72E-05	4.27E-05	7.39E-07	1.50E-19	1.00E-02	0.93	0.06	0.01	0.00	0.00	0.00	1.00
A6	9.26E-03	6.08E-04	9.79E-05	5.25E-05	1.19E-06	1.87E-19	1.00E-02	0.92	0.06	0.01	0.01	0.00	0.00	1.00
A7	9.36E-03	5.69E-04	9.81E-05	2.24E-05	2.40E-07	7.74E-20	1.01E-02	0.93	0.06	0.01	0.00	0.00	0.00	1.00
A8	9.30E-03	5.84E-04	9.65E-05	4.64E-05	7.95E-07	2.00E-19	1.00E-02	0.93	0.06	0.01	0.00	0.00	0.00	1.00
A9	9.44E-03	5.73E-04	9.89E-05	2.40E-05	2.58E-07	1.02E-19	1.01E-02	0.93	0.06	0.01	0.00	0.00	0.00	1.00
A10	4.68E-02	1.81E-03	1.72E-03	4.13E-05	2.31E-07	3.96E-17	5.03E-02	0.93	0.04	0.03	0.00	0.00	0.00	1.00
A11	9.55E-03	6.12E-04	9.28E-05	2.60E-05	2.64E-07	1.14E-19	1.03E-02	0.93	0.06	0.01	0.00	0.00	0.00	1.00
A12	9.55E-03	5.99E-04	9.99E-05	4.09E-05	5.05E-07	1.88E-19	1.03E-02	0.93	0.06	0.01	0.00	0.00	0.00	1.00
A13	8.92E-03	5.62E-04	9.05E-05	3.85E-05	4.74E-07	1.42E-19	9.61E-03	0.93	0.06	0.01	0.00	0.00	0.00	1.00
A14	9.19E-03	6.24E-04	9.78E-05	5.83E-05	1.27E-06	2.51E-19	9.97E-03	0.92	0.06	0.01	0.01	0.00	0.00	1.00
A15	9.54E-03	5.78E-04	1.00E-04	3.11E-05	3.34E-07	2.91E-19	1.02E-02	0.93	0.06	0.01	0.00	0.00	0.00	1.00
A16	9.85E-03	5.78E-04	1.13E-04	1.73E-05	4.51E-08	1.74E-19	1.06E-02	0.93	0.05	0.01	0.00	0.00	0.00	1.00
A17	9.58E-03	5.97E-04	1.02E-04	2.33E-05	7.90E-08	2.06E-19	1.03E-02	0.93	0.06	0.01	0.00	0.00	0.00	1.00
A18	9.46E-03	6.13E-04	1.08E-04	1.32E-05	2.13E-08	1.10E-19	1.02E-02	0.93	0.06	0.01	0.00	0.00	0.00	1.00
A19	4.70E-02	1.76E-03	1.58E-03	1.62E-04	2.13E-07	3.00E-16	5.05E-02	0.93	0.03	0.03	0.00	0.00	0.00	1.00
A20	--	--	--	--	--	--	--		--	--	--	--	--	--
B1	1.91E-02	2.31E-03	5.33E-04	1.33E-05	3.80E-08	1.10E-21	2.20E-02	0.87	0.10	0.02	0.00	0.00	0.00	1.00
B2	1.82E-02	1.79E-03	1.35E-03	9.20E-06	3.32E-08	9.50E-22	2.14E-02	0.85	0.08	0.06	0.00	0.00	0.00	1.00
B3	1.94E-02	2.19E-03	5.31E-04	2.18E-05	6.64E-08	1.01E-20	2.21E-02	0.88	0.10	0.02	0.00	0.00	0.00	1.00
B4	1.85E-02	1.70E-03	1.36E-03	1.51E-05	5.81E-08	8.88E-21	2.15E-02	0.86	0.08	0.06	0.00	0.00	0.00	1.00
B5	1.86E-02	2.14E-03	1.53E-03	1.33E-05	5.91E-08	1.03E-20	2.23E-02	0.83	0.10	0.07	0.00	0.00	0.00	1.00
B6	1.43E-02	1.38E-03	4.24E-04	5.89E-06	2.11E-08	1.07E-22	1.61E-02	0.89	0.09	0.03	0.00	0.00	0.00	1.00
B7	1.83E-02	1.65E-03	1.49E-03	7.28E-06	2.89E-08	5.64E-22	2.14E-02	0.85	0.08	0.07	0.00	0.00	0.00	1.00
B8	2.19E-02	2.76E-03	1.79E-03	7.86E-06	3.57E-08	1.38E-21	2.64E-02	0.83	0.10	0.07	0.00	0.00	0.00	1.00
B9	1.49E-02	1.47E-03	4.56E-04	3.75E-06	1.31E-08	1.62E-23	1.68E-02	0.89	0.09	0.03	0.00	0.00	0.00	1.00
B10	1.84E-02	1.76E-03	1.51E-03	4.87E-06	1.82E-08	9.16E-23	2.16E-02	0.85	0.08	0.07	0.00	0.00	0.00	1.00
B11	2.33E-02	3.00E-03	2.06E-03	5.93E-06	2.50E-08	3.28E-22	2.83E-02	0.82	0.11	0.07	0.00	0.00	0.00	1.00
B12	1.44E-02	1.55E-03	4.43E-04	4.25E-06	1.37E-08	1.98E-23	1.64E-02	0.88	0.09	0.03	0.00	0.00	0.00	1.00
B13	1.78E-02	1.83E-03	1.46E-03	5.42E-06	1.90E-08	1.06E-22	2.11E-02	0.84	0.09	0.07	0.00	0.00	0.00	1.00
B14	2.16E-02	2.70E-03	1.96E-03	5.69E-06	2.33E-08	2.49E-22	2.62E-02	0.82	0.10	0.07	0.00	0.00	0.00	1.00
B15	9.89E-03	7.88E-04	2.20E-04	4.51E-06	1.95E-08	6.26E-23	1.09E-02	0.91	0.07	0.02	0.00	0.00	0.00	1.00
B16	9.78E-03	8.41E-04	2.19E-04	5.15E-06	2.07E-08	8.02E-23	1.08E-02	0.90	0.08	0.02	0.00	0.00	0.00	1.00
B17	1.80E-02	2.06E-03	1.39E-03	1.49E-05	7.03E-08	2.08E-20	2.14E-02	0.84	0.10	0.06	0.00	0.00	0.00	1.00
B18	1.75E-02	2.69E-03	1.16E-03	1.19E-05	6.65E-08	1.66E-20	2.14E-02	0.82	0.13	0.05	0.00	0.00	0.00	1.00
B19	1.71E-02	3.27E-03	9.60E-04	9.16E-06	6.12E-08	1.16E-20	2.13E-02	0.80	0.15	0.05	0.00	0.00	0.00	1.00
M1	5.09E-03	2.53E-04	6.67E-05	5.16E-06	3.43E-08	5.37E-22	5.41E-03	0.94	0.05	0.01	0.00	0.00	0.00	1.00
M2	4.77E-03	2.67E-04	4.61E-05	5.84E-06	3.51E-08	4.71E-22	5.09E-03	0.94	0.05	0.01	0.00	0.00	0.00	1.00
M3	5.12E-03	2.76E-04	7.24E-05	4.34E-06	2.64E-08	2.03E-22	5.47E-03	0.94	0.05	0.01	0.00	0.00	0.00	1.00
M4	9.13E-03	5.16E-04	1.94E-04	2.07E-06	1.18E-08	1.16E-23	9.84E-03	0.93	0.05	0.02	0.00	0.00	0.00	1.00
M5	9.03E-03	7.27E-04	1.46E-04	3.99E-06	1.61E-08	3.32E-23	9.90E-03	0.91	0.07	0.01	0.00	0.00	0.00	1.00
M6	1.59E-02	9.59E-04	3.27E-04	3.10E-06	1.67E-08	4.43E-23	1.72E-02	0.93	0.06	0.02	0.00	0.00	0.00	1.00
M7	1.41E-02	4.81E-04	4.20E-04	4.57E-07	4.30E-09	2.61E-25	1.50E-02	0.94	0.03	0.03	0.00	0.00	0.00	1.00
M8	1.81E-02	9.30E-04	4.85E-04	1.31E-06	8.23E-09	3.23E-24	1.95E-02	0.93	0.05	0.02	0.00	0.00	0.00	1.00
M9	2.69E-02	1.50E-03	8.75E-04	2.33E-06	1.35E-08	2.72E-23	2.92E-02	0.92	0.05	0.03	0.00	0.00	0.00	1.00
M10	1.33E-02	1.61E-03	4.15E-04	8.28E-06	2.21E-08	1.99E-22	1.53E-02	0.87	0.11	0.03	0.00	0.00	0.00	1.00
M11	2.47E-02	3.84E-03	8.13E-04	2.50E-05	5.23E-08	6.49E-21	2.93E-02	0.84	0.13	0.03	0.00	0.00	0.00	1.00
M12	1.73E-02	1.99E-03	4.68E-04	9.66E-06	2.71E-08	4.06E-22	1.98E-02	0.88	0.10	0.02	0.00	0.00	0.00	1.00
M13	1.10E-02	1.17E-03	2.05E-04	1.23E-05	3.76E-08	1.13E-21	1.24E-02	0.89	0.09	0.02	0.00	0.00	0.00	1.00
M14	1.72E-02	2.28E-03	4.67E-04	1.83E-05	1.26E-08	2.92E-21	2.00E-02	0.86	0.11	0.02	0.00	0.00	0.00	1.00
Mavromatis et al. 2013														
CaMg76s	1.34E-03	1.40E-04	4.83E-05	3.66E-07	1.36E-09	9.06E-28	1.53E-03	0.88	0.09	0.03	0.00	0.00	0.00	1.00
CaMg77s	3.54E-03	3.75E-04	1.32E-04	1.01E-06	3.67E-09	5.00E-26	4.04E-03	0.87	0.09	0.03	0.00	0.00	0.00	1.00
CaMg78s	6.67E-03	7.34E-04	2.58E-04	2.07E-06	7.25E-09	7.91E-25	7.66E-03	0.87	0.10	0.03	0.00	0.00	0.00	1.00
CaMg87s	3.70E-03	3.89E-04	1.39E-04	1.04E-06	3.82E-09	5.90E-26	4.23E-03	0.87	0.09	0.03	0.00	0.00	0.00	1.00
CaMg89s	1.05E-02	1.03E-03	9.01E-04	2.90E-06	1.18E-08	7.86E-24	1.24E-02	0.84	0.08	0.07	0.00	0.00	0.00	1.00
CaMg94s	9.86E-03	9.83E-04	8.42E-04	2.78E-06	1.12E-08	6.35E-24	1.17E-02	0.84	0.08	0.07	0.00	0.00	0.00	1.00
CaMg95s	3.60E-03	3.88E-04	1.32E-04	1.06E-06	3.79E-09	5.65E-26	4.12E-03	0.87	0.09	0.03	0.00	0.00	0.00	1.00
CaMg96s	6.78E-03	7.02E-04	4.21E-04	1.95E-06	7.38E-09	1.09E-24	7.91E-03	0.86	0.09	0.05	0.00	0.00	0.00	1.00
CaMg98s	1.21E-02	1.30E-03	1.15E-03	3.29E-06	1.41E-08	1.69E-23	1.46E-02	0.83	0.09	0.08	0.00	0.00	0.00	1.00
CaMg99s	9.23E-03	1.04E-03	3.71E-04	3.00E-06	1.03E-08	3.39E-24	1.06E-02	0.87	0.10	0.03	0.00	0.00	0.00	1.00
CaMg100s	8.55E-03	8.58E-04	5.43E-04	2.56E-06	1.00E-08	3.69E-24	9.96E-03	0.86	0.09	0.05	0.00	0.00	0.00	1.00
CaMg102s	8.08E-03	8.49E-04	7.33E-04	2.17E-06	9.70E-09	3.79E-24	9.67E-03	0.84	0.09	0.08	0.00	0.00	0.00	1.00
CaMg113s	6.98E-03	1.02E-03	5.45E-04	1.54E-06	8.24E-09	1.96E-24	8.54E-03	0.82	0.12	0.06	0.00	0.00	0.00	1.00
CaMg114s	6.80E-03	9.91E-04	5.27E-04	1.48E-06	7.97E-09	1.72E-24	8.31E-03	0.82	0.12	0.06	0.00	0.00	0.00	1.00

Supplemental Figures

Figure SM1 – Accuracy of measured in-house Mg isotope standard HPS-909104 test solutions (TS) after full procedural processing as unknowns, compared to calculated yield, as measured by MC-ICP-MS signal intensity. Magnesium loss due to dry down and/or sorption to collection beakers and pipet tips likely explain yields below 80%. Additional variability close to 100% recovery is likely due to imprecision of pipet volumes during preparation of 1 ppm Mg solutions used for analysis.

Figure SM2 – X-ray maps (left) showing Mg concentrations and secondary electron images (right) produced by CAMECA SXFive field emission electron mircroprobe analysis of Mg-free seed crystals (top) and Mg-bearing seed crystals (middle). The bottom pair of images is of the final product from a Mg-bearing seed crystal experiment. The mol% Mg uncertainty is a function of the count rates and counting duration and expressed by: ± mol % Mg = 0.84*[measured mol% Mg]$^{0.505}$. For example, 4.0 ± 1.7 mol % Mg.

Figure SM3 – Relation between Mg/Ca ratio and Mg distribution coefficient for synthetic magnesian calcite formed near room temperature (23-25°C). The purple regression line is same as shown in Figure 3. The "plates" and "straws" reported by Huang and Fairchild (2001) refer to synthetic speleothem formations precipitated on drip substrates and solution delivery tubing, respectively. This figure is modified after Mucci and Morse (1983).

Figure SM4 – Relation between Mg/Ca ratios and Mg distribution coefficient for synthetic magnesian calcite formed near room temperature (22-28°C). The calcite produced by Loste et al. (2003) and Purgstaller et al. (2016) formed via an amorphous calcium carbonate (ACC) precursor. Similarly, the calcite produced by Jimenez-Lopez et al. (2004) form a monohydrocalcite (MHC) precursor. For comparison, the D_{Mg} values reported by Blue and Dove (2015) from ACC are also shown. The purple regression line is from Figure 3. This figure is modified after Mucci and Morse (1983).

Figure SM5 – Comparison between Mg distribution coefficient between calcite and solution compared to the absolute concentration of Mg in the formation solution at steady state conditions. This was determined using a chemo-stat approach for this study, Li et al. (2012), and Gavitov et al. (2014). For Mavromatis et al. (2013), steady state was inferred based on time. For room temperature experiments (23-25°C). Individual values determined by this study are given in Table 2.

Figure SM6 – As in Figure SM5 but comparing Mg distribution coefficient between calcite and Mg in solution to ionic strength of precipitation fluid.

Figure SM7 – As in Figure SM5 but comparing Mg distribution coefficient between calcite and Mg in solution to partial pressure of CO_2. Mavromatis et al. (2013) used a pCO_2 of 100% for all experiments.

Figure SM8 – As in Figure SM5 but comparing Mg distribution coefficient between calcite and Mg in solution to calcite precipitation rate.

Figure SM9 – As in Figure SM5 but comparing Mg distribution coefficient between calcite and Mg in solution to calcite saturation state.

Figure SM10 – Mg isotope fractionation between calcite and solution compared to the Mg concentration in the formation solution (at steady state condition for Mavromatis et al., 2013). The solutions from which experiments CaMg113s and CaMg114s precipitated are reported to have non-mass dependent relations between $^{26}Mg/^{24}Mg$ and $^{25}Mg/^{24}Mg$ by Mavromatis et al. (2013, Table 2). Individual propagated 2SD external uncertainty for experimental values is represented by error bars. Individual values determined by this study are given in Table 2.

Figure SM11 – As in Figure S10 but comparing Mg isotope fractionation between calcite and Mg in solution to the homogeneous distribution coefficient (D_{Mg}).

Figure SM12 – As in Figure S10 but comparing Mg isotope fractionation between calcite and Mg in solution to solution ionic strength.

Figure SM13 – As in Figure S10 but comparing Mg isotope fractionation between calcite and Mg in solution to partial pressure of CO_2. Mavromatis et al. (2013) used a pCO_2 of 100% for all experiments.

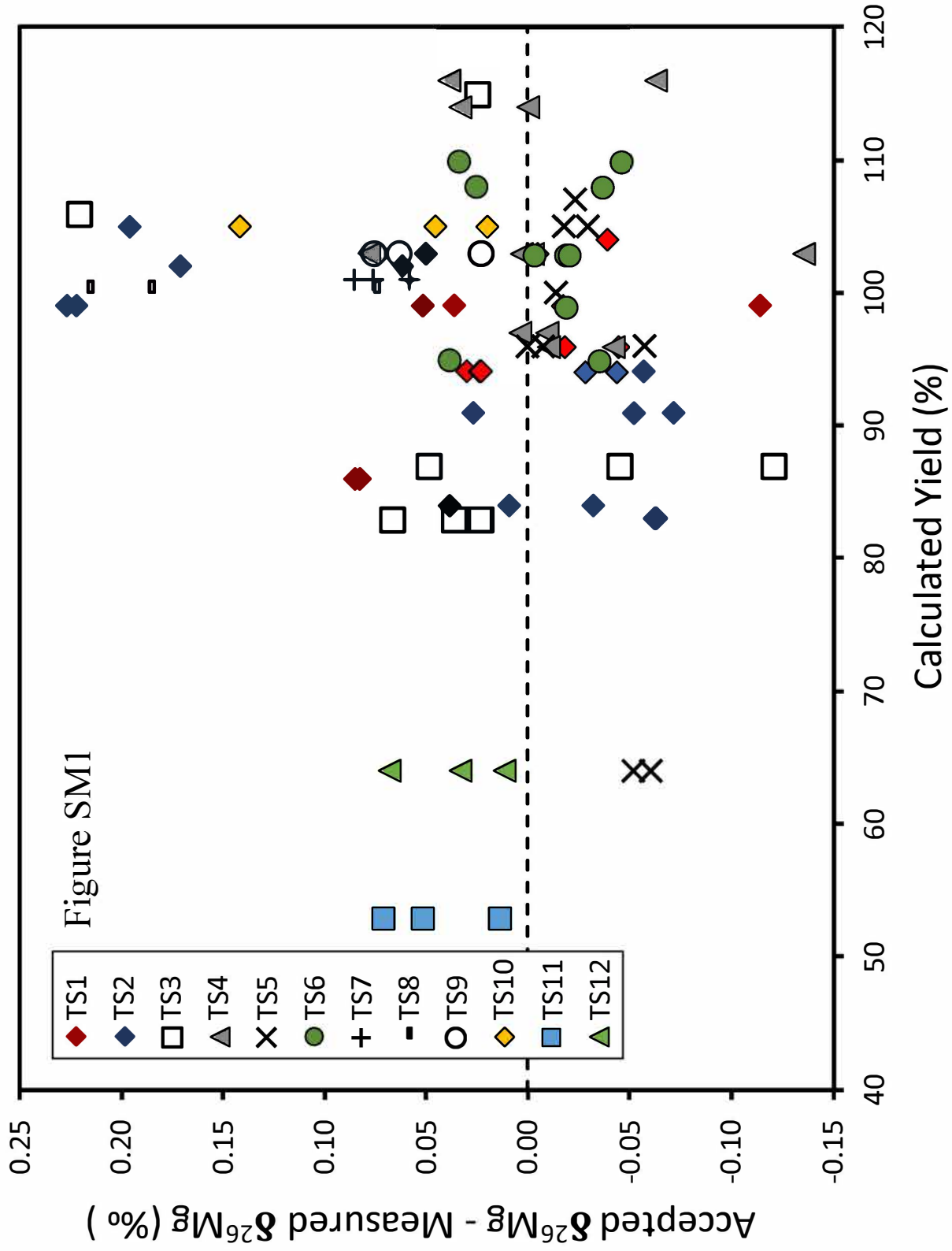
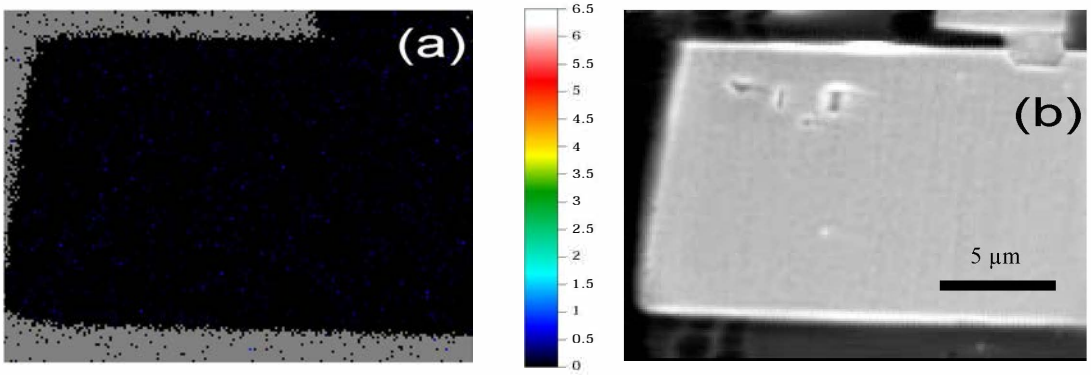
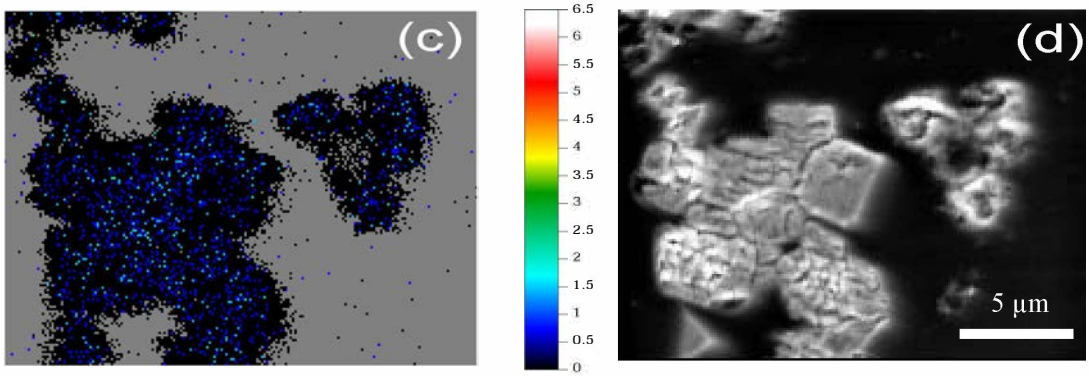

Figure SM1
Accepted δ26Mg - Measured δ26Mg (‰)
Calculated Yield (%)
0.25
0.20
0.15
0.10
0.05
0.00
-0.05
-0.10
-0.15
40
50
60
70
80
90
100
110
120
TS1
TS2
TS3
TS4
TS5
TS6
TS7
TS8
TS9
TS10
TS11
TS12

Figure SM2



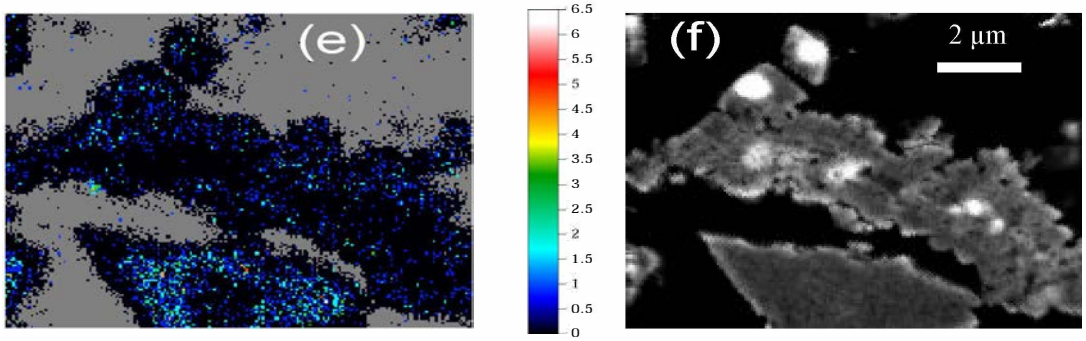
Set "B" Seeds

Mg Wt%

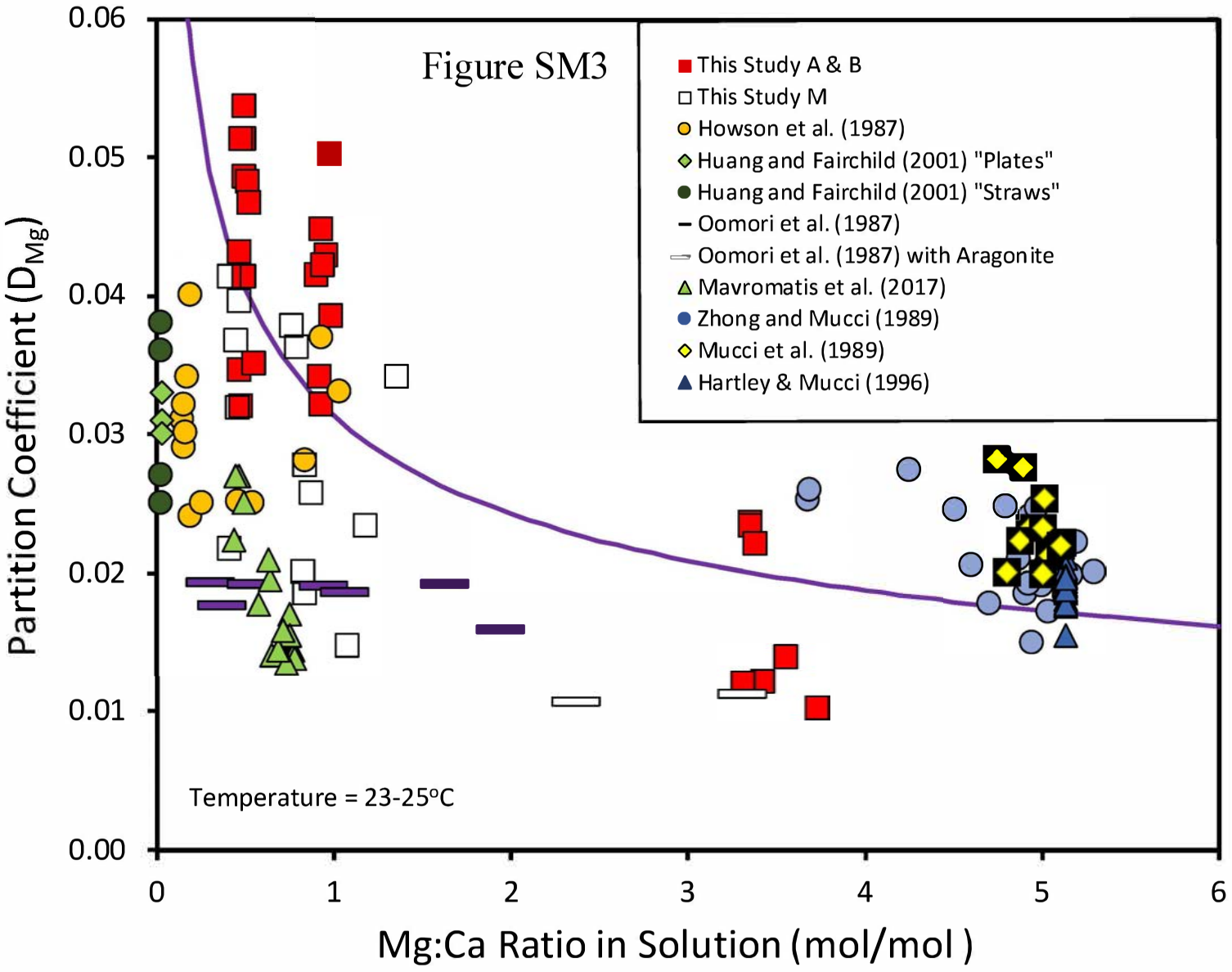


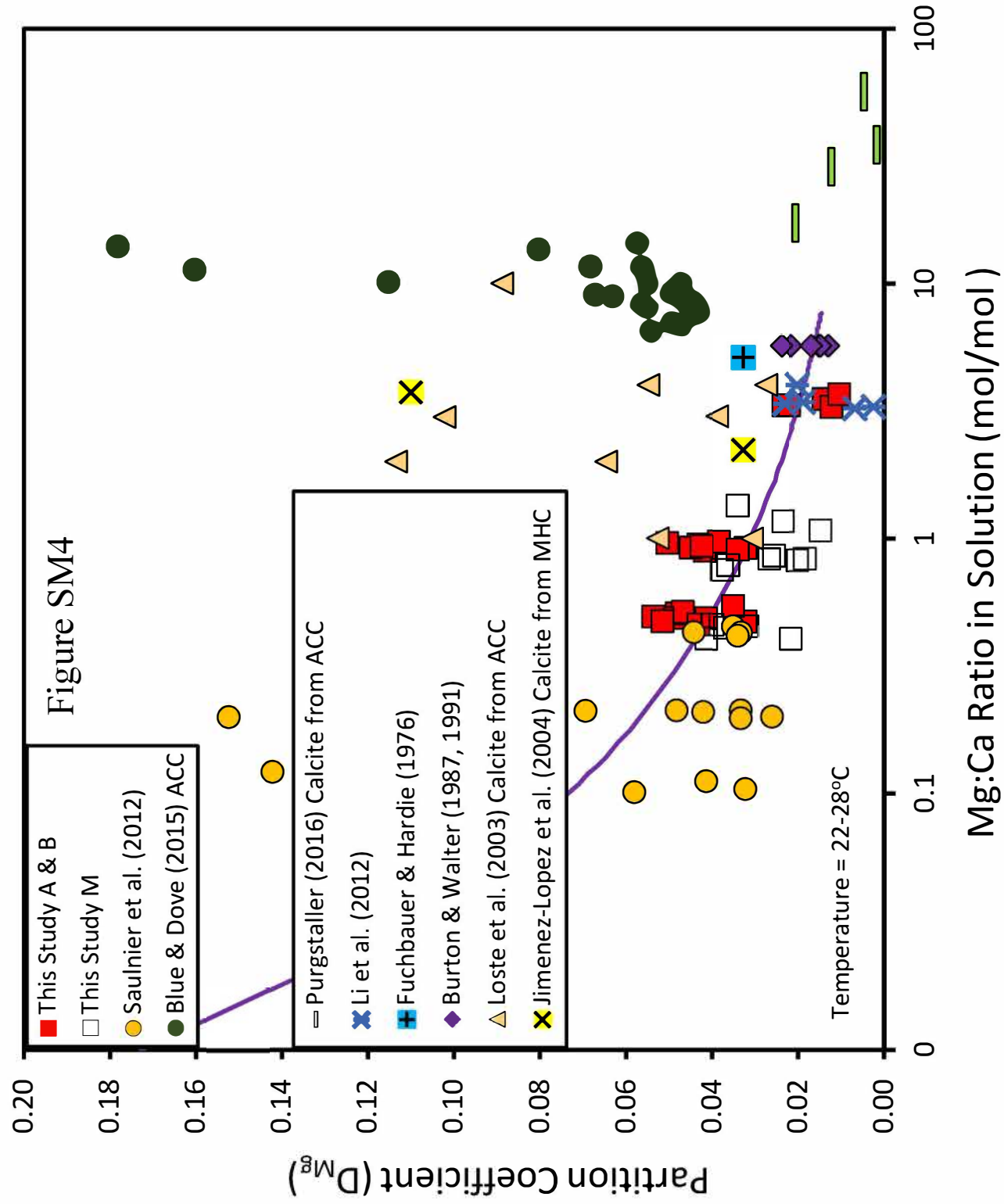
Set "M" Seeds

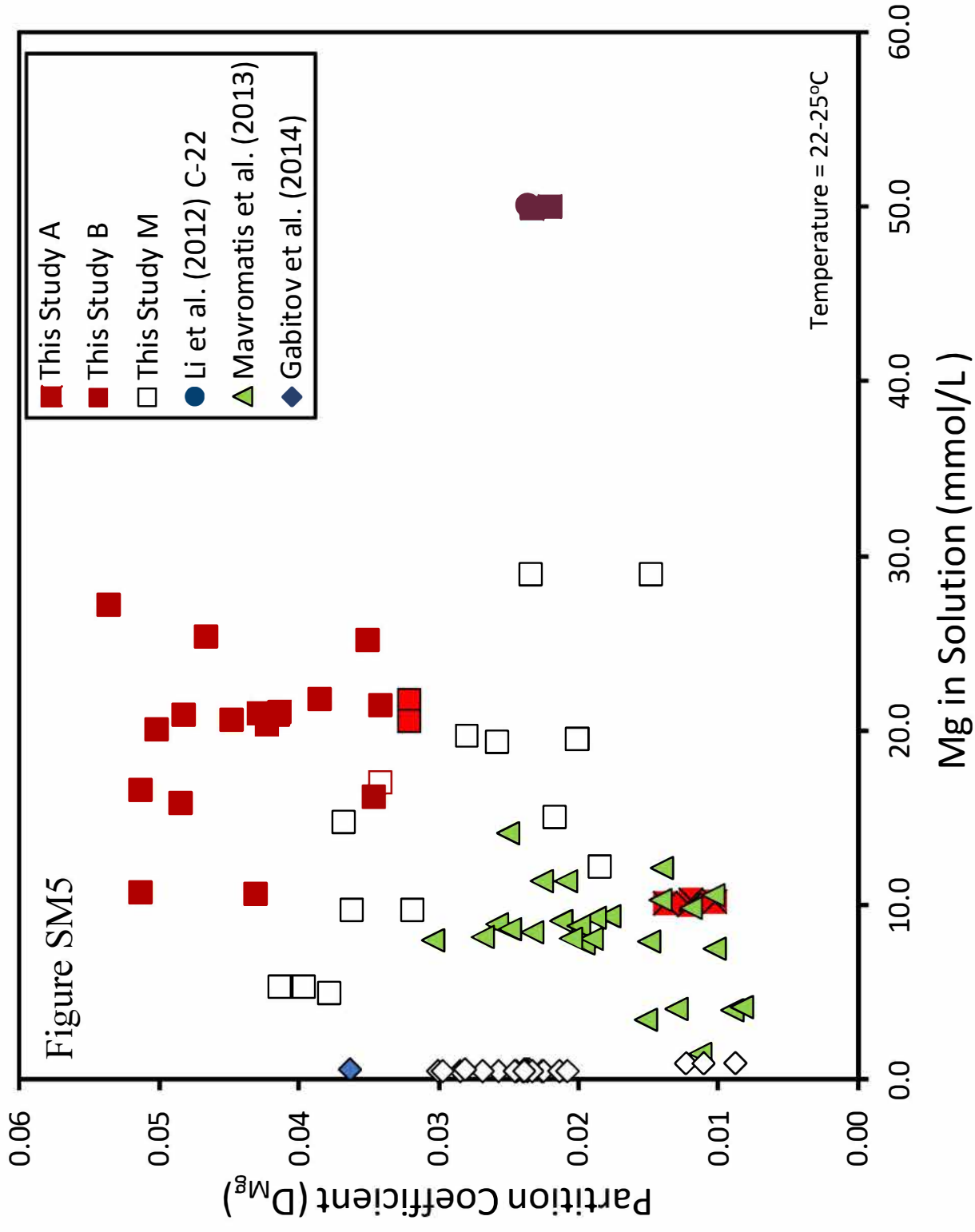
Mg Wt%

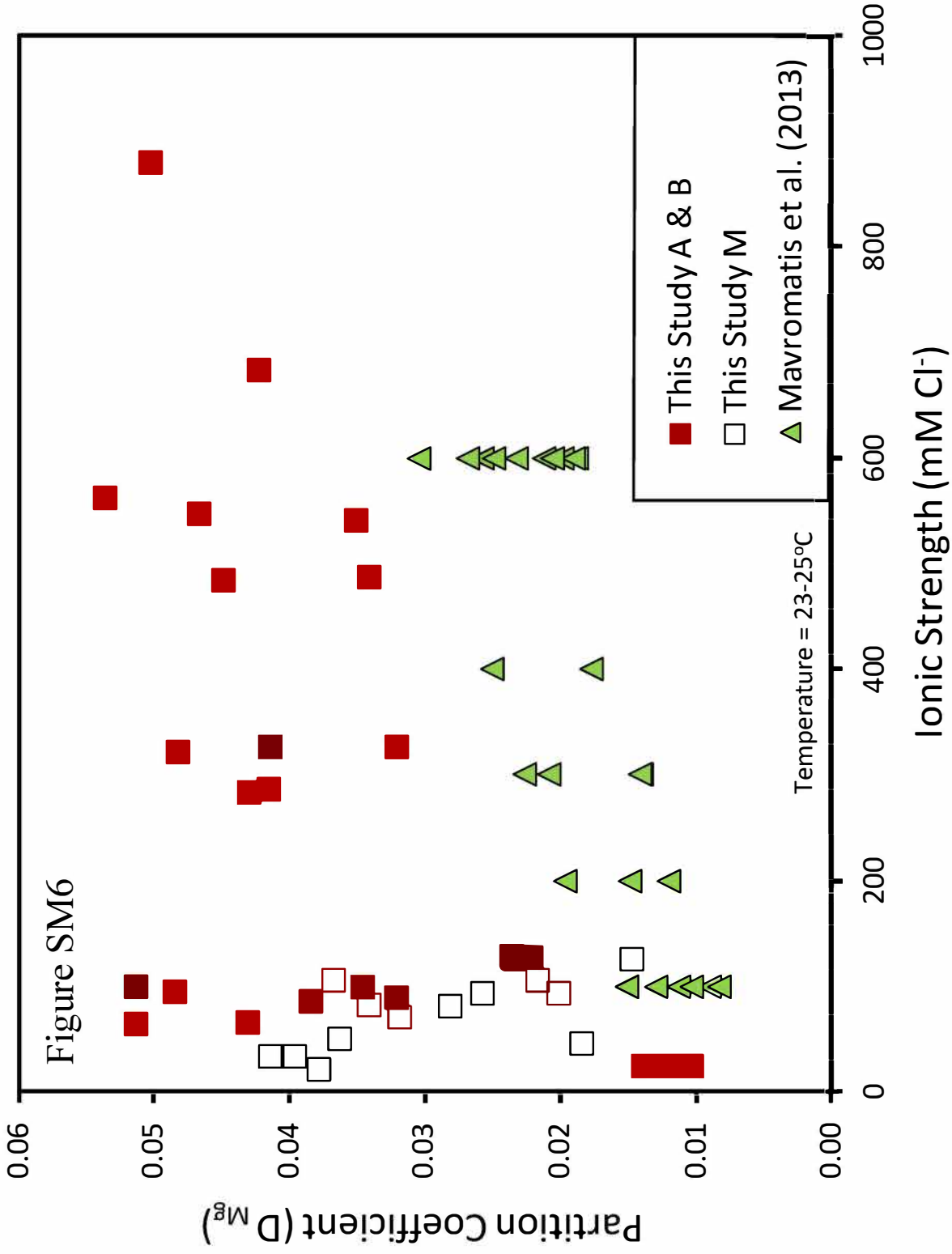


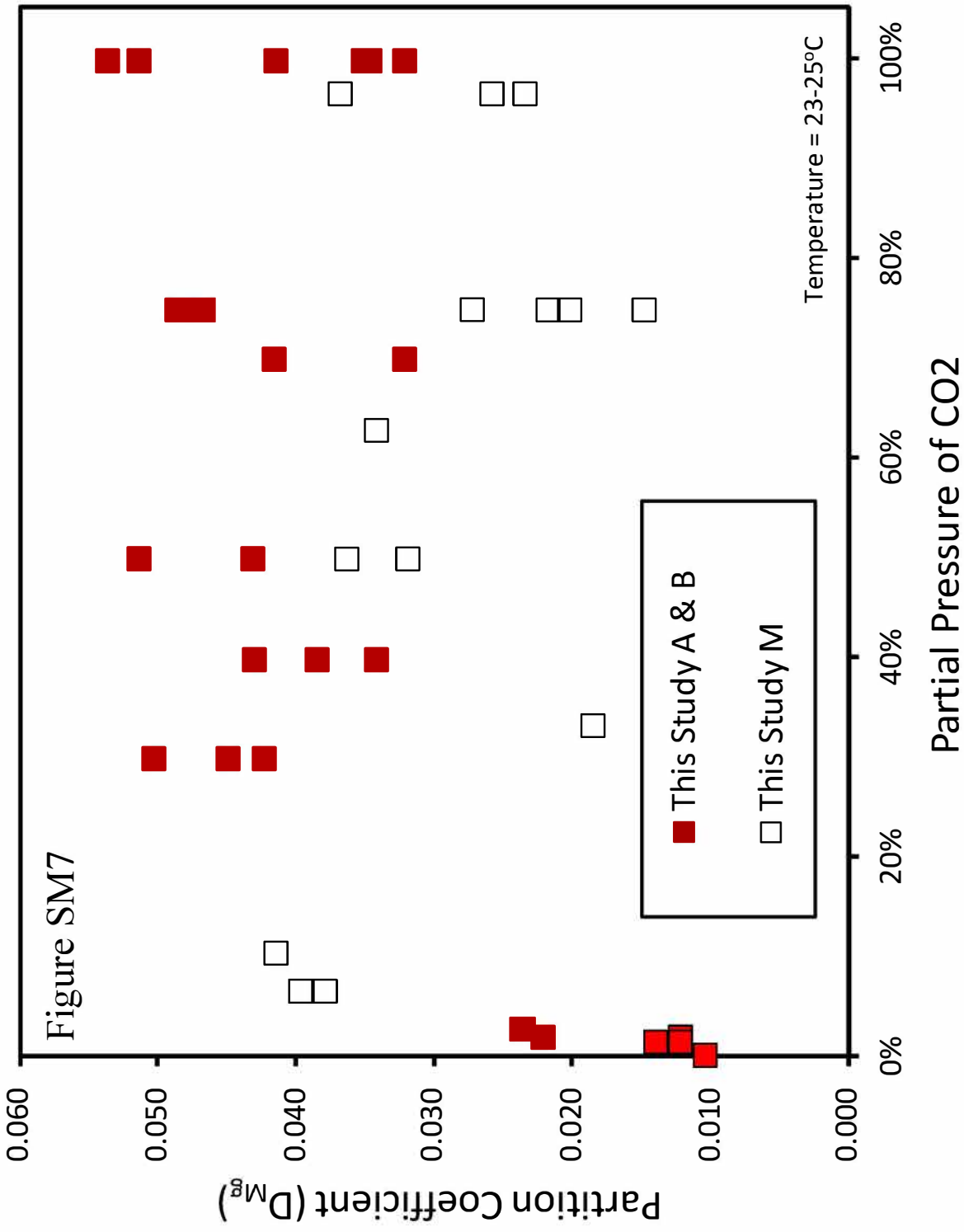
Experiment M14 Product

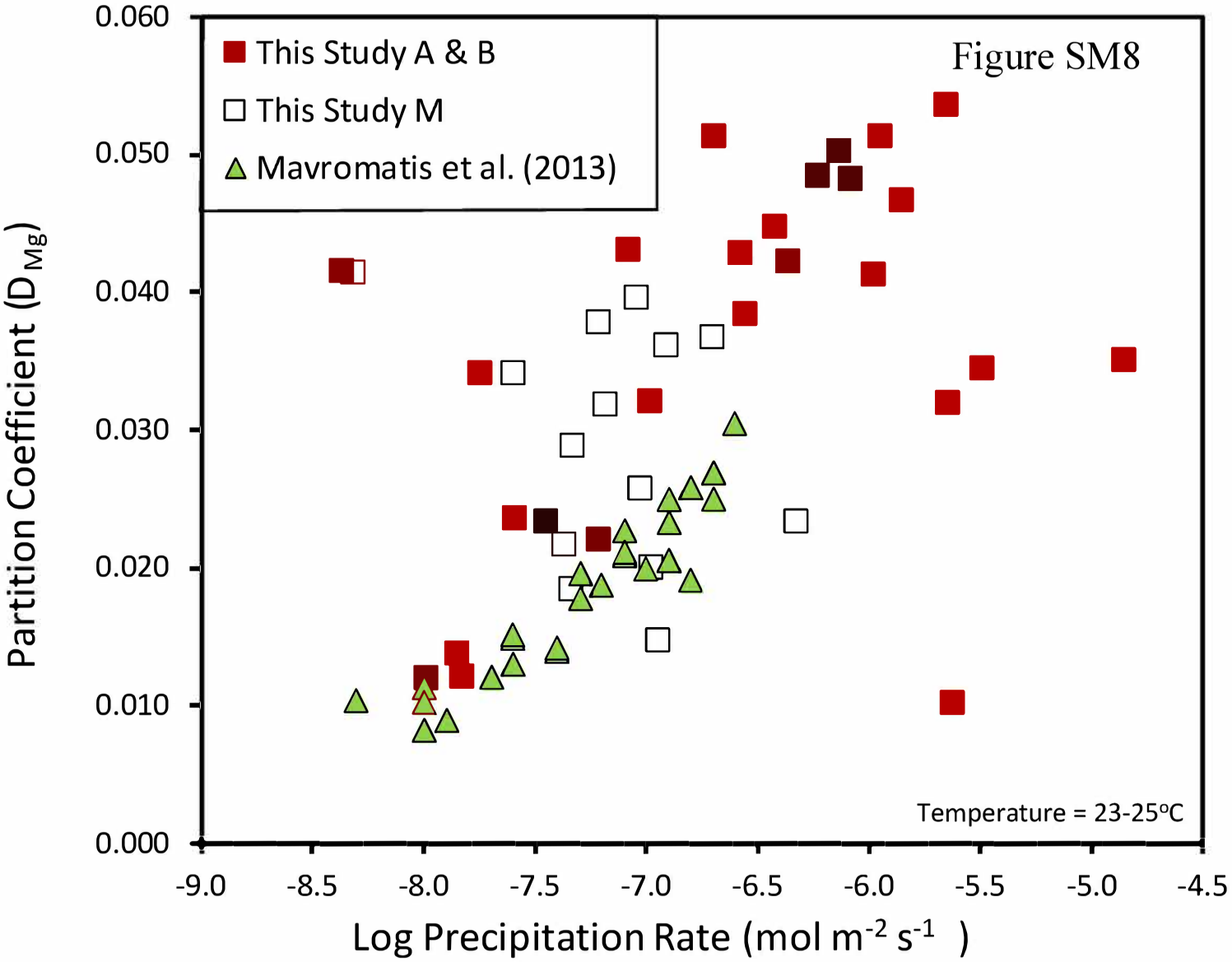

Figure SM3
This Study A & B
This Study M
Howson et al. (1987)
Huang and Fairchild (2001) "Plates"
Huang and Fairchild (2001) "Straws"
Oomori et al. (1987)
Oomori et al. (1987) with Aragonite
Mavromatis et al. (2017)
Zhong and Mucci (1989)
Mucci et al. (1989)
Hartley & Mucci (1996)
Temperature = 23-25°C
Partition Coefficient (D_{Mg})
0.06
0.05
0.04
0.03
0.02
0.01
0.00
0
1
2
3
4
5
6
Mg:Ca Ratio in Solution (mol/mol)

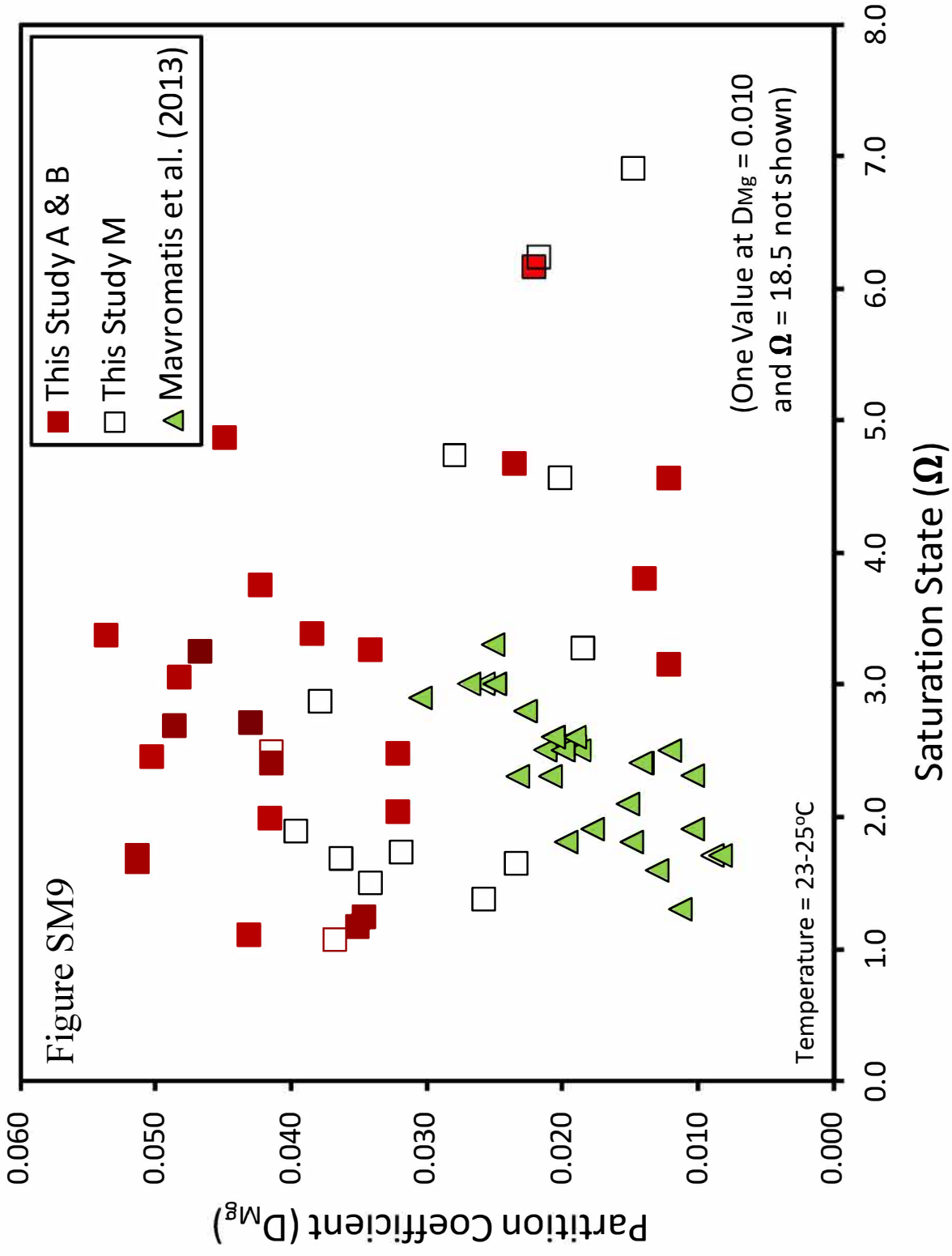

Figure SM4
This Study A & B
This Study M
Saulnier et al. (2012)
Blue & Dove (2015) ACC
Purgstaller (2016) Calcite from ACC
Li et al. (2012)
Fuchbauer & Hardie (1976)
Burton & Walter (1987, 1991)
Loste et al. (2003) Calcite from ACC
Jimenez-Lopez et al. (2004) Calcite from MHC
Temperature = 22-28°C
Partition Coefficient (D_{Mg})
0.20
0.18
0.16
0.14
0.12
0.10
0.08
0.06
0.04
0.02
0.00
Mg:Ca Ratio in Solution (mol/mol)
0
0.1
1
10
100

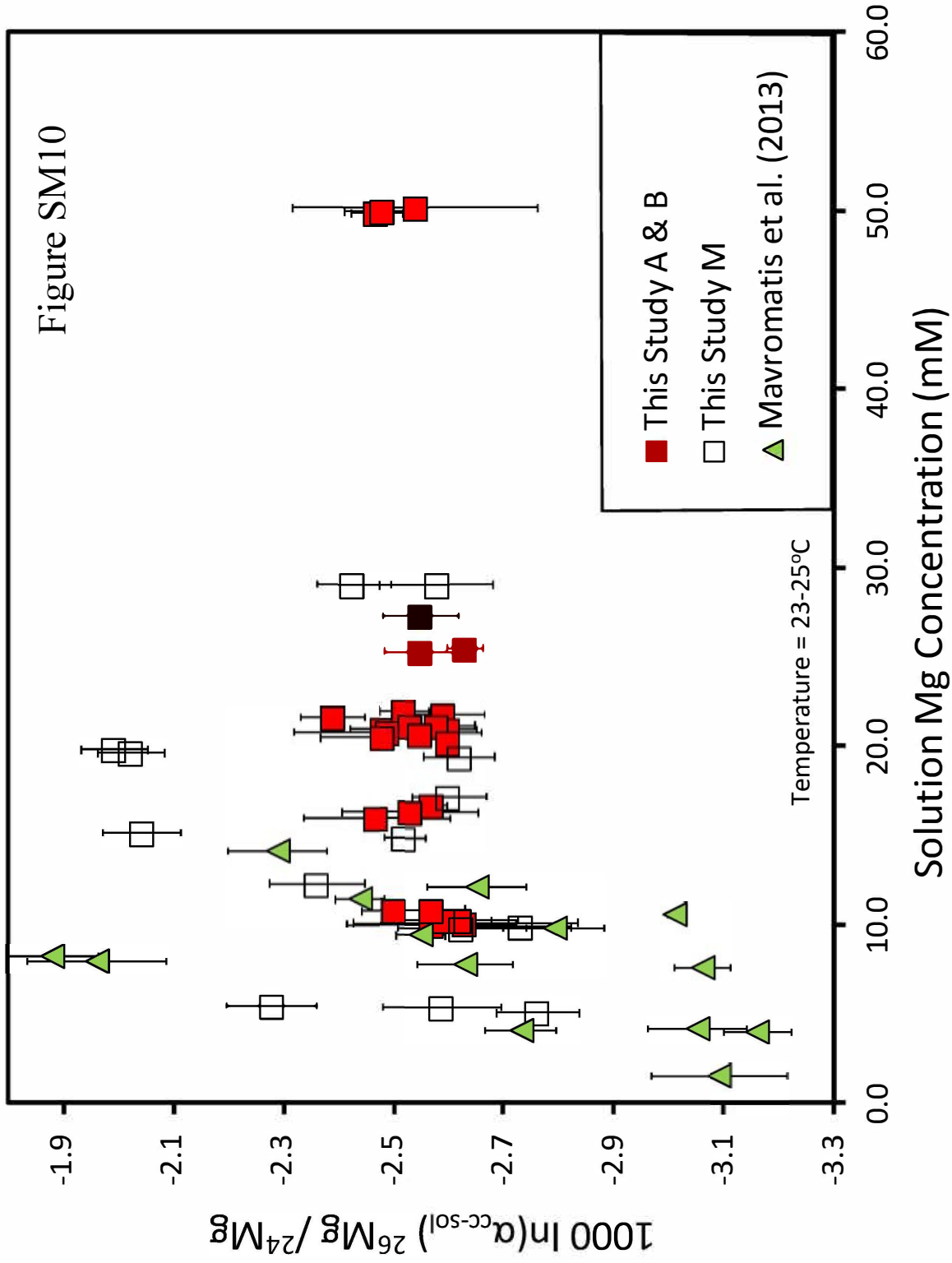

Figure SM5
This Study A
This Study B
This Study M
Li et al. (2012) C-22
Mavromatis et al. (2013)
Gabitov et al. (2014)
Temperature = 22-25°C
Partition Coefficient (D_{Mg})
Mg in Solution (mmol/L)
0.00
0.01
0.02
0.03
0.04
0.05
0.06
0.0
10.0
20.0
30.0
40.0
50.0
60.0

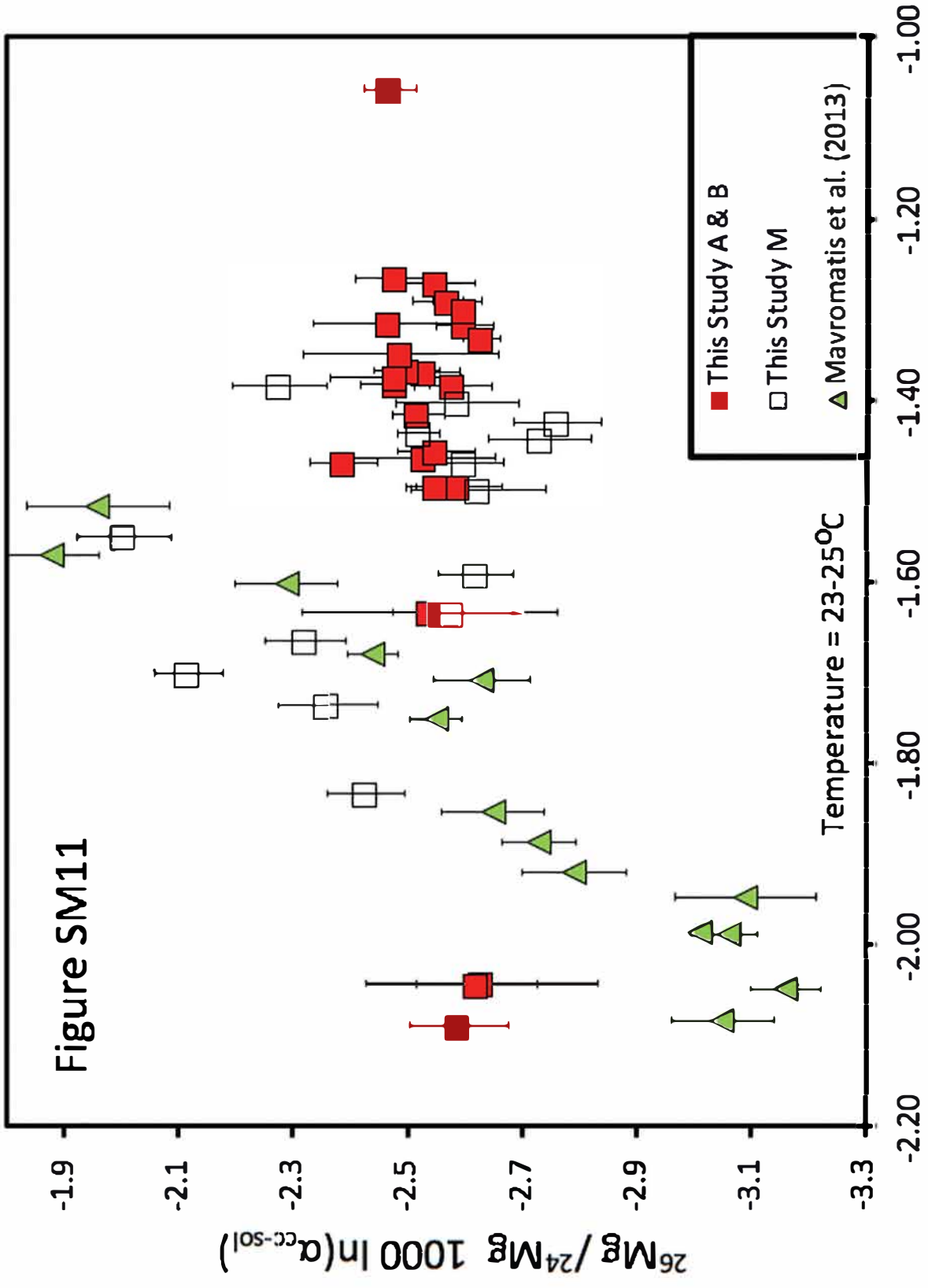

Figure SM6
Partition Coefficient (D_{Mg})
Ionic Strength (mM Cl^-)
0.00
0.01
0.02
0.03
0.04
0.05
0.06
0
200
400
600
800
1000
This Study A & B
This Study M
Mavromatis et al. (2013)
Temperature = 23-25°C

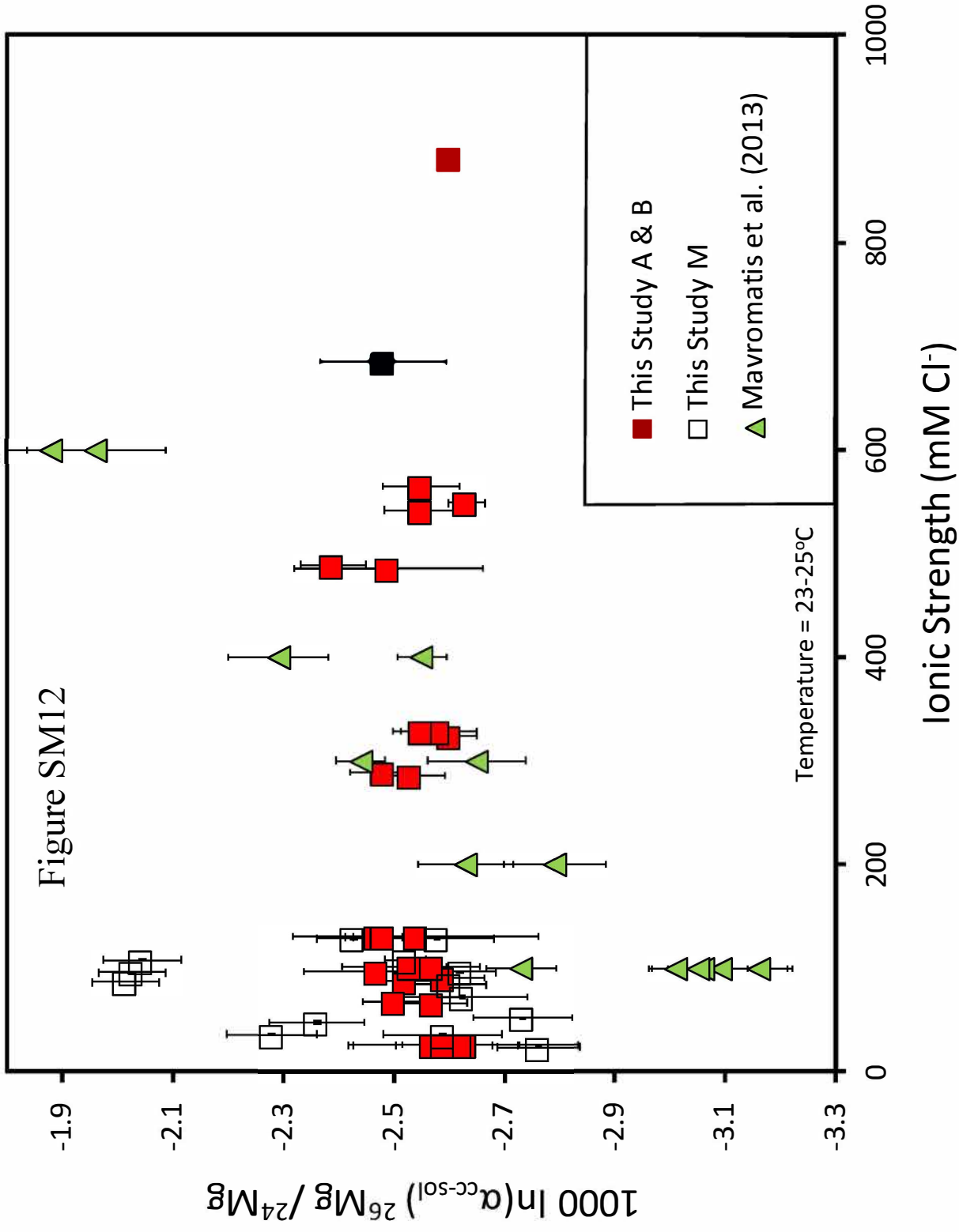

Figure SM7
Partition Coefficient (D_{M_g})
0.060
0.050
0.040
0.030
0.020
0.010
0.000
0%
20%
40%
60%
80%
100%
Partial Pressure of CO2
Temperature = 23-25°C
This Study A & B
This Study M

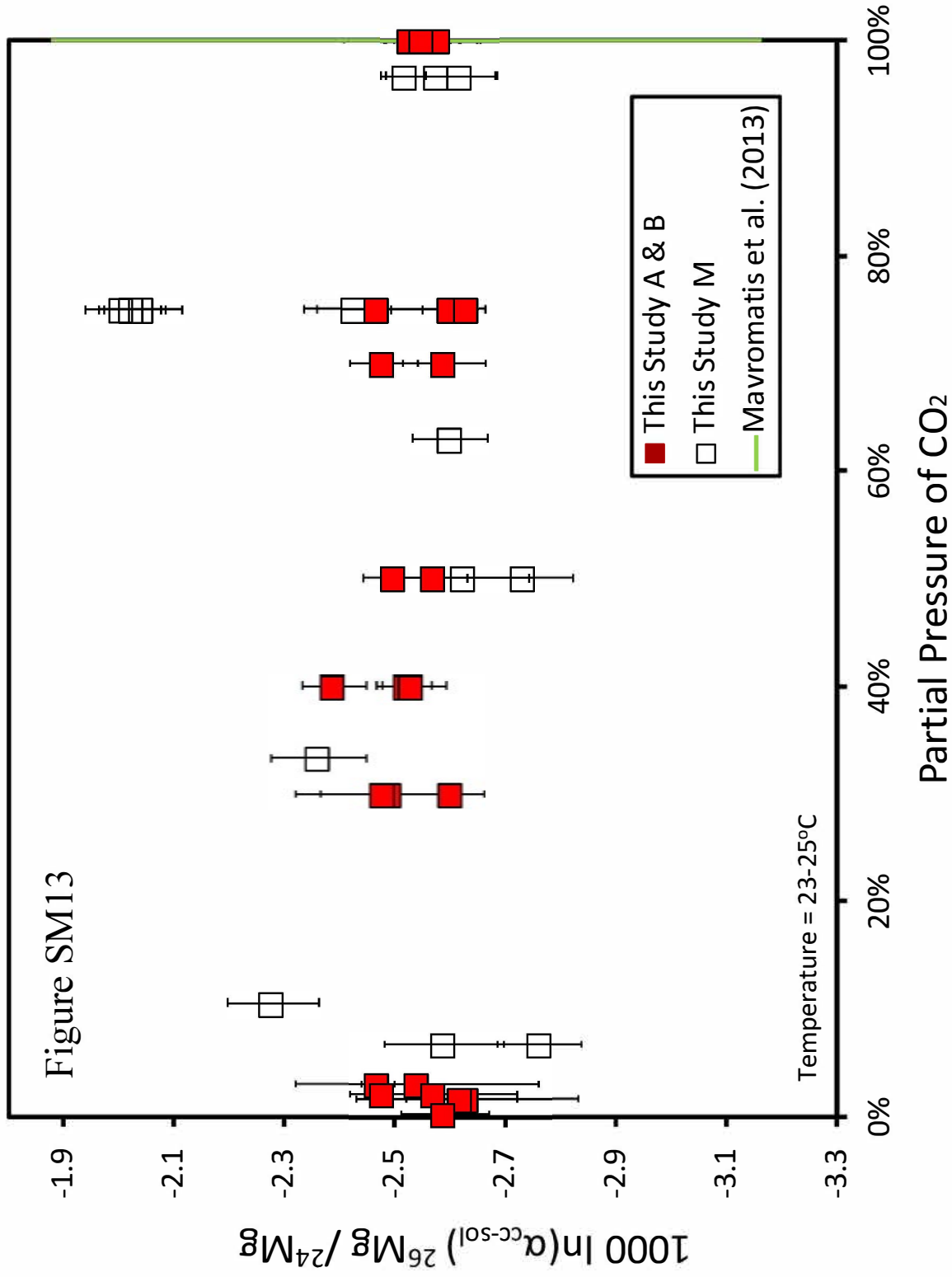

Figure SM8
This Study A & B
This Study M
Mavromatis et al. (2013)
Temperature = 23-25°C
Partition Coefficient (D_{Mg})
Log Precipitation Rate (mol m^{-2} s^{-1})
0.060
0.050
0.040
0.030
0.020
0.010
0.000
-9.0
-8.5
-8.0
-7.5
-7.0
-6.5
-6.0
-5.5
-5.0
-4.5


Figure SM9
This Study A & B
This Study M
Mavromatis et al. (2013)
(One Value at D_{Mg} = 0.010 and Ω = 18.5 not shown)
Temperature = 23-25°C
Partition Coefficient (D_{Mg})
Saturation State (Ω)
0.000
0.010
0.020
0.030
0.040
0.050
0.060
0.0
1.0
2.0
3.0
4.0
5.0
6.0
7.0
8.0


Figure SM10
This Study A & B
This Study M
Mavromatis et al. (2013)
Temperature = 23-25°C
1000 ln(α cc-sol) 26Mg /24Mg
Solution Mg Concentration (mM)
-1.9
-2.1
-2.3
-2.5
-2.7
-2.9
-3.1
-3.3
0.0
10.0
20.0
30.0
40.0
50.0
60.0


Figure SM11
Temperature = 23-25°C
This Study A & B
This Study M
Mavromatis et al. (2013)
-1.00
-1.20
-1.40
-1.60
-1.80
-2.00
-2.20
-1.9
-2.1
-2.3
-2.5
-2.7
-2.9
-3.1
-3.3
26Mg /24Mg 1000 ln(αcc-sol)


Figure SM12
1000 ln(α cc-sol) 26Mg /24Mg
Ionic Strength (mM Cl-)
Temperature = 23-25°C
This Study A & B
This Study M
Mavromatis et al. (2013)
-1.9
-2.1
-2.3
-2.5
-2.7
-2.9
-3.1
-3.3
0
200
400
600
800
1000


Figure SM13
1000 ln(α cc-sol) 26Mg /24Mg
-1.9
-2.1
-2.3
-2.5
-2.7
-2.9
-3.1
-3.3
0%
20%
40%
60%
80%
100%
Partial Pressure of CO2
Temperature = 23-25°C
This Study A & B
This Study M
Mavromatis et al. (2013)

Bibliography

Affek HP (**2013**) Clumped Isotope Equilibrium and the rate of Isotope Exchange between CO_2 and Water. *Am. J. Sci.*, 313, 309-325.

Affek HP and Eiler JM (**2006**) Abundance of mass 47 CO^2 in urban air, car exhaust, and human breath. *Geochim. Cosmochim. Acta*, 70, 1-12.

Affek HP and Zaarur S (**2014**) Kinetic isotope effect in CO_2 degassing: Insights from clumped and oxygen isotopes in laboratory precipitation experiments. *Geochim. Cosmochim. Acta*, 143, 319-330.

Affek HP, Matthews A, Ayalon A, Bar-Matthews M, Burstyn Y, Zaarur S, and Zilberman T (**2014**) Accounting for kinetic isotope effects in Soreq Cave (Israel) speleothems. *Geochim. Cosmochim. Acta*, 143, 303-318.

Albarède F and Beard BL (**2004**) Analytical methods for non-traditional isotopes. *Reviews in Mineralogy and Geochemistry. Mineral. Soc. Am. Washington, 113-152.*

Altermann W and Nelson DR (**1998**) Sedimentation rates, basin analysis and regional correlations of three Neoarchaean and Palaeoproterozoic sub-basins of the Kaapvaal craton as inferred from precise U–Pb zircon ages from volcaniclastic sediments. *Sedimentary Geology* 120, 225-256.

Altermann W and Wotherspoon JMcD (**1995**) The carbonates of the Transvaal and Griqualand West Sequences of the Kaapvaal craton, with special reference to the Lime Acres limestone deposit. *Mineral. Deposita* 30, 124-134.

Anderson TF and Arthur MA (**1983**) Stable isotopes of oxygen and carbon and their application to sedimentologic and paleoenvironmental problems. In: Arthur, M.A., Anderson, T.F., Kaplan, J.R., Veizer, J., Land, L.S. (Eds.), *Stable Isotopes in Sedimentary Geology. Society of Economic Paleontologists and Mineralogists*, Tusla, Oklahoma, pp. 1-1–1-151.

Andersson M.P., Rodriguez-Blanco, J.D., and Stipp, S.L.S. (**2016**) Is bicarbonate stable in and on the calcite surface? *Geochim. Cosmochim. Acta*, 176, 198-205.

Aoya M, Kouketsu Y, Endo S, Shimizu H, Mizukami T, Nakamura D, and Wallis S (**2010**) Extending the applicability of the Raman carbonaceous-material geothermometer using data from contact metamorphic rocks. *J. Met. Geol.* 28, 895-914.

Arora A, Banerjee S, and Dutta S (**2015**) Black shale in late Jurassic Jhuran Formation of Kutch: Possible indicator of ocean anoxic event? *J. Geol. S. India* 85, 265-278.

Artemieva IM and Vinnik LP (**2016**) Density structure of the cratonic mantle in southern Africa: 1. Implications for dynamic topography. *Gondwana Research* 39, 204-216.

Bai G, Yi H-B, Li H-J, and Xu J-J (**2013**) Hydration characteristics of Ca^{2+} and Mg^{2+}: a density functional theory, polarized continuum model and molecular dynamics investigation. *Molecular Physics* 111, 4, 553-568.

Bajnai D, Fiebig J, Tomasovych A, Garcia SM, Rollion-Bard C, Raddatz J, Loffler N, Primo-Ramos C, and Brand U (**2018**) Assessing kinetic fractionation in brachiopod calcite using clumped isotopes. *Sci. Reports* 8, 533, 1-12.

Baltrusaitis J and Grassian VH (**2009**) Calcite (1014) surface in humid environments. *Surface Science* 603, L99-L104.

Baskin DK (**1997**) Atomic H/C ratio of kerogen as an estimate of thermal maturity and organic matter conversion. *AAPG Bull.*, 81, 9, 1437-1450.

Beck WC, Grossman EL and Morse JW (**2005**) Experimental studies of oxygen isotope fractionation in the carbonic acid system at 15, 25, and 40 °C. *Geochim. Cosmochim. Acta*, 69, 3493-3503.

Bergmann KD, Finnegan S, Creel R, Eiler JM, Hughes NC, Popov LE, and Fischer WW (**2018**) A paired apatite and calcite clumped isotope thermometry approach to estimating Cambro-Ordovician seawater temperatures and isotopic composition. *Geochim. Cosmochim. Acta* 224, 18-41.

Bertram MA, Mackenzie FT, Bishop FC, Bischoff WD (**1991**) Influence of temperature on the stability of magnesian calcite. *Am. Mineralogist* 76, 1889-1896.

Beukes NJ (**1977**) Transition from siliciclastic to carbonate sedimentation near the base of the Transvaal Supergroup, Northern Cape Province, South Africa. *Sed. Geol.* 18, 201-221.

Beukes NJ (**1980**) Lithofacies and stratigraphy of the Kuruman and Griquatown Iron-Formations, Northern Cape Province, *South Africa. Trans. Geol. Soc. S. Afr.* 83, 69-86.

Beukes NJ (**1984**) Sedimentology of the Kuruman and Griquatown Iron-Formations, Transvaal Supergroup, Griqualand West, *South Africa. Precam. Res.* 24, 47-84.

Beukes NJ (**1987**) Facies relations, depositional environments, and diagenesis in a major early Proterozoic stromatolitic carbonate platform to basinal sequence, Campbellrand Subgroup, Transvaal Supergroup, *Southern Africa. Sed. Geol.* 54, 1-46.

Beukes NJ and Klein C (**1990**) Geochemistry and sedimentology of a facies transition – from microbanded to granular iron-formation – in the early Protozoic Transvaal Supergroup, *South Africa. Precam. Res.* 47, 99-139.

Beukes NJ, Klein C, Kaufman AJ, and Hayes JM (**1990**) Carbonate Petrography, Kerogen Distribution, and Carbon and Oxygen Isotope Variations in the Early Proterozoic Transition from Limestone to Iron-Formation Deposition, Transvaal Supergroup, *South Africa. Bull. Soc. Econ. Geol.* 85, 4, 663-690.

Beyssac O, Goffe B, Chopin C, and Rouzaud JN (**2002**) Raman spectra of carbonaceous material in metasediments: a new geothermometer. *J. Met. Geol.*, 2002, 20, 859-871.

Bierman PR, Coppersmith R, Hanson K, Neveling J, Portenga EW, and Rood DH (**2014**) A cosmogenic view of erosion, relief generation, and the age of faulting in southern Africa. *GSA Today* 24, 9, 4-11.

Birdwell JE and Washburn KE (**2015**) Rapid analysis of kerogen hydrogen-to-carbon ratios in shale and mudrocks by laser-induced breakdown spectroscopy. *Energy Fuels*, 29, 6999-7004.

Bischoff WD, Bishop FC, and Mackenzie FT (**1983**) Biogenically produced magnesian calcite: inhomogenities in chemical and physical properties; comparison with synthetic phases. *Am. Mineralogist* 68, 1183-1188.

Bischoff WD, Sharma SK, and Mackenzie FT (**1985**) Carbonate ion disorder in synthetic and biogenic magnesian calcites: a Raman spectral study. *Am. Mineralogist* 70, 581-589.

Bischoff WD, Mackenzie FT, and Bishop FC (**1987**) Stabilities of synthetic magnesian calcites in aqueous solution: Comparison with biogenic materials. *Geochim. Cosmochim. Acta* 51, 1413-1423.

Bischoff WD, Bertram MA, Mackenzie FT, and Bishop FC (**1993**) Diagenetic stabilization pathways of magnesian calcites. *Carbonates and Evaporites* 8, 1, 82-89.

Bischoff WD (**1998**) Dissolution Enthalpies of Magnesian Calcites. *Aquat. Geochem.* 4, 321-336.

Blake RE, Chang SJ, and Lepland A (**2010**) Phosphate oxygen isotopic evidence for a temperate and biologically active Archaean ocean. *Nature* 464, 1029-1033.

Blue CR and Dove PM (**2015**) Chemical controls on the magnesium content of amorphous calcium carbonate. *Geochim. Cosmochim. Acta* 148, 23-33.

Blue CR, Giuffre A, Mergelsberg S, Han N., De Yoreo JJ, and Dove PM (**2017**) Chemical and physical controls on the transformation of amorphous calcium carbonate into crystalline $CaCO_3$ polymorphs. *Geochim. Cosmochim. Acta* 196, 179-196.

Bonifacie M, Calmels D, Eiler JM, Horita J, Chaduteau C, Vasconcelos C, Agrinier P, Katz A, Passey BH, Ferry JM, and Bourrand JJ (**2017**) Calibration of the dolomite clumped isotope thermometer from 25 to 350°C, and implications for a universal calibration for all (Ca, Mg, Fe)CO3 carbonates. *Geochim. Cosmochim. Acta*, 200, 255-279.

Bonoldi L, Di Paolo L, and Flego C (**2016**) Vibrational spectroscopy assessment of kerogen maturity in organic-rich source rocks. *Vibrat. Spect.*, 87, 14-19.

Bottinga Y (**1968**) Calculation of fractionation factors for carbon and oxygen isotopic exchange in the system calcite-carbon dioxide-water. *J. Phys. Chem.*, 72(3), 800-808.

Brand WA, Assonov SS, and Coplen TB (**2010**) Correction for the 17O interference in $\delta^{13}C$ measurements when analyzing CO_2 with stable isotope mass spectrometry (IUPAC Technical Report). *Pure Appl. Chem.* 82, 1719-1733.

Brand U, Azmy K, Bitner MA, Logan A, Zuschin M, Came R, and Ruggiero E (**2013**) Oxygen isotopes and $MgCO_3$ in brachiopod calcite and a new paleotemperature equation. *Chem. Geol.* 359, 23-31.

Braun RL and Burnham AK (**1987**) Analysis of Chemical Reaction Kinetics Using a Distribution of Activation Energies and Simpler Models. *Energy & Fuels*, 1, 153-161.

Braun J, Guillocheau F, Robin C, Baby G, and Jelsma H (**2014**) Rapid erosion of the Southern African Plateau as it climbs over a mantle superswell. *J. Geophys. Res. Solid Earth* 119, 6093-6112.

Brenner DC, Passey BH, and Stolper DA (**2018**) Influence of water on clumped-isotope bond reordering kinetics in calcite. *Geochim. Cosmochim. Acta* 224, 42-63.

Brenninkmeijer CAM, Kraft P and Mook WG (**1983**) Oxygen isotope fractionation between CO_2 and H_2O. *Isotope Geoscience* 1:181-190.

Brown E, Colling A, Park D, Phillips J, Rothery D, and Wright J (**2004**) *The Ocean Basins: Their Structure and Evolution.* Butterworth-Heinemann, Linacre House, Jordan Hill, Oxford OX2 8DP, p. 172.

Brunauer S, Emmett P, and Teller E (**1938**) Adsorption of gases in multimolecular layers. *J. Am. Chem. Soc.* 60, 309–319.

Bucher K and Grapes R (**2011**) Petrogenesis of Metamorphic Rocks. 8th Edition, Springer Science + Business Media, pp. 162-165.

Budd DA and Haitt EE (**1993**) Mineralogical stabilization of high-magnesium calcite: geochemical evidence for intracrystal recrystallization within holocene porcellaneous foraminifera. *J. Sed. Petrol.* 63, 2, 261-274.

Bumby AJ, Eriksson PG, Catuneanu O, Nelson DR, and Rigby MJ (**2012**) Meso-Archaean and Palaeo-Proterozoic sedimentary sequence stratigraphy of the Kaapvaal Craton. *Marine and Petroleum Geology* 33, 92-116.

Burklé-Vitzthum V, Bounaceur R, Michels R, Scacchi G, and Marquaire P-M (**2017**) Kinetic parameters for the thermal cracking of simple hydrocarbons: From laboratory to geological time-temperature conditions. *J. Anal. App. Pyrolysis*, 125, 40-49.

Burnham AK (**2017**) Global Chemical Kinetics of Fossil Fuels: How to Model Maturation and Pyrolysis. Springer International Publishing, Gewerbestrasse, Switzerland.

Burnham AK and Sweeney JJ (**1989**) A chemical kinetic model of vitrinite maturation and reflectance. *Geochim. Cosmochim. Acta* 53, 2649-2657.

Burnham AK, Braun RL, and Coburn TT (**1996**) An appropriate kinetic model for well-preserved algal kerogens. *Energy & Fuels*, 10, 49-59.

Burton EA and Walter LM (**1987**) Relative precipitation rates of aragonite and Mg calcite from seawater: Temperature or carbonate ion control? *Geology* 15, 2, 111-114.

Burton EA and Walter LM (**1991**) The effects of PCO_2 and temperature on magnesium incorporation in calcite in seawater and $MgCl_2$-$CaCl_2$ solutions. *Geochim. Cosmochim. Acta* 55, 777-785.

Busenberg E and Plummer LN (**1989**) Thermodynamics of magnesian calcite solid-solutions at 25C and 1 atm total pressure. *Geochim. Cosmochim. Acta* 53, 1189-1208.

Button A (**1973**) The stratigraphic history of the Malmani Dolomite in the eastern and north-eastern Transvaal. *Trans. Geol. Soc. S. Afr.* 76, 229-247.

Came RE, Eiler JM, Veizer J, Azmy K, Brand U, and Weidman CR (**2007**) Coupling of surface temperatures and atmospheric CO^2 concentrations during the Palaeozoic era. *Nature*, 449, 198-201.

Came RE, Brand U, and Affek HP (**2014**) Clumped isotope signatures in modern brachiopod carbonate. *Chem. Geol.* 377, 20-30.

Chaco T and Deines P (**2008**) Theoretical calculation of oxygen isotope fractionation factors in carbonate systems. *Geochim. Cosmochim. Acta*, 72, 3642-3660.

Chanda P and Fantle MS (**2016**) Quantifying the effect of diagenetic recrystallization on the Mg isotopic composition of marine carbonates. *Geochim Cosmochim Acta* 204, 219-239.

Chang VTC, Williams RJP, Makishima A, Belshawl NS, O'Nions RK (**2004**) Mg and Ca isotope fractionation during $CaCO_3$ biomineralization. *Biochem. Biophys. Res. Commun.* 323, 79-85.

Chen Z, Liu X, and Jiang C (**2017**) Quick evaluation of source rock kerogen kinetics using hydrocarbon pyrograms from regular Rock-Eval anlaysis. *Energy Fuels*, 31, 1832-1841.

Chen Z, Liu X, Guo Q, Jiang C, and Mort A (**2017**) Inversion of source rock hydrocarbon generation kinetics from Rock-Eval data. *Fuel*, 194, 91-101.

Coplen T (**2007**) Calibration of the calcite–water oxygen-isotope geothermometer at Devils Hole, Nevada, a natural laboratory. *Geochim Cosmochim Acta* 71, 3948-3957.

Clog M, Stolper D, and Eiler JM (**2015**) Kinetics of $CO_{2(g)} – H_2O_{(l)}$ Isotopic Exchange, Including Mass 47 Isotopologues. *Chem. Geol.*, 395, 1-10.

Craig H (**1957**) The Natural Distribution of Radiocarbon and the Exchange Time of Carbon Dioxide Between Atmosphere and Sea. *Tellus*, 9, 1, 1-17.

Criss RE (**1991**) Temperature dependence of isotopic fractionation factor. In Stable Isotope Geochemistry: A Tribute to Samuel Epstein, *The Geochemical Society, Special Publication No.3*, 11-16.

Cummins RC, Finnegan S, Fike DA, Eiler JM, and Fischer WW (**2014**) Carbonate clumped isotope constraints on Silurian ocean temperature and seawater $\delta^{18}O$. *Geochim. Cosmochim. Acta* 140, 241-258.

Cusack M, Parkinson D, Perez-Huerta A, England J, Curry GB, and Fallick AE (**2007**) Relationship between $\delta^{18}O$ and minor element composition of *Terebratalia transversa*. *Earth Env. Sci. Trans. R. Soc. Edin.* 98, 443-449.

Cusack M, Dauphin Y, Chung P, Perez-Huerta A, and Cuif J-P (**2008**) Multiscale structure of calcite fibres of the shell of the brachiopod *Terebratulina retusa*. *J. Struct. Biol*. 164, 96-100.

Cusack M, Chung P, Dauphin Y, and Perez-Huerta A (**2010**) Brachiopod primary layer crystallography and nanostructure. *Spec. Pap. Palaeontol.* 84, 99-105.

Czaja AD, Beukes NJ, and Osterhout JT (**2016**) Sulfur-oxidizing bacteria prior to the Great Oxidation Event from the 2.52 Ga Gamohaan Formation of South Africa. *Geology* 44, 12, 983-986.

Daeron M, Guo W, Eiler JM, Genty D, Blamart D, Boch R, Drysdale R, Maire R, Wainer K, and Zanchetta G (**2011**) $^{13}C^{18}O$ clumping in speleothems: Observations from natural caves and precipitation experiments. *Geochim. Cosmochim. Acta* 75, 3303-3317.

Dalai P, Ustriyana P, and Sahai N (**2018**) Aqueous magnesium as an environmental selection pressure in the evolution of phospholipid membranes on early earth. *Geochim. Cosmochim. Acta* 223, 216-228.

Daeron M, Blamart D, Peral M, and Affek HP (**2016**) Absolute isotopic abundance ratios and the accuracy of Δ_{47} measurements. *Chem Geol.* 442, 83-96.

Deflies WF, Hren MT, and Lohmann KC (**2015**) Compositional and temperature effects of phosphoric acid fractionation on Δ_{47} analysis and implications for discrepant calibrations. *Chem. Geol.*, 396, 51-60.

Delarue F, Rouzaud J-N, Derenne S, Bourbin M, Westall F, Kremer B, Sugitani K, Deldicque D, and Robert F (**2016**) The Raman-Derived Carbonization Continuum: A Tool to Select the Best Preserved Molecular Structures in Archean Kerogens. *Astrobiology*, 16, 6, 407-417.

Delvaux D, Martin H, Leplat P, and Paulet J (**1990**) Geochemical characterization of sedimentary organic matter by means of pyrolysis kinetic parameters. *Org. Geochem.* 16, 1-3, 175-189.

Dennis KJ and Schrag DP (**2010**), Clumped isotope thermometry of carbonatites as an indicator of diagenetic alteration, *Geochim. Cosmochim. Acta*, 74(14), 4110-4122.

Dennis KJ, Affek HP, Passey BP, Schrag DP, and Eiler JM (**2011**), Defining an absolute reference frame for 'clumped' isotope studies of CO_2, *Geochim. Cosmochim. Acta*, 75(22), 7117-7131.

deGroot PA (**2009**) Handbook of Stable Isotope Techniques, Volume 2, Elsevier,

Radarweg 29, PO Box 211, 1000 AE Amsterdam, The Netherlands

Devriendt LS, Watkins JM, and McGregor HV (**2017**) Oxygen isotope fractionation in the $CaCO_3$-DIC-H_2O system. *Geochim. Cosmochim. Acta*, 214, 115-142.

Dietzel M and Usdowski E (**1996**) Coprecipitation of Ni^{2+}, Co^{2+}, and Mn^{2+} with galena and covellite, and of Sr^{2+} with calcite during crystallization via diffusion of H_2S and CO_2 through polyethylene at 20°C: Power law and Nernst law control of trace element partitioning. *Chem. Geol.* 131, 55–65.

Dietzel M, Tang J, Leis A and Köhler SJ (**2009**) Stable isotopic fractionation during inorganic calcite precipitation - effects of temperature, precipitation rate and pH. *Chem. Geol.*, 268 (2009), 107-115.

Disnar JR (**1994**) Determination of maximum paleotemperatures of burial (MPTB) of sedimentary rocks from pyrolysis data on the associated organic matter: basic principles and application. *Chem. Geol.*, 118, 289-299.

Doerner HA and Hoskins WM (**1925**) Co-precipitation of radium and barium sulfates. *J. Am. Chem. Soc.* 47, 3, 662-675.

Dressel I, Scheck-Wenderoth M, Cacace M, Lewerenz B, Gotze H-J, and Reichert C (**2015**) Reconstruction of the southwest African continental margin by backward modeling. *Marine Petrol. Geol.* 67, 544.

Du J, Geng A, Liao Z, and Cheng B (**2014**) Potential Raman parameters to assess the thermal evolution of kerogens from different pyrolysis experiments. *J. Anal. Appl. Pyrol.*, 107, 242-249.

Eagle RA, Eiler JM, Tripati AK, Ries JB, Freitas PS, Hiebenthal C, Wannamaker AD, Taviani M, Elliot M, Marenssi S, Nakamura K, Ramirez P, and Roy K (**2013**) The influence of temperature and seawater carbonate saturation state on ^{13}C-^{18}O bond ordering in bivalve mollusks. *Biogeosciences* 10, 4591-4606.

Eiler JM (**2007**) "Clumped-isotope" geochemistry—The study of naturally-occurring, multiply-substituted isotopologues. *Earth and Planetary Science Letters* 262.

Eiler JM (**2011**) Paleoclimate reconstruction using carbonate clump isotope thermometry. *Quat. Sci. Rev.* 30, 3575-3588.

Elstnerova P, Friak M, Fabritius HO, Lymperakis L, Hickel T, Petrov M, Nikolov S, Raabe D, Zieler A, Hild S, and Neugebauer J (**2010**) Ab initio study of thermodynamic, structural, and elastic properties of Mg-substituted crystalline calcite. *Acta Biomat.* 6, 4506-4512.

England J, Cusack M, and Lee MR (**2007**) Magnesium and sulphur in the calcite shells of two brachiopods, *Terebratulina retusa* and *Novocrania anomala*. *Lethaia* 40, 2-10.

Epstein S and Mayeda T (**1953**) Variation of O^{18} content of waters from natural sources. *Geochim. Cosmochim. Acta* 4, 213–224.

Epstein S, Buchsbaum R, Lowenstam HA, and Urey HC (**1953**) Revised Carbonate-Water Isotopic Temperature Scale. *Bull. Geol. Soc. Am.* 64, 1315-1326.

Eriksson PG, Altermann W, Catuneanu O, van der Merwe R, and Bumby AJ (**2001**) Major influences on the evolution of the 2.67-2.1 Ga Transvaal basin, Kaapvaal craton. *Sed. Geol.* 141-142, 205-231.

Erlanger ED, Granger DE, and Gibbon RJ (**2012**) Rock uplift rates in South Africa from isochron burial dating of fluvial and marine terraces. *Geology* 40, 11, 1019–1022.

Eroglu S, van Zuilen MA, Taubald H, Drost K, Wille Martin, Swanner ED, Beukes NJ, and Schoenberg R (**2017**) Depth-dependent δ13C trends in platform and slope settings of the Campbellrand-Malmani carbonate platform and possible implications for Early Earth oxidation. *Precam. Res.* 302, 122-139.

Farver JR and Yund RA (**1996**) Volume and grain boundary diffusion of calcium in natural and hot-pressed calcite aggregates. *Contrib. Mineral Petrol.* 123, 77-91.

Faure G and Mensing TM (**2009**) ISOTOPES Principles and Applications, Third Edition, John Wiley & Sons, Inc., New York, USA

Fernandez A, Tang J, and Rosenheim B (**2014**) Siderite "clumped" isotope thermometry: A new paleoclimate proxy for humid continental environments. *Geochimica et Cosmochimica Acta* **126**, 411421.

Ferralis N, Matys ED, Knoll AH, Hallmann C, and Summons RE (**2016**) Rapid, direct and non-destructive assessment of fossil organic matter via microRaman spectroscopy. *Carbon*, 108, 440-449.

Ferrari AC and Robertson J (**2000**) Interpretation of Raman spectra of disordered and amorphous carbon. *Phys. Rev. B* 61, 20, 14095-14107.

Ferry JM (**2001**) Calcite inclusions in forsterite. *Am. Mineralogist* 86, 773-779.

Finnegan S, Bergmann K, Eiler JM, Jones DS, Fike DA, Eisenman I, Hughes NC, Tripati AK, and Fischer WW (**2011**) The Magnitude and Duration of Late Ordovician-Early Silurian Glaciation. *Science* 331, 903-906.

Finnigan Gasbench II Operating Manual Revision A, Thermo Electron Corporation. Product Marketing, Bremen, Germany, **2004**.

Fischer WW, Schroeder S, Lacassie JP, Beukes NJ, Goldberg T, Strauss H, Horstmann UE, Schrag DP, and Knoll AH (**2009**) Isotopic constraints on the Late Archean carbon cycle from the Transvaal Supergroup along the western margin of the Kaapvaal Craton, South Africa. *Precam. Res.* 169, 15-27.

Fisler DK and Cygan RT (**1999**) Diffusion of Ca and Mg in calcite. *Am. Mineralogist* 84, 1392-1399.

Flowers RM and Schoene B (**2010**) (U-Th)/He thermochronometry constraints on unroofing of the eastern Kaapvaal craton and significance for uplift of the southern African Plateau. *Geology* 38, 9, 827-830.

Frauenstein F, Veizer J, Beukes NJ, Van Niekerk HS, and Coetzee LL (**2009**) Transvaal Supergroup carbonates: Implications for Paleoproterozoic $\delta^{18}O$ and $\delta^{13}C$ records. *Precam. Res.* 175, 149-160.

French KL, Hallmann C, Hope JM, Schoon PL, Zumberge JA, Hoshino Y, Peters CA, George SC, Love GD, Brocks JJ, Buick R, and Summons RE (**2015**) Reappraisal of hydrocarbon biomarkers in Archean rocks. *Proc. Nat. Acad. Sci.* 112, 19, 5915-5920.

Friedman I and O'Neil JR (**1977**) Compilation of stable isotope fractionation factors of geochemical interest. *U. S. Geol. Surv. Prof. Pap. 440*, KK1–KK9.

Fuchtbauer H and Hardie LA (**1976**) Experimentally determined homogeneous distribution coefficients for precipitated magnesian calcites: Application to marine carbonate cements. *Ann. Mtg. Geol. Soc. Amer.* 8, 877.

Fukushi K, Suzuki Y Kawano J, Ohno T, Ogawa M, Yaji T, and Takahashi Y (**2017**) Speciation of magnesium in monohydrocalcite: XANES, ab initio and geochemical modeling. *Geochim. Cosmochim. Acta* 213, 457-474.

Gabitov RI, Watson EB, and Sadekov A (**2012**) Oxygen isotope fractionation between calcite and fluid as a function of growth rate and temperature: An in situ study. *Chemical Geology* 306-307, 92-102.

Gabitov RI, Sadekov A, and Leinweber A (**2014**) Crystal Growth rate effect on Mg/Ca and Sr/Ca partitioning between calcite and fluid: An in situ approach. *Chem. Geol.* 367, 70-82.

Gagnon AC, DePaolo DJ, and Adkins JF (**2012**) Precise overgrowth composition during biomineral culture and inorganic precipitation. *Chem. Geol.* 330-331, 188-196.

Galy A, Bar-Matthews M, Halicz L, and O'Nions RK (**2002**) Mg isotopic composition of carbonate: insight from speleothem formation. *Earth Planet. Science Lett.* 201, 105-115.

Galy A, Yoffe O, Janney PE, Williams RW, Cloquet C, Alard O, Halicz L, Wadhwa M, Hutcheon ID, Ramon E, and Carignan J (**2003**) Magnesium isotope heterogeneity of the isotopic standard SRM980 and new reference materials for magnesium-isotope-ratio measurements. *J. Anal. At. Spectrom.* 18, 1352–1356.

Geisler T, Perdikouri C, Kasioptas A and Dietzel M (**2012**) Real-time monitoring of the overall exchange of oxygen isotopes between aqueous CO_3^{2-} and H_2O by Raman spectroscopy. *Geochim. Cosmochim. Acta*, 90, 1-11.

Ghosh P, Adkins J, Affek HP, Balta B, Guo WF, Schauble EA, Schrag DP, and Eiler JM (**2006**), ^{13}C-^{18}O bonds in carbonate minerals: A new kind of paleothermometer, *Geochim. Cosmochim. Acta*, 70(6), 1439-1456.

Giuffre AJ, Gagnon AC, De Yoreo JJ, and Dove PM (**2015**) Isotopic tracer evidence for the amorphous calcium carbonate to calcite transformation by dissolution-reprecipitation. *Geochim. Cosmochim. Acta* 165, 407-417.

Gonfiantini R (**1981**) The δ - notation and the mass-spectrometric measurement techniques. In : Stable isotope hydrology, deuterium and oxygen-18 in the water cycle. J. R. Gat & R. Gonfiantini (eds.). IAEA , Vienna. *Technical Report Series No. 210*: 35–84. [1-1/2, 6-2, App C]

Gorski CA and Fantle MS (**2017**) Stable mineral recrystallization in low temperature aqueous systems: A critical review. *Geochim. Cosmochim. Acta* 198, 439-465.

Green PF, Duddy IR, Japsen P, Bonow JM, and Malan JA (**2017**) Post-breakup burial and exhumation of the sourthern margin of Africa. *Basin Research* 29, 96-127.

Gregg JM, Bish DL, Kaczmarek SE, and Machel HG (**2015**) Mineralogy, nucleation and growth of dolomite in the laboratory and sedimentary environment: A review. *Sedimentology*, 62, 1749-1769.

Griesshaber E, Schmahl WW, Neuser R, Pettke T, Blum M, Mutterlose J, and Brand U (**2007**) Crystallographic texture and microstructure of terebratulide brachiopod shell calcite: An optimized materials design with hierarchical architecture. *Eur. J. Mineral.* 21, 715-723.

Griesshaber E, Kelm K, Sehrbrock A, Mader W, Mutterlose J, Brand U, and Schmahl WW (**2009**) Amorphous calcium carbonate in the shell material of the brachiopod *Megerlia truncata*. *Eur. J. Mineral.* 21, 715-723.

Guggenheim EA (**1937**) The theoretical basis of Raoult's law. *Trans. Faraday Soc.* 33, 151-155.

Gunasekaran S, Anbalagan G, and Pandi S (**2006**) Raman and infrared spectra of carbonates of calcite structure. *J. Raman Spect.* 37, 892-899.

Guo WF (**2008**). Carbonate clumped isotope thermometry: application to carbonaceous chondrites and effects of kinetic isotope fractionation. Ph. D. thesis, Div. of Geology and Planetary Science, Caltech, Pasadena, CA.

Guo WF, Mosenfelder J, Goddard W, and Eiler JM (**2009**) Isotopic fractionations associated with phosphoric acid digestion of carbonate minerals: Insights from first-principles theoretical modeling and clumped isotope measurements. *Geochimica et Cosmochimica Acta* **73.**

Hartley G and Mucci A (**1996**) The influence of P_{CO2} on the partitioning of magnesium in calcite overgrowth precipitated from artificial seawater at 25°C and 1 atm total pressure. *Geochim. Cosmochim. Acta* 60, 2, 315-324.

Heimann A, Johnson CM, Beard BL, Valley JW, Roden EE, Spicuzza MJ, and Beukes NJ (**2010**) Fe, C, and O isotope compositions of banded iron formation carbonates demonstrate a major role for dissimilatory iron reduction in ~2.5 Ga marine environments. *Earth Planet. Science Lett.* 490, 40-50.

Henkes GA, Passey BH, Grossman EL, Shenton BJ, Perez-Huerta A, and Yancey TE (**2014**) Temperature Limits for preservation of primary calcite clumped isotope paleotemperatures. *Geochim. Cosmochim. Acta* 139, 362-382.

Helpa V, Rybacki E, Morales LFG, and Dresen G (**2015**) Influence of grain size, water, and deformation, on dolomite reaction rim formation. *Am. Mineralogist* 101, 2655-2665.

Henderson LM and Kracek FC (**1927**) The fractional precipitation of barium and radium chromates. *J. Amer. Chem. Soc.* 49, 739-749.

Henkes GA, Passey BH, Wanamaker AD, Grossman EL, Ambrose WG and Carroll ML (**2013**) Carbonate clumped isotope compositions of modern marine mollusk and brachiopod shells. *Geochim. Cosmochim. Acta* 106, 307–325.

Henkes GA, Passey BH, Grossman EL, Shenton BJ, Yancey TE, and Perez-Huerta A (**2018**) Temperature evolution and the oxygen isotope composition of Phanerozoic oceans from carbonate clumped isotope thermometry. *Earth Planet. Science Lett.* 490, 40-50.

Higgins JA, Blatter CL, Lundstrom EA, Santiago-Ramos DP, Akhtar AA, Ahm A-S C, Bialik O, Holmden C, Bradbury H, Murray ST, and Swart PK (**2018**) Mineralogy, early marine diagenesis, and the chemistry of shallow-water carbonate sediments. *Geochim. Cosmochim. Acta* 220, 512-534.

Hill PS, Tripati AK, and Schauble EA (**2014**) Theoretical Constraints on the effects of pH, salinity, and temperature on clumped isotope signatures of dissolved inorganic carbon species and precipitating carbonate minerals. *Geochim. Cosmochim. Acta*, 125, 610-652.

Hippler D, Buhl D, Witbaard R, Richter DK, and Immenhauser A (**2009**) Towards a better understanding of magnesium-isotope ratios from marine skeletal carbonates. *Geochim. Cosmochim. Acta* 73, 6134-6146.

Hong M and Teng HH (**2014**) Implications of solution chemistry effects: Direction-specific restraints on the step kinetics of calcite growth. *Geochim. Cosmochim. Acta* 141, 228-239.

Hong M, Xu J, and Teng HH (**2016**) Evolution of calcite growth morphology in the presence of magnesium: Implications for the dolomite problem. *Geochim. Cosmochim. Acta* 172, 55-64.

Howson MR, Pethybridge AD, and House WA (**1987**) Synthesis and distribution coefficient of low-magnesium calcites. *Chem. Geol.* 64, 79-87.

Horita J (**2005**) Stable isotope thermometry: There is more to it than temperature. *Geochem. J.*, 39, 481-496.

Horita J and Wesolowski DJ (**1994**) Liquid-vapor fractionation of oxygen and hydrogen isotopes of water from the freezing to the critical temperature. *Geochim. Cosmochim. Acta*, 58, 16, 3425-3437.

Hu Z, Hu W, Wang X, Lu Y, Wang L, Liao Z, and Li W (**2017**) Resetting of Mg isotopes between calcite and dolomite during burial metamorphism: Outlook of Mg isotopes as geothermometer and seawater proxy. *Geochim. Cosmochim. Acta* 208, 24-40.

Huang Y and Fairchild IJ (**2001**) Partitioning of Sr^{2+} and Mg^{2+} into calcite under karst-analogue experimental conditions. *Geochim. Cosmochim. Acta* 65, 47-62.

Huntington KW and Lechler AR (**2015**) Carboante clumped isotope thermometry in continental tectonics. *Tectonophysics*, 647-648, 1-20.

Huntington KW, Eiler JM, Affek HP, Guo W, Bonifacie M, Yeung LY, Thiagarajan N, Passey B, Tripati A, Daeron M, and Came R (**2009**), Methods and limitations of 'clumped' CO_2 isotope (Δ_{47}) analysis by gas-source isotope ratio mass spectrometry, *J. Mass Spect.*, 44(9), 1318-1329.

Immenhauser A, Buhl D, Richter D, Niedermayr A, Riechelmann D, Dietzel M, and Schulte U (**2010**) Magnesium-isotope fractionation during low-Mg calcite precipitation in a limestone cave – Field study and experiments. *Geochim. Cosmochim. Acta* 74, 4346-4364.

Immenhauser A, Schone BR, Hoffmann R, and Niedermayr A (**2016**) Mollusc and brachiopod skeletal hard parts: Intricate archives of their marine environment. *Sedimentology* 63, 1-59.

Jacobs J and Thomas RJ (**2001**) A titanite fission track profile across the southeastern Archean Kaapvaal Craton and the Mesoproterozoic Natal Metamorphic Province, South Africa: evidence for differential cryptic Meso- to Neoproterozoic tectonism. *J. Afr. Earth Sci.* 33, 2, 323-333.

Jaffres JBD, Shields GA, and Wallmann C (**2007**) The oxygen isotope evolution of seawater: A critical review of a long-standing controversy and an improved geological water cycle model for the past 3.4 billion years. *Earth-Science Reviews* 83, 83-122.

Jimenez-Lopez C and Romanek CS (**2004**), Precipitation kinetics and carbon isotope partitioning of inorganic siderite at 25 degrees C and 1 atm, *Geochim. Cosmochim. Acta*, 68(3), 557-571.

Jimenez-Lopez C, Romanek CS, Huertas FJ, Ohmoto H, and Caballero E (**2004**) Oxygen isotope fractionation in synthetic magnesian calcite. *Geochim. Cosmochim. Acta* 68, 3367-3377.

Jimenez-Lopez C, Romanek CS, and Caballero E (**2006**) Carbon isotope fractionation in synthetic magnesian calcite. *Geochim. Cosmochim. Acta* 70, 1163-1171.

Johnson CM, Ludois JM, Beard BL, Beukes NJ, and Heimann A (**2013**) Iron formation carbonates: Paleoceanographic proxy or recorder of microbial diagenesis. *Geology* 41, 11, 1147-1150.

Jonas L, Muller T, Dohmen R, Baumgartner L, and Putlitz B (**2015**) Transport-controlled hydrothermal replacement of calcite by Mg-carbonates. *Geology* 43, 779–782.

Jung G, Prange M, and Schulz M (**2014**) Uplift of Africa as a potential cause for Neogene intensification of the Benguela upwelling system. *Nature Geoscience* 7, 741-747.

Kamber BS and Webb GE (**2001**) The geochemistry of late Archean microbial carbonate: Implications for ocean chemistry and continental erosion history. *Geochim. Cosmochim. Acta* 65, 15, 2509-2525.

Kasting JF, Howard MT, Wallman K, Veizer J, Shields GA, and Jaffres JBD (**2006**) Paleoclimates, ocean depth, and the oxygen isotopic composition of seawater. *Earth Planet. Sci. Lett.* 252, 82-93.

Katz A (**1973**) The interaction of magnesium with calcite during crystal growth at 25-90°C and one atmosphere. *Geochim. Cosmochim. Acta* 37, 1563-1586.

Kelson JR, Huntington KW, Schauer AJ, Saenger C, and Lechler AR (**2017**) Toward a universal carbonate clumped isotope calibration: Diverse synthesis and preparatory methods suggest a single temperature relationship. *Geochim. Cosmochim. Acta*, 197, 104-131.

Khelifi N, Sarnthein M, Frank M, Andersen N, Garbe-Schonberg D (**2014**) Late Pliocene variations of the Mediterranean outflow. *Mar. Geol.* 357, 182-194.

Kim S-T and O'Neil J (**1997**) Equilibrium and nonequilibrium oxygen isotope effects in synthetic carbonates. *Geochimica et Cosmochimica Acta* **61**.

Kim S-T, Hillaire-Marcel C, and Mucci A (**2006**) Mechanisms of equilibrium and kinetic oxygen isotope effects in synthetic aragonite at 25°C. *Geochimica et Cosmochimica Acta* **70**.

Kim ST, Gebbinck CK, Mucci A, Coplen TB (**2014**) Oxygen isotope systematics in the aragonite-CO_2-H_2O-NaCl sysem up to 0.7 mol/kg ionic strength at 25C. *Geochim. Cosmochim. Acta*, 137, 147-158.

Klein C and Beukes NJ. (**1989**) Geochemistry and Sedimentology of a Facies Transition from Limestone to Iron-Formation Deposition in the Early Proterozoic Transvaal Supergroup, South Africa. *South-African Econ. Geol.*, 84, 1733-1774.

Kluge T and Affek HP (**2012**) Quantifying kinetic fractionation in Bunker Cave speleothems using Δ_{47}. *Quat Sci. Rev.*, 49, 82-94.

Kluge T, Affek HP, Marx T, Aeschbach-Hertig W, Riechelmann DFC, Scholz D, Riechelmann S, Immenhauser A, Richter DK, Fohlmeister J, Wackerbarth A, Mangini A, and Spötl C (**2013**) Reconstruction of drip-water $\delta^{13}C$ based on calcite and clumped isotopes from Bunker Cave (Germany). *Clim. Past.* **9,** 377-391.

Kluge T, Affek HP, Dublyansky Y, and Spötl C (**2014**) Devils Hole paleotemperatures and implications for oxygen isotope equilibrium fractionation. *Earth and Planetary Science Letters* 400, 251260.

Kluge T, John CM, Jourdan AL, Davis S, and Crawshaw J (**2015**), Laboratory calibration of the calcium carbonate clumped isotope thermometer in the 25-250C temperature range, *Geochim. Cosmochim. Acta*, 157, 213-227.

Knauth LP (**2005**) Temperature and salinity history of the Precambrian ocean: Implications for the course of microbial evolution. *Palaeogeog. Palaeoclim. Palaeoecol.* 219, 1-2, 53-69.

Knoll AH and Beukes NJ (**2009**) Introduction: Initial investigations of a Neoarchean shelf margin-basin transition (Transvaal Supergroup, South Africa). *Precam. Res.* 169, 1-14.

Konigsberger E and Gamsjager H (**1992**) Solid-solute phase equilibria in aqueous solution: VII. A re-interpretation of magnesian calcite stabilities. *Geochim. Cosmochim. Acta* 56, 4095-4098.

Konigsberger E, Konigsberger L-C, and Gamsjager H (**1999**) Low-temperature thermodynamic model for the system Na_2CO_3-$MgCO_3$-$CaCO_3$-H_2O. *Geochim. Cosmochim. Acta* 63, 19/20, 3105-3119.

Kouketsu Y, Mizukami T, Mori H, Endo S, Aoya M, Hara H, Nakamura D, and Wallis S (**2014**) A new approach to develop the Raman carbonaceous material geothermometer for low-grade metamorphism using peak width. *Island Arc*, 23, 33-50.

Kunitake ME, Baker SP, and Estroff LA (**2012**) The effect of magnesium substitution on the hardness of synthetic and biogenic calcite. *MRS Comm.* 2, 113-116.

Kunitake ME, Mangano LM, Peloquin JM, Baker SP, and Estroff LA (**2013**) Evaluation of strengthening mechanisms in calcite single crystals from mollusk shells. *Acta Biomat.* 9, 5353-5359.

Land LS (**1998**) Failure to precipitate dolomite at 25°C from dilution solution despite 1000-fold oversaturation after 32 years. *Aquat. Geochem.,* 4, 361-368.

Lahfid A, Beyssac O, Deville E, Negro F, Chopin C, and Goffe B (**2010**) Evolution of the Raman spectrum of carbonaceous material in low-grade metasediments of the Glarus Alps (Switzerland). *Terra Nova*, 22, 354-360.

Lai D, Zhan J-H, Tian Y, Gao S, and Xu G (**2017**) Mechanism of kerogen pyrolysis in terms of chemical structure transformation. *Fuel*, 199, 504-511.

Lafargue E, Marquis F, and Pillot D (**1998**) Rock-Eval 6 applications in hydrocarbon exploration, production and soil contamination studies. *Oil Gas Sci. Technol.* 53, 421-437.

Lee H-T and Sun L-C (**2013**) The atomic H/C ratio of kerogen and its relation to organic geochemical parameters: implications for evaluating hydrocarbon generation of source rock. *Carbonates Evaporites*, 28, 433-445.

Levitt NP (**2014**) Sample Matrix Effects on Measured Carbon and Oxygen Isotope Ratios during Continuous-Flow Isotope-Ratio Mass Spectrometry. *Rapid Commun. Mass Spectrom.*, 28, 2259-2274.

Levitt NP, Eiler JM, Romanek CS, Beard BL, Xu H, and Johnson CM (**2018**) Near Equilibrium ^{13}C-^{18}O Bonding During Inorganic Calcite Precipitation under Chemo-Stat Conditions. *Geochem. Geophys.* 19, 10.1002/2017GC007089.

Levitt NP and Romanek CS (**2016**) An "On-Line" Method for Oxygen Isotope Exchange Between Gas Phase CO_2 and Water. *Aquatic Geochemistry*, 22, 253-269.

Li W, Chakraborty S, Beard BL, Romanek CS, and Johnson CM (**2012**) Magnesium isotope fractionation during precipitation of inorganic calcite under laboratory conditions. *Earth Planet. Science Lett.,* 333-334, 304316.

Li W, Beard BL, Li C, and Johnson CM (**2014**) Magnesium isotope fractionation between brucite [$Mg(OH)_2$] and Mg aqueous species: Implications for silicate weathering and biogeochemical processes. *Earth Planet. Science Lett.,* 394, 82-93.

Li W, Beard BL, Li C, Xu H, and Johnson CM (**2015**) Experimental calibration of Mg isotope fractionation between dolomite and aqueous solution and its geological implications. *Geochim. Cosmochim. Acta* 157, 164–181.

Lippmann F (**1991**) Aqueous Solubility of Magnesian calcites with different endmembers. *Acta Mineral. Petrog. Szeged* XXXII, 5-19.

Lloyd MK, Eiler JM, and Nabelek PI (**2017**) Clumped isotope thermometry of calcite and dolomite in a contact metamorphic environment. *Geochim. Cosmochim. Acta* 197, 323-344.

Lloyd MK, Ryb U, and Eiler JM (**2018**) Experimental calibration of clumped isotope reordering in dolomite. *Geochim. Cosmochim. Acta* 242, 1-20.

Lohmann KC and Meyers WJ (**1977**) Microdolomite inclusions in cloudy prismatic calcites: A proposed criterion for former high-magnesium calcites. *J. Sed. Pet.*, 47, 3, 1078-1088.

Long X, Nasse MJ, Ma Y, and Qi L (**2012**) From synthetic to biogenic Mg-containing calcites: a comparative study using FTIR microspectroscopy. *Phys. Chem. Chem. Phys.* 14, 2255-2263.

Long X, Ma Y, and Qi L (**2014**) Biogenic and synthetic high magnesium calcite – A review. *J. Struct. Biol.* 185, 1-14.

Lopez O, Zuddas P, and Faivre D (**2009**) The influence of temperature and seawater composition on calcite crystal growth mechanisms and kinetics: Implications for Mg incorporation in calcite lattice. *Geochim. Cosmochim. Acta* 73, 337-347.

Loste E, Wilson RM, Seshadri R, and Meldrum FC (**2003**) The role of magnesium in stabilizing amorphous calcium carbonate and controlling calcite morphologies. *J. Crystal. Growth* 254, 206-218.

Lunsdorf NK, Dunkl I, Schmidt BC, Rantitsch G, and Eynatten H (**2017**) Towards a Higher Comparability of Geothermometric Data Obtained by Raman Spectroscopy of Carbonaceous Material. Part 2: A Revised Geothermometer. *Geostands. Geoanal. Res.* 41, 4, 593-612.

Ma H, Xu Y, Huang K, Sun Y, Ke S, Peng Y, Lang X, Yan Z, and Shen B (**2018**) Heterogeneous Mg isotopic composition of the early Carboniferous limestone: implications for carbonate as a seawater archive. *Acta Geochimica* 37, 1, 1-18.

Martin DMB, Clendenin CW, Krapez B, and McNaughton NJ (**1998**) Tectonic and geochronological constraints on late Archaean and Palaeoproterozoic stratigraphic correlation within and between the Kaapvaal and Pilbara Cratons. *J. Geol. Soc. London* 155, 311.

Mavromatis V, Gautier Q, Bosc O, and Schott J (**2013**) Kinetics of Mg partition and Mg stable isotope fractionation during its incorporation in calcite. *Geochim. Cosmochim. Acta* 114, 188–203.

Mavromatis V, van Zuilen K, Purgstaller B, Baldermann A, Nagler TF, and Dietzel M (**2016**) Barium isotope fractionation during witherite ($BaCO_3$) dissolution, precipitation, and at equilibrium. *Geochim. Cosmochim. Acta* 190, 72–84.

Mavromatis V, Gautier Q, Bosc O, and Schott J (**2017a**) Impact of amorphous precursor phases on magnesium isotope signatures of Mg-calcite. *Earth Planet. Sci. Lett.* 464, 227–236.

Mavromatis V, Immenhauser A, Buhl D, Purgstaller B, Baldermann A, and Dietzel M (**2017b**) Effect of organic ligands on Mg partitioning and Mg isotope fractionation during low-temperature precipitation of calcite in the absence of growth rate effects. *Geochim. Cosmochim. Acta* 207, 139-153.

McCrea JM (1950) On the Isotopic Chemistry of Carbonates and a Paleotemperature Scale. *J. Chem. Phys.* 18, 849-857.

Millero F, Huang F, Graham T, and Pierrot D (**2007**) The dissociation of carbonic acid in NaCl solutions as a function of concentration and temperature. *Geochim. Cosmochim. Acta* 71, 46–55.

Mills GA and Urey HC (**1940**) The Kinetics of Isotopic Exchange between Carbon Dioxide, Bicarbonate Ion, Carbonate Ion and Water. *J. Am. Chem. Soc.*, 62, 1019-1026.

Missbach H, Duda JP, Lunsdorf NK, Schmidt BC, and Thiel V (**2016**) Testing the preservation of biomarkers during experimental maturation of an immature kerogen. I. J. *Astrobio.*, 15, 3, 165-175.

Miyano T and Beukes NJ (**1984**) Phase Relations of Stilpnomelane, Ferri-annite, and Riebeckite in Very Low-Grade Metamorphosed Iron-Formations. *Trans. Geol. Soc. S. Africa* 87, 111-124.

Mori H, Mori N, Wallis S, Westaway R, and Annen C (**2017**) The importance of heating duration for Raman CM thermometry: evidence from contact metamorphism around the Great Whin Sill intrusion, UK. *J. Met. Geol.* 35, 165-180.

Morse JW (**1974**) Dissolution kinetics of calcium carbonate in sea water. III. A new method for the study of carbonate reaction kinetics. *Amer. J. Sci.* 274, 97-107.

Morse JW, Arvidson RS, and Luttge A (**2007**) Calcium carbonate formation and dissolution. *Chem. Rev.* 107, 342-381.

Morse JW and Mackenzie FT (**1990**) Geochemistry of Sedimentary Carbonates. Elsevier Science Publishers Inc., New York, NY.

Moucha R and Forte AM (**2011**) Changes in African topography driven by mantle convection. *Nature Geoscience* 4, 707-712.

Mucci A (**1986**) Growth kinetics and composition of magnesian calcite overgrowths precipitated from seawater: Quantitative influence of orthophosphate ions. *Geochim. Cosmochim. Acta* 50, 2255-2265.

Mucci A (**1987**) Influence of temperature on the composition of magnesian calcite overgrowth precipitated from seawater. *Geochim. Cosmochim. Acta* 51, 1977-1984.

Mucci A and Morse JW (**1983**) The incorporation of Mg^{2+} and Sr^{2+} into calcite overgrowths: influences of growth rate and solution composition. *Geochim. Cosmochim. Acta* 47, 217-233.

Mucci A and Morse JW (**1984**) The solubility of calcite in seawater solutions of various magnesium concentration, I_t = 0.697 m at 25ºC and one atmosphere total pressure. *Geochim. Cosmochim. Acta* 48, 815-822.

Mucci A, Morse JW, and Kaminsky MS (**1985**) Auger spectroscopy analysis of magnesian calcite overgrowths precipitated from seawater and solutions of similar composition. *Am. J. Sci.* 285, 289-305.

Mucci A, Canuel R, and Zhong S (**1989**) The solubility of calcite and aragonite in sulfate free seawater and the seeded growth kinetics and composition of the precipitates at 25°C. *Chem. Geol.* 74, 309-320.

Muller MN, Kisakurek B, Buhl D, Gutperlet R, Kolevica A, Riebesell U, Stoll H, Eisenhauer A (**2011**) Response of the coccolithophores *Emiliania huxleyi* and *Coccolithus braarudii* to

changing seawater Mg^{2+} and Ca^{2+} concentrations: Mg/Ca, Sr/Ca ratios and $\delta^{44/40}Ca$, $\delta^{26/24}Mg$ of coccolith calcite. *Geochim. Cosmochim. Acta* 75, 2088-2102.

Murray ST, Arienzo MM, and Swart PK (**2016**) Determining the Δ_{47} acid fractionation in dolomites. *Geochim. Cosmochim. Acta* 174, 42-53.

Navrotsky A and Capobianco C (**1987**) Enthalpies of formation of dolomite and of magnesian calcites. *Am. Mineral.* 72, 782-787.

Nutman AP, Bennett VC, Friend CR, Van Kranendonk MJ, and Chivas AR (**2016**) Rapid emergence of life shown by discovery of 3,700-million-year-old microbial structures. *Nature* 537, 7621, 535-539.

Oelkers EH, Berninger U-N, Perez-Fernandez A, Chmeleff J, Mavromatis V (**2018**) The temporal evolution of magnesium isotope fractionation during hydromagnesite dissolution, precipitation, and at equilibrium. *Geochim. Cosmochim. Acta* 226, 36-49.

Ogino T, Suzuki T, and Sawada K (**1987**) The formation and transformation mechanism of calcium carbonate in water. *Geochim. Cosmochim. Acta,* 51, 2757–2767.

Olack G and Coleman A (**2016**) Influence of 17O correction parameters on calculation and calibration of Δ_{47}. Abstract presented at Goldschmidt. Yokohama, Japan 26 June – 1 July, 2016 2378.

O'Neil JR and Adami LH (**1969**) Oxygen isotope partition function ratio of water and the structure of liquid water. *J. Phys. Chem.* 73(5): 1553-1558.

Oomori T, Kaneshima H, and Maezato Y (**1987**) Distribution coefficient of Mg^{2+} ions between calcite and solution at 10-50°C. *Marine Chem.* 20, 327-336.

Palmer DA, and Wesolowski DJ (**1997**) Potentiometric measurements of the first hydrolysis quotient of magnesium (II) to 250ºC and 5 molal ionic strength (NaCl). *J. Solut. Chem.* 26, 217–232.

Parkhurst DL and Appelo CAJ (**2013**) Description of input and examples for PHREEQC version 3—A computer program for speciation, batch-reaction, one-dimensional transport, and inverse geochemical calculations: U.S. Geological Survey Techniques and Methods, book 6, chap. A43, 497 p., available only at http://pubs.usgs.gov/tm/06/a43/.

Passey BH, Levin NE, Cerling TE, Brown FH, and Eiler JM (**2010**) High-temperature environments of human evolution in East Africa based on bond ordering in paleosol carbonates. *Proc. Natl. Acad. Sci. U.S.A.* 107, 11245–9.

Pearce CR, Saldi GD, Schott J, and Oelkers EH (**2012**) Isotopic fractionation during congruent dissolution, precipitation, and at equilibrium: Evidence from Mg isotopes. *Geochim. Cosmochim. Acta* 92, 170-183.

Perez-Fernandez A, Berninger U-N, Mavromatis V, Pogge von Strandmann PAE, and Oelkers EH (**2017**) Ca and Mg isotope fractionation during the stoichiometric dissolution of dolomite at temperatures from 51 to 126ºC and 5 bars CO_2 pressure. *Chem. Geol.* 467, 76-88.

Perez-Huerta A, Cusack M, Jeffries TE, Williams CT (**2008**) High resolution distribution of magnesium and strontium and the evaluation of Mg/Ca thermometry in Recent brachiopod shells. *Chem. Geol.* 247, 229-241.

Perez-Huerta A, Cusack M, and Dalbeck P (**2011**) Crystallographic contribution to the vital effect in biogenic carbonates Mg/Ca thermometry. *Earth Environ. Sci. Trans. Royal Soc. Edinburgh* 102, 35–41.

Peters KE, Burnham AK, Walters CC, and Schenk O (**2017**) Guidelines for kinetic input to petroleum system models from open-system pyrolysis. *Marine Petrol. Geol.*, in press, https://doi.org/10.1016/j.marpetgeo.2017.11.024

Petryshyn VA, Lim D, Laval BL, Brady A, Slater G, and Tripati AK (**2015**) Reconstruction of limnology and microbialite formation conditions from carbonate clumped isotope thermometry. *Geobiology* 13, 53-67.

Pinilla C, Blanchard M, Balan E, Natarajan SK, Vuilleumier R, and Mauri F (**2015**) Equilibrium magnesium isotope fractionation between aqueous Mg^{2+} and carbonate minerals: Insights from path integral molecular dynamics. *Geochim. Cosmochim. Acta* 163, 126-139.

Pogge von Strandmann PAE, James RH, van Calsteren P, Gislason SR, and Burton KW (**2008**) Lithium, magnesium, and uranium isotope behavior in the estuarine environment of basaltic islands. *Earth Planet. Sci. Lett.* 274, 462-471.

Pogge von Strandmann PAE, Forshaw J, and Schmidt DN (**2014**) Modern and Cenozoic records of seawater magnesium from foraminiferal Mg isotopes. *Biogeosciences* 11, 5155-5168.

Politi Y, Batchelor DR, Zaslansky P, Chmelka BF, Weaver JC, Sagi I, Weiner S, and Addadi L (**2010**) Role of Magnesium Ion in the Stabilization of Biogenic Amorphous Calcium Carbonate: A Structure-Function Investigation. *Chem. Mater.* 22, 161-166.

Pope EC, Bird DK, and Rosing MT (**2012**) Isotope composition and volume of Earth's early oceans. *Proc. Nat. Acad. Sci.* 109, 12, 4371-4376.

Purgstaller B, Mavromatis V, Immenhauser A, and Dietzel M (**2016**) Transformation of Mg-bearing amorphous calcium carbonate to Mg-calcite – In situ monitoring. *Geochim. Cosmochim. Acta* 174, 180-195.

Putnis A (**2014**) Why Mineral Interfaces Matter. *Science* 343, 1441-1442.

Ra K, Kitagawa H, and Shiraiwa Y (**2010**) Mg isotopes in chlorophyll-a and coccoliths of cultured coccolithophores (*Emiliania huxleyi*) by MC-ICP-MS. *Mar. Chem.* 122, 130-137.

Radha AV, Fernandez-Martinez A, Hu Y, Jun Y-S, Waychunas GA, and Navrotsky A (**2012**) Energetic and structural studies of amorphous $Ca_{1-x}Mg_xCO_3 \bullet nH_2O (0 \leq x \leq 1)$. *Geochim. Cosmochim. Acta* 90, 83-95.

Radha AV and Navrotsky A (**2013**) Thermodynamics of Carbonates. *Rev. Min. Geochem.* 77, 73-121.

Rahl JM, Anderson KM, Brandon MT, and Fassoulas C (**2005**) Raman spectroscopic carbonaceous material thermometry of low-grade metamorphic rocks: Calibration and application to tectonic exhumation in Crete, Greece. *Earth Planet. Sci. Lett.*, 240, 339-354.

Raja MA, Zhao Y, Zhang X, Li C, and Zhang S (**2018**) Practices for modeling oil shale pyrolysis and kinetics. *Rev. Chem. Eng.*, 34, 1, 21-42.

Richardson JC, Hodgson DM, Paton D, Craven B, Rawcliffe A, and Lang A (**2017**) Where is my sink? Reconstruction of landscape development in southwestern Africa since the Late Jurassic. *Gondwanan Research* 45, 43-64.

Riechelmann S, Mavromatis V, Buhl D, Dietzel M, Eisenhauer A, and Immenhauser A (**2016**) Impact of diagenetic alteration on brachiopod shell magnesium isotope ($\delta^{26}Mg$) signatures: Experimental versus field data. *Chem. Geol.* 440, 191-206.

Ries JB (**2004**) Effect of ambient Mg/Ca ratio on Mg fractionation in calcareous marine invertebrates: A record of the oceanic Mg/Ca ratio over the Phanerozoic. *Geology*, 32, 11, 981-984.

Roberts GG and White N (**2010**) Estimating uplift rate histories from river profiles using African examples. *J. Geophys. Res.* 115, B02406.

Rodriguez-Blanco JD, Shaw S, and Benning LG (**2011**) The kinetics and mechanisms of amorphous calcium carbonate (ACC) crystallization to calcite, via vaterite. *Nanoscale* **3**, 265–71.

Rollion-Bard C, Saulnier S, Vigier N, Schumacher A, Chaussidon M, and Lecuyer C (**2016**) Variability in magnesium, carbon and oxygen isotope compositions of brachiopod shells: Implications for paleoceanographic studies. *Chem. Geol.* 443, 49-60.

Romanek CS, Grossman EL, and Morse JW (**1992**), Carbon isotopic fractionation in synthetic aragonite and calcite – effects of temperature and precipitation rate. *Geochim. Cosmochim. Acta*, 56(1), 419-430.

Romanek CS, Jimenez-Lopez C, Navarro AR, Sanchez-Roman M, Sahai N, and Colman M (**2009**), Inorganic synthesis of Fe-Ca-Mg carbonates at low temperature. *Geochim. Cosmochim. Acta*, 73(18), 5361-5376.

Romanek CS, Morse JW, and Grossman EL (**2011**), Aragonite Kinetics in Dilute Solutions, *Aquat. Geochem.* 17(4-5), 339-356.

Rudge JF, Roberts GG, White NJ, and Richardson CN (**2015**) Uplift histories of Africa and Australia from linear inverse modeling of drainage inventories. *J. Geophys. Res. Earth Surf.* 120, 894-914.

Rustad JR, Casey WH, Yin Q-Z, Bylaska EJ, Felmy AR, Bogatko SA, Jackson VE, and Dixon DA (**2010**) Isotopic fractionation of Mg^{2+}(aq), Ca^{2+}(aq), and Fe^{2+}(aq) with carbonate minerals. *Geochim. Cosmochim. Acta*, 74, 6301-6323.

Sade Z and Halevy I (**2017**) New constraints on kinetic isotope effects during CO2(aq) hydration and hydroxylation: Revisiting theoretical and experimental data. *Geochim. Cosmochim. Acta*, 214, 246-265.

Saenger C and Wang Z (**2014**) Magnesium isotope fractionation in biogenic and abiogenic carbonates: implications for paleoenvironmental proxies. *Quat. Sci. Rev.* 90, 1-21.
Saenger C and Wang Z (**2014**) Magnesium isotope fractionation in biogenic and abiogenic carbonates: implications for paleoenvironmental proxies. *Quat. Sci. Rev.* 90, 1-21.

Said A, Moder C, Clark S, and Ghorbal B (**2015**) Cretaceous-Cenozoic sedimentary budgets of the Southern Mozambique Basin: Implications for uplift history of the South African Plateau. *J. African Earth Sci.* 109, 1-10.

Sand KK, Tobler DJ, Dobberschutz S, Larsen KK, Makovicky E, Andersson MP, Wolthers M, and Stipp SLS (**2016**) Calcite Growth Kinetics: Dependence on Saturation Index, Ca^{2+}:CO_3^{2-} Activity Ratio, and Surface Atomic Structure. *Cryst. Growth Des.* 16, 3602-3612.

Santos GM, Ferguson J, Acaylar K, Johnson KR, Griffin S, and Druffel E (**2011**) $\Delta^{14}C$ and $\delta^{13}C$ of seawater DIC as tracers of coastal upwelling: a 5-year time-series from Southern California. *Radiocarbon* 53, 669–677.

Santrock J, Studley SA, and Hayes JM (**1985**) Isotopic analyses based on the mass spectrum of carbon dioxide. *Anal. Chem.* 57, 1444-1448.

Saulnier S, Rollion-Bard D, Vigier N, and Chaussidon M (**2012**) Mg isotope fractionation during calcite precipitation: an experimental study. *Geochim. Cosmochim. Acta* 91, 75-91.

Saunders AM and DeRose VJ (**2016**) Beyond Mg^{2+}: functional interactions between RNA and transition metals. *Curr. Opin. Chem. Biol.* 31, 153-159.

Schauble EA (**2004**) Applying stable isotope fractionation theory to new systems, geochemistry of non-traditional stable isotopes. *Mineral. Soc. Am.* Washington, 65-111.

Schauble EA (**2011**) First-principles estimates of equilibrium magnesium isotope fractionation in silicate, oxide, carbonate and hexaaquamagnesium(2+) crystals. *Geochim. Cosmochim. Acta* 75, 844-869.

Schauer AJ, Kelson J, Saenger C, and Huntington KW (**2016**) Choice of ^{17}O correction affects clumped isotope (Δ_{47}) values of CO_2 measured with mass spectrometry. *Rapid Comm. Mass Spec.* 30, 2607-2616.

Schito A, Corrado S, Aldega L, and Grigo D (**2016**) Overcoming pitfalls of vitrine reflectance measurements in the assessment of thermal maturity: the case history of the lower Congo basin. *Marine Petrol. Geol.*, 74, 59-70.

Schito A, Romano C, Corrado S, Grigo D, and Poe B (**2017**) Diagenetic thermal evolution of organic matter by Raman spectroscopy. *Organic Geochem.*, 106, 57-67.

Schopf JM, Kudryavtsev AB, Agresti DG, Czaja AD, and Wdowiak TJ (**2005**) Raman Imagery: A New Approach to Assess the Geochemical Maturity and Biogenicity of Permineralized Precambrian Fossils. *Astrobiology*, 5, 3, 333-371.

Schott J, Mavromatis V, Fujii T, Pearce CR, and Oelkers EH (**2016**) The control of carbonate mineral Mg isotope composition by aqueous speciation: Theoretical and experimental modeling. *Chem. Geol.* 445, 120-134.

Schroder S, Bukes NJ, and Sumner DY (**2009**) Microbialite-sediment interactions on the slope of the Campbellrand carbonate platform (Neoarchean, South Africa). *Precam. Res.* 169, 68-79.

Schroder S, Lacassie JP, and Bukes NJ (**2006**) Stratigraphic and geochemical framework of the Agouron drill cores, Transvall Supergroup (Neoarchean-Paleoproterozoic, South Africa). *S. Afr. J. Geol.* 109, 23-54.

Sedaghatpour F, Teng F-Z, Liu Y, Sears DWG, and Taylor LA (**2013**) Magnesium Isotopic Composition of the Moon. *Geochim. Cosmochim. Acta* 120, 1-16.

Sforna MC, van Zuilen MA, and Philippot P (**2014**) Structural characterization by Raman hyperspectral mapping of organic carbon in the 3.46 billion-year-old Apex chert, Western Australia. *Geochim. Cosmochim. Acta* 124, 18-33.

Shen Z, Szlufarska I, Brown PE, Xu H (**2015**) Investigation of the Role of Polysaccharide in the Dolomite Growth at Low Temperature by Using Atomistic Simulations. *Langmuir* 31, 10435-10442.

Shields GA (**2007**) The marine carbonate and chert isotope records and their implications for tectonics, life and climate on the early Earth. *Earth's Oldest Rocks, Developments in Precambrian Geology* 15, 971-983.

Spencer C and Kim ST (**2015**) Carbonate clumped isotope paleothermometry: a review of recent advances in CO_2 evolution, purification, measurement and standardization techniques. *Geosci. Journal*, 19,2, 357-374.

Stanley JR, Flowers RM, and Bell DR (**2013**) Kimberlite (U-Th)/He dating links surface erosion with lithospheric heating, thinning, and metasomatism in the southern African Plateau. *Geology* 41, 12, 1243-1246.

Stanley SM and Hardie LA (**1998**) Secular oscillations in the carbonate mineralogy of reef-building and sediment-producing organisms driven by tectonically forced shifts in seawater chemistry. *Paleogeog. Paleoclim.*, 144, 3-19.

Stefánsson A, Bénézeth P, and Schott J. (**2013**). Carbonic acid ionization and the stability of sodium bicarbonate and carbonate ion pairs to 200 °C — a potentiometric and spectrophotometric study. *Geochim. Cosmochim. Acta* 120, 600–611.

Stefánsson A, Bénézeth P, and Schott J (**2014**). Potentiometric and spectrophotometric study of the stability of magnesium carbonate and bicarbonate ion pairs to 150 °C and aqueous inorganic carbon speciation and magnesite solubility. *Geochim. Cosmochim. Acta* 138, 21–31.

Stolper DA and Eiler JM (**2015**) The Kinetics of Solid-State Isotope-Exchange Reactions for Clumped Isotopes: A Study of Inorganic Calcites and Apatites from Natural and Experimental Samples. *Am. J. Sci.*, 315, 363-411.

Stolper DA, Eiler JM, and Higgins JA (**2018**) Modeling the effects of diagenesis on carbonate clumped-isotope values in deep- and shallow-water settings. *Geochim. Cosmochim. Acta* 227, 264-291.

Strauss H and Beukes NJ (**1996**) Carbon and sulfur isotopic compositions of organic carbon and pyrite in sediments from the Transvaal Supergroup, South Africa. *Precam. Res.* 79, 57-71.

Sulpis O, Lix C, Mucci A, and Boudreau BP (**2017**) Calcite dissolution kinetics at the sediment-water interface in natural seawater. *Marine Chem.* 195, 70-83.

Sumner DY (**1995**) Facies, Paleogeography, and Carbonate precipitation on the Archean (2520 Ma) Campbellrand-Malmani Carbonate Platform, Transvaal Supergroup, South Africa. Ph. D. thesis, Department of Earth, Atmospheric and Planetary Sciences, Massachusetts Institute of Technology, Cambridge, MA.

Sumner DY (**2002**) Neoarchean Carbonates - Clues to Early Life and Early Ocean Chemistry. Excursion 6A Field Guide, International Association of Sedimentologists, 16th International Sedimentological Congress, Rand Afrikaans University, Auckland Park, Johannesburg, South Africa.

Sumner DY and Grotzinger JP (**1996**) Herringbone Calcite: Petrography and Environmental Significance. *J. Sed. Res.* 66, 3, 419-429.

Sumner DY and Grotzinger JP (**2004**) Implications for Neoarchaean ocean chemistry from primary carbonate mineralogy of the Campbellrand-Malmani Platform, South Africa. *Sedimentology* 51, 1273-1299.

Sumner DY and Beukes (**2006**) Sequence Stratigraphic Development of the Neoarchean Transvaal carbonate platform, Kaapvaal Craton, South Africa. *S. Afr. J. of Geol.* 190, 11-22.

Sumner DY and Bowring SA (**1996**) U-Pb geochronology constraints on deposition of the Campbellrand Subgroup, Transvaal Supergroup, South Africa. *Precambrian Research* 79, 25-35.

Swart PK (**2015**) The geochemistry of carbonate diagenesis: The past, present, and future. *Sedimentology* 62, 1233-1304.

Swart PK, Burns SJ, and Leder JJ (**1991**) Fractionation of the stable isotopes of oxygen and carbon in carbon dioxide during the reaction of calcite with phosphoric acid as a function of temperature and technique. *Chemical Geology: Isotope Geoscience section* 86, 89-96.

Sweeney JJ and Burnham AK (**1990**) Evaluation of a simple model of vitrine reflectance based on chemical kinetics. *AAPG Bull.*, 74, 10, 1559-1570.

Tang J, Köhler S, and Dietzel M (**2008**) Sr^{2+}/Ca^{2+} and $^{44}Ca/^{40}Ca$ fractionation during inorganic calcite formation: I. Sr incorporation. *Geochim. Cosmochim. Acta,* 72, 3733-3745.

Tang J, Dietzel M, Fernandez A, Tripati AK, and Rosenheim BE (**2014**) Evaluation of kinetic effects on clumped isotope fractionation (Δ_{47}) during inorganic calcite precipitation. *Geochim. Cosmochim. Acta* 134, 120-136.

Tartese R, Chaussidon M, Gurenko A, Delarue F, and Robert F (**2017**) Warm Archean oceans reconstructed from oxygen isotope composition of early-life remnants. *Geochem. Perspect. Lett.* 3, 55-65.

Tarutani T, Clayton RN, and Mayeda TK (**1969**) The effect of polymorphism and magnesium substitution on oxygen isotope fractionation between calcium carbonate and water. *Geochim. Cosmochim. Acta* 33, 987–996.

Teng F-Z (**2017**) Magnesium Isotope Geochemistry. *Rev. Min. Geochem.* 82, 219-287.

Teng HH, Dove PM, and Yoreo JJ (**2000**) Kinetics of calcite growth: Surface processes and relationships to macroscopic rate laws. *Geochim. Cosmochim. Acta* 64, 2255-2266.

Thiagarajan N, Adkins J, and Eiler JM (**2011**) Carbonate clumped isotope thermometry of deep sea corals and implications for vital effects. *Geochim. Cosmochim. Acta* 75, 4416–4425.

Tribble JS and Mackenzie FT (**1998**) Recrystallization of Magnesian Calcite Overgrowths on Calcite Seeds Suspended in Seawater. *Aquat. Geochem.* 4, 337-360.

Tripati AK, Eagle RA, Thiagarajan N, Gagnon AC, Bauch H, Halloran PR, and Eiler JM (**2010**) ^{13}C-^{18}O isotope signatures and "clumped isotope" thermometry in foraminifera and coccoliths. *Geochim. Cosmochim. Acta* 74, 5697-5717.

Tripati AK, Hill PS, Eagle RA, Mosenfelder JL, Tang J, Schauble EA, Eiler JM, Zeebe RE, Uchikawa J, Coplen TB, Ries JB, and Henry D (**2015**) Beyond temperature: Clumped isotope signatures in dissolved inorganic carbon species and the influence of solution chemistry on carbonate mineral composition. *Geochim. Cosmochim. Acta*, 166, 344-371.

Uchikawa J and Zeebe RE (**2013**) No discernible effect of Mg^{2+} ions on the equilibrium oxygen isotope fractionation in the CO_2–H_2O system. *Chem. Geol.* 343, 1–11.

Ullmann CV and Korte C (**2015**) Diagenetic alteration in low-Mg calcite from macrofossils: a review. *Geol. Quart.* 59, 1, 3-20.

Urey HC (**1947**), The Thermodynamic Properties of Isotopic Substances. *J. Chem. Soc.*, May, 562-581.

Usdowski E, Michaelis J, Böttcher ME, and Hoefs J (**1991**) Factors for the oxygen isotope equilibrium fractionation between aqueous and gaseous CO_2, carbonic acid, bicarbonate, carbonate, and water (19 °C). *Zeitschrift für physikalische Chemie*, 170, pp. 237-249.

Usdowski E and Hoefs J (**1993**) Oxygen isotope exchange between carbonic acid, bicarbonate, carbonate, and water: a re-examination of the data of MCCREA (1950) and an expression for the overall partitioning of oxygen isotopes between the carbonate species and water. *Geochim. Cosmochim. Acta*, 57, 3815-3818.

Van der Weijden CH and van der Weijden RD (**2014**) Calcite Growth: Rate dependence on saturation, on ratios of dissolved calcium and (bi)carbonate and on their complexes. *J. Crystal Growth* 394, 137-144.

Vandenbroucke M and Largeau C (**2007**) Kerogen origin, evolution and structure. *Org. Chem.* 38, 719-833.

Wacker U, Fiebig J, Tödter J, Schöne B, Bahr A, Friedrich O, Tütken T, Gischler E, and Joachimski M (**2014**) Empirical calibration of the clumped isotope paleothermometer using calcites of various origins. *Geochimica et Cosmochimica Acta* **141**.

Walter LM and Morse JW (**1984**) Magnesian calcite stabilities: A reevaluation. *Geochim. Cosmochim. Acta* 48, 1059–1069.

Wang M, Lu S, Chen G, Zheng M, Zhang S, and Huang W (**2015**) Thermal effect of intrusive rock on hydrocarbon generation from organic matter. *Arab J. Geosci.*, 8, 39-56.

Wang RZ, Addadi L, and Weiner S (**1997**) Design strategies of sea urchin teeth: structure, composition and micromechanical relations to function. *Phil. Trans. R. Soc. London, Series B*, 352, 469-480.

Wang W, Qin T, Zhou C, Huang S, Wu Z, and Huang F (**2017**) Concentration effect on equilibrium fractionation of Mg-Ca isotopes in carbonate minerals: Insights from first-principles calculations. *Geochim. Cosmochim. Acta* 208, 185-197.

Wang Y and Xu H (2001) Prediction of trace metal partitioning between minerals and aqueous solutions: A linear free energy approach. *Geochim. Cosmochim. Acta* 65, 10, 1529-1543.

Wang Z, Hu P, Gaetani G, Liu C, Saenger C, Cohen A, and Hart S (**2013**) Experimental calibration of Mg isotope fractionation between aragonite and seawater. *Geochim. Cosmochim. Acta* 102, 113-123.

Wang ZG, Schauble EA, and Eiler JM (**2004**) Equilibrium Thermodynamics of Multiply Substituted Isotopologues of Molecular Gases. *Geochim. Cosmochim. Acta*, 68(23), 4779-4797.

Watkins JM and Hunt JD (**2015**) A process-based model for non-equilibrium clumped isotope effects in carbonates. *Earth and Planetary Science Reviews*, 432, 152-165.

Watkins JM, Hunt JD, Ryerson FJ, and DePaolo DJ (**2014**) The influence of temperature, pH, and growth rate on the $\delta^{18}O$ composition of inorganically precipitated calcite. *Earth and Planetary Science Reviews*, 404, 332-343.

Watkins JM, Nielsen LC, Ryerson FJ, and DePaolo DJ (**2013**) The influence of kinetics on the oxygen isotope composition of calcium carbonate. *Earth Planet. Sci. Lett.,* 375, 349–360.

Wildman M, Brown R, Watkins R, Carter A, Gleadow A, and Summerfield M (**2015**) Post break-up tectonic inversion across the southwestern cape of South Africa: New insights from apatite and zircon fission track thermochronometry. *Tectonophysics* 654, 30-55.

Wildman M, Brown R, Beucher R, Persano C, Stuart FM, Mackintosh V, Gallagher K, Schwanethal J, and Carter A (**2017**) Contrasting Mesozoic evolution across the boundary between on and off craton regions of the South African plateau inferred from apatite fission track and (U-Th-Sm)/He thermochronology. *J. Geophys. Res. Solid Earth* 122, 1517-1547.

Wildman M, Brown R, Persano C, Beucher R, Stuart FM, Gallagher K, Schwanethal J, and Carter A (**2016**) The chronology and tectonic style of landscape evolution along the elevated Atlantic continental margin of South Africa resolved by joint apatite fission track and (U-Th-Sm)/He thermochronology. *Tectonophysics* 35, 511-545.

Winkelstern IZ, Kaczmarek SE, Lohmann KC, and Humphrey JD (**2016**) Calibration of dolomite clumped isotope thermometry. *Chem. Geol.*, 443, 32-38.

Wolthers M, Nehrke G, Gustafsson JP, and Cappellen PV (**2012**) Calcite growth kinetics: Modeling the effect of solution stoichiometry. *Geochim. Cosmochim. Acta*, 77, 121-134.

Wombacher F, Eisenhauer A, Bohm F, Gussone N, Kinkel H, Lezius J, Noe S, Regenberg M, and Ruggeberg A (**2006**) Magnesium stable isotope compositions in biogenic $CaCO_3$. *European Geoscience Union. Geophys. Res. Abstr.* 8, 06353.

Wombacher F, Eisenhauer A, Bohm F, Gussone N, Regenberg M, Dullo WC, and Ruggeberg A (**2011**) Magnesium stable isotope fractionation in marine biogenic calcite. *Geochim. Cosmochim. Acta* 75, 5797-5818.

Wood DA (**2018**) Kerogen conversion and thermal maturity modelling of petroleum generation: Integrated analysis applying relevant kerogen kinetics. *Marine Petrol. Geol.*, 89, 313-329.

Xu M and Higgins SR (**2011**) Effects of magnesium ions on near-equilibrium calcite dissolution: Step kinetics and morphology. *Geochim. Cosmochim. Acta* 75, 719-733.

Xu J, Yan C, Zhang F, Konishi H, Xu H, Teng HH (**2013**) Testing the cation-hydration effect on the crystallization of Ca-$MgCO_3$ systems. *Proc. Natl. Acad. Sci. U.S.A.* 110, 17750-17755.

Ye F, Crippa G, Angiolini L, Brand U, Capitani GC, Cusack M, Garbelli C, Griesshaber E, Harper E, and Schmahl W (**2017**) Mapping of recent brachiopod microstructure: A tool for environmental studies. *J. Struct. Biol.* https://www.sciencedirect.com/science/article/pii/S104784771730206X

Zaarur S, Affek HP, and Brandon MT (**2013**) A revised calibration of the clumped isotope thermometer. *Earth and Planetary Science Reviews*, 382, 47-57.

Zeebe RE (**2014**) Kinetic fractionation of carbon and oxygen isotopes during hydration of carbon dioxide. *Geochim. Cosmochim. Acta*, 139, 540-552.

Zeebe RE and Wolf-Gladrow D (**2001**) CO_2 in Seawater: Equilibrium, Kinetics, Isotopes. Elsevier Science B.V. (Oceanography Series), Amsterdam.

Zhang F, Xu H, Konishi H, Kemp JM, Roden EE and Shen ZZ (**2012**) Dissolved sulfide-catalyzed precipitation of disordered dolomite: Implications for the formation mechanism of sedimentary dolomite. *Geochim. Cosmochim. Acta* 97, 148-165.

Zhang F, Yan C, Teng HH, Roden EE, and Xu H (**2013**) In situ AFM observations of Ca-Mg carbonate crystallization catalyzed by dissolved sulfide: Implications for sedimentary dolomite formation. *Geochim. Cosmochim. Acta* 105, 44-55.

Zhang F, Xu H, Shelobolina ES, Konishi H, Converse B, Shen Z, Roden EE (**2015**) The catalytic effect of bound extracellular polymeric substances excreted by anaerobic microorganisms on Ca-Mg carbonate precipitation: Implications for the "dolomite problem". *Am. Mineralogist* 100, 483-494.

Zhang N, Zhong S, and Flowers RM (**2012**) Predicting and testing continental vertical motion histories since the Paleozoic. *Earth Planet. Science Lett.* 317-318, 426-435.

Zhong S and Mucci A (**1989**) Calcite and aragonite precipitation from seawater solutions of various salinities: Precipitation rates and overgrowth compositions. *Chem. Geol.* 78, 283-299.

Zhu F, Kong Y, Liang J, Li C, Hu Y, Zhou Y, Liu X, Xie L, and Zhang R (**2010**) Tuning calcite magnesium content by soluble shell matrices: Insights into biomineral impurity control. *Mat. Sci. Eng. C* 30, 963-696.

Appendix A: Application of Clumped Isotope Thermometry to Archean Carbonates: Formation Temperatures, Thermal Histories, and Potential for Biomarker Preservation

The Campbellrand-Malmani carbonate platform (CMCP) is located on the Kaapvaal Craton of South Africa (Fig. A1) and preserves an extensive Neoarchean to Paleoproterozoic sequence of carbonate deposits and sediments. The Campbellrand Subgroup is located below the Asbestos Hills Subgroup which hosts the Kuruman and Gamohaan banded iron formations. The objective of this study was to estimate carbonate formation temperatures, thermal histories, and potential for biomarker preservation based on "clumped isotope" thermometry, organic material (OM) thermal maturation according to Rock-Eval pyrolysis and Raman spectroscopy, and chemical kinetic modeling.

The samples analyzed in this study for isotope compositions were collected from two hillside outcrops ("Kuruman Kop" and "Danielskuil"; Fig. A1) and three stratigraphically equivalent drill cores, DI-1, AD-5, and WB-98 (Fig. A2; Klein and Beukes, 1989). Calcite samples were collected from spar, herringbone calcite, and micritic sections. Dolomite and siderite are massive in nature. In all cases, these materials formed from early precipitation of carbonates from seawater or porewater shortly after sediment deposition (Sumner and Grotzinger, 2004). These textures have been verified by microscopic inspection of thin sections created from individual hand samples (Table A1-1, Figs. A3-A6) collected from strata comprised primarily of stromatolitic limestone with localized early diagenetic dolomitization.

Bulk C, bulk O, and clumped isotope compositions for calcite were determined at the California Institute of Technology by isotope ratio mass spectrometry on both of two nearly identical Thermo-Finnigan MAT 253 instruments (Tables A1-2 through 4). Total organic content (TOC), oxygen index (OI), hydrogen index (HI) and Tmax were estimated by a Rock-Eval-6 Pyrolyzer at the Department of Earth Sciences, IIT Bombay (Arora et al., 2015) for a collection of CMCP specimens provided by Nic Beukes of the Department of Geology,

University of Johannesburg (Table A1-5). Micro-Raman spectra (Table A1-6) were acquired from thin section billets by Nicola Ferallis of Department of Materials Science and Engineering, MIT using a Horiba LabRAM 800 HR spectrometer (see Ferallis et al. [2016] for details).

Average apparent temperatures from clumped isotope (Δ_{47}) analysis (excluding hydrothermal carbonates and the modern caliche) considered for modeling purposes are 143°C and 98°C (Table A1-2) for calcite and dolomite, respectively, as estimated by the calibration reported by Lloyd et al. (2017) and expressed in the Caltech reference frame as $\Delta_{47} = 0.000746*(10^6/T^2)^2 + 0.03069*(10^6/T^2) + 0.20084$. Applying this calibration to the average Δ_{47} value determined for siderite samples yields an apparent temperature of 85°C. However, clumped isotope bonding can be altered during diagenesis. Heating short of recrystallization on long enough time scales will allow minerals to retain much of their primary information such as bulk isotope composition and only alter $^{13}C–^{18}O$ bonding frequency. This resetting or reordering has been studied experimentally as well as through the rock record (see References). Two models proposed to explain the mechanisms of calcite reordering are those of Henkes et al. (2014) and Stolper and Eiler (2015). Additionally, rate constants for dolomite reordering have been reported by Lloyd et al. (2018). These studies provide a framework that can be used to reconstruct the time-temperature (t-T) history of calcite and dolomite natural samples. However, there are currently no published studies of siderite reordering or thermometry calibrations at higher temperatures. Therefore, measured $^{13}C–^{18}O$ bonding frequency for siderite samples (Table A1-2) is difficult to reliably interpret at this time.

The maximum paleotemperature of burial (MPTB) of the CMCP has been estimated by Miyano and Beukes (1984) according to metamorphic mineral assemblages in the Kuruman Iron Formation. The authors identified greenalite-quartz-magnetite-hemitite systems in the upper Kuruman and occurrences of minnesotaite from which they concluded that the iron formation

saw maximum burial temperatures of 110-170 °C. For the purposes of this study, maximum burial depth will be considered early in the history of the carbonate platform following the subsidence modeling of Sumner and Beukes (2006), which indicates a minimum burial duration of ~200 Ma and maximum burial temperatures ranging up to ~250°C assuming continental geothermal gradients similar to today. The timing of uplift of the South Africa Plateau is uncertain but has been investigated by a number of studies (see References). Therefore, recent and rapid as well as protracted uplift histories were considered during modeling simulations.

Figure A7 illustrates the clumped isotope thermometry modeled t-T path for calcite and dolomite which best fits estimated system conditions and model constraints outlined above. Specifically, this simulation assumes a prolonged burial period of 600 Ma to a MPTB of 163.5°C, a duration of 1,905 Ma at MPTB, and a rapid exhumation of 15 Ma to produce blocking temperatures of 140°C and 99°C for calcite and dolomite, respectively, compared to measured mean blocking temperatures of ~143 and 98°C. Varying burial and exhumation durations identified minimum and maximum MPTB values of ~150 and 200°C for clumped isotope blocking temperatures in the range of values measured in this study (Table A1-2). Modeling simulations assume a starting (carbonate formation) temperature of 30°C. However, calcite reordering kinetics are not sensitive to the initial temperature under most t-T scenarios considered here and a more reliable dolomite formation temperature cannot be determined without further constraints on burial and uplift timing, more precise clumped isotope analytical methods, and/or less uncertainty associated with kinetic model parameters.

Organic material associated with CMCP specimens has been analyzed by Rock-Eval pyrolysis and micro-Raman spectroscopy in order to aid assessment of thermal maturation of kerogen. Rock-Eval data was used to determine MPTB (Fig. A8) according to the method of Disnar (1994). Spectral features of Raman data can be interpreted by a number of different

methods in order to estimate MPTB, equivalent vitrine reflectance (Ro%), and fraction (F) of total possible volatile component production during burial heating catagenesis (Table A1-6). In general, these methods overestimate thermal maturation compared to clumped isotope thermometry and metamorphic mineral assemblages. For example, the method of Rahl et al. (2005) gives an average MPTB of 243°C, which is the lowest average determined according to Raman data. However, these methods (Table A1-6) have been developed based on much younger materials (and much shorter periods of heating) and therefore time sensitive kinetics-based approaches should also be considered.

Specimen specific characteristics derived from Rock-Eval pyrolysis and Raman spectra such as O/C ratio, H/C ratio, and remaining wt.% C can be used to constrain boundary conditions and test chemical kinetic models. Additionally, the maturation conversion parameter, F, can be used to compare Raman derived estimates (Shito et al., 2016) to model output values. The average F value for samples of this study is ~0.8 (Table A1-6). The work of Wood (2018) and the "Vitrimat" model of Burnham and Sweeney (1989) were considered to compare thermal maturation estimates between OM based analyses and carbonate clumped isotope thermometry. The t-T regime determined for Figure A7 has been assumed during kerogen maturation calculations. The approach presented by Wood (2018) requires a MPTB of ~137°C or lower to calculate F values ≤ 0.9 (Fig. A9). The Vitrimat model, however, is generally consistent with carbonate clumped isotope thermometry and calculates F values from ~0.8-0.9 with a MPTB of 160°C (Figs. 10-12). Collectively, these results indicate that of the original OM, including biomarkers, ≥ 80% have completed devolatilization reactions during a progression toward graphite formation.

Table A1-1: Hand Samples and Petrographic Thin Sections

Hand Sample Identification	Thin Section Identification	Thin Section Polish/Finish	Geologic Unit	Sample Description	Collection Location - City or lattitude, longitude, elevation
14AS-SA02	NA	NA	--	Grainstone, carbonate sand with early and partial silicification	--
14AS-SA03	14AS*SA03B	"SEM"	Gamohaan Fm.	Fenestral microbialite, dolomite infill, small chert nodules	27°22'58" S 23°20'44" E, 1459.0 m
14AS-SA03	14AS*SA03C	"SEM"	Gamohaan Fm.	Fenestral microbialite, dolomite infill, small chert nodules	27°22'58" S 23°20'44" E, 1459.0 m
14AS-SA03	14AS*SA03D1	"SEM"	Gamohaan Fm.	Fenestral microbialite, dolomite infill, small chert nodules	27°22'58" S 23°20'44" E, 1459.0 m
14AS-SA03	14AS*SA03D2	"SEM"	Gamohaan Fm.	Fenestral microbialite, dolomite infill, small chert nodules	27°22'58" S 23°20'44" E, 1459.0 m
14AS-SA03	14AS*SA03D3	"SEM"	Gamohaan Fm.	Fenestral microbialite, dolomite infill, small chert nodules	27°22'58" S 23°20'44" E, 1459.0 m
14AS-SA04Top	14AS*SA04A1	"EBSD"	Gamohaan Fm.	Fenestral microbialite, dolomite infill, small chert nodules	27°22'58" S 23°20'45" E, 1471.0 m
14AS-SA04Top	14AS*SA04B1	"EBSD"	Gamohaan Fm.	Fenestral microbialite, dolomite infill, small chert nodules	27°22'58" S 23°20'45" E, 1471.0 m
14AS-SA04Top	14AS*SA04C1	"EBSD"	Gamohaan Fm.	Fenestral microbialite, dolomite infill, small chert nodules	27°22'58" S 23°20'45" E, 1471.0 m
14AS-SA04Middle	14AS*SA04A2	"EBSD"	Gamohaan Fm.	Fenestral microbialite, dolomite infill, small chert nodules	27°22'58" S 23°20'45" E, 1471.0 m
14AS-SA04Middle	14AS*SA04B2	"EBSD"	Gamohaan Fm.	Fenestral microbialite, dolomite infill, small chert nodules	27°22'58" S 23°20'45" E, 1471.0 m
14AS-SA04Middle	14AS*SA04C2	"EBSD"	Gamohaan Fm.	Fenestral microbialite, dolomite infill, small chert nodules	27°22'58" S 23°20'45" E, 1471.0 m
14AS-SA04Bottom	14AS*SA04A3	"EBSD"	Gamohaan Fm.	Fenestral microbialite, dolomite infill, small chert nodules	27°22'58" S 23°20'45" E, 1471.0 m
14AS-SA04Bottom	14AS*SA04B3	"EBSD"	Gamohaan Fm.	Fenestral microbialite, dolomite infill, small chert nodules	27°22'58" S 23°20'45" E, 1471.0 m
14AS-SA05	14AS*SA05B1	"SEM"	Gamohaan Fm.	Small domal stromatolite with draping dolomite	27°22'56" S 23°20'43" E, 1447.0 m
14AS-SA05	14AS*SA05B2	"SEM"	Gamohaan Fm.	Small domal stromatolite with draping dolomite	27°22'56" S 23°20'43" E, 1447.0 m
14AS-SA05	14AS*SA05B3	"SEM"	Gamohaan Fm.	Small domal stromatolite with draping dolomite	27°22'56" S 23°20'43" E, 1447.0 m
14AS-SA05	14AS*SA05B4	"SEM"	Gamohaan Fm.	Small domal stromatolite with draping dolomite	27°22'56" S 23°20'43" E, 1447.0 m
14AS-SA05	14AS*SA05B5	"SEM"	Gamohaan Fm.	Small domal stromatolite with draping dolomite	27°22'56" S 23°20'43" E, 1447.0 m
14AS-SA05	14AS*SA05B6	"SEM"	Gamohaan Fm.	Small domal stromatolite with draping dolomite	27°22'56" S 23°20'43" E, 1447.0 m
14AS-SA06	14AS*SA06A	"EBSD"	Kogelbeen Fm.	Domal/columnar stromatolite with dolomite infill	27°22'52" S 23°20'42" E, 1374.0 m
14AS-SA06	14AS*SA06B	"EBSD"	Kogelbeen Fm.	Domal/columnar stromatolite with dolomite infill	27°22'52" S 23°20'42" E, 1374.0 m
14AS-SA07	14AS*SA07A	~150-200 um, "single polish"	Kogelbeen Fm.	Chertified stromatolite	--
14AS-SA07	14AS*SA07C		Kogelbeen Fm.	Chertified stromatolite	--
14AS-SA08	NA	NA	Kogelbeen Fm.	Hydrothermal vein calcite and dolomite	27°22'51" S 23°20'40" E, 1370.0 m
14AS-SA09	14AS*SA09A	"EBSD"	Kogelbeen Fm.	Chertified stromatolite	--
14AS-SA09	14AS*SA09B	~150-200 um, "single polish"	Kogelbeen Fm.	Chertified stromatolite	--
14AS-SA10	14AS*SA10A		Kogelbeen Fm.	Silicified stromatolite	--
14AS-SA11	14AS*SA11A	"EBSD"	Kogelbeen Fm.	Sparry fenestral microbialite and micrite	27°22'49" S 23°20'40" E, 1338.0 m
14AS-SA11	14AS*SA11B	"EBSD"	Kogelbeen Fm.	Sparry fenestral microbialite and micrite	27°22'49" S 23°20'40" E, 1338.0 m
14AS-SA12	14AS*SA12'A'	"SEM"	Gamohaan Fm.	Stromatolite with dolomite infill, caliche at base	28°6'17" S 23°34'20" E, 1546.0 m
14AS-SA13	14AS*SA13B1	"SEM"	Gamohaan Fm.	Draping stromatolites with dolomite sand, spar and fenestrae	28°6'14" S 23°34'18" E, 1574.0 m
14AS-SA13	14AS*SA13B2	"SEM"	Gamohaan Fm.	Draping stromatolites with dolomite sand, spar and fenestrae	28°6'14" S 23°34'18" E, 1574.0 m
14AS-SA13	14AS*SA13B3	"SEM"	Gamohaan Fm.	Draping stromatolites with dolomite sand, spar and fenestrae	28°6'14" S 23°34'18" E, 1574.0 m
14AS-SA13	14AS*SA13B4	"SEM"	Gamohaan Fm.	Draping stromatolites with dolomite sand, spar and fenestrae	28°6'14" S 23°34'18" E, 1574.0 m
14AS-SA14A	14AS*SA14AB1	"SEM"	Gamohaan Fm.	Early silicified fenestral microbialite	28°6'13" S 23°34'16" E, 1596.0 m
14AS-SA14A	14AS*SA14AB2	"SEM"	Gamohaan Fm.	Early silicified fenestral microbialite	28°6'13" S 23°34'16" E, 1596.0 m
14AS-SA14A	14AS*SA14AB3	"SEM"	Gamohaan Fm.	Early silicified fenestral microbialite	28°6'13" S 23°34'16" E, 1596.0 m
14AS-SA14A	14AS*SA14AB4	"SEM"	Gamohaan Fm.	Early silicified fenestral microbialite	28°6'13" S 23°34'16" E, 1596.0 m
14AS-SA14B	14AS*SA14B1	~150-200 um	Gamohaan Fm.	Thick chert with dolomite vein(s)	28°6'13" S 23°34'16" E, 1596.0 m
14AS-SA15	14AS*SA15BA1	"SEM"	Gamohaan Fm.	Cauliflower stromatolite, fenestrae, dolomite infill	--
14AS-SA15	14AS*SA15BA2	"SEM"	Gamohaan Fm.	Cauliflower stromatolite, fenestrae, dolomite infill	--
14AS-SA15	14AS*SA15BA3	"SEM"	Gamohaan Fm.	Cauliflower stromatolite, fenestrae, dolomite infill	--
14AS-SA15	14AS*SA15BB	"SEM"	Gamohaan Fm.	Cauliflower stromatolite, fenestrae, dolomite infill	--

Table A1-1 (cont.): Hand Samples and Petrographic Thin Sections

Hand Sample Identification	Thin Section Identification	Thin Section Polish/Finish	Geologic Unit	Sample Description	Collection Location - City or lattitude, longitude, elevation
AS16-01A	6-1A1	"EBSD"	Gamohaan Fm. (??)	Cement-grainstone rhythmite with graded bedding	27°22.9019' S 23°20.6808" E, 1224.1 ± 4.9 m
AS16-01A	6-1A2	"EBSD"	Gamohaan Fm. (??)	Cement-grainstone rhythmite with graded bedding	27°22.9019' S 23°20.6808" E, 1224.1 ± 4.9 m
AS16-01B	6-1B1	"EBSD"	Gamohaan Fm. (??)	Cement-grainstone rhythmite with graded bedding	27°22.9019' S 23°20.6808" E, 1224.1 ± 4.9 m
AS16-01B	6-1B2	"EBSD"	Gamohaan Fm. (??)	Cement-grainstone rhythmite with graded bedding	27°22.9019' S 23°20.6808" E, 1224.1 ± 4.9 m
AS16-01B	6-1B3	"EBSD"	Gamohaan Fm. (??)	Cement-grainstone rhythmite with graded bedding	27°22.9019' S 23°20.6808" E, 1224.1 ± 4.9 m
AS16-02	6-2A	"EBSD"	Gamohaan Fm.	Cement-grainstone rhythmite with graded bedding	28°06.2835' S 23°34.2760" E, 1557.2 ± 4.9 m
AS16-02	62A (duplicate)	"EBSD"	Gamohaan Fm.	Cement-grainstone rhythmite with graded bedding	28°06.2835' S 23°34.2760" E, 1557.2 ± 4.9 m
AS16-02	6-2B	"EBSD"	Gamohaan Fm.	Cement-grainstone rhythmite with graded bedding	28°06.2835' S 23°34.2760" E, 1557.2 ± 4.9 m
AS16-02	6-2B (duplicate)	"EBSD"	Gamohaan Fm.	Cement-grainstone rhythmite with graded bedding	28°06.2835' S 23°34.2760" E, 1557.2 ± 4.9 m
AS16-03	6-3A	"EBSD"	Gamohaan Fm.	Dolomitized rhythmite with graded bedding	28°06.2835' S 23°34.2760" E, 1558.7 ± 4.9 m
AS16-03	6-3B	"EBSD"	Gamohaan Fm.	Dolomitized rhythmite with graded bedding	28°06.2835' S 23°34.2760" E, 1558.7 ± 4.9 m
AS16-03	6-3C	"EBSD"	Gamohaan Fm.	Dolomitized rhythmite with graded bedding	28°06.2835' S 23°34.2760" E, 1558.7 ± 4.9 m
NL16-04	6-4A	"EBSD"	Gamohaan Fm.	Dolomitized laminar stromatolites	28°06.2835' S 23°34.2760" E, 1566.4 ± 4.9 m
NL16-04	6-4B	"EBSD"	Gamohaan Fm.	Dolomitized laminar stromatolites	28°06.2835' S 23°34.2760" E, 1566.4 ± 4.9 m
NL16-05	65A1	"EBSD"	Lime Acres Mem.	Sparry crystalline carbonate (fenestrate microbialites)	28°16.0680' S 23°31.8818" E, 1468.8 ± 4.9 m
NL16-05	65A1 (duplicate)	"EBSD"	Lime Acres Mem.	Sparry crystalline carbonate (fenestrate microbialites)	28°16.0680' S 23°31.8818" E, 1468.8 ± 4.9 m
NL16-05	65A2	"EBSD"	Lime Acres Mem.	Sparry crystalline carbonate (fenestrate microbialites)	28°16.0680' S 23°31.8818" E, 1468.8 ± 4.9 m
NL16-05	65A2 (duplicate)	"EBSD"	Lime Acres Mem.	Sparry crystalline carbonate (fenestrate microbialites)	28°16.0680' S 23°31.8818" E, 1468.8 ± 4.9 m
NL16-05	65A3	"EBSD"	Lime Acres Mem.	Sparry crystalline carbonate (fenestrate microbialites)	28°16.0680' S 23°31.8818" E, 1468.8 ± 4.9 m
NL16-05	65A4	"EBSD"	Lime Acres Mem.	Sparry crystalline carbonate (fenestrate microbialites)	28°16.0680' S 23°31.8818" E, 1468.8 ± 4.9 m
NL16-05	65B1	"EBSD"	Lime Acres Mem.	Sparry crystalline carbonate (fenestrate microbialites)	28°16.0680' S 23°31.8818" E, 1468.8 ± 4.9 m
NL16-05	65B2	"EBSD"	Lime Acres Mem.	Sparry crystalline carbonate (fenestrate microbialites)	28°16.0680' S 23°31.8818" E, 1468.8 ± 4.9 m
NL16-06	NA	NA	Reivilo Formation	Aragonite pseudomorphs in massive microcrystalline beds	27°57.8317' S 27°27.2672" E, 1174.1 ± 4.9 m
NL16-07A	NA	NA	Reivilo Formation	Aragonite pseudomorphs in massive microcrystalline beds	27°57.8343' S 27°27.2879" E, 1171.7 ± 4.9 m
NL16-07B	67B1	"EBSD"	Reivilo Formation	Aragonite pseudomorphs in massive microcrystalline beds	27°57.8343' S 27°27.2879" E, 1171.7 ± 4.9 m
NL16-07B	67B2	"EBSD"	Reivilo Formation	Aragonite pseudomorphs in massive microcrystalline beds	27°57.8343' S 27°27.2879" E, 1171.7 ± 4.9 m
NL16-07B	67B3	"EBSD"	Reivilo Formation	Aragonite pseudomorphs in massive microcrystalline beds	27°57.8343' S 27°27.2879" E, 1171.7 ± 4.9 m
NL16-07B	67B4	"EBSD"	Reivilo Formation	Aragonite pseudomorphs in massive microcrystalline beds	27°57.8343' S 27°27.2879" E, 1171.7 ± 4.9 m
NL16-07B	67B5	"EBSD"	Reivilo Formation	Aragonite pseudomorphs in massive microcrystalline beds	27°57.8343' S 27°27.2879" E, 1171.7 ± 4.9 m
NL16-08	6*8A	"EBSD"	Reivilo Formation	Columnar stromatolites with dolomite infill	28°35.0415' S 23°57.7265" E, 1451.5 ± 4.9 m
NL16-08	6*8B	"EBSD"	Reivilo Formation	Columnar stromatolites with dolomite infill	28°35.0415' S 23°57.7265" E, 1451.5 ± 4.9 m
NL16-08	6*8C	"EBSD"	Reivilo Formation	Columnar stromatolites with dolomite infill	28°35.0415' S 23°57.7265" E, 1451.5 ± 4.9 m
NL16-08	6*8D	"EBSD"	Reivilo Formation	Columnar stromatolites with dolomite infill	28°35.0415' S 23°57.7265" E, 1451.5 ± 4.9 m
NL16-08	6*8E	"EBSD"	Reivilo Formation	Columnar stromatolites with dolomite infill	28°35.0415' S 23°57.7265" E, 1451.5 ± 4.9 m
AD-5-190.30-190.35	AD5-1		Tsineng Member	Black chert with calcite veins	AD-5 Core, near Adelaide, South Africa
AD-5-190.38-190.41	AD5-2	~150-200 um,	Tsineng Member	Black chert with calcite veins	AD-5 Core, near Adelaide, South Africa
AD-5-190.41-190.46	AD5-3	"single polish"	Tsineng Member	Black chert with calcite veins	AD-5 Core, near Adelaide, South Africa
AD-5-190.46-190.52	AD5-4		Tsineng Member	Black chert with calcite veins	AD-5 Core, near Adelaide, South Africa
WB98-966.5CS1	NA	NA	Gamohaan Fm.	Fenestral microbialite and pyrite	WB-98 Core, near Kuruman Kop, South Africa
DM-1	NA	NA	Monteville Fm.	"Sparitic Carbonate conophyton"	Douglas (area), South Africa
DM-2	NA	NA	Monteville Fm.	"Carbonaceous limestone"	Douglas (area), South Africa
GAM-3	NA	NA	Gamohaan Fm.	"Contorted mats in carbonate"	Gamohaan Reserve, South Africa
GAM-4	GAM*4A	"EBSD"	Gamohaan Fm.	"Carbonaceous carbonate pod"	Gamohaan Reserve, South Africa
GAM-4	GAM*4B	"EBSD"	Gamohaan Fm.	"Carbonaceous carbonate pod"	Gamohaan Reserve, South Africa
LIME 2	NA	NA	Lime Acres Mem.	"Limestone from Lime Acres"	Danielskuil, South Africa
LIME DK-1	NA	NA	Lime Acres Mem.	"Limestone from Danielskuil"	Danielskuil, South Africa
LIME DK-3	DK*3A	"EBSD"	Lime Acres Mem.	"Limestone from Danielskuil"	Danielskuil, South Africa
LIME DK-3	DK*3B	"EBSD"	Lime Acres Mem.	"Limestone from Danielskuil"	Danielskuil, South Africa
RE-1	NA	NA	Gamohaan Fm.	"Black chert from Retreat Farm near Kuruman"	Kuruman, South Africa
RE-2	NA	NA	Gamohaan Fm.	"Black chert from Retreat Farm near Kuruman"	Kuruman, South Africa
RE-3	NA	NA	Gamohaan Fm.	"Dolomite from Retreat Farm (partly weathered)"	Kuruman, South Africa

Table A1-2: Summary of Isotope Compositions of Carbonates and Apparent Temperatures

Identification	Sample Location	Type	Analyses (n)	δ^{26}Mg (‰, DSM)	Analyses (n)	δ^{13}C (‰, VPDB)	δ^{18}O (‰, VSMOW)	Δ_{47} (‰, CIT90)	Apparent T (° C, CIT90)[A]	Δ_{47} (‰, CDES90)	Apparent T (° C, CDES90) by Calibration: A	B	C
14AS-SA03CS1	Kuruman Kop	sparry calcite	--	--	3	0.37 ± 0.02	23.90 ± 0.13	0.394 ± 0.036	152	0.415 ± 0.021	190	109	214
14AS-SA03CS2	Kuruman Kop	sparry calcite	--	--	3	0.32 ± 0.06	23.64 ± 0.12	0.408 ± 0.024	138	0.439 ± 0.025	163	94	183
14AS-SA03D1	Kuruman Kop	dolomite	3	-1.91 ± 0.10	3	0.39 ± 0.02	23.78 ± 0.05	0.448 ± 0.027	108	0.483 ± 0.026	124	71	138
14AS-SA03D2	Kuruman Kop	dolomite	3	-1.83 ± 0.09	3	-0.07 ± 0.01	24.10 ± 0.01	0.488 ± 0.011	83	0.512 ± 0.012	105	58	115
14AS-SA04TA2CS1	Kuruman Kop	sparry calcite	--	--	3	0.04 ± 0.02	23.26 ± 0.10	0.395 ± 0.052	151	0.459 ± 0.046	144	83	161
14AS-SA04TA2CS2	Kuruman Kop	sparry calcite	--	--	3	0.15 ± 0.01	23.23 ± 0.01	0.414 ± 0.045	134	0.440 ± 0.064	161	93	181
14AS-SA05CS1	Kuruman Kop	sparry calcite	3	-2.18 ± 0.03	3	-0.41 ± 0.03	21.51 ± 0.09	0.407 ± 0.041	139	0.431 ± 0.047	171	99	192
14AS-SA05CS2	Kuruman Kop	sparry calcite	3	-2.11 ± 0.10	3	0.36 ± 0.01	24.00 ± 0.07	0.391 ± 0.008	155	0.420 ± 0.007	184	106	208
14AS-SA05D1	Kuruman Kop	dolomite	--	--	3	0.45 ± 0.03	21.92 ± 0.04	0.449 ± 0.016	107	0.478 ± 0.018	128	73	142
14AS-SA05D2	Kuruman Kop	dolomite	3	-2.40 ± 0.07	3	0.52 ± 0.27	22.27 ± 1.00	0.463 ± 0.030	98	0.485 ± 0.033	123	70	136
14AS-SA06L1	Kuruman Kop	herringbone calcite	7	-1.91 ± 0.14	3	-0.14 ± 0.06	21.13 ± 0.07	0.386 ± 0.062	160	0.454 ± 0.056	148	85	166
14AS-SA06L2	Kuruman Kop	herringbone calcite	3	-1.72 ± 0.02	3	-0.17 ± 0.02	21.08 ± 0.04	0.410 ± 0.016	136	0.444 ± 0.017	158	91	177
14AS-SA06L3	Kuruman Kop	herringbone calcite	3	-1.74 ± 0.10	3	-0.13 ± 0.01	21.65 ± 0.09	0.395 ± 0.036	151	0.421 ± 0.025	182	105	205
14AS-SA06ST1	Kuruman Kop	stromatolite calcite	--	--	3	0.49 ± 0.01	22.74 ± 0.10	0.391 ± 0.066	154	0.422 ± 0.071	182	105	205
14AS-SA06ST2	Kuruman Kop	stromatolite calcite	--	--	3	0.47 ± 0.02	22.78 ± 0.09	0.385 ± 0.026	161	0.400 ± 0.028	212	120	238
14AS-SA06D1	Kuruman Kop	dolomite	3	-1.69 ± 0.05	3	0.31 ± 0.08	21.21 ± 0.15	0.432 ± 0.026	119	0.473 ± 0.026	132	76	147
14AS-SA08CS1	Kuruman Kop	hydrothermal calcite	4	-1.56 ± 0.13	3	0.18 ± 0.01	23.40 ± 0.03	0.378 ± 0.050	169	0.444 ± 0.044	157	91	177
14AS-SA08D1	Kuruman Kop	hydrothermal dolomite	--	--	3	1.43 ± 0.14	24.32 ± 0.11	0.402 ± 0.005	144	0.433 ± 0.005	169	98	190
14AS-SA11CS1	Kuruman Kop	sparry calcite	--	--	3	-0.42 ± 0.02	22.49 ± 0.07	0.382 ± 0.063	164	0.458 ± 0.038	145	84	162
14AS-SA11CS2	Kuruman Kop	sparry calcite	--	--	3	-0.36 ± 0.04	22.25 ± 0.02	0.400 ± 0.032	146	0.429 ± 0.040	174	100	195
14AS-SA12por1	Danielskuil	modern caliche	6	-3.53 ± 0.13	3	3.40 ± 0.06	28.26 ± 0.05	0.636 ± 0.036	27[D]	0.669 ± 0.039		33[D]	
14AS-SA13CS1	Danielskuil	sparry calcite	5	-2.04 ± 0.07	3	-0.15 ± 0.08	23.62 ± 0.13	0.402 ± 0.044	144	0.434 ± 0.050	168	97	189
14AS-SA14ACS1	Danielskuil	sparry calcite	3	-1.87 ± 0.08	3	-0.16 ± 0.04	23.10 ± 0.15	0.426 ± 0.031	123	0.460 ± 0.032	143	82	160
14AS-SA14BD1	Danielskuil	dolomite	--	--	3	-2.19 ± 0.11	22.47 ± 0.32	0.490 ± 0.034	82	0.526 ± 0.037	96	52	105
14AS-SA15CS1	Danielskuil	sparry calcite	--	--	3	0.03 ± 0.07	23.49 ± 0.15	0.399 ± 0.030	146	0.438 ± 0.032	164	95	184
AD5-161.9A	Lamination 2	siderite†	--	--	1	-3.78 ± 0.003	22.17 ± 0.02	0.468 ± 0.040	95	0.423 ± 0.040	180	104	203
AD5-172.3L1	AD-5 core	calcite micrite	--	--	3	-1.23 ± 0.01	20.43 ± 0.05	0.411 ± 0.006	135	0.466 ± 0.014	138	79	154
AD5-176.9D1	AD-5 core	dolomite	--	--	3	-2.67 ± 0.01	20.35 ± 0.06	0.480 ± 0.042	88	0.541 ± 0.037	88	46	95
AD5-201.5CS1	AD-5 core	sparry calcite	6	-0.82 ± 0.10	3	-0.53 ± 0.01	22.59 ± 0.07	0.403 ± 0.034	143	0.442 ± 0.036	159	92	179
AD5-201.5D1	AD-5 core	dolomite	--	--	3	-0.96 ± 0.22	25.66 ± 0.13	0.453 ± 0.049	105	0.473 ± 0.053	132	76	147
DI1-213.8A	Lamination 4	siderite†	--	--	1	-5.89 ± 0.002	20.15 ± 0.01	0.469 ± 0.026	94	0.420 ± 0.026	184	106	208
DI1-236.7A	Lamination 2	siderite	--	--	2	-7.12 ± 0.053	20.83 ± 0.26	0.506 ± 0.006	74	0.468 ± 0.006	136	78	152
DI1-236.7A	Lamination 3	siderite†	--	--	1	-8.18 ± 0.006	20.86 ± 0.01	0.510 ± 0.039	73	0.467 ± 0.039	136	79	152
DI1-230.2CS1	DI-1 core	sparry calcite	4	-1.73 ± 0.03	3	-0.59 ± 0.02	24.89 ± 0.08	0.403 ± 0.029	143	0.439 ± 0.031	163	94	183
DI1-246.5L1	DI-1 core	calcite micrite	--	--	4	-0.60 ± 0.03	21.68 ± 0.14	0.407 ± 0.036	139	0.453 ± 0.048	149	86	167
WB98-815A	Lamination 1	siderite†	--	--	1	-6.68 ± 0.003	20.51 ± 0.02	0.472 ± 0.024	93	0.435 ± 0.024	167	97	188
WB98-815B	Lamination 3	siderite†	--	--	1	-6.85 ± 0.002	19.98 ± 0.01	0.473 ± 0.028	92	0.473 ± 0.028	182	105	205
WB98-886A	Lamination 14	siderite†	--	--	1	-4.17 ± 0.007	19.27 ± 0.004	0.511 ± 0.037	72	0.477 ± 0.037	128	73	143
WB98-886B	Lamination 6	siderite†	--	--	1	-4.35 ± 0.002	20.22 ± 0.02	0.468 ± 0.027	95	0.420 ± 0.027	184	106	207
WB98-966.5CS1	WB-98 core	sparry calcite	--	--	3	-0.43 ± 0.01	24.59 ± 0.05	0.415 ± 0.017	133	0.452 ± 0.018	150	87	168
WB98-981CS1	WB-98 core	sparry calcite	4	-2.73 ± 0.09	3	-1.01 ± 0.04	22.70 ± 0.14	0.418 ± 0.043	130	0.459 ± 0.046	143	83	161
WB98-981L1	WB-98 core	calcite micrite	--	--	3	-1.02 ± 0.02	22.19 ± 0.02	0.414 ± 0.031	133	0.465 ± 0.043	138	80	154
Average*	--	calcite	--	--	--	--	--	0.403 ± 0.023	143	0.441 ± 0.035	161	93	181
Average*	--	dolomite	--	--	--	--	--	0.463 ± 0.043	98	0.496 ± 0.053	115	65	127
Average	--	siderite	--	--	--	--	--	0.485 ± 0.041	85	0.442 ± 0.050	160	93	180

Calibrations reported by A - Lloyd et al. (2017), B - Bonifacie et al. (2017) , C - Kluge et al. (2015), D - Zaarur et al. (2013)

†Internal errors reported for siderite samples with only one analysis.

* Average values do not include hydrothermal samples or the modern caliche sample

Table A1-3: Full Carbon, Oxygen, and Clumped Isotope Analysis Details

Measurement			$\delta^{13}C$	$\delta^{13}C$	$\delta^{18}O$ gas	$\delta^{18}O$ mineral	$\delta^{18}O$ mineral	$\delta^{18}O$	δ 47 raw	δ 47 raw	Δ 47 raw	D47	D47	d48	d48	D48	D48	CIT	CIT	HG	Stretch	Acid	EGL	ETF	Acid	ARF	ARF
Week	Type	Name	VPDB (‰)	1σ	VSMOW (‰)	VPDB (‰)	VSMOW (‰)	1σ	(‰)	1σ	(v. Oz)	1σ	sterror	(v. Oz)	1σ	(v. Oz)	1σ	slope	intercept	Correct	Correct	Correct*	Correct	Correct	Correct*	slope	intercept
1	Sample	14AS-SA04TA2CS1	0.03	0.01	31.63	-7.40	23.23	0.03	9.821	0.052	-0.332	0.023	0.008	18.367	0.242	5.234	0.214	0.0138	-0.7844	0.317	0.341	0.422	-0.476	0.401	0.482	0.965	0.861
1	Sample	14AS-SA04TA2CS1	0.05	0.02	31.72	-7.31	23.32	0.03	9.882	0.045	-0.379	0.026	0.009	18.507	0.308	5.195	0.259	0.0138	-0.7844	0.269	0.290	0.371	-0.524	0.356	0.437	0.965	0.861
1	Sample	14AS-SA04TA2CS1	0.04	0.00	31.64	-7.39	23.24	0.00	9.814	0.027	-0.359	0.028	0.010	18.258	0.256	5.110	0.248	0.0140	-0.7828	0.286	0.309	0.390	-0.503	0.376	0.457	0.965	0.861
1	Sample	14AS-SA06D1	0.33	0.01	30.76	-9.31	21.27	0.02	9.243	0.053	-0.335	0.037	0.013	16.040	0.173	4.625	0.148	0.0115	-0.7699	0.329	0.361	0.442	-0.471	0.407	0.488	0.965	0.861
1	Sample	14AS-SA06D1	0.33	0.00	30.73	-9.34	21.23	0.01	9.186	0.030	-0.358	0.029	0.010	16.246	0.183	4.893	0.180	0.0115	-0.7699	0.307	0.337	0.418	-0.493	0.386	0.467	0.965	0.861
1	Sample	14AS-SA06D1	0.26	0.01	30.62	-9.45	21.12	0.02	8.999	0.046	-0.363	0.042	0.015	15.594	0.282	4.473	0.264	0.0124	-0.8200	0.345	0.356	0.437	-0.495	0.383	0.464	0.965	0.861
1	Sample	14AS-SA06L1	-0.14	0.01	29.54	-9.41	21.16	0.01	7.497	0.024	-0.408	0.027	0.010	12.776	0.206	3.781	0.197	0.0140	-0.7828	0.269	0.291	0.372	-0.519	0.361	0.442	0.965	0.861
1	Sample	14AS-SA06L1	-0.11	0.01	29.48	-9.47	21.09	0.01	7.451	0.014	-0.416	0.018	0.006	13.284	0.300	4.405	0.283	0.0140	-0.7828	0.262	0.283	0.364	-0.526	0.354	0.435	0.965	0.861
1	Sample	14AS-SA06L1	-0.17	0.01	29.54	-9.42	21.15	0.01	7.506	0.026	-0.362	0.034	0.012	13.033	0.297	4.044	0.274	0.0140	-0.7828	0.315	0.341	0.422	-0.473	0.405	0.486	0.965	0.861
1	Sample	14AS-SA08CS1	0.18	0.02	31.82	-7.22	23.41	0.03	10.114	0.041	-0.366	0.034	0.012	18.686	0.251	5.189	0.206	0.0138	-0.7844	0.279	0.301	0.382	-0.514	0.365	0.446	0.965	0.861
1	Sample	14AS-SA08CS1	0.19	0.01	31.82	-7.22	23.41	0.01	10.096	0.036	-0.392	0.035	0.013	19.350	0.348	5.846	0.331	0.0140	-0.7828	0.250	0.270	0.351	-0.540	0.340	0.421	0.965	0.861
1	Sample	14AS-SA08CS1	0.18	0.01	31.79	-7.25	23.38	0.01	10.113	0.041	-0.345	0.027	0.010	19.224	0.269	5.779	0.246	0.0140	-0.7828	0.296	0.319	0.400	-0.494	0.384	0.465	0.965	0.861
1	Sample	14AS-SA11CS1	-0.41	0.01	30.84	-8.16	22.45	0.01	8.489	0.018	-0.452	0.014	0.005	17.321	0.332	5.740	0.322	0.0124	-0.8200	0.263	0.271	0.352	-0.576	0.305	0.449	0.965	0.861
1	Sample	14AS-SA11CS1	-0.43	0.02	30.90	-8.10	22.51	0.03	8.591	0.043	-0.389	0.028	0.010	16.251	0.268	4.570	0.209	0.0138	-0.7844	0.277	0.298	0.379	-0.515	0.364	0.445	0.965	0.861
1	Sample	14AS-SA11CS1	-0.42	0.01	30.91	-8.09	22.52	0.02	8.650	0.039	-0.352	0.025	0.009	16.606	0.143	4.895	0.159	0.0140	-0.7828	0.309	0.334	0.415	-0.480	0.399	0.480	0.965	0.861
2	Sample	14AS-SA03D1	0.38	0.00	33.29	-6.88	23.77	0.00	11.819	0.028	-0.281	0.032	0.011	23.989	0.199	7.724	0.193	0.0140	-0.7920	0.345	0.368	0.450	-0.467	0.408	0.490	1.133	0.937
2	Sample	14AS-SA03D1	0.39	0.00	33.29	-6.88	23.77	0.01	11.812	0.026	-0.301	0.024	0.008	24.152	0.242	7.886	0.241	0.0140	-0.7983	0.332	0.351	0.433	-0.486	0.385	0.467	1.133	0.937
2	Sample	14AS-SA15CS1	-0.01	0.00	31.81	-7.23	23.41	0.00	9.876	0.055	-0.373	0.054	0.019	19.729	0.239	6.410	0.235	0.0145	-0.8039	0.288	0.303	0.385	-0.528	0.338	0.420	1.133	0.937
2	Sample	14AS-SA15CS1	0.03	0.00	31.92	-7.13	23.51	0.00	10.046	0.034	-0.352	0.033	0.012	20.120	0.194	6.587	0.192	0.0141	-0.7896	0.296	0.317	0.399	-0.510	0.359	0.441	1.133	0.937
2	Sample	14AS-SA15CS1	0.06	0.00	31.96	-7.09	23.55	0.00	10.120	0.052	-0.341	0.052	0.018	20.164	0.369	6.552	0.362	0.0145	-0.8031	0.316	0.332	0.414	-0.500	0.370	0.452	1.133	0.937
2	Sample	AD5-176.9-D	-2.67	0.00	28.75	-11.26	19.26	0.01	4.247	0.024	-0.366	0.024	0.009	10.663	0.201	3.405	0.199	0.0149	-0.7795	0.350	0.380	0.462	-0.433	0.446	0.528	1.133	0.937
2	Sample	AD5-176.9-D	-2.67	0.00	28.70	-11.30	19.22	0.01	4.199	0.053	-0.363	0.053	0.019	10.455	0.220	3.306	0.219	0.0141	-0.7896	0.368	0.394	0.476	-0.429	0.451	0.533	1.133	0.937
2	Sample	AD5-176.9-D	-2.66	0.00	28.73	-11.24	19.27	0.00	4.273	0.035	-0.336	0.037	0.013	10.547	0.152	3.320	0.152	0.0141	-0.7896	0.394	0.421	0.503	-0.403	0.480	0.562	1.133	0.937
2	Sample	AD5-201.5-CS1	-0.54	0.00	30.97	-8.04	22.57	0.01	8.541	0.044	-0.356	0.048	0.017	17.289	0.334	5.638	0.322	0.0145	-0.8039	0.324	0.341	0.423	-0.490	0.381	0.463	1.133	0.937
2	Sample	AD5-201.5-CS1	-0.53	0.00	30.97	-8.04	22.57	0.01	8.514	0.034	-0.386	0.038	0.013	17.221	0.301	5.580	0.296	0.0145	-0.8039	0.294	0.310	0.392	-0.520	0.348	0.430	1.133	0.937
2	Sample	AD5-201.5-CS1	-0.53	0.00	31.03	-7.98	22.63	0.01	8.586	0.014	-0.381	0.020	0.007	17.552	0.201	5.787	0.198	0.0145	-0.8039	0.298	0.314	0.396	-0.516	0.352	0.434	1.133	0.937
2	Sample	AD5-172.3-L1	-1.24	0.00	28.83	-10.10	20.45	0.01	5.696	0.029	-0.392	0.033	0.012	10.937	0.248	3.521	0.247	0.0149	-0.7795	0.303	0.328	0.410	-0.481	0.391	0.473	1.133	0.937
2	Sample	AD5-172.3-L1	-1.23	0.00	28.78	-10.14	20.41	0.01	5.645	0.036	-0.401	0.042	0.015	10.802	0.293	3.477	0.291	0.0140	-0.7920	0.312	0.333	0.415	-0.490	0.382	0.464	1.133	0.937
2	Sample	AD5-172.3-L1	-1.23	0.00	28.81	-10.12	20.43	0.01	5.671	0.029	-0.404	0.027	0.010	10.871	0.199	3.496	0.195	0.0141	-0.7896	0.306	0.328	0.410	-0.493	0.378	0.460	1.133	0.937
2	Sample	DI1-230.2-CS1	-0.60	0.00	33.26	-5.84	24.84	0.00	10.781	0.034	-0.340	0.035	0.012	24.036	0.242	7.829	0.240	0.0145	-0.8039	0.308	0.323	0.405	-0.509	0.360	0.442	1.133	0.937
2	Sample	DI1-230.2-CS1	-0.59	0.00	33.32	-5.78	24.90	0.01	10.835	0.044	-0.356	0.040	0.014	24.294	0.240	7.970	0.246	0.0145	-0.8039	0.291	0.306	0.388	-0.526	0.340	0.422	1.133	0.937
2	Sample	DI1-230.2-CS1	-0.58	0.00	33.34	-5.76	24.93	0.01	10.892	0.045	-0.328	0.037	0.013	24.218	0.182	7.851	0.178	0.0145	-0.8039	0.318	0.334	0.416	-0.499	0.371	0.453	1.133	0.937
2	Sample	DI1-246.5-L1	-0.62	0.00	29.99	-8.98	21.60	0.00	7.461	0.028	-0.381	0.029	0.010	14.183	0.252	4.473	0.247	0.0149	-0.7795	0.287	0.312	0.394	-0.498	0.372	0.454	1.133	0.937
2	Sample	DI1-246.5-L1	-0.61	0.00	30.03	-8.94	21.65	0.00	7.536	0.036	-0.360	0.036	0.013	14.291	0.190	4.498	0.184	0.0141	-0.7896	0.324	0.347	0.429	-0.478	0.395	0.477	1.133	0.937
2	Sample	DI1-246.5-L1	-0.60	0.00	30.10	-8.88	21.71	0.01	7.594	0.022	-0.373	0.019	0.007	14.627	0.258	4.708	0.257	0.0140	-0.7920	0.312	0.333	0.415	-0.492	0.379	0.461	1.133	0.937
2	Sample	WB98-966.5-CS1	-0.43	0.00	32.98	-6.05	24.62	0.01	10.665	0.026	-0.337	0.031	0.011	23.079	0.198	7.437	0.195	0.0145	-0.8039	0.312	0.328	0.410	-0.504	0.365	0.447	1.133	0.937
2	Sample	WB98-966.5-CS1	-0.43	0.00	33.03	-6.11	24.57	0.01	10.722	0.031	-0.337	0.031	0.011	23.402	0.192	7.647	0.187	0.0145	-0.8039	0.311	0.327	0.409	-0.505	0.364	0.446	1.133	0.937
2	Sample	WB98-966.5-CS1	-0.43	0.00	33.01	-6.08	24.60	0.00	10.715	0.049	-0.323	0.050	0.018	23.359	0.293	7.655	0.286	0.0145	-0.8039	0.326	0.342	0.424	-0.491	0.380	0.462	1.133	0.937
2	Sample	WB98-981CS1	-0.99	0.00	31.11	-7.90	22.72	0.01	8.255	0.026	-0.344	0.029	0.010	17.717	0.305	5.784	0.297	0.0145	-0.8039	0.340	0.358	0.440	-0.474	0.400	0.482	1.133	0.937
2	Sample	WB98-981CS1	-1.03	0.00	31.02	-7.99	22.63	0.00	8.085	0.029	-0.387	0.029	0.010	17.361	0.294	5.611	0.289	0.0145	-0.8039	0.300	0.315	0.397	-0.514	0.354	0.436	1.133	0.937
2	Sample	WB98-981CS1	-1.00	0.00	31.16	-7.86	22.76	0.01	8.274	0.023	-0.364	0.022	0.008	17.788	0.117	5.768	0.125	0.0145	-0.8039	0.320	0.336	0.418	-0.494	0.377	0.459	1.133	0.937
2	Sample	WB98-981-L1	-1.03	0.00	30.57	-8.42	22.18	0.01	7.652	0.024	-0.365	0.024	0.008	16.052	0.226	5.198	0.227	0.0140	-0.7920	0.320	0.341	0.423	-0.485	0.387	0.469	1.133	0.937
2	Sample	WB98-981-L1	-1.02	0.00	30.59	-8.40	22.20	0.01	7.700	0.032	-0.350	0.025	0.009	16.116	0.263	5.220	0.259	0.0149	-0.7795	0.315	0.341	0.423	-0.471	0.403	0.485	1.133	0.937
2	Sample	WB98-981-L1	-1.01	0.00	30.59	-8.41	22.19	0.00	7.666	0.050	-0.388	0.050	0.018	15.854	0.193	4.970	0.191	0.0141	-0.7896	0.294	0.315	0.397	-0.508	0.361	0.443	1.133	0.937
3	Sample	14AS-SA03CS1	0.38	0.00	32.31	-6.75	23.90	0.00	10.758	0.020	-0.363	0.018	0.006	21.255	0.369	6.946	0.364	0.0146	-0.8053	0.285	0.299	0.381	-0.522	0.318	0.400	1.200	0.945
3	Sample	14AS-SA03CS1	0.36	0.00	32.29	-6.76	23.89	0.01	10.763	0.039	-0.331	0.039	0.014	20.988	0.333	6.709	0.325	0.0146	-0.8053	0.317	0.332	0.414	-0.490	0.357	0.439	1.200	0.945
3	Sample	14AS-SA03CS1	0.37	0.00	32.32	-6.74	23.91	0.00	10.767	0.030	-0.358	0.032	0.011	21.211	0.360	6.879	0.353	0.0146	-0.8053	0.290	0.304	0.386	-0.517	0.324	0.406	1.200	0.945
3	Sample	14AS-SA03D1	0.39	0.00	33.33	-6.84	23.81	0.01	11.886	0.037	-0.271	0.043	0.015	24.104	0.247	7.759	0.237	0.0146	-0.8053	0.360	0.378	0.460	-0.447	0.409	0.491	1.200	0.945
3	Sample	14AS-SA05CS1	-0.41	0.00	29.92	-9.05	21.53	0.00	7.612	0.045	-0.368	0.043	0.015	14.106	0.291	4.535	0.290	0.0146	-0.8053	0.326	0.342	0.424	-0.481	0.368	0.450	1.200	0.945
3	Sample	14AS-SA05CS1	-0.40	0.00	29.92	-9.04	21.54	0.00	7.580	0.050	-0.406	0.051	0.018	14.056	0.226	4.480	0.227	0.0146	-0.8053	0.288	0.303	0.385	-0.518	0.323	0.405	1.200	0.945
3	Sample	14AS-SA05CS1	-0.43	0.00	29.84	-9.12	21.46	0.01	7.499	0.029	-0.380	0.030	0.011	13.970	0.341	4.548	0.337	0.0146	-0.8053	0.316	0.331	0.413	-0.491	0.356	0.438	1.200	0.945
3	Sample	14AS-SA05D1	0.45	0.00	31.41	-8.68	21.91	0.01	10.000	0.034	-0.305	0.036	0.013	18.507	0.220	5.970	0.219	0.0146	-0.8053	0.353	0.371	0.453	-0.453	0.401	0.483	1.200	0.945
3	Sample	14AS-SA05D1	0.46	0.00	31.45	-8.65	21.95	0.01	10.050	0.071	-0.304	0.071	0.025	18.614	0.337	6.005	0.334	0.0146	-0.8053	0.354	0.372	0.454	-0.452	0.402	0.484	1.200	0.945
3	Sample	14AS-SA05D1	0.43	0.00	31.42	-8.68	21.91	0.01	9.970	0.025	-0.319	0.027	0.010	18.656	0.233	6.111	0.215	0.0146	-0.8053	0.341	0.358	0.440	-0.466	0.386	0.468	1.200	0.945
3	Sample	14AS-SA13CS1	-0.16	0.00	32.00	-7.04	23.60	0.01	9.937	0.021	-0.364	0.029	0.010	20.373	0.299	6.667	0.284	0.0148	-0.7947	0.284	0.302	0.384	-0.511	0.332	0.414	1.200	0.945
3	Sample	14AS-SA13CS1	-0.19	0.00	31.97	-7.08	23.56	0.01	9.910	0.025	-0.324	0.022	0.008	20.209	0.214	6.575	0.207	0.0148	-0.7947	0.324	0.345	0.427	-0.471	0.380	0.462	1.200	0.945
3	Sample	14AS-SA14ACS1	-0.19	0.00	31.42	-7.60	23.02	0.01	9.338	0.061	-0.349	0.059	0.021	18.606	0.274	6.060	0.264	0.0148	-0.7947	0.308	0.327	0.409	-0.487	0.361	0.443	1.200	0.945

Table A1-3 (cont.): Full Carbon, Oxygen, and Clumped Isotope Analysis Details

Measurement			$\delta^{13}C$	$\delta^{13}C$	$\delta^{18}O$ gas	$\delta^{18}O$ mineral	$\delta^{18}O$ mineral	$\delta^{18}O$	δ 47 raw	δ 47 raw	Δ 47 raw	D47	D47	d48	d48	D48	D48	CIT	CIT	HG	Stretch	Acid	EGL	ETF	Acid	ARF	ARF
Week	Type	Name	VPDB (‰)	1σ	VSMOW (‰)	VPDB (‰)	VSMOW (‰)	1σ	(‰)	1σ	(v. Oz)	1σ	sterror	(v. Oz)	1σ	(v. Oz)	1σ	slope	intercept	Correct	Correct	Correct*	Correct	Correct	Correct*	slope	intercept
4	Sample	14AS-SA03D2	-0.07	0.00	33.62	-6.56	24.10	0.01	11.734	0.040	-0.270	0.039	0.014	22.298	0.172	5.410	0.163	0.0142	-0.8340	0.397	0.403	0.485	-0.441	0.426	0.508	1.081	0.921
4	Sample	14AS-SA03D2	-0.08	0.00	33.63	-6.55	24.11	0.00	11.744	0.030	-0.260	0.031	0.011	22.417	0.253	5.502	0.250	0.0142	-0.8340	0.407	0.413	0.495	-0.431	0.436	0.518	1.081	0.921
4	Sample	14AS-SA03D2	-0.08	0.00	33.63	-6.55	24.10	0.01	11.727	0.027	-0.269	0.024	0.008	22.537	0.203	5.636	0.206	0.0142	-0.8340	0.398	0.404	0.486	-0.440	0.427	0.509	1.081	0.921
4	Sample	14AS-SA04TA2CS2	0.15	0.00	31.62	-7.41	23.22	0.01	9.825	0.036	-0.392	0.040	0.014	17.073	0.193	4.155	0.191	0.0142	-0.8340	0.302	0.307	0.389	-0.535	0.322	0.404	1.081	0.921
4	Sample	14AS-SA05D2	0.67	0.00	32.37	-7.77	22.85	0.01	11.160	0.022	-0.308	0.028	0.010	19.052	0.280	4.658	0.275	0.0142	-0.8340	0.368	0.373	0.455	-0.471	0.393	0.475	1.081	0.921
4	Sample	14AS-SA05D2	0.44	0.00	31.46	-8.64	21.95	0.00	10.033	0.038	-0.298	0.039	0.014	16.615	0.097	4.023	0.095	0.0142	-0.8340	0.394	0.399	0.481	-0.444	0.422	0.504	1.081	0.921
4	Sample	14AS-SA05D2	0.44	0.00	31.52	-8.58	22.02	0.01	10.078	0.055	-0.323	0.056	0.020	16.789	0.149	4.068	0.147	0.0142	-0.8340	0.368	0.373	0.455	-0.470	0.394	0.476	1.081	0.921
4	Sample	14AS-SA06ST2	0.45	0.00	31.23	-7.79	22.83	0.01	9.718	0.031	-0.405	0.029	0.010	15.811	0.141	3.669	0.136	0.0142	-0.8340	0.291	0.295	0.377	-0.547	0.309	0.391	1.081	0.921
4	Sample	14AS-SA06ST2	0.47	0.00	31.16	-7.86	22.76	0.01	9.681	0.043	-0.383	0.042	0.015	15.742	0.297	3.748	0.282	0.0142	-0.8340	0.314	0.318	0.400	-0.524	0.334	0.416	1.081	0.921
4	Sample	14AS-SA06ST2	0.48	0.00	31.14	-7.87	22.75	0.01	9.651	0.046	-0.405	0.046	0.016	15.856	0.214	3.887	0.215	0.0142	-0.8340	0.292	0.296	0.378	-0.546	0.310	0.392	1.081	0.921
4	Sample	14AS-SA06L3	-0.14	0.00	30.07	-8.90	21.68	0.01	7.999	0.026	-0.394	0.025	0.009	12.901	0.273	3.047	0.269	0.0142	-0.8340	0.326	0.331	0.413	-0.511	0.349	0.431	1.081	0.921
4	Sample	14AS-SA08D1	1.48	0.00	33.90	-6.29	24.37	0.01	13.473	0.046	-0.310	0.041	0.015	23.326	0.223	5.878	0.221	0.0150	-0.8276	0.316	0.322	0.404	-0.507	0.353	0.435	1.081	0.921
4	Sample	14AS-SA08D1	1.35	0.00	33.80	-6.39	24.27	0.01	13.242	0.043	-0.316	0.041	0.015	23.083	0.219	5.842	0.210	0.0150	-0.8276	0.313	0.320	0.402	-0.509	0.351	0.433	1.081	0.921
4	Sample	14AS-SA08D1	1.47	0.01	33.83	-6.36	24.30	0.01	13.381	0.062	-0.316	0.068	0.024	23.112	0.313	5.815	0.324	0.0150	-0.8276	0.311	0.318	0.400	-0.511	0.348	0.430	1.081	0.921
4	Sample	14AS-SA12por1	3.43	0.01	37.85	-2.50	28.28	0.01	19.642	0.038	-0.003	0.030	0.011	33.520	0.227	8.186	0.216	0.0142	-0.8340	0.552	0.560	0.642	-0.290	0.593	0.675	1.081	0.921
4	Sample	14AS-SA12por1	3.37	0.01	37.81	-2.53	28.25	0.01	19.550	0.038	0.004	0.035	0.012	33.841	0.287	8.574	0.281	0.0142	-0.8340	0.560	0.568	0.650	-0.281	0.602	0.684	1.081	0.921
4	Sample	14AS-SA12por1	3.39	0.00	37.81	-2.54	28.24	0.01	19.530	0.022	-0.030	0.024	0.008	33.781	0.240	8.522	0.237	0.0142	-0.8340	0.527	0.534	0.616	-0.315	0.565	0.647	1.081	0.921
4	Sample	14AS-SA14BD1	-2.14	0.00	32.06	-8.06	22.55	0.01	8.143	0.036	-0.287	0.029	0.010	18.646	0.310	4.856	0.303	0.0150	-0.8276	0.418	0.427	0.509	-0.406	0.465	0.547	1.081	0.921
4	Sample	14AS-SA14BD1	-2.25	0.00	32.09	-8.03	22.58	0.01	8.037	0.024	-0.312	0.022	0.008	18.809	0.124	4.959	0.116	0.0150	-0.8276	0.395	0.403	0.485	-0.429	0.439	0.521	1.081	0.921
4	Sample	14AS-SA14BD1	-2.18	0.00	31.79	-8.32	22.28	0.01	7.794	0.062	-0.325	0.059	0.021	17.795	0.296	4.537	0.293	0.0150	-0.8276	0.386	0.394	0.476	-0.439	0.428	0.510	1.081	0.921
4	Sample	AD5-201.5-D1	-1.08	0.00	34.01	-5.11	25.59	0.01	11.059	0.047	-0.338	0.039	0.014	23.676	0.209	6.016	0.203	0.0142	-0.8340	0.339	0.344	0.426	-0.499	0.361	0.443	1.081	0.921
4	Sample	AD5-201.5-D1	-0.92	0.00	34.11	-5.01	25.69	0.01	11.377	0.033	-0.287	0.030	0.011	24.111	0.304	6.238	0.306	0.0142	-0.8340	0.385	0.391	0.473	-0.453	0.413	0.495	1.081	0.921
4	Sample	AD5-201.5-D1	-0.88	0.00	34.13	-5.00	25.71	0.01	11.365	0.051	-0.300	0.055	0.019	23.852	0.207	5.947	0.210	0.0142	-0.8340	0.373	0.378	0.460	-0.466	0.398	0.480	1.081	0.921
4	Sample	DI1-246.5-L1	-0.58	0.00	30.15	-8.83	21.76	0.01	7.629	0.043	-0.410	0.044	0.016	13.442	0.206	3.431	0.200	0.0150	-0.8276	0.303	0.310	0.392	-0.521	0.337	0.419	1.081	0.921
5	Sample	14AS-SA03CS2	0.31	0.00	31.93	-7.11	23.53	0.01	10.312	0.037	-0.367	0.037	0.013	17.262	0.221	3.737	0.216	0.0141	-0.8399	0.328	0.330	0.412	-0.520	0.360	0.442	1.103	0.913
5	Sample	14AS-SA03CS2	0.30	0.01	31.98	-7.06	23.58	0.01	10.335	0.036	-0.382	0.032	0.011	17.632	0.282	4.008	0.285	0.0142	-0.8395	0.311	0.313	0.395	-0.535	0.343	0.425	1.103	0.913
5	Sample	14AS-SA03CS2	0.35	0.00	32.20	-6.85	23.80	0.00	10.635	0.038	-0.355	0.035	0.013	18.175	0.192	4.111	0.189	0.0142	-0.8395	0.333	0.336	0.418	-0.512	0.367	0.449	1.103	0.913
5	Sample	14AS-SA04TA2CS2	0.15	0.00	31.63	-7.40	23.23	0.01	9.876	0.042	-0.353	0.043	0.015	16.553	0.301	3.625	0.291	0.0141	-0.8399	0.348	0.350	0.432	-0.499	0.382	0.464	1.103	0.913
5	Sample	14AS-SA04TA2CS2	0.14	0.00	31.64	-7.39	23.24	0.01	9.866	0.035	-0.363	0.033	0.012	16.648	0.275	3.700	0.265	0.0142	-0.8395	0.336	0.339	0.421	-0.509	0.371	0.453	1.103	0.913
5	Sample	14AS-SA05CS2	0.36	0.00	32.40	-6.66	23.99	0.01	10.817	0.030	-0.378	0.029	0.010	18.474	0.135	4.029	0.136	0.0141	-0.8399	0.309	0.311	0.393	-0.538	0.340	0.422	1.103	0.913
5	Sample	14AS-SA05CS2	0.37	0.00	32.38	-6.68	23.98	0.01	10.804	0.024	-0.384	0.028	0.010	18.804	0.229	4.380	0.226	0.0142	-0.8395	0.302	0.304	0.386	-0.544	0.333	0.415	1.103	0.913
5	Sample	14AS-SA05CS2	0.36	0.01	32.45	-6.61	24.04	0.01	10.872	0.029	-0.377	0.037	0.013	18.906	0.326	4.348	0.317	0.0142	-0.8395	0.308	0.310	0.392	-0.538	0.340	0.422	1.103	0.913
5	Sample	14AS-SA06ST1	0.49	0.00	31.09	-7.92	22.69	0.01	9.589	0.040	-0.425	0.038	0.014	15.478	0.222	3.615	0.230	0.0142	-0.8395	0.278	0.280	0.362	-0.567	0.308	0.390	1.103	0.913
5	Sample	14AS-SA06ST1	0.48	0.01	31.12	-7.89	22.72	0.01	9.683	0.030	-0.359	0.030	0.009	15.486	0.314	3.562	0.308	0.0142	-0.8395	0.343	0.345	0.427	-0.502	0.378	0.460	1.103	0.913
5	Sample	14AS-SA06ST1	0.49	0.00	31.18	-7.83	22.79	0.01	9.713	0.051	-0.401	0.057	0.020	15.843	0.219	3.791	0.208	0.0142	-0.8395	0.301	0.303	0.385	-0.545	0.332	0.414	1.103	0.913
5	Sample	14AS-SA06L2	-0.18	0.00	29.44	-9.51	21.06	0.01	7.319	0.031	-0.403	0.028	0.010	11.071	0.268	2.466	0.266	0.0142	-0.8395	0.333	0.335	0.417	-0.511	0.369	0.451	1.103	0.913
5	Sample	14AS-SA06L2	-0.18	0.01	29.48	-9.47	21.10	0.02	7.350	0.033	-0.418	0.037	0.013	11.167	0.191	2.475	0.187	0.0142	-0.8395	0.317	0.319	0.401	-0.527	0.352	0.434	1.103	0.913
5	Sample	14AS-SA06L2	-0.16	0.00	29.47	-9.48	21.09	0.01	7.369	0.031	-0.406	0.034	0.012	11.406	0.262	2.736	0.257	0.0142	-0.8395	0.329	0.331	0.413	-0.515	0.365	0.447	1.103	0.913
5	Sample	14AS-SA06L3	-0.14	0.00	29.99	-8.98	21.60	0.01	7.897	0.025	-0.417	0.028	0.010	12.785	0.120	3.090	0.120	0.0142	-0.8395	0.310	0.313	0.395	-0.534	0.344	0.426	1.103	0.913
5	Sample	14AS-SA06L3	-0.13	0.01	30.06	-8.91	21.67	0.01	7.953	0.049	-0.434	0.048	0.017	12.811	0.269	2.984	0.252	0.0142	-0.8395	0.293	0.295	0.377	-0.552	0.325	0.407	1.103	0.913
5	Sample	14AS-SA11CS2	-0.34	0.00	30.65	-8.34	22.26	0.01	8.339	0.056	-0.429	0.049	0.017	13.318	0.652	2.332	0.637	0.0140	-0.8467	0.301	0.300	0.382	-0.552	0.324	0.406	1.103	0.913
5	Sample	14AS-SA11CS2	-0.38	0.00	30.65	-8.35	22.25	0.01	8.326	0.036	-0.402	0.038	0.014	13.896	0.154	2.916	0.149	0.0141	-0.8395	0.320	0.322	0.404	-0.525	0.354	0.436	1.103	0.913
5	Sample	14AS-SA11CS2	-0.36	0.00	30.64	-8.36	22.24	0.01	8.346	0.040	-0.393	0.037	0.013	13.812	0.133	2.852	0.132	0.0141	-0.8399	0.329	0.331	0.413	-0.517	0.363	0.445	1.103	0.913
5	Sample	14AS-SA13CS1	-0.10	0.01	32.10	-6.95	23.69	0.01	10.058	0.031	-0.386	0.024	0.008	18.146	0.133	4.291	0.129	0.0142	-0.8395	0.311	0.313	0.395	-0.535	0.343	0.425	1.103	0.913
5	Sample	14AS-SA14ACS1	-0.15	0.00	31.54	-7.49	23.14	0.01	9.490	0.046	-0.350	0.044	0.015	16.438	0.124	3.687	0.119	0.0142	-0.8395	0.355	0.357	0.439	-0.490	0.391	0.473	1.103	0.913
5	Sample	14AS-SA14ACS1	-0.15	0.00	31.55	-7.48	23.15	0.01	9.500	0.014	-0.358	0.019	0.007	16.731	0.344	3.952	0.334	0.0142	-0.8395	0.347	0.349	0.431	-0.499	0.382	0.464	1.103	0.913
6	sample	--	--	--	--	--	--	--	--	--	--	--	--	--	--	--	--	--	--	--	--	--	--	--	--	--	--	--
7	sample	WB98-815B	-6.85	0.00	28.63	-10.55	19.98	0.01	-0.093	0.031	-0.583	0.028	0.010	12.020	0.421	4.848	0.424	0.0152	-0.8493	--	0.348	0.473	--	0.297	0.422	--	--
7	sample	AD5-161.9A	-3.78	0.00	30.84	-8.43	22.17	0.02	5.168	0.053	-0.507	0.040	0.014	19.289	0.384	7.721	0.361	0.0152	-0.8493	--	0.343	0.468	--	0.298	0.423	--	--
7	sample	WB98-886B	-4.35	0.00	28.87	-10.32	20.22	0.02	2.616	0.034	-0.546	0.027	0.009	12.529	0.402	4.871	0.383	0.0152	-0.8493	--	0.343	0.468	--	0.295	0.420	--	--
7	sample	DI1-213.8A	-5.89	0.00	28.80	-10.39	20.15	0.01	1.032	0.025	-0.569	0.026	0.009	12.257	0.412	4.742	0.406	0.0152	-0.8493	--	0.345	0.469	--	0.295	0.420	--	--
8	sample	WB98-815A	-6.68	0.00	29.17	-10.04	20.51	0.02	0.608	0.021	-0.578	0.024	0.008	11.070	0.238	2.864	0.233	0.0105	-0.8523	--	0.347	0.472	--	0.310	0.435	--	--
8	sample	WB98-886A	-4.17	0.01	27.91	-11.25	19.27	0.00	1.854	0.038	-0.525	0.037	0.013	7.825	0.277	2.077	0.272	0.0105	-0.8523	--	0.387	0.511	--	0.353	0.477	--	--
8	sample	DI1-236.7A L2	-7.15	0.00	29.67	-9.55	21.01	0.01	0.679	0.018	-0.549	0.018	0.006	12.529	0.176	3.326	0.176	0.0105	-0.8523	--	0.375	0.500	--	0.340	0.465	--	--
9	sample	DI1-236.7A L2 (repeat)	-7.08	0.00	29.29	-9.92	20.64	0.00	0.372	0.030	-0.553	0.032	0.011	12.288	0.341	3.826	0.338	0.0131	-0.8775	--	0.389	0.513	--	0.347	0.472	--	--
9	sample	DI1-236.7A L3	-8.18	0.01	29.51	-9.70	20.86	0.01	-0.502	0.047	-0.568	0.039	0.014	13.135	0.287	4.242	0.274	0.0131	-0.8775	--	0.385	0.510	--	0.343	0.467	--	--

* Acid correction factors were calculated according to Deflies et al. (2015). Specifically, samples digested at 90ºC (i.e. calcite and dolomite) and 115ºC (i.e. siderite) were corrected by a values of 0.0820 and 0.1247, respectively.

Table A1-4: Full Standards, Heated Gasses, and Equilibrated Gasses Analyzed During Clumped Isotope Analyses

Measurement			$\delta^{13}C$	$\delta^{13}C$	$\delta^{18}O$ gas	$\delta^{18}O$ mineral	$\delta^{18}O$ mineral	$\delta^{18}O$	δ 47 raw	δ 47 raw	Δ 47 raw	D47	D47	d48	d48	D48	D48	CIT	CIT	HG	Stretch	Acid	EGL	ETF	Acid	ARF	ARF
Week	Type	Name	VPDB (‰)	1σ	VSMOW (‰)	PDB (‰)	VSMOW (‰)	1σ	(‰)	1σ	(v. Oz)	1σ	sterror	(v. Oz)	1σ	(v. Oz)	1σ	slope	intercept	Correct	Correct	Correct*	Correct	Correct	Correct*	slope	intercept
1	Standard	CIT Carrara	2.15	0.02	37.38	-1.87	28.93	0.03	17.640	0.064	-0.319	0.020	0.007	33.865	0.194	9.259	0.193	0.0115	-0.7699	0.248	0.272	0.353	-0.5787	0.303	0.384	0.965	0.861
1	Standard	CIT Carrara	3.44	0.02	30.57	-8.43	22.17	0.03	12.288	0.044	-0.113	0.041	0.014	15.907	0.244	4.866	0.197	0.0115	-0.7699	0.516	0.566	0.647	-0.2933	0.578	0.659	0.965	0.861
1	Standard	TV03	3.44	0.02	30.49	-8.50	22.10	0.03	12.243	0.058	-0.089	0.038	0.013	15.343	0.228	4.456	0.208	0.0138	-0.7844	0.526	0.567	0.648	-0.2691	0.602	0.683	0.965	0.861
1	Standard	TV03	2.12	0.02	37.32	-1.93	28.87	0.03	17.593	0.039	-0.281	0.022	0.008	33.602	0.294	9.120	0.276	0.0138	-0.7844	0.260	0.281	0.362	-0.5399	0.340	0.421	0.965	0.861
1	Standard	TV03	3.43	0.01	30.51	-8.48	22.12	0.02	12.288	0.027	-0.050	0.017	0.006	15.632	0.300	4.701	0.302	0.0138	-0.7844	0.565	0.609	0.690	-0.2307	0.639	0.720	0.965	0.861
1	Standard	CIT Carrara	2.16	0.01	37.39	-1.86	28.95	0.01	17.708	0.035	-0.278	0.024	0.008	34.320	0.326	9.676	0.305	0.0140	-0.7828	0.257	0.277	0.358	-0.5383	0.342	0.423	0.965	0.861
1	Standard	TV03	3.46	0.01	30.54	-8.45	22.15	0.01	12.313	0.021	-0.086	0.025	0.009	15.794	0.277	4.798	0.256	0.0140	-0.7828	0.524	0.566	0.647	-0.2675	0.603	0.684	0.965	0.861
1	Standard	TV03	3.45	0.01	30.55	-8.45	22.15	0.02	12.313	0.054	-0.081	0.036	0.013	15.765	0.310	4.765	0.273	0.0140	-0.7828	0.530	0.572	0.653	-0.2616	0.609	0.690	0.965	0.861
1	Standard	CIT Carrara	2.15	0.00	37.38	-1.87	28.93	0.01	17.679	0.040	-0.283	0.029	0.010	34.455	0.156	9.842	0.162	0.0140	-0.7828	0.253	0.273	0.354	-0.5427	0.338	0.419	0.965	0.861
1	Standard	TV03	3.48	0.01	30.54	-8.45	22.15	0.02	12.357	0.027	-0.067	0.016	0.006	15.967	0.502	4.965	0.470	0.0140	-0.7828	0.543	0.586	0.667	-0.2487	0.621	0.702	0.965	0.861
1	Standard	CIT Carrara	2.15	0.01	37.45	-1.80	29.00	0.02	17.752	0.037	-0.280	0.024	0.009	33.845	0.331	9.104	0.301	0.0140	-0.7828	0.254	0.275	0.356	-0.5409	0.339	0.420	0.965	0.861
1	Standard	TV03	3.50	0.01	30.57	-8.42	22.18	0.03	12.392	0.030	-0.073	0.026	0.009	15.895	0.350	4.842	0.308	0.0140	-0.7828	0.536	0.579	0.660	-0.2556	0.615	0.696	0.965	0.861
1	Heated Gas	BOC	-10.94	0.01	30.16	-8.82	21.77	0.02	-2.793	0.047	-0.822	0.024	0.008	14.318	0.188	4.152	0.201	--	--	--	--	--	--	--	--	--	--
1	Heated Gas	eBOC	-10.37	0.02	58.13	18.10	49.52	0.03	25.765	0.040	-0.452	0.016	0.006	91.064	0.306	23.827	0.265	--	--	--	--	--	--	--	--	--	--
1	Heated Gas	BOC	-10.61	0.01	29.99	-8.98	21.60	0.02	-2.591	0.034	-0.779	0.024	0.008	13.670	0.385	3.838	0.359	--	--	--	--	--	--	--	--	--	--
1	Heated Gas	eBOC	-10.97	0.01	58.38	18.34	49.77	0.03	25.394	0.049	-0.473	0.040	0.014	93.871	1.686	25.975	1.580	--	--	--	--	--	--	--	--	--	--
1	Heated Gas	BOC	-10.58	0.01	29.44	-9.51	21.06	0.01	-3.164	0.044	-0.837	0.042	0.015	12.573	0.166	3.821	0.145	--	--	--	--	--	--	--	--	--	--
1	Heated Gas	eBOC	-11.16	0.04	57.21	17.21	48.60	0.08	24.077	0.092	-0.441	0.042	0.015	91.319	0.775	25.857	0.628	--	--	--	--	--	--	--	--	--	--
1	Heated Gas	BOC	-10.83	0.00	29.93	-9.03	21.55	0.01	-2.939	0.033	-0.860	0.031	0.011	14.412	0.307	4.681	0.293	--	--	--	--	--	--	--	--	--	--
1	Heated Gas	eBOC	-10.70	0.00	57.08	17.09	48.47	0.01	24.438	0.050	-0.418	0.050	0.018	94.832	0.569	29.403	0.532	--	--	--	--	--	--	--	--	--	--
1	Heated Gas	eBOC	-10.78	0.00	57.50	17.49	48.89	0.00	24.766	0.050	-0.416	0.046	0.016	95.905	0.431	29.606	0.398	--	--	--	--	--	--	--	--	--	--
1	Heated Gas	BOC	-10.87	0.00	29.96	-9.01	21.57	0.00	-2.919	0.027	-0.819	0.024	0.008	14.402	0.132	4.622	0.128	--	--	--	--	--	--	--	--	--	--
1	Heated Gas	BOC	-11.16	0.01	29.70	-9.26	21.32	0.03	-3.504	0.055	-0.876	0.032	0.011	14.180	0.307	4.904	0.279	--	--	--	--	--	--	--	--	--	--
1	Equilibrated Gas	25C eBOC	-10.70	0.02	59.53	19.44	50.90	0.04	27.705	0.059	0.409	0.019	0.007	95.831	0.208	25.596	0.138	--	--	--	--	--	--	--	--	--	--
1	Equilibrated Gas	25C BOC	-10.64	0.01	28.75	-10.17	20.37	0.02	-3.110	0.041	-0.043	0.031	0.011	11.516	0.496	4.114	0.473	--	--	--	--	--	--	--	--	--	--
1	Equilibrated Gas	25C eBOC	-10.55	0.02	59.35	19.27	50.73	0.05	27.676	0.086	0.409	0.035	0.012	95.263	0.502	25.405	0.403	--	--	--	--	--	--	--	--	--	--
1	Equilibrated Gas	25C eBOC	-10.61	0.00	58.36	18.31	49.74	0.00	26.675	0.050	0.453	0.050	0.018	100.438	0.567	32.188	0.534	--	--	--	--	--	--	--	--	--	--
1	Equilibrated Gas	25C BOC	-10.73	0.00	28.67	-10.25	20.29	0.01	-3.265	0.027	-0.033	0.024	0.009	11.168	0.203	3.930	0.194	--	--	--	--	--	--	--	--	--	--
1	Equilibrated Gas	25C eBOC	-10.62	0.00	59.15	19.08	50.52	0.01	27.549	0.035	0.550	0.030	0.011	105.978	1.259	35.834	1.181	--	--	--	--	--	--	--	--	--	--
2	Standard	TV03	3.33	0.00	30.55	-8.44	22.16	0.01	12.135	0.061	-0.105	0.059	0.021	16.202	0.295	5.378	0.290	0.0140	-0.7983	0.523	0.554	0.636	-0.296	0.602	0.684	1.133	0.937
2	Standard	CIT Carrara	2.10	0.00	37.39	-1.86	28.95	0.00	17.580	0.023	-0.301	0.022	0.008	36.149	0.325	11.636	0.318	0.0140	-0.7920	0.244	0.261	0.343	-0.577	0.283	0.365	1.133	0.937
2	Standard	TV03	3.41	0.00	30.58	-8.41	22.19	0.00	12.259	0.042	-0.092	0.045	0.016	16.173	0.322	5.294	0.311	0.0141	-0.7896	0.525	0.562	0.644	-0.284	0.614	0.696	1.133	0.937
2	Standard	CIT Carrara	2.11	0.00	37.49	-1.76	29.04	0.01	17.691	0.028	-0.295	0.022	0.008	36.500	0.218	11.795	0.212	0.0145	-0.8039	0.252	0.265	0.347	-0.573	0.288	0.370	1.133	0.937
2	Standard	TV03	3.38	0.00	30.61	-8.38	22.22	0.01	12.259	0.035	-0.093	0.037	0.013	16.303	0.299	5.361	0.288	0.0145	-0.8039	0.533	0.561	0.643	-0.285	0.613	0.695	1.133	0.937
2	Standard	CIT Carrara	2.12	0.00	37.51	-1.75	29.06	0.01	17.742	0.041	-0.277	0.041	0.014	36.587	0.193	11.844	0.190	0.0145	-0.8039	0.270	0.284	0.366	-0.556	0.307	0.389	1.133	0.937
2	Standard	TV03	3.39	0.00	30.58	-8.42	22.18	0.00	12.249	0.039	-0.079	0.036	0.013	16.248	0.174	5.375	0.176	0.0145	-0.8039	0.547	0.575	0.657	-0.271	0.629	0.711	1.133	0.937
2	Standard	NBS-19	2.01	0.00	37.03	-2.21	28.58	0.01	17.101	0.040	-0.327	0.036	0.013	35.112	0.326	11.340	0.315	0.0145	-0.8039	0.229	0.241	0.323	-0.595	0.262	0.344	1.133	0.937
2	Standard	TV03	3.44	0.00	30.59	-8.40	22.20	0.01	12.312	0.029	-0.075	0.030	0.011	16.320	0.239	5.418	0.242	0.0145	-0.8039	0.550	0.579	0.661	-0.268	0.633	0.715	1.133	0.937
2	Standard	CIT Carrara	2.10	0.00	37.45	-1.80	29.00	0.01	17.679	0.032	-0.263	0.028	0.010	36.222	0.156	11.592	0.151	0.0149	-0.7795	0.253	0.274	0.356	-0.541	0.324	0.406	1.133	0.937
2	Standard	TV03	3.38	0.00	30.62	-8.37	22.23	0.00	12.318	0.040	-0.050	0.042	0.015	16.328	0.273	5.361	0.267	0.0149	-0.7795	0.546	0.592	0.674	-0.243	0.661	0.743	1.133	0.937
2	Heated Gas	BOC	-11.04	0.00	33.16	-5.93	24.74	0.01	0.038	0.027	-0.812	0.029	0.010	23.643	0.370	7.648	0.364	--	--	--	--	--	--	--	--	--	--
2	Heated Gas	BOC	-11.55	0.00	32.74	-6.33	24.33	0.01	-0.881	0.028	-0.832	0.030	0.011	22.385	0.338	7.213	0.328	--	--	--	--	--	--	--	--	--	--
2	Heated Gas	eBOC	-10.91	0.00	55.37	15.44	46.78	0.01	22.461	0.039	-0.448	0.034	0.012	89.758	0.422	28.045	0.393	--	--	--	--	--	--	--	--	--	--
2	Heated Gas	eBOC	-10.72	0.00	57.21	17.21	48.60	0.01	24.456	0.034	-0.461	0.033	0.012	95.326	0.337	29.713	0.311	--	--	--	--	--	--	--	--	--	--
2	Heated Gas	BOC	-10.96	0.00	32.95	-6.13	24.54	0.01	-0.075	0.039	-0.802	0.036	0.013	23.020	0.211	7.426	0.194	--	--	--	--	--	--	--	--	--	--
2	Heated Gas	eBOC	-10.47	0.00	57.10	17.11	48.50	0.01	24.598	0.024	-0.464	0.026	0.009	94.960	0.329	29.569	0.312	--	--	--	--	--	--	--	--	--	--
2	Heated Gas	BOC	-10.67	0.00	33.03	-6.06	24.61	0.01	0.305	0.034	-0.777	0.038	0.013	23.195	0.248	7.459	0.245	--	--	--	--	--	--	--	--	--	--
2	Heated Gas	eBOC	-10.60	0.00	55.21	15.29	46.62	0.01	22.601	0.020	-0.460	0.022	0.008	89.266	0.319	27.892	0.292	--	--	--	--	--	--	--	--	--	--
2	Heated Gas	BOC	-10.56	0.00	32.66	-6.41	24.25	0.00	0.030	0.040	-0.797	0.038	0.014	21.961	0.335	6.963	0.328	--	--	--	--	--	--	--	--	--	--
2	Heated Gas	eBOC	-10.91	0.01	57.76	17.73	49.14	0.01	24.812	0.026	-0.454	0.029	0.010	96.716	0.224	29.952	0.211	--	--	--	--	--	--	--	--	--	--
2	Heated Gas	BOC	-11.21	0.00	32.75	-6.32	24.34	0.01	-0.531	0.042	-0.822	0.042	0.015	22.664	0.128	7.466	0.130	--	--	--	--	--	--	--	--	--	--
2	Equilibrated Gas	25C eBOC	-11.03	0.00	58.44	18.40	49.83	0.01	26.266	0.048	0.411	0.043	0.015	100.325	0.302	32.091	0.285	--	--	--	--	--	--	--	--	--	--
2	Equilibrated Gas	25C BOC	-11.02	0.00	29.57	-9.38	21.19	0.01	-2.714	0.034	-0.046	0.028	0.010	13.421	0.313	4.583	0.302	--	--	--	--	--	--	--	--	--	--
2	Equilibrated Gas	25C eBOC	-11.01	0.00	58.34	18.30	49.73	0.01	26.145	0.040	0.373	0.041	0.014	99.632	0.270	31.542	0.336	--	--	--	--	--	--	--	--	--	--
2	Equilibrated Gas	25C BOC	-11.05	0.00	28.48	-10.43	20.11	0.01	-3.887	0.047	-0.119	0.049	0.017	10.391	0.284	3.658	0.294	--	--	--	--	--	--	--	--	--	--
3	Standard	CIT Carrara	2.12	0.00	37.48	-1.78	29.03	0.01	17.719	0.035	-0.264	0.033	0.012	36.497	0.282	11.819	0.271	0.0146	-0.8053	0.2819	0.2958	0.3778	-0.5262	0.3135	0.3955	1.2001	0.9450
3	Standard	TV03	3.40	0.00	30.60	-8.39	22.21	0.00	12.291	0.043	-0.071	0.044	0.016	16.093	0.397	5.175	0.389	0.0146	-0.8053	0.5543	0.5819	0.6639	-0.2529	0.6415	0.7235	1.2001	0.9450
3	Standard	CIT Carrera	2.08	0.00	37.39	-1.86	28.94	0.01	17.567	0.059	-0.294	0.059	0.021	36.174	0.375	11.665	0.375	0.0146	-0.8053	0.2539	0.2665	0.3485	-0.5542	0.2799	0.3619	1.2001	0.9450
3	Standard	TV03	3.41	0.00	30.61	-8.38	22.22	0.01	12.290	0.046	-0.086	0.052	0.018	16.286	0.474	5.326	0.463	0.0146	-0.8053	0.5395	0.5663	0.6483	-0.2678	0.6237	0.7057	1.2001	0.9450
3	Standard	CIT Carrara	2.11	0.00	37.47	-1.78	29.02	0.01	17.709	0.058	-0.262	0.059	0.021	36.400	0.213	11.734	0.200	0.0148	-0.7947	0.2702	0.2875	0.3695	-0.5245	0.3156	0.3976	1.2001	0.9450
3	Standard	TV03	3.43	0.00	30.61	-8.38	22.22	0.01	12.321	0.033	-0.078	0.024	0.009	16.433	0.265	5.468	0.266	0.0148	-0.7947	0.5340	0.5680	0.6500	-0.2607	0.6321	0.7141	1.2001	0.9450
3	Standard	CIT Carrara	2.11	0.00	37.46	-1.79	29.01	0.01	17.702	0.055	-0.258	0.050	0.018	36.163	0.330	11.519	0.320	0.0148	-0.7947	0.2748	0.2923	0.3743	-0.5199	0.3210	0.4030	1.2001	0.9450
3	Standard	TV03	3.40	0.00	30.61	-8.38	22.22	0.00	12.275	0.035	-0.091	0.036	0.013	16.166	0.484	5.214	0.476	0.0148	-0.7947	0.5218	0.5550	0.6370	-0.2729	0.6175	0.6995	1.2001	0.9450
3	Standard	CIT Carrera	2.08	0.00	37.43	-1.82	28.98	0.01	17.654	0.040	-0.246	0.037	0.013	36.434	0.397	11.843	0.380	0.0148	-0.7947	0.2871	0.3053	0.3873	-0.5076	0.3358	0.4178	1.2001	0.9450
3	Standard	TV03	3.41	0.00	30.58	-8.42	22.18	0.00	12.274	0.026	-0.074	0.024	0.009	15.913	0.187	5.030	0.181	0.0148	-0.7947	0.5392	0.5735	0.6555	-0.2555	0.6383	0.7203	1.2001	0.9450
3	Standard	CIT Carrera	2.05	0.00	37.40	-1.85	28.95	0.01	17.542	0.035	-0.301	0.034	0.012	36.348	0.283	11.818	0.266	0.0148	-0.7947	0.2338	0.2487	0.3307	-0.5609	0.2719	0.3539	1.2001	0.9450
3	Heated Gas	eBOC	-10.72	0.00	57.21	17.21	48.60	0.01	24.456	0.034	-0.461	0.033	0.012	95.326	0.337	29.713	0.311	--	--	--	--	--	--	--	--	--	--
3	Heated Gas	BOC	-10.96	0.00	32.95	-6.13	24.54	0.01	-0.075	0.039	-0.802	0.036	0.013	23.020	0.211	7.426	0.194	--	--	--	--	--	--	--	--	--	--
3	Heated Gas	eBOC	-10.47	0.00	57.10	17.11	48.50	0.01	24.598	0.024	-0.464	0.026	0.009	94.960	0.329	29.569	0.312	--	--	--	--	--	--	--	--	--	--
3	Heated Gas	BOC	-10.67	0.00	33.03	-6.06	24.61	0.01	0.305	0.034	-0.777	0.038	0.013	23.195	0.248	7.459	0.245	--	--	--	--	--	--	--	--	--	--
3	Heated Gas	eBOC	-10.60	0.00	55.21	15.29	46.62	0.01	22.601	0.020	-0.460	0.022	0.008	89.266	0.319	27.892	0.292	--	--	--	--	--	--	--	--	--	--
3	Heated Gas	BOC	-10.56	0.00	32.66	-6.41	24.25	0.00	0.030	0.040	-0.797	0.038	0.014	21.961	0.335	6.963	0.328	--	--	--	--	--	--	--	--	--	--
3	Heated Gas	eBOC	-10.91	0.01	57.76	17.73	49.14	0.01	24.812	0.026	-0.454	0.029	0.010	96.716	0.224	29.952	0.211	--	--	--	--	--	--	--	--	--	--
3	Heated Gas	BOC	-11.21	0.00	32.75	-6.32	24.34	0.01	-0.531	0.042	-0.822	0.042	0.015	22.664	0.128	7.466	0.130	--	--	--	--	--	--	--	--	--	--
3	Heated Gas	eBOC	-10.85	0.01	56.61	16.63	48.01	0.01	23.741	0.031	-0.459	0.032	0.011	93.016	0.253	28.703	0.238	--	--	--	--	--	--	--	--	--	--
3	Heated Gas	BOC	-11.27	0.00	33.22	-5.87	24.81	0.01	-0.110	0.035	-0.799	0.037	0.013	23.688	0.259	7.615	0.260	--	--	--	--	--	--	--	--	--	--
3	Heated Gas	eBOC	-11.38	0.00	53.95	14.08	45.37	0.01	20.566	0.036	-0.477	0.032	0.011	85.595	0.171	26.965	0.163	--	--	--	--	--	--	--	--	--	--
3	Heated Gas	BOC	-10.85	0.00	53.13	13.28	44.55	0.00	20.269	0.025	-0.489	0.027	0.009	82.415	0.217	25.557	0.203	--	--	--	--	--	--	--	--	--	--
3	Equilibrated Gas	25C BOC	-11.05	0.00	28.48	-10.43	20.11	0.01	-3.887	0.047	-0.119	0.049	0.017	10.391	0.284	3.658	0.294	--	--	--	--	--	--	--	--	--	--
3	Equilibrated Gas	25C eBOC	-11.09	0.00	58.00	17.97	49.38	0.01	25.705	0.033	0.358	0.037	0.013	98.633	0.273	31.283	0.260	--	--	--	--	--	--	--	--	--	--
3	Equilibrated Gas	25C BOC	-11.03	0.01	28.18	-10.72	19.81	0.00	-4.183	0.027	-0.128	0.026	0.009	9.434	0.272	3.336	0.271	--	--	--	--	--	--	--	--	--	--
3	Equilibrated Gas	25C eBOC	-11.13	0.01	56.48	16.50	47.87	0.02	24.136	0.040	0.335	0.039	0.014	93.622	0.270	29.534	0.248	--	--	--	--	--	--	--	--	--	--
3	Equilibrated Gas	25C BOC	-11.00	0.00	27.89	-11.00	19.52	0.01	-4.398	0.056	-0.088	0.055	0.020	8.287	0.223	2.730	0.216	--	--	--	--	--	--	--	--	--	--

Table A1-4 (cont.): Full Standards, Heated Gasses, and Equilibrated Gasses Analyzed During Clumped Isotope Analyses

Measurement			$\delta^{13}C$	$\delta^{13}C$	$\delta^{18}O$ gas	$\delta^{18}O$ mineral	$\delta^{18}O$ mineral	$\delta^{18}O$	δ 47 raw	δ 47 raw	Δ 47 raw	D47	D47	d48	d48	D48	D48	CIT	CIT	HG	Stretch	Acid	EGL	ETF	Acid	ARF	ARF
Week	Type	Name	VPDB (‰)	1σ	VSMOW (‰)	PDB (‰)	VSMOW (‰)	1σ	(‰)	1σ	(v. Oz)	1σ	sterror	(v. Oz)	1σ	(v. Oz)	1σ	slope	intercept	Correct	Correct	Correct*	Correct	Correct	Correct*	slope	intercept
4	Standard	TV03	3.36	0.01	30.80	-8.20	22.41	0.01	12.426	0.031	-0.096	0.030	0.010	13.958	0.246	2.668	0.249	0.0140	-0.8467	0.577	0.576	0.658	-0.286	0.474	0.556	1.081	0.921
4	Standard	CIT Carrara	2.18	0.00	37.34	-1.91	28.89	0.01	17.547	0.045	-0.355	0.037	0.013	30.132	0.260	5.873	0.243	0.0140	-0.8467	0.246	0.246	0.328	-0.615	0.257	0.339	1.081	0.921
4	Standard	TV03	3.42	0.01	30.65	-8.35	22.25	0.01	12.327	0.039	-0.102	0.040	0.014	13.703	0.224	2.720	0.222	0.0140	-0.8467	0.572	0.571	0.653	-0.284	0.614	0.696	1.081	0.921
4	Standard	CIT Carrara	2.09	0.00	37.73	-1.53	29.28	0.01	17.890	0.039	-0.316	0.038	0.014	31.135	0.192	6.089	0.174	0.0140	-0.8467	0.280	0.280	0.362	-0.581	0.294	0.376	1.081	0.921
4	Standard	TV03	3.43	0.00	30.67	-8.32	22.28	0.01	12.365	0.035	-0.093	0.035	0.012	13.811	0.223	2.780	0.206	0.0140	-0.8467	0.581	0.580	0.662	-0.276	0.623	0.705	1.081	0.921
4	Standard	CIT Carrara	2.13	0.00	37.47	-1.78	29.02	0.01	17.675	0.044	-0.311	0.041	0.014	31.105	0.211	6.566	0.207	0.0140	-0.8467	0.288	0.288	0.370	-0.573	0.302	0.384	1.081	0.921
4	Standard	TV03	3.40	0.01	30.68	-8.32	22.28	0.01	12.340	0.030	-0.094	0.031	0.011	13.899	0.233	2.856	0.224	0.0140	-0.8467	0.580	0.579	0.661	-0.277	0.622	0.704	1.081	0.921
4	Standard	CIT Carrara	2.13	0.00	37.55	-1.70	29.10	0.01	17.774	0.027	-0.296	0.032	0.011	31.486	0.263	6.776	0.271	0.0141	-0.8399	0.293	0.295	0.377	-0.559	0.317	0.399	1.081	0.921
4	Standard	TV03	3.41	0.00	30.66	-8.33	22.27	0.01	12.350	0.043	-0.076	0.035	0.012	14.248	0.162	3.231	0.147	0.0141	-0.8399	0.590	0.594	0.676	-0.259	0.642	0.724	1.081	0.921
4	Standard	CIT Carrara	2.13	0.01	37.53	-1.72	29.08	0.01	17.745	0.047	-0.308	0.048	0.017	31.979	0.290	7.297	0.270	0.0142	-0.8395	0.280	0.281	0.363	-0.571	0.304	0.386	1.081	0.921
4	Standard	TV03	3.44	0.00	30.64	-8.35	22.25	0.01	12.350	0.043	-0.093	0.046	0.016	14.293	0.242	3.309	0.239	0.0142	-0.8395	0.571	0.575	0.657	-0.276	0.623	0.705	1.081	0.921
4	Standard	CIT Carrara	2.13	0.00	37.53	-1.73	29.08	0.01	17.772	0.032	-0.272	0.035	0.012	32.124	0.255	7.450	0.246	0.0142	-0.8395	0.315	0.317	0.399	-0.535	0.343	0.425	1.081	0.921
4	Standard	TV03	3.42	0.01	30.60	-8.39	22.21	0.01	12.294	0.044	-0.085	0.048	0.017	14.298	0.262	3.399	0.262	0.0142	-0.8395	0.580	0.584	0.666	-0.267	0.633	0.715	1.081	0.921
4	Standard	CIT Carrara	2.13	0.00	37.54	-1.71	29.09	0.01	17.742	0.049	-0.316	0.051	0.018	32.642	0.202	7.925	0.195	0.0142	-0.8395	0.272	0.273	0.355	-0.579	0.296	0.378	1.081	0.921
4	Heated Gas	BOC	-9.91	0.01	34.06	-5.07	25.64	0.01	2.026	0.030	-0.814	0.029	0.010	21.643	0.290	3.926	0.280	--	--	--	--	--	--	--	--	--	--
4	Heated Gas	eBOC	-11.26	0.00	57.86	17.83	49.24	0.01	24.511	0.024	-0.501	0.027	0.010	83.064	0.392	16.936	0.376	--	--	--	--	--	--	--	--	--	--
4	Heated Gas	BOC	-10.99	0.00	32.80	-6.27	24.39	0.00	-0.274	0.039	-0.823	0.038	0.014	19.509	0.099	4.262	0.096	--	--	--	--	--	--	--	--	--	--
4	Heated Gas	eBOC	-11.06	0.00	60.81	20.67	52.17	0.03	27.659	0.039	-0.472	0.023	0.008	92.816	0.320	20.389	0.265	--	--	--	--	--	--	--	--	--	--
4	Heated Gas	BOC	-10.85	0.00	33.23	-5.86	24.82	0.01	0.258	0.043	-0.847	0.040	0.014	20.617	0.159	4.522	0.168	--	--	--	--	--	--	--	--	--	--
4	Heated Gas	eBOC	-11.10	0.01	60.65	20.52	52.01	0.02	27.479	0.052	-0.453	0.044	0.015	93.338	0.426	21.184	0.376	--	--	--	--	--	--	--	--	--	--
4	Heated Gas	BOC	-11.19	0.01	33.19	-5.90	24.78	0.01	-0.140	0.053	-0.877	0.054	0.019	20.676	0.163	4.662	0.156	--	--	--	--	--	--	--	--	--	--
4	Heated Gas	eBOC	-11.09	0.00	59.88	19.78	51.25	0.02	26.678	0.053	-0.510	0.055	0.019	92.249	0.248	21.638	0.229	--	--	--	--	--	--	--	--	--	--
4	Heated Gas	BOC	-10.80	0.00	32.18	-6.87	23.77	0.01	-0.753	0.031	-0.875	0.031	0.011	18.244	0.198	4.229	0.194	--	--	--	--	--	--	--	--	--	--
4	Heated Gas	eBOC	-10.85	0.00	59.45	19.37	50.83	0.01	26.539	0.055	-0.464	0.057	0.020	91.069	0.170	21.364	0.159	--	--	--	--	--	--	--	--	--	--
4	Heated Gas	BOC	-11.13	0.01	34.16	-4.96	25.74	0.01	0.895	0.036	-0.864	0.033	0.012	23.573	0.329	5.615	0.325	--	--	--	--	--	--	--	--	--	--
4	Heated Gas	eBOC	-10.79	0.01	59.29	19.22	50.67	0.01	26.424	0.047	-0.480	0.041	0.014	91.588	0.355	22.159	0.334	--	--	--	--	--	--	--	--	--	--
4	Heated Gas	BOC	-10.56	0.00	32.57	-6.49	24.17	0.01	-0.039	0.023	-0.783	0.024	0.009	19.677	0.139	4.875	0.138	--	--	--	--	--	--	--	--	--	--
4	Heated Gas	eBOC	-11.28	0.00	51.43	11.65	42.87	0.01	18.100	0.035	-0.548	0.037	0.013	71.085	0.172	18.020	0.164	--	--	--	--	--	--	--	--	--	--
4	Heated Gas	BOC	-11.07	0.00	33.60	-5.51	25.18	0.01	0.430	0.027	-0.831	0.023	0.008	22.478	0.421	5.635	0.410	--	--	--	--	--	--	--	--	--	--
4	Heated Gas	eBOC	-11.23	0.00	54.84	14.93	46.25	0.01	21.612	0.033	-0.448	0.036	0.013	81.600	0.332	21.388	0.326	--	--	--	--	--	--	--	--	--	--
4	Equilibrated Gas	25C BOC	-11.15	0.01	29.33	-9.62	20.95	0.01	-3.101	0.036	-0.063	0.048	0.017	10.791	0.341	2.412	0.326	--	--	--	--	--	--	--	--	--	--
4	Equilibrated Gas	25C eBOC	-11.10	0.00	57.97	17.94	49.36	0.02	25.693	0.048	0.377	0.051	0.018	85.818	0.329	19.299	0.303	--	--	--	--	--	--	--	--	--	--
4	Equilibrated Gas	25C BOC	-11.04	0.01	28.94	-9.99	20.56	0.01	-3.370	0.031	-0.061	0.034	0.012	10.162	0.258	2.533	0.261	--	--	--	--	--	--	--	--	--	--
4	Equilibrated Gas	25C eBOC	-11.13	0.01	57.93	17.90	49.31	0.01	25.651	0.026	0.410	0.028	0.010	87.009	0.254	20.506	0.243	--	--	--	--	--	--	--	--	--	--
4	Equilibrated Gas	25C BOC	-10.92	0.00	27.03	-11.83	18.67	0.00	-5.153	0.055	-0.068	0.057	0.020	5.389	0.257	1.522	0.259	--	--	--	--	--	--	--	--	--	--
5	Standard	TV03	3.43	0.00	30.61	-8.39	22.21	0.01	12.317	0.042	-0.077	0.042	0.015	14.562	0.143	3.650	0.144	0.01420	-0.83400	0.582	0.590	0.672	-0.257	0.629	0.711	1.103	0.913
5	Standard	CIT Carrara	2.14	0.00	37.54	-1.72	29.09	0.01	17.767	0.039	-0.302	0.041	0.015	32.573	0.224	7.860	0.214	0.01420	-0.83400	0.280	0.283	0.365	-0.561	0.293	0.375	1.103	0.913
5	Standard	TV03	3.43	0.00	30.66	-8.34	22.27	0.01	12.384	0.034	-0.060	0.034	0.012	14.613	0.271	3.598	0.262	0.01420	-0.83400	0.598	0.606	0.688	-0.241	0.647	0.729	1.103	0.913
5	Standard	NBS-19	2.03	0.00	37.16	-2.08	28.71	0.01	17.280	0.045	-0.302	0.050	0.018	31.779	0.228	7.830	0.230	0.01420	-0.83400	0.287	0.291	0.373	-0.554	0.301	0.383	1.103	0.913
5	Standard	TV03	3.39	0.00	30.75	-8.25	22.35	0.00	12.422	0.041	-0.076	0.041	0.014	15.116	0.202	3.924	0.196	0.01420	-0.83400	0.582	0.589	0.671	-0.257	0.629	0.711	1.103	0.913
5	Standard	CIT Carrara	2.13	0.00	37.54	-1.72	29.09	0.01	17.793	0.021	-0.269	0.023	0.008	33.001	0.278	8.285	0.271	0.01500	-0.82760	0.292	0.298	0.380	-0.529	0.329	0.411	1.103	0.913
5	Standard	TV03	3.43	0.00	30.70	-8.29	22.31	0.01	12.405	0.022	-0.087	0.026	0.009	15.298	0.422	4.187	0.425	0.01500	-0.82760	0.555	0.566	0.648	-0.268	0.617	0.699	1.103	0.913
5	Standard	CIT Carrara	2.07	0.00	37.44	-1.81	28.99	0.01	17.606	0.029	-0.298	0.033	0.012	32.926	0.143	8.399	0.153	0.01500	-0.82760	0.266	0.271	0.353	-0.555	0.300	0.382	1.103	0.913
5	Heated Gas	eBOC	-11.09	0.00	59.88	19.78	51.25	0.02	26.678	0.053	-0.510	0.055	0.019	92.249	0.248	21.638	0.229	--	--	--	--	--	--	--	--	--	--
5	Heated Gas	BOC	-10.80	0.00	32.18	-6.87	23.77	0.01	-0.753	0.031	-0.875	0.031	0.011	18.244	0.198	4.229	0.194	--	--	--	--	--	--	--	--	--	--
5	Heated Gas	eBOC	-10.85	0.00	59.45	19.37	50.83	0.01	26.539	0.055	-0.464	0.057	0.020	91.069	0.170	21.364	0.159	--	--	--	--	--	--	--	--	--	--
5	Heated Gas	BOC	-11.13	0.01	34.16	-4.96	25.74	0.01	0.895	0.036	-0.864	0.033	0.012	23.573	0.329	5.615	0.325	--	--	--	--	--	--	--	--	--	--
5	Heated Gas	eBOC	-10.79	0.01	59.29	19.22	50.67	0.01	26.424	0.047	-0.480	0.041	0.014	91.588	0.355	22.159	0.334	--	--	--	--	--	--	--	--	--	--
5	Heated Gas	BOC	-10.56	0.00	32.57	-6.49	24.17	0.01	-0.039	0.023	-0.783	0.024	0.009	19.677	0.139	4.875	0.138	--	--	--	--	--	--	--	--	--	--
5	Heated Gas	eBOC	-11.28	0.00	51.43	11.65	42.87	0.01	18.100	0.035	-0.548	0.037	0.013	71.085	0.172	18.020	0.164	--	--	--	--	--	--	--	--	--	--
5	Heated Gas	BOC	-11.07	0.00	33.60	-5.51	25.18	0.01	0.430	0.027	-0.831	0.023	0.008	22.478	0.421	5.635	0.410	--	--	--	--	--	--	--	--	--	--
5	Heated Gas	eBOC	-11.23	0.00	54.84	14.93	46.25	0.01	21.612	0.033	-0.448	0.036	0.013	81.600	0.332	21.388	0.326	--	--	--	--	--	--	--	--	--	--
5	Equilibrated Gas	25C BOC	-11.15	0.01	29.33	-9.62	20.95	0.01	-3.101	0.036	-0.063	0.048	0.017	10.791	0.341	2.412	0.326	--	--	--	--	--	--	--	--	--	--
5	Equilibrated Gas	25C eBOC	-11.10	0.00	57.97	17.94	49.36	0.02	25.693	0.048	0.377	0.051	0.018	85.818	0.329	19.299	0.303	--	--	--	--	--	--	--	--	--	--
5	Equilibrated Gas	25C BOC	-11.04	0.01	28.94	-9.99	20.56	0.01	-3.370	0.031	-0.061	0.034	0.012	10.162	0.258	2.533	0.261	--	--	--	--	--	--	--	--	--	--
5	Equilibrated Gas	25C eBOC	-11.13	0.01	57.93	17.90	49.31	0.01	25.651	0.026	0.410	0.028	0.010	87.009	0.254	20.506	0.243	--	--	--	--	--	--	--	--	--	--
6	Roxbury siderite 1 hr 90C autoline		-9.56	0.02	23.47	-16.06	14.31	0.04	-4.107	0.104	3.217	0.060	0.021	22.212	0.572	25.396	0.528	0.01245	-0.83046	--	4.253	4.378	--	4.566	4.691	--	--
6	Roxbury siderite 15min 115C		-12.12	0.03	19.91	-18.94	11.34	0.05	-14.116	0.110	-0.848	0.037	0.013	-13.609	0.374	-3.623	0.303	0.01245	-0.83046	--	0.242	0.367	--	0.212	0.337	--	--
6	Roxbury siderite 75min 115C		-12.18	0.01	19.87	-18.98	11.29	0.02	-14.222	0.049	-0.846	0.021	0.008	-13.921	0.323	-3.845	0.290	0.01245	-0.83046	--	0.246	0.371	--	0.216	0.341	--	--
6	Roxbury siderite 90min 115C		-12.18	0.03	19.94	-18.91	11.36	0.04	-14.149	0.085	-0.847	0.027	0.009	-13.664	0.381	-3.726	0.325	0.01245	-0.83046	--	0.243	0.368	--	0.214	0.338	--	--
6	Carrara 115C 10min		2.15	0.04	36.91	-1.78	29.03	0.02	17.086	0.039	-0.369	0.026	0.009	31.321	0.272	7.863	0.261	0.01245	-0.83046	--	0.334	0.459	--	0.300	0.425	--	--
6	Elguin siderite 75min 115C		7.07	0.02	37.51	-2.01	28.79	0.03	22.785	0.079	-0.104	0.048	0.017	33.341	0.132	8.643	0.139	0.01245	-0.83046	--	0.532	0.656	--	0.512	0.637	--	--
6	TV04 75min 115C		1.43	0.02	29.82	-8.61	21.99	0.03	9.453	0.052	-0.222	0.020	0.007	12.468	0.282	3.104	0.236	0.01245	-0.83046	--	0.580	0.705	--	0.570	0.695	--	--
6	SID 4 Alvaro 75min 115C		-7.19	0.03	22.83	-16.13	14.23	0.05	-6.344	0.081	-0.706	0.026	0.009	-5.895	0.315	-1.568	0.273	0.01245	-0.83046	--	0.288	0.413	--	0.259	0.384	--	--
7	standard	Elguin (Alvaro)	8.19	0.00	37.42	-2.10	28.69	0.00	23.916	0.016	-0.034	0.018	0.007	40.848	0.362	15.996	0.352	0.01522	-0.84926	--	0.530	0.655	--	0.520	0.645	--	--
7	standard	SID4	-7.10	0.00	23.12	-15.85	14.52	0.02	-5.950	0.031	-0.749	0.020	0.007	-6.441	0.444	-2.831	0.463	0.01522	-0.84926	--	0.271	0.396	--	0.208	0.333	--	--
7	CIT Carrara 115C offline		2.15	0.00	36.93	-1.76	29.05	0.00	17.187	0.025	-0.346	0.022	0.007	39.473	0.316	15.628	0.307	0.01522	-0.84926	--	0.321	0.446	--	0.289	0.414	--	--
7	standard	CIT Carrara	2.11	0.00	37.46	-1.79	29.01	0.00	17.711	0.020	-0.312	0.019	0.007	40.973	0.426	16.055	0.413	0.01522	-0.84926	--	0.347	0.472	--	0.317	0.442	--	--
7	standard	CIT Carrara	2.11	0.00	37.44	-1.81	28.99	0.01	17.673	0.033	-0.333	0.032	0.011	40.839	0.417	15.971	0.411	0.01522	-0.84926	--	0.327	0.452	--	0.296	0.421	--	--
7	standard	CIT Carrara	2.11	0.00	37.41	-1.84	28.96	0.01	17.642	0.032	-0.337	0.028	0.010	40.869	0.218	16.054	0.212	0.01522	-0.84926	--	0.323	0.448	--	0.292	0.417	--	--
7	standard	CIT Carrara	2.11	0.00	37.37	-1.88	28.93	0.01	17.605	0.023	-0.334	0.030	0.010	40.061	0.382	15.337	0.373	0.01522	-0.84926	--	0.328	0.452	--	0.297	0.421	--	--
7	TV04 115C offline		1.51	0.00	29.72	-8.70	21.89	0.01	9.472	0.040	-0.237	0.040	0.013	15.564	0.436	6.206	0.421	0.01522	-0.84926	--	0.547	0.672	--	0.521	0.645	--	--
7	standard	TV04	1.48	0.01	30.22	-8.76	21.83	0.00	10.023	0.035	-0.157	0.035	0.012	16.901	0.309	6.560	0.303	0.01522	-0.84926	--	0.618	0.743	--	0.598	0.722	--	--
7	standard	TV04	1.47	0.00	30.19	-8.79	21.80	0.00	9.946	0.021	-0.192	0.017	0.006	17.249	0.394	6.959	0.386	0.01522	-0.84926	--	0.585	0.710	--	0.562	0.687	--	--
7	standard	TV04	1.48	0.00	30.24	-8.74	21.85	0.01	10.011	0.023	-0.198	0.026	0.009	17.200	0.328	6.801	0.323	0.01522	-0.84926	--	0.578	0.702	--	0.554	0.679	--	--
7	standard	TV04	1.43	0.00	30.19	-8.79	21.80	0.00	9.911	0.025	-0.196	0.027	0.010	17.300	0.402	7.005	0.394	0.01522	-0.84926	--	0.581	0.706	--	0.558	0.683	--	--
8	standard	CIT Carrara	2.10	0.00	37.36	-1.89	28.91	0.00	17.482	0.035	-0.430	0.035	0.013	32.898	0.233	8.375	0.224	0.01048	-0.85234	--	0.318	0.442	--	0.281	0.406	--	--
8	standard	CIT Carrara	2.13	0.00	37.43	-1.82	28.99	0.00	17.605	0.023	-0.410	0.024	0.008	33.330	0.144	8.651	0.141	0.01048	-0.85234	--	0.337	0.461	--	0.302	0.426	--	--
8	standard	CIT Carrara	2.11	0.00	37.39	-1.86	28.94	0.00	17.553	0.029	-0.402	0.029	0.010	33.508	0.183	8.911	0.178	0.01048	-0.85234	--	0.345	0.470	--	0.311	0.435	--	--
8	standard	TV04	1.42	0.00	30.20	-8.78	21.81	0.01	9.845	0.026	-0.255	0.024	0.009	13.743	0.181	3.467	0.182	0.01048	-0.85234	--	0.571	0.696	--	0.551	0.676	--	--
8	standard	TV04	1.45	0.00	30.11	-8.86	21.72	0.00	9.782	0.022	-0.257	0.022	0.008	13.515	0.194	3.413	0.196	0.01048	-0.85234	--	0.570	0.694	--	0.550	0.674	--	--
8	standard	TV04	1.47	0.00	30.17	-8.80	21.79	0.00	9.899	0.017	-0.226	0.016	0.006	14.022	0.168	3.791	0.165	0.01048	-0.85234	--	0.599	0.724	--	0.581	0.706	--	--
9	Elguin siderite 14.0mg		8.23	0.00	36.99	-2.51	28.27	0.01	23.477	0.020	-0.087	0.015	0.005	35.483	0.252	11.585	0.252	0.01314	-0.87746	--	0.545	0.670	--	0.529	0.653	--	--
9	standard	TV04	1.46	0.00	30.33	-8.65	21.94	0.01	10.064	0.032	-0.210	0.031	0.011	15.750	0.220	5.198	0.214	0.01314	-0.87746	--	0.596	0.721	--	0.574	0.699	--	--
9	standard	TV04	1.47	0.01	30.18	-8.80	21.79	0.00	9.900	0.027	-0.235	0.024	0.009	15.099	0.288	4.843	0.285	0.01314	-0.87746	--	0.574	0.699	--	0.551	0.675	--	--
9	standard	TV04	1.49	0.01	30.22	-8.76	21.83	0.00	9.993	0.021	-0.196	0.018	0.006	15.485	0.279	5.156	0.271	0.01314	-0.87746	--	0.611	0.736	--	0.590	0.715	--	--
9	standard	CIT Carrara	2.11	0.00	37.55	-1.71	29.10	0.00	17.732	0.045	-0.376	0.047	0.017	36.557	0.125	11.575	0.124	0.01314	-0.87746	--	0.339	0.464	--	0.306	0.430	--	--
9	CIT Carrara 115C offline		2.15	0.00	36.93	-1.76	29.04	0.01	17.124	0.033	-0.406	0.024	0.008	34.780	0.162	11.056	0.140	0.01314	-0.87746	--	0.318	0.443	--	0.283	0.407	--	--
9	standard	CIT Carrara	2.13	0.00	37.48	-1.78	29.03	0.00	17.682	0.021	-0.374	0.021	0.007	36.479	0.278	11.639	0.274	0.01314	-0.87746	--	0.342	0.467	--	0.308	0.433	--	--
9	standard	CIT Carrara	2.13	0.01	37.42	-1.83	28.98	0.00	17.628	0.029	-0.376	0.030	0.011	36.202	0.296	11.473	0.289	0.01314	-0.87746	--	0.341	0.466	--	0.307	0.432	--	--

* Add correction factors were calculated according to Defliés et al. (2015). Specifically, samples digested at 90°C (i.e. calcite and dolomite) and 115°C (i.e. siderite) were corrected by a values of 0.0820 and 0.1247, respectively.

Table A1-5: Rock-Eval Pyrolysis Data and Maximum Paleotemperature of Burial (MPTB) as calculated by Disnar (1994) Method.

Sample ID	Formation	Locality	Description	S1 (mg/g)	S2 (mg/g)	Tmax (°C)	S3 (mg/g)	TOC (%)	HI	OI	O/C Ratio	Delta_Ea (kcal/mol)	Delta_Ea (kJ/mol)	MPTB 0.21 °C/Ma	MPTB 0.64 °C/Ma
DI-1/247.5	Gamohaan	Danielskuil	Carbonaceous carbonate with microbial laminae	0.04	0.21	428	1.00	0.34	62	294	0.16	79	330	237	230
DI-1/250.9	Gamohaan	Danielskuil	Microbial laminated carbonaceous carbonate + thin s	0.05	0.23	410	0.81	0.50	46	162	0.09	77	321	223	217
DI-1/259.8	Gamohaan	Danielskuil	Stilpnomelane Not valid	0.04	0.22	386	0.43	0.05	440	860	0.47	74	310	206	199
GAM-1	Gamohaan	Gamohaan Reserve	Black shale	0.05	0.08	339	0.23	7.37	1	3	0.00	68	287	171	165
GAM-2	Gamohaan	Gamohaan Reserve	Black shale	0.01	0.01	422	0.95	0.03	33	3167	1.73	78	327	232	225
GAM-3	Gamohaan	Gamohaan Reserve	Contorted mats in carb	0.01	0.05	381	0.42	0.22	23	191	0.10	73	307	202	196
GAM-4	Gamohaan	Gamohaan Reserve	Carbonaceous carbonate pod	0.01	0.04	496	0.72	0.67	6	107	0.06	87	363	286	279
HF-1	Gamohaan	Hopefield Estate	Contorted mats in limest	0.02	0.03	273	0.64	0.05	60	1280	0.70	61	255	123	118
HF-2	Gamohaan	Hopefield Estate	Carbonaceous limestone	0.01	0.00	465	0.48	0.10	0	480	0.26	83	348	264	257
HF-3	Gamohaan	Hopefield Estate	Contorted mats in limest	0.01	0.02	452	0.59	0.19	11	311	0.17	82	342	254	247
ALPHEN 1A-1	Gamohaan	Kuruman	Limestone from Alphen Farm near Kuruman	0.04	0.08	489	0.53	0.21	38	252	0.14	86	360	281	274
ALPHEN 1A-2	Gamohaan	Kuruman	Limestone from Alphen Farm near Kuruman	0.01	0.06	461	0.75	0.09	67	833	0.45	83	346	261	254
RE 1	Gamohaan	Kuruman	Black chert from Retreat Farm near Kuruman	0.02	0.06	455	0.29	0.04	150	725	0.40	82	343	256	249
RE 2	Gamohaan	Kuruman	Black chert from Retreat Farm near Kuruman	0.02	0.07	488	0.76	0.12	58	633	0.35	86	359	281	273
RE3	Gamohaan	Kuruman	Dolomite from Retreat Farm near Kuruman (partly w	0.02	0.06	548	0.80	0.09	67	889	0.48	93	389	325	317
WB98/850	Gamohaan	Kuruman Kop	Black shale	0.07	0.27	424	0.64	4.21	6	15	0.01	78	328	234	227
WB98/898	Gamohaan	Kuruman Kop	Black shale	0.07	0.27	425	2.56	2.91	9	88	0.05	78	328	234	228
WB98/906	Gamohaan	Kuruman Kop	Carbonaceous shale + carbonate (limestone mostly)	0.05	0.26	408	0.69	0.58	45	119	0.06	76	320	222	215
WB98/920	Gamohaan	Kuruman Kop	Carbonaceous shale + carbonate (limestone mostly)	0.09	0.38	408	0.75	1.21	31	62	0.03	76	320	222	215
WB98/953	Gamohaan	Kuruman Kop	Carbonaceous shale + carbonate (limestone mostly)	0.05	0.35	393	0.64	0.77	45	83	0.05	75	313	211	204
WB98/958	Gamohaan	Kuruman Kop	Carbonaceous shale + carbonate (limestone mostly)	0.06	0.34	402	0.73	1.01	34	72	0.04	76	317	217	211
WB98/975	Gamohaan	Kuruman Kop	Limestone with contorted microbial laminae	0.10	0.22	399	1.05	0.96	23	109	0.06	75	316	215	209
WB98/999	Gamohaan	Kuruman Kop	Limestone with contorted microbial laminae	0.06	0.31	413	0.77	0.73	42	105	0.06	77	323	226	219
AD5/180	Gamohaan	Pomfret	Carbonaceous carbonate with contorted microbial lar	0.04	0.23	399	0.65	0.79	29	82	0.04	75	316	215	209
AD5/201.6	Gamohaan	Pomfret	Carbonaceous carbonate with contorted microbial lar	0.04	0.27	410	1.46	0.55	49	265	0.14	77	321	223	217
AD5/216.5	Gamohaan	Pomfret	Carbonaceous carbonate with contorted microbial lar	0.05	0.29	400	1.25	0.52	56	240	0.13	76	316	216	209
AD5/219.2	Gamohaan	Pomfret	Black shale and fine carbonate	0.08	0.31	401	0.69	3.67	8	19	0.01	76	317	217	210

Table A1-5 (cont.): Rock-Eval Pyrolysis Data and Maximum Paleotemperature of Burial (MPTB) as calculated by Disnar (1994) Method.

Sample ID	Formation	Locality	Description	S1 (mg/g)	S2 (mg/g)	Tmax (°C)	S3 (mg/g)	TOC (%)	HI	OI	O/C Ratio	Delta_Ea (kcal/mol)	Delta_Ea (kJ/mol)	MPTB 0.21 °C/Ma	MPTB 0.64 °C/Ma
LIME 1	Lime Acres	Danielskuil	Black chert in limestone from Lime Acres	0.01	0.06	455	0.43	0.10	60	430	0.23	82	343	256	249
LIME 2	Lime Acres	Danielskuil	Limestone from Lime Acres	0.02	0.07	319	0.36	0.07	100	514	0.28	66	277	157	151
LIME DK1	Lime Acres	Danielskuil	Limestone from Danielskuil	0.02	0.08	435	0.62	0.11	73	564	0.31	80	333	242	235
LIME DK2	Lime Acres	Danielskuil	Carbonaceous limestone from Danielskuil	0.04	0.11	345	0.32	0.99	11	32	0.02	69	290	176	170
LIME DK2 OM	Lime Acres	Danielskuil	Organic matter from Lime DK2	0.03	0.10	374	0.42	0.86	12	49	0.03	73	304	197	191
LIME DK3	Lime Acres	Danielskuil	Limestone from Danielskuil	0.01	0.07	602	0.24	0.01	700	2400	1.31	99	415	364	356
LIME DK4	Lime Acres	Danielskuil	Limestone with carbonaceous black inclusions	0.03	0.10	415	0.52	1.11	9	47	0.03	77	324	227	220
LIME DK4 OM	Lime Acres	Danielskuil	Organic matter from Lime DK4	0.02	0.12	465	0.68	1.80	7	38	0.02	83	348	264	257
LIME DK5	Lime Acres	Danielskuil	Limestone with black carbonaceous black inclusions	0.04	0.09	495	0.55	0.50	18	110	0.06	87	363	286	278
LIME DK5 OM	Lime Acres	Danielskuil	Organic matter from Lime DK5	0.03	0.08	360	0.69	0.49	16	141	0.08	71	297	187	181
DM-1	Monteville	DouglasArea	Sparitic Carbonate conophyton	0.01	0.06	441	0.43	0.04	150	1075	0.59	80	336	246	239
DM-2	Monteville	DouglasArea	Carbonaceous limestone	0.02	0.04	496	0.72	0.10	40	720	0.39	87	363	286	279
B0603	Monteville	Reivilo	Monteville near Reivilo: Strauss and Beukes	0.01	0.03	443	0.18	2.58	1	7	0.00	81	337	248	241
B0606	Monteville	Reivilo	Monteville near Reivilo	0.02	0.04	390	0.15	2.11	2	7	0.00	74	311	209	202
B0615	Monteville	Reivilo	Monteville near Reivilo	0.02	0.04	421	0.11	3.29	1	3	0.00	78	327	231	225
GKF-1/1408.79	Nauga	Griquatown	Carbonaceous carbonate	0.01	0.01	414	0.94	0.14	7	671	0.37	77	323	226	220
GKF-1/838.65	Nauga	Griquatown	BlackShale	0.06	0.11	404	0.16	0.31	35	52	0.03	76	318	219	212
GKF-1/919.35	Nauga	Griquatown	Carbonaceous carbonate	0.01	0.03	379	2.62	0.17	18	1541	0.84	73	306	201	194
GKF1/1151.85	Nauga	Griquatown	BlackShale	0.06	0.12	384	0.22	2.75	4	8	0.00	74	309	204	198
GKF1/1348.81	Nauga	Griquatown	BlackShale	0.10	0.13	417	0.18	0.25	52	72	0.04	78	325	228	222
GKF1/1430.82	Nauga	Griquatown	Carbonaceous carbonate	0.04	0.10	387	0.94	0.45	22	209	0.11	74	310	206	200
GKF1/268.30	Nauga	Griquatown	BlackShale	0.13	0.16	348	0.23	4.57	4	5	0.00	70	291	178	172
GKF1/288.10	Nauga	Griquatown	BlackShale	0.10	0.13	367	0.27	3.49	4	8	0.00	72	300	192	186
GKF1/395.40	Nauga	Griquatown	Carbonaceous carbonate	0.02	0.11	417	1.75	0.35	31	500	0.27	78	325	228	222
GKP-1/427.40	Nauga	Griquatown	Carbonaceous carbonate	0.02	0.09	503	2.39	0.36	25	664	0.36	88	367	292	284
GKP1/1055.70	Nauga	Griquatown	Carbonaceous carbonate	0.04	0.12	405	2.01	0.46	26	437	0.24	76	319	220	213
GKP1/341.45	Nauga	Griquatown	Carbonaceous carbonate	0.02	0.08	389	1.53	1.04	8	147	0.08	74	311	208	201
GKP1/645.23	Nauga	Griquatown	Carbonaceous carbonate	0.02	0.09	414	2.26	0.37	24	611	0.33	77	323	226	220
SPR-1/53.04	Nauga	Griquatown	Carbonaceous carbonate	0.01	0.02	441	0.89	0.04	50	2225	1.21	80	336	246	239
SPR-1/56	Nauga	Griquatown	BlackShale	0.03	0.04	406	1.34	0.11	36	1218	0.66	76	319	220	214
SPR-1/64.9	Nauga	Griquatown	BlackShale+Carbonate	0.02	0.07	402	1.78	0.60	12	297	0.16	76	317	217	211
SPR-1/74.63	Nauga	Griquatown	Black shale	0.05	0.16	355	2.60	0.15	107	1733	0.95	70	294	183	177
SPR-1/79.5	Nauga	Griquatown	Carbonaceous carbonate	0.03	0.07	408	1.45	0.19	37	763	0.42	76	320	222	215
SPR-2/17.90	Nauga	Griquatown	Black shale	0.06	0.09	470	2.20	2.00	4	110	0.06	84	350	267	260
SPR-2/19.72	Nauga	Griquatown	BlackShale+Carbonate	0.06	0.10	487	4.20	1.14	9	368	0.20	86	359	280	272
SPR-2/35.98	Nauga	Griquatown	Sparitic Carbonate conophyton	0.02	0.07	432	1.79	0.09	78	1989	1.08	79	332	239	233

Table A1-6: Raman peak details, H:C Ratio Determination, Maximum Burial Temperature Estimates, and Vitrine Reflectance Estimates

	This Study									Ferralis et al. (2016)			
	Measurments	Position	Position	FWHM		Peak Ratio		Area	Area	H:C Rato		Average	
Sample ID	Averaged (n)	G Peak (cm^{-1})	D Peak (cm^{-1})	D Peak	stdev	ID/IG	stdev	D5/G	(D4+D5)G	HC1	HC2	H:C	stdev
14AS-SA03B	5	1607	1329	80	7	1.4	0.1	0.21	0.40	0.167	0.134	0.15	0.05
14AS-SA03C	4	1606	1327	77	2	1.4	0.1	0.21	0.37	0.150	0.131	0.14	0.02
14AS-SA03D1	5	1606	1328	83	5	1.3	0.1	0.21	0.41	0.171	0.134	0.15	0.04
14AS-SA03D2	5	1605	1328	81	4	1.2	0.1	0.22	0.40	0.168	0.142	0.16	0.03
14AS-SA03D3	6	1605	1327	77	4	1.3	0.1	0.23	0.38	0.158	0.146	0.15	0.03
14AS-SA04A1	5	1605	1326	79	5	1.1	0.1	0.26	0.42	0.179	0.176	0.18	0.04
14AS-SA04A2	4	1603	1329	82	7	1.3	0.1	0.37	0.37	0.148	0.270	0.21	0.03
14AS-SA04A3	5	1605	1328	89	8	1.2	0.2	0.27	0.39	0.161	0.186	0.17	0.02
14AS-SA04B1	5	1605	1326	72	7	1.5	0.1	0.29	0.36	0.147	0.112	0.13	0.03
14AS-SA04B2	6	1604	1326	82	16	1.2	0.3	0.18	0.40	0.167	0.103	0.14	0.04
14AS-SA04B3	5	1603	1328	88	8	1.2	0.2	0.20	0.37	0.149	0.120	0.13	0.03
14AS-SA04C1	5	1605	1327	81	7	1.2	0.1	0.17	0.40	0.168	0.100	0.13	0.04
14AS-SA04C2	6	1605	1328	79	11	1.3	0.2	0.27	0.40	0.167	0.187	0.18	0.05
14AS-SA05B1	4	1605	1328	84	13	1.3	0.1	0.17	0.41	0.175	0.097	0.14	0.04
14AS-SA05B2	6	1606	1327	82	7	1.4	0.1	0.28	0.36	0.142	0.196	0.17	0.02
14AS-SA05B3	6	1604	1326	85	8	1.2	0.2	0.19	0.37	0.149	0.113	0.13	0.06
14AS-SA05B4	6	1606	1327	88	7	1.3	0.1	0.25	0.37	0.147	0.171	0.16	0.04
14AS-SA05B5	6	1605	1328	92	8	1.2	0.1	0.12	0.38	0.155	0.058	0.11	0.03
14AS-SA05B6	6	1606	1328	90	7	1.2	0.1	0.21	0.38	0.157	0.136	0.15	0.03
14AS-SA06A	3	1604	1327	84	15	1.1	0.1	0.24	0.42	0.144	0.180	0.16	0.00
14AS-SA06B	5	1607	1332	95	11	1.1	0.2	0.26	0.36	0.144	0.180	0.16	0.00
14AS-SA11A	6	1606	1329	97	4	1.1	0.1	0.24	0.51	0.233	0.154	0.19	0.03
14AS-SA11B	6	1606	1328	89	11	1.1	0.2	0.28	0.40	0.165	0.191	0.18	0.02
14AS-SA12A	6	1606	1327	77	2	1.3	0.0	0.22	0.35	0.136	0.140	0.14	0.02
14AS-SA13B1	6	1605	1327	87	11	1.2	0.2	0.20	0.33	0.128	0.123	0.13	0.01
14AS-SA13B2	3	1606	1325	73	13	1.2	0.2	0.24	0.39	0.159	0.162	0.16	0.02
14AS-SA13B3	6	1606	1324	81	5	1.1	0.1	0.25	0.35	0.139	0.168	0.15	0.02
14AS-SA13B4	5	1605	1328	88	11	1.1	0.1	0.20	0.40	0.165	0.120	0.14	0.03
14AS-SA14AB1	6	1606	1326	86	8	1.2	0.1	0.22	0.35	0.139	0.140	0.14	0.01
14AS-SA14AB2	6	1606	1325	79	3	1.2	0.1	0.19	0.38	0.156	0.118	0.14	0.03
14AS-SA14AB3	5	1605	1324	83	10	1.2	0.1	0.24	0.35	0.139	0.156	0.15	0.04
14AS-SA14AB4	6	1606	1325	80	5	1.3	0.1	0.24	0.37	0.152	0.158	0.15	0.02
14AS-SA14B1	6	1606	1326	72	5	1.3	0.2	0.26	0.37	0.151	0.171	0.16	0.03
14AS-SA15BA1	6	1605	1327	81	10	1.3	0.1	0.19	0.37	0.147	0.112	0.13	0.03
14AS-SA15BA2	5	1606	1324	81	5	1.3	0.4	0.29	0.40	0.169	0.202	0.19	0.05
14AS-SA15BA3	5	1606	1326	86	8	1.2	0.2	0.15	0.38	0.153	0.082	0.12	0.04
14AS-SA15BB	5	1605	1325	78	4	1.3	0.1	0.24	0.32	0.144	0.096	0.12	0.03
WB98_850ft	6	1604	1322	94	2	1.1	0.2	0.36	0.44	0.267	0.193	0.23	0.07
WB98_898ft	5	1606	1325	85	2	1.1	0.2	0.22	0.39	0.140	0.165	0.15	0.03
WB98_906ft	6	1605	1325	82	2	1.2	0.2	0.30	0.40	0.213	0.171	0.19	0.07
WB98_920ft	10	1606	1325	81	2	1.2	0.2	0.23	0.41	0.147	0.175	0.16	0.07
WB98_953ft	8	1605	1324	83	2	1.1	0.1	0.20	0.41	0.123	0.177	0.15	0.07
WB98_958ft	8	1605	1325	80	1	1.2	0.1	0.24	0.38	0.160	0.162	0.16	0.09
WB98_975ft	9	1605	1325	82	2	1.2	0.2	0.19	0.33	0.114	0.130	0.12	0.07
WB98_999_2ft	11	1606	1325	83	2	1.2	0.1	0.17	0.35	0.095	0.140	0.12	0.08
AD5_180m	7	1605	1329	79	2	1.4	0.2	0.19	0.35	0.115	0.141	0.13	0.04
AD5_201_6m	6	1605	1331	72	2	1.6	0.0	0.18	0.39	0.107	0.163	0.14	0.08
AD5_216_5m	8	1604	1330	73	4	1.5	0.2	0.22	0.33	0.139	0.128	0.13	0.09
AD5_219_2m	6	1604	1328	79	2	1.4	0.2	0.22	0.35	0.115	0.141	0.13	0.04
DI1_247_5m	10	1605	1324	89	3	1.0	0.1	0.22	0.44	0.143	0.196	0.17	0.10
DI1_250_9m	10	1606	1325	89	2	1.0	0.1	0.22	0.42	0.141	0.181	0.16	0.08
Alphen_1A	5	1605	1329	80	6	1.3	0.1	0.15	0.31	0.082	0.115	0.10	0.10
RE-3	4	1606	1327	83	4	1.2	0.2	0.26	0.34	0.173	0.134	0.15	0.08
Average	6	1605	1327	83 ±6		1.2 ±0.1		0.23	0.38	0.15	0.15	0.15 ±0.02	

Table A1-6 (cont.): Raman peak details, H:C Ratio Determination, Maximum Burial Temperature Estimates, and Vitrine Reflectance Estimates

	Aoya et al. (2010)		Beyssac et al. (2002)		Kouketsu et al. (2014)				Lahfid et al. (2010)				Rahl et al. (2005)	
	R2 T (°C)		T (°C)		D1 T (°C)		D2 T (°C)		RA1 T (°C)		RA2 T (°C)		T (°C)	
Sample ID	avg.	stdev	avg.	stdev	avg.	stdev	avg.	stdev	avg.	stdev	avg.	stdev	avg.	stdev
14AS-SA03B	323	7	368	134	453	61	486	112	351	31	368	49	241	35
14AS-SA03C	323	19	313	26	436	85	446	168	371	62	407	92	237	122
14AS-SA03D1	327	15	318	21	443	78	468	142	382	25	418	45	241	77
14AS-SA03D2	330	5	324	7	443	78	470	138	383	22	418	37	248	26
14AS-SA03D3	334	3	323	14	449	70	481	124	371	21	398	36	253	54
14AS-SA04A1	341	12	338	16	445	74	475	130	336	49	348	63	266	60
14AS-SA04A2	337	6	332	8	449	59	427	213	324	48	331	61	278	59
14AS-SA04A3	329	13	322	18	436	93	474	129	374	36	405	60	238	85
14AS-SA04B1	316	4	303	6	452	58	471	129	389	6	429	11	225	46
14AS-SA04B2	353	21	352	24	442	88	490	110	306	33	306	41	304	157
14AS-SA04B3	344	7	341	10	444	75	463	155	322	29	326	40	291	58
14AS-SA04C1	333	13	328	18	444	76	469	140	345	37	359	52	259	90
14AS-SA04C2	332	15	329	21	452	64	476	140	353	58	377	90	268	80
14AS-SA05B1	327	16	319	23	429	98	455	151	369	48	400	73	245	77
14AS-SA05B2	322	10	310	13	445	81	486	110	366	18	390	29	234	59
14AS-SA05B3	336	7	331	9	449	70	491	100	310	44	313	57	260	18
14AS-SA05B4	323	11	316	16	444	82	481	126	340	19	349	28	237	65
14AS-SA05B5	324	7	321	18	443	84	481	124	332	53	345	71	244	89
14AS-SA05B6	326	6	318	7	444	83	473	143	363	15	384	23	236	34
14AS-SA06A	347	10	346	12	427	88	440	160	311	1	309	2	285	37
14AS-SA06B	355	24	355	29	434	96	448	190	273	81	276	85	301	133
14AS-SA11A	338	14	333	17	442	88	480	127	314	20	315	25	250	61
14AS-SA11B	336	4	330	5	453	60	474	140	347	31	361	46	248	65
14AS-SA12A	326	6	319	9	451	67	483	118	365	24	388	38	242	24
14AS-SA13B1	329	16	322	20	446	77	483	120	348	49	367	68	242	66
14AS-SA13B2	340	30	335	40	435	74	420	190	316	70	326	94	267	164
14AS-SA13B3	329	9	319	13	451	67	486	109	350	41	369	62	223	60
14AS-SA13B4	336	15	331	20	445	74	475	127	347	60	368	83	251	81
14AS-SA14AB1	328	11	320	14	448	73	487	110	344	51	361	71	237	45
14AS-SA14AB2	330	10	323	12	449	70	488	106	367	28	392	42	239	34
14AS-SA14AB3	329	8	322	11	443	77	467	140	371	32	399	50	237	55
14AS-SA14AB4	321	7	311	9	448	73	489	102	375	25	405	40	225	52
14AS-SA14B1	322	6	311	8	450	68	485	111	395	21	440	37	231	17
14AS-SA15BA1	327	5	317	8	452	63	484	116	362	13	383	21	237	20
14AS-SA15BA2	329	13	321	18	444	77	476	127	349	71	374	95	241	63
14AS-SA15BA3	322	9	312	13	438	90	472	131	376	28	407	49	214	57
14AS-SA15BB	322	13	312	18	445	74	475	126	377	20	409	34	228	59
WB98_850ft	326	11	318	15	276	11	252	14	359	35	381	50	217	54
WB98_898ft	321	9	311	13	295	7	271	14	378	33	412	53	205	56
WB98_906ft	322	7	311	11	303	9	269	3	395	19	440	34	212	19
WB98_920ft	329	12	322	16	304	8	254	25	344	57	363	77	236	79
WB98_953ft	324	4	315	6	300	7	269	7	390	26	432	43	214	24
WB98_958ft	325	5	316	8	306	5	261	12	367	45	396	71	225	32
WB98_975ft	326	8	317	11	302	7	255	12	361	37	384	54	222	33
WB98_999_2ft	321	4	310	6	299	6	261	14	385	28	424	50	213	17
AD5_180m	327	11	318	15	309	7	217	27	354	45	375	68	254	72
AD5_201_6m	324	2	314	3	324	9	216	15	334	81	357	106	258	13
AD5_216_5m	326	10	318	15	321	16	214	17	302	114	324	123	262	72
AD5_219_2m	327	11	318	15	309	7	217	27	354	45	375	68	254	72
DI1_247_5m	329	7	322	9	286	12	275	6	362	22	384	35	209	33
DI1_250_9m	326	5	318	8	286	8	275	7	375	16	405	26	204	28
Alphen_1A	331	8	324	11	306	24	223	38	287	24	282	28	257	55
RE-3	334	11	328	15	299	15	231	26	258	123	272	130	250	67
Average	329 ± 8		323 ± 12		401 ± 67		404 ± 106		351 ± 31		372 ± 41		243 ± 23	

Table A1-6 (cont.): Raman peak details, H:C Ratio Determination, Maximum Burial Temperature Estimates, and Vitrine Reflectance Estimates

	Bonoldi et al. (2016)	Du et al. (2014)		Schito et al. (2017)				Schito et al. (2016)
	Ro%	Ro%		Ro%				
Sample ID	G-D peak distance	H:C Ratio	G-shift	RA2	Dw/Gw Area	Avg	stdev	F
14AS-SA03B	3.63	2.416	3.66	5.71	1.59	3.65	2.39	0.78
14AS-SA03C	3.67	2.446	3.56	7.07	1.70	4.38	3.36	0.83
14AS-SA03D1	3.65	2.408	3.54	7.24	1.84	4.54	3.02	0.84
14AS-SA03D2	3.62	2.414	3.36	7.22	1.62	4.42	3.05	0.83
14AS-SA03D3	3.66	2.433	3.40	6.56	1.43	3.99	2.91	0.81
14AS-SA04A1	3.68	2.394	3.26	5.21	1.74	3.48	2.13	0.77
14AS-SA04A2	3.47	2.450	2.86	4.75	1.23	2.99	2.20	0.73
14AS-SA04A3	3.60	2.427	3.33	6.87	2.15	4.51	2.84	0.84
14AS-SA04B1	3.67	2.452	3.34	7.52	1.50	4.51	3.20	0.84
14AS-SA04B2	3.65	2.416	3.12	4.07	1.77	2.92	1.48	0.72
14AS-SA04B3	3.51	2.448	2.81	4.57	1.22	2.90	1.96	0.72
14AS-SA04C1	3.66	2.414	3.33	5.48	1.78	3.63	2.21	0.78
14AS-SA04C2	3.59	2.416	3.21	6.17	1.44	3.81	2.89	0.79
14AS-SA05B1	3.59	2.401	3.32	6.74	1.61	4.18	3.07	0.82
14AS-SA05B2	3.68	2.460	3.46	6.31	1.84	4.07	2.48	0.81
14AS-SA05B3	3.66	2.449	3.20	4.29	1.68	2.98	1.89	0.73
14AS-SA05B4	3.65	2.452	3.43	5.15	2.11	3.63	1.70	0.78
14AS-SA05B5	3.61	2.438	3.41	5.16	1.95	3.56	2.06	0.78
14AS-SA05B6	3.61	2.435	3.42	6.13	2.05	4.09	2.21	0.81
14AS-SA06A	3.63	2.458	3.16	4.10	1.62	2.86	1.37	0.72
14AS-SA06B	3.54	2.458	3.84	3.57	1.72	2.64	1.59	0.69
14AS-SA11A	3.62	2.297	3.60	4.25	2.15	3.20	1.22	0.75
14AS-SA11B	3.64	2.419	3.48	5.52	1.95	3.74	2.00	0.79
14AS-SA12A	3.69	2.472	3.56	6.28	1.57	3.92	2.54	0.80
14AS-SA13B1	3.63	2.487	3.33	5.76	1.76	3.76	2.31	0.79
14AS-SA13B2	3.73	2.430	3.43	4.73	1.48	3.11	2.42	0.74
14AS-SA13B3	3.76	2.467	3.48	5.79	2.07	3.93	2.36	0.80
14AS-SA13B4	3.60	2.420	3.26	5.87	1.98	3.92	2.59	0.80
14AS-SA14AB1	3.71	2.467	3.45	5.60	2.00	3.80	2.17	0.79
14AS-SA14AB2	3.74	2.436	3.43	6.42	1.84	4.13	2.56	0.82
14AS-SA14AB3	3.73	2.467	3.29	6.64	2.13	4.39	2.62	0.83
14AS-SA14AB4	3.73	2.443	3.49	6.80	1.83	4.31	2.79	0.83
14AS-SA14B1	3.72	2.445	3.60	7.93	1.51	4.72	3.48	0.85
14AS-SA15BA1	3.66	2.452	3.38	6.10	1.68	3.89	2.37	0.80
14AS-SA15BA2	3.76	2.412	3.43	6.08	1.96	4.02	2.76	0.81
14AS-SA15BA3	3.71	2.440	3.45	6.90	2.35	4.63	2.68	0.85
14AS-SA15BB	3.73	2.457	3.33	6.90	1.73	4.32	2.82	0.83
WB98_850ft	3.77	2.236	3.02	6.11	2.70	4.40	2.02	0.83
WB98_898ft	3.77	2.464	3.56	7.07	2.54	4.81	2.63	0.86
WB98_906ft	3.74	2.333	3.40	7.93	2.22	5.07	3.08	0.87
WB98_920ft	3.72	2.452	3.45	5.70	1.98	3.84	2.40	0.80
WB98_953ft	3.76	2.495	3.28	7.71	2.32	5.01	2.94	0.87
WB98_958ft	3.73	2.429	3.31	6.66	2.00	4.33	2.82	0.83
WB98_975ft	3.74	2.511	3.31	6.21	2.00	4.11	2.41	0.81
WB98_999_2ft	3.72	2.545	3.48	7.46	2.19	4.82	2.94	0.86
AD5_180m	3.57	2.510	3.39	6.00	1.36	3.68	2.76	0.78
AD5_201_6m	3.49	2.523	3.30	5.69	1.05	3.37	3.09	0.76
AD5_216_5m	3.51	2.467	3.18	4.95	1.13	3.04	2.77	0.73
AD5_219_2m	3.57	2.510	3.14	6.00	1.36	3.68	2.76	0.78
DI1_247_5m	3.75	2.459	3.40	6.14	2.95	4.54	1.82	0.84
DI1_250_9m	3.74	2.462	3.47	6.76	2.93	4.85	2.06	0.86
Alphen_1A	3.58	2.570	3.30	3.50	1.45	2.48	1.16	0.68
RE-3	3.67	2.405	3.47	3.74	1.74	2.74	2.13	0.70
Average	3.66 ± 0.08	2.44 ± 0.05	3.37 ± 0.18	5.95 ± 1.13	1.84 ± 0.65	3.89 ± 0.65		0.80 ± 0.05

Figure Captions

Figure A1 – Map of field site and sample collection locations. Figure modified from Beukes et al. (1990).

Figure A2 – Stratigraphic columns depicting lithologies of drill cores and outcrop localities. Drill core stratigraphy modified from Heimann et al. (2010) and outcrop stratigraphy modified from Sumner (1995).

Figure A3 – Hand sample of stromatolitic specimen 14AS-SA06. Primary calcite (gray) and early dolomite (red/brown) mineralogies are indicated.

Figure A4 – Full thin section (left) showing cross section of stromatolitic specimen 14AS-SA06 and magnified portion of thin section (right) under plane polarized light. The scale bar in the right image is 500 μm.

Figure A5 – Polished hand sample of specimen 14AS-SA13B1 showing herringbone calcite (left edge of image) grading into sparry calcite. The edge of a ruler with 1mm graduations is located at the bottom right corner of the image.

Figure A6 – Magnified portion of thin section from specimen 14AS-SA13B1. The top image was collected under plane polarized light and the bottom image was taken with cross polarized light. Laminated organic material is located in the lower left corner of the images. Herringbone calcite at the bottom of the images grades into sparry calcite near the top of the images. Both scale bars are 500 μm.

Figure A7 – Modeled burial history of the Cambellrand-Malmani carbonate platform based on clumped isotope thermometry and reordering kinetics. The pictured model assumes a burial from 30°C to 163.5°C over the course of 600 million years. The carbonates reside buried at depth until 15 million years ago when they are uplifted and cooled to 18.6°C. The solid red line traces the ambient temperature along a 20°C/km geotherm. Broken lines predict the apparent clumped isotope temperature according to reordering models. The blue dot-dashed line follows calcite reordering according to the model of Henkes et al. (2014). The black dotted line depicts calcite ^{13}C-^{18}O bonding frequency based on the model of Stolper and Eiler (2015). Finally, the (lower) green dashed line was calculated for dolomite using the model of Henkes et al. (2014) with mineral specific reaction rate constants determined by Lloyd et al. (2018). Final apparent clumped (Δ_{47}) temperatures for these three scenarios are 140°C, 140°C, and 99°C, respectively. A second time-temperature history, shown by the upper green dashed line has been modeled for dolomite assuming a burial from 80°C to 163.5°C. The final apparent clumped temperature for this scenario is 129°C.

Figure A8 – Frequency distribution of maximum temperature of burial according to Rock-Eval data as calculated according to Disnar (1994) and Raman data as calculated according to Rahl et al. (2005). The blue and red histogram values were calculated according to a 600 and 200 million year heating periods, respectively, producing heating rates of 0.21 and 0.64 °C/Ma.

Figure A9 – Kinetically modeled kerogen maturation according to Wood (2018). The red line traces the ambient temperature path as in Figure 7 but with a maximum burial temperature of 137°C. The blue dashed and solid lines show progress of kerogen maturation as a fraction of total kerogen with maximum burial temperatures of 160 and 137°C, respectively. The calculated

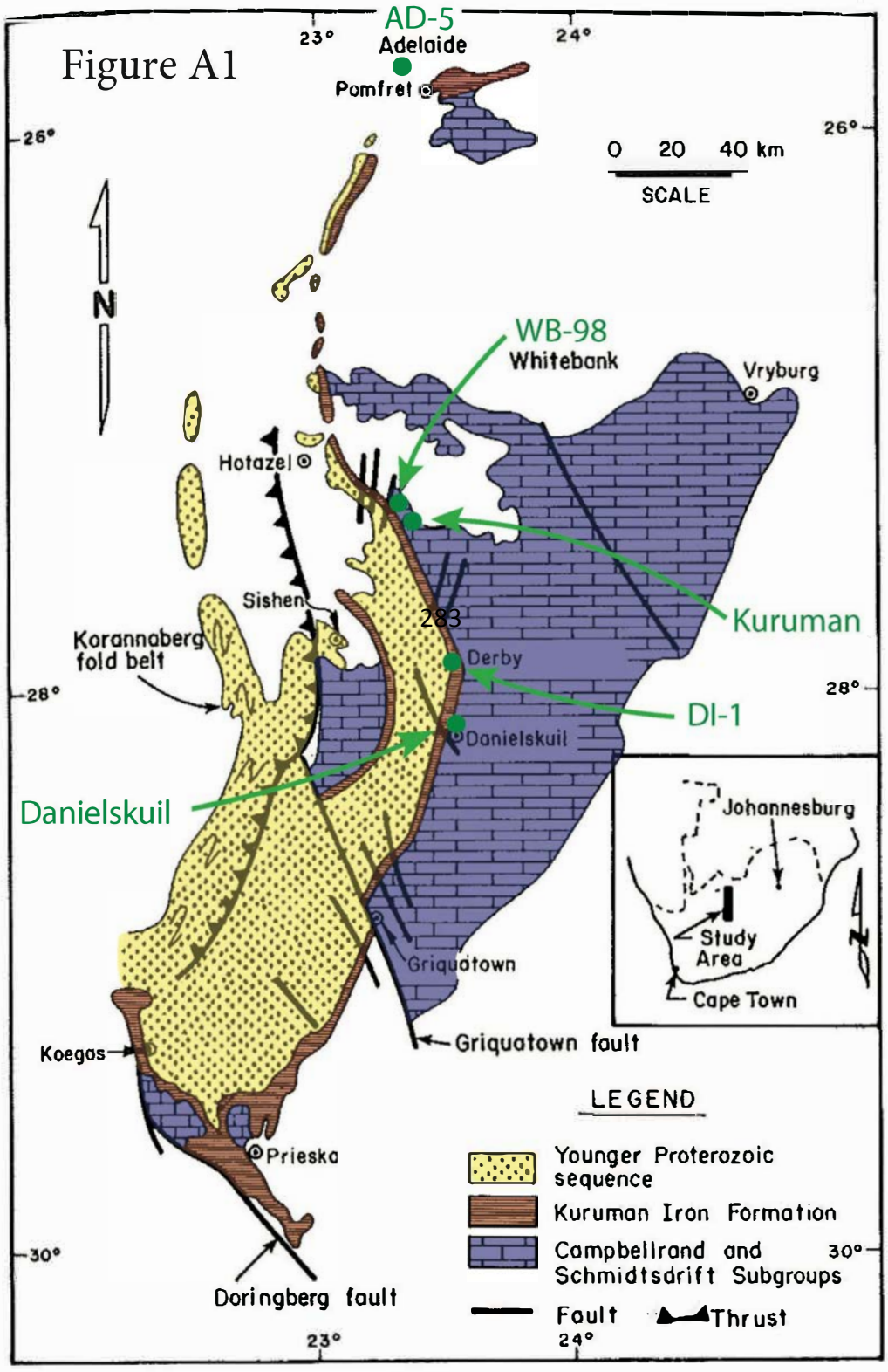
end equivalent vitrine reflectance (Ro%) values for these two heating regimes are 4.41 and 3.17, respectively.

Figure A10 – Kinetically modeled type III kerogen maturation according to Burnham and Sweeney (1989). The red line traces the ambient temperature path as in Figure 7 but with a maximum burial temperature of 160°C. The solid blue lines show progress of kerogen maturation as a fraction of total kerogen assuming initial H/C and O/C ratios of 0.9 and 0.35, respectively. The end equivalent vitrine reflectance (Ro%) values for this material are 3.41, 3.13, and 3.21, respectively, as calculated from final weight % C, final H/C and O/C values, and the "Easy Ro%" method of Sweeney and Burnham (1990).

Figure A11 – This figure is analogous to Figure 10 except that type II kerogen maturation was modeled.

Figure A12 – This figure is analogous to Figure 10 except that type I kerogen maturation was modeled.

Figure A1


AD-5
Adelaide
Pomfret
23°
24°
26°
26°
0 20 40 km
SCALE
N
WB-98
Whitebank
Vryburg
Hotazel
Sishen
283
Kuruman
Korannaberg
fold belt
Derby
28°
28°
DI-1
Danielskuil
Danielskuil
Johannesburg
Study
Area
Cape Town
Griquatown
Griquatown fault
Koegas
LEGEND
Younger Proterozoic
sequence
Kuruman Iron Formation
Campbellrand and
Schmidtsdrift Subgroups
30°
Fault
Thrust
Prieska
30°
Doringberg fault
23°
24°

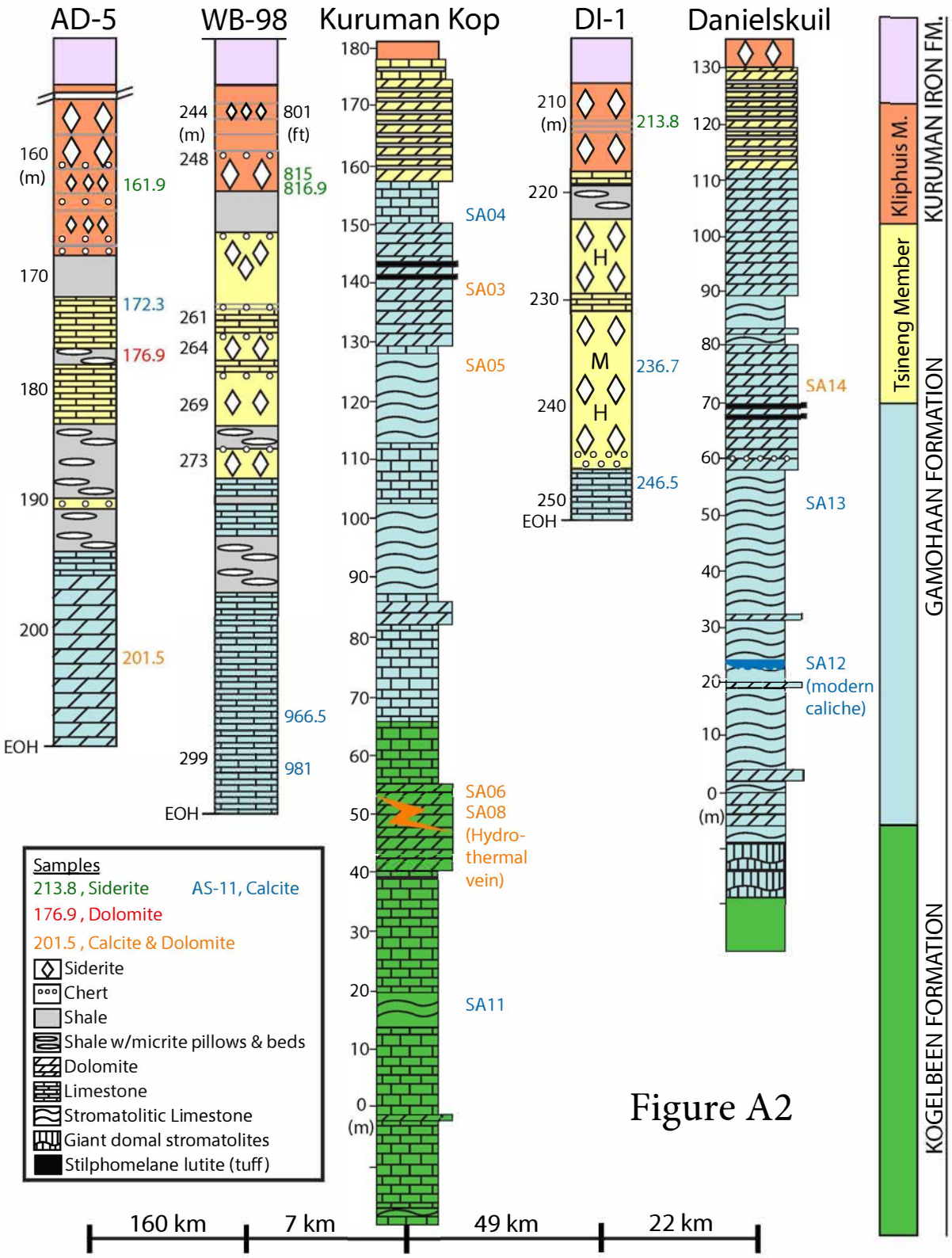

AD-5
WB-98
Kuruman Kop
DI-1
Danielskuil
160 (m)
170
180
190
200
EOH
161.9
172.3
176.9
201.5
244 (m)
248
261
264
269
273
299
EOH
801 (ft)
815
816.9
966.5
981
180
170
160
150
140
130
120
110
100
90
80
70
60
50
40
30
20
10
0 (m)
SA04
SA03
SA05
SA06
SA08
(Hydro-thermal vein)
SA11
210 (m)
220
230
240
250
EOH
H
M
H
213.8
236.7
246.5
130
120
110
100
90
80
70
60
50
40
30
20
10
0 (m)
SA14
SA13
SA12
(modern caliche)
Kliphuis M.
Tsineng Member
KURUMAN IRON FM.
GAMOHAAN FORMATION
KOGELBEEN FORMATION
Samples
213.8 , Siderite
AS-11, Calcite
176.9 , Dolomite
201.5 , Calcite & Dolomite
Siderite
Chert
Shale
Shale w/micrite pillows & beds
Dolomite
Limestone
Stromatolitic Limestone
Giant domal stromatolites
Stilphomelane lutite (tuff)
160 km
7 km
49 km
22 km

Figure A2

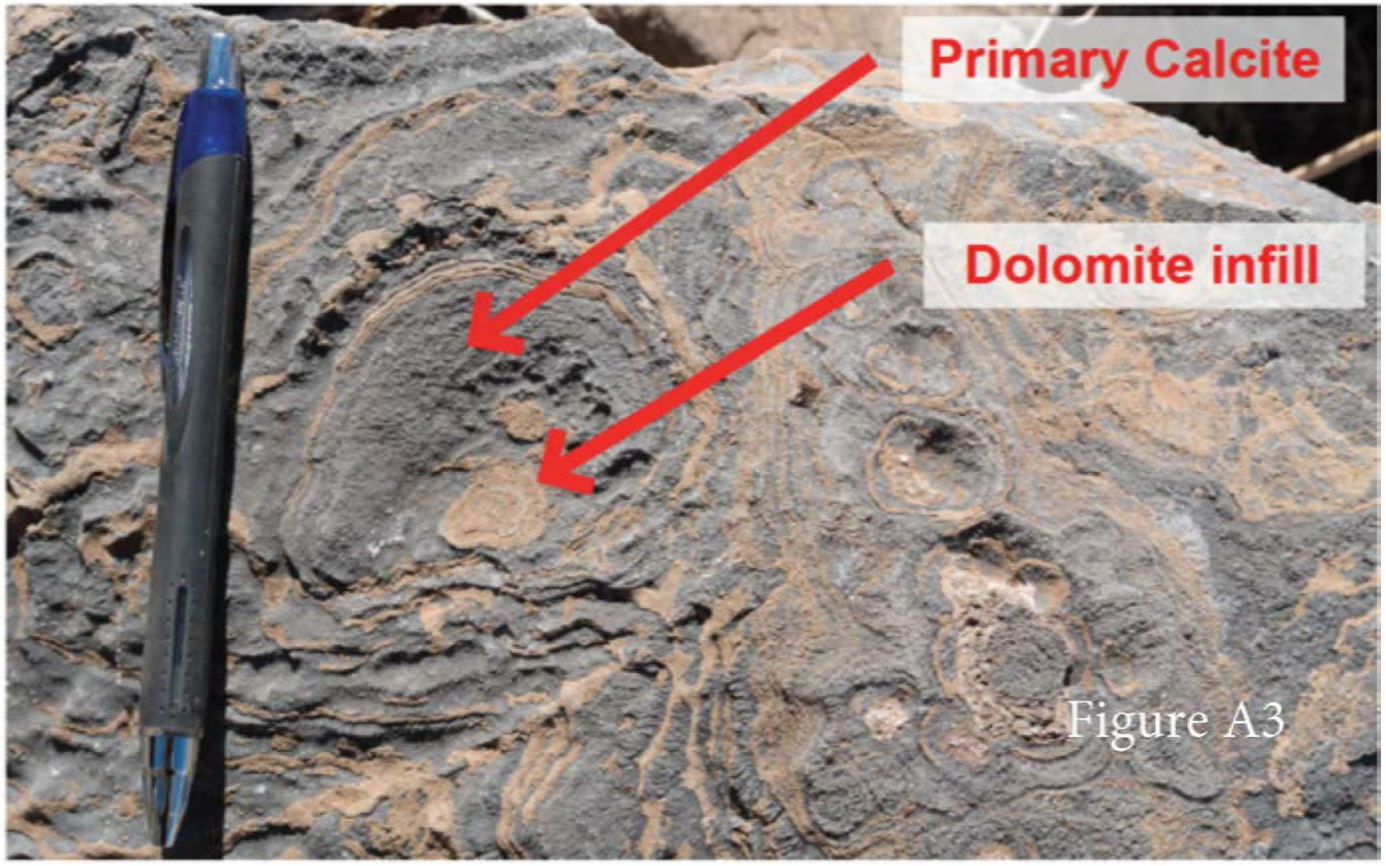
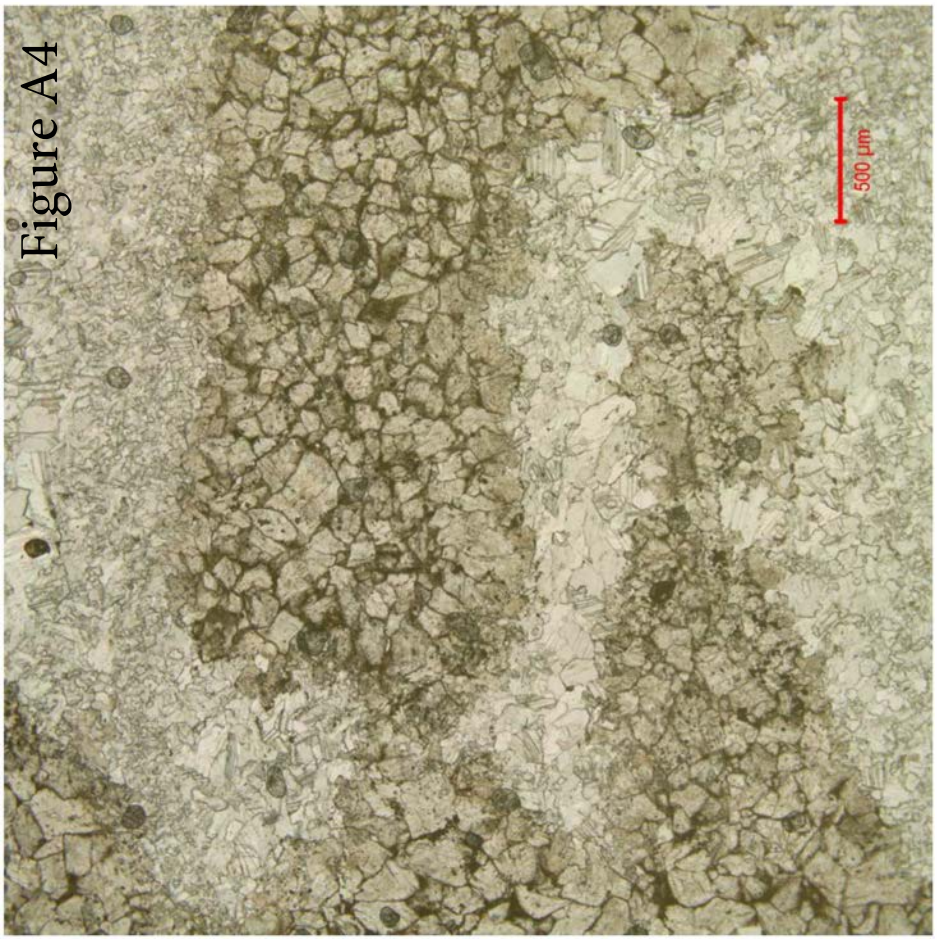


Figure A3

Figure A4



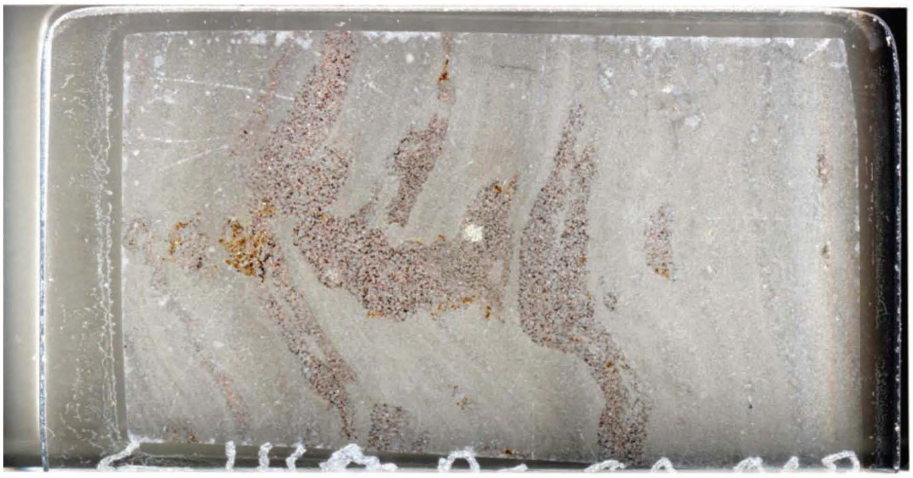
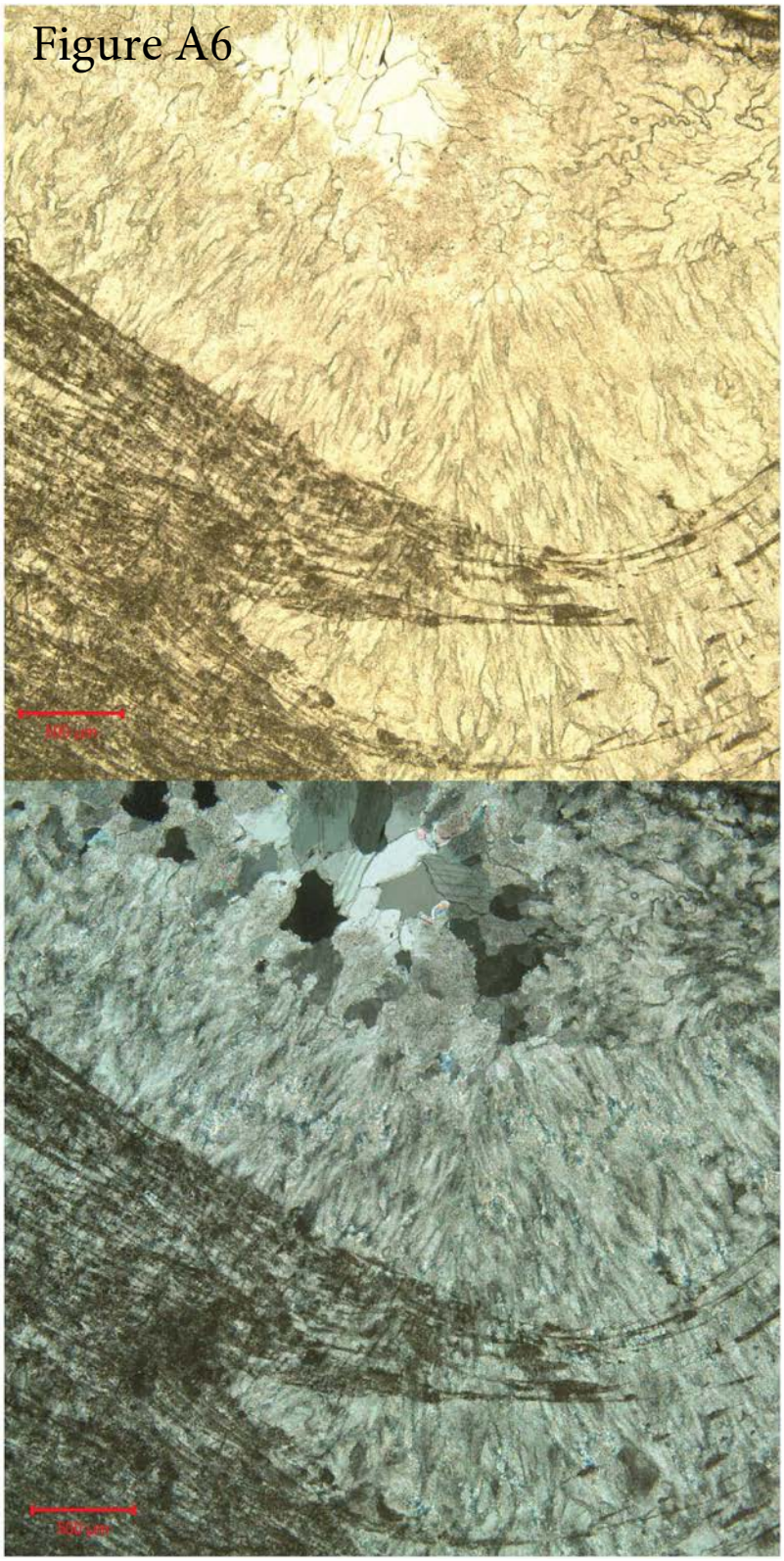
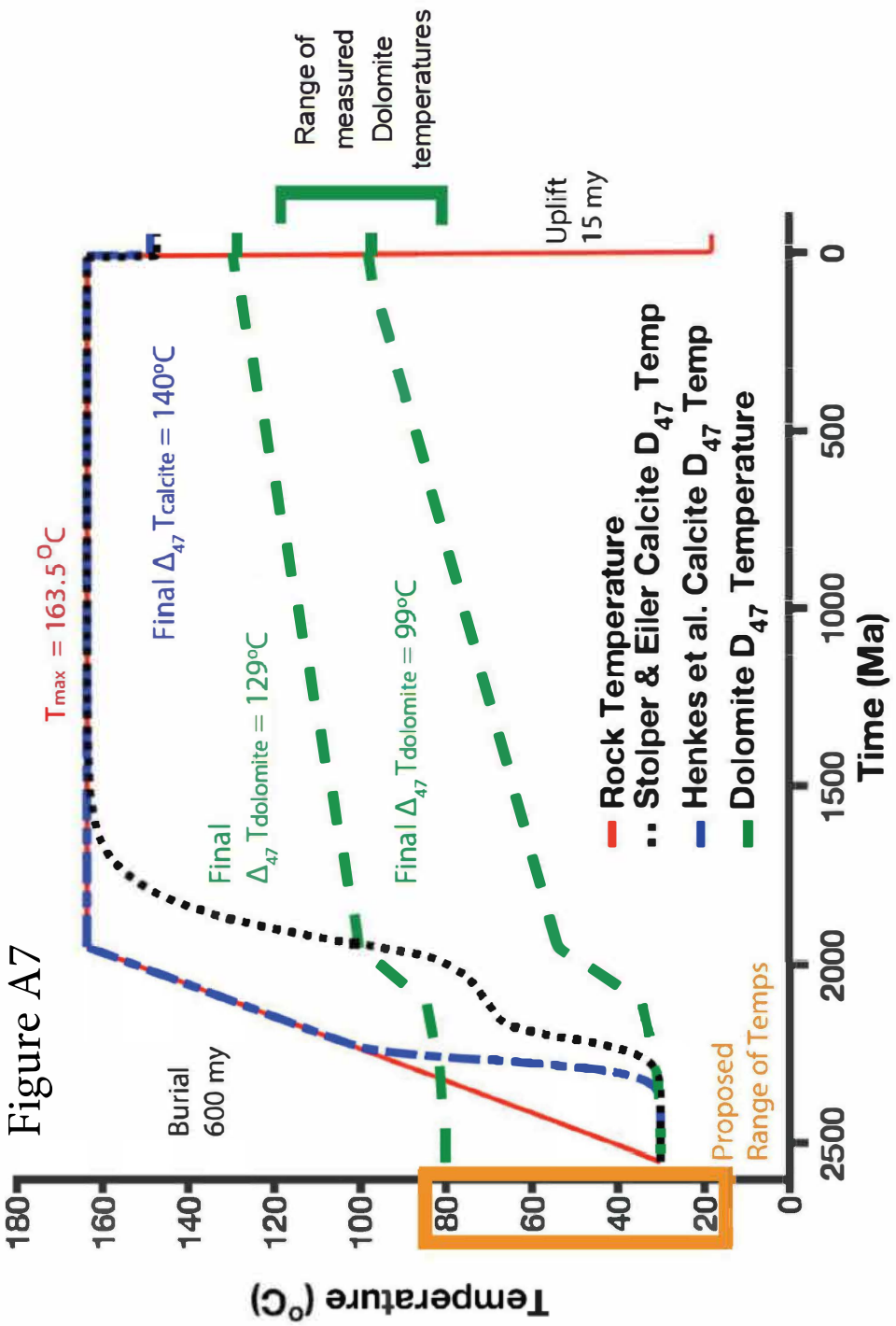


Figure A5



Figure A6




Figure A7
Temperature (°C)
Time (Ma)
Rock Temperature
Stolper & Eiler Calcite D47 Temp
Henkes et al. Calcite D47 Temp
Dolomite D47 Temperature
Tmax = 163.5°C
Final Δ47 Tcalcite = 140°C
Final Δ47 Tdolomite = 129°C
Final Δ47 Tdolomite = 99°C
Range of measured Dolomite temperatures
Uplift 15 my
Burial 600 my
Proposed Range of Temps

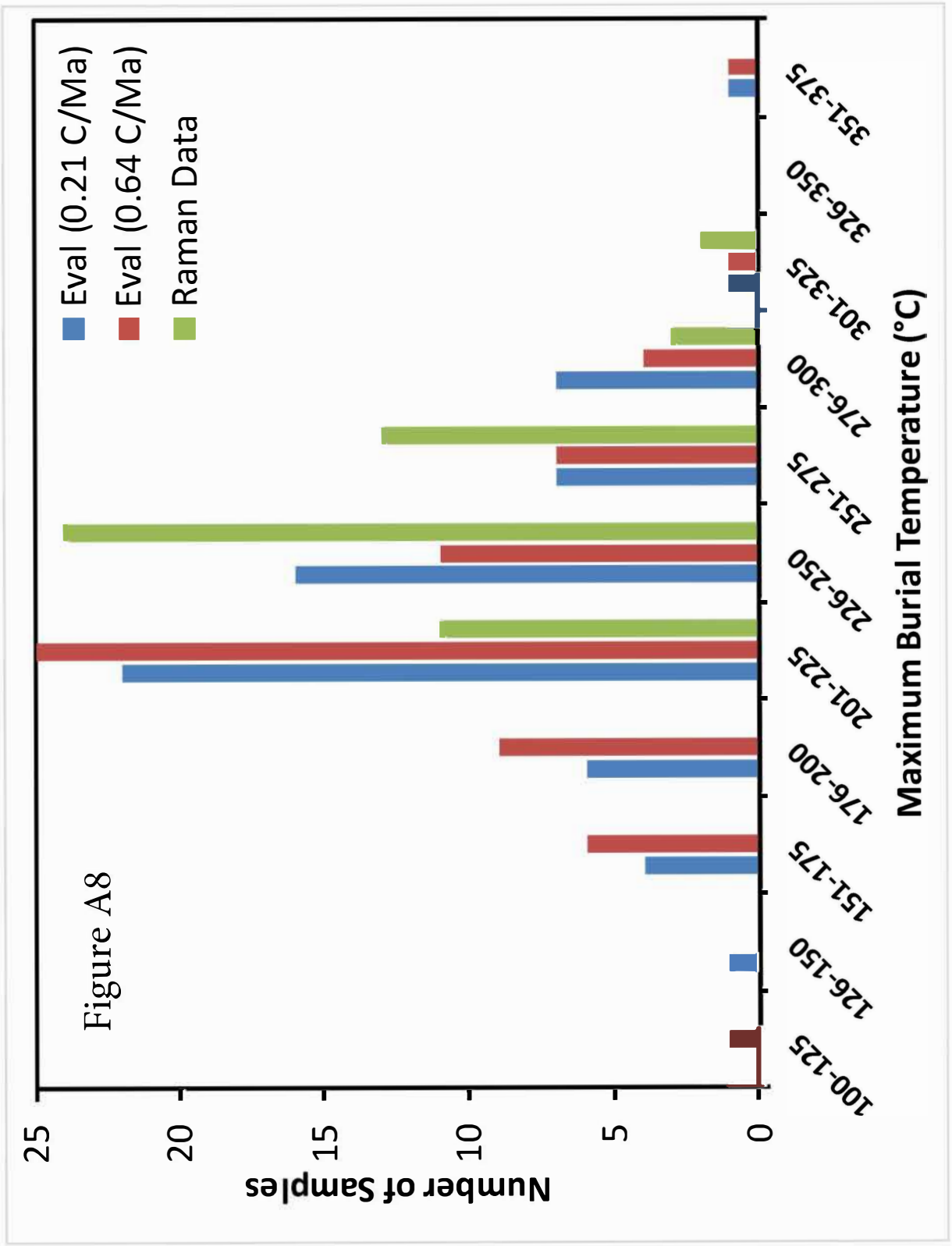

Eval (0.21 C/Ma)
Eval (0.64 C/Ma)
Raman Data
Number of Samples
0
5
10
15
20
25
100-125
126-150
151-175
176-200
201-225
226-250
251-275
276-300
301-325
326-350
351-375
Maximum Burial Temperature (°C)

Figure A8

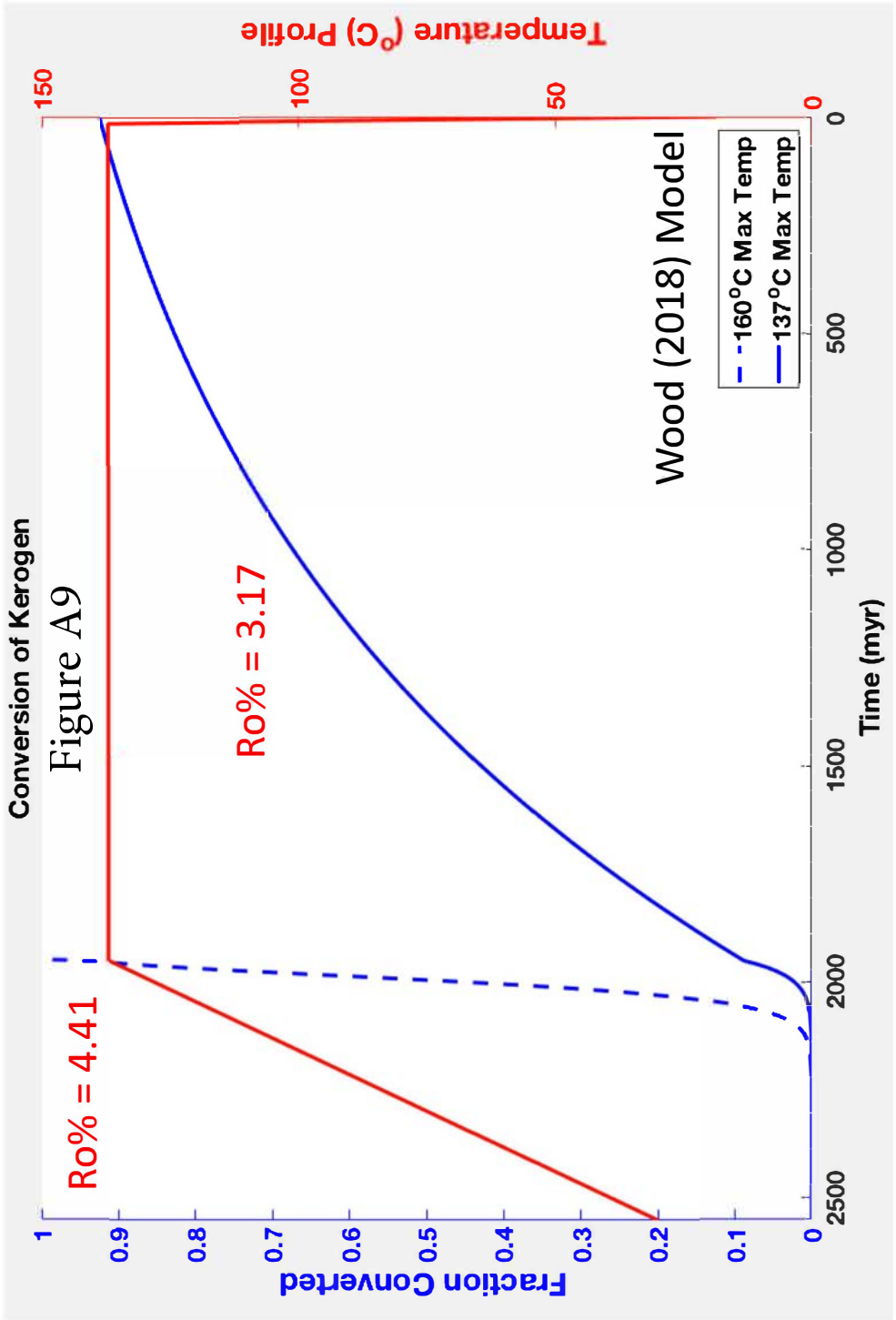

Conversion of Kerogen
Fraction Converted
Time (myr)
Temperature (°C) Profile
Wood (2018) Model
160°C Max Temp
137°C Max Temp
Ro% = 4.41
Ro% = 3.17
0
0.1
0.2
0.3
0.4
0.5
0.6
0.7
0.8
0.9
1
0
500
1000
1500
2000
2500
0
50
100
150

Figure A9

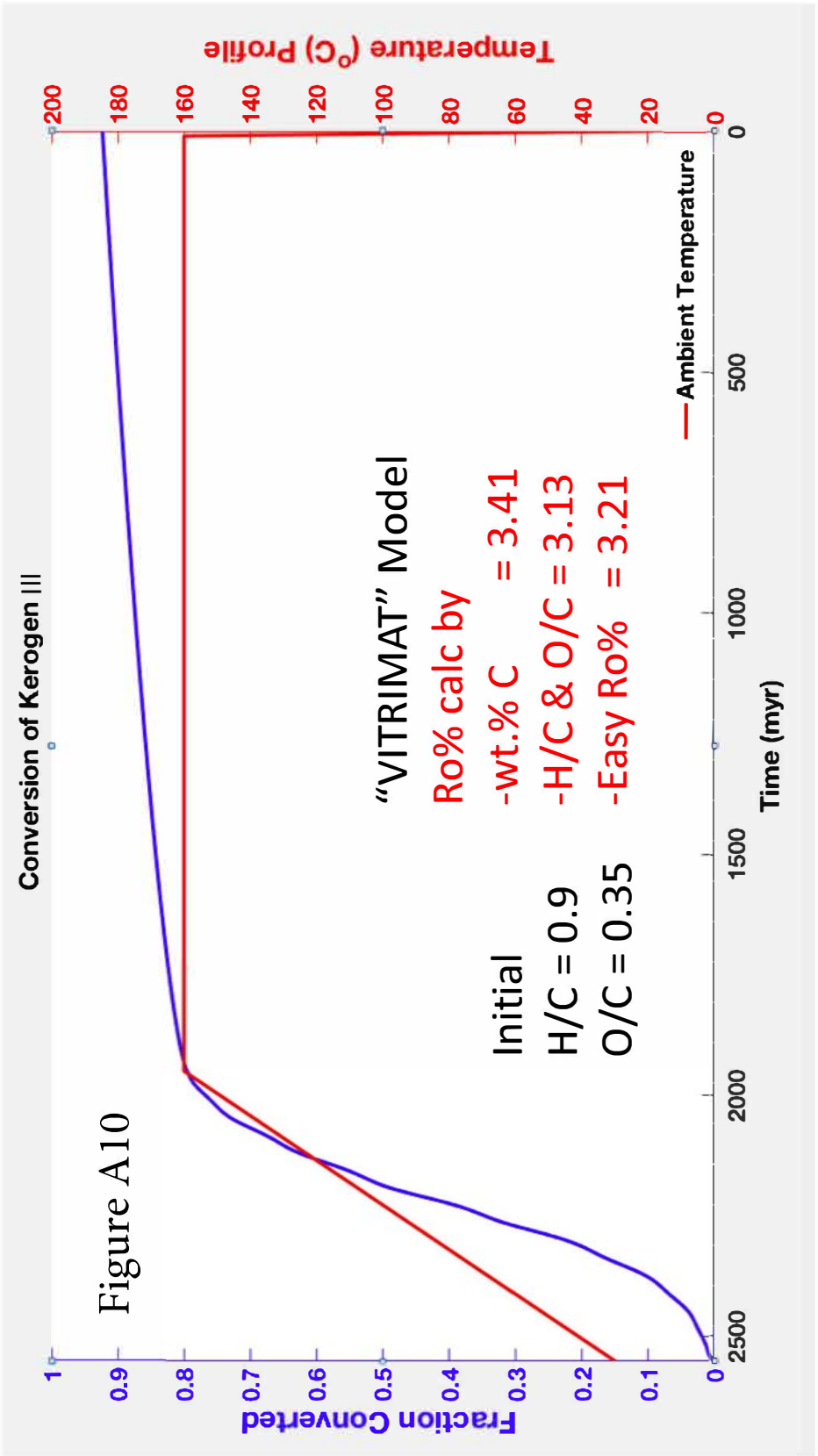

Conversion of Kerogen III
Temperature (°C) Profile
Fraction Converted
Time (myr)
Ambient Temperature
"VITRIMAT" Model
Ro% calc by
-wt.% C = 3.41
-H/C & O/C = 3.13
-Easy Ro% = 3.21
Initial
H/C = 0.9
O/C = 0.35

Figure A10

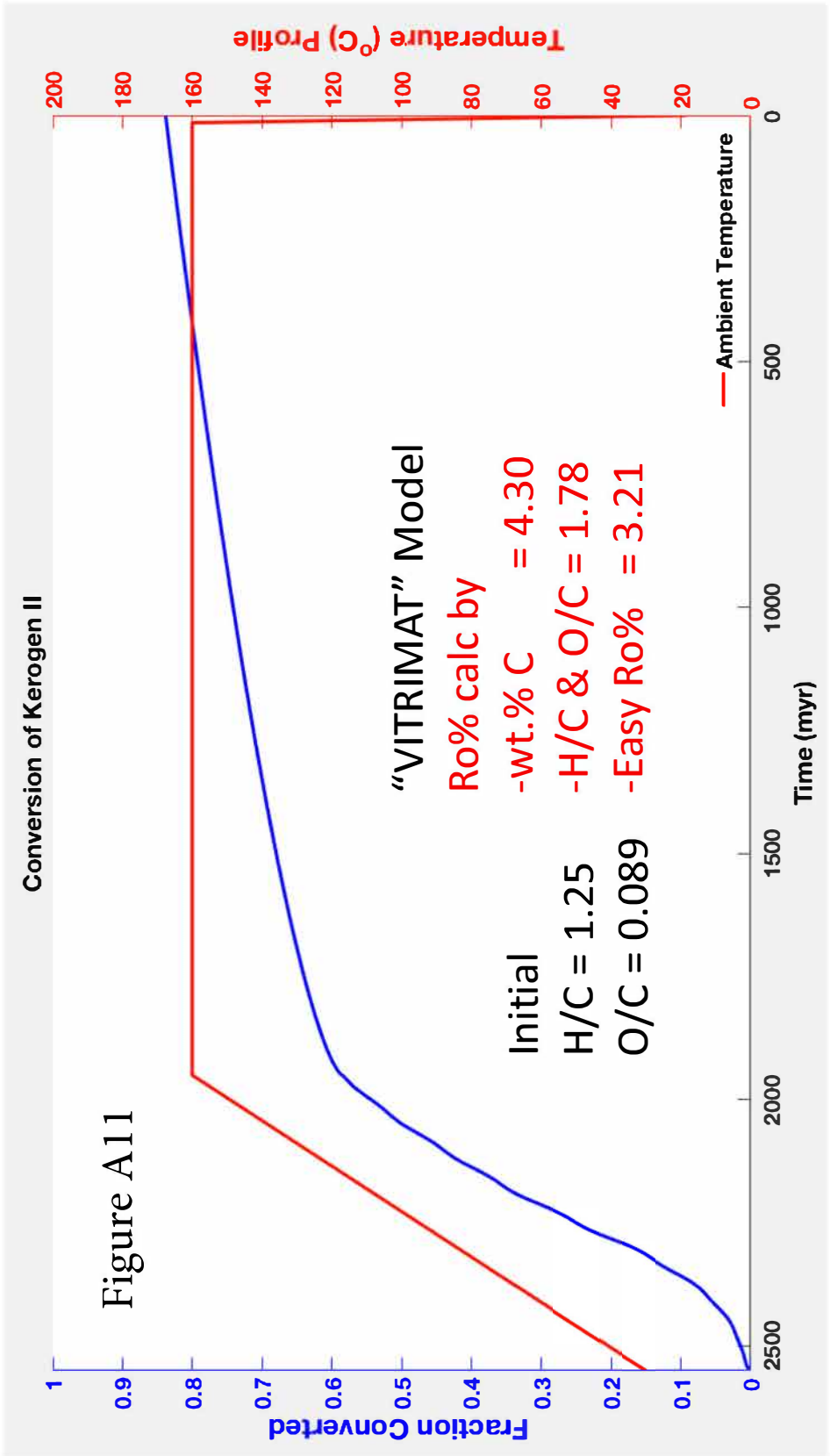

Conversion of Kerogen II
Fraction Converted
Temperature (°C) Profile
Time (myr)
Ambient Temperature
"VITRIMAT" Model
Ro% calc by
-wt.% C = 4.30
-H/C & O/C = 1.78
-Easy Ro% = 3.21
Initial
H/C = 1.25
O/C = 0.089

Figure A11

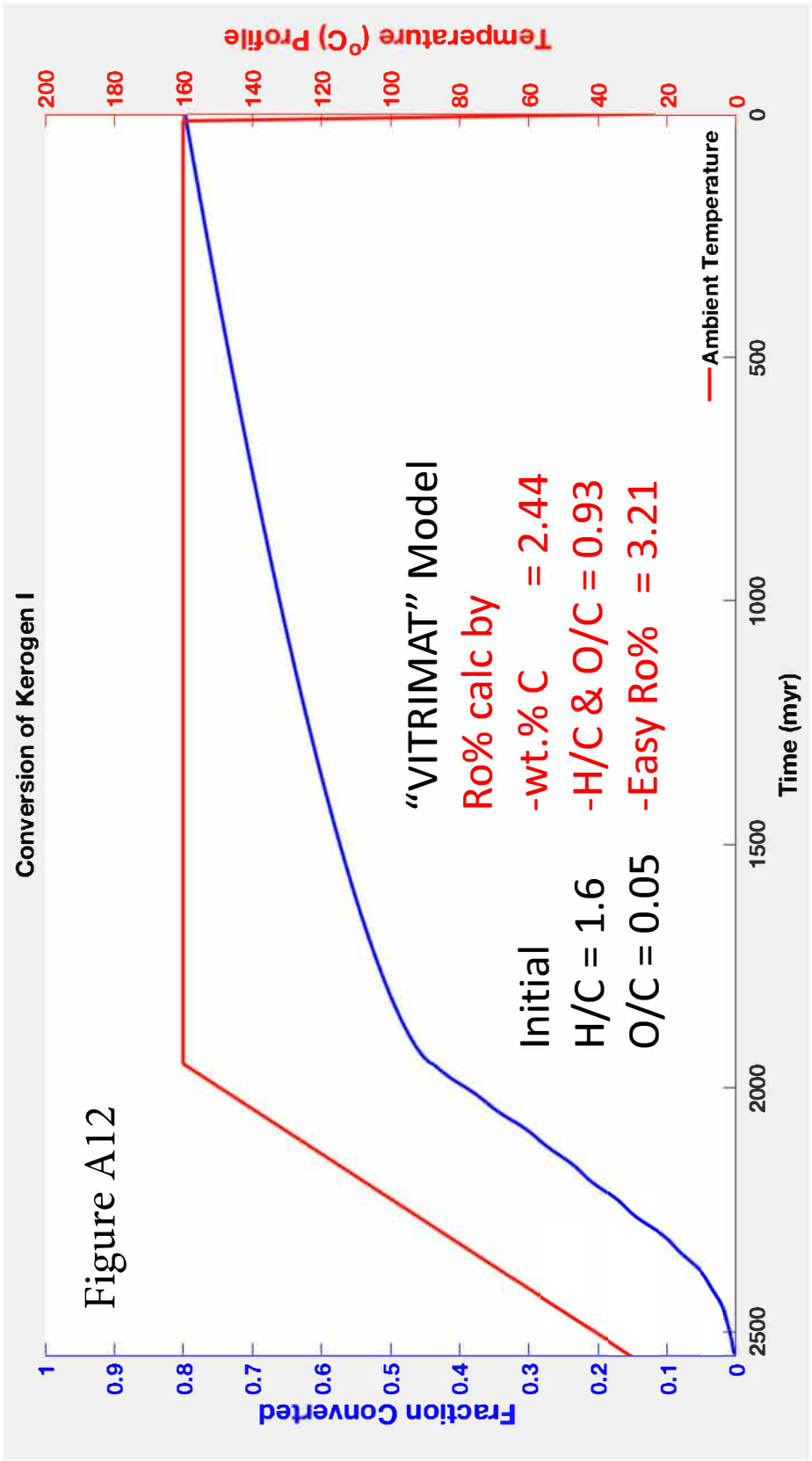

Conversion of Kerogen I
Fraction Converted
Temperature (°C) Profile
Time (myr)
Ambient Temperature
"VITRIMAT" Model
Ro% calc by
-wt.% C = 2.44
-H/C & O/C = 0.93
-Easy Ro% = 3.21
Initial
H/C = 1.6
O/C = 0.05

Figure A12

Appendix B: Laboratory Reports from Outside Sources and Collaborators

- University of California-Davis Stable Isotope Facility
    - H_2O stable isotope analysis by laser spectroscopy (Los Gatos Reseach Instruments)
        - First CI Sample Set (6/10/2014)
        - Second CI Sample Set (7/15/2015)
    - Carbon stable isotope analysis of DIC by Delta V Plus IRMS
        - First CI Sample Set (7/10/2014)
        - Second CI Sample Set (8/06/2015)
- Geoscience Department, University of Wisconsin-Madison
    - CAMECA SXFive field emission electron probe
        - Preliminary survey by Drs. Aurélien Moy and John Fournelle of some seed crystal and magnesian calcite powders related to "Chapter 3: Factors Influencing the Mg Isotope Composition of Magnesian Calcite"
- Department of Earth Sciences, IIT Bombay
    - Rock-Eval-6 Pyrolyzer
        - Pyrograms provided by Professor Nic Beukes
- Department of Material Sciences and Engineering, Massachusetts Institute of Technology
    - Micro-Raman analsis by Horiba LabRam 800HR
        - Spectra for "14AS-SA" samples listed in Table A1-6

University of California-Davis Stable Isotope Facility
One Shields Ave. Davis, CA 95616
530-754-7517
6/10/14

University of Wisconsin - Madison, Geoscience
First CI Sample Set 2014
Nicholas Levitt
859-492-2674
nlevitt@wisc.edu

H_2O stable isotope analysis by laser spectroscopy (Los Gatos Reseach Instruments)

LabID	Sample ID	VSMOW $d^{18}O$
W-22747	20140213start	-8.95
W-22748	20140213Aend	-8.94
W-22749	20140221start	-9.14
W-22750	20120221Aend	-8.98
W-22751	20140227start	-9.00
W-22752	20140227Aend	-8.88
W-22753	20140305start	-9.02
W-22754	20140305Aend	-8.75
W-22755	20140314start	-8.77
W-22756	20140314Aend	-8.58
W-22757	20140314Bend	-8.65
W-22758	20140320start	-8.64
W-22759	20140320Aend	-8.64
W-22760	20140320Bend	-8.93
W-22761	20140325start	-8.80
W-22762	20140325Aend	-8.70
W-22763	20140325Bend	-9.01
W-22764	20140403start	-9.15
W-22765	20140403Aend	-8.40
W-22766	20140403Bend	-8.60
W-22767	20140409start	-8.67
W-22768	20140409Aend	-8.73
W-22769	20140409Bend	-8.91
W-22770	20140414start	-8.72
W-22771	20140414Aend	-9.03
W-22772	20140414Bend	-8.96
W-22773	20140420start	-9.17
W-22774	20140420Aend	-9.21
W-22775	20140420Bend	-8.90
W-22776	20140427start	-9.10
W-22777	eqsystem20140315	-1.25
W-22778	Eqsystem20140427	-2.89

Internal check	$d^{18}O$ per mil
Known value	-4.95
Mean	-4.95
1 SD	0.17

University of California-Davis Stable Isotope Facility
One Shields Ave. Davis, CA 95616
530-754-7517
7/15/15

University of Wisconsin-Madison, Geoscience
Second Cl Sample Set - H2O
Nicholas Levitt
859-492-2674
nlevitt@wisc.edu

H_2O stable isotope analysis by laser spectroscopy (Los Gatos Reseach Instruments)

LabID	Sample ID	VSMOW d ^{18}O
W-25575	20140420start	-8.71
W-25576	20140420Aend	-8.74
W-25577	20140420Bend	-8.84
W-25578	20140626Bend	-8.85
W-25579	20140607start	-8.88
W-25580	20140607Bend	-8.93
W-25581	20140626start	-8.84
W-25582	20140626Aend	-8.75
W-25583	20140717Bend	-8.90
W-25584	20140724start	-8.80
W-25585	20140724Aend	-8.74
W-25586	20140724Bend	-8.81
W-25587	20140823Aend	-8.64
W-25588	20140901Aend	-8.51

Internal check	d ^{18}O per mil
Known value	-2.83
Mean	-2.83
1 SD	0.05

changed vial label from electronic sample list file with client confirmation;ed

University of California-Davis Stable Isotope Facility
One Shields Ave. Davis, CA 95616
530-754-7517
7/10/14

University of Wisconsin - Madison, Geoscience
First CI Sample Set 2014
Nicholas Levitt
859-492-2674
nlevitt@wisc.edu

Sample	$\delta^{13}C_{VPDB}$	µg C/mL	Comments
20140213	-1.48	19.6	
20140213A	-2.84	8.9	
20140221	-5.23	15.0	
20120221A	-2.93	9.3	
20140227	-2.07	11.4	
20140227A	-2.83	8.4	
20140305	-1.89	11.5	
20140305A	-3.30	8.3	
20140314	-1.45	11.2	
20140314A	-2.83	9.3	
20140314B	-2.57	10.0	
20140320	-4.62	24.5	
20140320A	-2.98	8.8	
20140320B	-2.84	8.7	
20140325	-2.36	11.8	
20140325A	-2.96	8.0	
20140325B	-2.93	8.1	
20140403	-2.38	12.6	
20140403A	-2.49	9.1	
20140403B	-2.52	9.5	
20140409	-3.72	13.7	
20140409A	-3.14	13.3	
20140409B	-2.99	16.1	
20140414	-2.05	14.2	
20140414A	-2.02	13.4	
20140414B	-1.95	12.5	
20140420	-2.81	11.5	
20140420A	-1.99	11.1	
20140420B	-1.86	11.9	
20140427	-3.46	13.1	

Project: First CI Sample Set 2014

CHECK STD
0.2 ml 10mM Li2CO3 (Acros2)

MEASURED	KNOWN	
-3.74	-3.7	
-3.68		
-3.63	MEAN	
-3.68	-3.69	
-3.69		
-3.70	SD	
-3.64	0.04	
-3.74		

CALIBRATION STDS

MEASURED	KNOWN	
-46.65	-46.6	LSVEC
-46.54	-46.6	LSVEC
-46.71	-46.6	LSVEC
0.72	0.7	SEA WATER
0.65	0.7	SEA WATER
0.73	0.7	SEA WATER

SECONDARY CHECK STDS

-13.23	-13.3	Acros1
-13.28	-13.3	Acros1
-13.30	-13.3	Acros1
-13.30	-13.3	Acros1

University of California-Davis Stable Isotope Facility
One Shields Ave. Davis, CA 95616
530-754-7517
8/6/15

University of Wisconsin - Madison, Geoscience
Second CI Sample Set
Nicholas Levitt
859-492-2674
nlevitt@wisc.edu

Sample	$\delta^{13}C_{VPDB}$	µg C/mL	Comments	Project: Second CI Sample Set		
20140427A	-5.54	13.3				
20140427B	-6.01	13.6				
20140531	-2.92	14.8		CHECK STD		
20140531A	-3.21	12.4		0.2 ml 10mM Li2CO3 (Acros2)		
20140531B	-3.36	11.9				
20140607	-2.68	15.6		MEASURED	KNOWN	
20140607A	-3.39	11.1		-4.08	-4.0	
20140607B	-3.24	12.0		-4.01		
20140617	-2.02	15.0		-4.02	MEAN	
20140617A	-3.47	10.5		-4.03	-4.04	
20140617B	-3.36	11.3		-4.04		
20140626	-2.24	14.7			SD	
20140626A	-2.65	14.5			0.03	
20140626B	-2.94	10.7				
20140630	-3.26	14.4				
20140630A	-4.17	14.0				
20140630B	-3.95	14.5				
20140711	-1.58	12.5				
20140711A	-2.53	11.6				
20140711B	-2.42	11.5				
20140717	-3.85	13.0				
20140717A	-5.05	12.4				
20140717B	-4.58	13.1		CALIBRATION STDS		
20140724	-3.97	14.6		MEASURED	KNOWN	
20140724A	-4.94	11.2		-46.84	-46.6	LSVEC
20140724B	-5.05	10.9		-46.66	-46.6	LSVEC
20140804	-3.99	15.8		-46.58	-46.6	LSVEC
20140804A	-5.04	11.4				
20140804B	-4.52	11.9		-2.37	-2.2	NAU-1
20140810	-4.04	13.9		-2.19	-2.2	NAU-1
20140810A	-4.86	11.0		-2.29	-2.2	NAU-1
20140810B	-4.49	12.5				
20140817	-4.05	13.8		-26.32	-26.6	NAU-2
20140817A	-5.28	11.9		-26.26	-26.6	NAU-2
20140817B	-4.44	13.4		-26.39	-26.6	NAU-2
20140823	-3.38	15.2				
20140823A	-4.74	13.6				
20140823B	-4.98	15.3		SECONDARY CHECK STDS		
20140901	-5.12	15.3				
20140901A	-6.60	12.8		0.58	0.7	SEAWATER
20140901B	-6.52	13.9				
20150221	-5.85	17.4		-13.36	-13.4	ACROS-1
20150320	-4.93	25.5		-13.41	-13.4	ACROS-1
20150409	-4.33	15.3				

Date: 12/15/2017
From: Aurélien Moy and John Fournelle
Re: Nick Levitt's Mg-calcite experimental grains mounted in epoxy

EPMA conditions: 7kV, 10nA. Background corrected by the Mean Atomic Number method. Validated for trace levels of Mg with seeds containing no Mg. Mg detection limit is 0.07 wt% or ~0.3 mol% Mg.

Two techniques were used: spot/point analyses and X-ray maps. We mainly operated the WDS spectrometers (Mg Ka on LTAP crystal and Ca Ka on LPET crystal) for WDS spot analyses as well as WDS X-ray maps, but also occasionally utilized our EDS system for EDS X-ray mapping. The WDS maps were background and matrix corrected, and output in wt% Mg.

We are using a fully focused beam with a CAMECA SXFive field emission electron probe, and calculate the analytical spatial resolution as ~500 nm (0.5 micron). We estimate that the "rims" on the seed crystals are roughly from maybe a quarter to 1 micron in width.

Information on the homogeneity of the seed crystals follows the experimental data.

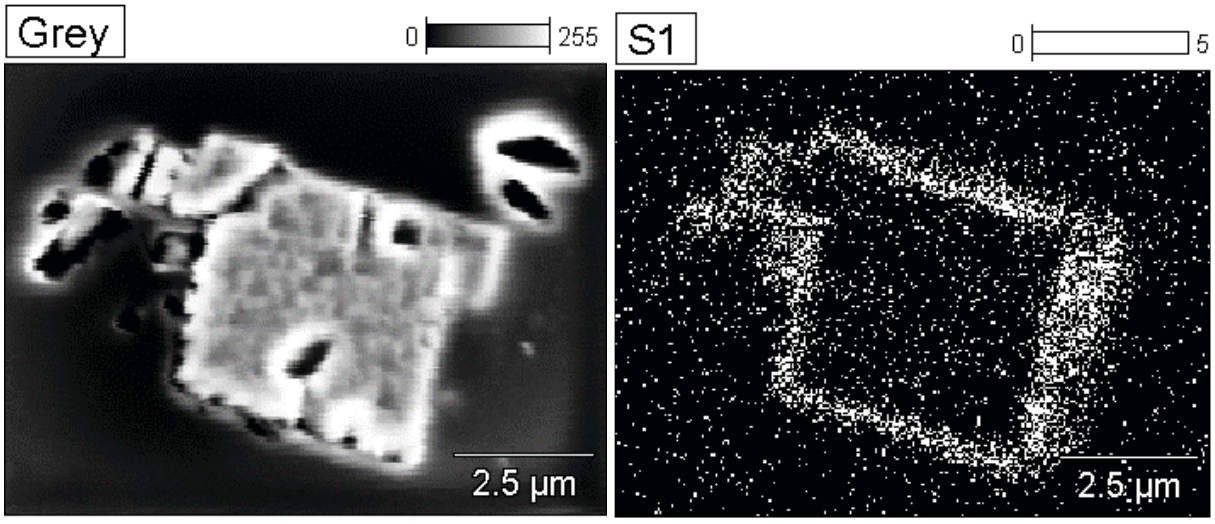
Experimental samples analyzed (spots/points):

- UK-32: 12 grains were analyzed with at least 3 points on each grains (rim). Almost no Mg was found on the rim.
- UK-36: 12 grains were analyzed with at least 3 points on each grains (rim). A high concentration of Mg (.1 to .6 wt%) was found on most of the analyzed points on the rim. Two grains showed an unusually high Mg concentration on the rim (up to 5.5 wt%).
- FU-24: 9 grains were analyzed with at least 3 points on each grains (rim and core). The concentration of Mg inside the grains is around 0.1 wt% and increases when the analyzed spots are closer to the rim (around 0.4 wt%).
- FU-23: 3 grains were analyzed with at least 6 points on each grains (rim and core). Little Mg is present on the rim (0.05 to 0.1 wt%). A highest concentration of Mg is present inside the grain but heterogeneously distributed (up to 1.2 wt%).

Samples analyzed (maps):

UK-36

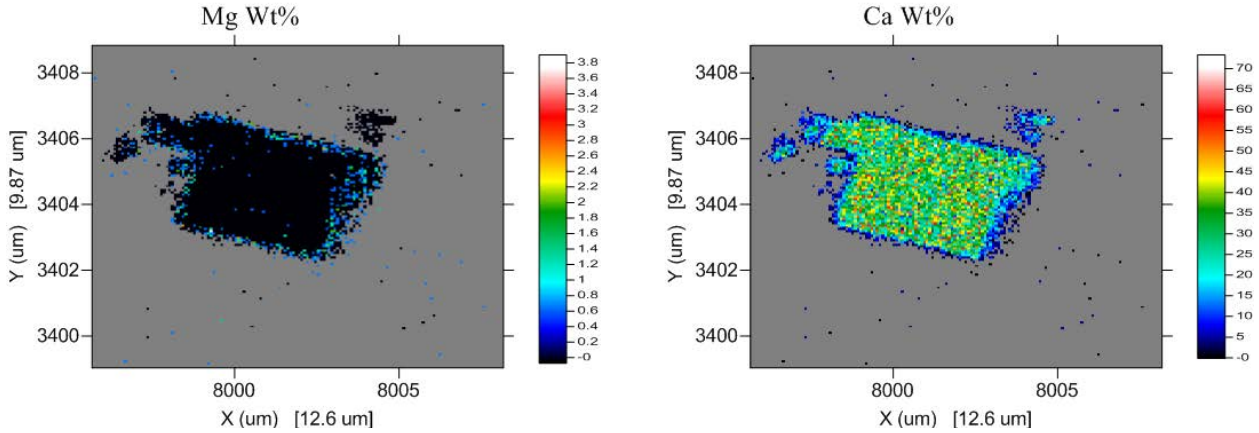
- 6 semi-quantitative EDS maps (and one WDS map for element Mg) were acquired on 6 grains on UK-36.



On all the mapped grains, the Mg was forming a rim around the grain. Almost no Mg was present inside the grain.

- 1 quantitative map for Mg and Ca was acquired on 1 grain on UK-36.

carbonate_7KV_121317_UK-36-Gr16_, Elemental Wt.%

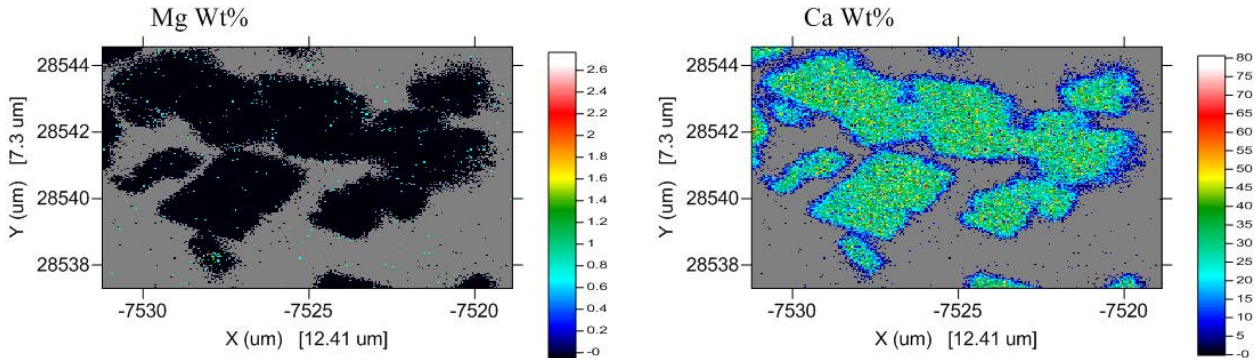


The map confirms the EDS semi-quantitative results: the Mg is only present on the rim of the grain.

UK-32

- 1 quantitative map for Mg and Ca was acquired on 1 grain on UK-32.

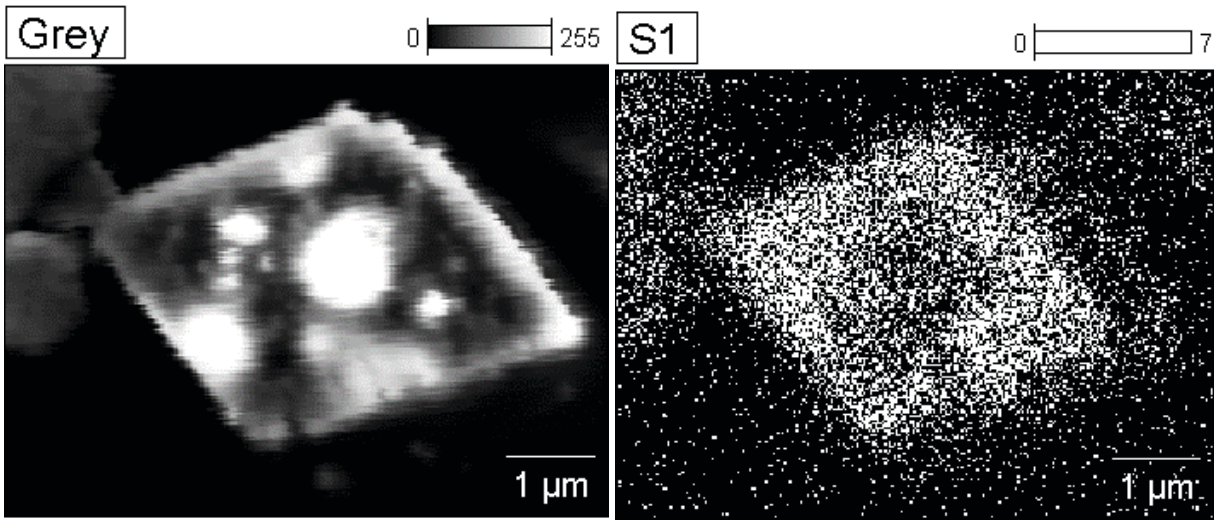
carbonate_7KV_MAN_121117_UK-32-8_00040_, Elemental Wt.%



Almost no Mg was detected on this grain.

FU-24

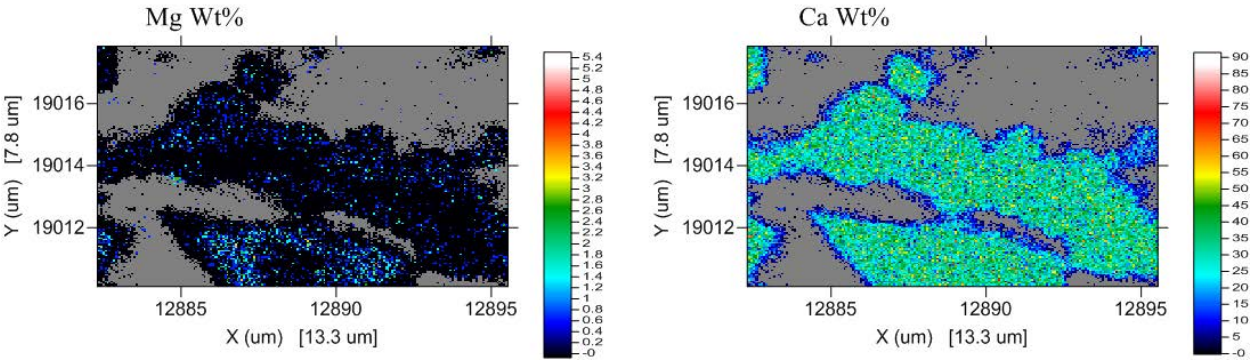
- 1 semi-quantitative EDS maps (and one WDS map for element Mg) were acquired on 1 grains on FU-24.

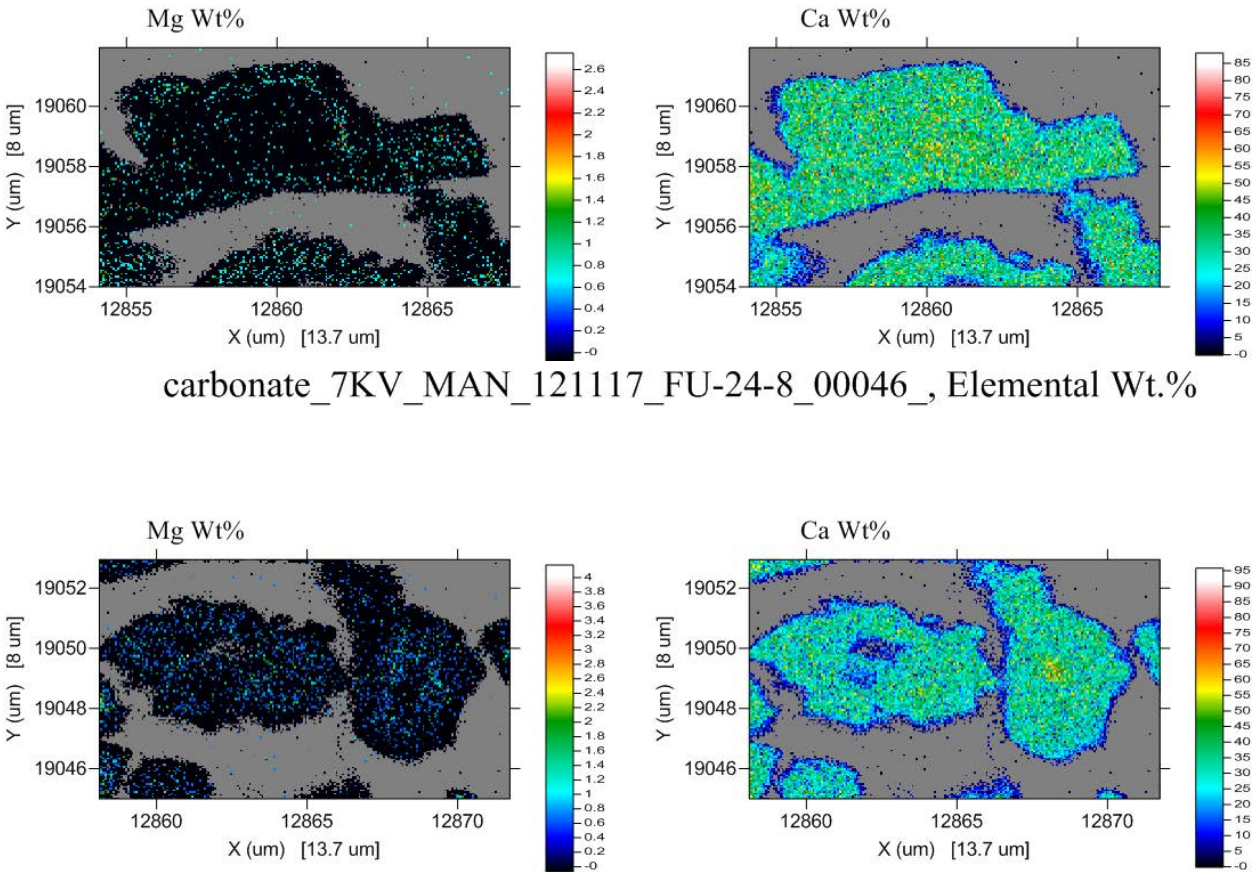


The mapped grain shows Mg formed inside the sample but almost no Mg was present on the rim of the grain (see below for more visual examples).

- 3 quantitative maps for Mg and Ca were acquired on 3 grains on FU-24.

carbonate_7KV_MAN_121117_FU-24-6_00045_, Elemental Wt.%



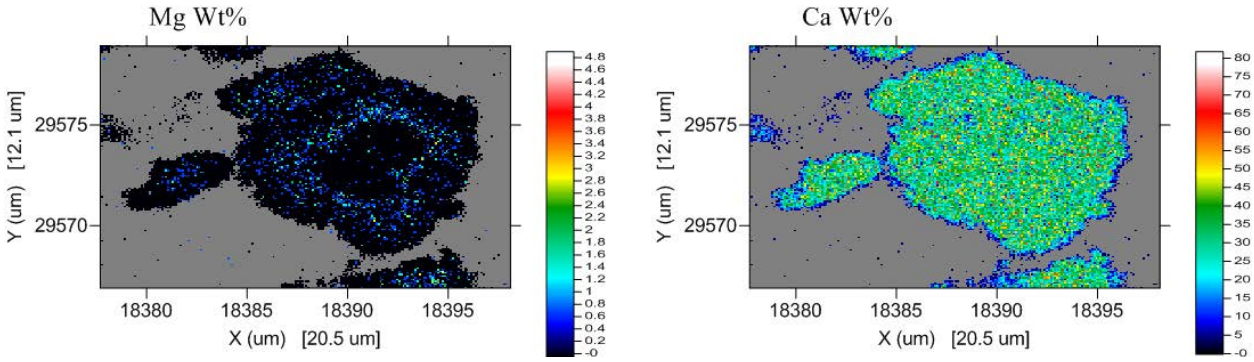


The Mg is mainly present inside the grain. The rim usually contains no Mg.

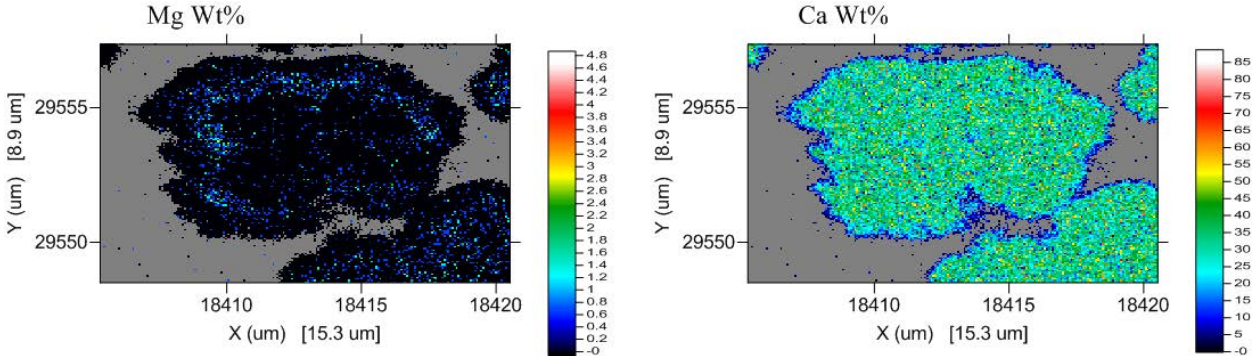
FU-23

- 3 quantitative maps for Mg and Ca were acquired on 3 grains on FU-23.

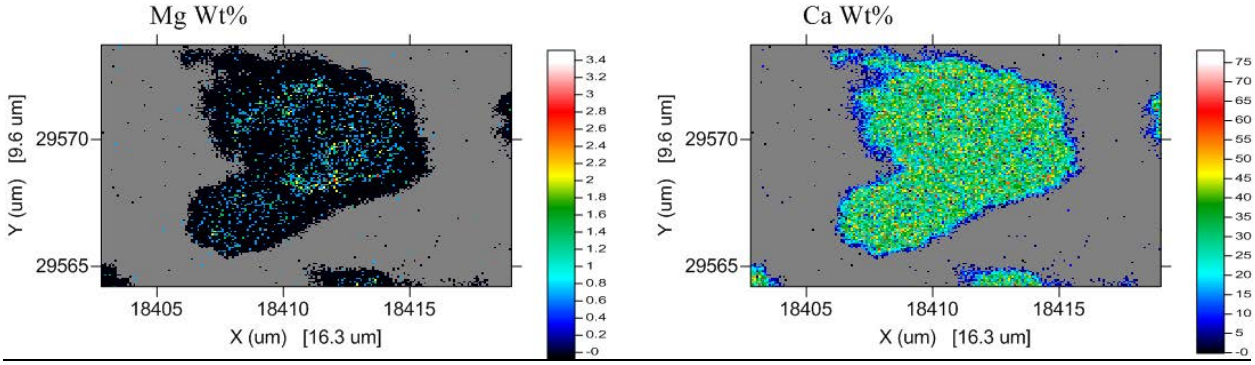
carbonate_7KV_MAN_121117_FU-23-1_00047_, Elemental Wt.%



carbonate_7KV_MAN_121117_FU-23-2_00048_, Elemental Wt.%



carbonate_7KV_MAN_121117_FU-23-3_00049_, Elemental Wt.%



<u>The Mg is only present inside the grain: no Mg present in the rim. There is also a diminishing of the Mg concentration on the middle of the grains 1 and 2.</u>

Homogeneity of the seed crystals by EPMA

Where mol% Mg is defined at (mol Mg / (mol Mg + mol Ca))*100

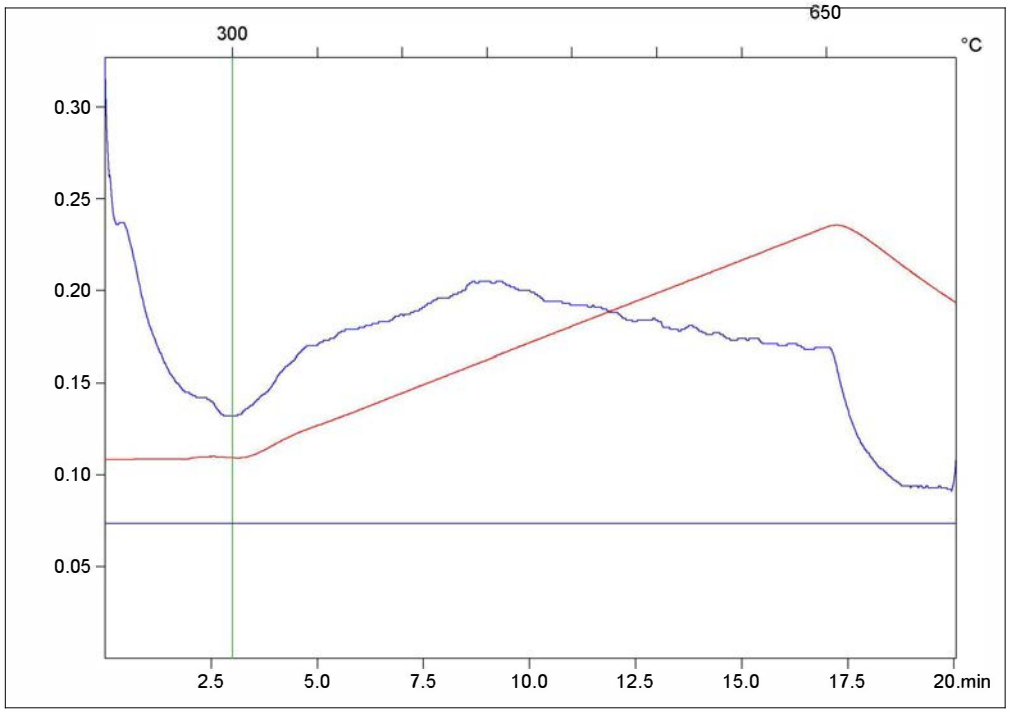
Brief summary: AGT seed crystals average 1.6 mol% Mg with standard deviation of 0.9 mol% (25 measurements). Minimum of 0.1 to maximum of 3.5 mol%.
AGB seed crystals average 1.5 mol% Mg with a standard deviation of 0.8 mol% (20 measurements. Minimum of 0.2 to maximum of 2.6 mol%.
See attached excel table.

Customer :	Customer part :
IIT Mumbai	65131

Comment :

RE6 Turbo n E907/65131/102/07

S1(mg/g)=0.04	Sample =AD5/180
S2(mg/g)=0.23	Method =Bulk Rock
Tmax(°C)=399	Cycle=oxi fast
TpkS2(°C)=439.0	KFID(10*9)=1472
PI=0.16	Qty(mg)=61.4
HI=29	TOC(%)=0.79



C:\2016-17\SD33\48.R00 : FID pyrolysis graphic

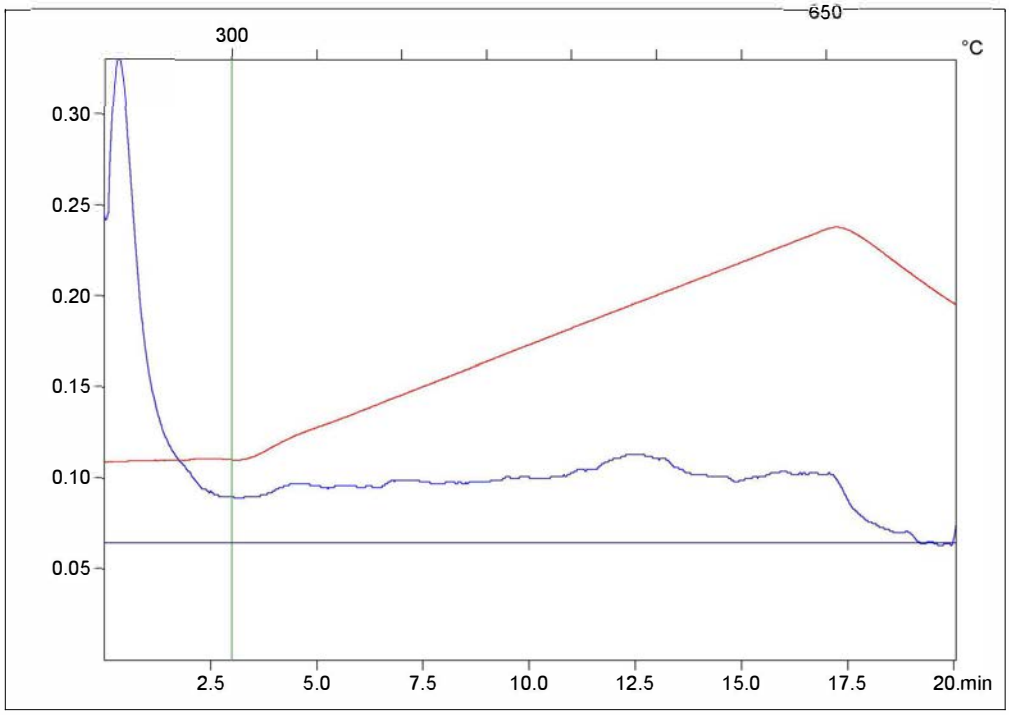
State	Ok
Pyro Status	No blank substraction
Oxi Status	No blank substraction

Customer :	Customer part :
IIT Mumbai	65131

Comment :

RE6 Turbo n E907/65131/102/07

S1(mg/g)=0.04	Sample =ALPHEN 1A-1
S2(mg/g)=0.08	Method =Bulk Rock
Tmax(°C)=489	Cycle=oxi fast
TpkS2(°C)=529.0	KFID(10*9)=1472
PI=0.35	Qty(mg)=61.5
HI=38	TOC(%)=0.21



C:\2016-17\SD34\23.R00 : FID pyrolysis graphic

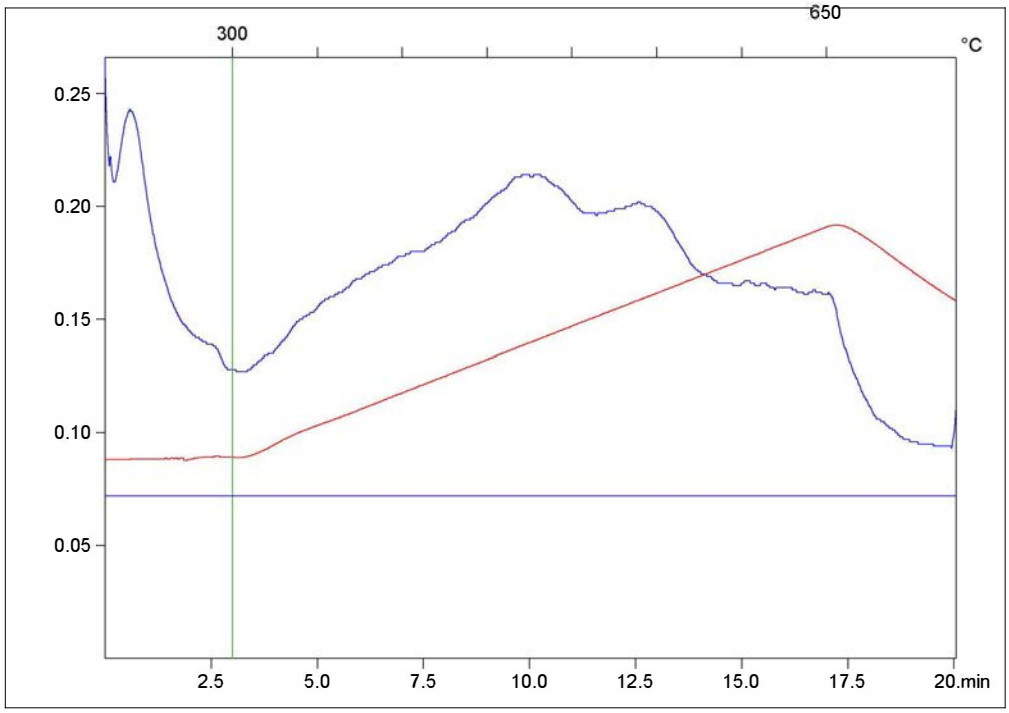
State	Ok
Pyro Status	No blank substraction
Oxi Status	No blank substraction

Customer :	Customer part :
IIT Mumbai	65131

Comment :

RE6 Turbo n E907/65131/102/07

S1(mg/g)=0.04	Sample =DI-1/247.5
S2(mg/g)=0.21	Method =Bulk Rock
Tmax(°C)=428	Cycle=oxi fast
TpkS2(°C)=468.0	KFID(10*9)=1472
PI=0.16	Qty(mg)=67.2
HI=62	TOC(%)=0.34



C:\2016-17\SD33\45.R00 : FID pyrolysis graphic

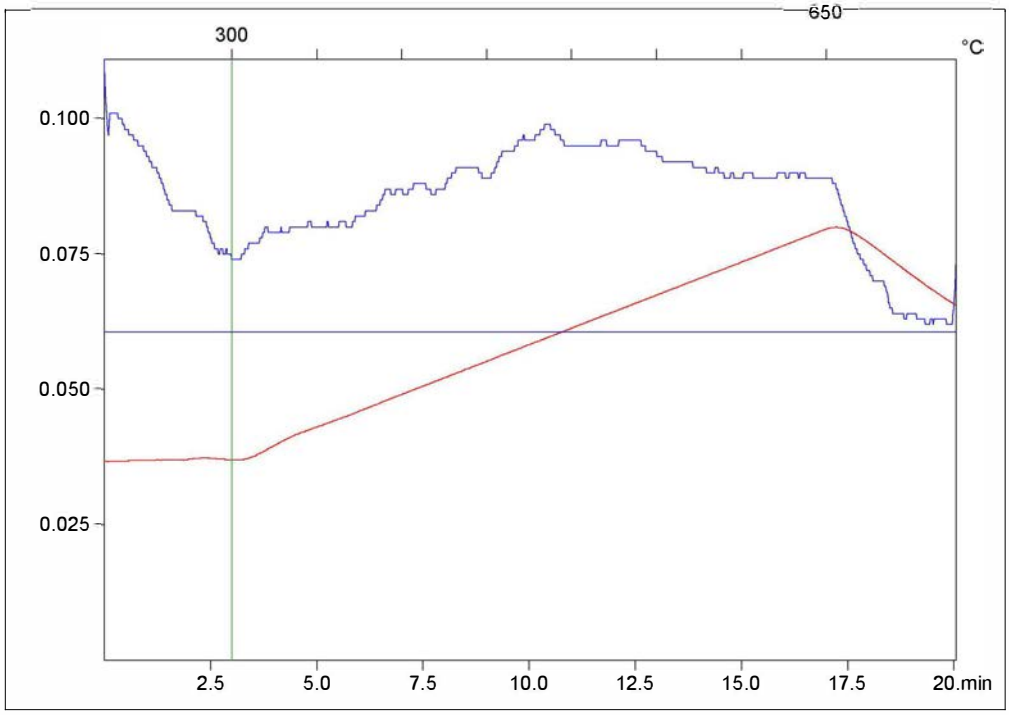
State	Ok
Pyro Status	No blank substraction
Oxi Status	No blank substraction

Customer :	Customer part :
IIT Mumbai	65131

Comment :

RE6 Turbo n E907/65131/102/07

S1(mg/g)=0.01	Sample =DM-1(3)
S2(mg/g)=0.06	Method =Bulk Rock
Tmax(°C)=441	Cycle=oxi fast
TpkS2(°C)=481.0	KFID(10*9)=1472
PI=0.16	Qty(mg)=62.0
HI=150	TOC(%)=0.04



C:\2016-17\SD34\94.R00 : FID pyrolysis graphic

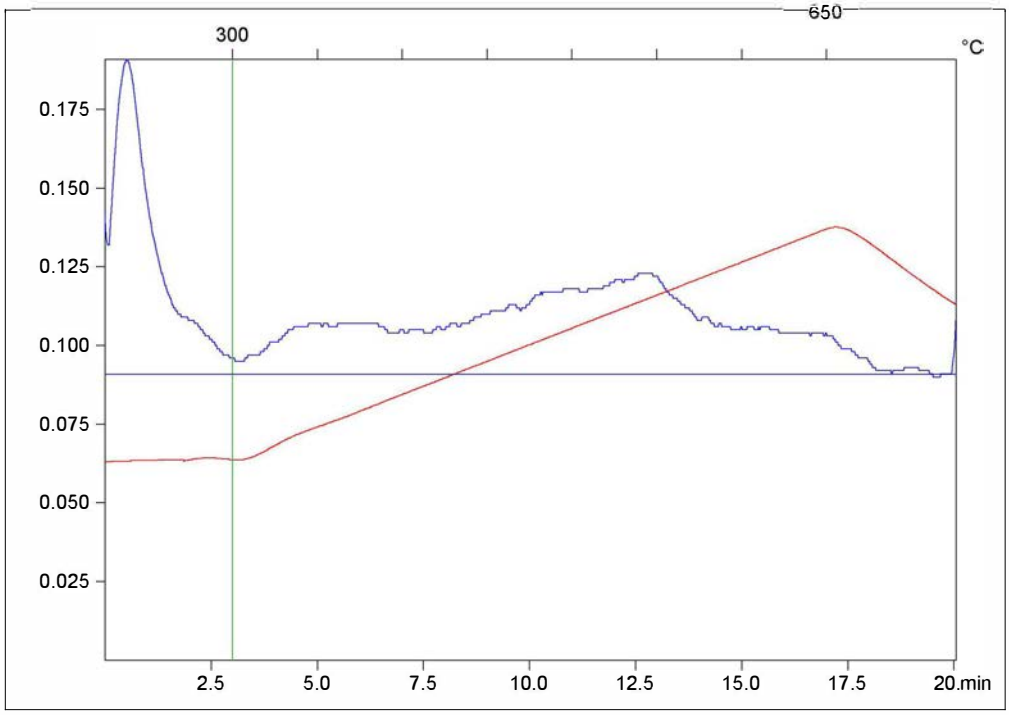
State	Ok
Pyro Status	No blank substraction
Oxi Status	No blank substraction

Customer :	Customer part :
IIT Mumbai	65131

Comment :

RE6 Turbo n E907/65131/102/07

S1(mg/g)=0.02	Sample =DM-2
S2(mg/g)=0.04	Method =Bulk Rock
Tmax(°C)=496	Cycle=oxi fast
TpkS2(°C)=536.0	KFID(10*9)=1472
PI=0.3	Qty(mg)=61.4
HI=40	TOC(%)=0.1



C:\2016-17\SD34\83.R00 : FID pyrolysis graphic

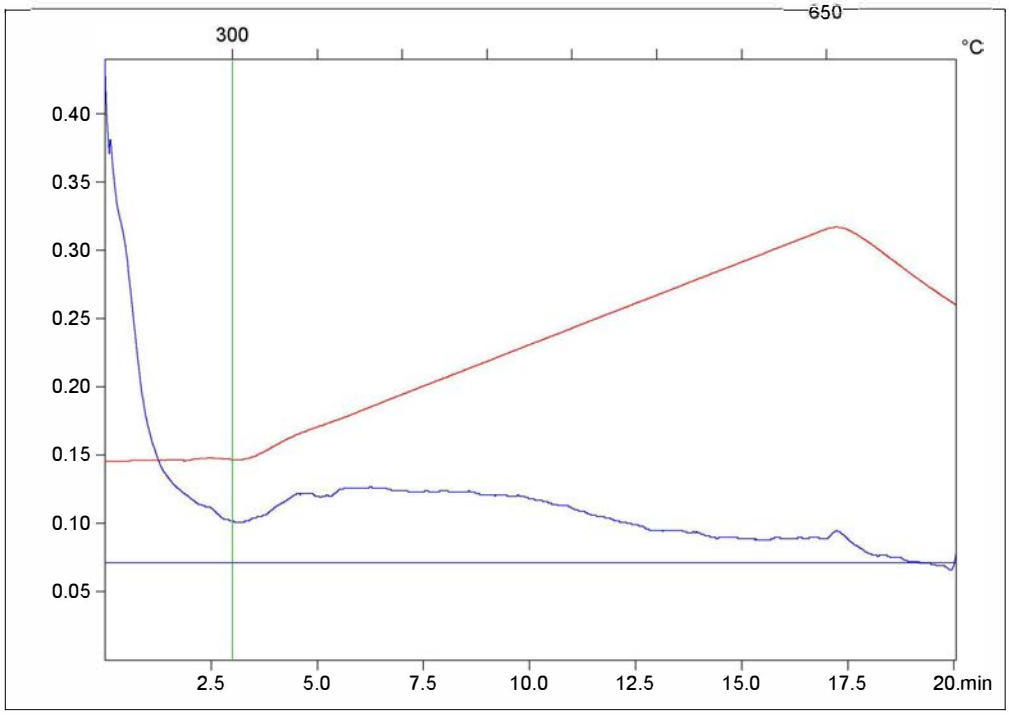
State	Ok
Pyro Status	No blank substraction
Oxi Status	No blank substraction

Customer :	Customer part :
IIT Mumbai	65131

Comment :

RE6 Turbo n E907/65131/102/07

S1(mg/g)=0.05	Sample =GAM-1
S2(mg/g)=0.08	Method =Bulk Rock
Tmax(°C)=339	Cycle=oxi fast
TpkS2(°C)=379.0	KFID(10*9)=1472
PI=0.37	Qty(mg)=60.2
HI=1	TOC(%)=7.37



C:\2016-17\SD34\59.R00 : FID pyrolysis graphic

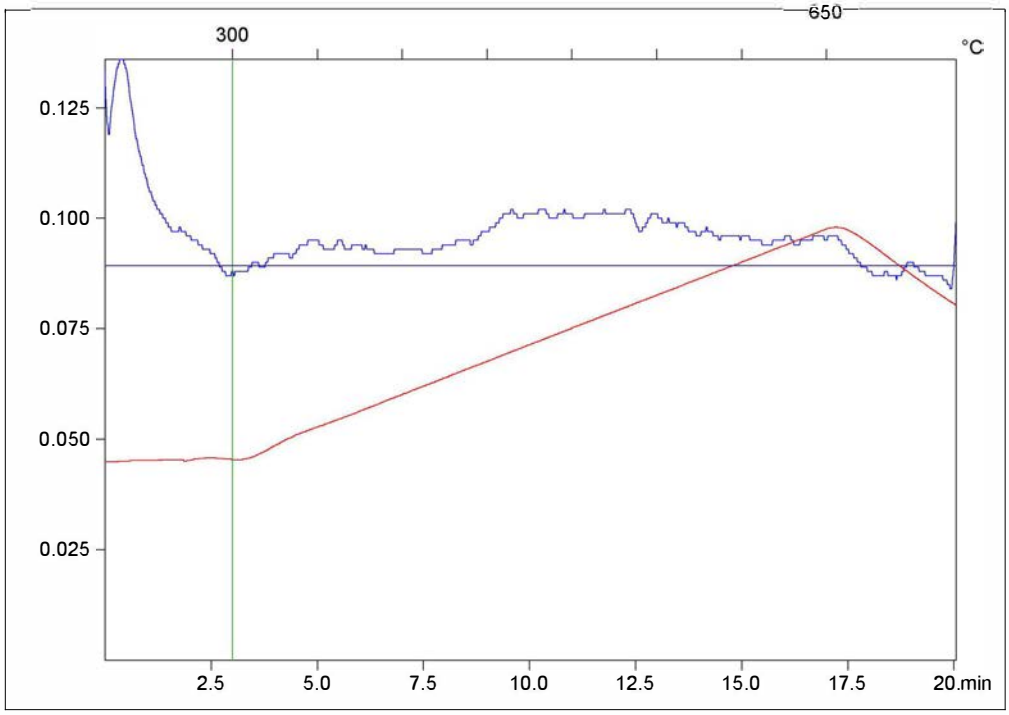
State	Ok
Pyro Status	No blank substraction
Oxi Status	No blank substraction

Customer :	Customer part :
IIT Mumbai	65131

Comment :

RE6 Turbo n E907/65131/102/07

S1(mg/g)=0.01	Sample =GAM-2
S2(mg/g)=0.01	Method =Bulk Rock
Tmax(°C)=422	Cycle=oxi fast
TpkS2(°C)=462.0	KFID(10*9)=1472
PI=0.33	Qty(mg)=61.5
HI=33	TOC(%)=0.03



C:\2016-17\SD34\84.R00 : FID pyrolysis graphic

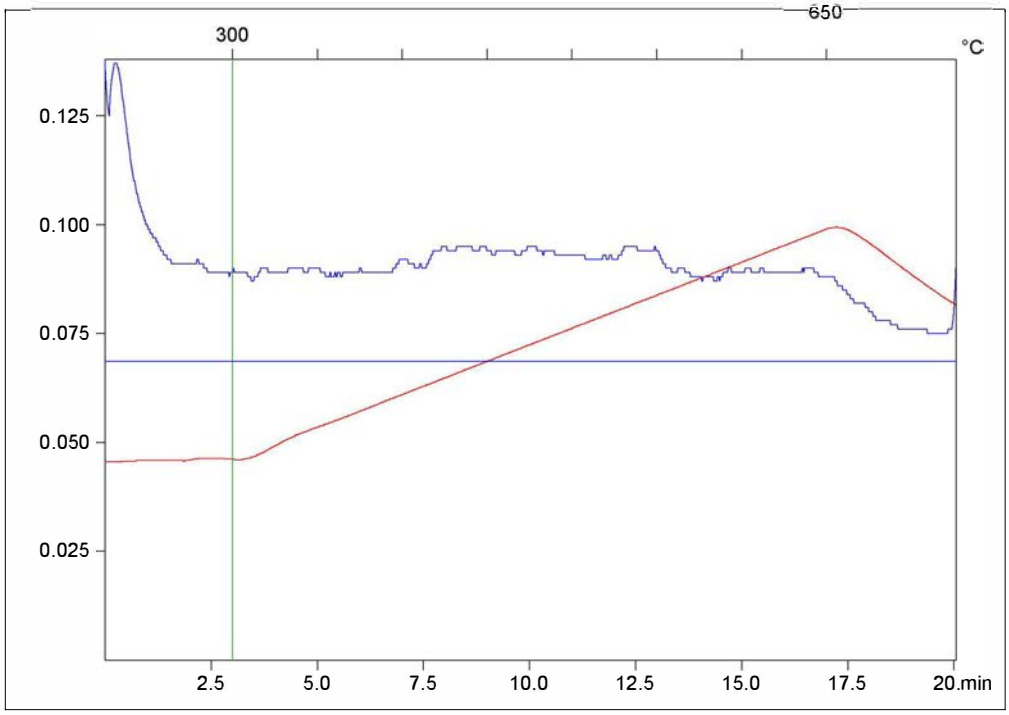
State	P artial
Pyro Status	No blank substraction
Oxi Status	Oxidation analysis not made

Customer :	Customer part :
IIT Mumbai	65131

Comment :

RE6 Turbo n E907/65131/102/07

S1(mg/g)=0.01	Sample =GAM-3
S2(mg/g)=0.05	Method =Bulk Rock
Tmax(°C)=381	Cycle=oxi fast
TpkS2(°C)=421.0	KFID(10*9)=1472
PI=0.22	Qty(mg)=62.3
HI=23	TOC(%)=0.22



C:\2016-17\SD34\85.R00 : FID pyrolysis graphic

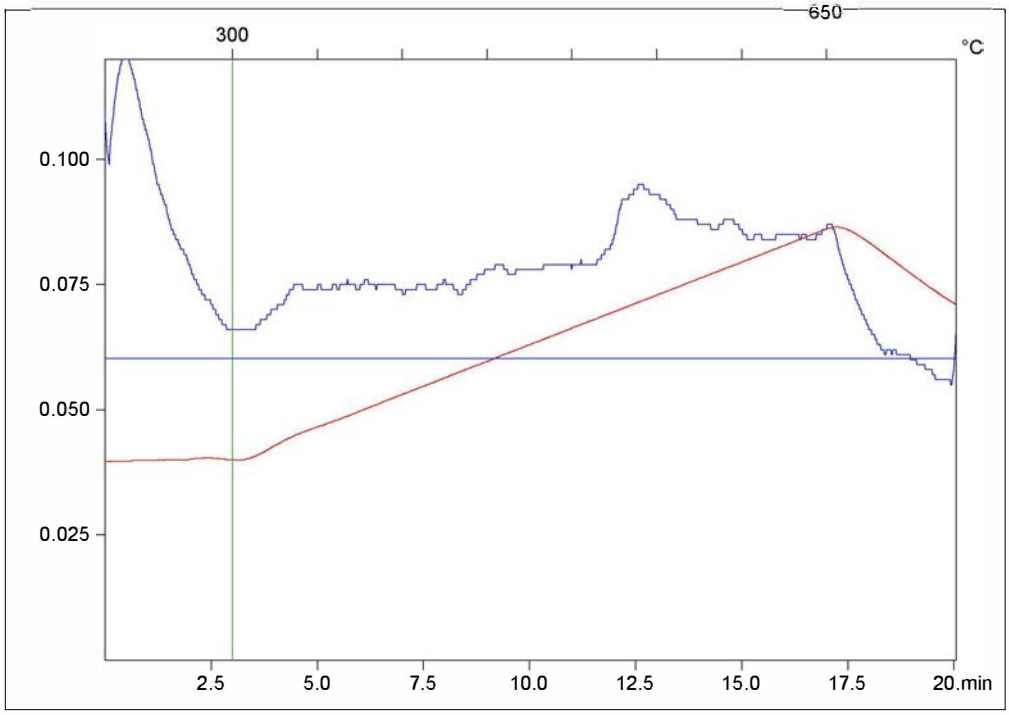
State	Ok
Pyro Status	No blank substraction
Oxi Status	No blank substraction

Customer :	Customer part :
IIT Mumbai	65131

Comment :

RE6 Turbo n E907/65131/102/07

S1(mg/g)=0.01	Sample =GAM-4(2)
S2(mg/g)=0.04	Method =Bulk Rock
Tmax(°C)=496	Cycle=oxi fast
TpkS2(°C)=536.0	KFID(10*9)=1472
PI=0.24	Qty(mg)=62.8
HI=6	TOC(%)=0.67



C:\2016-17\SD34\93.R00 : FID pyrolysis graphic

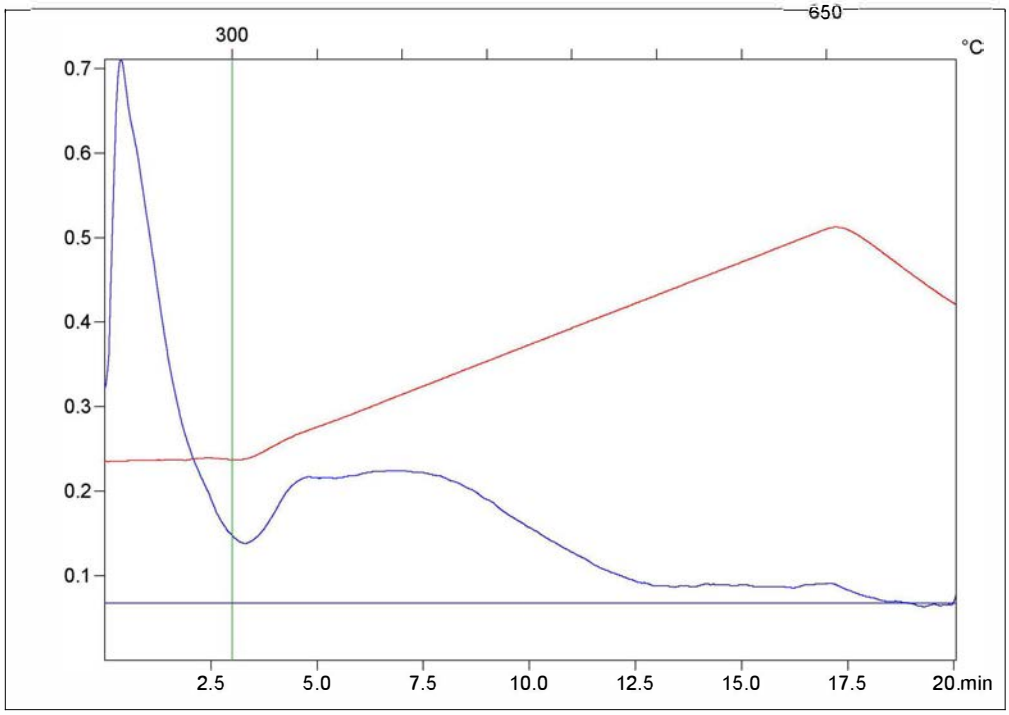
State	Ok
Pyro Status	No blank substraction
Oxi Status	No blank substraction

Customer :	Customer part :
IIT Mumbai	65131

Comment :

RE6 Turbo n E907/65131/102/07

S1(mg/g)=0.13	Sample =GKF1/268.30
S2(mg/g)=0.16	Method =Bulk Rock
Tmax(°C)=348	Cycle=oxi fast
TpkS2(°C)=388.0	KFID(10*9)=1472
PI=0.45	Qty(mg)=62.6
HI=4	TOC(%)=4.57



C:\2016-17\SD34\61.R00 : FID pyrolysis graphic

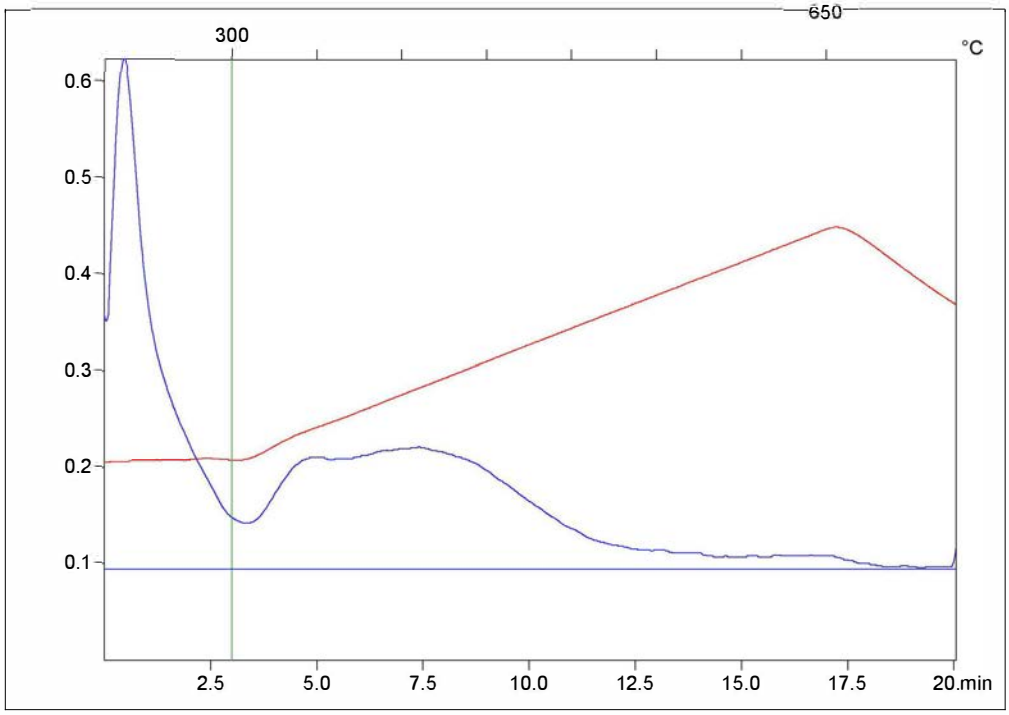
State	Ok
Pyro Status	No blank substraction
Oxi Status	No blank substraction

Customer :	Customer part :
IIT Mumbai	65131

Comment :

RE6 Turbo n E907/65131/102/07

S1(mg/g)=0.1	Sample =GKF1/288.10
S2(mg/g)=0.13	Method =Bulk Rock
Tmax(°C)=367	Cycle=oxi fast
TpkS2(°C)=407.0	KFID(10*9)=1472
PI=0.43	Qty(mg)=60.6
HI=4	TOC(%)=3.49



C:\2016-17\SD34\77.R00 : FID pyrolysis graphic

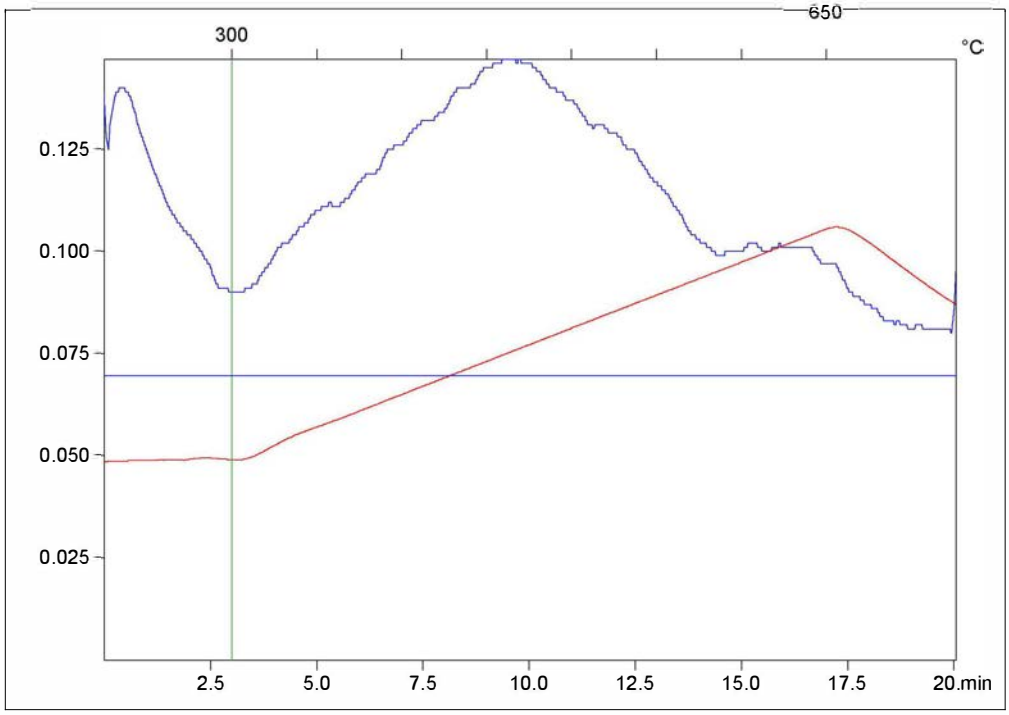
State	Ok
Pyro Status	No blank substraction
Oxi Status	No blank substraction

Customer :	Customer part :
IIT Mumbai	65131

Comment :

RE6 Turbo n E907/65131/102/07

S1(mg/g)=0.02	Sample =GKF1/395.40
S2(mg/g)=0.11	Method =Bulk Rock
Tmax(°C)=417	Cycle=oxi fast
TpkS2(°C)=457.0	KFID(10*9)=1472
PI=0.15	Qty(mg)=61.6
HI=31	TOC(%)=0.35



C:\2016-17\SD34\87.R00 : FID pyrolysis graphic

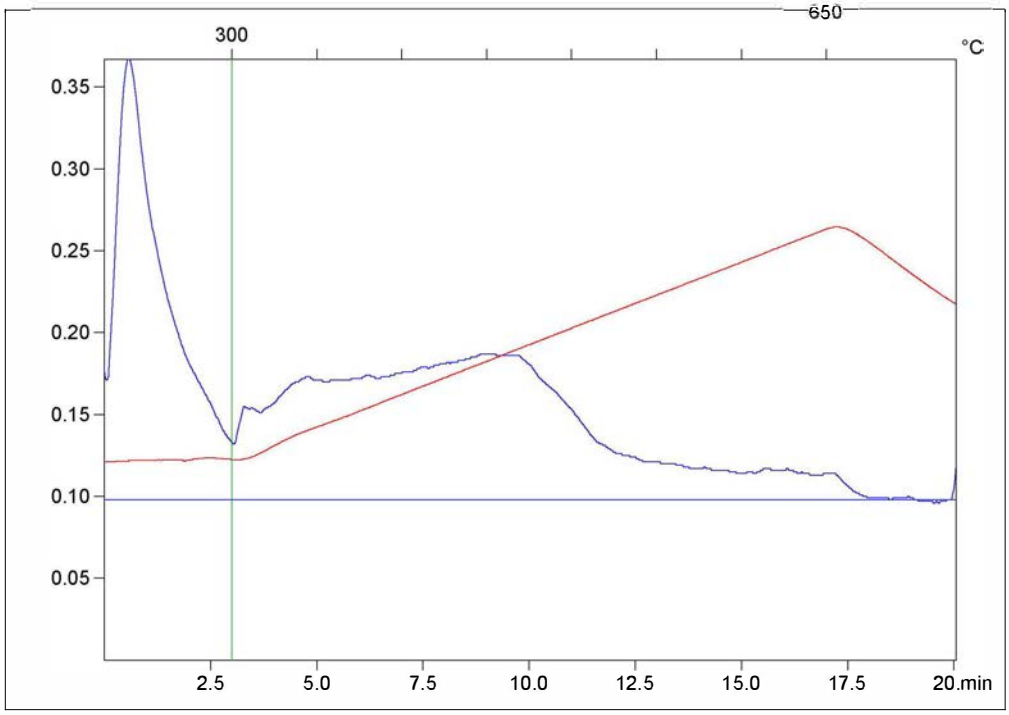
State	Ok
Pyro Status	No blank substraction
Oxi Status	No blank substraction

Customer :	Customer part :
IIT Mumbai	65131

Comment :

RE6 Turbo n E907/65131/102/07

S1(mg/g)=0.06	Sample =GKF-1/838.65
S2(mg/g)=0.11	Method =Bulk Rock
Tmax(°C)=404	Cycle=oxi fast
TpkS2(°C)=444.0	KFID(10*9)=1472
PI=0.34	Qty(mg)=60.8
HI=35	TOC(%)=0.31



C:\2016-17\SD34\75.R00 : FID pyrolysis graphic

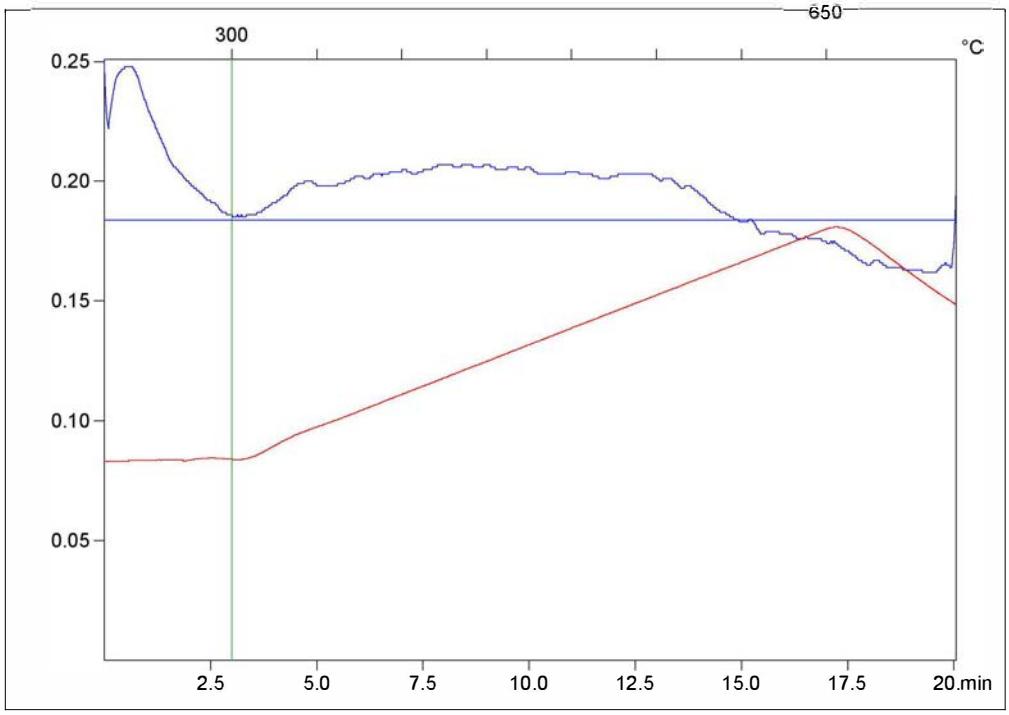
State	Ok
Pyro Status	No blank substraction
Oxi Status	No blank substraction

Customer :	Customer part :
IIT Mumbai	65131

Comment :

RE6 Turbo n E907/65131/102/07

S1(mg/g)=0.01	Sample =GKF-1/919.35
S2(mg/g)=0.03	Method =Bulk Rock
Tmax(°C)=379	Cycle=oxi fast
TpkS2(°C)=419.0	KFID(10*9)=1472
PI=0.33	Qty(mg)=60.8
HI=18	TOC(%)=0.17



C:\2016-17\SD34\65.R00 : FID pyrolysis graphic

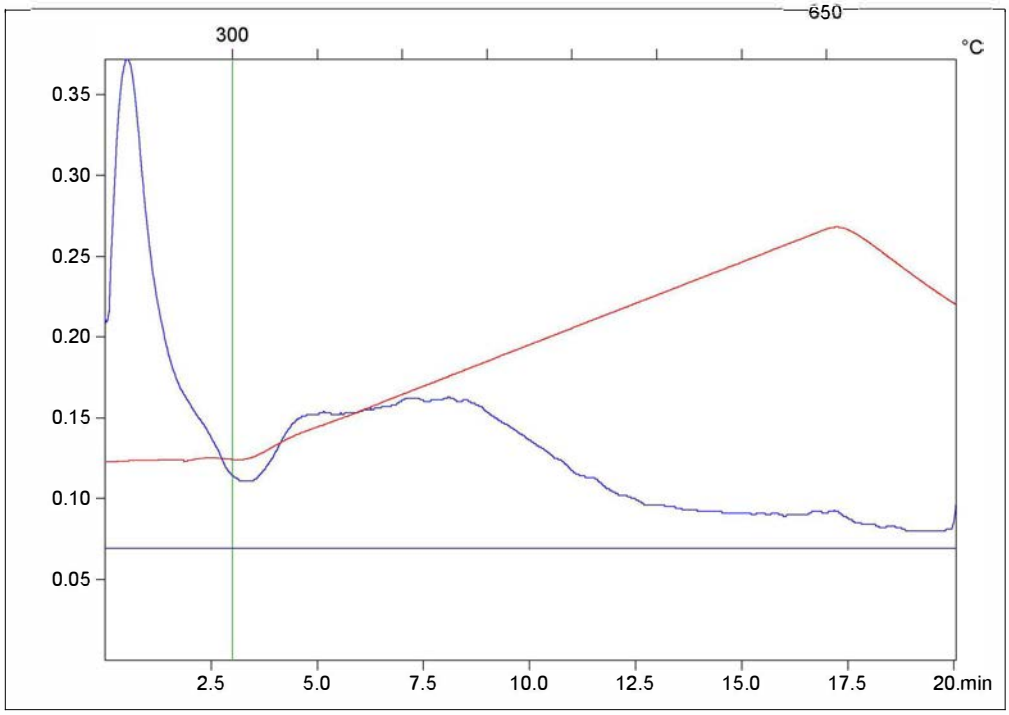
State	Ok
Pyro Status	No blank substraction
Oxi Status	No blank substraction

Customer :	Customer part :
IIT Mumbai	65131

Comment :

RE6 Turbo n E907/65131/102/07

S1(mg/g)=0.06	Sample =GKF1/1151.85
S2(mg/g)=0.12	Method =Bulk Rock
Tmax(°C)=384	Cycle=oxi fast
TpkS2(°C)=424.0	KFID(10*9)=1472
PI=0.35	Qty(mg)=60.9
HI=4	TOC(%)=2.75



C:\2016-17\SD34\86.R00 : FID pyrolysis graphic

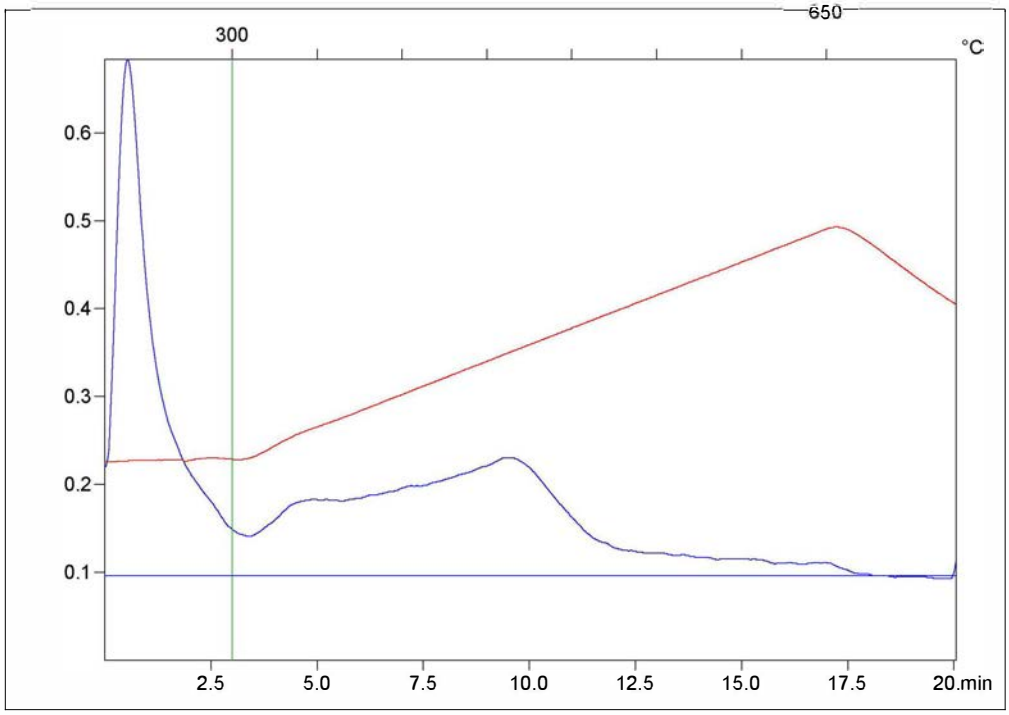
State	Ok
Pyro Status	No blank substraction
Oxi Status	No blank substraction

Customer :	Customer part :
IIT Mumbai	65131

Comment :

RE6 Turbo n E907/65131/102/07

S1(mg/g)=0.1	Sample =GKF1/1348.81
S2(mg/g)=0.13	Method =Bulk Rock
Tmax(°C)=417	Cycle=oxi fast
TpkS2(°C)=457.0	KFID(10*9)=1472
PI=0.43	Qty(mg)=61.6
HI=52	TOC(%)=0.25



C:\2016-17\SD34\76.R00 : FID pyrolysis graphic

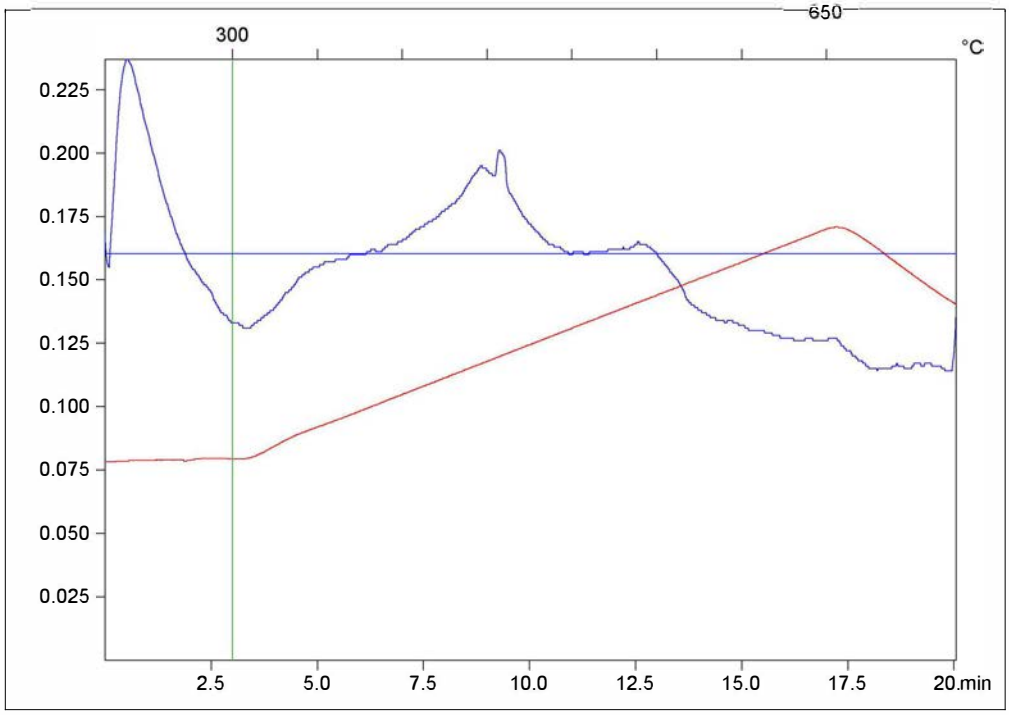
State	Ok
Pyro Status	No blank substraction
Oxi Status	No blank substraction

Customer :	Customer part :
IIT Mumbai	65131

Comment :

RE6 Turbo n E907/65131/102/07

S1(mg/g)=0.01	Sample =GKF-1/1408.7
S2(mg/g)=0.01	Method =Bulk Rock
Tmax(°C)=414	Cycle=oxi fast
TpkS2(°C)=454.0	KFID(10*9)=1472
PI=0.49	Qty(mg)=62.2
HI=7	TOC(%)=0.14



C:\2016-17\SD34\70.R00 : FID pyrolysis graphic

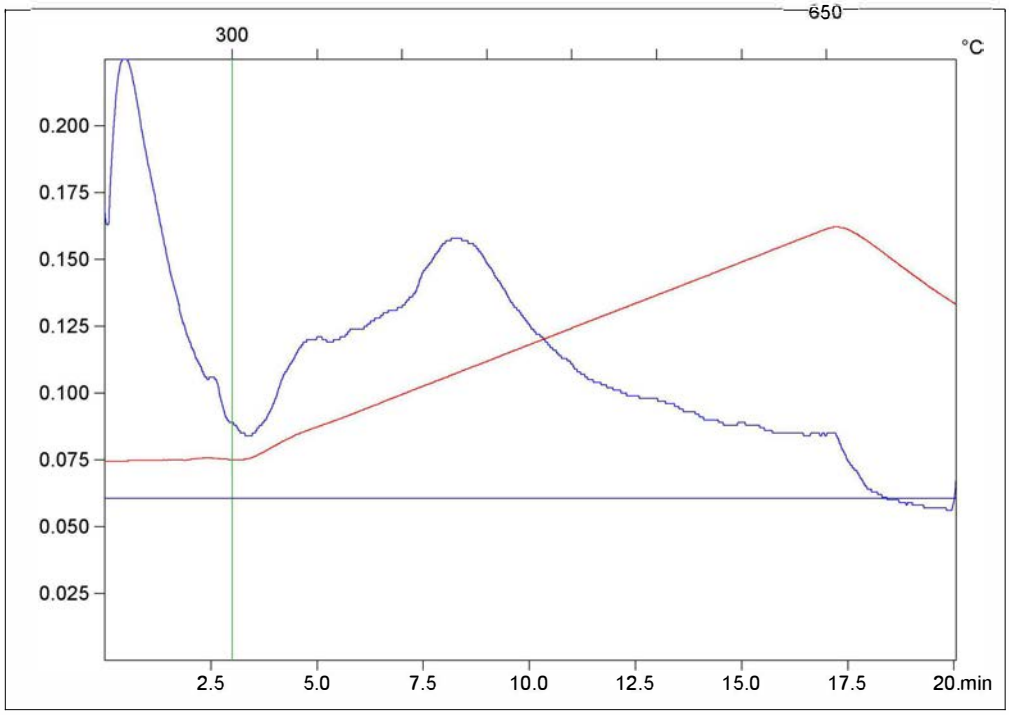
State	Ok
Pyro Status	No blank substraction
Oxi Status	No blank substraction

Customer :	Customer part :
IIT Mumbai	65131

Comment :

RE6 Turbo n E907/65131/102/07

S1(mg/g)=0.04	Sample =GKF1/1430.82
S2(mg/g)=0.1	Method =Bulk Rock
Tmax(°C)=387	Cycle=oxi fast
TpkS2(°C)=427.0	KFID(10*9)=1472
PI=0.27	Qty(mg)=61.8
HI=22	TOC(%)=0.45



C:\2016-17\SD34\96.R00 : FID pyrolysis graphic

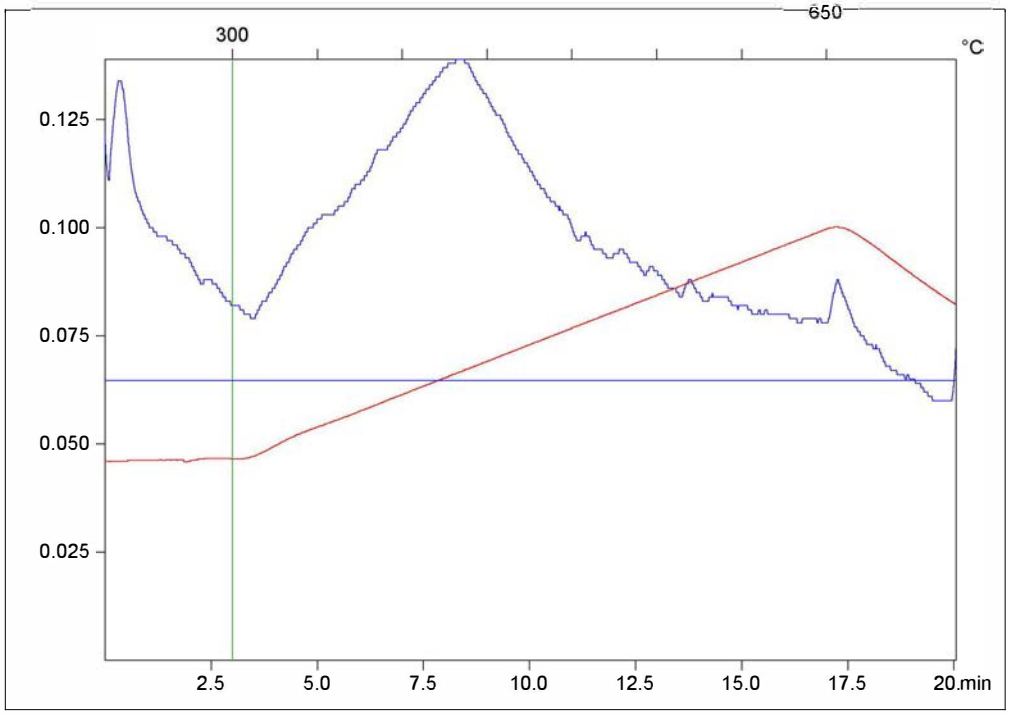
State	Ok
Pyro Status	No blank substraction
Oxi Status	No blank substraction

Customer :	Customer part :
IIT Mumbai	65131

Comment :

RE6 Turbo n E907/65131/102/07

S1(mg/g)=0.02	Sample =GKP1/341.45
S2(mg/g)=0.08	Method =Bulk Rock
Tmax(°C)=389	Cycle=oxi fast
TpkS2(°C)=429.0	KFID(10*9)=1472
PI=0.17	Qty(mg)=60.7
HI=8	TOC(%)=1.04



C:\2016-17\SD34\90.R00 : FID pyrolysis graphic

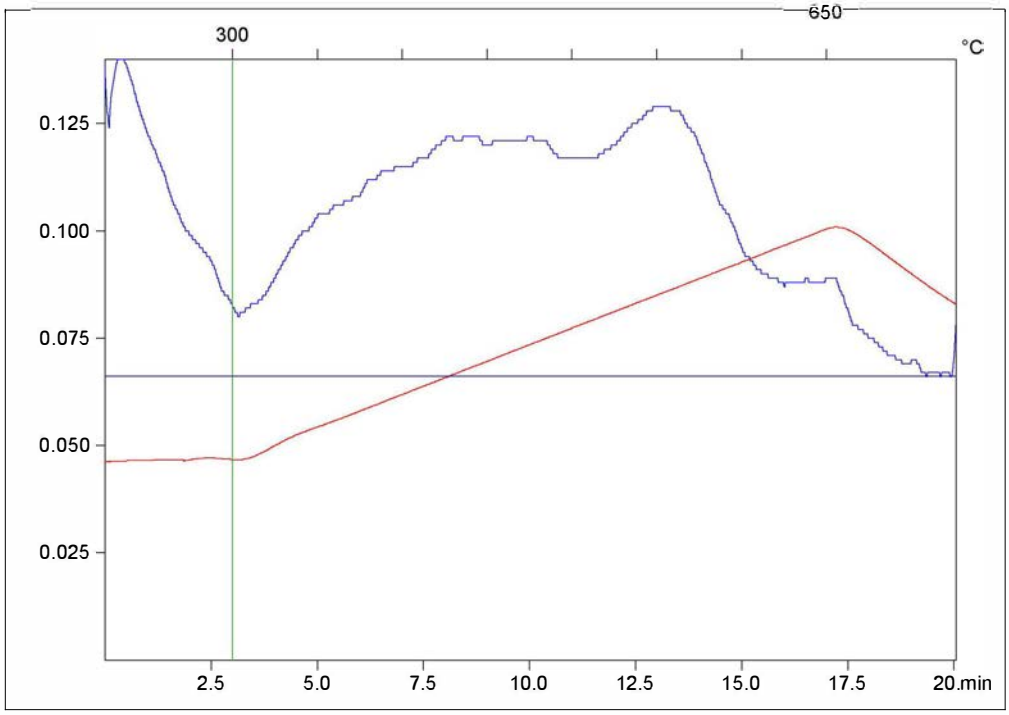
State	Ok
Pyro Status	No blank substraction
Oxi Status	No blank substraction

Customer :	Customer part :
IIT Mumbai	65131

Comment :

RE6 Turbo n E907/65131/102/07

S1(mg/g)=0.02	Sample =GKP1/427.40
S2(mg/g)=0.09	Method =Bulk Rock
Tmax(°C)=504	Cycle=oxi fast
TpkS2(°C)=544.0	KFID(10*9)=1472
PI=0.18	Qty(mg)=64.6
HI=26	TOC(%)=0.35



C:\2016-17\SD34\89.R00 : FID pyrolysis graphic

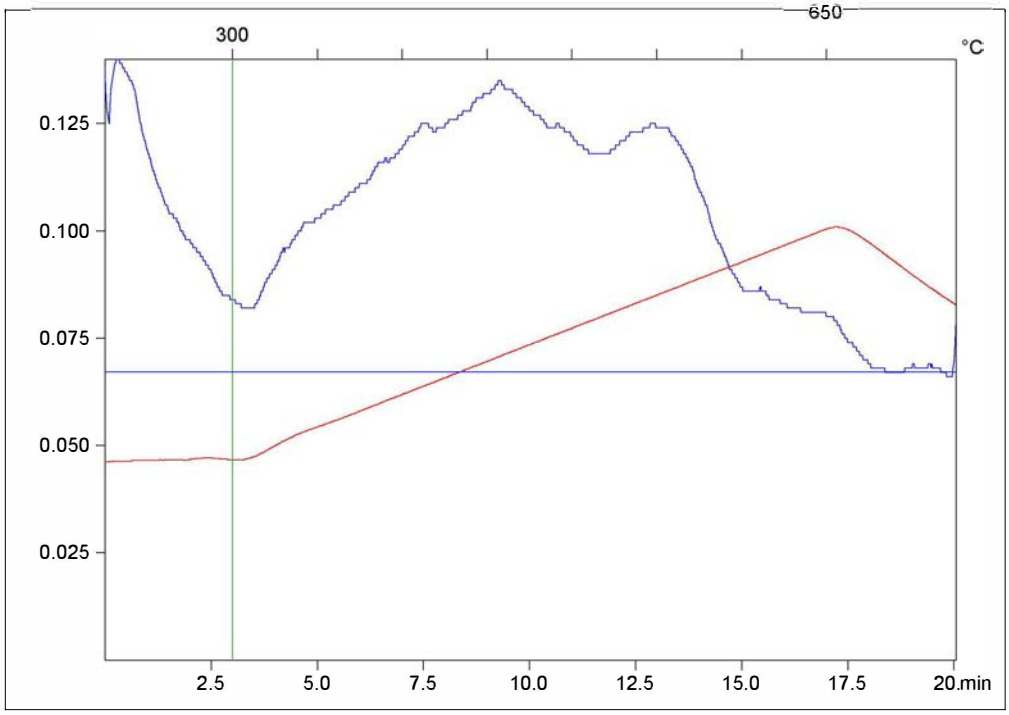
State	Ok
Pyro Status	No blank substraction
Oxi Status	No blank substraction

Customer :	Customer part :
IIT Mumbai	65131

Comment :

RE6 Turbo n E907/65131/102/07

S1(mg/g)=0.02	Sample =GKP1/645.23
S2(mg/g)=0.09	Method =Bulk Rock
Tmax(°C)=414	Cycle=oxi fast
TpkS2(°C)=454.0	KFID(10*9)=1472
PI=0.17	Qty(mg)=60.8
HI=24	TOC(%)=0.37



C:\2016-17\SD34\88.R00 : FID pyrolysis graphic

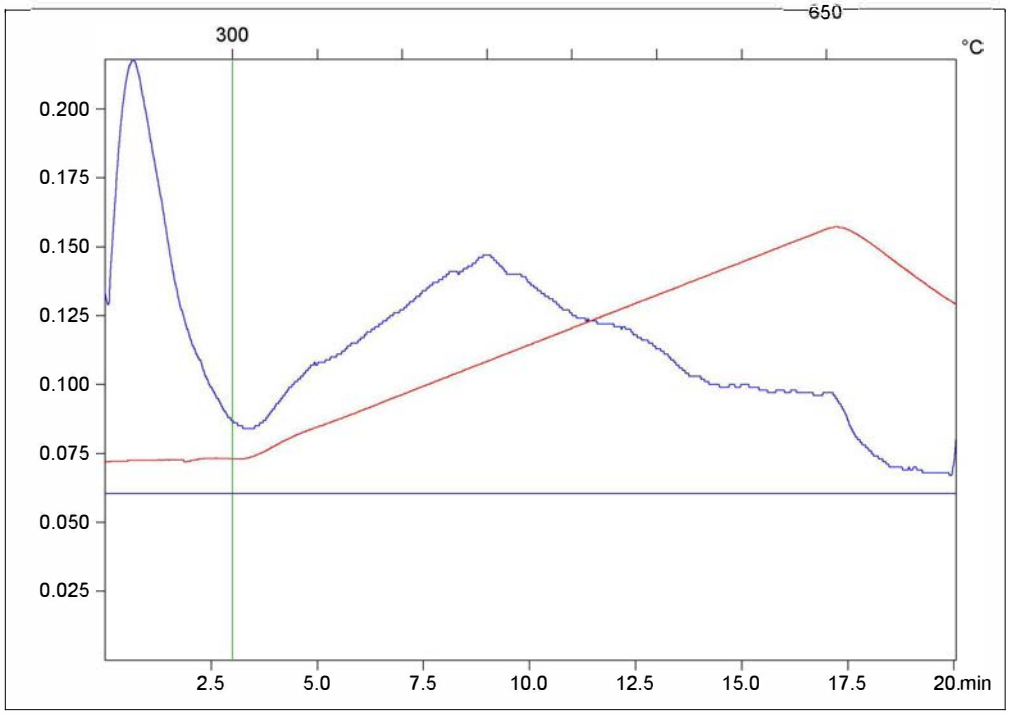
State	Ok
Pyro Status	No blank substraction
Oxi Status	No blank substraction

Customer :	Customer part :
IIT Mumbai	65131

Comment :

RE6 Turbo n E907/65131/102/07

S1(mg/g)=0.04	Sample =GKP1/1055.70
S2(mg/g)=0.12	Method =Bulk Rock
Tmax(°C)=405	Cycle=oxi fast
TpkS2(°C)=445.0	KFID(10*9)=1472
PI=0.24	Qty(mg)=61.4
HI=26	TOC(%)=0.46



C:\2016-17\SD34\95.R00 : FID pyrolysis graphic

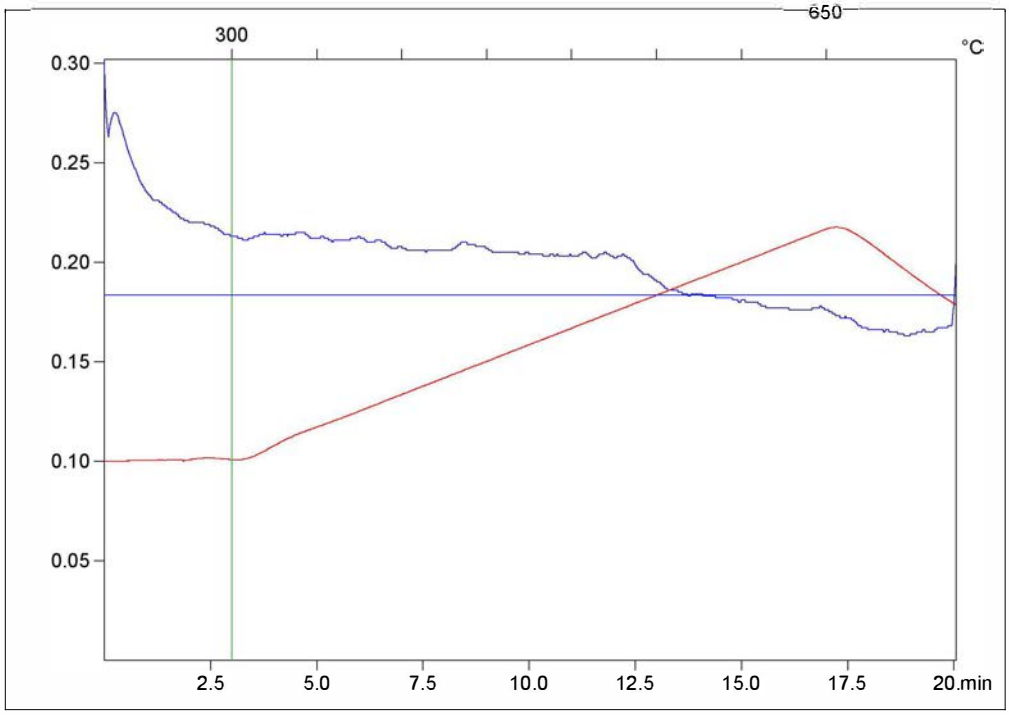
State	Ok
Pyro Status	No blank substraction
Oxi Status	No blank substraction

Customer :	Customer part :
IIT Mumbai	65131

Comment :

RE6 Turbo n E907/65131/102/07

S1(mg/g)=0.02	Sample =HF-1
S2(mg/g)=0.03	Method =Bulk Rock
Tmax(°C)=273	Cycle=oxi fast
TpkS2(°C)=313.0	KFID(10*9)=1472
PI=0.39	Qty(mg)=61.2
HI=60	TOC(%)=0.05



C:\2016-17\SD34\63.R00 : FID pyrolysis graphic

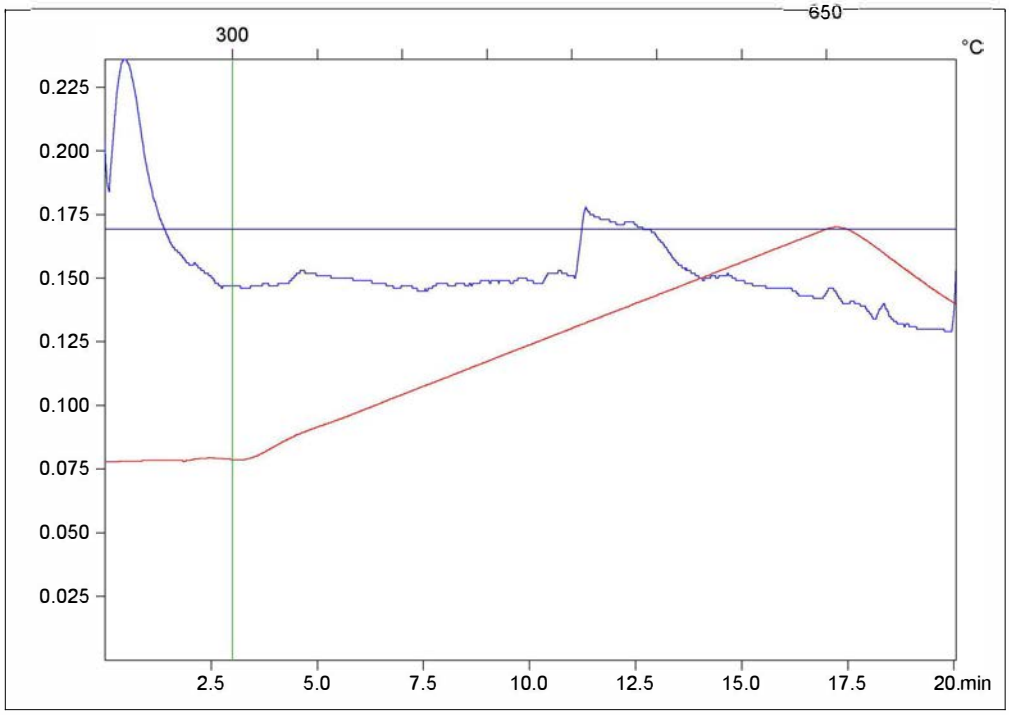
State	Ok
Pyro Status	No blank substraction
Oxi Status	No blank substraction

Customer :	Customer part :
IIT Mumbai	65131

Comment :

RE6 Turbo n E907/65131/102/07

S1(mg/g)=0.01	Sample =HF-2
S2(mg/g)=0	Method =Bulk Rock
Tmax(°C)=465	Cycle=oxi fast
TpkS2(°C)=505.0	KFID(10*9)=1472
PI=0.91	Qty(mg)=62.6
HI=0	TOC(%)=0.1



C:\2016-17\SD34\69.R00 : FID pyrolysis graphic

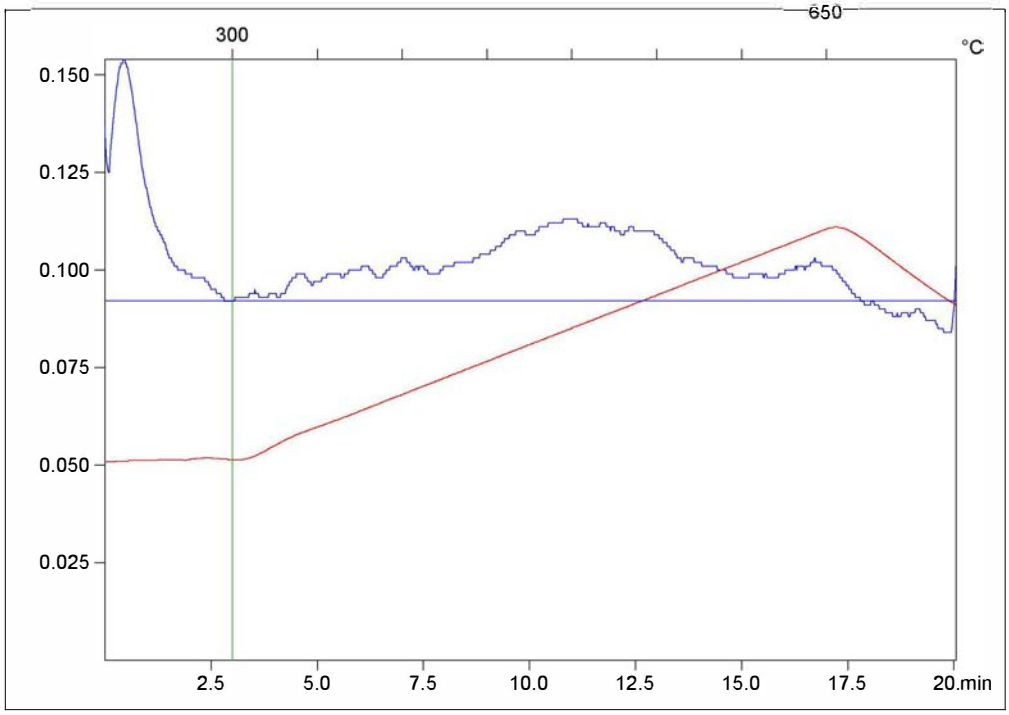
State	Ok
Pyro Status	No blank substraction
Oxi Status	No blank substraction

Customer :	Customer part :
IIT Mumbai	65131

Comment :

RE6 Turbo n E907/65131/102/07

S1(mg/g)=0.01	Sample =HF-3
S2(mg/g)=0.02	Method =Bulk Rock
Tmax(°C)=452	Cycle=oxi fast
TpkS2(°C)=492.0	KFID(10*9)=1472
PI=0.3	Qty(mg)=61.6
HI=11	TOC(%)=0.19



C:\2016-17\SD34\82.R00 : FID pyrolysis graphic

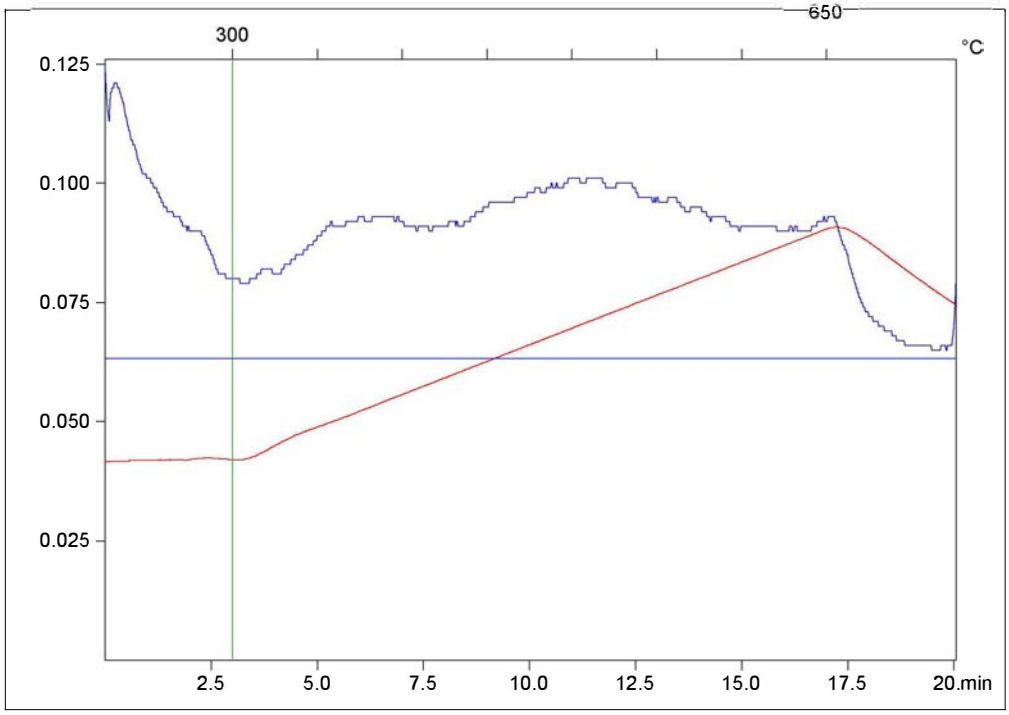
State	Ok
Pyro Status	No blank substraction
Oxi Status	No blank substraction

Customer :	Customer part :
IIT Mumbai	65131

Comment :

RE6 Turbo n E907/65131/102/07

S1(mg/g)=0.01	Sample =LIME 1
S2(mg/g)=0.06	Method =Bulk Rock
Tmax(°C)=455	Cycle=oxi fast
TpkS2(°C)=495.0	KFID(10*9)=1472
PI=0.19	Qty(mg)=61.5
HI=60	TOC(%)=0.1



C:\2016-17\SD34\6.R00 : FID pyrolysis graphic

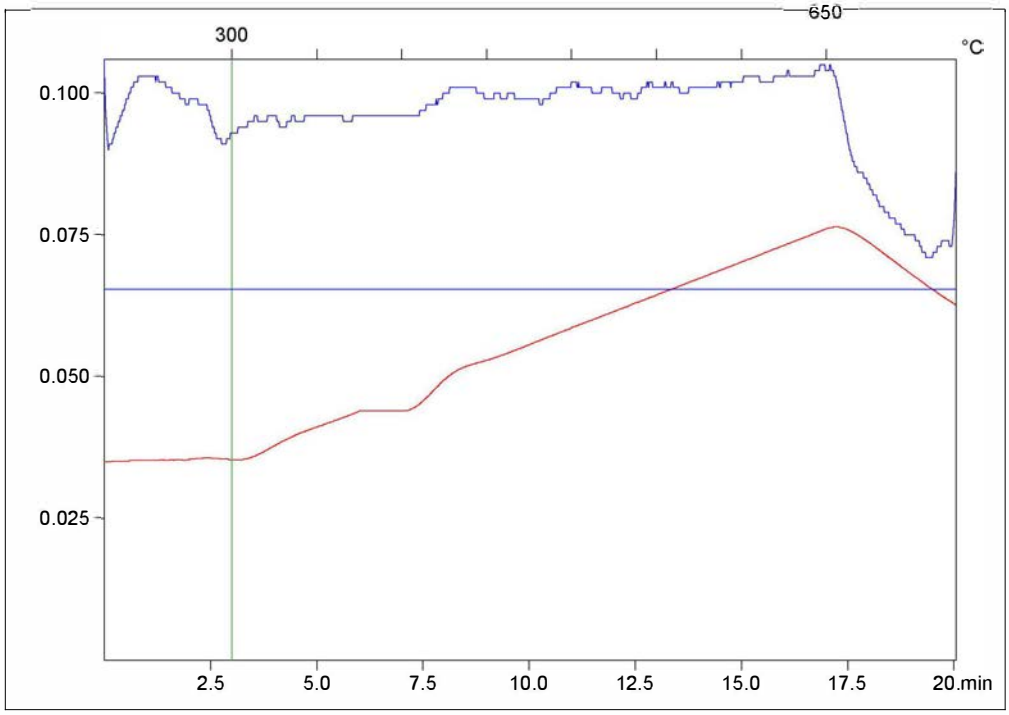
State	Ok
Pyro Status	No blank substraction
Oxi Status	No blank substraction

Customer :	Customer part :
IIT Mumbai	65131

Comment :

RE6 Turbo n E907/65131/102/07

S1(mg/g)=0.01	Sample =LIME DK3
S2(mg/g)=0.07	Method =Bulk Rock
Tmax(°C)=602	Cycle=oxi fast
TpkS2(°C)=642.0	KFID(10*9)=1472
PI=0.16	Qty(mg)=61.5
HI=700	TOC(%)=0.01



C:\2016-17\SD34\25.R00 : FID pyrolysis graphic

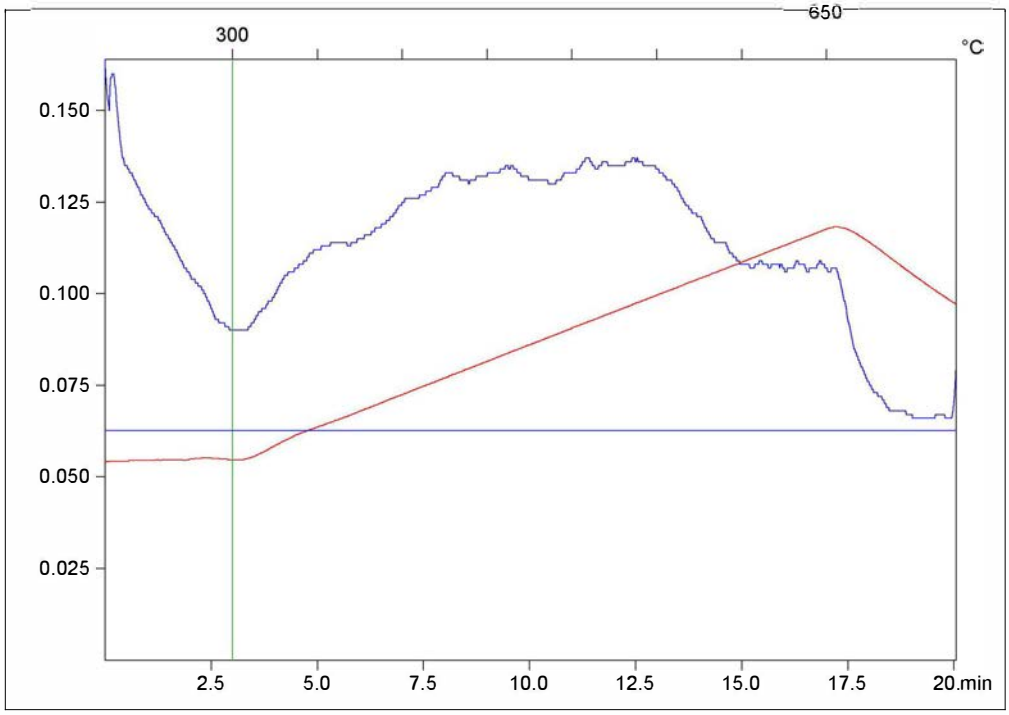
State	Ok
Pyro Status	No blank substraction
Oxi Status	No blank substraction

Customer :	Customer part :
IIT Mumbai	65131

Comment :

RE6 Turbo n E907/65131/102/07

S1(mg/g)=0.02	Sample =LIME DK4 OM
S2(mg/g)=0.12	Method =Bulk Rock
Tmax(°C)=465	Cycle=oxi fast
TpkS2(°C)=505.0	KFID(10*9)=1472
PI=0.16	Qty(mg)=62.2
HI=7	TOC(%)=1.8



C:\2016-17\SD34\4.R00 : FID pyrolysis graphic

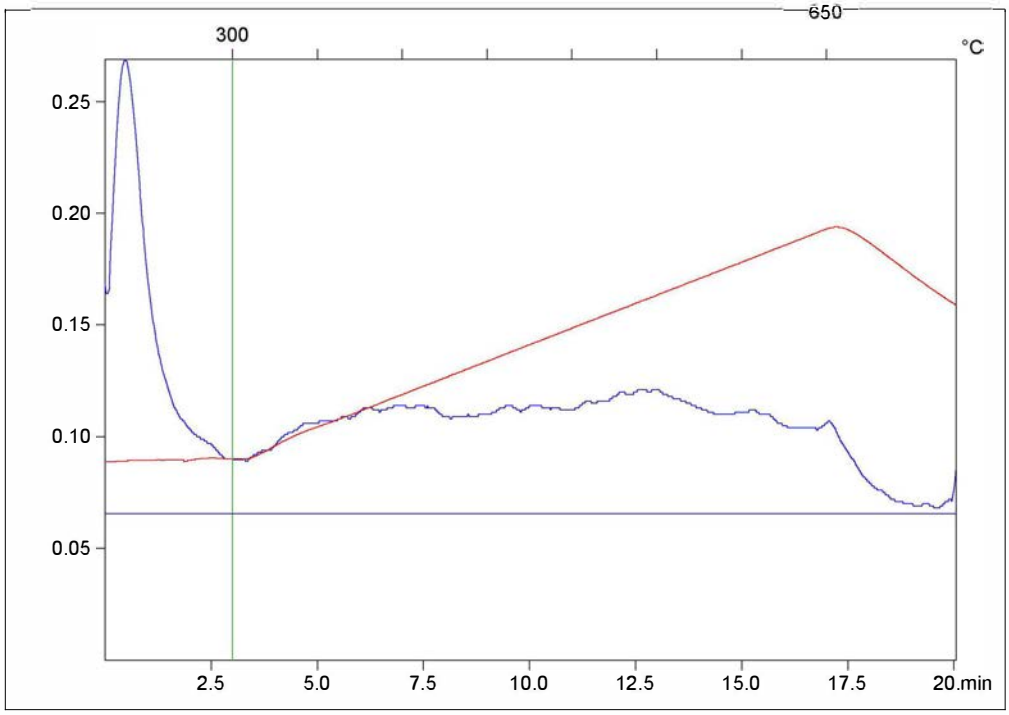
State	Ok
Pyro Status	No blank substraction
Oxi Status	No blank substraction

Customer :	Customer part :
IIT Mumbai	65131

Comment :

RE6 Turbo n E907/65131/102/07

S1(mg/g)=0.04	Sample =LIME DK5
S2(mg/g)=0.09	Method =Bulk Rock
Tmax(°C)=495	Cycle=oxi fast
TpkS2(°C)=535.0	KFID(10*9)=1472
PI=0.27	Qty(mg)=62.0
HI=18	TOC(%)=0.5



C:\2016-17\SD34\26.R00 : FID pyrolysis graphic

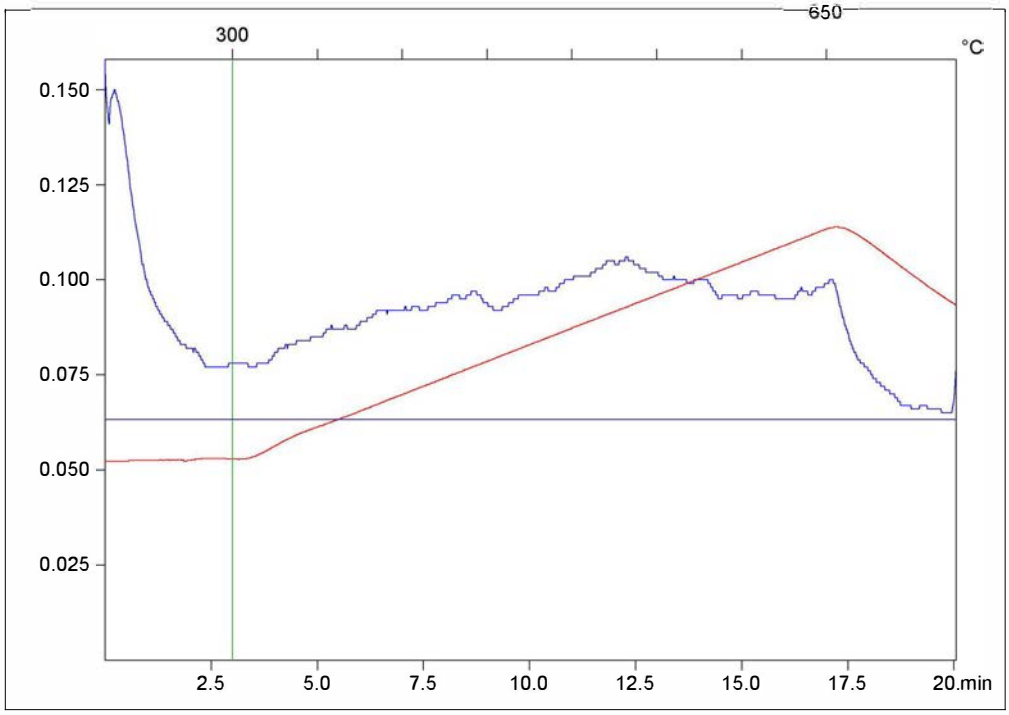
State	Ok
Pyro Status	No blank substraction
Oxi Status	No blank substraction

Customer :	Customer part :
IIT Mumbai	65131

Comment :

RE6 Turbo n E907/65131/102/07

S1(mg/g)=0.02	Sample =RE 2
S2(mg/g)=0.07	Method =Bulk Rock
Tmax(°C)=488	Cycle=oxi fast
TpkS2(°C)=528.0	KFID(10*9)=1472
PI=0.19	Qty(mg)=61.0
HI=58	TOC(%)=0.12



C:\2016-17\SD34\22.R00 : FID pyrolysis graphic

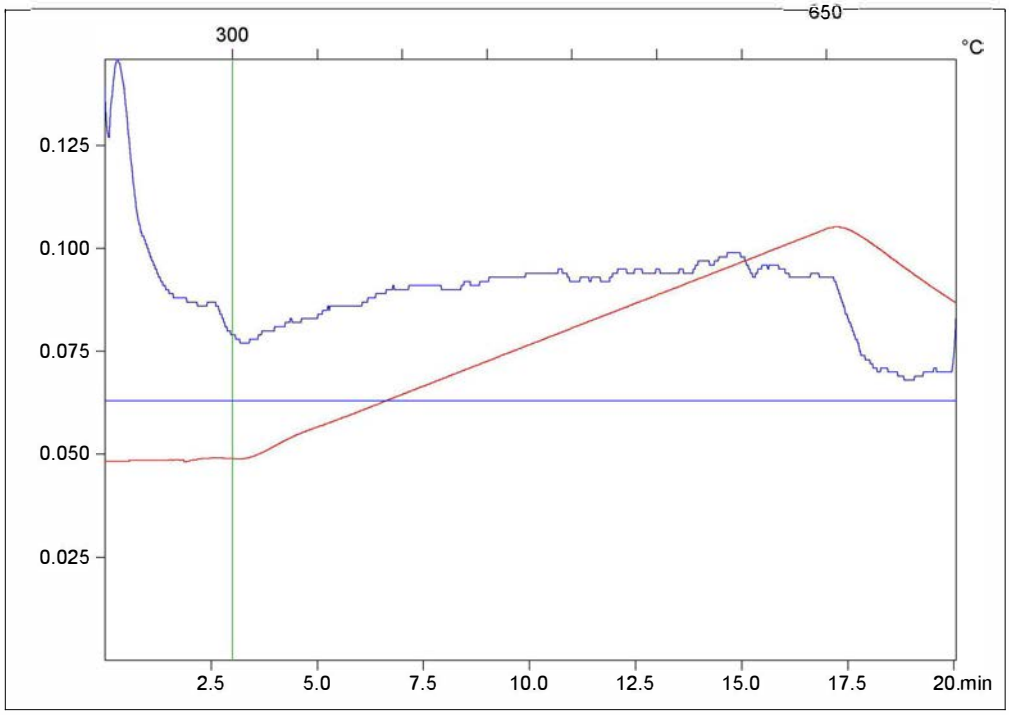
State	Ok
Pyro Status	No blank substraction
Oxi Status	No blank substraction

Customer :	Customer part :
IIT Mumbai	65131

Comment :

RE6 Turbo n E907/65131/102/07

S1(mg/g)=0.02	Sample =RE3
S2(mg/g)=0.06	Method =Bulk Rock
Tmax(°C)=548	Cycle=oxi fast
TpkS2(°C)=588.0	KFID(10*9)=1472
PI=0.21	Qty(mg)=60.3
HI=67	TOC(%)=0.09



C:\2016-17\SD34\5.R00 : FID pyrolysis graphic

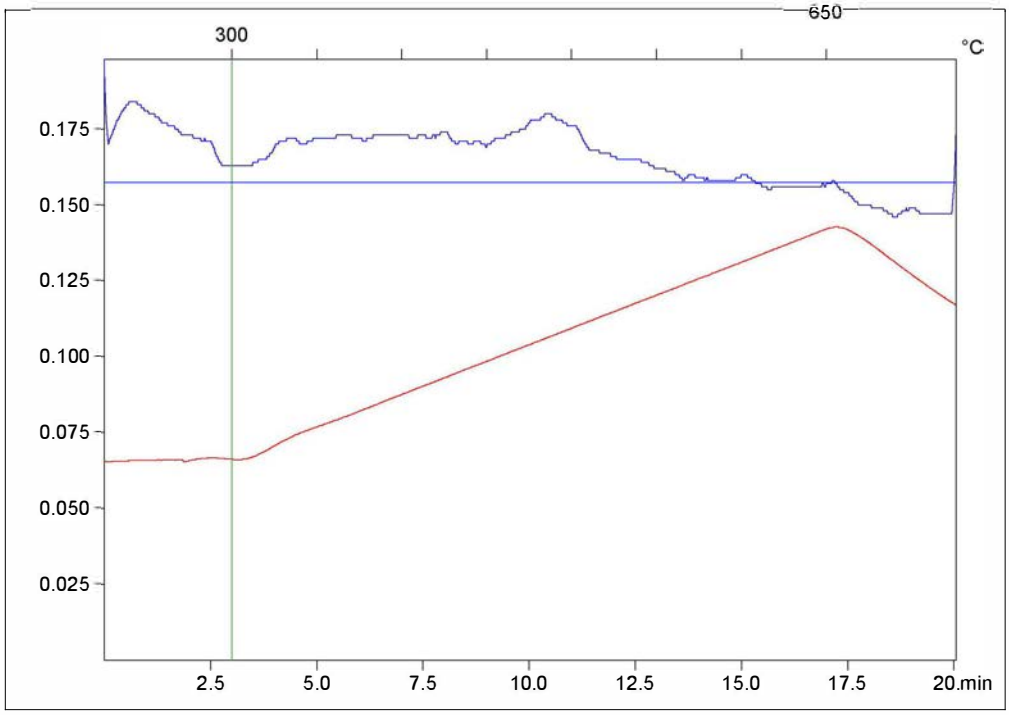
State	Ok
Pyro Status	No blank substraction
Oxi Status	No blank substraction

Customer :	Customer part :
IIT Mumbai	65131

Comment :

RE6 Turbo n E907/65131/102/07

S1(mg/g)=0.01	Sample =SPR-1/53.04
S2(mg/g)=0.02	Method =Bulk Rock
Tmax(°C)=441	Cycle=oxi fast
TpkS2(°C)=481.0	KFID(10*9)=1472
PI=0.27	Qty(mg)=60.6
HI=50	TOC(%)=0.04



C:\2016-17\SD34\71.R00 : FID pyrolysis graphic

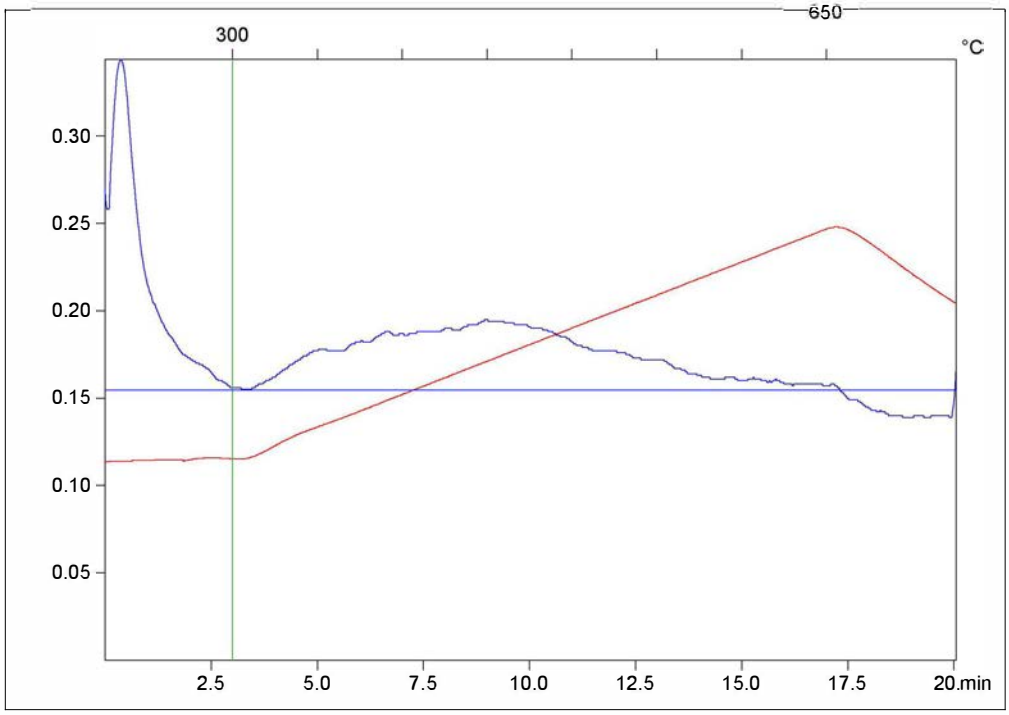
State	Ok
Pyro Status	No blank substraction
Oxi Status	No blank substraction

Customer :	Customer part :
IIT Mumbai	65131

Comment :

RE6 Turbo n E907/65131/102/07

S1(mg/g)=0.03	Sample =SPR-1/56
S2(mg/g)=0.04	Method =Bulk Rock
Tmax(°C)=406	Cycle=oxi fast
TpkS2(°C)=446.0	KFID(10*9)=1472
PI=0.38	Qty(mg)=60.1
HI=36	TOC(%)=0.11



C:\2016-17\SD34\72.R00 : FID pyrolysis graphic

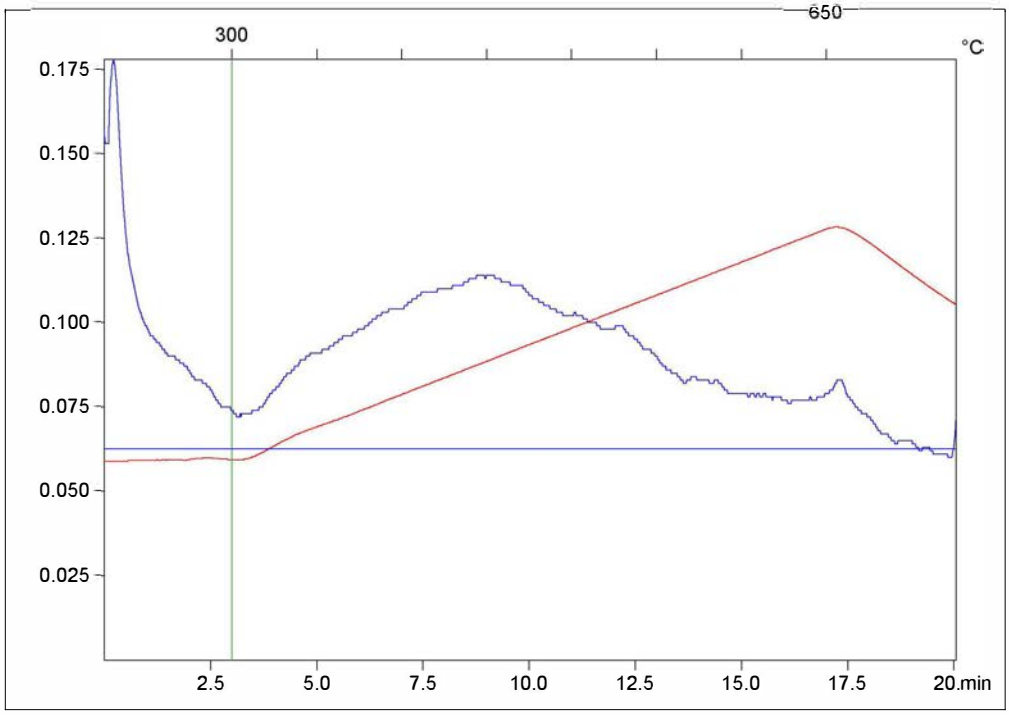
State	Ok
Pyro Status	No blank substraction
Oxi Status	No blank substraction

Customer :	Customer part :
IIT Mumbai	65131

Comment :

RE6 Turbo n E907/65131/102/07

S1(mg/g)=0.02	Sample =SPR-1/64.9
S2(mg/g)=0.07	Method =Bulk Rock
Tmax(°C)=402	Cycle=oxi fast
TpkS2(°C)=442.0	KFID(10*9)=1472
PI=0.2	Qty(mg)=61.5
HI=12	TOC(%)=0.6



C:\2016-17\SD34\91.R00 : FID pyrolysis graphic

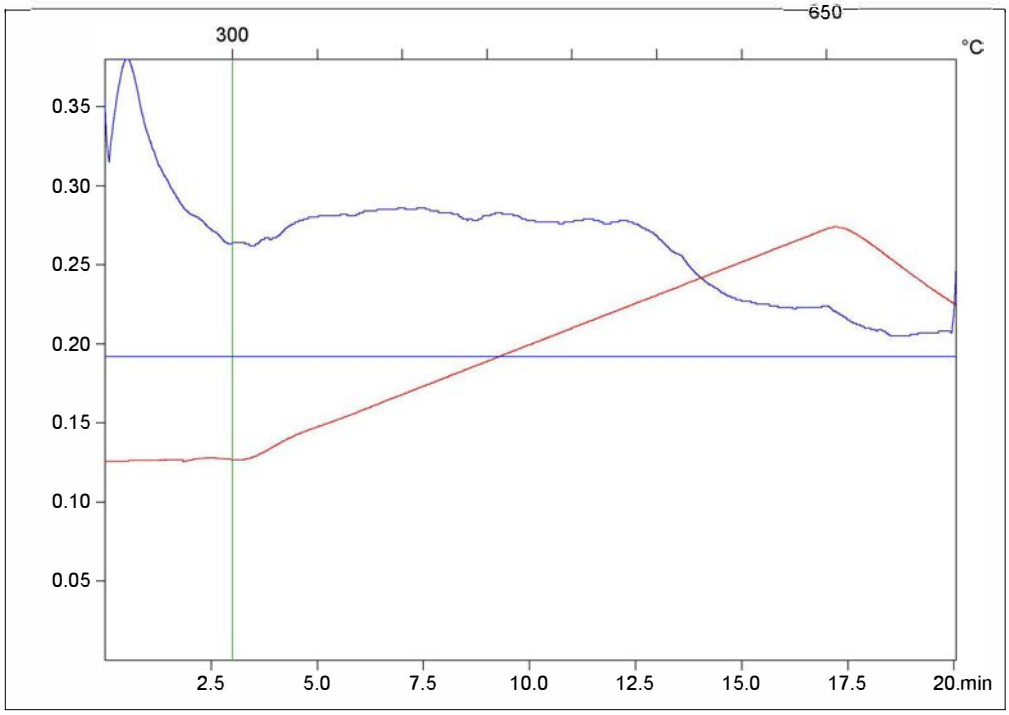
State	Ok
Pyro Status	No blank substraction
Oxi Status	No blank substraction

Customer :	Customer part :
IIT Mumbai	65131

Comment :

RE6 Turbo n E907/65131/102/07

S1(mg/g)=0.05	Sample =SPR-1/74.63
S2(mg/g)=0.16	Method =Bulk Rock
Tmax(°C)=355	Cycle=oxi fast
TpkS2(°C)=395.0	KFID(10*9)=1472
PI=0.25	Qty(mg)=61.9
HI=107	TOC(%)=0.15



C:\2016-17\SD34\64.R00 : FID pyrolysis graphic

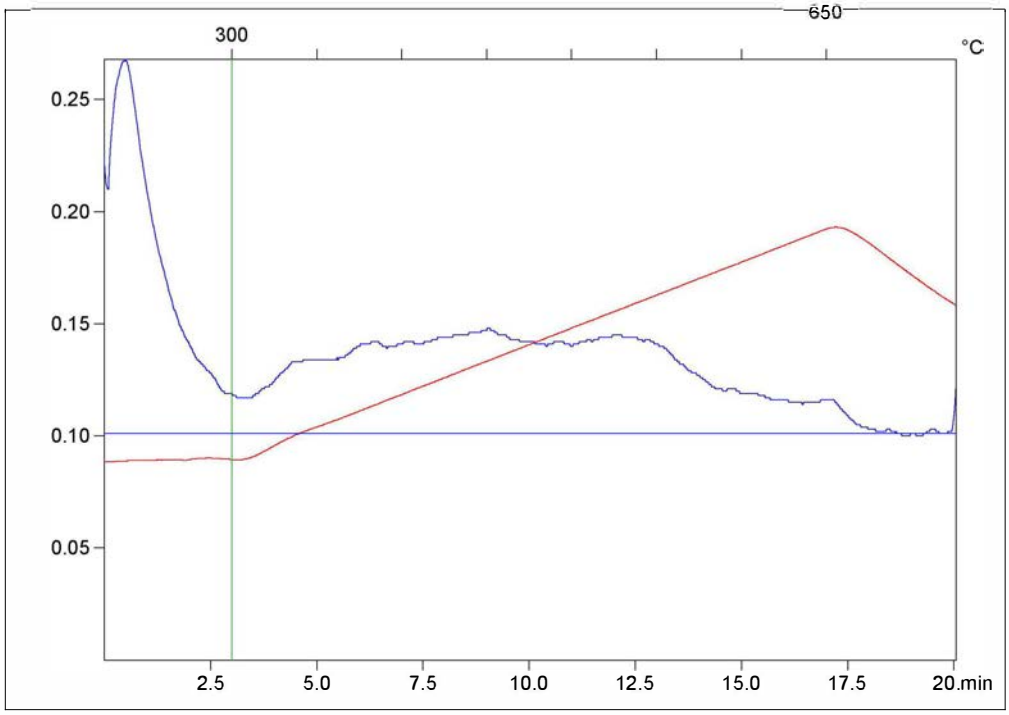
State	Ok
Pyro Status	No blank substraction
Oxi Status	No blank substraction

Customer :	Customer part :
IIT Mumbai	65131

Comment :

RE6 Turbo n E907/65131/102/07

S1(mg/g)=0.03	Sample =SPR-1/79.5
S2(mg/g)=0.07	Method =Bulk Rock
Tmax(°C)=408	Cycle=oxi fast
TpkS2(°C)=448.0	KFID(10*9)=1472
PI=0.33	Qty(mg)=61.9
HI=37	TOC(%)=0.19



C:\2016-17\SD34\74.R00 : FID pyrolysis graphic

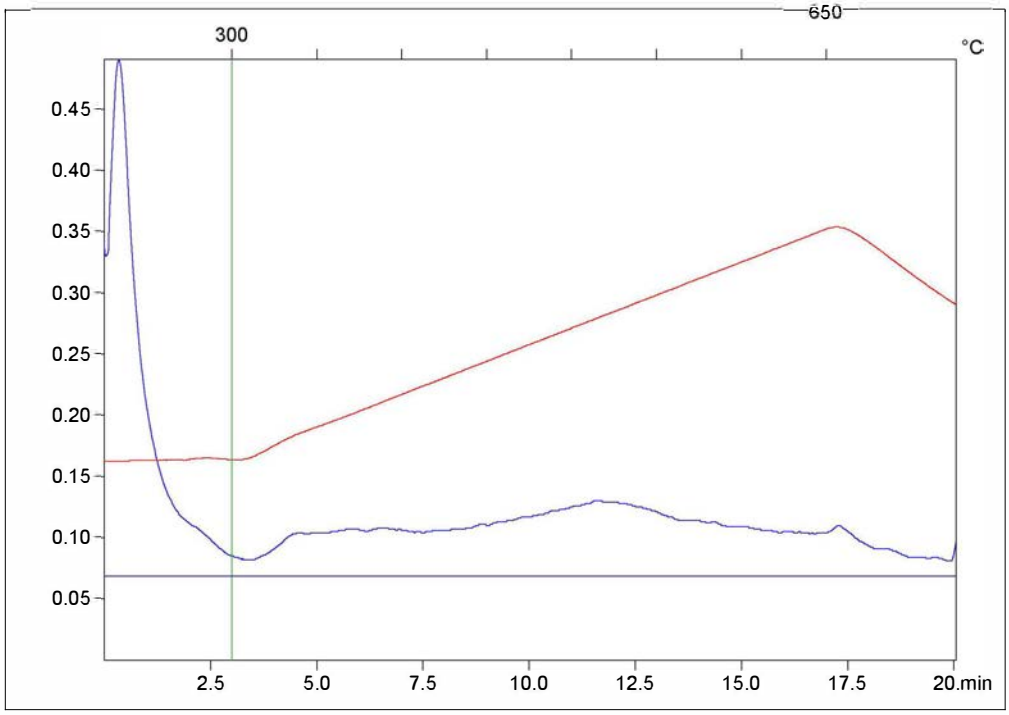
State	Ok
Pyro Status	No blank substraction
Oxi Status	No blank substraction

Customer :	Customer part :
IIT Mumbai	65131

Comment :

RE6 Turbo n E907/65131/102/07

S1(mg/g)=0.06	Sample =SPR-2/17.90
S2(mg/g)=0.09	Method =Bulk Rock
Tmax(°C)=470	Cycle=oxi fast
TpkS2(°C)=510.0	KFID(10*9)=1472
PI=0.38	Qty(mg)=61.7
HI=4	TOC(%)=2



C:\2016-17\SD34\60.R00 : FID pyrolysis graphic

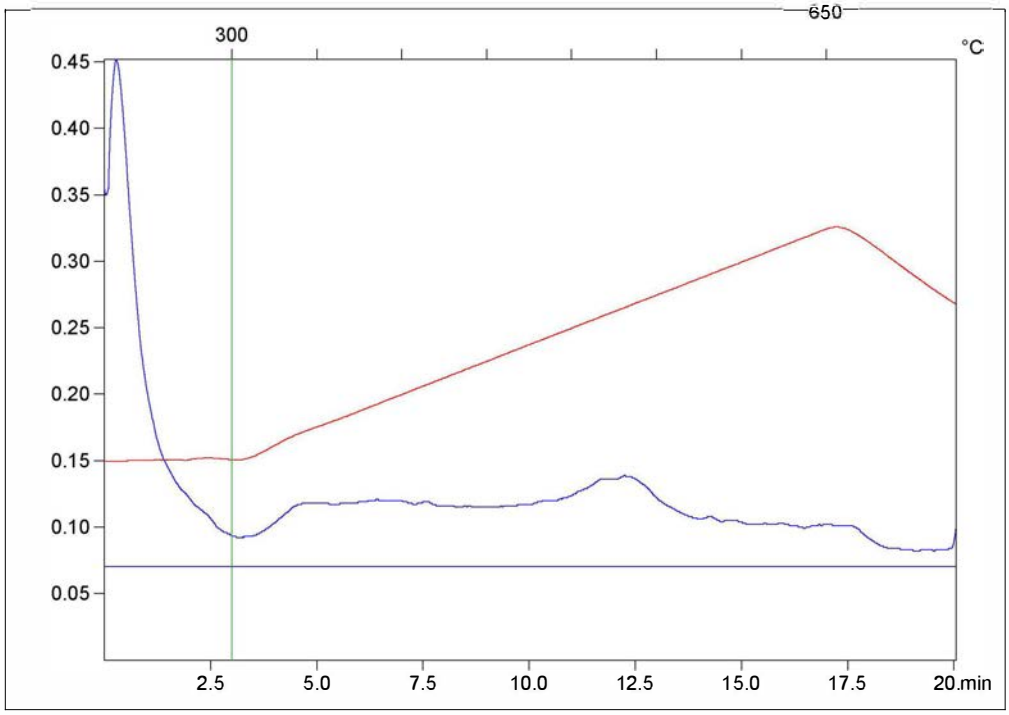
State	Ok
Pyro Status	No blank substraction
Oxi Status	No blank substraction

Customer :	Customer part :
IIT Mumbai	65131

Comment :

RE6 Turbo n E907/65131/102/07

S1(mg/g)=0.06	Sample =SPR-2/19.72
S2(mg/g)=0.1	Method =Bulk Rock
Tmax(°C)=487	Cycle=oxi fast
TpkS2(°C)=527.0	KFID(10*9)=1472
PI=0.37	Qty(mg)=61.8
HI=9	TOC(%)=1.14



C:\2016-17\SD34\58.R00 : FID pyrolysis graphic

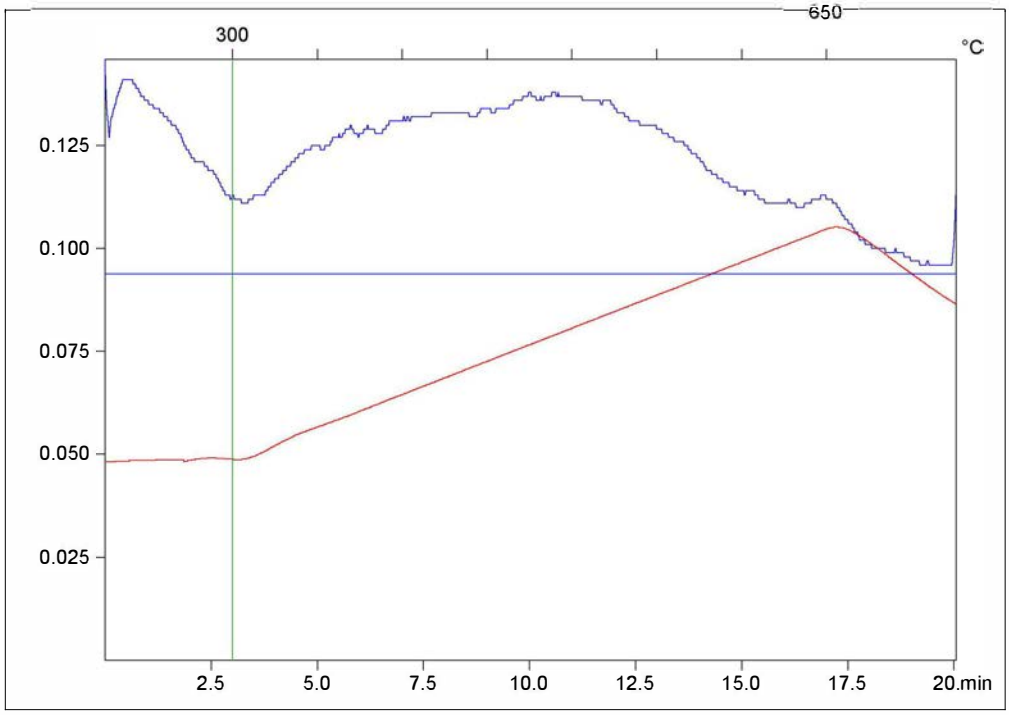
State	Ok
Pyro Status	No blank substraction
Oxi Status	No blank substraction

Customer :	Customer part :
IIT Mumbai	65131

Comment :

RE6 Turbo n E907/65131/102/07

S1(mg/g)=0.02	Sample =SPR-2/35.98
S2(mg/g)=0.07	Method =Bulk Rock
Tmax(°C)=432	Cycle=oxi fast
TpkS2(°C)=472.0	KFID(10*9)=1472
PI=0.18	Qty(mg)=60.5
HI=78	TOC(%)=0.09



C:\2016-17\SD34\81.R00 : FID pyrolysis graphic

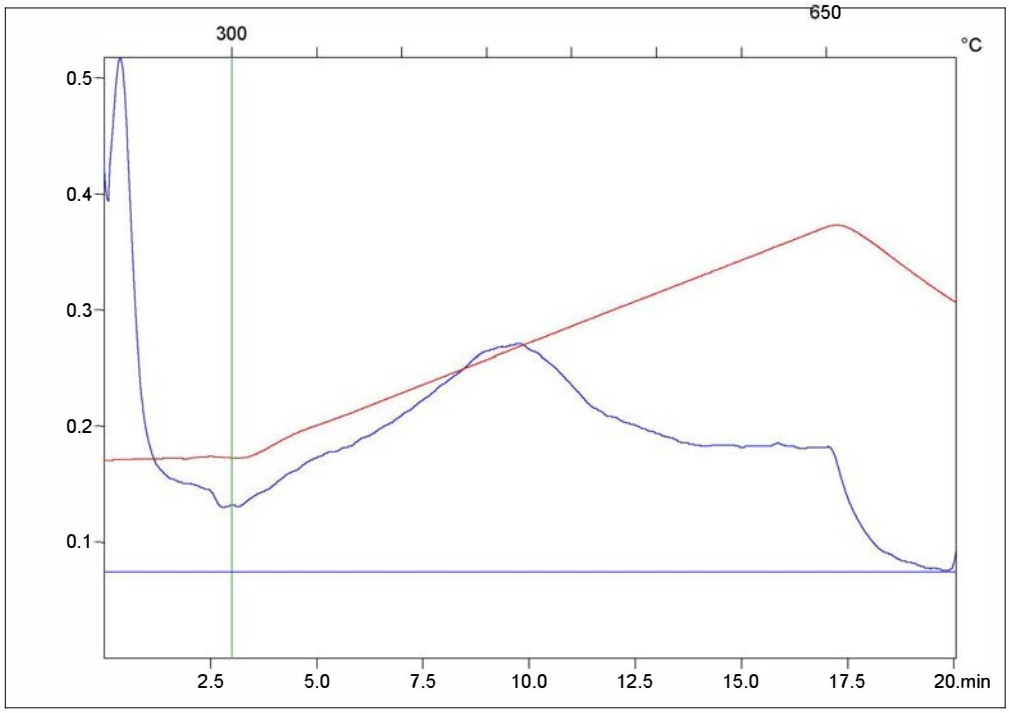
State	Ok
Pyro Status	No blank substraction
Oxi Status	No blank substraction

Customer :	Customer part :
IIT Mumbai	65131

Comment :

RE6 Turbo n E907/65131/102/07

S1(mg/g)=0.07	Sample =WB98/850
S2(mg/g)=0.27	Method =Bulk Rock
Tmax(°C)=424	Cycle=oxi fast
TpkS2(°C)=464.0	KFID(10*9)=1472
PI=0.2	Qty(mg)=60.9
HI=6	TOC(%)=4.21



C:\2016-17\SD33\52.R00 : FID pyrolysis graphic

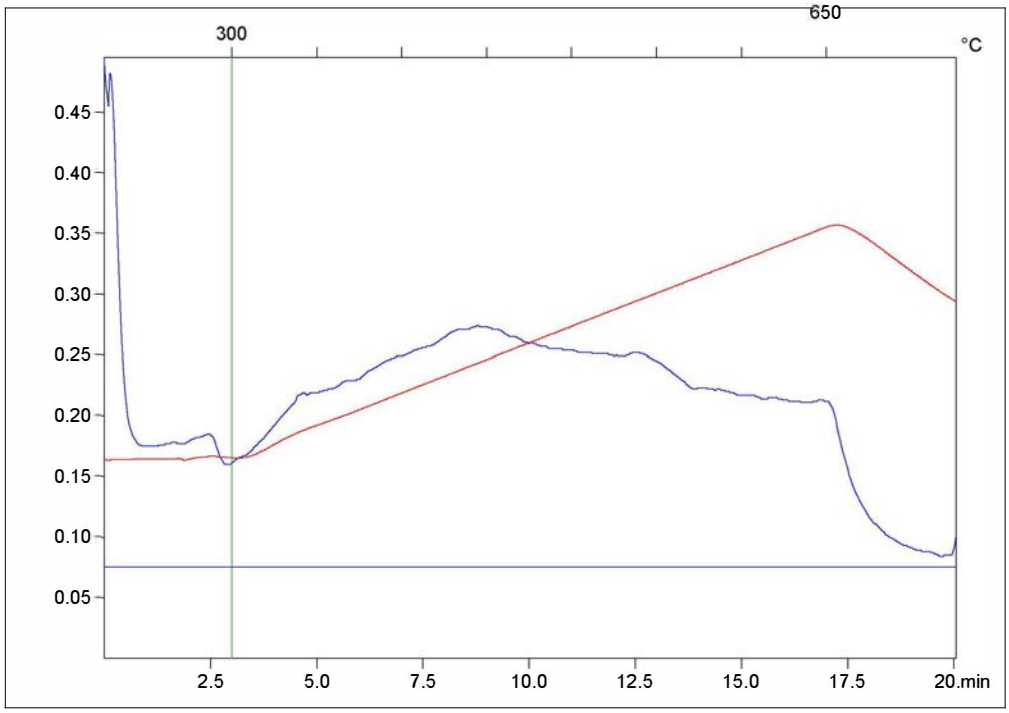
State	Ok
Pyro Status	No blank substraction
Oxi Status	No blank substraction

Customer :	Customer part :
IIT Mumbai	65131

Comment :

RE6 Turbo n E907/65131/102/07

S1(mg/g)=0.06	Sample =WB98/958
S2(mg/g)=0.34	Method =Bulk Rock
Tmax(°C)=402	Cycle=oxi fast
TpkS2(°C)=442.0	KFID(10*9)=1472
PI=0.15	Qty(mg)=61.1
HI=34	TOC(%)=1.01



C:\2016-17\SD33\57.R00 : FID pyrolysis graphic

State	Ok
Pyro Status	No blank substraction
Oxi Status	No blank substraction



Massachusetts Institute of Technology

Raman Analysis of Organic Matter in Carbonates from Clark Johnson – UW Madison

Ryan M. Schubert, Nicola Ferralis

Department of Materials Science and Engineering

Massachusetts Institute of Technology

ferralis@mit.edu

05-04-2017

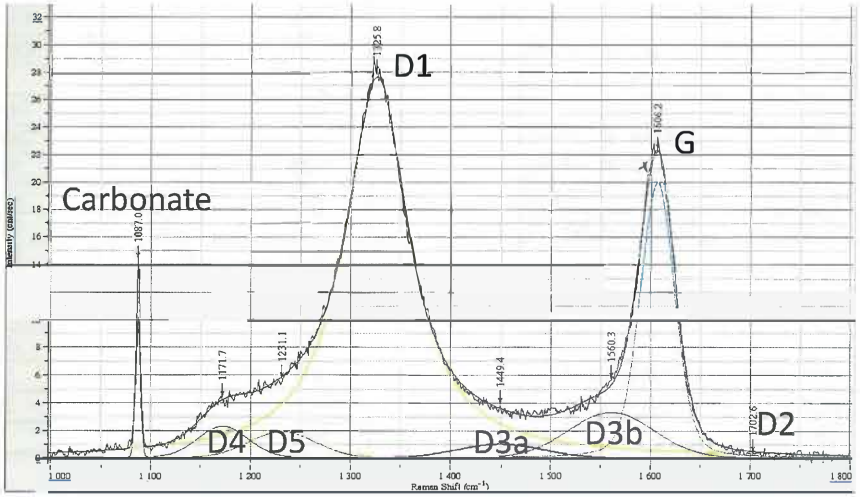
Methodology

- Using Horiba LabRam 800HR
  - Excitation: 633 nm
  - Power density: <1mW/cm^2
  - Spectral range: 1000-1800 1/cm
  - Resolution: 1 1/cm
- Acquisition:
  - 6-10 point spectra per sample.
  - Position of point spectra are tracked if in needs for future studies
- Analysis:
  - Follows: Ferralis *et al.* Carbon 108 (2016), 440-449
  - H:C listed as average across 4 to 6 spectra.
  - Uncertainty on H:C
    - Standard deviation: listed (next slide)
    - Additional systematic: ~0.03

Reference spectral components

OM: D1, D2, D3, **D4, D5, G (used for determination of H:C)**[1]
Carbonates:

- Two families of carbonates have been identified
- 1087 1/cm (Calcium Carbonates), 1097 1/cm (possibly Dolomite[2])



[1] Ferralis *et al.* Carbon 108 (2016), 440-449
[2]RRUFF database: http://rruff.info/

H:C Summary

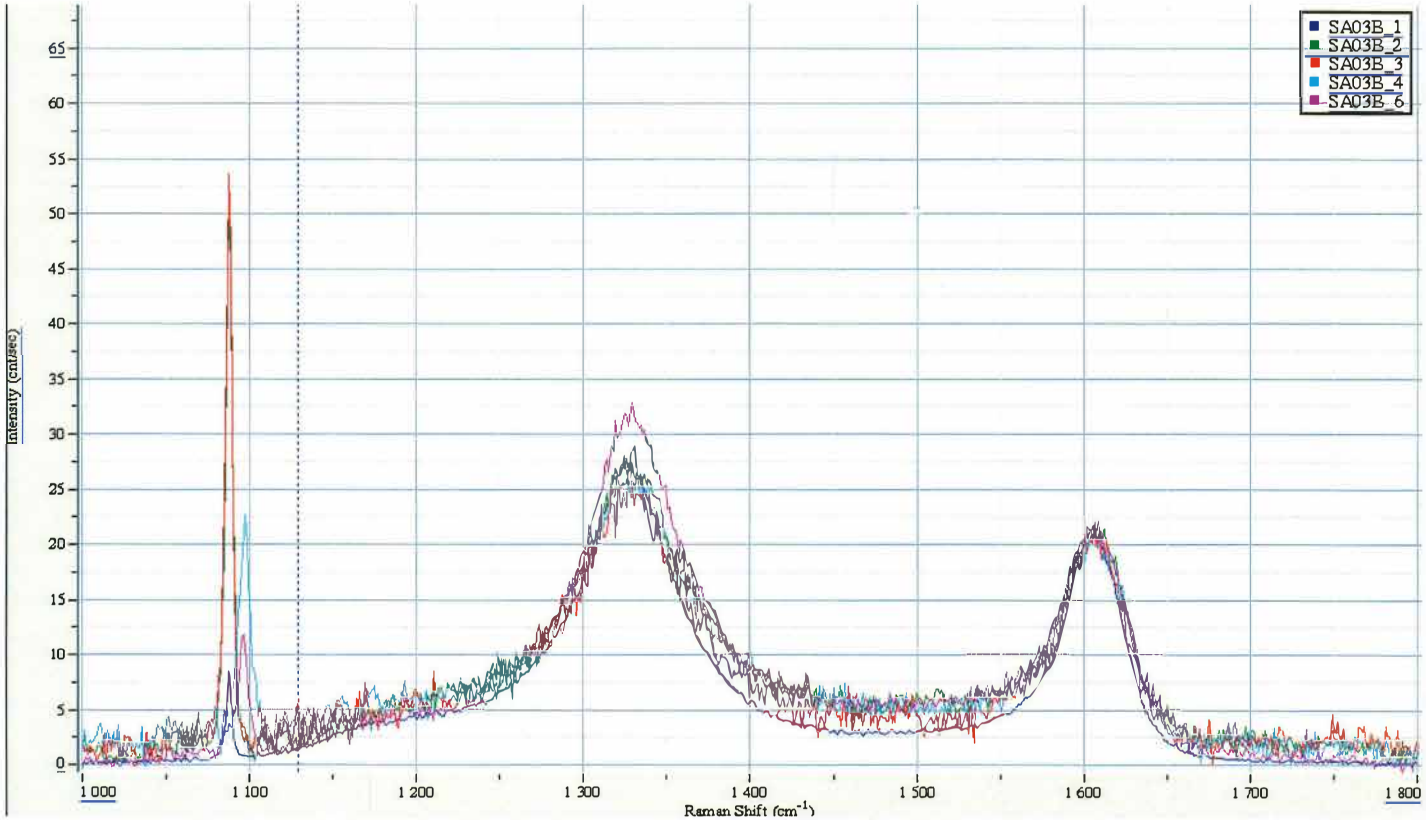
Sample	Average H:C	stdev
Sample 1- SA03B	0.17	0.05
Sample 2- SA03C	0.15	0.02
Sample 3- SA03D1	0.18	0.04
Sample 4- SA03D2	0.16	0.03
Sample 5- SA03D3	0.16	0.03
Sample 6- SA04A1	0.18	0.03
Sample 7- SA04A2	0.16	0.03
Sample 8- SA04A3	0.16	0.02
Sample 9- SA04B1	0.14	0.01
Sample 9a- SA04B1		
Sample 10- SA04B2	0.17	0.04
Sample 11- SA04B3	0.15	0.03
Sample 12- SA04C1	0.17	0.04
Sample 13- SA04C2	0.17	0.05
Sample 14- SA05B1	0.18	0.04
Sample 15- SA05B2	0.15	0.02
Sample 16- SA05B3	0.15	0.06
Sample 17- SA05B4	0.15	0.04
Sample 18- SA05B5	0.15	0.03
Sample 19- SA05B6	0.16	0.03
Sample 20- SA06A	0.17	0.01
Sample 20- SA06A	0.21	
Sample 21- SA06B	0.14	0.00
Sample 21- SA06B	0.23	0.04

Sample	Average H:C	stdev
Sample 23- SA11B	0.17	0.02
Sample 24- SA12A	0.14	0.02
Sample 25- SA13B1	0.13	0.01
Sample 25- SA13B1	0.20	0.02
Sample 26- SA13B2	0.16	0.02
Sample 27- SA13B3	0.14	0.02
Sample 28- SA13B4	0.16	0.02
Sample 28- SA13B4	0.23	
Sample 29- SA14AB1	0.14	0.01
Sample 30- SA14AB2	0.16	0.03
Sample 31- SA14AB3	0.14	0.04
Sample 32- SA14AB4	0.15	0.02
Sample 33- SA14B1	0.15	0.03
Sample 34- SA15BA1	0.15	0.03
Sample 34- SA15BA1	0.23	
Sample 35- SA15BA2	0.17	0.05
Sample 36- SA15BA3	0.15	0.04
Sample 37- SA15BB	0.14	0.03

Spectral analysis

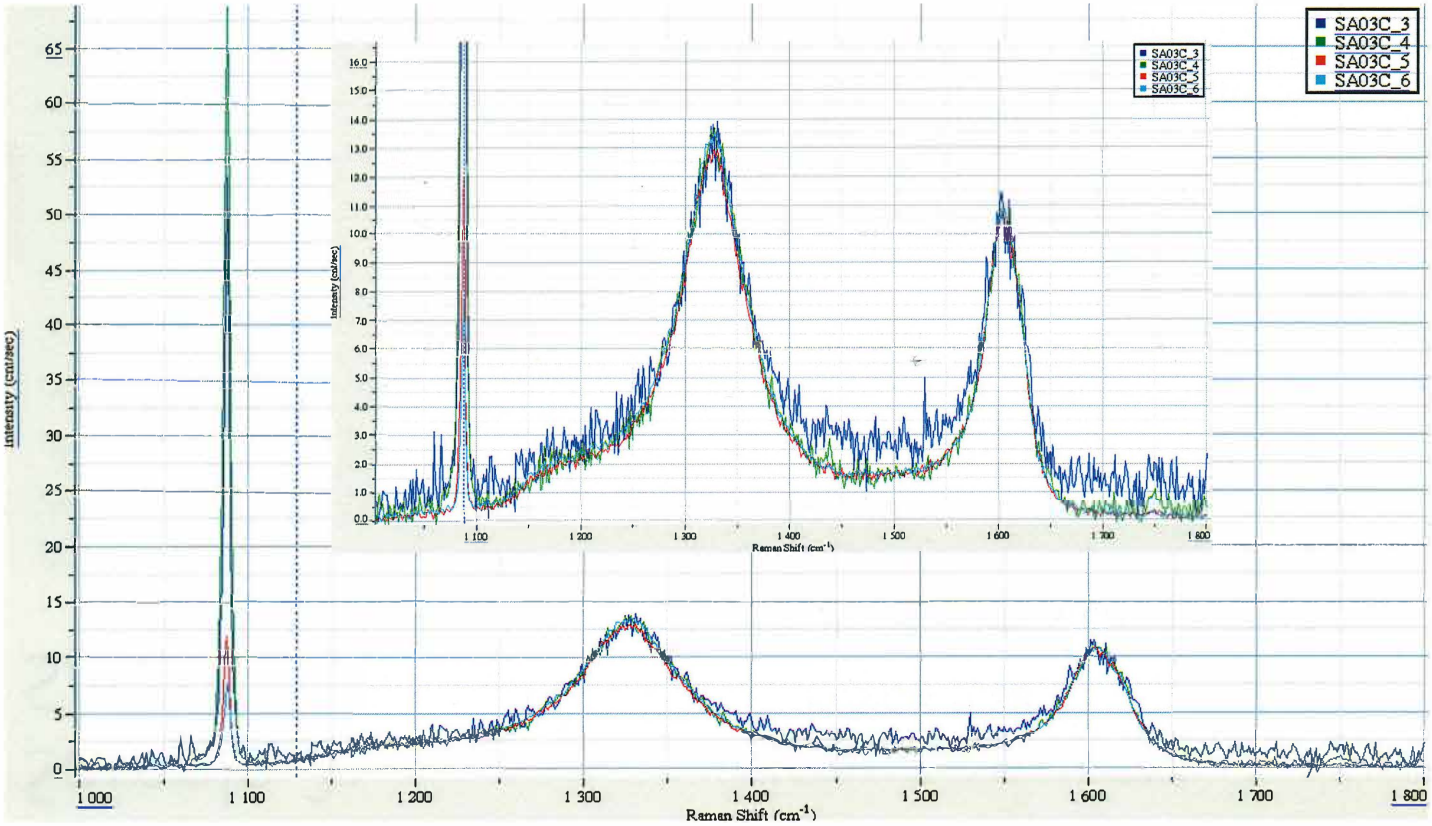
Sample 1: SA03B

- Homogeneous OM
  - H:C = 0.17
- Mixed carbonates



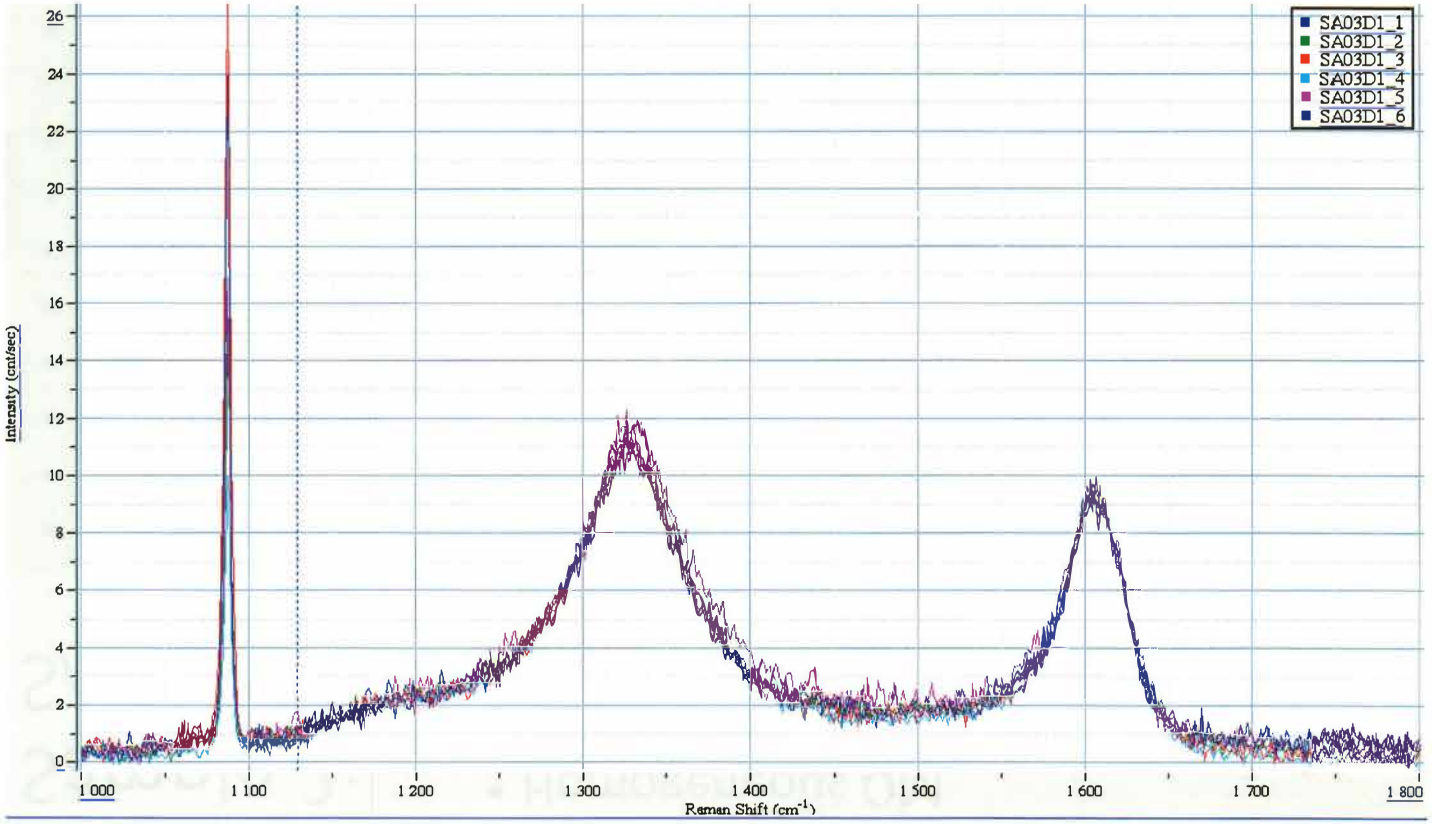
Sample 2: SA03C

- Homogeneous OM
  - H:C = 0.15
- Homogenous carbonates (1087)



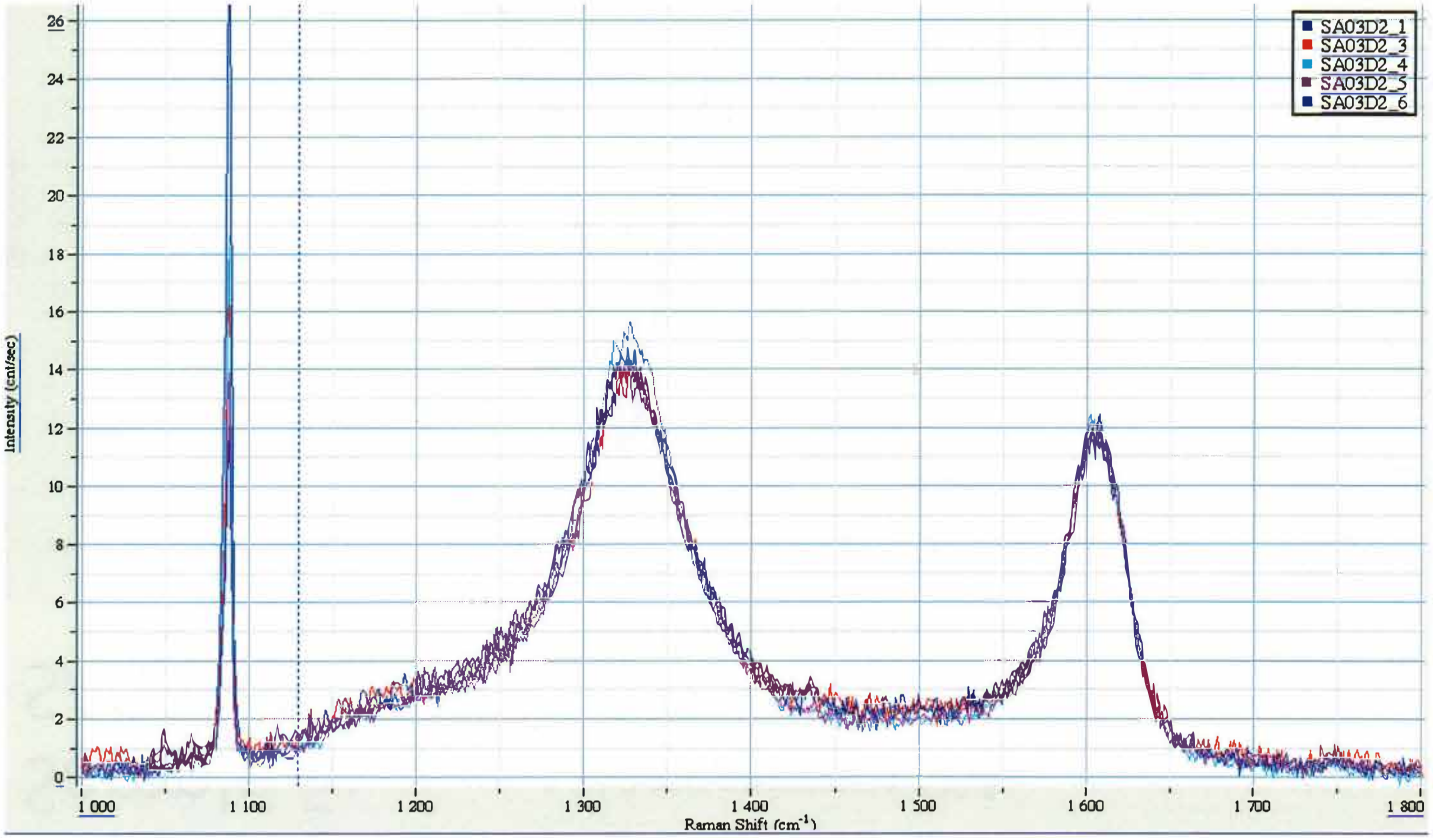
Sample 3: SA03D1

- Homogeneous OM
  - H:C = 0.18
- Homogenous carbonates



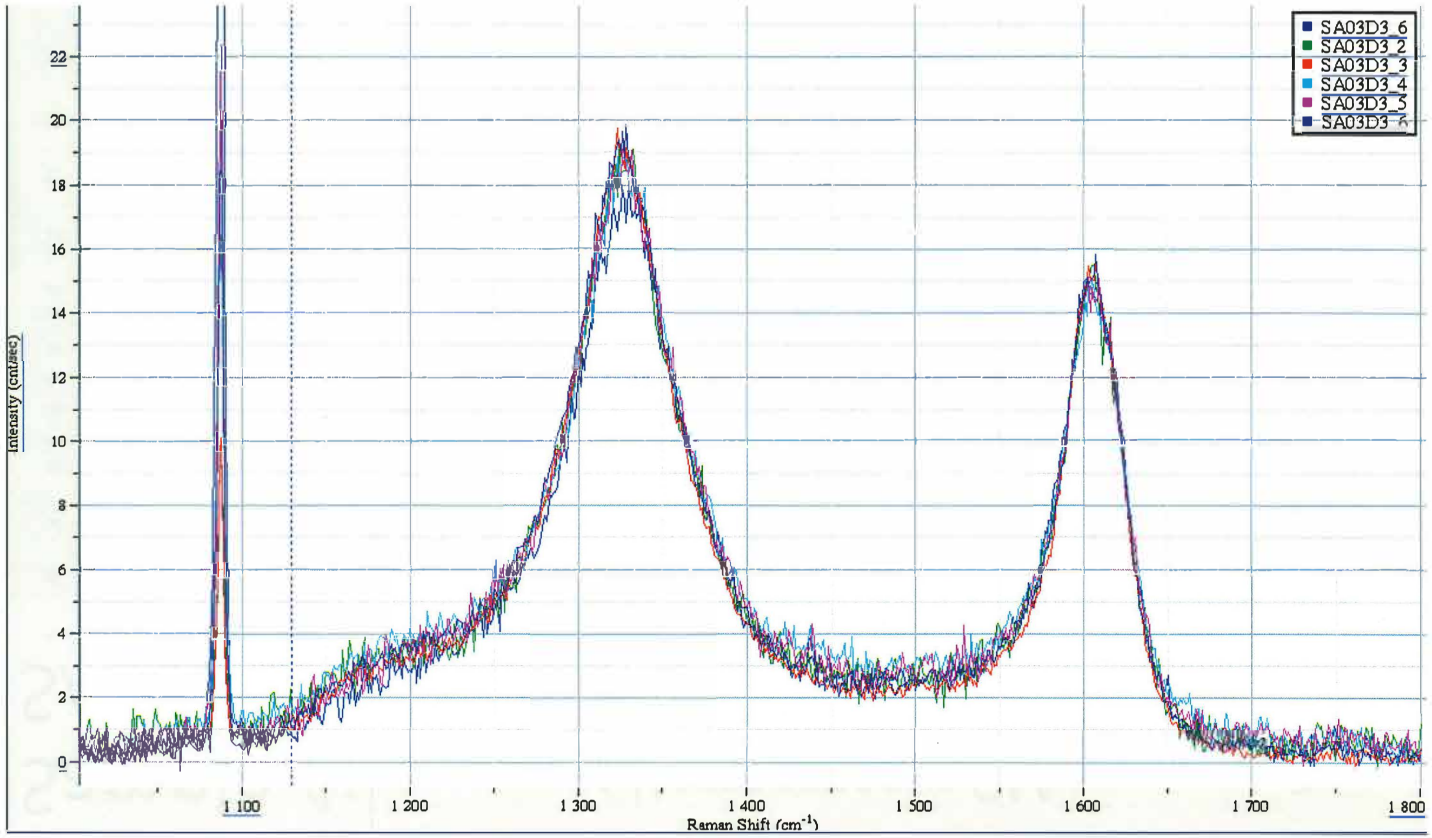
Sample 4: SA03D2

- Homogeneous OM
  - H:C = 0.16
- Homogenous carbonates (1087)



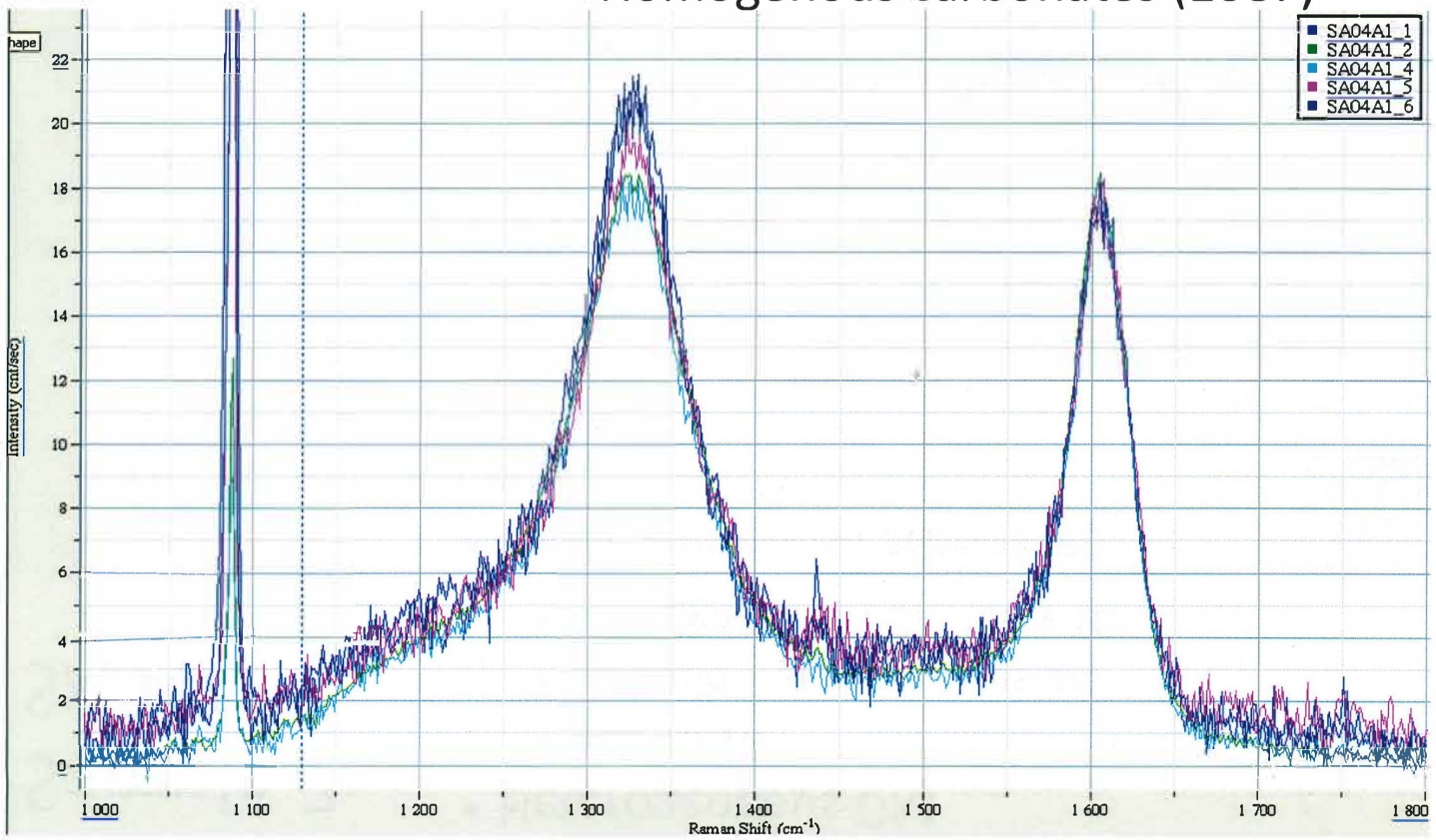
Sample 5: SA03D3

- Homogeneous OM
  - H:C = 0.16
- Homogenous carbonates (1087)



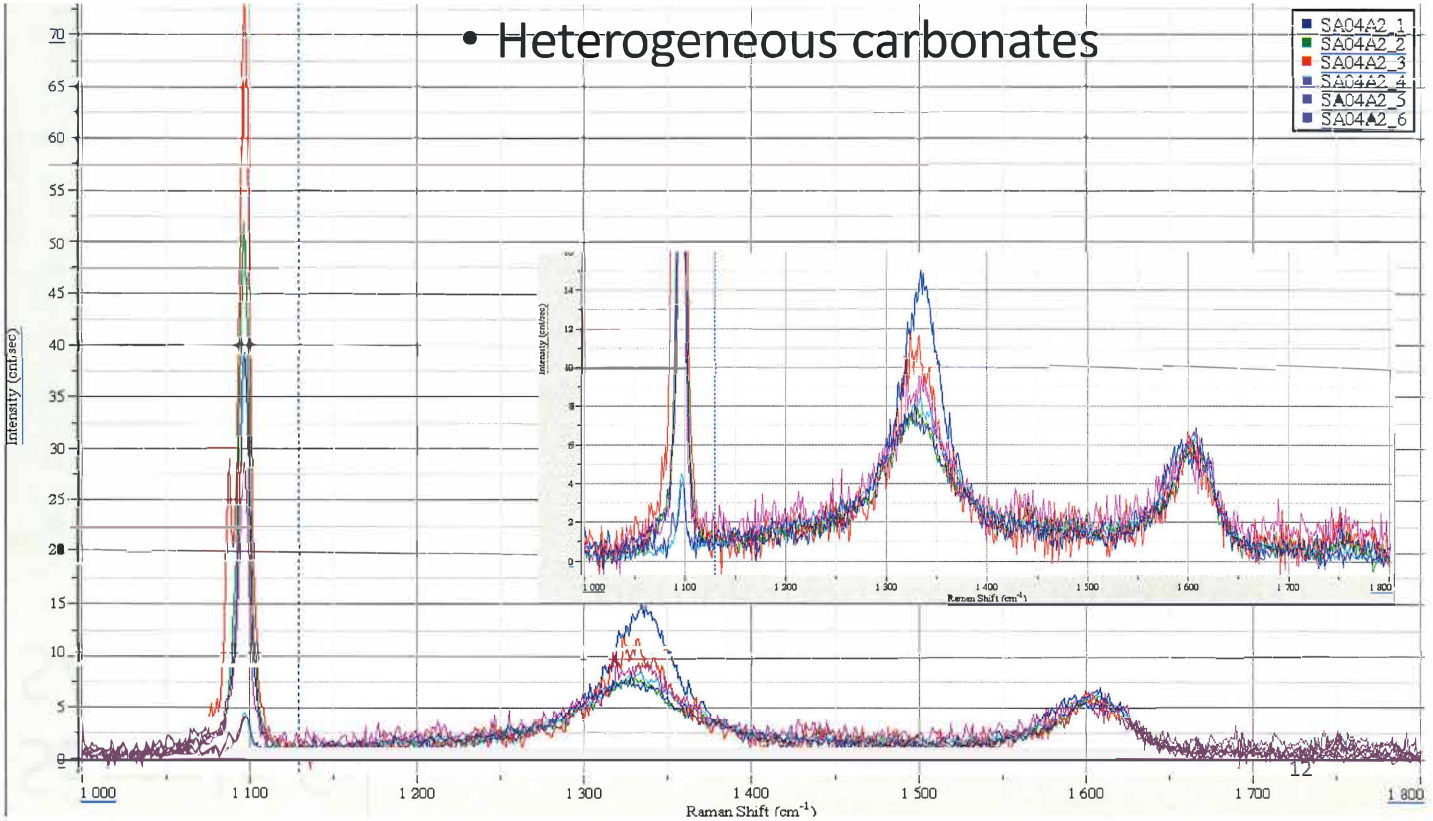
Sample 6: SA04A1

- Homogeneous OM
  - H:C = 0.17
- Homogenous carbonates (1087)



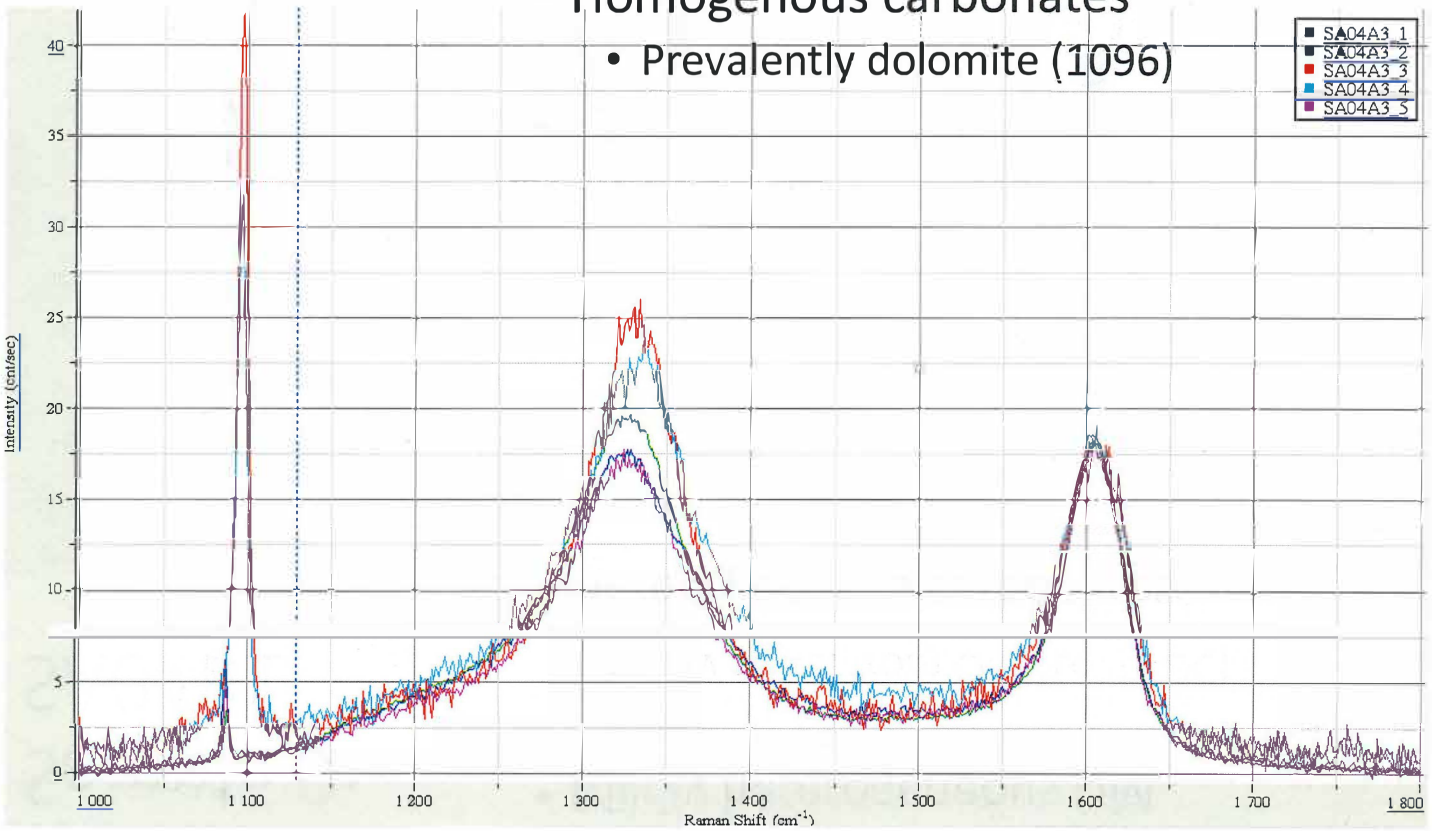
Sample 7: SA04A2

- Heterogeneous OM
  - H:C = 0.16
  - D1 band – aromatic clusters
  - Low signal from OM (Low TOC)
- Heterogeneous carbonates



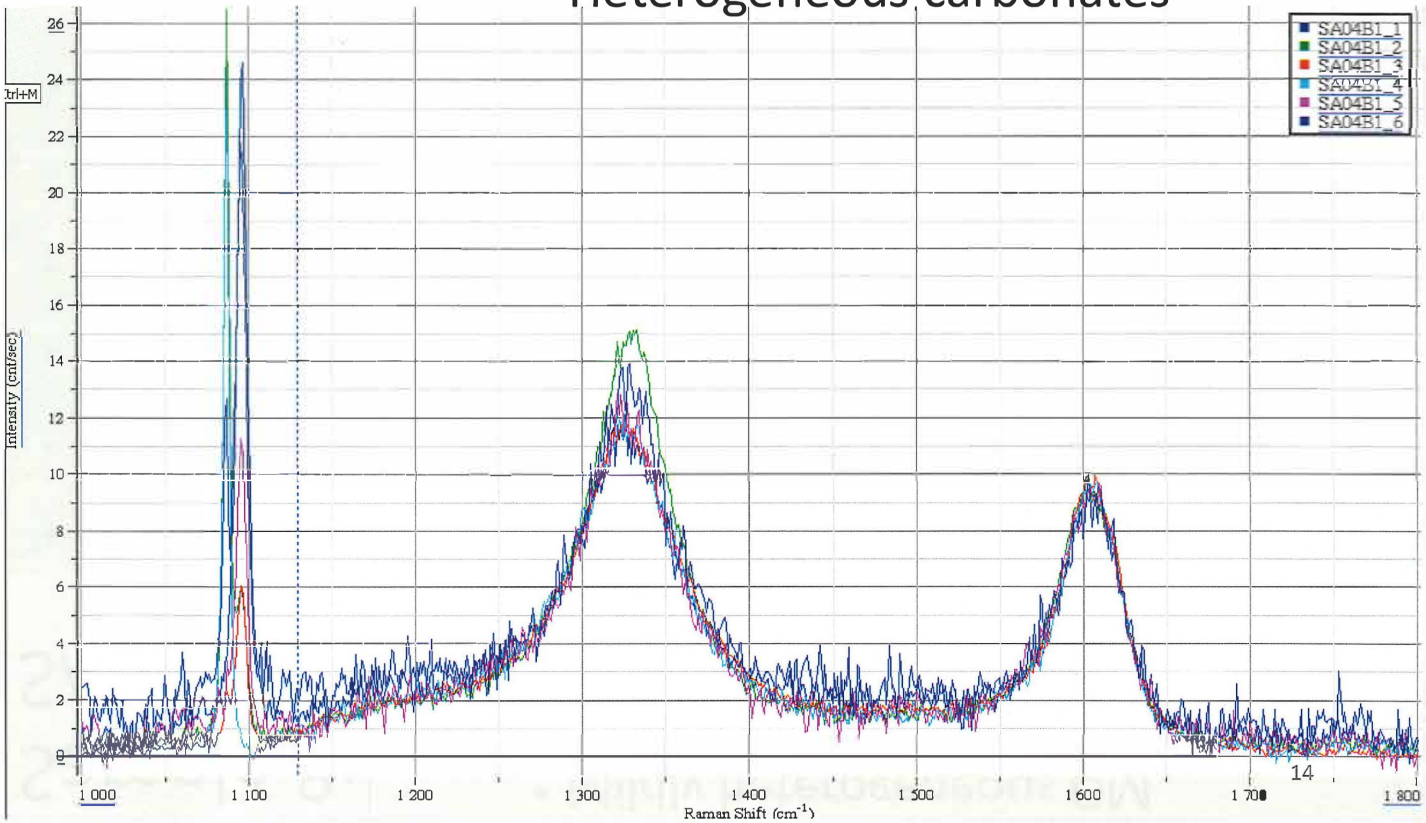
Sample 8: SA04A3

- Mildly heterogeneous OM
  - D1 band – aromatic clusters
  - H:C = 0.16
- Homogenous carbonates
  - Prevalently dolomite (1096)



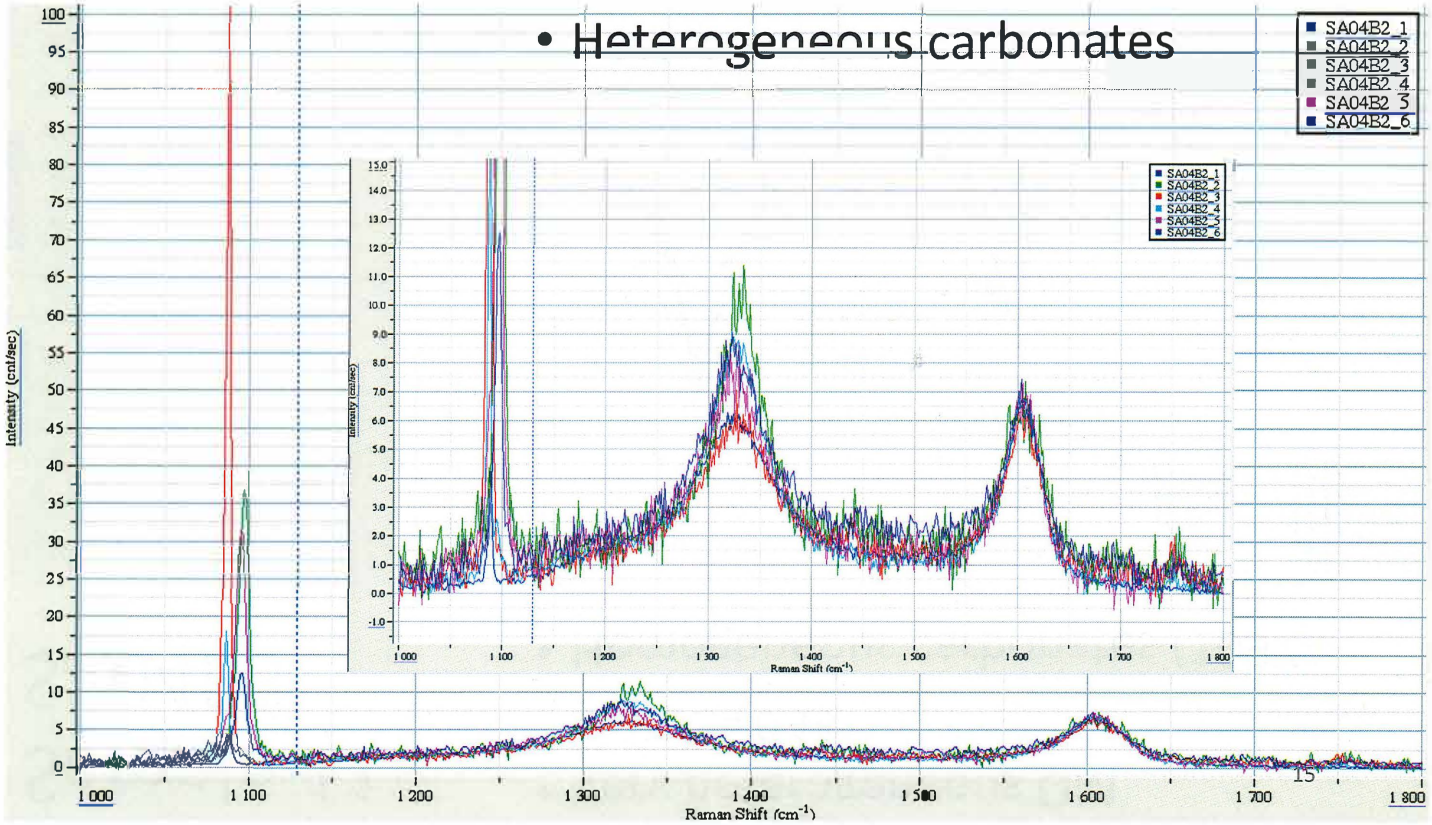
Sample 9: SA04B1

- Mildly heterogeneous OM
  - H:C = 0.15
  - Low signal from OM (Low TOC)
- Heterogeneous carbonates



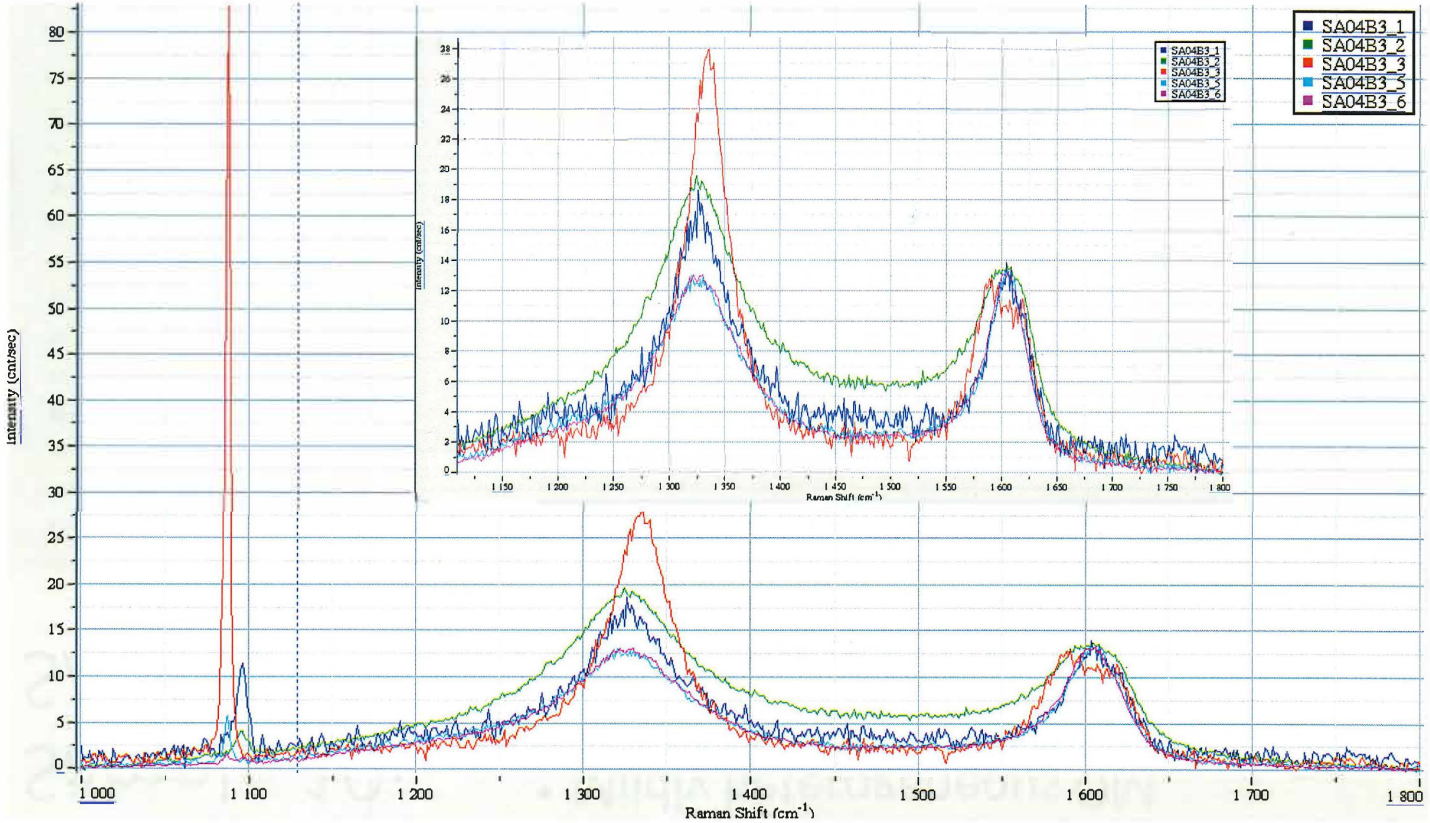
Sample 10: SA04B2

- Mildly heterogeneous OM
  - H:C = 0.16
  - Very low signal from OM (Low TOC)
- Heterogeneous carbonates



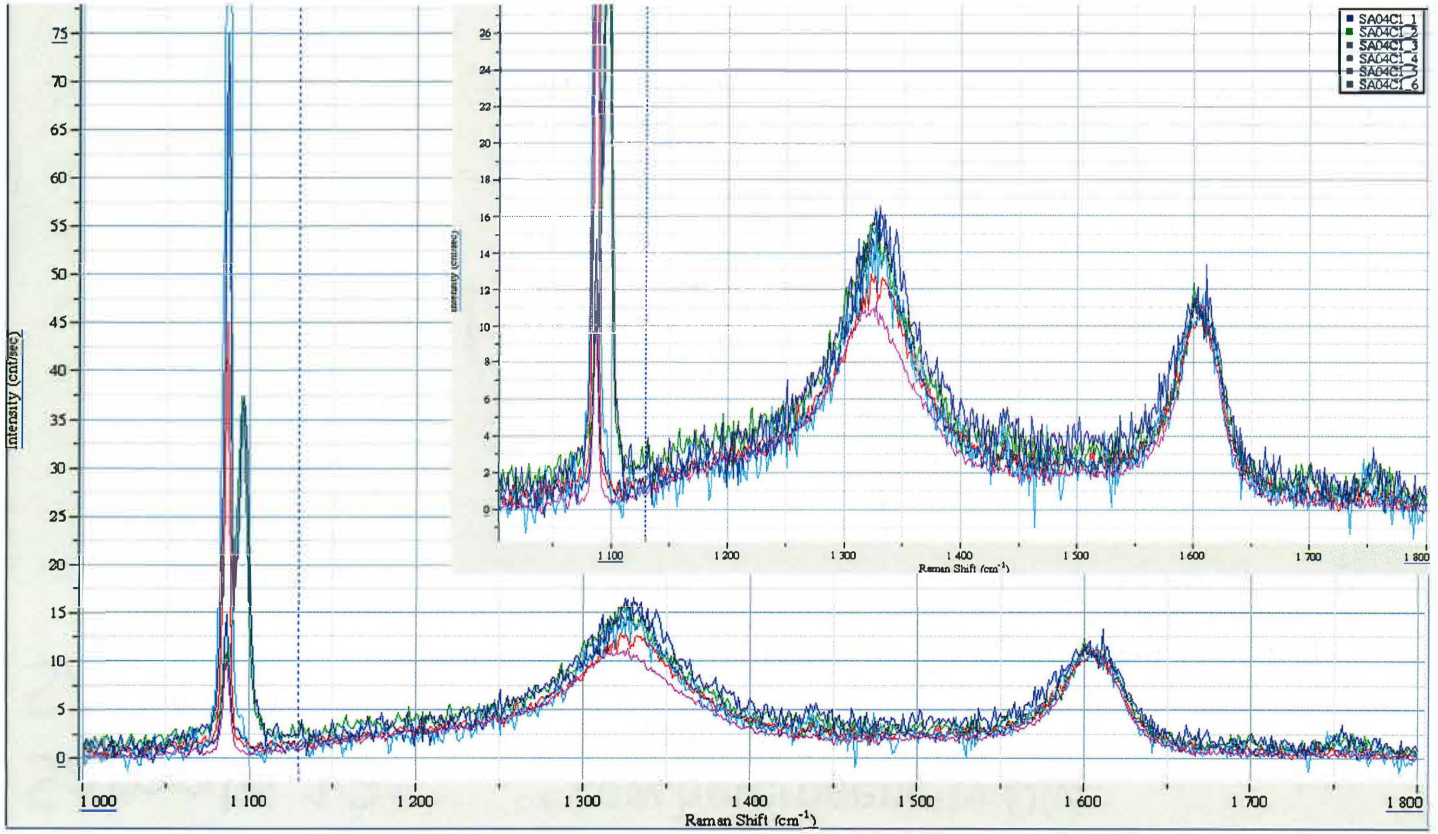
Sample 11: SA04B3

- Very heterogeneous OM
  - H:C = 0.15
- Homogeneous carbonates (1097)



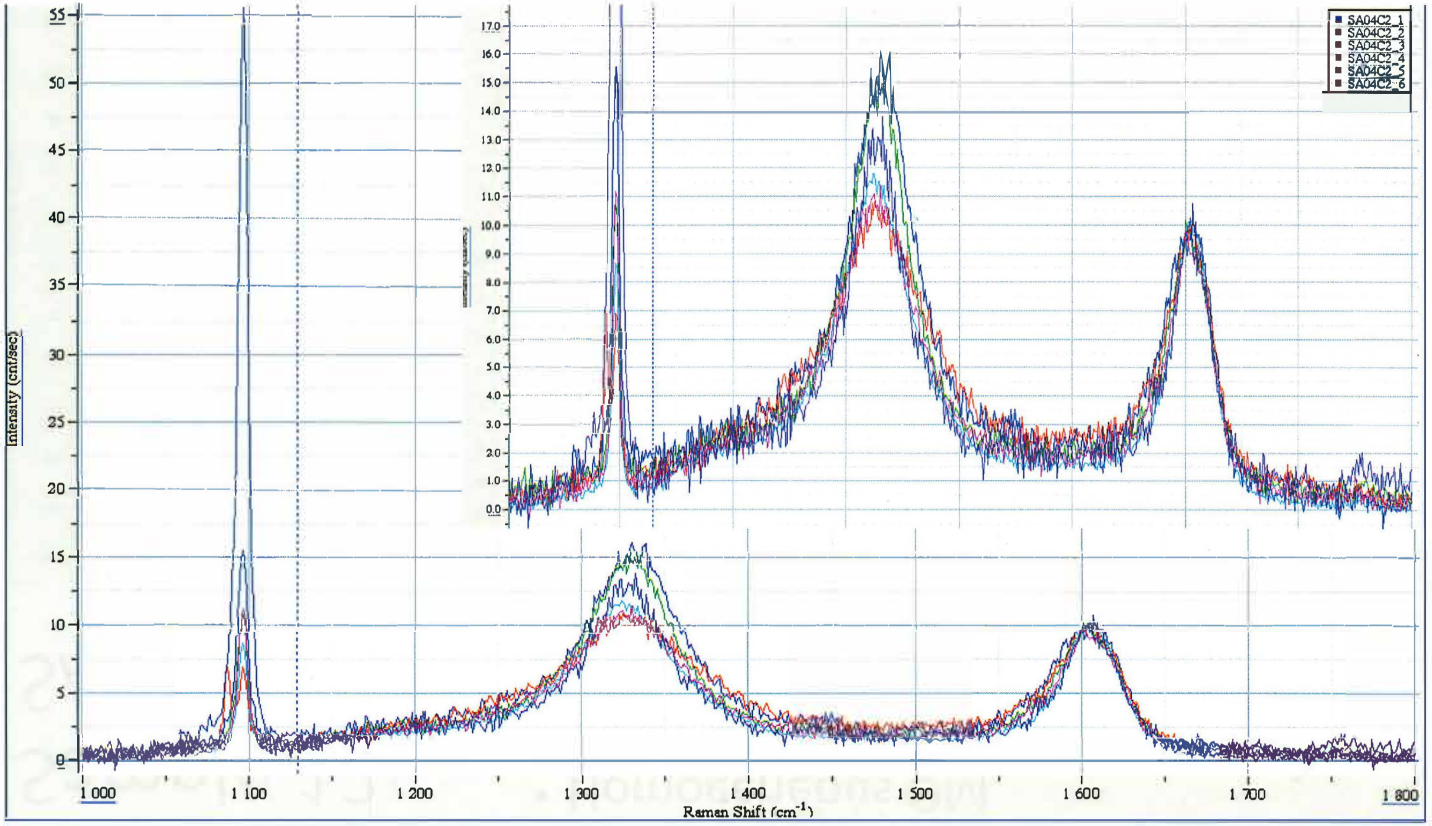
Sample 12: SA04C1

- Homogeneous OM
  - H:C = 0.17
- Heterogeneous carbonates



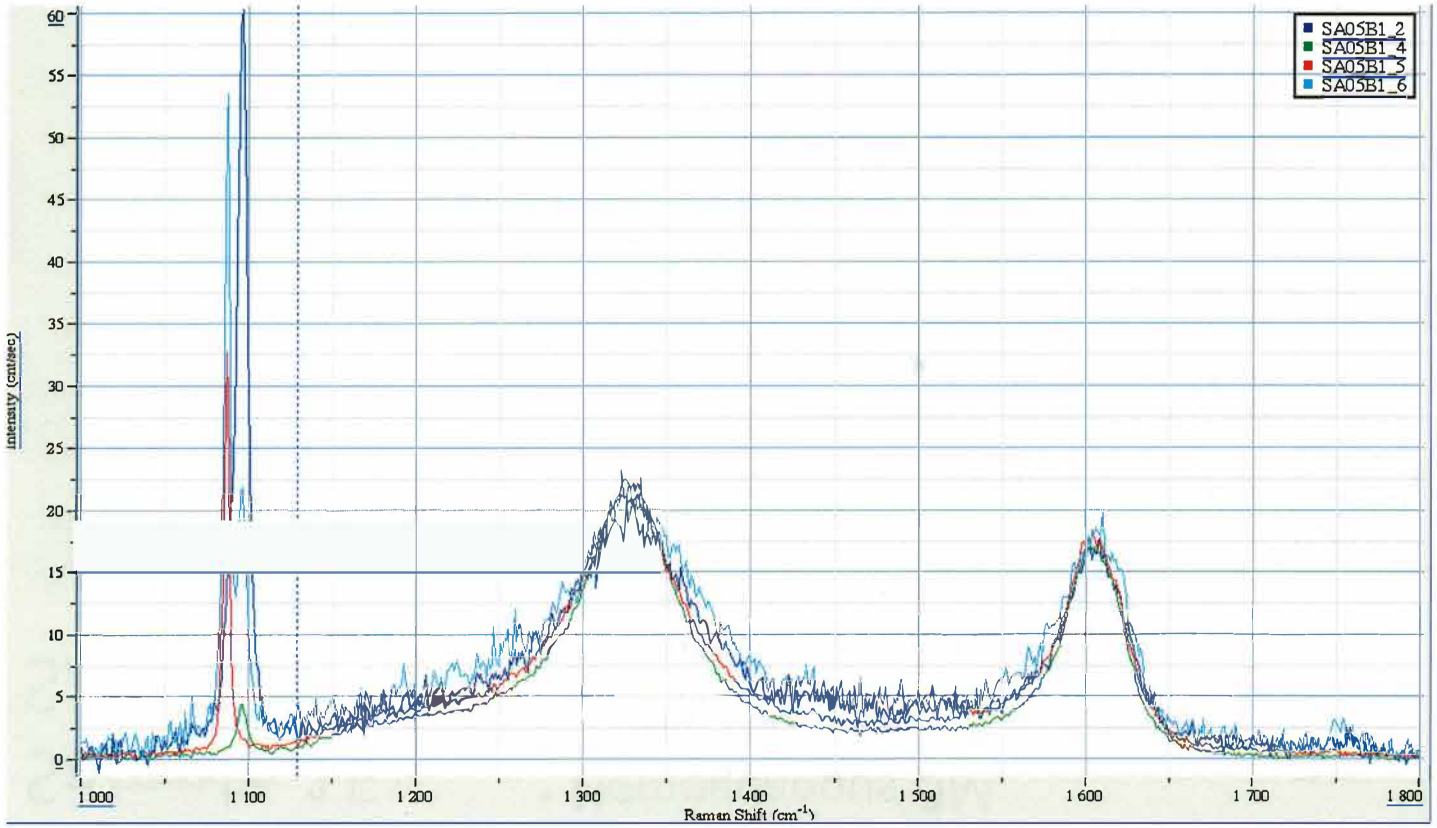
Sample 13: SA04C2

- Low heterogeneity OM
  - H:C = 0.17
- Homogeneous Carbonates (1097)



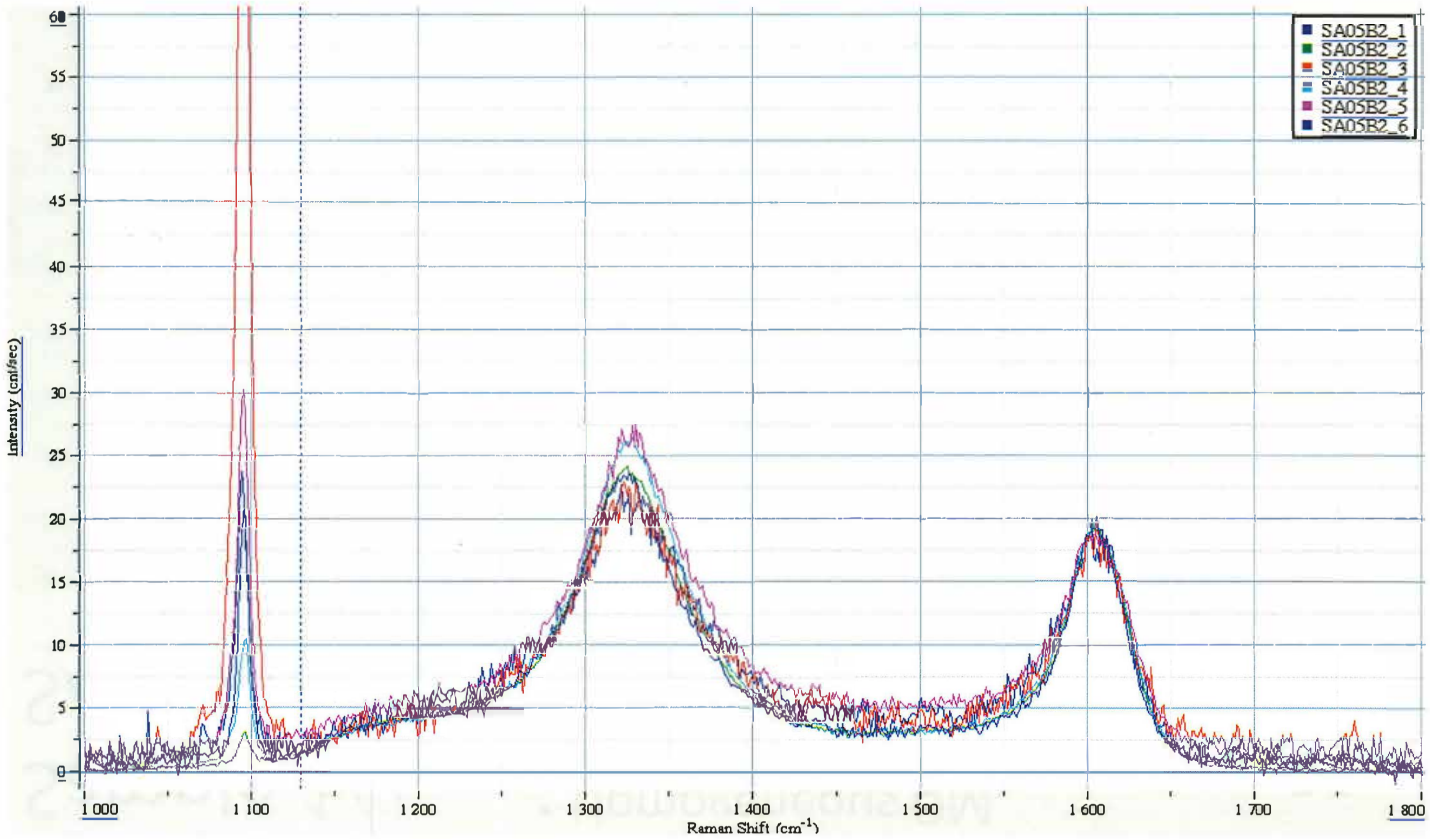
Sample 14: SA05B1

- Homogeneous OM
  - H:C = 0.17
- Heterogeneous Carbonates



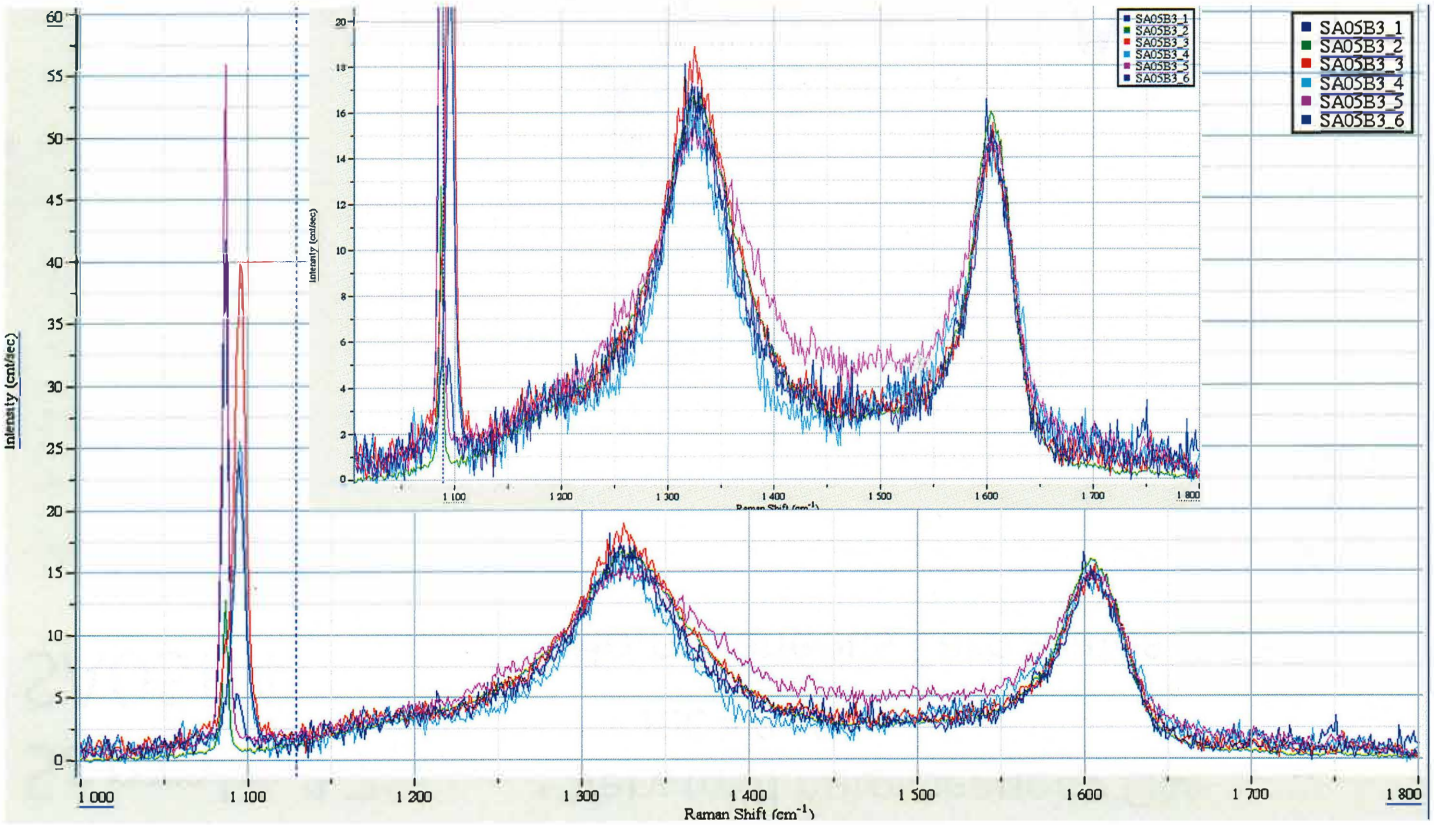
Sample 15: SA05B2

- Homogeneous OM
  - H:C = 0.15
- Homogeneous Carbonates



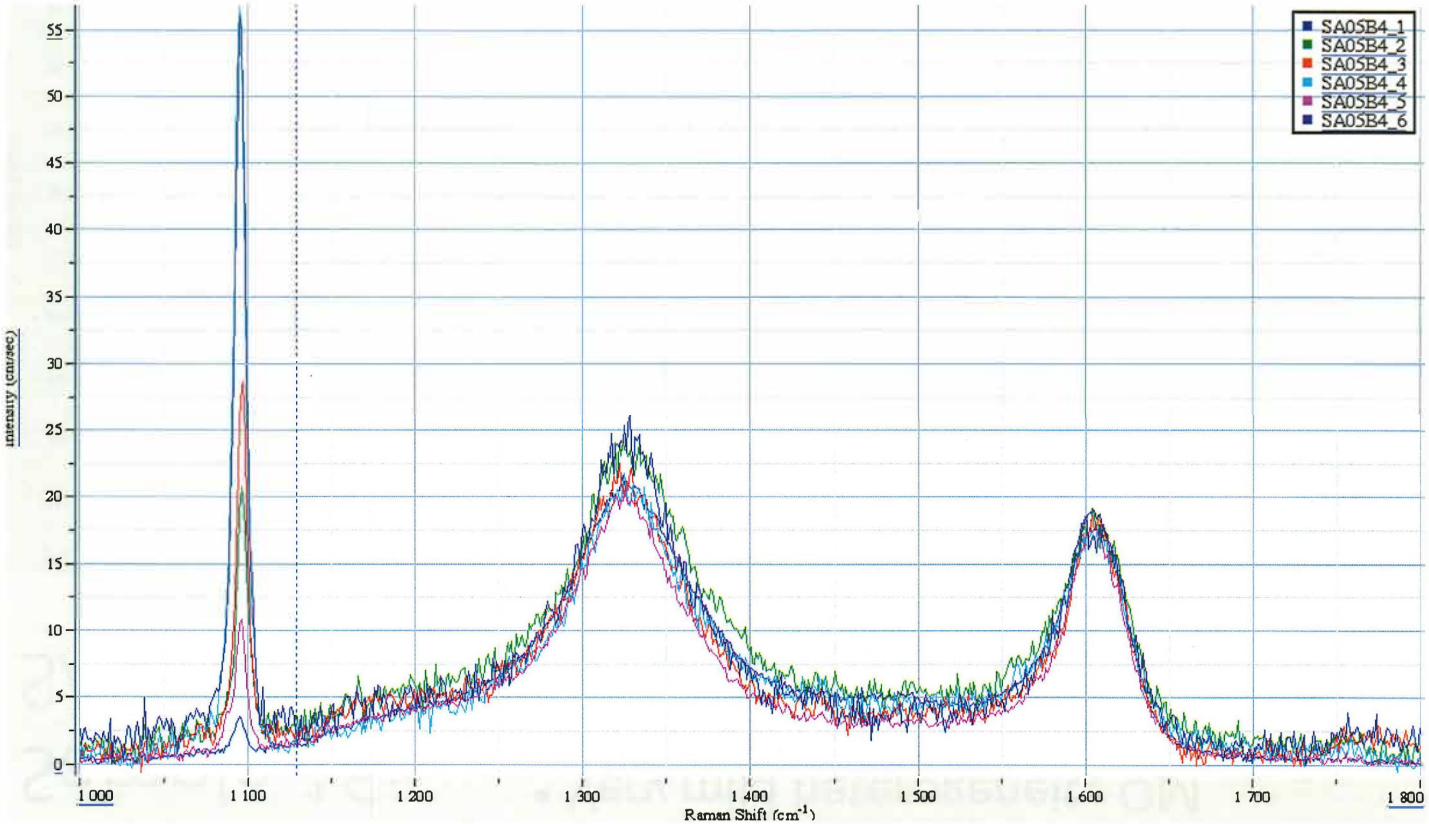
Sample 16: SA05B3

- Very mild heterogeneity OM
  - H:C = 0.16
- Heterogeneous Carbonates



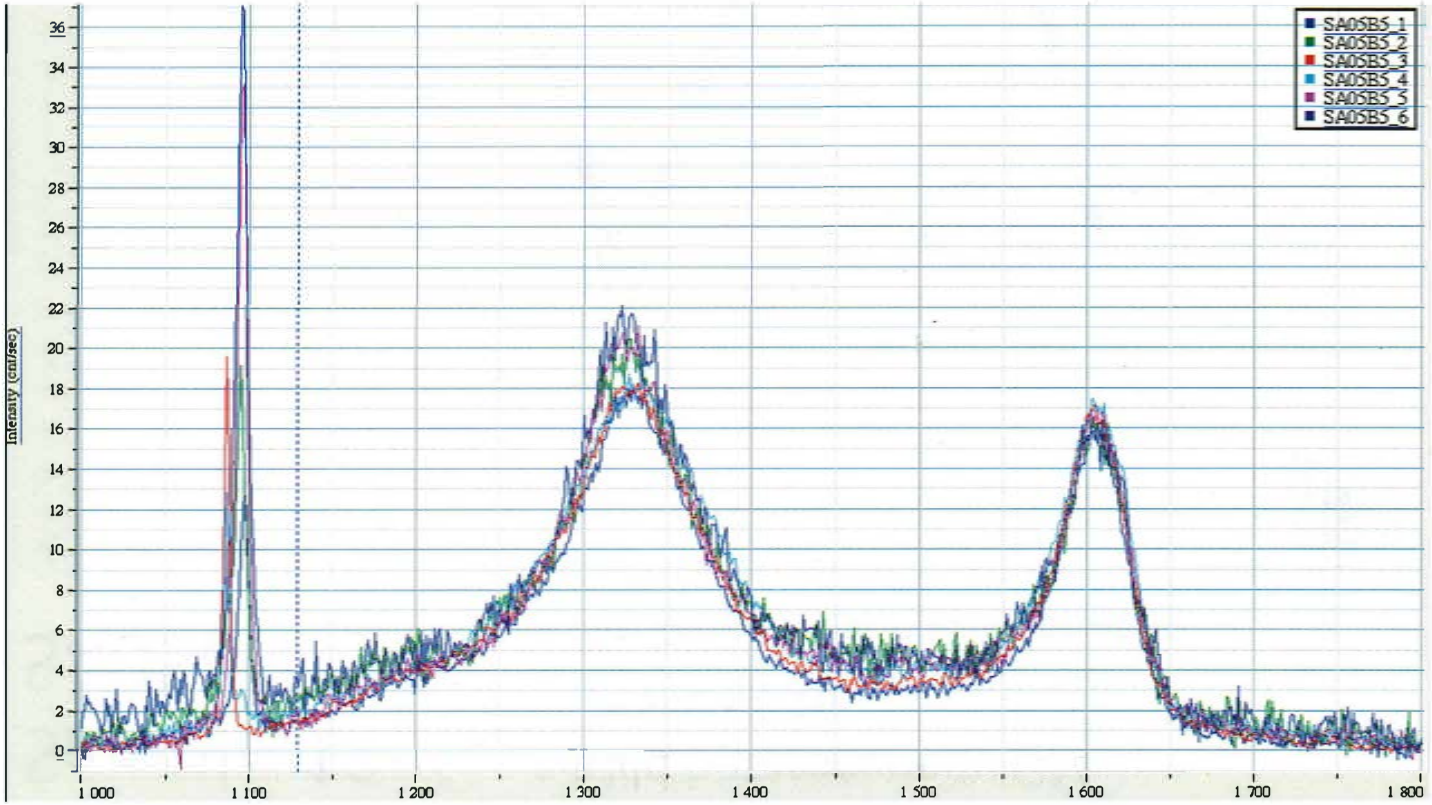
Sample 17: SA05B4

- Very mild heterogeneity OM
  - H:C = 0.15
- Homogeneous Carbonates (1097)



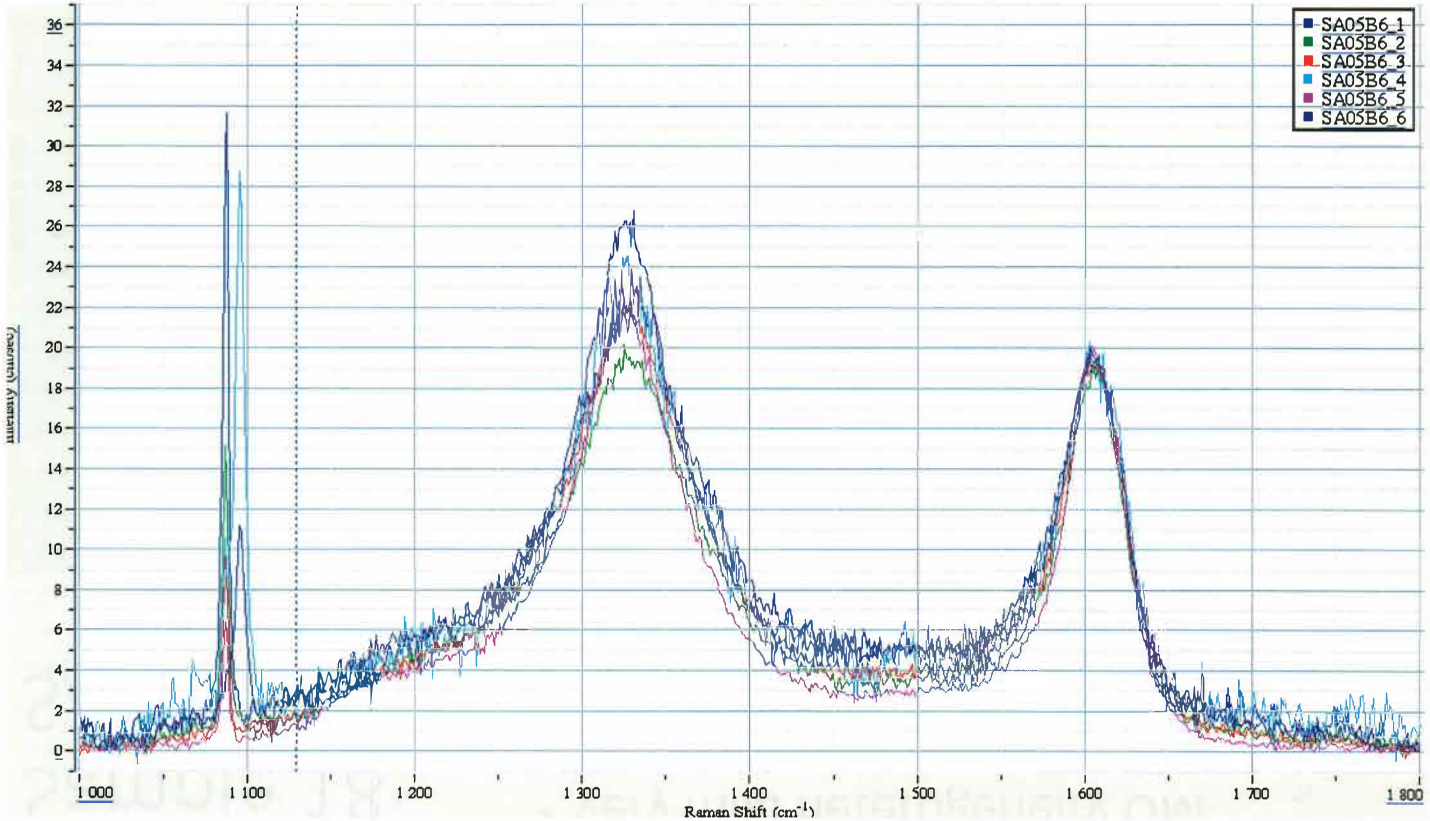
Sample 18: SA05B5

- Very mild heterogeneity OM
  - H:C = 0.15
- Heterogeneous Carbonates



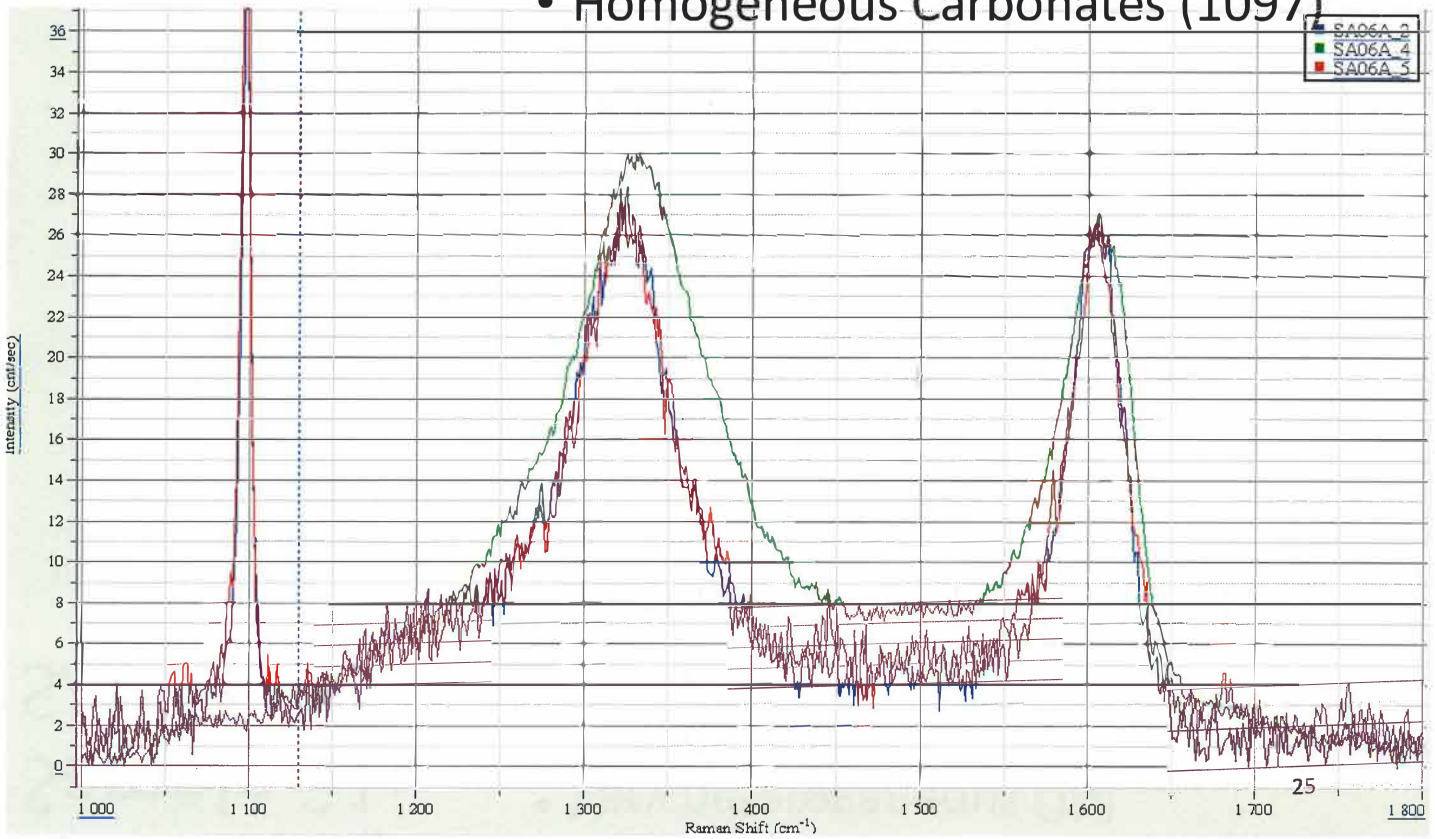
Sample 19: SA05B6

- Mild heterogeneity OM
  - H:C = 0.16
- Heterogeneous Carbonates



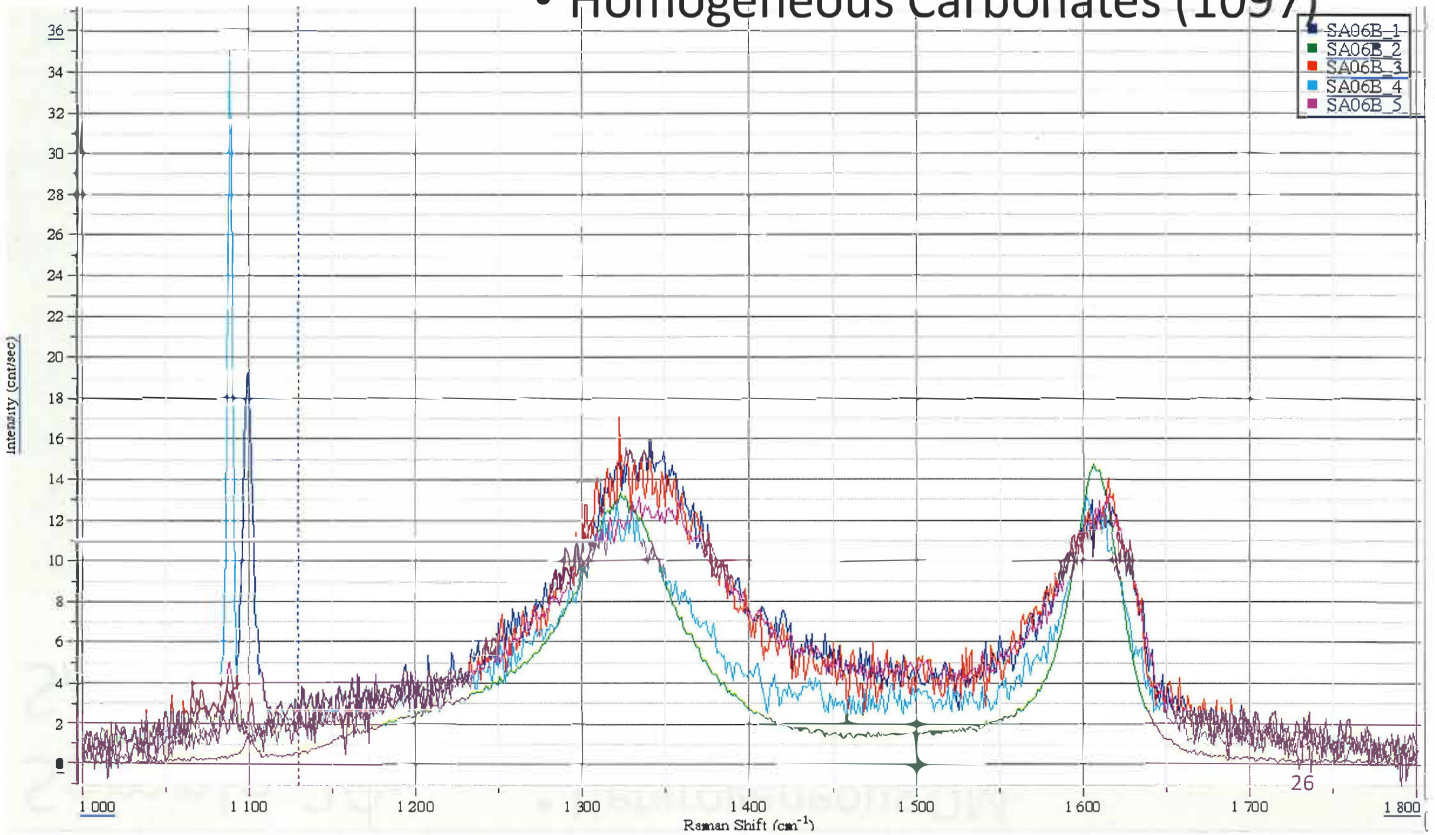
Sample 20: SA06A

- Heterogeneous OM
  - H:C = 0.16
  - H:C = 0.2 (Green – no carbonate)
- Homogeneous Carbonates (1097)



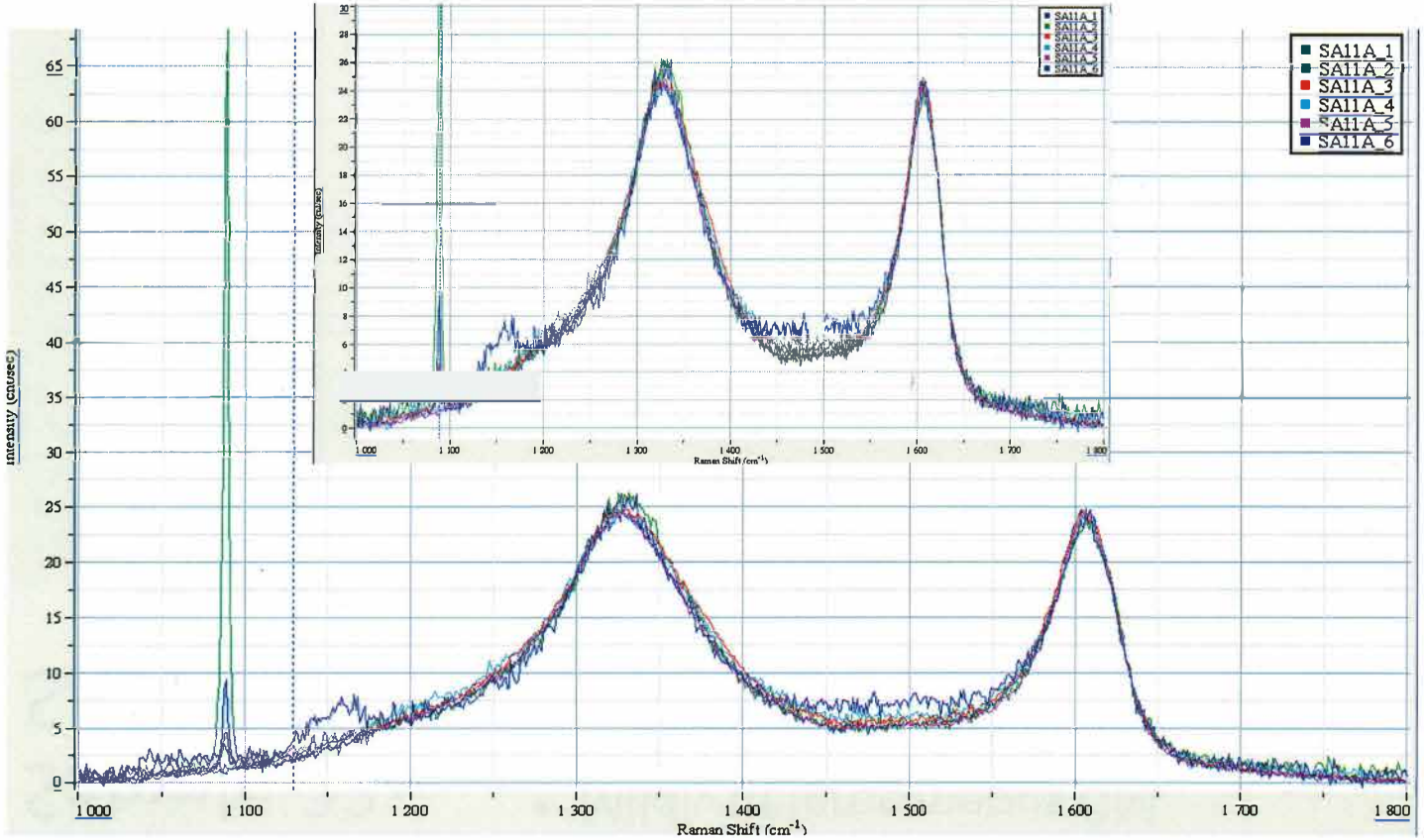
Sample 21: SA06B

- Very heterogeneous OM
  - H:C = 0.15
  - H:C = 0.23
- Homogeneous Carbonates (1097)



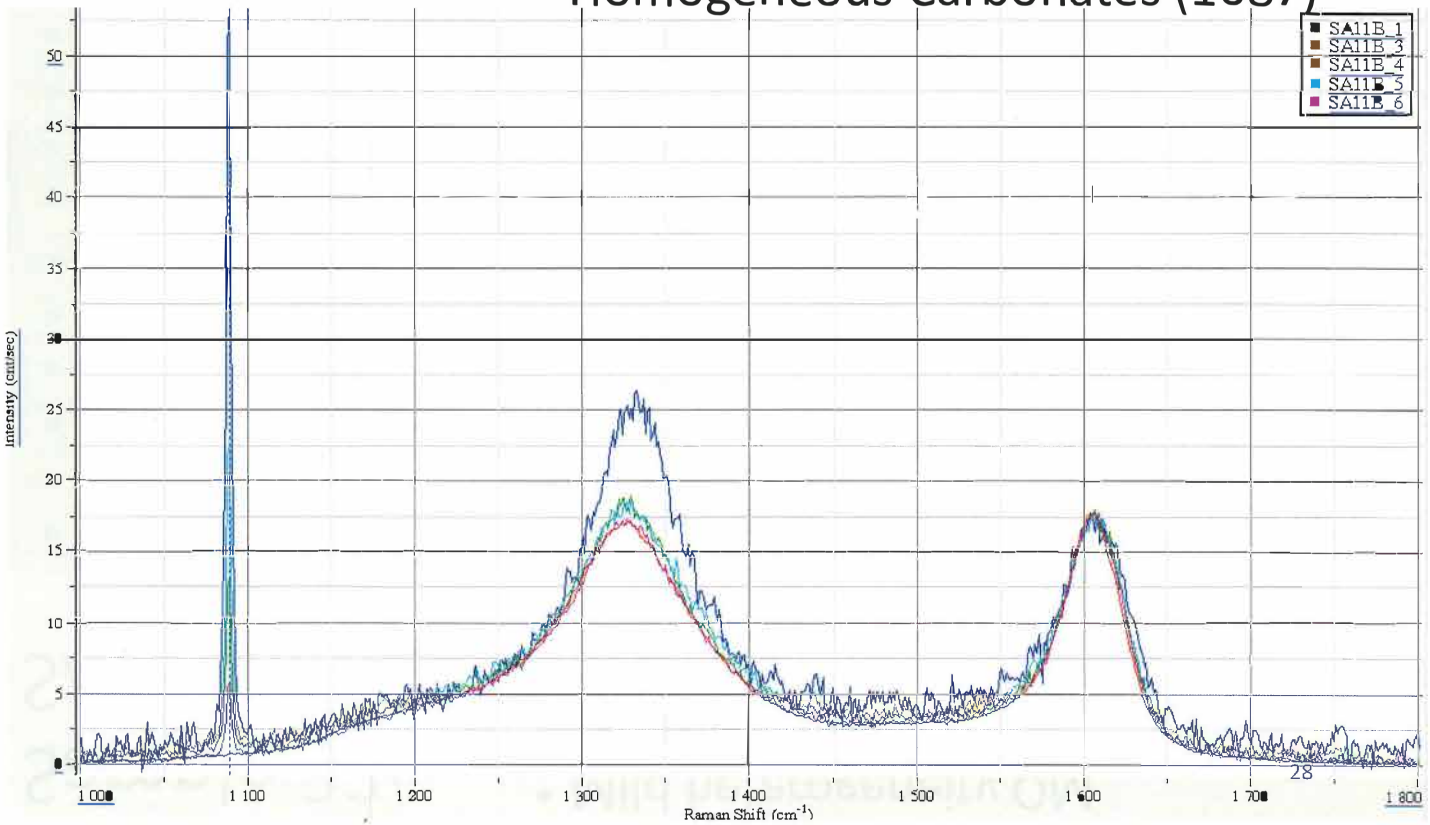
Sample 22: SA11A

- Mild heterogeneity OM
  - H:C = 0.23
- Homogeneous Carbonates (1087)



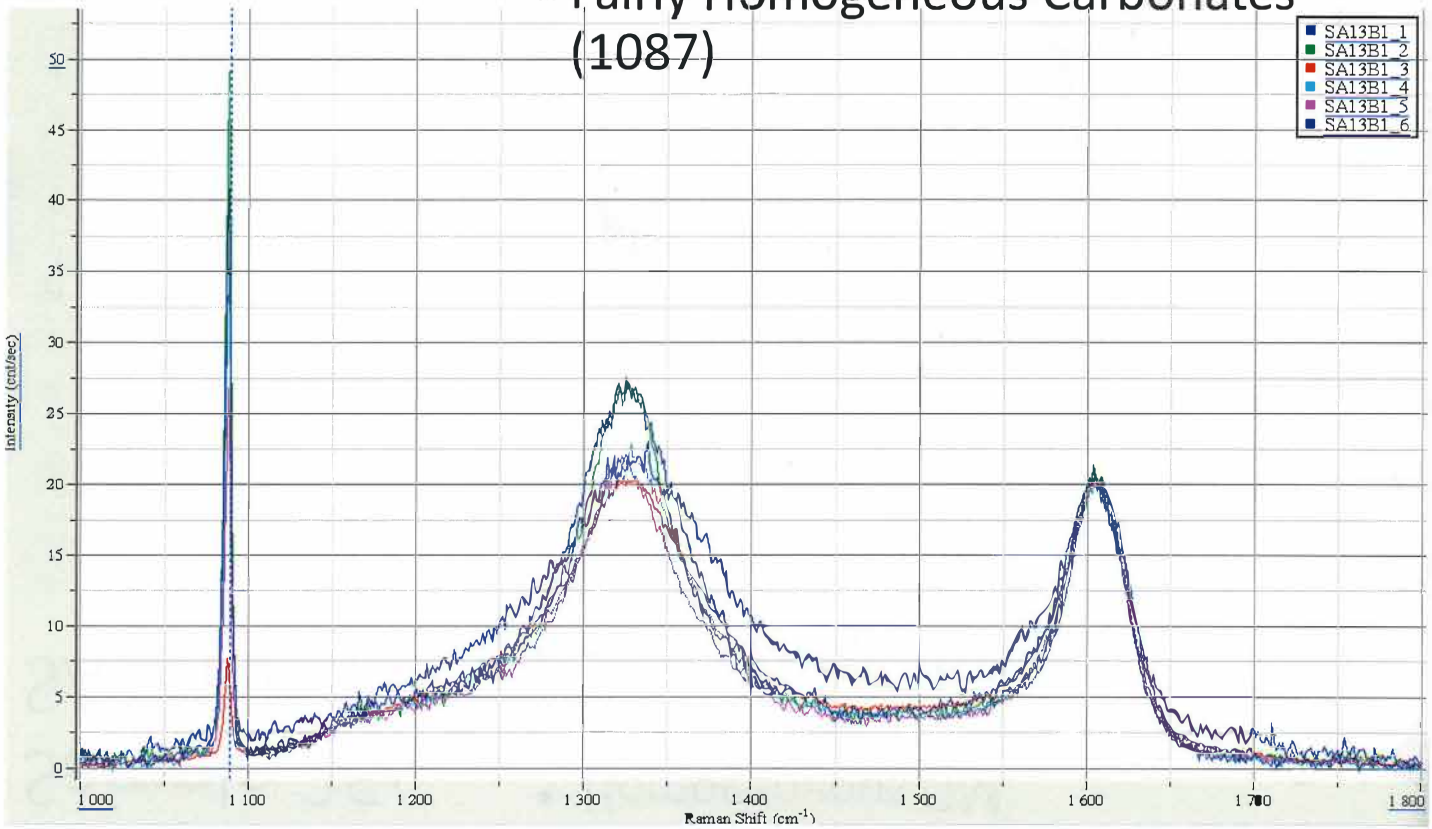
Sample 23: SA11B

- Mildly heterogeneous OM
  - D1 band – aromatic clusters
  - H:C = 0.17
- Homogeneous Carbonates (1087)



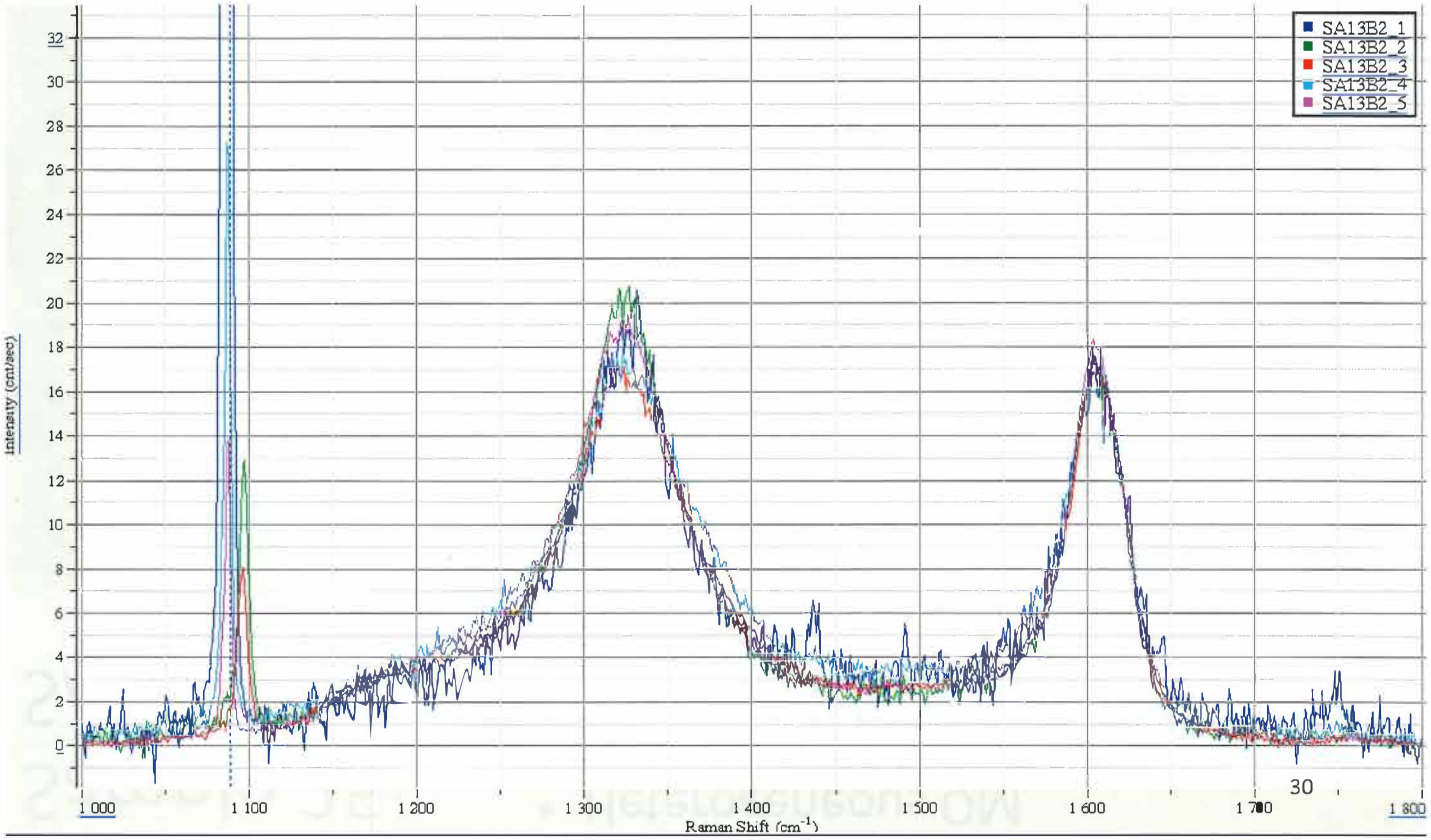
Sample 25: SA13B1

- Heterogeneous OM
  - H:C = 0.13
  - H:C = 0.20
- Fairly Homogeneous Carbonates (1087)



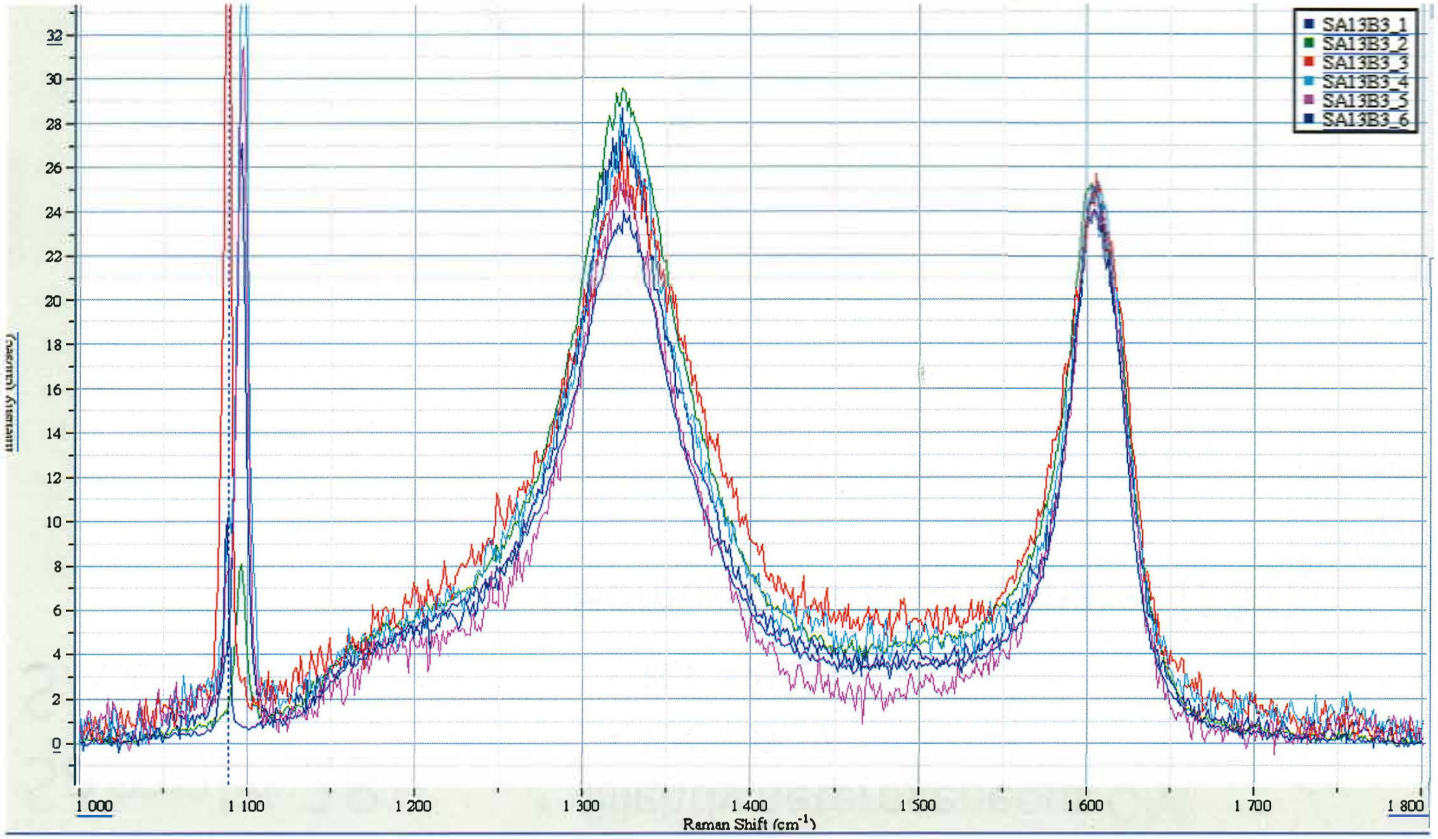
Sample 26: SA13B2

- Homogeneous OM
  - H:C = 0.16
- Heterogeneous Carbonates



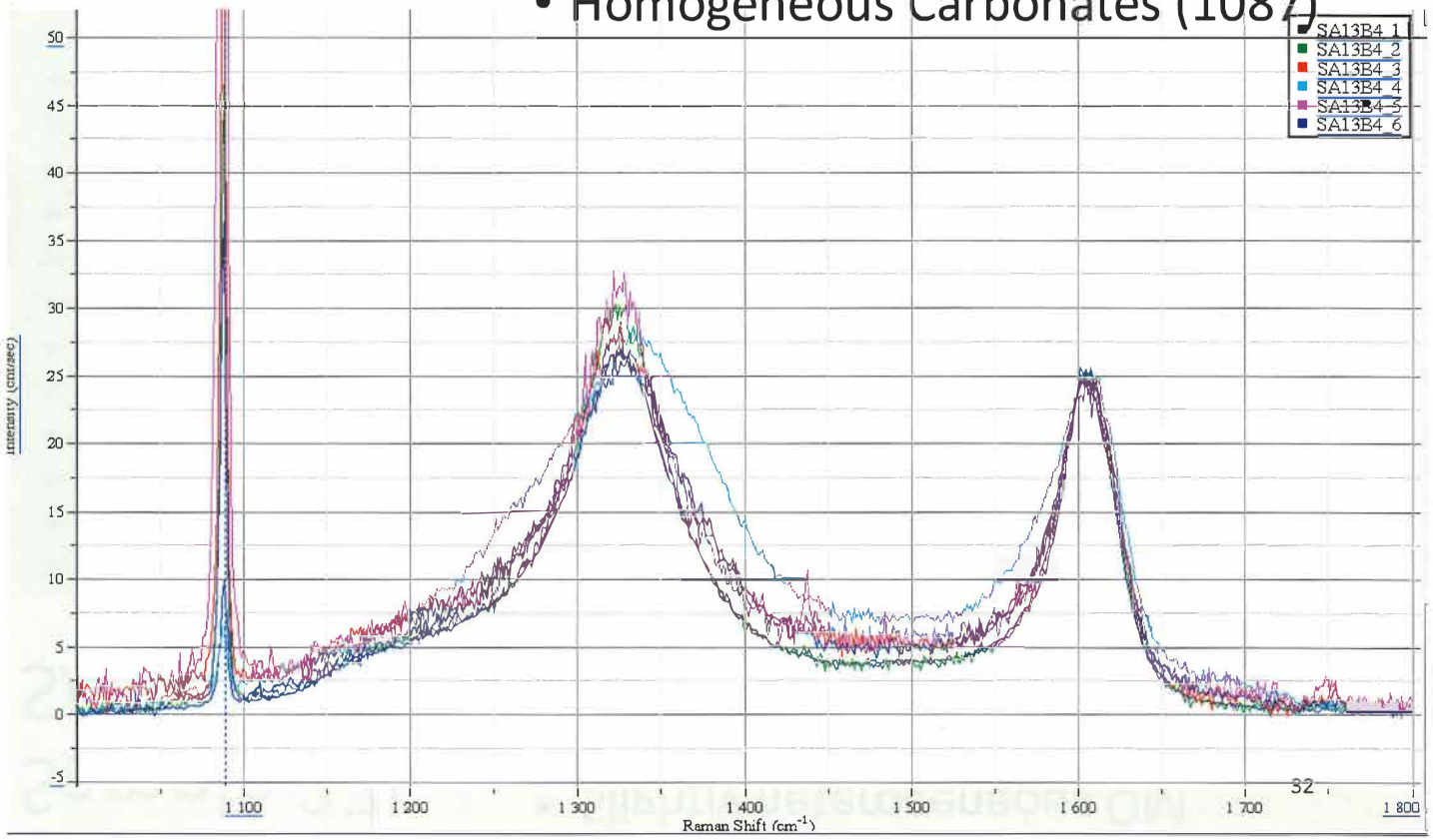
Sample 27: SA13B3

- Slightly heterogeneous OM
  - H:C = 0.14
- Heterogeneous Carbonates



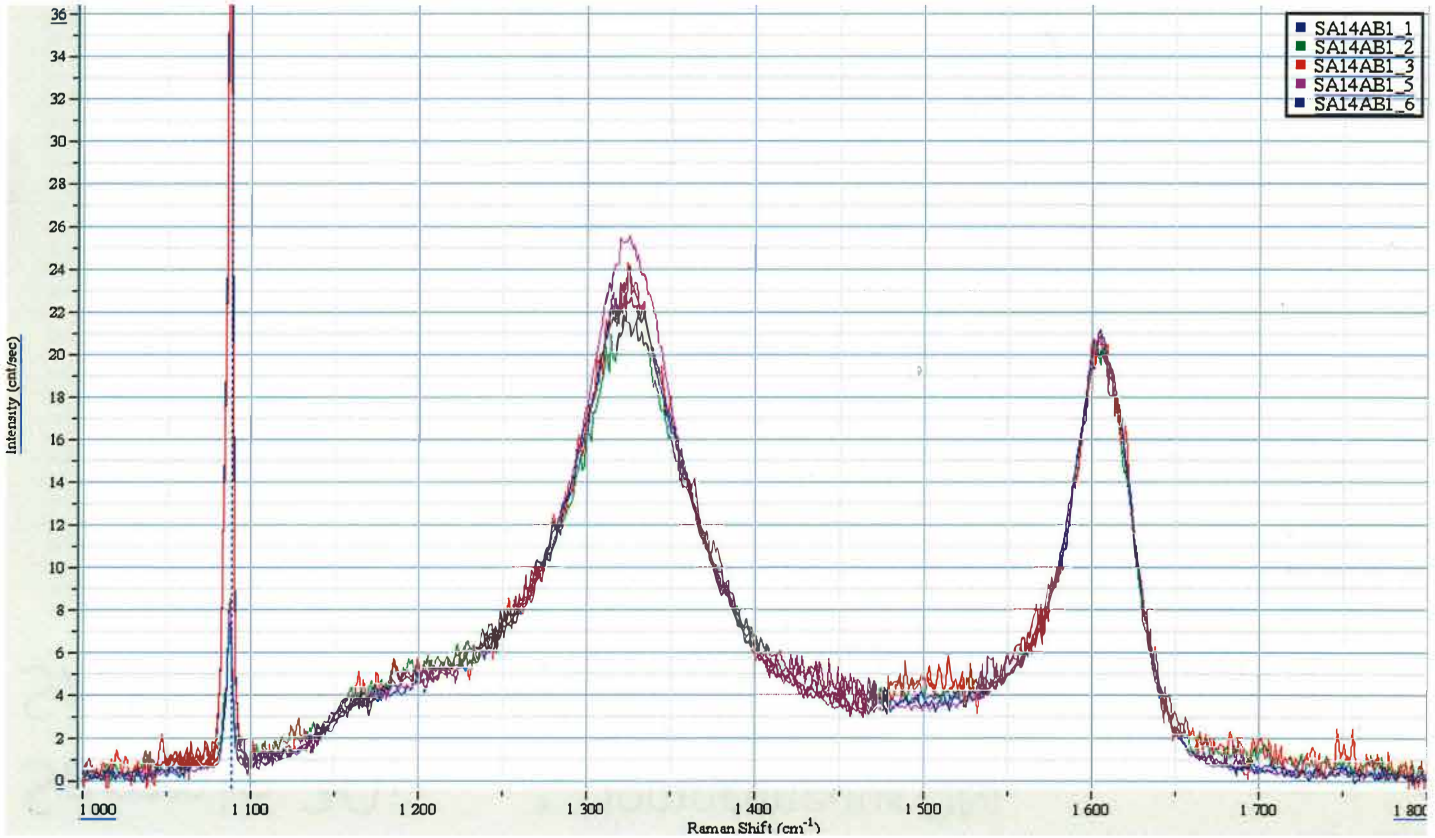
Sample 28: SA13B4

- Slightly heterogeneous OM
  - H:C = 0.17
  - H:C = 0.23 (cyan)
- Homogeneous Carbonates (1087)



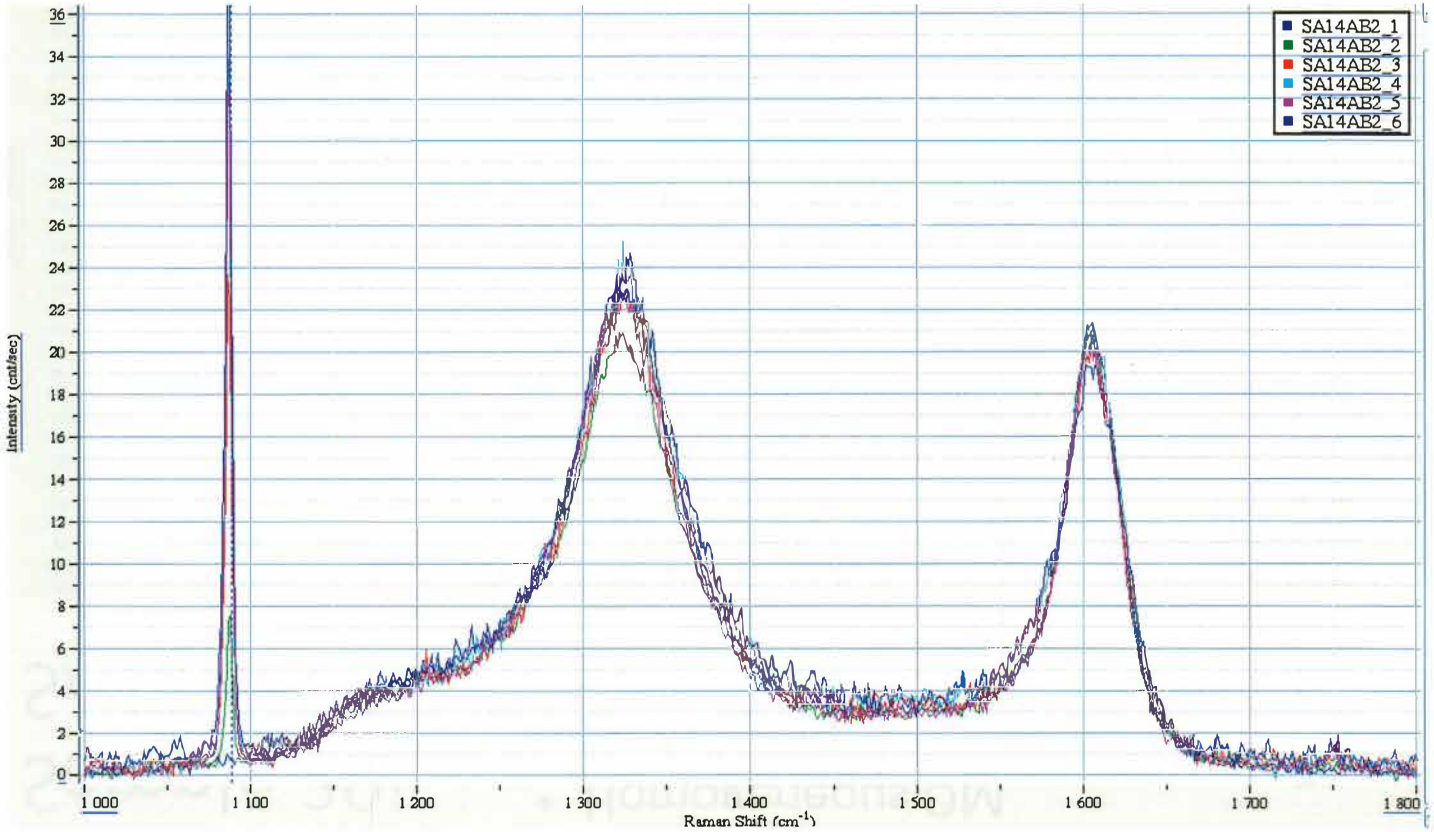
Sample 29: SA14AB1

- Homogeneous OM
  - H:C = 0.14
- Homogeneous Carbonates (1087)



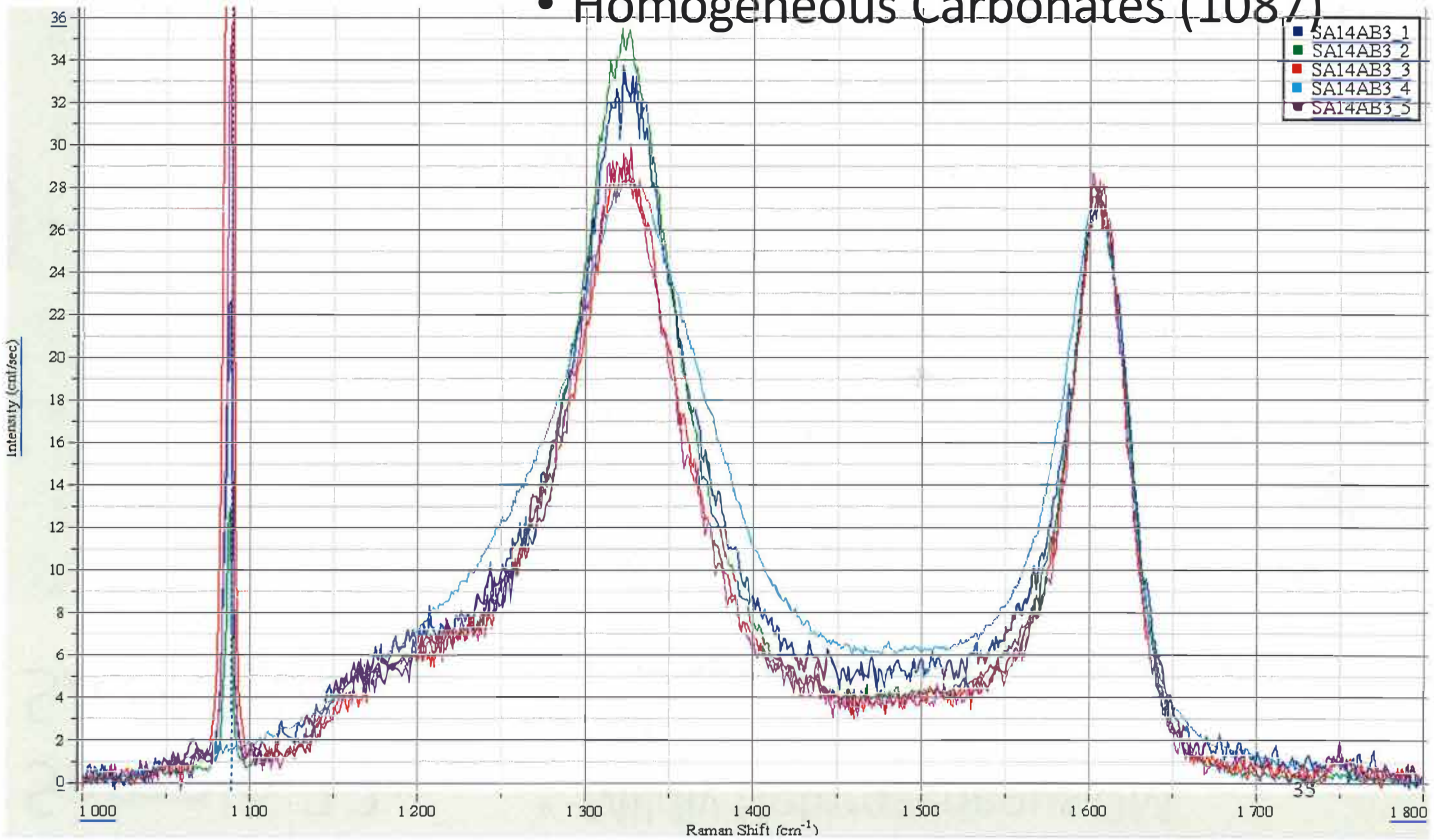
Sample 30: SA14AB2

- Homogeneous OM
  - H:C = 0.16
- Homogeneous Carbonates (1087)



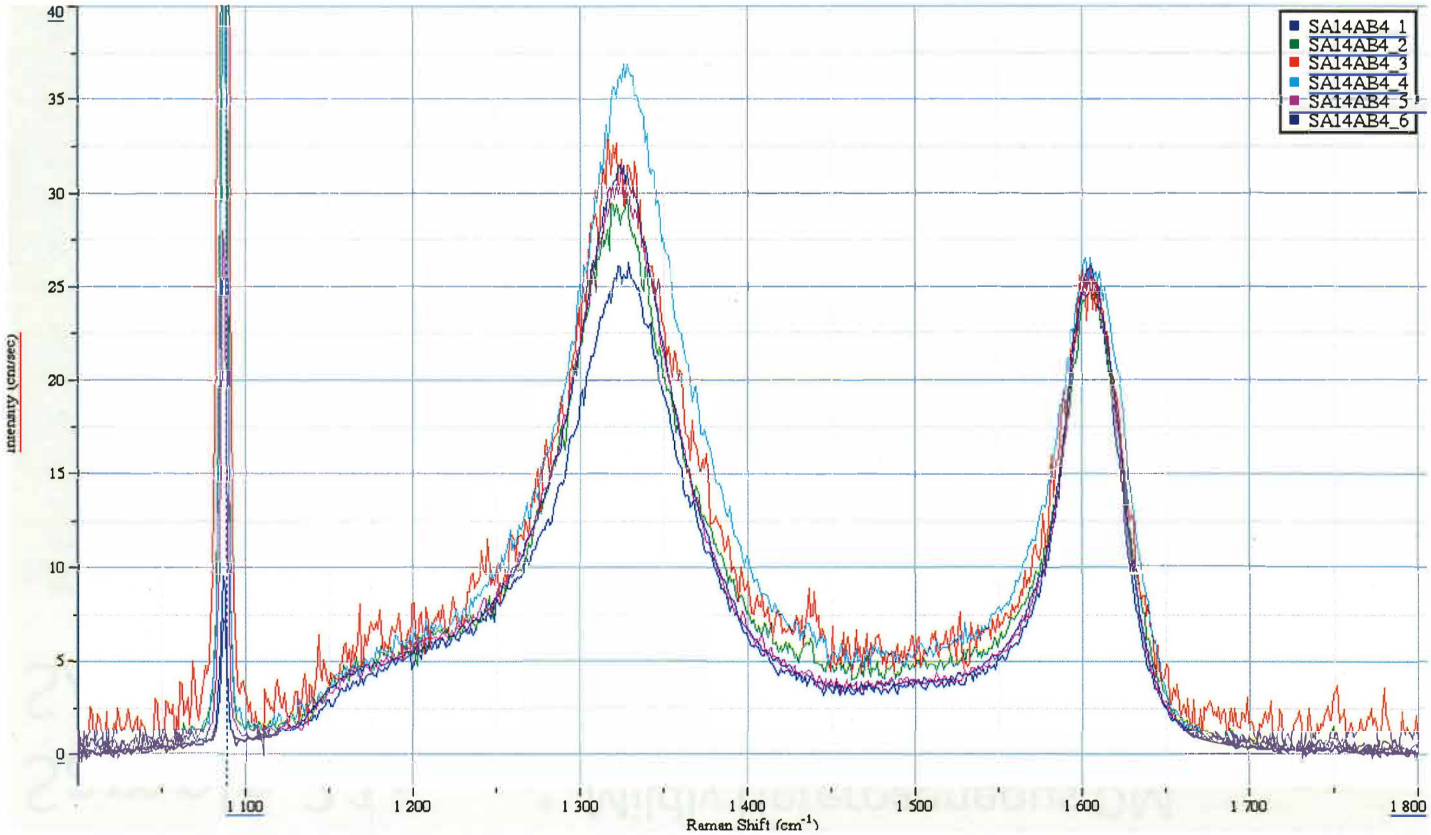
Sample 31: SA14AB3

- Mildly Heterogeneous OM
  - H:C = 0.14
  - H:C = 0.24 (cyan)
- Homogeneous Carbonates (1087)



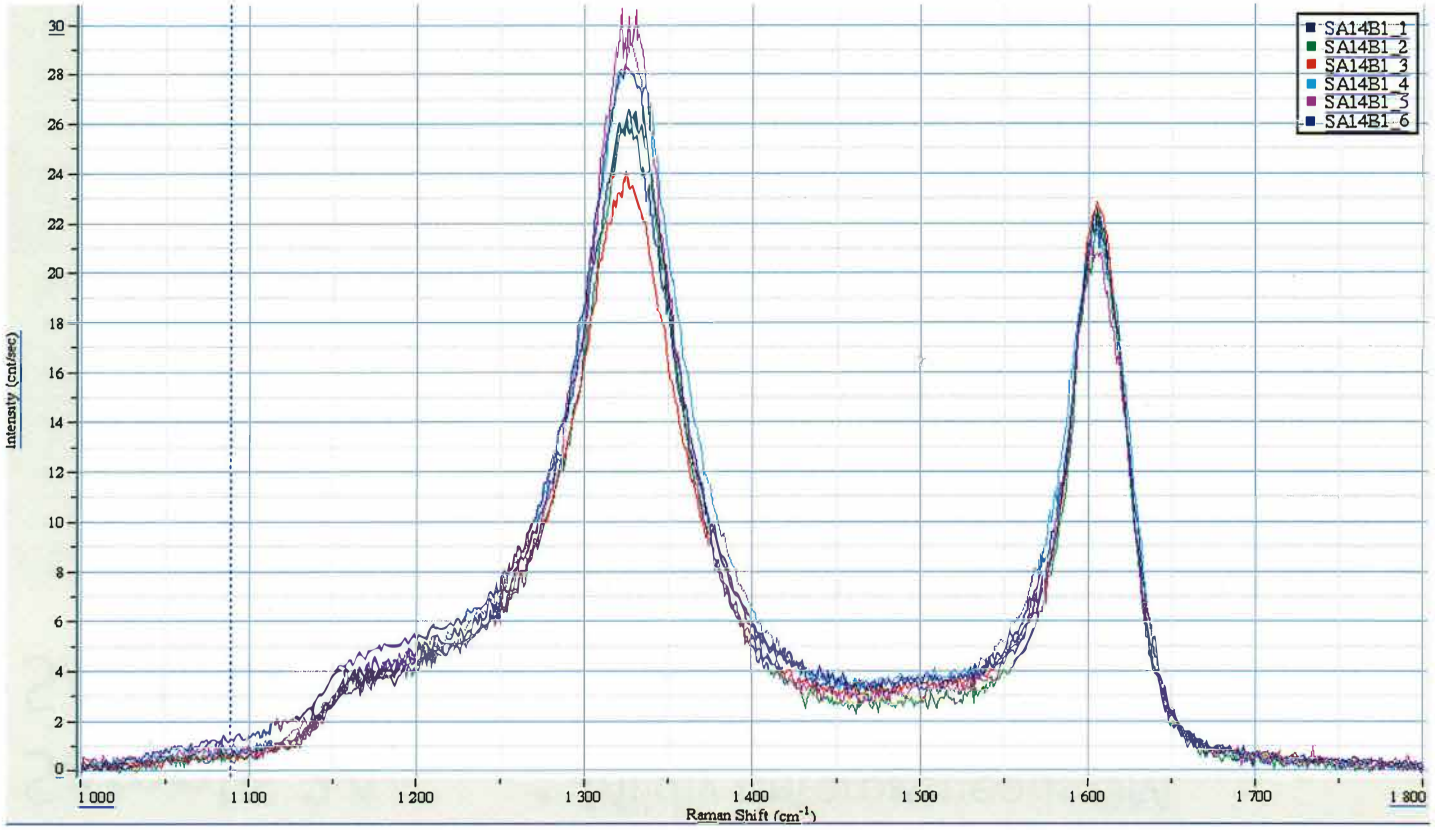
Sample 32: SA14AB4

- Mildly Heterogeneous OM
  - H:C = 0.15
- Homogeneous Carbonates (1087)



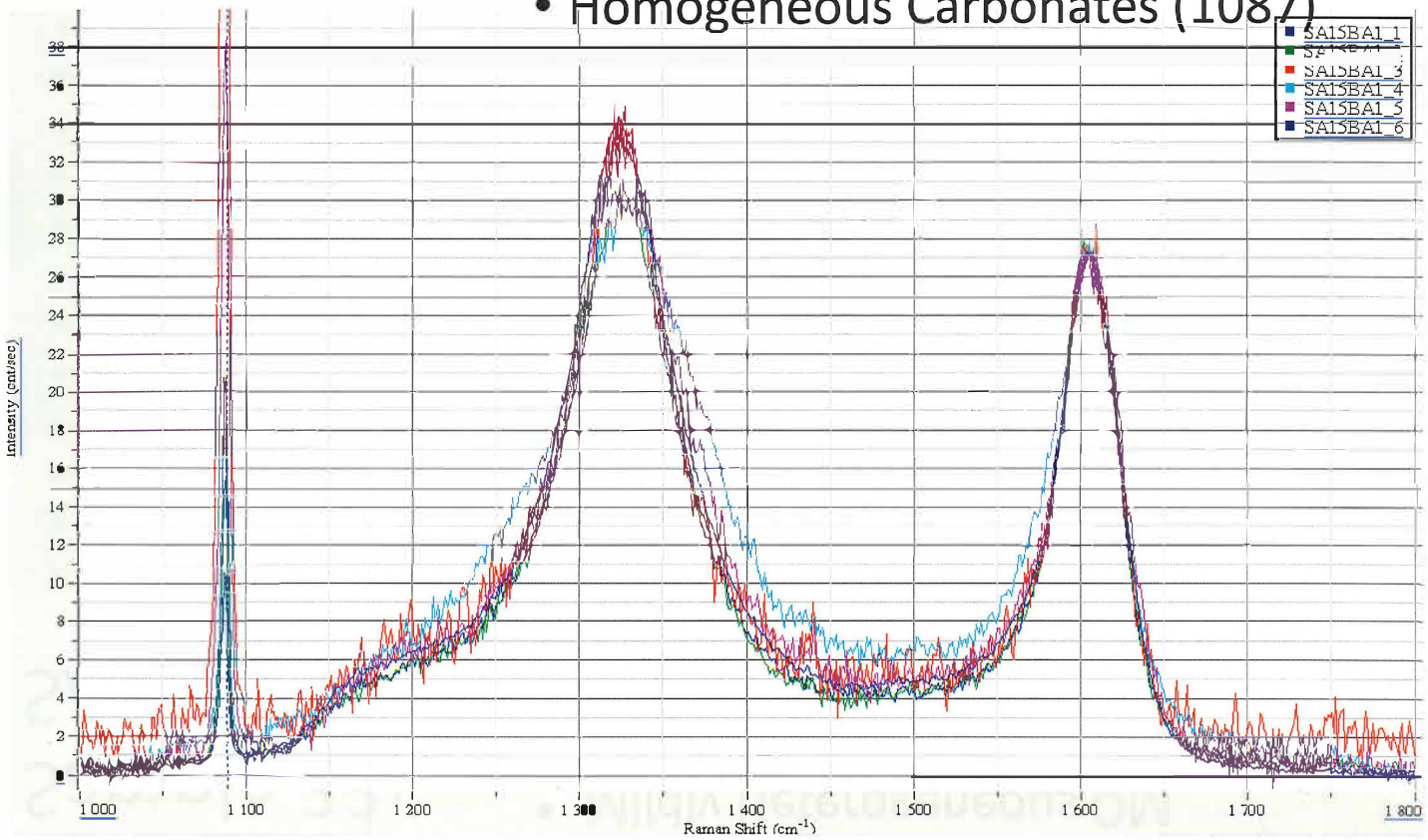
Sample 33: SA14B1

- Mildly Heterogeneous OM
  - H:C = 0.15
- No Carbonates (within the spectra)



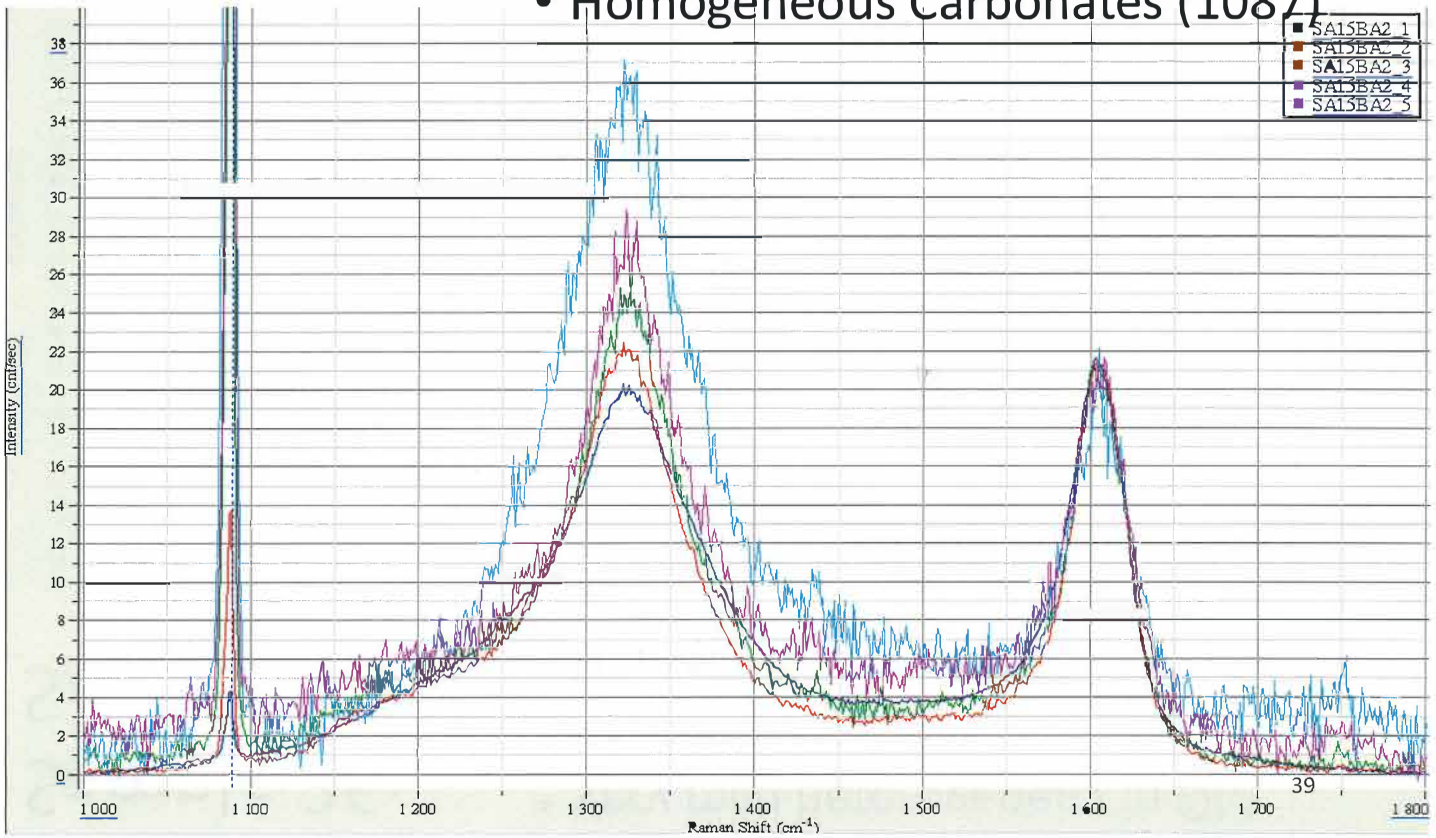
Sample 34: SA15BA1

- Mildly Heterogeneous OM
  - H:C = 0.15
  - H:C = 0.23
- Homogeneous Carbonates (1087)



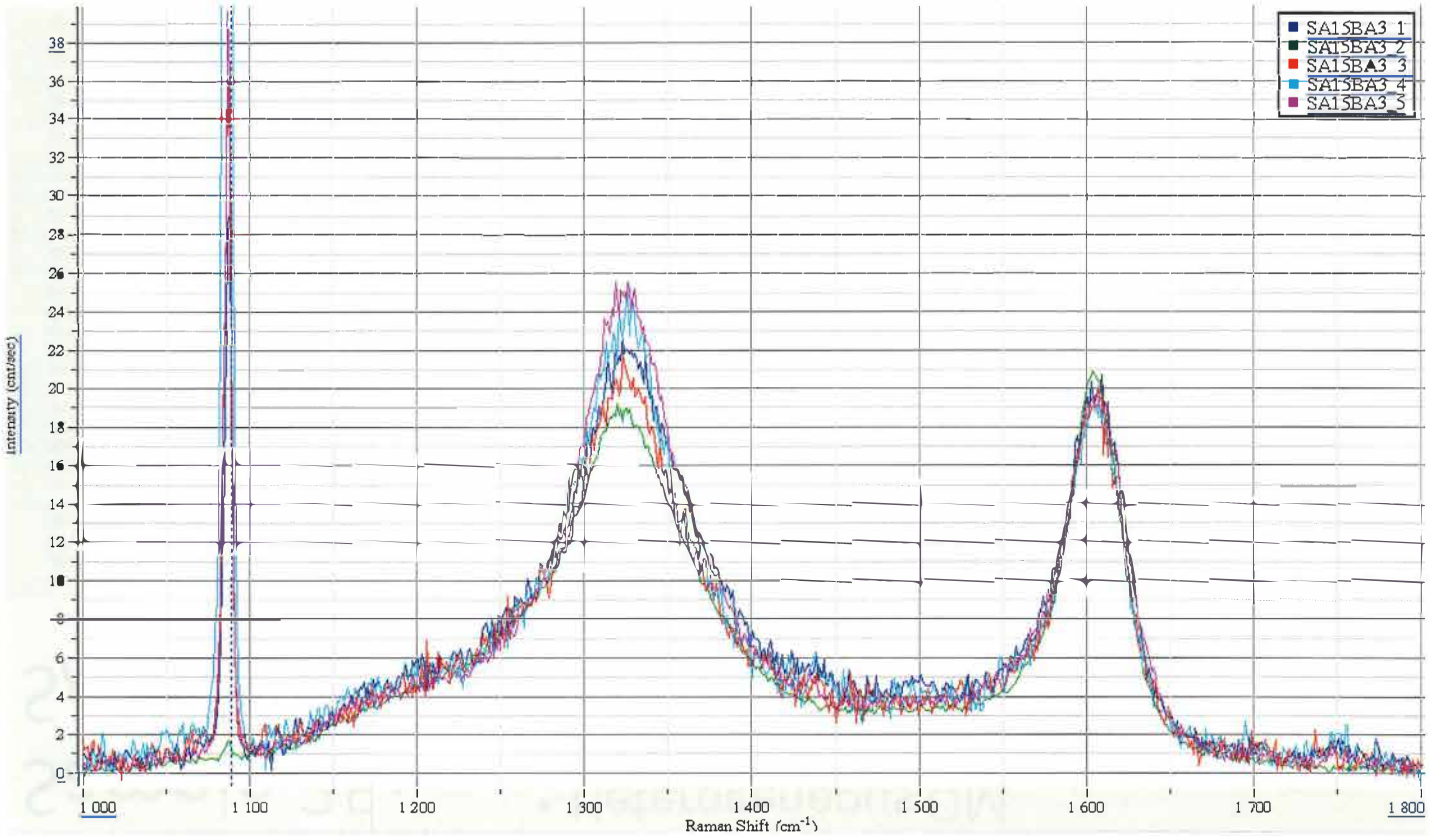
Sample 35: SA15BA2

- Heterogeneous OM
  - From D1 band – aromatic clusters
  - H:C = 0.17
- Homogeneous Carbonates (1087)



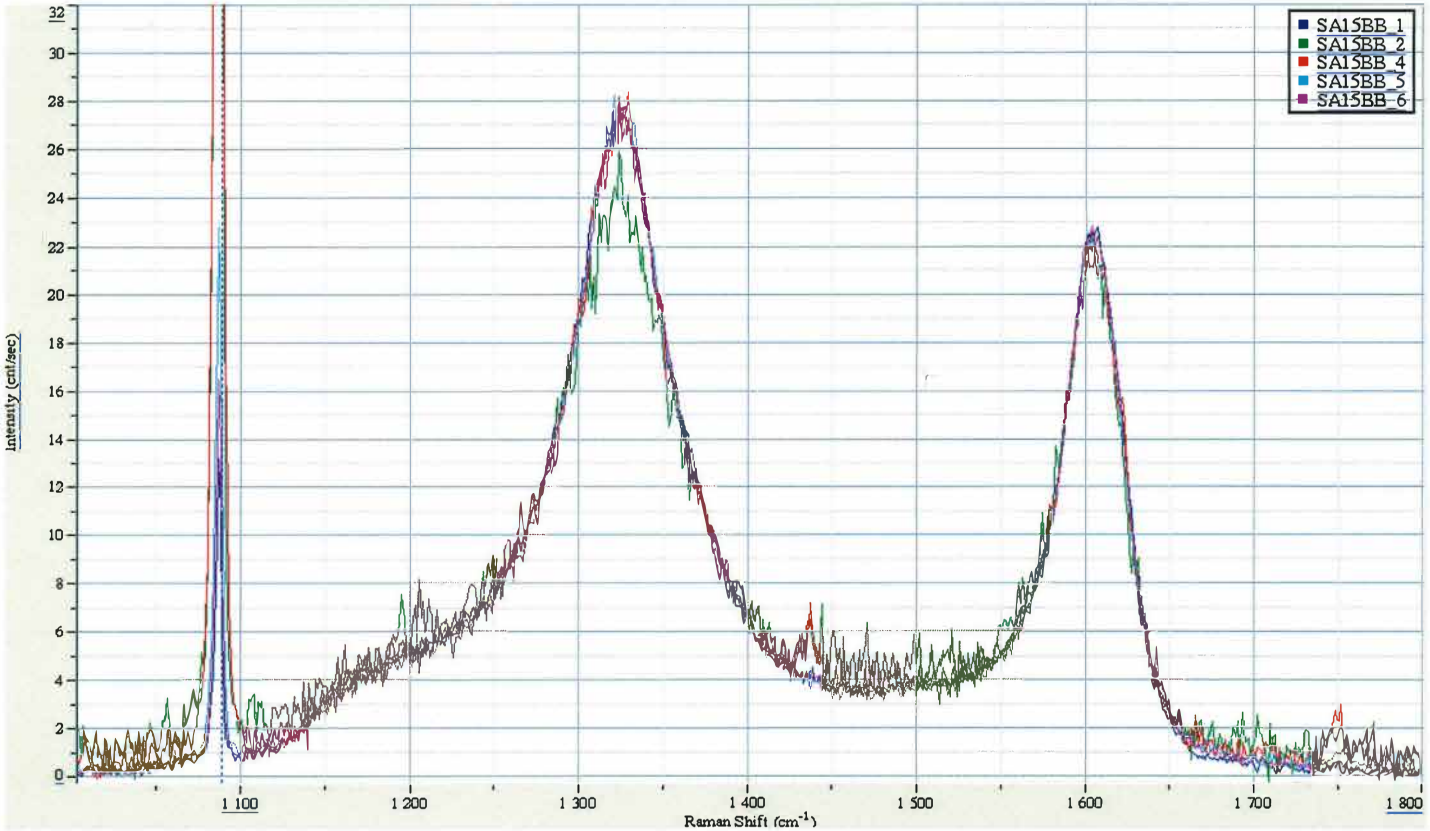
Sample 36: SA15BA3

- Very mild heterogeneity in OM
  - H:C = 0.15
- Homogeneous Carbonates (1087)



Sample 37: SA15BB

- Very mild heterogeneity in OM
  - H:C = 0.14
- Homogeneous Carbonates (1087)



Appendix C: UW-Madison Thesis Collection Sample Identification Table

GEOLOGY MUSEUM
UW MADISON

DEPARTMENT OF GEOSCIENCE
1215 W. DAYTON STREET
MADISON, WISCONSIN 53706
MUSEUM OFFICE 608.262.1412
COLLECTIONS 608.262.4912
FAX 608.262.0693

Preparing thesis samples for the UW Thesis Collection

In order to complete your degree, any specimens relevant to your thesis must be cataloged and deposited with the UW Thesis Collection. In order to fulfill this requirement, you will be responsible for the following:

1) Meeting with the Museum Curator at least *two months* before your defense date to receive your collection number and discuss your specimens

2) Numbering and labeling your own specimens according to the instructions in this packet

3) Returning all of your specimens, once they are numbered, to the Museum Curator for review and depositing

UW Thesis Catalog Number:

You are given one UW Thesis Collection "lot" numer. This number refers to the collection of specimens from your M.S. or Ph.D. thesis. A catalog number contains three parts: the "lot" number, the "primary" number, and an optional "secondary" number. Your lot number is UW _____. You will use this lot number on every specimen to be stored in the repository. Please number your specimens with consecutive primary numbers: UW_____/1, UW_____/2, etc. If you have multiple parts to one sample (e.g. a hand sample, a billet, and a thin section), please label each component part consecutively under the same primary number with consecutive secondary numbers: UW_____/1.1, UW_____1.2, etc. If, for example, you have a hand sample with a corresponding billet and thin section, the hand sample might be numbered UWXXXX/1.1, the billet would be UWXXXX/1.2, and the thin section would be UWXXXX/1.3

Do not use your own field or lab numbers behind the UW prefix.

How to reference specimens in your thesis text:

Please put the following sentence at the end of your introduction or thesis abstract section:

"All specimens referenced in this thesis are in the collections of the Department of Geoscience, University of Wisconsin-Madison, under file number UW_____."

Do not use this sentence if you have not turned in any specimens to the Museum Curator.

A table **must** be put in an Appendix listing all samples you have used to complete your research. This table should list thie UW specimen number, any correlating lab or field numbers, a short sample description, location, and the figures in which those specimens appear. ***You should also provide a copy of this table, printed on archival acid-free paper, to be filed with your thesis specimens in the repository.***

Appendix C: UW-Madison Thesis Collection Sample Identification Table

	Identification Numbers					
UW-Madison	**Publication**	**Lab or Field**	**Sample Type**	**Locality**	**Description**	**Featured In**
UW2038/1.1	UWAI-001/022	20140203	synthetic calcite powder	Room 456, Weeks Hall, Madison, Wi, USA	43Ca spiked seeds, bulk, Mg-free	Ch. 2, Sec. 2.1 & Fig. S1 & Tables S1 and S3
UW2038/1.2	UWAI-001/022	SS1	EPMA plug mount	Room 456, Weeks Hall, Madison, Wi, USA	43Ca spiked seeds, bulk, Mg-free	Ch. 2, Sec. 2.1 & Fig. S1 & Tables S1 and S3
UW2038/1.3	UWAI-001/022	SS2	EPMA plug mount	Room 456, Weeks Hall, Madison, Wi, USA	43Ca spiked seeds, bulk, Mg-free, duplicate of SS1	Ch. 2, Sec. 2.1 & Fig. S1 & Tables S1 and S3
UW2038/1.4	UWAI-001/022	ST	EPMA plug mount	Room 456, Weeks Hall, Madison, Wi, USA	43Ca spiked seeds, “tiny” size fraction, Mg-free	Ch. 2, Sec. 2.1 & Fig. S1 & Tables S1 and S3
UW2038/1.5	UWAI-001/022	SB	EPMA plug mount	Room 456, Weeks Hall, Madison, Wi, USA	43Ca spiked seeds, “big” size fraction, Mg-free	Ch. 2, Sec. 2.1 & Fig. S1 & Tables S1 and S3
UW2038/2	UWAI-002	20140214	synthetic calcite powder	Room 456, Weeks Hall, Madison, Wi, USA	20.0°C, 5% pCO2, 6.8 pH	Chapter 2, Tables 1 & 2
UW2038/3	UWAI-003	20140221	synthetic calcite powder	Room 456, Weeks Hall, Madison, Wi, USA	20.0°C, 5% pCO2, 6.9 pH	Chapter 2, Tables 1 & 2
UW2038/4	UWAI-004	20140227	synthetic calcite powder	Room 456, Weeks Hall, Madison, Wi, USA	20.0°C, 5% pCO2, 6.9 pH	Chapter 2, Tables 1 & 2
UW2038/5	UWAI-005	20140305	synthetic calcite powder	Room 456, Weeks Hall, Madison, Wi, USA	20.0°C, 5% pCO2, 6.9 pH	Chapter 2, Tables 1 & 2
UW2038/6	UWAI-006	20140314A	synthetic calcite powder	Room 456, Weeks Hall, Madison, Wi, USA	20.0°C, 5% pCO2, 6.9 pH	Chapter 2, Tables 1 & 2
UW2038/7	UWAI-007	20140314B	synthetic calcite powder	Room 456, Weeks Hall, Madison, Wi, USA	19.9°C, 5% pCO2, 6.8 pH	Chapter 2, Tables 1 & 2
UW2038/8	UWAI-008	20140320A	synthetic calcite powder	Room 456, Weeks Hall, Madison, Wi, USA	20.0°C, 5% pCO2, 6.9 pH	Chapter 2, Tables 1 & 2
UW2038/9	UWAI-009	20140320B	synthetic calcite powder	Room 456, Weeks Hall, Madison, Wi, USA	19.9°C, 5% pCO2, 6.9 pH	Chapter 2, Tables 1 & 2
UW2038/10	UWAI-010	20140325A	synthetic calcite powder	Room 456, Weeks Hall, Madison, Wi, USA	20.0°C, 5% pCO2, 6.9 pH	Chapter 2, Tables 1 & 2
UW2038/11	UWAI-011	20140325B	synthetic calcite powder	Room 456, Weeks Hall, Madison, Wi, USA	19.9°C, 5% pCO2, 7.0 pH	Chapter 2, Tables 1 & 2
UW2038/12	UWAI-012	20140403A	synthetic calcite powder	Room 456, Weeks Hall, Madison, Wi, USA	20.0°C, 5% pCO2, 7.0 pH	Chapter 2, Tables 1 & 2
UW2038/13	UWAI-013	20140403B	synthetic calcite powder	Room 456, Weeks Hall, Madison, Wi, USA	19.9°C, 5% pCO2, 7.0 pH	Chapter 2, Tables 1 & 2
UW2038/14	UWAI-014	20140409A	synthetic calcite powder	Room 456, Weeks Hall, Madison, Wi, USA	20.0°C, 10% pCO2, 6.6 pH	Chapter 2, Tables 1 & 2
UW2038/15	UWAI-015	20140409B	synthetic calcite powder	Room 456, Weeks Hall, Madison, Wi, USA	19.9°C, 10% pCO2, 6.6 pH	Chapter 2, Tables 1 & 2
UW2038/16	UWAI-016	20140414A	synthetic calcite powder	Room 456, Weeks Hall, Madison, Wi, USA	9.9°C , 10% pCO2, 6.5 pH	Chapter 2, Tables 1 & 2
UW2038/17	UWAI-017	20140414B	synthetic calcite powder	Room 456, Weeks Hall, Madison, Wi, USA	9.9°C, 10% pCO2, 6.6 pH	Chapter 2, Tables 1 & 2
UW2038/18	UWAI-018	20140420A	synthetic calcite powder	Room 456, Weeks Hall, Madison, Wi, USA	10.0°C, 10% pCO2, 6.5 pH	Chapter 2, Tables 1 & 2
UW2038/19	UWAI-019	20140420B	synthetic calcite powder	Room 456, Weeks Hall, Madison, Wi, USA	9.9°C, 10% pCO2, 6.7 pH	Chapter 2, Tables 1 & 2
UW2038/20	UWAI-020	20140427A	synthetic calcite powder	Room 456, Weeks Hall, Madison, Wi, USA	30.0°C, 16% pCO2, 6.3 pH	Chapter 2, Tables 1 & 2
UW2038/21	UWAI-021	20140427B	synthetic calcite powder	Room 456, Weeks Hall, Madison, Wi, USA	30.1°C, 16% pCO2, 6.5 pH	Chapter 2, Tables 1 & 2
UW2038/22	Water δ18O	"deionized water"	liquid (20 mL)	Madison, Wi, USA	water used to precipitate experimental calcite	Chapter 2, Table 1; Appendix B
UW2038/23	UWAI-023	20140531A	synthetic calcite powder	Room 456, Weeks Hall, Madison, Wi, USA	20.0°C, 6% pCO2, 6.8 pH	Chapter 2, Tables 1 & 2
UW2038/24	UWAI-024	20140531B	synthetic calcite powder	Room 456, Weeks Hall, Madison, Wi, USA	19.9°C, 6% pCO2, 6.9 pH	Chapter 2, Tables 1 & 2
UW2038/25	UWAI-025	20140607A	synthetic calcite powder	Room 456, Weeks Hall, Madison, Wi, USA	9.5°C, 6% pCO2, 6.7 pH	Chapter 2, Tables 1 & 2
UW2038/26	UWAI-026	20140607B	synthetic calcite powder	Room 456, Weeks Hall, Madison, Wi, USA	10.4°C, 6% pCO2, 6.8 pH	Chapter 2, Tables 1 & 2
UW2038/27	UWAI-027	20140617A	synthetic calcite powder	Room 456, Weeks Hall, Madison, Wi, USA	10.0°C, 6% pCO2, 6.8 pH	Chapter 2, Tables 1 & 2
UW2038/28	UWAI-028	20140617B	synthetic calcite powder	Room 456, Weeks Hall, Madison, Wi, USA	10.0°C, 6% pCO2, 6.8 pH	Chapter 2, Tables 1 & 2
UW2038/29	UWAI-029	20140626A	synthetic calcite powder	Room 456, Weeks Hall, Madison, Wi, USA	10.0°C, 6% pCO2, 6.8 pH	Chapter 2, Tables 1 & 2
UW2038/30	UWAI-030	20140626B	synthetic calcite powder	Room 456, Weeks Hall, Madison, Wi, USA	10.9°C, 6% pCO2, 6.8 pH	Chapter 2, Tables 1 & 2
UW2038/31	UWAI-031	20140630A	synthetic calcite powder	Room 456, Weeks Hall, Madison, Wi, USA	9.8°C, 6% pCO2, 6.7 pH	Chapter 2, Tables 1 & 2
UW2038/32	UWAI-032	20140630B	synthetic calcite powder	Room 456, Weeks Hall, Madison, Wi, USA	9.9°C, 6% pCO2, 6.7 pH	Chapter 2, Tables 1 & 2
UW2038/33	UWAI-033	20140711A	synthetic calcite powder	Room 456, Weeks Hall, Madison, Wi, USA	9.9°C, 6% pCO2, 6.8 pH	Chapter 2, Tables 1 & 2
UW2038/34	UWAI-034	20140711B	synthetic calcite powder	Room 456, Weeks Hall, Madison, Wi, USA	10.5°C, 6% pCO2, 6.8 pH	Chapter 2, Tables 1 & 2
UW2038/35	UWAI-035	20140717A	synthetic calcite powder	Room 456, Weeks Hall, Madison, Wi, USA	30.0°C, 13% pCO2, 6.6 pH	Chapter 2, Tables 1 & 2
UW2038/36	UWAI-036	20140717B	synthetic calcite powder	Room 456, Weeks Hall, Madison, Wi, USA	30.2°C, 13% pCO2, 6.6 pH	Chapter 2, Tables 1 & 2
UW2038/37	UWAI-037	20140724A	synthetic calcite powder	Room 456, Weeks Hall, Madison, Wi, USA	29.9°C, 13% pCO2, 6.5 pH	Chapter 2, Tables 1 & 2
UW2038/38	UWAI-038	20140724B	synthetic calcite powder	Room 456, Weeks Hall, Madison, Wi, USA	29.9°C, 13% pCO2, 6.5 pH	Chapter 2, Tables 1 & 2
UW2038/39	UWAI-039	20140804A	synthetic calcite powder	Room 456, Weeks Hall, Madison, Wi, USA	30.0°C, 13% pCO2, 6.5 pH	Chapter 2, Tables 1 & 2
UW2038/40	UWAI-040	20140804B	synthetic calcite powder	Room 456, Weeks Hall, Madison, Wi, USA	30.1°C, 13% pCO2, 6.6 pH	Chapter 2, Tables 1 & 2
UW2038/41	UWAI-041	20140810A	synthetic calcite powder	Room 456, Weeks Hall, Madison, Wi, USA	30.0°C, 13% pCO2, 6.5 pH	Chapter 2, Tables 1 & 2
UW2038/42	UWAI-042	20140810B	synthetic calcite powder	Room 456, Weeks Hall, Madison, Wi, USA	30.0°C, 13% pCO2, 6.5 pH	Chapter 2, Tables 1 & 2
UW2038/43	UWAI-043	20140817A	synthetic calcite powder	Room 456, Weeks Hall, Madison, Wi, USA	30.0°C, 13% pCO2, 6.5 pH	Chapter 2, Tables 1 & 2
UW2038/44	UWAI-044	20140817B	synthetic calcite powder	Room 456, Weeks Hall, Madison, Wi, USA	30.2°C, 13% pCO2, 6.6 pH	Chapter 2, Tables 1 & 2
UW2038/45	UWAI-045	20140823A	synthetic calcite powder	Room 456, Weeks Hall, Madison, Wi, USA	19.6°C, 13% pCO2, 6.5 pH	Chapter 2, Tables 1 & 2
UW2038/46	UWAI-046	20140823B	synthetic calcite powder	Room 456, Weeks Hall, Madison, Wi, USA	19.8°C, 13% pCO2, 6.5 pH	Chapter 2, Tables 1 & 2
UW2038/47	UWAI-047	20140901A	synthetic calcite powder	Room 456, Weeks Hall, Madison, Wi, USA	29.5°C, 13% pCO2, 6.5 pH	Chapter 2, Tables 1 & 2
UW2038/48	UWAI-048	20140901B	synthetic calcite powder	Room 456, Weeks Hall, Madison, Wi, USA	30.2°C, 13% pCO2, 6.5 pH	Chapter 2, Tables 1 & 2

Appendix C (cont): UW-Madison Thesis Collection Sample Identification Table

	Identification Numbers					
UW-Madison	**Publication**	**Lab or Field**	**Sample Type**	**Locality**	**Description**	**Featured In**
UW2038/49.1	Agros calcite	Agros calcite	commercial calcite powder	Manufacturer: AGROS Organics	CaCO3, 99+%, Lot: A0350502	Ch. 3, Table 2 & Sec. 2.1, Fig. S2
UW2038/49.2	Agros calcite	AGT	EPMA plug mount	Room 456, Weeks Hall, Madison, Wi, USA	Agros seeds, "tiny" size fraction, ~1.6 mol% Mg	Ch. 3, Table 2 & Sec. 2.1, Fig. S2
UW2038/49.3	Agros calcite	AGB	EPMA plug mount	Room 456, Weeks Hall, Madison, Wi, USA	Agros seeds, "big" size fraction, ~1.6 mol% Mg	Ch. 3, Table 2 & Sec. 2.1, Fig. S2
UW2038/50.1	Baker calcite	Baker calcite	commercial calcite powder	Manufacturer: J.T. Baker	Baker Analyzed™ reagent CaCO3, Lot H22339	Ch. 3, Sec. 2.1, Fig. S2
UW2038/50.2	Baker calcite	BT	EPMA plug mount	Room 456, Weeks Hall, Madison, Wi, USA	Baker seeds, "tiny" size fraction, Mg-free	Ch. 3, Sec. 2.1, Fig. S2
UW2038/50.3	Baker calcite	BB	EPMA plug mount	Room 456, Weeks Hall, Madison, Wi, USA	Baker seeds, "big" size fraction, Mg-free	Ch. 3, Sec. 2.1, Fig. S2
UW2038/51	A20	Chem/UK-2	EPMA plug mount	Slone Research Bldg, U. Kentucky (Lexington, Ky, USA)	Mg-free seeds from Li et al. (2012), overgrowth Mg content unknown	Ch.3, Tables 1-S3, Fig. 2
UW2038/52	NA	Chem/UK-32	EPMA plug mount	Slone Research Bldg, U. Kentucky (Lexington, Ky, USA)	Mg-free seeds from Li et al. (2012), overgrowth Mg content unknown	Ch.3; Page ii (Statement of Authorship)
UW2038/53	NA	Chem/UK-33	EPMA plug mount	Slone Research Bldg, U. Kentucky (Lexington, Ky, USA)	Mg-free seeds, Mg content of overgrowth estimated to be 11.5 mol%	Ch.3; Appendix B
UW2038/54	A19	Chem/UK-36	EPMA plug mount	Slone Research Bldg, U. Kentucky (Lexington, Ky, USA)	Mg-free seeds, Mg content of overgrowth estimated to be 2.5 mol%	Ch.3, Tables 1-S3, Fig. 2: Appendix B
UW2038/55	M1	FU-1	EPMA plug mount	Furman University (Greeneville, SC, USA)	Agros seeds, Mg content of overgrowth estimated to be 1.8 mol%	Ch.3, Tables 1-S3
UW2038/56	M2	FU-2	EPMA plug mount	Furman University (Greeneville, SC, USA)	Agros seeds, Mg content of overgrowth estimated to be 2.8 mol%	Ch.3, Tables 1-S3
UW2038/57	M3	FU-8	EPMA plug mount	Furman University (Greeneville, SC, USA)	Agros seeds, Mg content of overgrowth estimated to be 1.7 mol%	Ch.3, Tables 1-S3
UW2038/58	M4	FU-11	EPMA plug mount	Furman University (Greeneville, SC, USA)	Agros seeds, Mg content of overgrowth estimated to be 1.4 mol%	Ch.3, Tables 1-S3
UW2038/59	M5	FU-12	EPMA plug mount	Furman University (Greeneville, SC, USA)	Agros seeds, Mg content of overgrowth estimated to be 2.8 mol%	Ch.3, Tables 1-S3
UW2038/60	NA	FU-17	EPMA plug mount	Furman University (Greeneville, SC, USA)	Agros seeds, Mg content of overgrowth estimated to be 2.9 mol%	Ch.3; Page ii (Statement of Authorship)
UW2038/61	M6	FU-19	EPMA plug mount	Furman University (Greeneville, SC, USA)	Agros seeds, Mg content of overgrowth estimated to be 4.4 mol%	Ch.3, Tables 1-S3, Fig. 2
UW2038/62	M7	FU-20	EPMA plug mount	Furman University (Greeneville, SC, USA)	Agros seeds, Mg content of overgrowth estimated to be 1.6 mol%	Ch.3, Tables 1-S3
UW2038/63	NA	FU-21	EPMA plug mount	Furman University (Greeneville, SC, USA)	Agros seeds, Mg content of overgrowth estimated to be 2.2 mol%	Ch.3; Page ii (Statement of Authorship)
UW2038/64	M9	FU-22	EPMA plug mount	Furman University (Greeneville, SC, USA)	Agros seeds, Mg content of overgrowth estimated to be 2.7 mol%	Ch.3, Tables 1-S3
UW2038/65	M10	FU-23	EPMA plug mount	Furman University (Greeneville, SC, USA)	Agros seeds, Mg content of overgrowth estimated to be 0.9 mol%	Ch.3, Tables 1-S3; Appendix B
UW2038/66	M14	FU-24	EPMA plug mount	Furman University (Greeneville, SC, USA)	Agros seeds, Mg content of overgrowth estimated to be 13.1 mol%	Ch.3, Tables 1-S3, Fig. S2; Appendix B
UW2038/67	M11	FU-25	EPMA plug mount	Furman University (Greeneville, SC, USA)	Agros seeds, Mg content of overgrowth estimated to be 1.6 mol%	Ch.3, Tables 1-S3
UW2038/68	NA	FU-26	EPMA plug mount	Furman University (Greeneville, SC, USA)	Agros seeds, Mg content of overgrowth estimated to be 0.9 mol%	Ch.3; Page ii (Statement of Authorship)
UW2038/69	NA	FU-37	EPMA plug mount	Furman University (Greeneville, SC, USA)	Agros seeds, Mg content of overgrowth estimated to be 3.0 mol%	Ch.3; Page ii (Statement of Authorship)
UW2038/70.1	14AS-SA02	14AS-SA02	hand sample	Vryburg, South Africa	Grainstone, carbonate sand with early and partial silicification	Appedix A, Table A1-1
UW2038/70.2	14AS-SA02	14AS-SA02	hand sample	Vryburg, South Africa	Grainstone, carbonate sand with early and partial silicification	Appedix A, Table A1-1
UW2038/70.3	14AS-SA02	14AS-SA02	hand sample	Vryburg, South Africa	Grainstone, carbonate sand with early and partial silicification	Appedix A, Table A1-1
UW2038/70.4	14AS-SA02	14AS-SA02	hand sample	Vryburg, South Africa	Grainstone, carbonate sand with early and partial silicification	Appedix A, Table A1-1
UW2038/70.5	14AS-SA02	14AS-SA02	hand sample	Vryburg, South Africa	Grainstone, carbonate sand with early and partial silicification	Appedix A, Table A1-1
UW2038/70.6	14AS-SA02	14AS-SA02	hand sample	Vryburg, South Africa	Grainstone, carbonate sand with early and partial silicification	Appedix A, Table A1-1
UW2038/71.1	14AS-SA03	14AS-SA03	hand sample	Kuruman Kop, South Africa	Fenestral microbialite, dolomite infill, small chert nodules	Appedix A, Table A1-1 through A1-3, Fig. A2
UW2038/71.2	14AS-SA03	14AS-SA03	hand sample	Kuruman Kop, South Africa	Fenestral microbialite, dolomite infill, small chert nodules	Appedix A, Table A1-1 through A1-3, Fig. A2
UW2038/71.3	14AS-SA03	14AS-SA03	hand sample	Kuruman Kop, South Africa	Fenestral microbialite, dolomite infill, small chert nodules	Appedix A, Table A1-1 through A1-3, Fig. A2
UW2038/71.4	14AS-SA03	14AS-SA03	hand sample	Kuruman Kop, South Africa	Fenestral microbialite, dolomite infill, small chert nodules	Appedix A, Table A1-1 through A1-3, Fig. A2
UW2038/71.5	14AS-SA03B	14AS-SA03B	billet	Kuruman Kop, South Africa	Fenestral microbialite, dolomite infill, small chert nodules	Appedix A, Table A1-1 through A1-3, Fig. A2
UW2038/71.6	14AS-SA03C	14AS-SA03C	billet	Kuruman Kop, South Africa	Fenestral microbialite, dolomite infill, small chert nodules	Appedix A, Table A1-1 through A1-3, Fig. A2
UW2038/71.7	14AS-SA03D1	14AS-SA03D1	billet	Kuruman Kop, South Africa	Fenestral microbialite, dolomite infill, small chert nodules	Appedix A, Table A1-1 through A1-3, Fig. A2
UW2038/71.8	14AS-SA03D2	14AS-SA03D2	billet	Kuruman Kop, South Africa	Fenestral microbialite, dolomite infill, small chert nodules	Appedix A, Table A1-1 through A1-3, Fig. A2
UW2038/71.9	14AS-SA03D3	14AS-SA03D3	billet	Kuruman Kop, South Africa	Fenestral microbialite, dolomite infill, small chert nodules	Appedix A, Table A1-1 through A1-3, Fig. A2
UW2038/71.10	14AS-SA03	14AS*SA03B	thin section	Kuruman Kop, South Africa	Fenestral microbialite, dolomite infill, small chert nodules	Appedix A, Table A1-1 through A1-3, Fig. A2
UW2038/71.11	14AS-SA03	14AS*SA03C	thin section	Kuruman Kop, South Africa	Fenestral microbialite, dolomite infill, small chert nodules	Appedix A, Table A1-1 through A1-3, Fig. A2
UW2038/71.12	14AS-SA03	14AS*SA03D1	thin section	Kuruman Kop, South Africa	Fenestral microbialite, dolomite infill, small chert nodules	Appedix A, Table A1-1 through A1-3, Fig. A2
UW2038/71.13	14AS-SA03	14AS*SA03D2	thin section	Kuruman Kop, South Africa	Fenestral microbialite, dolomite infill, small chert nodules	Appedix A, Table A1-1 through A1-3, Fig. A2
UW2038/71.14	14AS-SA03	14AS*SA03D3	thin section	Kuruman Kop, South Africa	Fenestral microbialite, dolomite infill, small chert nodules	Appedix A, Table A1-1 through A1-3, Fig. A2
UW2038/71.15	14AS-SA03_sphere1	14AS-SA03_sphere1	crushed sample powder	Kuruman Kop, South Africa	Fenestral microbialite, dolomite infill, small chert nodules	Appedix A, Table A1-1 through A1-3, Fig. A2
UW2038/71.16	14AS-SA03CS1	14AS-SA03S1	crushed sample powder	Kuruman Kop, South Africa	sparry calcite	Appedix A, Table A1-1 through A1-3, Fig. A2
UW2038/71.17	14AS-SA03CS2	14AS-SA03S2	crushed sample powder	Kuruman Kop, South Africa	sparry calcite	Appedix A, Table A1-1 through A1-3, Fig. A2
UW2038/71.18	14AS-SA03CS3	14AS-SA03S3	crushed sample powder	Kuruman Kop, South Africa	sparry calcite	Appedix A, Table A1-1 through A1-3, Fig. A2
UW2038/71.19	14AS-SA03D1	14AS-SA03D1	crushed sample powder	Kuruman Kop, South Africa	dolomite	Appedix A, Table A1-1 through A1-3, Fig. A2
UW2038/71.20	14AS-SA03D2	14AS-SA03D2	crushed sample powder	Kuruman Kop, South Africa	dolomite	Appedix A, Table A1-1 through A1-3, Fig. A2
UW2038/72.1	14AS-SA04_Top	14AS-SA04_Top	hand sample	Kuruman Kop, South Africa	Fenestral microbialite, dolomite infill, small chert nodules	Appedix A, Table A1-1 through A1-3, Fig. A2
UW2038/72.2	14AS-SA04_Top	14AS-SA04_Top	hand sample	Kuruman Kop, South Africa	Fenestral microbialite, dolomite infill, small chert nodules	Appedix A, Table A1-1 through A1-3, Fig. A2
UW2038/72.3	14AS-SA04_Top	14AS-SA04_Top	hand sample	Kuruman Kop, South Africa	Fenestral microbialite, dolomite infill, small chert nodules	Appedix A, Table A1-1 through A1-3, Fig. A2
UW2038/72.4	14AS-SA04A1	14AS-SA04A1	billet	Kuruman Kop, South Africa	Fenestral microbialite, dolomite infill, small chert nodules	Appedix A, Table A1-1 through A1-3, Fig. A2
UW2038/72.5	14AS-SA04B1	14AS-SA04B1	billet	Kuruman Kop, South Africa	Fenestral microbialite, dolomite infill, small chert nodules	Appedix A, Table A1-1 through A1-3, Fig. A2
UW2038/72.6	14AS-SA04C1	14AS-SA04C1	billet	Kuruman Kop, South Africa	Fenestral microbialite, dolomite infill, small chert nodules	Appedix A, Table A1-1 through A1-3, Fig. A2
UW2038/72.7	14AS-SA04Top	14AS*SA04A1	thin section	Kuruman Kop, South Africa	Fenestral microbialite, dolomite infill, small chert nodules	Appedix A, Table A1-1 through A1-3, Fig. A2
UW2038/72.8	14AS-SA04Top	14AS*SA04B1	thin section	Kuruman Kop, South Africa	Fenestral microbialite, dolomite infill, small chert nodules	Appedix A, Table A1-1 through A1-3, Fig. A2
UW2038/72.9	14AS-SA04Top	14AS*SA04C1	thin section	Kuruman Kop, South Africa	Fenestral microbialite, dolomite infill, small chert nodules	Appedix A, Table A1-1 through A1-3, Fig. A2
UW2038/72.10	14AS-SA04TA2CS1	14AS-SA04TA2S1	crushed sample powder	Kuruman Kop, South Africa	sparry calcite	Appedix A, Table A1-1 through A1-3, Fig. A2
UW2038/72.11	14AS-SA04TA2CS2	14AS-SA04TA2S2	crushed sample powder	Kuruman Kop, South Africa	sparry calcite	Appedix A, Table A1-1 through A1-3, Fig. A2
UW2038/72.12	14AS-SA04_Top_A1_Bulk	14AS-SA04_Top_A1_Bulk	crushed sample powder	Kuruman Kop, South Africa	Fenestral microbialite limestone	Appedix A, Table A1-1 through A1-3, Fig. A2
UW2038/72.13	14AS-SA04_Top_A2_Bulk	14AS-SA04_Top_A2_Bulk	crushed sample powder	Kuruman Kop, South Africa	Fenestral microbialite limestone	Appedix A, Table A1-1 through A1-3, Fig. A2
UW2038/72.14	14AS-SA04_Top_A3_Bulk	14AS-SA04_Top_A3_Bulk	crushed sample powder	Kuruman Kop, South Africa	Fenestral microbialite limestone	Appedix A, Table A1-1 through A1-3, Fig. A2

Appendix C (cont): UW-Madison Thesis Collection Sample Identification Table

	Identification Numbers					
UW-Madison	**Publication**	**Lab or Field**	**Sample Type**	**Locality**	**Description**	**Featured In**
UW2038/73.1	14AS-SA04_Middle	14AS-SA04_Middle	hand sample	Kuruman Kop, South Africa	Fenestral microbialite, dolomite infill, small chert nodules	Appedix A, Table A1-1, Fig. A2
UW2038/73.2	14AS-SA04_Middle	14AS-SA04_Middle	hand sample	Kuruman Kop, South Africa	Fenestral microbialite, dolomite infill, small chert nodules	Appedix A, Table A1-1, Fig. A2
UW2038/73.3	14AS-SA04A2	14AS-SA04A2	billet	Kuruman Kop, South Africa	Fenestral microbialite, dolomite infill, small chert nodules	Appedix A, Table A1-1, Fig. A2
UW2038/73.4	14AS-SA04B2	14AS-SA04B2	billet	Kuruman Kop, South Africa	Fenestral microbialite, dolomite infill, small chert nodules	Appedix A, Table A1-1, Fig. A2
UW2038/73.5	14AS-SA04C2	14AS-SA04C2	billet	Kuruman Kop, South Africa	Fenestral microbialite, dolomite infill, small chert nodules	Appedix A, Table A1-1, Fig. A2
UW2038/73.6	14AS-SA04Middle	14AS*SA04A2	thin section	Kuruman Kop, South Africa	Fenestral microbialite, dolomite infill, small chert nodules	Appedix A, Table A1-1, Fig. A2
UW2038/73.7	14AS-SA04Middle	14AS*SA04B2	thin section	Kuruman Kop, South Africa	Fenestral microbialite, dolomite infill, small chert nodules	Appedix A, Table A1-1, Fig. A2
UW2038/73.8	14AS-SA04Middle	14AS*SA04C2	thin section	Kuruman Kop, South Africa	Fenestral microbialite, dolomite infill, small chert nodules	Appedix A, Table A1-1, Fig. A2
UW2038/73.9	14AS-SA04_Middle_A1_Bulk	14AS-SA04_Middle_A1_Bulk	crushed sample powder	Kuruman Kop, South Africa	Fenestral microbialite limestone	Appedix A, Table A1-1, Fig. A2
UW2038/73.10	14AS-SA04_Middle_A2_Bulk	14AS-SA04_Middle_A2_Bulk	crushed sample powder	Kuruman Kop, South Africa	Fenestral microbialite limestone	Appedix A, Table A1-1, Fig. A2
UW2038/73.11	14AS-SA04_Middle_A3_Bulk	14AS-SA04_Middle_A3_Bulk	crushed sample powder	Kuruman Kop, South Africa	Fenestral microbialite limestone	Appedix A, Table A1-1, Fig. A2
UW2038/74.1	14AS-SA04_Bottom	14AS-SA04_Bottom	hand sample	Kuruman Kop, South Africa	Fenestral microbialite, dolomite infill, small chert nodules	Appedix A, Table A1-1, Fig. A2
UW2038/74.2	14AS-SA04_Bottom	14AS-SA04_Bottom	hand sample	Kuruman Kop, South Africa	Fenestral microbialite, dolomite infill, small chert nodules	Appedix A, Table A1-1, Fig. A2
UW2038/74.3	14AS-SA04A3	14AS-SA04A3	billet	Kuruman Kop, South Africa	Fenestral microbialite, dolomite infill, small chert nodules	Appedix A, Table A1-1, Fig. A2
UW2038/74.4	14AS-SA04B3	14AS-SA04B3	billet	Kuruman Kop, South Africa	Fenestral microbialite, dolomite infill, small chert nodules	Appedix A, Table A1-1, Fig. A2
UW2038/74.5	14AS-SA04_Bottom	14AS*SA04A3	thin section	Kuruman Kop, South Africa	Fenestral microbialite, dolomite infill, small chert nodules	Appedix A, Table A1-1, Fig. A2
UW2038/74.6	14AS-SA04_Bottom	14AS*SA04B3	thin section	Kuruman Kop, South Africa	Fenestral microbialite, dolomite infill, small chert nodules	Appedix A, Table A1-1, Fig. A2
UW2038/74.7	14AS-SA04_Bottom_A1_Bulk	14AS-SA04_Bottom_A1_Bulk	crushed sample powder	Kuruman Kop, South Africa	Fenestral microbialite limestone	Appedix A, Table A1-1, Fig. A2
UW2038/74.8	14AS-SA04_Bottom_A2_Bulk	14AS-SA04_Bottom_A2_Bulk	crushed sample powder	Kuruman Kop, South Africa	Fenestral microbialite limestone	Appedix A, Table A1-1, Fig. A2
UW2038/75.1	14AS-SA05	14AS-SA05	hand sample	Kuruman Kop, South Africa	Small domal stromatolite with draping dolomite	Appedix A, Table A1-1 through A1-3, Fig. A2
UW2038/75.2	14AS-SA05	14AS-SA05	hand sample	Kuruman Kop, South Africa	Small domal stromatolite with draping dolomite	Appedix A, Table A1-1 through A1-3, Fig. A2
UW2038/75.3	14AS-SA05B1	14AS-SA05B1	billet	Kuruman Kop, South Africa	Small domal stromatolite with draping dolomite	Appedix A, Table A1-1 through A1-3, Fig. A2
UW2038/75.4	14AS-SA05B2	14AS-SA05B2	billet	Kuruman Kop, South Africa	Small domal stromatolite with draping dolomite	Appedix A, Table A1-1 through A1-3, Fig. A2
UW2038/75.5	14AS-SA05B3	14AS-SA05B3	billet	Kuruman Kop, South Africa	Small domal stromatolite with draping dolomite	Appedix A, Table A1-1 through A1-3, Fig. A2
UW2038/75.6	14AS-SA05B4	14AS-SA05B4	billet	Kuruman Kop, South Africa	Small domal stromatolite with draping dolomite	Appedix A, Table A1-1 through A1-3, Fig. A2
UW2038/75.7	14AS-SA05B5	14AS-SA05B5	billet	Kuruman Kop, South Africa	Small domal stromatolite with draping dolomite	Appedix A, Table A1-1 through A1-3, Fig. A2
UW2038/75.8	14AS-SA05B6	14AS-SA05B6	billet	Kuruman Kop, South Africa	Small domal stromatolite with draping dolomite	Appedix A, Table A1-1 through A1-3, Fig. A2
UW2038/75.9	14AS-SA05	14AS*SA05B1	thin section	Kuruman Kop, South Africa	Small domal stromatolite with draping dolomite	Appedix A, Table A1-1 through A1-3, Fig. A2
UW2038/75.10	14AS-SA05	14AS*SA05B2	thin section	Kuruman Kop, South Africa	Small domal stromatolite with draping dolomite	Appedix A, Table A1-1 through A1-3, Fig. A2
UW2038/75.11	14AS-SA05	14AS*SA05B3	thin section	Kuruman Kop, South Africa	Small domal stromatolite with draping dolomite	Appedix A, Table A1-1 through A1-3, Fig. A2
UW2038/75.12	14AS-SA05	14AS*SA05B4	thin section	Kuruman Kop, South Africa	Small domal stromatolite with draping dolomite	Appedix A, Table A1-1 through A1-3, Fig. A2
UW2038/75.13	14AS-SA05	14AS*SA05B5	thin section	Kuruman Kop, South Africa	Small domal stromatolite with draping dolomite	Appedix A, Table A1-1 through A1-3, Fig. A2
UW2038/75.14	14AS-SA05	14AS*SA05B6	thin section	Kuruman Kop, South Africa	Small domal stromatolite with draping dolomite	Appedix A, Table A1-1 through A1-3, Fig. A2
UW2038/75.15	14AS-SA05CS1	14AS-SA05S1	crushed sample powder	Kuruman Kop, South Africa	sparry calcite	Appedix A, Table A1-1 through A1-3, Fig. A2
UW2038/75.16	14AS-SA05CS2	14AS-SA05S2	crushed sample powder	Kuruman Kop, South Africa	sparry calcite	Appedix A, Table A1-1 through A1-3, Fig. A2
UW2038/75.17	14AS-SA05D1	14AS-SA05D1	crushed sample powder	Kuruman Kop, South Africa	dolomite	Appedix A, Table A1-1 through A1-3, Fig. A2
UW2038/75.18	14AS-SA05D2	14AS-SA05D2	crushed sample powder	Kuruman Kop, South Africa	dolomite	Appedix A, Table A1-1 through A1-3, Fig. A2
UW2038/76.1	14AS-SA06	14AS-SA06	hand sample	Kuruman Kop, South Africa	Domal/columnar stromatolite with dolomite infill	Appedix A, Table A1-1 through A1-3, Fig. A2-A4
UW2038/76.2	14AS-SA06	14AS-SA06	hand sample	Kuruman Kop, South Africa	Domal/columnar stromatolite with dolomite infill	Appedix A, Table A1-1 through A1-3, Fig. A2-A4
UW2038/76.3	14AS-SA06	14AS-SA06A	billet	Kuruman Kop, South Africa	Domal/columnar stromatolite with dolomite infill	Appedix A, Table A1-1 through A1-3, Fig. A2-A4
UW2038/76.4	14AS-SA06	14AS-SA06B	billet	Kuruman Kop, South Africa	Domal/columnar stromatolite with dolomite infill	Appedix A, Table A1-1 through A1-3, Fig. A2-A4
UW2038/76.5	14AS-SA06A	14AS*SA06A	thin section	Kuruman Kop, South Africa	Domal/columnar stromatolite with dolomite infill	Appedix A, Table A1-1 through A1-3, Fig. A2-A4
UW2038/76.6	14AS-SA06B	14AS*SA06B	thin section	Kuruman Kop, South Africa	Domal/columnar stromatolite with dolomite infill	Appedix A, Table A1-1 through A1-3, Fig. A2-A4
UW2038/76.7	14AS-SA06D1	14AS-SA06D1	crushed sample powder	Kuruman Kop, South Africa	dolomite	Appedix A, Table A1-1 through A1-3, Fig. A2-A4
UW2038/76.8	14AS-SA06L1	14AS-SA06L1	crushed sample powder	Kuruman Kop, South Africa	herringbone calcite	Appedix A, Table A1-1 through A1-3, Fig. A2-A4
UW2038/76.9	14AS-SA06L2	14AS-SA06L2	crushed sample powder	Kuruman Kop, South Africa	herringbone calcite	Appedix A, Table A1-1 through A1-3, Fig. A2-A4
UW2038/76.10	14AS-SA06L3	14AS-SA06L3	crushed sample powder	Kuruman Kop, South Africa	herringbone calcite	Appedix A, Table A1-1 through A1-3, Fig. A2-A4
UW2038/76.11	14AS-SA06ST1	14AS-SA06D2	crushed sample powder	Kuruman Kop, South Africa	stromatolite calcite	Appedix A, Table A1-1 through A1-3, Fig. A2-A4
UW2038/76.12	14AS-SA06ST2	14AS-SA06D3	crushed sample powder	Kuruman Kop, South Africa	stromatolite calcite	Appedix A, Table A1-1 through A1-3, Fig. A2-A4
UW2038/76.13	14AS-SA06_Bulk	14AS-SA06_Bulk	crushed sample powder	Kuruman Kop, South Africa	Domal/columnar stromatolite with dolomite infill	Appedix A, Table A1-1 through A1-3, Fig. A2
UW2038/77.1	14AS-SA07	14AS-SA07	hand sample	Kuruman Kop, South Africa	Chertified stromatolite	Appedix A, Table A1-1 through A1-3, Fig. A2
UW2038/77.2	14AS-SA07	14AS-SA07	hand sample	Kuruman Kop, South Africa	Chertified stromatolite	Appedix A, Table A1-1 through A1-3, Fig. A2
UW2038/77.3	14AS-SA07	14AS-SA07	hand sample	Kuruman Kop, South Africa	Chertified stromatolite	Appedix A, Table A1-1 through A1-3, Fig. A2
UW2038/77.4	14AS-SA07	14AS-SA07	hand sample	Kuruman Kop, South Africa	Chertified stromatolite	Appedix A, Table A1-1 through A1-3, Fig. A2
UW2038/77.5	14AS-SA07	14AS-SA07	hand sample	Kuruman Kop, South Africa	Chertified stromatolite	Appedix A, Table A1-1 through A1-3, Fig. A2
UW2038/77.6	14AS-SA07	14AS-SA07	hand sample	Kuruman Kop, South Africa	Chertified stromatolite	Appedix A, Table A1-1 through A1-3, Fig. A2
UW2038/77.7	14AS-SA07B	14AS-SA07B	billet	Kuruman Kop, South Africa	Chertified stromatolite	Appedix A, Table A1-1 through A1-3, Fig. A2
UW2038/77.8	14AS-SA07A	14AS*SA07A	thin section	Kuruman Kop, South Africa	Chertified stromatolite	Appedix A, Table A1-1 through A1-3, Fig. A2
UW2038/77.9	14AS-SA07C	14AS*SA07C	thin section	Kuruman Kop, South Africa	Chertified stromatolite	Appedix A, Table A1-1 through A1-3, Fig. A2
UW2038/78.1	14AS-SA08	14AS-SA08	hand sample	Kuruman Kop, South Africa	Hydrothermal vein calcite and dolomite	Appedix A, Table A1-1 through A1-3, Fig. A2
UW2038/78.2	14AS-SA08	14AS-SA08	hand sample	Kuruman Kop, South Africa	Hydrothermal vein calcite and dolomite	Appedix A, Table A1-1 through A1-3, Fig. A2
UW2038/78.3	14AS-SA08CS1	14AS-SA08S1	crushed sample powder	Kuruman Kop, South Africa	hydrothermal calcite	Appedix A, Table A1-1 through A1-3, Fig. A2
UW2038/78.4	14AS-SA08CS2	14AS-SA08S2	crushed sample powder	Kuruman Kop, South Africa	hydrothermal calcite	Appedix A, Table A1-1 through A1-3, Fig. A2
UW2038/78.5	14AS-SA08D1	14AS-SA08D1	crushed sample powder	Kuruman Kop, South Africa	hydrothermal dolomite	Appedix A, Table A1-1 through A1-3, Fig. A2
UW2038/78.6	14AS-SA08D2	14AS-SA08D2	crushed sample powder	Kuruman Kop, South Africa	hydrothermal dolomite	Appedix A, Table A1-1 through A1-3, Fig. A2

Appendix C (cont): UW-Madison Thesis Collection Sample Identification Table

	Identification Numbers					
UW-Madison	**Publication**	**Lab or Field**	**Sample Type**	**Locality**	**Description**	**Featured In**
UW2038/79.1	14AS-SA09	14AS-SA09	hand sample	Kuruman Kop, South Africa	Chertified stromatolite	Appedix A, Table A1-1
UW2038/79.2	14AS-SA09	14AS-SA09	hand sample	Kuruman Kop, South Africa	Chertified stromatolite	Appedix A, Table A1-1
UW2038/79.3	14AS-SA09	14AS-SA09	hand sample	Kuruman Kop, South Africa	Chertified stromatolite	Appedix A, Table A1-1
UW2038/79.4	14AS-SA09	14AS-SA09	hand sample	Kuruman Kop, South Africa	Chertified stromatolite	Appedix A, Table A1-1
UW2038/79.5	14AS-SA09	14AS-SA09	hand sample	Kuruman Kop, South Africa	Chertified stromatolite	Appedix A, Table A1-1
UW2038/79.6	14AS-SA09	14AS-SA09	hand sample	Kuruman Kop, South Africa	Chertified stromatolite	Appedix A, Table A1-1
UW2038/79.7	14AS-SA09	14AS*SA09A	thin section	Kuruman Kop, South Africa	Chertified stromatolite	Appedix A, Table A1-1
UW2038/79.8	14AS-SA09	14AS*SA09B	thin section	Kuruman Kop, South Africa	Chertified stromatolite	Appedix A, Table A1-1
UW2038/80.1	14AS-SA10	14AS-SA10	hand sample	Kuruman Kop, South Africa	Silicified stromatolite	Appedix A, Table A1-1
UW2038/80.2	14AS-SA10	14AS-SA10	hand sample	Kuruman Kop, South Africa	Silicified stromatolite	Appedix A, Table A1-1
UW2038/80.3	14AS-SA10	14AS-SA10	billet	Kuruman Kop, South Africa	Silicified stromatolite	Appedix A, Table A1-1
UW2038/80.4	14AS-SA10	14AS*SA10A	thin section	Kuruman Kop, South Africa	Silicified stromatolite	Appedix A, Table A1-1
UW2038/81.1	14AS-SA11	14AS-SA11	hand sample	Kuruman Kop, South Africa	Sparry fenestral microbialite and micrite	Appedix A, Table A1-1 through A1-3, Fig. A2
UW2038/81.2	14AS-SA11	14AS-SA11	hand sample	Kuruman Kop, South Africa	Sparry fenestral microbialite and micrite	Appedix A, Table A1-1 through A1-3, Fig. A2
UW2038/81.3	14AS-SA11	14AS-SA11	hand sample	Kuruman Kop, South Africa	Sparry fenestral microbialite and micrite	Appedix A, Table A1-1 through A1-3, Fig. A2
UW2038/81.4	14AS-SA11A	14AS-SA11A	billet	Kuruman Kop, South Africa	Sparry fenestral microbialite and micrite	Appedix A, Table A1-1 through A1-3, Fig. A2
UW2038/81.5	14AS-SA11B	14AS-SA11B	billet	Kuruman Kop, South Africa	Sparry fenestral microbialite and micrite	Appedix A, Table A1-1 through A1-3, Fig. A2
UW2038/81.6	14AS-SA11	14AS*SA11A	thin section	Kuruman Kop, South Africa	Sparry fenestral microbialite and micrite	Appedix A, Table A1-1 through A1-3, Fig. A2
UW2038/81.7	14AS-SA11	14AS*SA11B	thin section	Kuruman Kop, South Africa	Sparry fenestral microbialite and micrite	Appedix A, Table A1-1 through A1-3, Fig. A2
UW2038/81.8	14AS-SA11CS1	14AS-SA11S1	crushed sample powder	Kuruman Kop, South Africa	sparry calcite	Appedix A, Table A1-1 through A1-3, Fig. A2
UW2038/81.9	14AS-SA11CS2	14AS-SA11S2	crushed sample powder	Kuruman Kop, South Africa	sparry calcite	Appedix A, Table A1-1 through A1-3, Fig. A2
UW2038/81.10	14AS-SA11_Bulk	14AS-SA11_Bulk	crushed sample powder	Kuruman Kop, South Africa	Sparry fenestral microbialite and micrite	Appedix A, Table A1-1 through A1-3, Fig. A2
UW2038/82.1	14AS-SA12	14AS-SA12	hand sample	Danielskuil, South Africa	Stromatolite with dolomite infill, caliche at base	Appedix A, Table A1-1 through A1-3, Fig. A2
UW2038/82.2	14AS-SA12	14AS-SA12	hand sample	Danielskuil, South Africa	Stromatolite with dolomite infill, caliche at base	Appedix A, Table A1-1 through A1-3, Fig. A2
UW2038/82.3	14AS-SA12	14AS-SA12	hand sample	Danielskuil, South Africa	Stromatolite with dolomite infill, caliche at base	Appedix A, Table A1-1 through A1-3, Fig. A2
UW2038/82.4	14AS-SA12	14AS-SA12	hand sample	Danielskuil, South Africa	Stromatolite with dolomite infill, caliche at base	Appedix A, Table A1-1 through A1-3, Fig. A2
UW2038/82.5	14AS-SA12A	14AS-SA12A	billet	Danielskuil, South Africa	Stromatolite with dolomite infill, caliche at base	Appedix A, Table A1-1 through A1-3, Fig. A2
UW2038/82.6	14AS-SA12A	14AS*SA12'A'	thin section	Danielskuil, South Africa	Stromatolite with dolomite infill, caliche at base	Appedix A, Table A1-1 through A1-3, Fig. A2
UW2038/82.7	14AS-SA12L1	14AS-SA12L1	crushed sample powder	Danielskuil, South Africa	Stromatolitic limestone	Appedix A, Table A1-1 through A1-3, Fig. A2
UW2038/82.8	14AS-SA12por1	14AS-SA12por1	crushed sample powder	Danielskuil, South Africa	modern caliche	Appedix A, Table A1-1 through A1-3, Fig. A2
UW2038/83.1	14AS-SA13	14AS-SA13	hand sample	Danielskuil, South Africa	Draping stromatolites with dolomite sand, spar and fenestrae	Appedix A, Table A1-1 through A1-3, Figs. A2
UW2038/83.2	14AS-SA13	14AS-SA13	hand sample	Danielskuil, South Africa	Draping stromatolites with dolomite sand, spar and fenestrae	Appedix A, Table A1-1 through A1-3, Figs. A2
UW2038/83.3	14AS-SA13	14AS-SA13	hand sample	Danielskuil, South Africa	Draping stromatolites with dolomite sand, spar and fenestrae	Appedix A, Table A1-1 through A1-3, Figs. A2
UW2038/83.4	14AS-SA13	14AS-SA13	hand sample	Danielskuil, South Africa	Draping stromatolites with dolomite sand, spar and fenestrae	Appedix A, Table A1-1 through A1-3, Figs. A2
UW2038/83.5	14AS-SA13B1	14AS-SA13B1	billet	Danielskuil, South Africa	Draping stromatolites with dolomite sand, spar and fenestrae	Appedix A, Table A1-1 through A1-3, Figs. A2, A5, A6
UW2038/83.6	14AS-SA13B2	14AS-SA13B2	billet	Danielskuil, South Africa	Draping stromatolites with dolomite sand, spar and fenestrae	Appedix A, Table A1-1 through A1-3, Figs. A2
UW2038/83.7	14AS-SA13B3	14AS-SA13B3	billet	Danielskuil, South Africa	Draping stromatolites with dolomite sand, spar and fenestrae	Appedix A, Table A1-1 through A1-3, Figs. A2
UW2038/83.8	14AS-SA13B4	14AS-SA13B4	billet	Danielskuil, South Africa	Draping stromatolites with dolomite sand, spar and fenestrae	Appedix A, Table A1-1 through A1-3, Figs. A2
UW2038/83.9	14AS-SA13	14AS*SA13B1	thin section	Danielskuil, South Africa	Draping stromatolites with dolomite sand, spar and fenestrae	Appedix A, Table A1-1 through A1-3, Figs. A2, A5, A6
UW2038/83.10	14AS-SA13	14AS*SA13B2	thin section	Danielskuil, South Africa	Draping stromatolites with dolomite sand, spar and fenestrae	Appedix A, Table A1-1 through A1-3, Figs. A2
UW2038/83.11	14AS-SA13	14AS*SA13B3	thin section	Danielskuil, South Africa	Draping stromatolites with dolomite sand, spar and fenestrae	Appedix A, Table A1-1 through A1-3, Figs. A2
UW2038/83.12	14AS-SA13	14AS*SA13B4	thin section	Danielskuil, South Africa	Draping stromatolites with dolomite sand, spar and fenestrae	Appedix A, Table A1-1 through A1-3, Figs. A2
UW2038/83.13	14AS-SA13CS1	14AS-SA13S1	crushed sample powder	Danielskuil, South Africa	sparry calcite	Appedix A, Table A1-1 through A1-3, Figs. A2
UW2038/83.14	14AS-SA13CS2	14AS-SA13S2	crushed sample powder	Danielskuil, South Africa	sparry calcite	Appedix A, Table A1-1 through A1-3, Figs. A2
UW2038/84.1	14AS-SA14	14AS-SA14	hand sample	Danielskuil, South Africa	Early silicified fenestral microbialite	Appedix A, Table A1-1 through A1-3, Fig. A2
UW2038/84.2	14AS-SA14	14AS-SA14	hand sample	Danielskuil, South Africa	Thick chert with dolomite vein(s)	Appedix A, Table A1-1 through A1-3, Fig. A2
UW2038/84.3	14AS-SA14AB1	14AS-SA14AB1	billet	Danielskuil, South Africa	Early silicified fenestral microbialite	Appedix A, Table A1-1 through A1-3, Fig. A2
UW2038/84.4	14AS-SA14AB2	14AS-SA14AB2	billet	Danielskuil, South Africa	Early silicified fenestral microbialite	Appedix A, Table A1-1 through A1-3, Fig. A2
UW2038/84.5	14AS-SA14AB3	14AS-SA14AB3	billet	Danielskuil, South Africa	Early silicified fenestral microbialite	Appedix A, Table A1-1 through A1-3, Fig. A2
UW2038/84.6	14AS-SA14AB4	14AS-SA14AB4	billet	Danielskuil, South Africa	Early silicified fenestral microbialite	Appedix A, Table A1-1 through A1-3, Fig. A2
UW2038/84.7	14AS-SA14B1	14AS-SA14B1	billet	Danielskuil, South Africa	Thick chert with dolomite vein(s)	Appedix A, Table A1-1 through A1-3, Fig. A2
UW2038/84.8	14AS-SA14A	14AS*SA14AB1	thin section	Danielskuil, South Africa	Early silicified fenestral microbialite	Appedix A, Table A1-1 through A1-3, Fig. A2
UW2038/84.9	14AS-SA14A	14AS*SA14AB2	thin section	Danielskuil, South Africa	Early silicified fenestral microbialite	Appedix A, Table A1-1 through A1-3, Fig. A2
UW2038/84.10	14AS-SA14A	14AS*SA14AB3	thin section	Danielskuil, South Africa	Early silicified fenestral microbialite	Appedix A, Table A1-1 through A1-3, Fig. A2
UW2038/84.11	14AS-SA14A	14AS*SA14AB4	thin section	Danielskuil, South Africa	Early silicified fenestral microbialite	Appedix A, Table A1-1 through A1-3, Fig. A2
UW2038/84.12	14AS-SA14B	14AS*SA14B1	thin section	Danielskuil, South Africa	Thick chert with dolomite vein(s)	Appedix A, Table A1-1 through A1-3, Fig. A2
UW2038/84.13	14AS-SA14ACS1	14AS-SA14ACS1	crushed sample powder	Danielskuil, South Africa	sparry calcite	Appedix A, Table A1-1 through A1-3, Fig. A2
UW2038/84.14	14AS-SA14ACS2	14AS-SA14ACS2	crushed sample powder	Danielskuil, South Africa	sparry calcite	Appedix A, Table A1-1 through A1-3, Fig. A2
UW2038/84.15	14AS-SA14B_D1	14AS-SA14B-D1	crushed sample powder	Danielskuil, South Africa	dolomite	Appedix A, Table A1-1 through A1-3, Fig. A2
UW2038/84.16	14AS-SA14B_D2	14AS-SA14B_D2	crushed sample powder	Danielskuil, South Africa	dolomite	Appedix A, Table A1-1 through A1-3, Fig. A2

Appendix C (cont): UW-Madison Thesis Collection Sample Identification Table

	Identification Numbers					
UW-Madison	**Publication**	**Lab or Field**	**Sample Type**	**Locality**	**Description**	**Featured In**
UW2038/85.1	14AS-SA15	14AS-SA15	hand sample	Danielskuil, South Africa	Cauliflower stromatolite, fenestrae, dolomite infill	Appedix A, Table A1-1 through A1-3, Fig. A2
UW2038/85.2	14AS-SA15BA1	14AS-SA15BA1	billet	Danielskuil, South Africa	Cauliflower stromatolite, fenestrae, dolomite infill	Appedix A, Table A1-1 through A1-3, Fig. A2
UW2038/85.3	14AS-SA15BA2	14AS-SA15BA2	billet	Danielskuil, South Africa	Cauliflower stromatolite, fenestrae, dolomite infill	Appedix A, Table A1-1 through A1-3, Fig. A2
UW2038/85.4	14AS-SA15BA3	14AS-SA15BA3	billet	Danielskuil, South Africa	Cauliflower stromatolite, fenestrae, dolomite infill	Appedix A, Table A1-1 through A1-3, Fig. A2
UW2038/85.5	14AS-SA15BB	14AS-SA15BB	billet	Danielskuil, South Africa	Cauliflower stromatolite, fenestrae, dolomite infill	Appedix A, Table A1-1 through A1-3, Fig. A2
UW2038/85.6	14AS-SA15	14AS*SA15BA1	thin section	Danielskuil, South Africa	Cauliflower stromatolite, fenestrae, dolomite infill	Appedix A, Table A1-1 through A1-3, Fig. A2
UW2038/85.7	14AS-SA15	14AS*SA15BA2	thin section	Danielskuil, South Africa	Cauliflower stromatolite, fenestrae, dolomite infill	Appedix A, Table A1-1 through A1-3, Fig. A2
UW2038/85.8	14AS-SA15	14AS*SA15BA3	thin section	Danielskuil, South Africa	Cauliflower stromatolite, fenestrae, dolomite infill	Appedix A, Table A1-1 through A1-3, Fig. A2
UW2038/85.9	14AS-SA15	14AS*SA15BB	thin section	Danielskuil, South Africa	Cauliflower stromatolite, fenestrae, dolomite infill	Appedix A, Table A1-1 through A1-3, Fig. A2
UW2038/85.10	14AS-SA15CS1	14AS-SA15S1	crushed sample powder	Danielskuil, South Africa	sparry calcite	Appedix A, Table A1-1 through A1-3, Fig. A2
UW2038/85.11	14AS-SA15CS2	14AS-SA15S2	crushed sample powder	Danielskuil, South Africa	sparry calcite	Appedix A, Table A1-1 through A1-3, Fig. A2
UW2038/86.1	AD5-190.30-190.35	AD5-1	rock core	AD-5 rock core near Adelaide and Pomfret, South Africa	Black chert with calcite veins	Appedix A, Table A1-1
UW2038/86.2	AD5-190.30-190.35	AD5-1	rock core	AD-5 rock core near Adelaide and Pomfret, South Africa	Black chert with calcite veins	Appedix A, Table A1-1
UW2038/86.3	AD5-190.30-190.35	AD5-1	thin section	AD-5 rock core near Adelaide and Pomfret, South Africa	Black chert with calcite veins	Appedix A, Table A1-1
UW2038/87.1	AD5-190.38-190.41	AD5-2	rock core	AD-5 rock core near Adelaide and Pomfret, South Africa	Black chert with calcite veins	Appedix A, Table A1-1
UW2038/87.2	AD5-190.38-190.41	AD5-2	rock core	AD-5 rock core near Adelaide and Pomfret, South Africa	Black chert with calcite veins	Appedix A, Table A1-1
UW2038/87.3	AD5-190.38-190.41	AD5-2	thin section	AD-5 rock core near Adelaide and Pomfret, South Africa	Black chert with calcite veins	Appedix A, Table A1-1
UW2038/88.1	AD5-190.41-190.46	AD5-3	rock core	AD-5 rock core near Adelaide and Pomfret, South Africa	Black chert with calcite veins	Appedix A, Table A1-1
UW2038/88.2	AD5-190.41-190.46	AD5-3	rock core	AD-5 rock core near Adelaide and Pomfret, South Africa	Black chert with calcite veins	Appedix A, Table A1-1
UW2038/88.3	AD5-190.41-190.46	AD5-3	thin section	AD-5 rock core near Adelaide and Pomfret, South Africa	Black chert with calcite veins	Appedix A, Table A1-1
UW2038/89.1	AD5-190.46-190.52	AD5-4	rock core	AD-5 rock core near Adelaide and Pomfret, South Africa	Black chert with calcite veins	Appedix A, Table A1-1
UW2038/89.2	AD5-190.46-190.52	AD5-4	thin section	AD-5 rock core near Adelaide and Pomfret, South Africa	Black chert with calcite veins	Appedix A, Table A1-1
UWGM884.39	AD5-161.9A	AD5-161.9A	rock core	AD-5 rock core near Adelaide and Pomfret, South Africa	Lamination 2, siderite	Appedix A, Table A1-1 through A1-3, Fig. A2
UWGM884.83	AD5-172.3L1	AD5-172.3L1	rock core	AD-5 rock core near Adelaide and Pomfret, South Africa	calcite micrite	Appedix A, Table A1-1 through A1-3, Fig. A2
UWGM884.41	AD5-176.9D1	AD5-176.9D1	rock core	AD-5 rock core near Adelaide and Pomfret, South Africa	dolomite	Appedix A, Table A1-1 through A1-3, Fig. A2
UWGM884.47	AD5-201.5CS1, AD5-201.5D1	AD5-201.5CS1, AD5-201.5D1	rock core	AD-5 rock core near Adelaide and Pomfret, South Africa	sparry calcite, dolomite	Appedix A, Table A1-1 through A1-3, Fig. A2
UW2038/90.1	AS16-01A	AS16-01A	hand sample	Kuruman Kop, South Africa	Cement-grainstone rhythmite with graded bedding	Appedix A, Table A1-1
UW2038/90.2	AS16-01A	AS16-01A	hand sample	Kuruman Kop, South Africa	Cement-grainstone rhythmite with graded bedding	Appedix A, Table A1-1
UW2038/90.3	AS16-01A	AS16-01A	hand sample	Kuruman Kop, South Africa	Cement-grainstone rhythmite with graded bedding	Appedix A, Table A1-1
UW2038/90.4	AS16-01A	6-1A1	billet	Kuruman Kop, South Africa	Cement-grainstone rhythmite with graded bedding	Appedix A, Table A1-1
UW2038/90.5	AS16-01A	6-1A2	billet	Kuruman Kop, South Africa	Cement-grainstone rhythmite with graded bedding	Appedix A, Table A1-1
UW2038/90.6	AS16-01A	6-1A1	thin section	Kuruman Kop, South Africa	Cement-grainstone rhythmite with graded bedding	Appedix A, Table A1-1
UW2038/90.7	AS16-01A	6-1A2	thin section	Kuruman Kop, South Africa	Cement-grainstone rhythmite with graded bedding	Appedix A, Table A1-1
UW2038/91.1	AS16-01B	AS16-01B	hand sample	Kuruman Kop, South Africa	Cement-grainstone rhythmite with graded bedding	Appedix A, Table A1-1
UW2038/91.2	AS16-01B	AS16-01B	hand sample	Kuruman Kop, South Africa	Cement-grainstone rhythmite with graded bedding	Appedix A, Table A1-1
UW2038/91.3	AS16-01B	AS16-01B	hand sample	Kuruman Kop, South Africa	Cement-grainstone rhythmite with graded bedding	Appedix A, Table A1-1
UW2038/91.4	AS16-01B	6-1B1	billet	Kuruman Kop, South Africa	Cement-grainstone rhythmite with graded bedding	Appedix A, Table A1-1
UW2038/91.5	AS16-01B	6-1B2	billet	Kuruman Kop, South Africa	Cement-grainstone rhythmite with graded bedding	Appedix A, Table A1-1
UW2038/91.6	AS16-01B	6-1B3	billet	Kuruman Kop, South Africa	Cement-grainstone rhythmite with graded bedding	Appedix A, Table A1-1
UW2038/91.7	AS16-01B	6-1B1	thin section	Kuruman Kop, South Africa	Cement-grainstone rhythmite with graded bedding	Appedix A, Table A1-1
UW2038/91.8	AS16-01B	6-1B2	thin section	Kuruman Kop, South Africa	Cement-grainstone rhythmite with graded bedding	Appedix A, Table A1-1
UW2038/91.9	AS16-01B	6-1B3	thin section	Kuruman Kop, South Africa	Cement-grainstone rhythmite with graded bedding	Appedix A, Table A1-1
UW2038/92.1	AS16-02	AS16-02	hand sample	Kuruman Kop, South Africa	Cement-grainstone rhythmite with graded bedding	Appedix A, Table A1-1
UW2038/92.2	AS16-02	AS16-02	hand sample	Kuruman Kop, South Africa	Cement-grainstone rhythmite with graded bedding	Appedix A, Table A1-1
UW2038/92.3	AS16-02	6-2A	billet	Kuruman Kop, South Africa	Cement-grainstone rhythmite with graded bedding	Appedix A, Table A1-1
UW2038/92.4	AS16-02	6-2A (duplicate)	billet	Kuruman Kop, South Africa	Cement-grainstone rhythmite with graded bedding	Appedix A, Table A1-1
UW2038/92.5	AS16-02	6-2B	billet	Kuruman Kop, South Africa	Cement-grainstone rhythmite with graded bedding	Appedix A, Table A1-1
UW2038/92.6	AS16-02	6-2B (duplicate)	billet	Kuruman Kop, South Africa	Cement-grainstone rhythmite with graded bedding	Appedix A, Table A1-1
UW2038/92.7	AS16-02	6-2A	thin section	Kuruman Kop, South Africa	Cement-grainstone rhythmite with graded bedding	Appedix A, Table A1-1
UW2038/92.8	AS16-02	6-2A (duplicate)	thin section	Kuruman Kop, South Africa	Cement-grainstone rhythmite with graded bedding	Appedix A, Table A1-1
UW2038/92.9	AS16-02	6-2B	thin section	Kuruman Kop, South Africa	Cement-grainstone rhythmite with graded bedding	Appedix A, Table A1-1
UW2038/92.10	AS16-02	6-2B (duplicate)	thin section	Kuruman Kop, South Africa	Cement-grainstone rhythmite with graded bedding	Appedix A, Table A1-1
UW2038/93.1	AS16-03	AS16-03	hand sample	Kuruman Kop, South Africa	Dolomitized rhythmite with graded bedding	Appedix A, Table A1-1
UW2038/93.2	AS16-03	AS16-03	hand sample	Kuruman Kop, South Africa	Dolomitized rhythmite with graded bedding	Appedix A, Table A1-1
UW2038/93.3	AS16-03	6-3A	billet	Kuruman Kop, South Africa	Dolomitized rhythmite with graded bedding	Appedix A, Table A1-1
UW2038/93.4	AS16-03	6-3B	billet	Kuruman Kop, South Africa	Dolomitized rhythmite with graded bedding	Appedix A, Table A1-1
UW2038/93.5	AS16-03	6-3C	billet	Kuruman Kop, South Africa	Dolomitized rhythmite with graded bedding	Appedix A, Table A1-1
UW2038/93.6	AS16-03	6-3A	thin section	Kuruman Kop, South Africa	Dolomitized rhythmite with graded bedding	Appedix A, Table A1-1
UW2038/93.7	AS16-03	6-3B	thin section	Kuruman Kop, South Africa	Dolomitized rhythmite with graded bedding	Appedix A, Table A1-1
UW2038/93.8	AS16-03	6-3C	thin section	Kuruman Kop, South Africa	Dolomitized rhythmite with graded bedding	Appedix A, Table A1-1
UWGM886.4	DI1-213.8A	DI1-213.8A	rock core	DI-1 rock core near Derby, South Africa	Lamination 4, siderite	Appedix A, Table A1-1 through A1-3, Fig. A2
UWGM886.21	DI1-230.2CS1	DI1-230.2CS1	rock core	DI-1 rock core near Derby, South Africa	sparry calcite	Appedix A, Table A1-1 through A1-3, Fig. A2
UWGM886.26	DI1-236.7A	DI1-236.7A	rock core	DI-1 rock core near Derby, South Africa	Lamination 2 and 3, siderite	Appedix A, Table A1-1 through A1-3, Fig. A2
UWGM886.42	DI1-246.5L1	DI1-246.5L1	rock core	DI-1 rock core near Derby, South Africa	calcite micrite	Appedix A, Table A1-1 through A1-3, Fig. A2
UW2038/98	DM1	DM1	hand sample	Douglas Area, South Africa	Sparitic Carbonate conophyton	Appedix A, Table A1-5
UW2038/94	DM2	DM2	hand sample	Douglas Area, South Africa	Carbonaceous limestone	Appedix A, Table A1-1 and A1-5
UW2038/95.1	GAM-3	GAM-3	hand sample	Gamohaan Reserve, South Africa	Contorted mats in carbonate	Appedix A, Table A1-1 and A1-5
UW2038/95.2	GAM-3	GAM-3	hand sample	Gamohaan Reserve, South Africa	Contorted mats in carbonate	Appedix A, Table A1-1 and A1-5

Appendix C (cont): UW-Madison Thesis Collection Sample Identification Table

Identification Numbers						
UW-Madison	**Publication**	**Lab or Field**	**Sample Type**	**Locality**	**Description**	**Featured In**
UW2038/96.1	GAM-4	GAM-4	hand sample	Gamohaan Reserve, South Africa	Carbonaceous carbonate pod	Appedix A, Table A1-1 and A1-5
UW2038/96.2	GAM-4	GAM-4	hand sample	Gamohaan Reserve, South Africa	Carbonaceous carbonate pod	Appedix A, Table A1-1 and A1-5
UW2038/96.3	GAM-4	GAM-4	hand sample	Gamohaan Reserve, South Africa	Carbonaceous carbonate pod	Appedix A, Table A1-1 and A1-5
UW2038/96.4	GAM-4	GAM4A	billet	Gamohaan Reserve, South Africa	Carbonaceous carbonate pod	Appedix A, Table A1-1 and A1-5
UW2038/96.5	GAM-4	GAM4B	billet	Gamohaan Reserve, South Africa	Carbonaceous carbonate pod	Appedix A, Table A1-1 and A1-5
UW2038/96.6	GAM-4	GAM*4A	thin section	Gamohaan Reserve, South Africa	Carbonaceous carbonate pod	Appedix A, Table A1-1 and A1-5
UW2038/96.7	GAM-4	GAM*4B	thin section	Gamohaan Reserve, South Africa	Carbonaceous carbonate pod	Appedix A, Table A1-1 and A1-5
UW2038/97.1	LIME 2	LIME 2	hand sample	Danielskuil, South Africa	Limestone from Lime Acres	Appedix A, Table A1-1 and A1-5
UW2038/97.2	LIME 2	LIME 2	hand sample	Danielskuil, South Africa	Limestone from Lime Acres	Appedix A, Table A1-1 and A1-5
UW2038/99.1	LIME DK-3	LIME DK-3	hand sample	Danielskuil, South Africa	Limestone from Danielskuil	Appedix A, Table A1-1 and A1-5
UW2038/99.2	LIME DK-3	LIME DK-3	hand sample	Danielskuil, South Africa	Limestone from Danielskuil	Appedix A, Table A1-1 and A1-5
UW2038/99.3	LIME DK-3	DK3A	billet	Danielskuil, South Africa	Limestone from Danielskuil	Appedix A, Table A1-1 and A1-5
UW2038/99.4	LIME DK-3	DK3B	billet	Danielskuil, South Africa	Limestone from Danielskuil	Appedix A, Table A1-1 and A1-5
UW2038/99.5	LIME DK-3	DK*3A	thin section	Danielskuil, South Africa	Limestone from Danielskuil	Appedix A, Table A1-1 and A1-5
UW2038/99.6	LIME DK-3	DK*3B	thin section	Danielskuil, South Africa	Limestone from Danielskuil	Appedix A, Table A1-1 and A1-5
UW2038/100.1	NL16-04	NL16-04	hand sample	Kuruman Kop, South Africa	Dolomitized laminar stromatolites	Appedix A, Table A1-1
UW2038/100.2	NL16-04	NL16-04	hand sample	Kuruman Kop, South Africa	Dolomitized laminar stromatolites	Appedix A, Table A1-1
UW2038/100.3	NL16-04	6-4A	billet	Kuruman Kop, South Africa	Dolomitized laminar stromatolites	Appedix A, Table A1-1
UW2038/100.4	NL16-04	6-4B	billet	Kuruman Kop, South Africa	Dolomitized laminar stromatolites	Appedix A, Table A1-1
UW2038/100.5	NL16-04	6-4A	thin section	Kuruman Kop, South Africa	Dolomitized laminar stromatolites	Appedix A, Table A1-1
UW2038/100.6	NL16-04	6-4B	thin section	Kuruman Kop, South Africa	Dolomitized laminar stromatolites	Appedix A, Table A1-1
UW2038/101.1	NL16-05	NL16-05	hand sample	Kuruman Kop, South Africa	Sparry crystalline carbonate (fenestrate microbialites)	Appedix A, Table A1-1
UW2038/101.2	NL16-05	65A1	billet	Kuruman Kop, South Africa	Sparry crystalline carbonate (fenestrate microbialites)	Appedix A, Table A1-1
UW2038/101.3	NL16-05	65A2	billet	Kuruman Kop, South Africa	Sparry crystalline carbonate (fenestrate microbialites)	Appedix A, Table A1-1
UW2038/101.4	NL16-05	65A3	billet	Kuruman Kop, South Africa	Sparry crystalline carbonate (fenestrate microbialites)	Appedix A, Table A1-1
UW2038/101.5	NL16-05	65A4	billet	Kuruman Kop, South Africa	Sparry crystalline carbonate (fenestrate microbialites)	Appedix A, Table A1-1
UW2038/101.6	NL16-05	65B1	billet	Kuruman Kop, South Africa	Sparry crystalline carbonate (fenestrate microbialites)	Appedix A, Table A1-1
UW2038/101.7	NL16-05	65B2	billet	Kuruman Kop, South Africa	Sparry crystalline carbonate (fenestrate microbialites)	Appedix A, Table A1-1
UW2038/101.8	NL16-05	65A1	thin section	Kuruman Kop, South Africa	Sparry crystalline carbonate (fenestrate microbialites)	Appedix A, Table A1-1
UW2038/101.9	NL16-05	65A1 (duplicate)	thin section	Kuruman Kop, South Africa	Sparry crystalline carbonate (fenestrate microbialites)	Appedix A, Table A1-1
UW2038/101.10	NL16-05	65A2	thin section	Kuruman Kop, South Africa	Sparry crystalline carbonate (fenestrate microbialites)	Appedix A, Table A1-1
UW2038/101.11	NL16-05	65A2 (duplicate)	thin section	Kuruman Kop, South Africa	Sparry crystalline carbonate (fenestrate microbialites)	Appedix A, Table A1-1
UW2038/101.12	NL16-05	65A3	thin section	Kuruman Kop, South Africa	Sparry crystalline carbonate (fenestrate microbialites)	Appedix A, Table A1-1
UW2038/101.13	NL16-05	65A4	thin section	Kuruman Kop, South Africa	Sparry crystalline carbonate (fenestrate microbialites)	Appedix A, Table A1-1
UW2038/101.14	NL16-05	65B1	thin section	Kuruman Kop, South Africa	Sparry crystalline carbonate (fenestrate microbialites)	Appedix A, Table A1-1
UW2038/101.15	NL16-05	65B2	thin section	Kuruman Kop, South Africa	Sparry crystalline carbonate (fenestrate microbialites)	Appedix A, Table A1-1
UW2038/102.1	NL16-06	NL16-06	hand sample	Kuruman Kop, South Africa	Aragonite pseudomorphs in massive microcrystalline beds	Appedix A, Table A1-1
UW2038/102.2	NL16-06	NL16-06	hand sample	Kuruman Kop, South Africa	Aragonite pseudomorphs in massive microcrystalline beds	Appedix A, Table A1-1
UW2038/103.1	NL16-07A	NL16-07A	hand sample	Kuruman Kop, South Africa	Aragonite pseudomorphs in massive microcrystalline beds	Appedix A, Table A1-1
UW2038/103.2	NL16-07A	NL16-07A	hand sample	Kuruman Kop, South Africa	Aragonite pseudomorphs in massive microcrystalline beds	Appedix A, Table A1-1
UW2038/104.1	NL16-07B	NL16-07B	hand sample	Kuruman Kop, South Africa	Aragonite pseudomorphs in massive microcrystalline beds	Appedix A, Table A1-1
UW2038/104.2	NL16-07B	6-7B1	billet	Kuruman Kop, South Africa	Aragonite pseudomorphs in massive microcrystalline beds	Appedix A, Table A1-1
UW2038/104.3	NL16-07B	67B2	billet	Kuruman Kop, South Africa	Aragonite pseudomorphs in massive microcrystalline beds	Appedix A, Table A1-1
UW2038/104.4	NL16-07B	67B3	billet	Kuruman Kop, South Africa	Aragonite pseudomorphs in massive microcrystalline beds	Appedix A, Table A1-1
UW2038/104.5	NL16-07B	67B4	billet	Kuruman Kop, South Africa	Aragonite pseudomorphs in massive microcrystalline beds	Appedix A, Table A1-1
UW2038/104.6	NL16-07B	67B5	billet	Kuruman Kop, South Africa	Aragonite pseudomorphs in massive microcrystalline beds	Appedix A, Table A1-1
UW2038/104.7	NL16-07B	67B1	thin section	Kuruman Kop, South Africa	Aragonite pseudomorphs in massive microcrystalline beds	Appedix A, Table A1-1
UW2038/104.8	NL16-07B	67B2	thin section	Kuruman Kop, South Africa	Aragonite pseudomorphs in massive microcrystalline beds	Appedix A, Table A1-1
UW2038/104.9	NL16-07B	67B3	thin section	Kuruman Kop, South Africa	Aragonite pseudomorphs in massive microcrystalline beds	Appedix A, Table A1-1
UW2038/104.10	NL16-07B	67B4	thin section	Kuruman Kop, South Africa	Aragonite pseudomorphs in massive microcrystalline beds	Appedix A, Table A1-1
UW2038/104.11	NL16-07B	67B5	thin section	Kuruman Kop, South Africa	Aragonite pseudomorphs in massive microcrystalline beds	Appedix A, Table A1-1
UW2038/105.1	NL16-08	NL16-08	hand sample	Kuruman Kop, South Africa	Columnar stromatolites with dolomite infill	Appedix A, Table A1-1
UW2038/105.2	NL16-08	6-8A	billet	Kuruman Kop, South Africa	Columnar stromatolites with dolomite infill	Appedix A, Table A1-1
UW2038/105.3	NL16-08	6-8B	billet	Kuruman Kop, South Africa	Columnar stromatolites with dolomite infill	Appedix A, Table A1-1
UW2038/105.4	NL16-08	6-8C	billet	Kuruman Kop, South Africa	Columnar stromatolites with dolomite infill	Appedix A, Table A1-1
UW2038/105.5	NL16-08	6-8D	billet	Kuruman Kop, South Africa	Columnar stromatolites with dolomite infill	Appedix A, Table A1-1
UW2038/105.6	NL16-08	6-8E	billet	Kuruman Kop, South Africa	Columnar stromatolites with dolomite infill	Appedix A, Table A1-1
UW2038/105.7	NL16-08	6*8A	thin section	Kuruman Kop, South Africa	Columnar stromatolites with dolomite infill	Appedix A, Table A1-1
UW2038/105.8	NL16-08	6*8B	thin section	Kuruman Kop, South Africa	Columnar stromatolites with dolomite infill	Appedix A, Table A1-1
UW2038/105.9	NL16-08	6*8C	thin section	Kuruman Kop, South Africa	Columnar stromatolites with dolomite infill	Appedix A, Table A1-1
UW2038/105.10	NL16-08	6*8D	thin section	Kuruman Kop, South Africa	Columnar stromatolites with dolomite infill	Appedix A, Table A1-1
UW2038/105.11	NL16-08	6*8E	thin section	Kuruman Kop, South Africa	Columnar stromatolites with dolomite infill	Appedix A, Table A1-1
UW2038/106.1	RE1	RE1	hand sample	Retreat Farm near Kuruman, South Africa	Black chert	Appedix A, Table A1-1 and A1-5
UW2038/106.2	RE1	RE1	hand sample	Retreat Farm near Kuruman, South Africa	Black chert	Appedix A, Table A1-1 and A1-5
UW2038/106.3	RE1	RE1	hand sample	Retreat Farm near Kuruman, South Africa	Black chert	Appedix A, Table A1-1 and A1-5
UW2038/106.4	RE1	RE1	hand sample	Retreat Farm near Kuruman, South Africa	Black chert	Appedix A, Table A1-1 and A1-5
UW2038/107.1	RE2	RE2	hand sample	Retreat Farm near Kuruman, South Africa	Black chert	Appedix A, Table A1-1 and A1-5
UW2038/107.2	RE2	RE2	hand sample	Retreat Farm near Kuruman, South Africa	Black chert	Appedix A, Table A1-1 and A1-5
UW2038/107.3	RE2	RE2	hand sample	Retreat Farm near Kuruman, South Africa	Black chert	Appedix A, Table A1-1 and A1-5
UW2038/108.1	RE3	RE3	hand sample	Retreat Farm near Kuruman, South Africa	Dolomite (partly weathered)	Appedix A, Table A1-1 and A1-5
UW2038/108.2	RE3	RE3	hand sample	Retreat Farm near Kuruman, South Africa	Dolomite (partly weathered)	Appedix A, Table A1-1 and A1-5
UWGM885.40	WB98-815A, WB98-815B	WB98-815A, WB98-815B	rock core	WB-98 rock core near Kuruman, South Africa	Lamination 1 and 3, siderite	Appedix A, Table A1-1 through A1-3, Fig. A2
UWGM885.45	WB98-886A, WB98-886B	WB98-886A, WB98-886B	rock core	WB-98 rock core near Kuruman, South Africa	Lamination 6 and 14, siderite	Appedix A, Table A1-1 through A1-3, Fig. A2
UW2038/109.1	WB98-966.5	WB98-966.5	rock core	WB-98 rock core near Kuruman, South Africa	Carbonaceous carbonate with contorted microbial laminae and pyrite	Appedix A, Table A1-1 through A1-3, Fig. A2
UW2038/109.2	WB98-966.5CS1	WB98-966.5spar1	crushed sample powder	WB-98 rock core near Kuruman, South Africa	sparry calcite	Appedix A, Table A1-1 through A1-3, Fig. A2
UW2038/109.3	WB98-966.5CS2	WB98-966.5spar2	crushed sample powder	WB-98 rock core near Kuruman, South Africa	sparry calcite	Appedix A, Table A1-1 through A1-3, Fig. A2
UWGM885.63	WB98-981CS1, WB98-981L1	WB98-981S1, WB98-981L1	rock core	WB-98 rock core near Kuruman, South Africa	sparry calcite, calcite micrite	Appedix A, Table A1-1 through A1-3, Fig. A2